Implementation, Verification, Validation, and Application of Two Constitutive Models for Earthquake Engineering Applications

Long Chen

A dissertation
submitted in partial fulfillment of the
requirements for the degree of

Doctor of Philosophy

University of Washington

2020

Reading Committee:

Pedro Arduino, Chair

Steven Kramer

Brett Maurer

Program Authorized to Offer Degree:
Civil and Environmental Engineering

University of Washington

Abstract

Implementation, Verification, Validation, and Application of Two Constitutive Models for Earthquake Engineering Applications

Long Chen

Chair of the Supervisory Committee:
Professor Pedro Arduino
Civil and Environmental Department

Human and economic losses caused by earthquake-induced soil liquefaction underscore the importance of assessing liquefaction hazards, both by determining whether a soil is likely to liquefy and by estimating consequences that these events may cause. Numerical simulations have proven to be useful for these purposes. Reliable numerical analysis requires constitutive models to represent the in-situ soil behavior as well as general loading and drainage conditions. In this context, the main objective of this research is to implement, verify, and validate two newly developed constitutive models, PM4Sand and PM4Silt (Boulanger and Ziotopoulou, 2017, 2018), in the finite element platform OpenSees (OpenSees, 2007). These models are developed for earthquake engineering applications and can achieve reasonable approximations of desired behavior including pore pressure generation and dissipation, limiting strains, and cyclic mobility with straightforward calibration process. The verification study compares the response of the same model implemented in three different frameworks, OpenSees, FLAC, and PLAXIS, using stress point, element model, and 1D analyses. The validation study demonstrates the models' capability in capturing realistic soil behavior under different scenarios including case-histories and a large-scale shake table test. For further validation of PM4Sand, the second part of this dissertation concentrates on the contribution of the UW numerical simulation team to three recent LEAP workshops that have focused

on validating constitutive models using high quality laboratory and centrifuge experiments. The simulated models include a constant slope subject to lateral spreading and a sheet pile retaining structure supporting liquefiable soils. Lastly, this dissertation addresses two case studies using PM4Sand and PM4Silt to shed light on their application for analyzing lateral spreading induced by liquefaction. The first case focuses on a typical highway bridge embankment and investigates the efficiency of different intensity measures for estimating lateral displacement. The second case focuses on a real case study that showed zero-displacement lateral spreading during a recent earthquake event due, possibly, to interbedded sand, silt, and clay deposits.

TABLE OF CONTENTS

LIST OF FIGURES

LIST OF TABLES

ACKNOWLEDGMENTS

The completion of this dissertation would not have been possible without the assistance, support and guidance of Dr. Pedro Arduino who patiently advised me during all the years behind this work. His high standards drove me towards higher quality both professionally and in life. I would like to give my gratitude to Dr. Steven L. Kramer, Dr. Brett W. Maurer, and Dr. Kathy Troost for reading this dissertation. I absolutely enjoyed their consult and valuable comments and suggestions. I also want to thank Dr. Peter Mackenzie-Helnwein, Dr. Joseph Wartman and Dr. Michael Gomez for their help during my study. I am fortunate to be a part of the University of Washington community.

My friends and colleagues were a big part of this effort. My thanks go to Alborz Ghofrani, Minyong Lee, Andrew Makdisi, Krishnendu Shekhar, Gregor Vilhar and many other who were always there for me. My special thanks to Yiming Liu, who would always be the lab master in my memory. I appreciate the funding support from the Pacific Earthquake Engineering Research Center for part of this work. I also acknowledge the Hyak center at the University of Washington and the Texas Advanced Computing Center (TACC) at University of Texas at Austin for providing the HPC resources that have contributed to the research results reported within this work.

And you shall know the truth, and the truth shall set you free. - John 8:32

DEDICATION

This work could not have been possible without my parents and my wife, Lisi.

Chapter 1

INTRODUCTION

Through history earthquakes have caused tremendous losses of property and life. Hence, reduction of earthquake hazards have been a common theme in earth sciences, social sciences, and engineering communities. Earthquake engineering, in particular, has played and important role dealing with the effects of earthquakes on people and their environment and with methods for reducing these effects (Kramer, 1996). Geotechnical earthquake engineering, as a subset of the latter, focuses on the engineering behavior of earth materials, especially soils, subject to earthquake shaking. Soils are complex multi-phase composites comprised of air, water and solid particles. The fact that soils are three-phased is important, since the interaction between these phases can cause complex behavior during earthquakes that may lead to instabilities. Soil liquefaction is one of these complex conditions that happens when the soil is fully or partially saturated and the increase in pore water pressure, caused by shaking, reduces the inter-particle contact stress (effective stress) within solid particles leading to substantial reduction in strength and stiffness. Ultimately, under these circumstances soils behave similarly to viscous fluids. Liquefaction has been observed in many earthquakes including the 1964 Niigata earthquake, 1964 Alaska earthquake, 1989 Loma Prieta earthquake, 1995 Great Hanshin earthquake, 2010-11 Canterbury earthquake sequence, and recent 2018 Sulawesi earthquake. Human and economic losses caused by earthquake-induced soil liquefaction underscore the importance of assessing liquefaction hazards, both by determining whether a soil is likely to liquefy and by estimating consequences that these events may cause.

Semi-empirical liquefaction triggering models have been developed based on frameworks of analysis that rely on case histories (Seed and Idriss (1971), Robertson and Wride (1998),

Andrus and Stokoe (2000), Cetin et al. (2004), Moss et al. (2006), Idriss and Boulanger (2008), Boulanger and Idriss (2014)). In general, these models are based on either SPT (Standard Penetration Test), CPT (Cone Penetration Test) or V_s (shear wave velocity) field data and include deterministic and probabilistic procedures.

In parallel to these efforts, methods to evaluate the consequences of liquefaction have also been proposed and methods exists to estimate ground failure and permanent deformation, including volumetric compression, lateral spreading and flow failures, caused by liquefaction. In this context numerical modeling has gained popularity and become an important tool to extend our understanding on the consequences of liquefaction. Fully nonlinear modeling and advances in high performance computing (HPC) provide today the opportunity to tackle liquefaction problems at a much greater scale and complexity and at a faster computing speed.

Constitutive models play a vital role in these analyses. Accurate and reliable numerical analyses require advanced constitutive models representing the soil response to different granular configurations, drainage conditions, and loading conditions. Constitutive models must capture the behavior observed in laboratory tests, as well as, the response expected in 1D, 2D, and 3D geologic scenarios as observed in the field during earthquakes or reproduced by centrifuge tests. In this regard, the response of soils to both monotonic and dynamic loading, including cyclic mobility and modulus reduction (Darendeli, 2001; Menq, 2003), are important to consider. Furthermore, constitutive models *perse* only define stress-strain relationships and need to be implemented within boundary value solution frameworks usually including domain discretization. This means models need to be implemented into numerical platforms in order to be used to solve real problems. These platforms can be based on different numerical techniques, such as the finite-element (FEM), finite-difference (FEM), finite-volume (FVM), and material point method (MPM). In geotechnical practice, FLAC (Itasca, 2016), PLAXIS (Plaxis.B.V, 2018), and OpenSees (OpenSees, 2007), are among the most popular codes currently available for these analyses.

Over the years many constitutive models have been proposed and comprehensive consti-

tutive formulations have been established for geotechnical materials, laying the foundation for simulating complex soil behavior. However, as formulations have become more refined they have also become more elaborated, adding complexity to their implementation. Therefore, before a newly proposed or implemented model can be used in research and practice, verification and validation processes are necessary. ***Verification*** is meant to identify and remove programming errors in computer codes and verify numerical algorithms. ***Validation*** is meant to assess the accuracy at which a numerical model represents reality and includes the essential features of a real model.

Verification of a newly implemented constitutive model must be carried with care such that system complexity is gradually increased and results are carefully examined to identify inconsistencies. These inconsistencies can be introduced from aspects other than the model formulation. For example: (i) the choice of numerical integration scheme can introduce different orders of accuracy, (ii) tolerance parameters for internal operations, which are chosen by individual developers/operators to balance performance and convergence within each framework, can increase (or reduce) accuracy, performance and efficiency, and (iii) extra algorithmic evaluations and conditions, often introduced to improve stability, result in varying results and affect the performance of a constitutive model at various levels. Hence, the response obtained from a model is a combination of the formulation used, numerical solution strategy selected, domain discretization (in space and time) and more. Individual implementations can yield different model response, even when identical formulations are used. Therefore, it is important to identify inconsistencies between implementations and separate differences associated to model response and system response.

Following a verification phase, case histories and laboratory tests are commonly used to validate a model and ensure it reproduces the intended soil behavior. Several aspects of the model require attention at this level; particularly, the calibration of the constitutive parameters. For geotechnical earthquake engineering applications, well-documented case histories, as well as full scale shake table tests provide valuable insight on model validation. Centrifuge tests also provide valuable data that complement case histories and full scale

experiments. These tests are commonly used to generate realistic stress levels using geometry scales much smaller than the actual prototype. Properly configured and instrumented, these experiments are proven to reproduce realistic full-scale soil behavior in smaller scale models. For example, LEAP (Liquefaction Experiments and Analysis Projects) (Manzari et al., 2017) is an effort to produce a well maintained database of clean centrifuge experimental data validated using numerical models.

The research presented in this document aims to extend tools for nonlinear effective stress analysis and focuses on the verification, validation, and application of two advanced constitutive models for liquefiable soils, PM4Sand and PM4Silt, using OpenSees. PM4Sand is a sand plasticity model for earthquake engineering applications recently proposed by Boulanger and Ziotopoulou (2015, 2017). This 2D plane-strain model follows the plasticity framework proposed by Dafalias and Manzari (2004) and is based on bounding surface plasticity and critical state concepts. Since its introduction, this model has drawn wide attention in geotechnical engineering practice and research communities due to its relatively easy calibration and good agreement with field observations. The PM4Silt model recently proposed by Boulanger and Ziotopoulou (2018) follows the basic framework of PM4Sand. Similar to PM4Sand, this model is able to capture the behavior of low-plasticity silts and clays by changing a few primary input parameters.

In this work, PM4Sand and PM4Silt were implemented in OpenSees using advanced methodologies. The models were used in a series of verification and validation studies including element tests and 1D and 2D simulations. Laboratory tests, full scale experiments and centrifuge test results were used in the verification and validation exercises. This work was complemented with two application case-studies that explore the capabilities of these models and OpenSees in the simulation of the effects of lateral spreading in geotechnical engineering problems.

1.1 Thesis organization

This document is organized in 12 chapters divided in 3 parts. Part I includes a review of general and bounding surface plasticity and a brief introduction to the PM4Sand and PM4Silt models and their implementation, verification, and validation in OpenSees. Part II presents contributions from the UW simulation team to LEAP projects. Part III presents two case studies performed using the newly implemented PM4Sand and PM4Silt models to study the onset of liquefaction and consequences of lateral spreading.

1.1.1 Part I

This part consists of five chapters:

- **Chapter 2** presents a brief review on bounding surface plasticity and constitutive models for geotechnical earthquake engineering applications.

- **Chapter 3** presents an introduction to the PM4Sand model and details of its implementation in OpenSees. A parametric study was performed to shed light on the model capabilities and calibration process.

- **Chapter 4** presents simulation results that verify the implementation of PM4Sand in OpenSees. Carefully controlled loading conditions and 1D canonical cases were used to verify the model's behavior in several computational frameworks. Results from FLAC and PLAXIS were also included and compared for verification purposes.

- **Chapter 5** presents a brief introduction to the PM4Silt model and and its implementation in OpenSees. Results of a verification study using element tests and 1D cases are presented here.

- **Chapter 6** presents a validation study of PM4Sand and PM4Silt as implemented in OpenSees. Two well-known case histories, Wildlife array and Port Island array, as well as

results from a blind prediction of a large-scale liquefaction shake table test, are considered in this chapter.

1.1.2 Part II

This part consists of three chapters that correspond to three LEAP workshops:

- **Chapter 7** presents the work performed according to LEAP-UCD-2017 guidelines using two bounding surface constitutive models. Comparisons between experimental results and numerical simulations obtained using these models, i.e., Manzari-Dafalias and PM4Sand are presented and discussed.

- **Chapter 8** presents the work performed according to LEAP-Asia-2019 guidelines using PM4Sand. For this purpose, type-C predictions were obtained and compared to recorded data from centrifuge experiments. The results were compared at different scales and the similitude laws proposed by Iai et al. (2005) were examined. Finally the importance of using realistic cyclic stress ratios (CSR) in the calibration of constitutive model parameters is discussed.

- **Chapter 9** presents the work performed according to LEAP-RPI-2020 guidelines using Manzari-Dafalias and PM4Sand. A series of centrifuge experiments were used to investigate the seismic response of a sheet pile retaining structure supporting liquefiable soils (LEAP-RPI-2020 Organizing Team, 2020). Simulation results and preliminary comparisons with experiments are presented and examined.

1.1.3 Part III

This part concentrates on two case studies that utilize the two newly implemented models. It consists of two chapters:

- **Chapter 10** presents a case study to evaluate the efficiency of motion intensity measures for a typical highway bridge embankment subject to liquefaction and lateral spreading.

For this purpose the performance based earthquake engineering (PBEE) framework proposed by PEER was used. Both record-to-record and spatial variability uncertainties were evaluated.

- **Chapter 11** presents simulation results for a zero-displacement lateral spread case study, referred as Çark Canal case, using PM4Sand and PM4Silt. The interbedded deposits of sand, silt, and clay encountered at this site are thought to be the reason for the overestimation of lateral spreading predicted using conventional linear regression procedures (Youd et al., 2009). This study proposed a simple workflow for model selection and calibration aiming to represent the gradual transition of soil properties within the interbedded layers and to shed light on the application of PM4Sand and PM4Silt for this particular type of problems. The effect of spatial variability within the interbedded layer based on the variation of fines content (FC) and plasticity index (PI) was examined. Sensitivity to input motion, motion polarity, shear strength, correlation length, and hydraulic conductivity were also investigated.

- **Chapter 12** presents a summary of research outcomes and recommendations for future research.

Chapter 2

BRIEF PLASTICITY REVIEW

2.1 Introduction

The stress-strain behavior of soils is nonlinear, inelastic, anisotropic, and nonhomogeneous with stress-dependent, and time-dependent characteristics. Description of such behavior in a realistic manner requires sophisticated constitutive models. Under short term loading, e.g., earthquakes, soil behavior is idealized as time-independent. This time-independent representation may be formulated as a combination of elastic and plastic behavior within classical plasticity. Classical plasticity, however, offers limited capabilities for describing the cyclic response of soils; something especially important in earthquake geotechnical engineering. Under cyclic loading, in addition to nonlinear response and failure, soils (particularly saturated granular soils) exhibit oscillating contractive and dilative response, accumulation or pore water pressure leading to liquefaction and cyclic mobility (Elgamal et al., 2003). In order to overcome such shortcomings, two major theories have been proposed: multi-surface plasticity and bounding surface plasticity. Both theories address the problem of cyclic loads using advanced nonlinear kinematic hardening formulations.

The multi-yield concept was originally proposes by Mroz and extended to soils by Prevost and coworkers. A series of pressure-dependent-multiyield models were developed by Elgamal et al. (2003) that capture the characteristics of cyclic mobility. These models were later implemented in the OpenSees platform by Yang et al. (2003), Yang et al. (2008) and Khosravifar et al. (2018). Bounding surface plasticity was originally proposed by Dafalias and Popov (1977) and coworkers and received much attention due to its simplicity and efficiency in modeling cyclic behavior. A total stress-based bounding surface plasticity model for clays was developed by Borja and Amies (1994) to accommodate multiaxial stress reversals. This

model has been implemented in OpenSees by Wang and Sitar (2006) and the research group at the University of Washington, independently. In 1997, Manzari and Dafalias (1997) presented a model within the framework of critical state soil mechanics and bounding surface plasticity to capture the cyclic response of cohesionless soils (sands). This model laid the basis for several other advanced constitutive models for sands that have proven to be effective in capturing many of the well-known behavior seen in sands under different drainage and cyclic loading conditions and different relative densities. Later, Dafalias and Manzari (2004) improved the model by including a fabric tensor for better representation of volumetric strains. This version is usually referred as the *ManzariDafalias* model and has been implemented in OpenSees by Ghofrani (2018). This model was then extended to SANISAND (Taiebat and Dafalias, 2008), a family of Simple ANIsotropic SAND constitutive models. In parallel to the Manzari-Dafalias developments, Cubrinovski and Ishihara (1998) proposed the Stress Density model. This is another useful stress-strain-dilatancy model for sands based on the idea of integral modeling over the relevant density and normal stress states. The model was established within the framework of the state concept and uses the relative initial e-p state to assess the combined influence of density and normal stress on sand behavior within the bounding surface context.

Due to its importance to this thesis, this chapter presents the general formulation of plasticity and bounding surface plasticity.

2.2 A brief review of bounding surface plasticity

General formulation of plasticity

As summarized in Dafalias (1986), the basic kinematic assumption in small-strain, rate-independent elastoplasticity is that the total strain rate can be decomposed into elastic and plastic parts as,

$$\boldsymbol{\varepsilon} = \boldsymbol{\varepsilon}^e + \boldsymbol{\varepsilon}^p \,. \tag{2.1}$$

The stress tensor, $\boldsymbol{\sigma}$, is related to the strain tensor through a constitutive relationship. The stress response is usually associated to the stored energy, ψ, such that,

$$\boldsymbol{\sigma} = \frac{\partial \psi(\boldsymbol{\varepsilon})}{\partial \boldsymbol{\varepsilon}} \,. \tag{2.2}$$

Within this framework, the stress tensor can be related to the elastic strains as $\boldsymbol{\sigma} = \mathbb{C} : \boldsymbol{\varepsilon}^e$, where $\mathbb{C} = \frac{\delta^2 \psi}{\delta \epsilon^e \otimes \delta \epsilon^e}$ is a 4^{th} order elastic tangent tensor. Since there is no one-to-one correspondence between stresses and strains in the plastic domain, it is not possible to derive a stress-strain relationship only in terms of the current state stress. Thus, in plasticity, only an incremental relationship between stress and strain increments may be written. Hence it is convenient to write this relationship in rate form as,

$$\dot{\boldsymbol{\sigma}} = \mathbb{C} : \dot{\boldsymbol{\varepsilon}}^e = \mathbb{C} : (\dot{\boldsymbol{\varepsilon}} - \dot{\boldsymbol{\varepsilon}}^p) \,. \tag{2.3}$$

Yield surface

A *yield condition*, *yield function* or *yield surface* is defined to separate elastic from hyper-elastic behavior. These functions usually depict surfaces in a multi-dimensional stress space. The exterior of the yield surface is inadmissible for the material and the material's behavior on the boundary is irreversible; meaning plastic response happens when the stress state is located on the boundary of the yield surface. The yield condition is commonly defined in terms of stress and corresponding internal variables as,

$$f(\boldsymbol{\sigma}, \mathbf{o}) = 0 \,, \tag{2.4}$$

where $\mathbf{o}$ is a vector of material internal variables. There are two possible states for this function:

- When $f < 0$, the material is inside the elastic domain and there is no plastic deformation, i.e. $\dot{\boldsymbol{\varepsilon}}^p = 0$.

- When $f = 0$, the material is on the surface and the is plastic deformation. The rate of plastic strain, $\dot{\boldsymbol{\varepsilon}}^p$, is defined by a non-negative parameter γ usually referred as the *consistency parameter* or *loading index* and a direction.

The criterion for loading or unloading can be expressed in terms of Kuhn-Tucker conditions as,

$$f \leq 0 \qquad \gamma \geq 0 \qquad f\gamma = 0 \tag{2.5}$$

This means that as the stress point tries to move outward of the current yield surface further plastic deformations occur. This case is referred as plastic loading. In the case of neutral loading or unloading, the stress point tries to move on or inward from the current yield surface and no further plastic deformation occurs. When combined with the yield condition (2.4), the Kuhn-Tucker conditions can determine the state of the material in terms of elastic or plastic response.

Flow and hardening rules

Flow and hardening rules define the evolution of the plastic strain rate and other internal variables and determine the evolution of the yield surface. The flow rule defines the evolution of the plastic strain rate, $\dot{\boldsymbol{\varepsilon}}^p$, whereas hardening rule defines the evolution of internal variable, $\dot{\mathbf{o}}$. Evolution of the plastic strain is defined by

$$\dot{\boldsymbol{\varepsilon}}^p = \gamma \mathbf{r}(\boldsymbol{\sigma}, \mathbf{o}) \,, \tag{2.6}$$

where $\mathbf{r}(\boldsymbol{\sigma}, \mathbf{o})$ is the direction of the plastic flow and is defined in terms of the gradient to a potential function defined in stress space, $g(\boldsymbol{\sigma}, \mathbf{o}) = 0$, usually referred as the *plastic potential* (i.e., $\mathbf{r} = \frac{\partial g}{\partial \boldsymbol{\sigma}}$). If the plastic potential is assumed to be the same as the yield function (associated with a particular yield criterion), the flow rule is called *associative*. Otherwise it is called *non-associative*. Similarly, the evolution of the internal variables $\dot{\mathbf{o}}$ can be expressed as,

$$\dot{\mathbf{o}} = \gamma \mathbf{h}(\boldsymbol{\sigma}, \mathbf{o}) \,, \tag{2.7}$$

where the function $\mathbf{h}$ defines the direction of the rate of change of the internal variables.

Consistency condition

During plastic deformation, a stress sate must persist on the yield surface. This can be mathematically expressed using the consistency (or persistency) condition,

$$\dot{f} = 0\,, \tag{2.8}$$

which yields an alternative form of the Kuhn Tucker conditions for any plastic state, i.e., for $f = 0$

$$\dot{f} \leq 0 \qquad\qquad \gamma \geq 0 \qquad\qquad \dot{f}\gamma = 0 \tag{2.9}$$

The flow and hardening rules can be related through the consistency condition such that,

$$\dot{f} = \frac{\partial f}{\partial \boldsymbol{\sigma}} : \dot{\boldsymbol{\sigma}} + \frac{\partial f}{\partial \mathbf{o}} : \dot{\mathbf{o}}\,. \tag{2.10}$$

Combining with Equations 2.6 and 2.7, the consistency parameter can be found as,

$$\gamma = \frac{\partial f/\partial \boldsymbol{\sigma} : \mathbb{C} : \dot{\boldsymbol{\varepsilon}}}{\partial f/\partial \boldsymbol{\sigma} : \mathbb{C} : \mathbf{r} - \partial f/\partial \mathbf{o} : \mathbf{h}}\,. \tag{2.11}$$

This equation is often written as,

$$\gamma = \frac{\partial f/\partial \boldsymbol{\sigma} : \mathbb{C} : \dot{\boldsymbol{\epsilon}}}{\partial f/\partial \boldsymbol{\sigma} : \mathbb{C} : \mathbf{r} + K_p}\,, \tag{2.12}$$

where K_p is the plastic modulus and is defined as,

$$K_p = \frac{1}{\gamma}\frac{\partial f}{\partial \boldsymbol{\sigma}} : \dot{\boldsymbol{\sigma}}\,. \tag{2.13}$$

Using Equation 2.10, K_p can be written in terms of the internal variables as,

$$K_p = -\frac{1}{\gamma}\frac{\partial f}{\partial \mathbf{o}} : \dot{\mathbf{o}}\,. \tag{2.14}$$

2.2.1 Bounding surface plasticity

The bounding surface concept (Dafalias, 1980, 1986) was motivated by the observation that any stress-strain curve for monotonic loading, or for monotonic loading followed by reverse

loading, eventually converges to certain "bounds" in the stress-strain space. Therefore, using the concept of a "bounding surface" limiting the response in stress space, flow and hardening rules can be defined by the distance between the current stress state and a properly defined *image stress state* on the so-called *"bounding surface"*. A unique image stress $\bar{\boldsymbol{\sigma}}$ on the bounding surface, $F = 0$ is defined for any $\boldsymbol{\sigma}$ satisfying $f = 0$ by a proper, noninvertible continuous mapping rule. For any $\dot{\boldsymbol{\sigma}}$ such that the loading index $\gamma \geq 0$, a corresponding $\dot{\bar{\boldsymbol{\sigma}}}$ occurs at the image stress point due to the change of $\boldsymbol{\sigma}$ and the hardening of $f = 0$.

Central to the bounding surface formulation is the definition of the hardening function. Hardening rules must be clearly defined, including the criteria for loading and unloading. For example, the evolution of plastic deviatoric strain can be defined as,

$$\dot{\varepsilon}_q^p = \frac{\dot{\eta}}{K_p}\,, \tag{2.15}$$

where $\dot{\eta}$ is the increment in stress ratio (with $\eta = q/p$, q =deviatoric stress and p = mean stress). Following the idea described in Dafalias and Popov (1977), this K_p should be infinite at the most recent transition from unloading, while equal to 0 on all of the bounding surface. Borja and Amies (1994) presented a framework for deriving expressions for K_p. Similar to Dafalias, in their work Borja & Amies define the image point $\hat{\boldsymbol{\sigma}}$ on the bounding surface such that

$$\hat{\boldsymbol{\sigma}} = \boldsymbol{\sigma} + \kappa(\boldsymbol{\sigma} - \bar{\boldsymbol{\sigma}})\,, \tag{2.16}$$

where κ is a dimensionless scalar quantity. The plastic hardening modulus K_p can then be made to vary with κ such that $K_p \to \infty$ as $\kappa \to \infty$, and $K_p \to 0$ as $\kappa \to 0$. Some specific forms for K_p are given below.

Exponential function

An interpolation for the hardening modulus of the form

$$K_p = h\kappa^m \tag{2.17}$$

is identical to the exponential function presented by Dafalias and Popov (1977), with $m = 1$. h is a modulus parameter which controls the rate of shear stiffness degradation, while m is a dimensionless quantity which controls the shape of the secant modulus versus the strain amplitude curve. In Dafalias and Manzari (2004),

$$\kappa = M^b - \eta\,, \tag{2.18}$$

where η is the current stress ratio, and M^b is the bounding or "image" stress ratio on the bounding surface. h is a positive scalar defined as,

$$h = \frac{b_0}{|\eta - \eta_{in}|}\,; \quad b_0 = G_0 h_0 (1 - c_h e)\big(\frac{p}{p_{atm}}\big)^{-1/2} \tag{2.19}$$

with scalar parameters h_0 and c_h. η_{in} is the value of η at the initiation of a loading process.

Hyperbolic function

Another form of the hardening function can be expressed as

$$K_p = 3G\frac{\kappa^2}{1 + 2\kappa}\,, \tag{2.20}$$

that is consistent with the hyperbolic stress-strain function for triaxial samples deforming under undrained conditions. Unlike the exponential function discussed above, this interpolation function does not require any additional parameter.

Davidenkov model

Other models with similar features may also be cast in the above form. For example, Borja and Amies (1994) presented a hardening modulus of the form

$$K_p = 3G\Big[\frac{1+\theta}{1+\theta+A}\Big(1 + \frac{1}{\theta}\Big)^A - 1\Big]\,, \tag{2.21}$$

where $\theta = \theta(\kappa) =$ nonextraneous root of

$$\kappa = \frac{A}{\theta}\Big[1 - \Big(\frac{\theta}{1+\theta}\Big)^A\Big]^{-1} - 1 \tag{2.22}$$

can be obtained from the backbone curve of the Davidenkov model of Martin and Seed (1982). Typical values of A are 0.9 for sands and 0.2 for clays (Martin and Seed, 1982). If $A = 1.0$, then $\theta = 1/\kappa$, and Equ. 2.22 degenerates to the hardening function for the hyperbolic case (Equ. 2.20); otherwise, A represents a curve-fitting parameter used to replicate more accurately the actual soil response.

Several bounding surface formulations have been proposed over the years. In this work we concentrate on two recent formulations proposed by Boulanger and Ziotopoulou (2017, 2018) which are based on the early work by Dafalias and Manzari (2004).

Part I

IMPLEMENTATION OF PM4SAND AND PM4SILT IN OPENSEES

The first part of this dissertation addresses the topic of model implementation in OpenSees. Two advanced bounding surface plasticity models are introduced and implementation details are given. Methods for integrating the resulting constitutive equations are discussed and verification and validation of these constitutive models follows afterward.

Reports and archival journal papers published by the author and coworkers as a result of this part of the research include:

- Chen, L. and Arduino, P. (2020b). "Implementation, verification, and validation of PM4Sand model in OpenSees". PEER Report - Submitted, under review

– *Miscellaneous Projects*

- Régnier, J., Bonilla, L. F., Bard, P. Y., Bertrand, E., Hollender, F., Kawase, H., Sicilia, D., Arduino, P., Amorosi, A., Asimaki, D., Boldini, D., Chen, L., Chiaradonna, A., Demartin, F., Ebrille, M., Elgamal, A., Falcone, G., Foerster, E., Foti, S., Garini, E., Gazetas, G., Gélis, C., Ghofrani, A., Giannakou, A., Gingery, J. R., Glinsky, N., Harmon, J., Hashash, Y., Iai, S., Jeremić, B., Kramer, S., Kontoe, S., Kristek, J., Lanzo, G., Di Lernia, A., Lopez-Caballero, F., Marot, M., McAllister, G., Mercerat, E. D., Moczo, P., Montoya-Noguera, S., Musgrove, M., Nieto-Ferro, A., Pagliaroli, A., Pisanò, F., Richterova, A., Sajana, S., Santisi D'avila, M. P., Shi, J., Silvestri, F., Taiebat, M., Tropeano, G., Verrucci, L., and Watanabe, K. (2016). "International benchmark on numerical simulations for 1d, nonlinear site response (prenolin): Verification phase

based on canonical cases." *Bulletin of the Seismological Society of America*, 106(5), 2112–2135

- Régnier, J., Bonilla, L. F., Bard, P. Y., Bertrand, E., Hollender, F., Kawase, H., Sicilia, D., Arduino, P., Amorosi, A., Asimaki, D., Boldini, D., Chen, L., Chiaradonna, A., Demartin, F., Elgamal, A., Falcone, G., Foerster, E., Foti, S., Garini, E., Gazetas, G., Gélis, C., Ghofrani, A., Giannakou, A., Gingery, J., Glinsky, N., Harmon, J., Hashash, Y., Iai, S., Kramer, S., Kontoe, S., Kristek, J., Lanzo, G., Lernia, A. D., Lopez-Caballero, F., Marot, M., McAllister, G., Mercerat, E. D., Moczo, P., Montoya-Noguera, S., Musgrove, M., Nieto-Ferro, A., Pagliaroli, A., Passeri, F., Richterova, A., Sajana, S., Santisi D'Avila, M. P., Shi, J., Silvestri, F., Taiebat, M., Tropeano, G., Vandeputte, D., and Verrucci, L. (2018). "Prenolin: International benchmark on 1d nonlinear: Site-response analysis-validation phase exercise." *Bulletin of the Seismological Society of America*, 108(2), 876–900

Chapter 3

IMPLEMENTATION OF PM4SAND IN OPENSEES

3.1 Introduction

This chapter presents a brief introduction to PM4Sand (Boulanger and Ziotopoulou, 2017) and its implementation in OpenSees. This 2D constitutive model follows the basic framework of the Dafalias and Manzari (2004) model (referred as MD model hereafter) based on bounding surface plasticity and critical state concepts. PM4Sand was developed specifically for plane-strain conditions and was simplified by using only in-plane stresses. It has the advantage of simplifying the MD formulation and improving computational speed by reducing the number of operations (Boulanger and Ziotopoulou, 2017). Implementation details of the model's current version 3.1 are presented here and readers are referred to the PM4Sand manual by Boulanger and Ziotopoulou (2017) for detailed information on the model.

3.2 Introduction to PM4Sand

3.2.1 Elastic response and yield surface

The model is based on effective stresses. Hence the conventional prime symbol is dropped from the stress terms for convenience. The matrix representation of the stress tensor, $\boldsymbol{\sigma}$, is simplified in plane-strain to,

$$[\boldsymbol{\sigma}] = \begin{bmatrix} \sigma_{xx} & \sigma_{xy} \\ \sigma_{xy} & \sigma_{yy} \end{bmatrix}, \tag{3.1}$$

where the brackets indicate the matrix representation of the tensor and a bold symbol represents a second order tensor.

The mean confining pressure, p, is defined as,

$$p = \frac{\sigma_{xx} + \sigma_{yy}}{2} \,. \tag{3.2}$$

and the deviatoric stress tensor $\mathbf{s}$ is defined as,

$$\mathbf{s} = \boldsymbol{\sigma} - p\mathbf{I} \,, \tag{3.3}$$

where $\mathbf{I}$ is the second order unit tensor. In matrix form results in

$$[\mathbf{s}] = [\boldsymbol{\sigma}] - p[\mathbf{I}] = \begin{bmatrix} s_{xx} & s_{xy} \\ s_{xy} & s_{yy} \end{bmatrix} = \begin{bmatrix} \sigma_{xx} - p & \sigma xy \\ \sigma xy & \sigma_{yy} - p \end{bmatrix} , \tag{3.4}$$

The volumetric strain in plane-strain is,

$$\epsilon_v = \epsilon_{xx} + \epsilon_{yy} \,, \tag{3.5}$$

and the deviatoric strain tensor, $\mathbf{e}$, is defined as,

$$\mathbf{e} = \boldsymbol{\epsilon} - \frac{\epsilon_v}{3}\mathbf{I} \,, \tag{3.6}$$

with matrix representation of the form

$$[\mathbf{e}] = [\boldsymbol{\epsilon}] - \frac{\epsilon_v}{3}[\mathbf{I}] = \begin{bmatrix} \epsilon_{xx} - \frac{\epsilon_v}{3} & \epsilon_{xy} \\ \epsilon_{xy} & \epsilon_{xx} - \frac{\epsilon_v}{3} \end{bmatrix} . \tag{3.7}$$

The elastic deviatoric strain increment is,

$$\dot{\mathbf{e}}^{el} = \frac{d\mathbf{s}}{2G} \,, \tag{3.8}$$

where the shear modulus G is calculated using the mean stress p and current stress ratio as,

$$G = G_o p_A (\frac{p}{p_A})^{1/2} C_{SR} \,, \tag{3.9}$$

where G_o is a scalar parameter, p_A is atmospheric pressure for normalization, ν is Poisson ratio, and C_{SR} is a factor which accounts for the stress ratio effect. C_{SR} is defined as,

$$C_{SR} = 1 - C_{SR,o} \cdot (\frac{\eta}{M^b})^{m_{SR}} \,, \tag{3.10}$$

where $C_{SR,o}, m_{SR}$ are constants, $\eta = q/p$ is the current stress ratio. q is the difference in the major and minor principal in-plane stresses,

$$q = \sqrt{(\sigma_{xx} - \sigma_{yy})^2 + (2\tau_{xy})^2}\,, \tag{3.11}$$

M^b is the bounding stress ratio which is described later. In the current implementation, $C_{SR,o} = 0.5$ and $m_{SR} = 4$. The bulk modulus K is computed as,

$$K = \frac{2(1+\nu)}{3(1-2\nu)}G\,. \tag{3.12}$$

The yield surface is described by a cone in principal stress space, and can be defined in stress terms as,

$$f = [(\mathbf{s} - p\boldsymbol{\alpha}) : (\mathbf{s} - p\boldsymbol{\alpha})]^{1/2} - \sqrt{1/2}pm = 0\,, \tag{3.13}$$

or in therms of stress ratio as,

$$f = [(\mathbf{r} - \boldsymbol{\alpha}) : (\mathbf{r} - \boldsymbol{\alpha})]^{1/2} - \sqrt{1/2}m = 0\,, \tag{3.14}$$

where $\mathbf{r} = \mathbf{s}/p$ is the stress ratio, $\boldsymbol{\alpha}$ is back-stress ratio tensor that defines the center of the yield surface in stress ratio space, and m defines the radius of the cone.

3.2.2 Critical state surface

The PM4Sand model incorporates the concept of critical state as defined by Schofield and Wroth (1968) and Muir Wood (1990) for soils. However, instead of critical void ratio, e_c, relative density at the critical state, $D_{R,cs}$, as presented by Bolton (1986) is used to define critical state in a $D_R - p$ space. Using this idea, Boulanger (2003) uses the relative state parameter index ξ_R defined as,

$$\xi_R = D_{R,cs} - D_R\,, \tag{3.15}$$

to relate soil behavior with the critical state. In Eq. 3.15 D_R is the current relative density and $D_{R,cs}$ is the relative density at a critical state for a current mean effective stress which is defined as,

$$D_{R_cs} = \frac{R}{Q - \ln(100\frac{p}{p_A})}\,, \tag{3.16}$$

where Q and R were shown by Bolton to be 10 and 1.0, respectively, for quartz sand. Using default values for $e_{max} = 0.8$ and $e_{min} = 0.5$, a default critical state line for the PM4Sand model can be plotted in $e - p$ space and thus be compared with critical state lines calibrated for the MD model. The MD model has been calibrated for several sands, e.g., Nevada sand, Toyoura sand, Ottawa sand, etc., using laboratory tests (Taiebat et al., 2010; Ramos, 2010; Ramirez et al., 2018a; Ghofrani, 2018). In Fig. 3.1 these critical lines are plotted together with the default critical state line for PM4Sand in $e - p$ space. As shown in the figure, the default critical state line provides a reasonable estimation of critical states for general sands when high quality lab tests data are not available for calibration. In the $q - p$ space, the

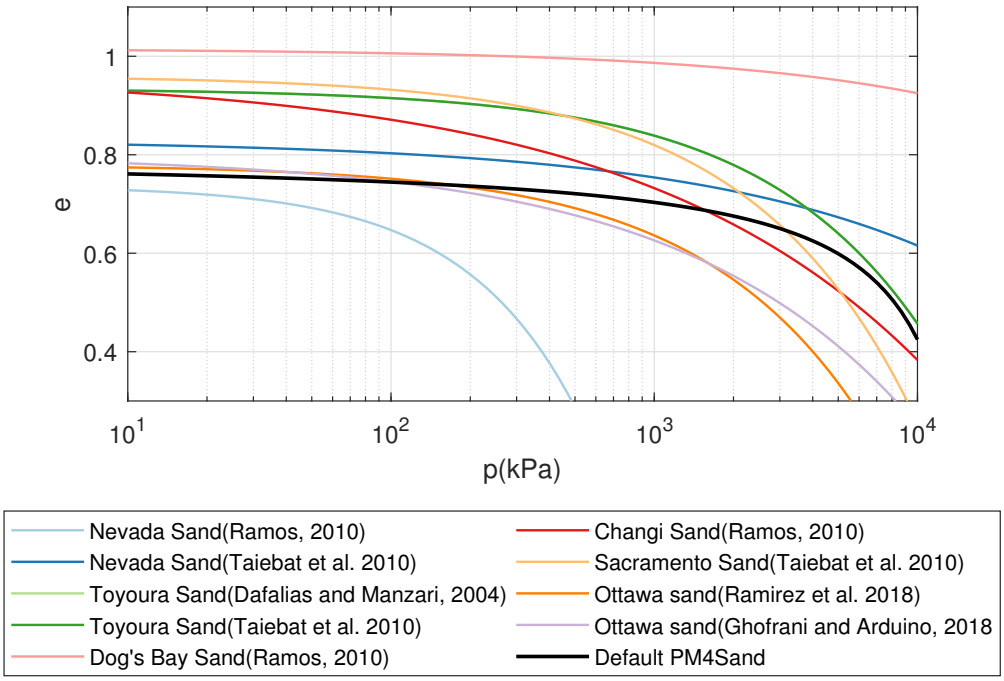

Figure 3.1: Default critical state line for PM4Sand compared to similar curves calibrated for MD.

critical stress state ratio is defined as $M = \frac{q_c}{p_c}$; where M can be related to the effective stress

friction angle at critical state ϕ_{cv} as,

$$M = 2 \cdot \sin(\phi_{cv}) \,, \tag{3.17}$$

where ϕ_{cv} is the constant volume friction angle.

3.2.3 Bounding and dilatancy surfaces

The model simplifies the bounding, dilatancy and critical state surfaces presented by Dafalias and Manzari (2004) by removing the Lode angle dependency. In PM4Sand, bounding and dilatancy ratios are related to critical stress ratio by,

$$M^b = M \cdot \exp(-n^b \xi_R) \,, \tag{3.18}$$

$$M^d = M \cdot \exp(n^d \xi_R) \,, \tag{3.19}$$

where n^b and n^d are model parameters. The default value of n^b is 0.50 and $n^b/4$ is used to compute M^b for loose of critical states. The default value of n^d is 0.10 and $4n^d$ is used to compute M^d for dense of critical states.

An image back-stress ratio tensor at the bounding surface is defined as,

$$\boldsymbol{\alpha}^b = \sqrt{1/2}[M^b - m]\mathbf{n} \,, \tag{3.20}$$

where $\mathbf{n}$ is a second order tensor representing the normal to the yield surface.

An image back-stress ratio tensor at the dilatancy surface is defined as,

$$\boldsymbol{\alpha}^d = \sqrt{1/2}[M^d - m]\mathbf{n} \,. \tag{3.21}$$

3.2.4 Flow rule

The loading index, L, is used to compute the plastic component of volumetric and deviatoric strain increments as,

$$\dot{\epsilon_v^p} = \langle L \rangle D \,, \tag{3.22}$$

$$\dot{\boldsymbol{\epsilon}^p} = \langle L \rangle \mathbf{R}' \,, \tag{3.23}$$

where D is a dilatancy parameter, $\mathbf{R}$ is the direction of plastic strain increment, $\dot{\boldsymbol{\epsilon}}^p$, $\mathbf{R}'$ is the deviatoric component of $\mathbf{R}$, and $\langle\rangle$ are MacCauley brackets. The tensor $\mathbf{R}$ for the assumption of no Lode angle dependency is,

$$\mathbf{R} = \mathbf{n} + \frac{1}{3} D\mathbf{I}\,. \tag{3.24}$$

The dilatancy parameter D relates the plastic volumetric strain increment to the magnitude of the plastic deviatoric strain increment,

$$D = \frac{\dot{\epsilon}_v^p}{|\dot{\boldsymbol{\epsilon}}^p|}\,, \tag{3.25}$$

The loading index, as derived in Dafalias and Manzari (2004) is,

$$L = \frac{1}{K_p}\frac{\partial f}{\partial \boldsymbol{\sigma}} : \dot{\boldsymbol{\sigma}} = \frac{1}{K_p}[\mathbf{n} : \dot{\mathbf{s}} - \mathbf{n} : \mathbf{r}\dot{p}]\,, \tag{3.26}$$

or

$$L = \frac{2G\mathbf{n} : \dot{\mathbf{e}} - \mathbf{n} : \mathbf{r}K\dot{\epsilon_v}}{K_p + 2G - KD\mathbf{n} : \mathbf{r}}\,, \tag{3.27}$$

and the stress increment for an imposed strain increment can be computed as,

$$\dot{\boldsymbol{\sigma}} = 2G\dot{\mathbf{e}} + K\dot{\epsilon}_v\mathbf{I} - \langle L\rangle(2G\mathbf{n} + KD\mathbf{I})\,, \tag{3.28}$$

3.2.5 Harding rule

In the original MD model, the plastic modulus is defined as,

$$K_p = \frac{2}{3}Gh_0\frac{(\boldsymbol{\alpha}^b - \boldsymbol{\alpha}) : \mathbf{n}}{(\boldsymbol{\alpha} - \boldsymbol{\alpha}_{in}) : \mathbf{n}}\,, \tag{3.29}$$

where $\boldsymbol{\alpha}_{in}$ is the initial back stress ratio at the start of a loading branch. In the current implementation of PM4Sand, $\boldsymbol{\alpha}_{in}$ is updated at each loading reversal, which is determined when,

$$(\boldsymbol{\alpha} - \boldsymbol{\alpha}_{in}) : \mathbf{n}_{trial} < 0\,, \tag{3.30}$$

where $\mathbf{n}_{trial}$ is the trial norm to the yield surface.

During loading reversals and "overshooting" problem may appear. This is a well known problem in bounding surface plasticity and recognized in Dafalias (1986).To demonstrate

the problem. Fig. 3.2 depicts an undrained DSS simulation with gradually increasing CSR for loading reversals. Suppose that after loading with a given $\boldsymbol{\alpha}_{in}$, a very small reverse loading eliminates the previous $\boldsymbol{\alpha}_{in}$ so that if loading in the original direction (or nearby directions) is resumed, the process will begin with a new $\boldsymbol{\alpha}_{in}$. As a result, the corresponding stress-strain curve will "overshoot" the continuation of the previous curve which would have occurred if no unloading/reverse loading/reloading had taken place (because at the initiation of the reloading $\boldsymbol{\alpha}_{in} = \boldsymbol{\alpha}$ and Eqs. 3.29 yields $K_p = \infty$). As the loading continues, the over estimated K_p would produce over-stiffening in the response comparing to a continuing branch without the small loading reversal. Such "overshooting," however, is not out of control because the existence of the bounds in stress-strain space restricts its extent; as shown in the black curve after around 0.5% of shear strain. Nevertheless, this is not a desirable feature and in the current version of PM4Sand an apparent initial back stress ratio $\boldsymbol{\alpha}_{in}^{app}$ and previous (apparent) initial back stress ratio $\boldsymbol{\alpha}_{in}^{p}$ are introduced to remedy the problem. The components of $\boldsymbol{\alpha}_{in}^{app}$ are taken as: (i) for positive loading directions, the minimum (positive) value they have ever had, but smaller than zero, (ii) for negative loading directions, the maximum (negative) value they have ever had, but no greater than zero. In this context, $\boldsymbol{\alpha}_{in}^{max}$, which is nonpositive, and $\boldsymbol{\alpha}_{in}^{min}$, which is nonnegative, are also tracked during loading. The $\boldsymbol{\alpha}_{in}$ from the MD model is then named $\boldsymbol{\alpha}_{in}^{true}$ in PM4Sand. A factor C_{rev} is introduced in K_p to soften the stress-strain response when $\boldsymbol{\alpha}$ doesn't exceed $\boldsymbol{\alpha}_{in}^{app}$, i.e., $(\boldsymbol{\alpha} - \boldsymbol{\alpha}_{in}^{app}) : \mathbf{n} \leq 0$.

$$\begin{aligned} C_{rev} &= \frac{(\boldsymbol{\alpha} - \boldsymbol{\alpha}_{in}^{app}) : \mathbf{n}}{(\boldsymbol{\alpha} - \boldsymbol{\alpha}_{in}^{true}) : \mathbf{n}} \quad for \quad (\boldsymbol{\alpha} - \boldsymbol{\alpha}_{in}^{p}) : \mathbf{n} \leq 0 \\ &= 1 \quad \text{otherwise.} \end{aligned} \tag{3.31}$$

The formulation for K_p is then modified to,

$$\begin{aligned} K_p &= Gh_o \frac{[(\boldsymbol{\alpha}^b - \boldsymbol{\alpha}) : \mathbf{n}]^{0.5}}{[\exp[(\boldsymbol{\alpha} - \boldsymbol{\alpha}_{in}^{app}) : \mathbf{n}] - 1] + C_{\gamma 1}} C_{rev} \\ &= Gh_o \frac{(\boldsymbol{\alpha}^b - \boldsymbol{\alpha}) : \mathbf{n}}{[[\exp[(\boldsymbol{\alpha} - \boldsymbol{\alpha}_{in}^{app}) : \mathbf{n}] - 1] + C_{\gamma 1}][(\boldsymbol{\alpha}^b - \boldsymbol{\alpha}) : \mathbf{n}]^{0.5}} C_{rev}\,, \end{aligned} \tag{3.32}$$

where $C_{\gamma 1}$ is added to prevent the denominator from becoming zero and generate nonlinearity even when $(\boldsymbol{\alpha} - \boldsymbol{\alpha}_{in}^{app}) : \mathbf{n}$ is small. Calibrations by Boulanger and Ziotopoulou (2017) show

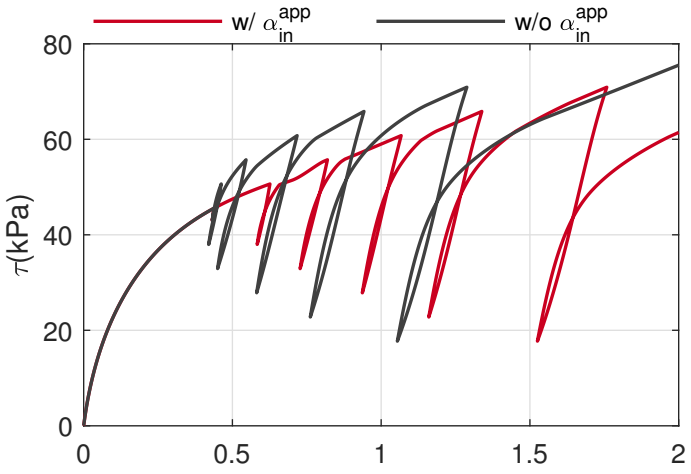

Figure 3.2: Effect of apparent initial back-stress ratio α_{in}^{app} to avoid "Overshooting" following a small loading reversal.

$C_{\gamma 1} = h_0/200$ produces a reasonable response. For a state with a stress ratio outside the bounding surface ($(\boldsymbol{\alpha}^b - \boldsymbol{\alpha}) : \mathbf{n} < 0$) and loose than critical ($\xi_R < 0$) condition, K_p is set to zero instead of allowing negative values. This restriction on K_p improves numerical stability while has little effect on the stress-strain response.

Assuming no isotropic hardening, $\dot{m} = 0$, and K_p is related to kinematic hardening aspects only as shown in Dafalias and Manzari (2004) and therefore,

$$\dot{\boldsymbol{\alpha}} = \langle L \rangle \frac{2}{3} h (\boldsymbol{\alpha}_\sigma^b - \boldsymbol{\alpha}) \,, \tag{3.33}$$

where h is the hardening coefficient and $\boldsymbol{\alpha}_\sigma^b - \boldsymbol{\alpha}$ is a distance between the bounding and current back-stress ratio tensors. The factor of 2/3 is included for convenience so that model constants are the same in triaxial and multi-axial formulations. Using the consistency condition $\dot{f} = 0$, one can get,

$$K_p = \frac{2}{3} p h (\boldsymbol{\alpha}^b - \boldsymbol{\alpha}) : \mathbf{n} = \frac{2}{3} p h \mathbf{b} : \mathbf{n} \,, \tag{3.34}$$

where $\mathbf{b} = \boldsymbol{\alpha}^b - \boldsymbol{\alpha}$. This expression can be rearranged to show that the consistency equation

can be satisfied by expressing the hardening coefficient as,

$$h = \frac{2}{3}\frac{K_p}{p(\boldsymbol{\alpha}^b - \boldsymbol{\alpha}) : \mathbf{n}}\,. \tag{3.35}$$

3.2.6 Dilatancy

Dilation

The dilatancy parameter D is made proportional to the difference between the current stress ratio and the dilatancy stress ratio defined by the dilatancy surface. Depending on $(\boldsymbol{\alpha}^d - \boldsymbol{\alpha}) : \mathbf{n} \lessgtr 0$, contraction ($D > 0$), dilation ($D < 0$) or zero volumetric rate ($D = 0$) can be obtained. Following the original MD formulation,

$$D = A_{do} \cdot [(\boldsymbol{\alpha}^d - \boldsymbol{\alpha}) : \mathbf{n}]\,, \tag{3.36}$$

where A_{do} can be related to the dilatancy relationship proposed by Bolton (1986),

$$A_{do} = \frac{1}{0.4}\frac{sin^{-1}(\frac{M^b}{2}) - sin^{-1}(\frac{M}{2})}{M^b - M^d}\,. \tag{3.37}$$

Contraction

In the MD model, plastic volumetric strain during both contraction and dilation is computed using,

$$D = A_{do} \cdot [(\boldsymbol{\alpha}^d - \boldsymbol{\alpha}) : \mathbf{n}]\,. \tag{3.38}$$

Although robust, this relatively simple expression has shown limitations in estimating cyclic resistance ratios (CRR) (Ghofrani and Arduino, 2017; Ramirez et al., 2018a). Therefore, in PM4Sand, the plastic volumetric strain during contraction is modified to the following expression,

$$D = A_{dc}[(\boldsymbol{\alpha} - \boldsymbol{\alpha}_{in}^{app}) : \mathbf{n}]^2 \frac{(\boldsymbol{\alpha}^d - \boldsymbol{\alpha}) : \mathbf{n}}{(\boldsymbol{\alpha}^d - \boldsymbol{\alpha}) : \mathbf{n} + C_D}\,, \tag{3.39}$$

where

$$A_{dc} = \frac{A_{do}}{h_p}. \tag{3.40}$$

The term $\frac{(\boldsymbol{\alpha}^d-\boldsymbol{\alpha}):\mathbf{n}}{(\boldsymbol{\alpha}^d-\boldsymbol{\alpha}):\mathbf{n}+C_D}$ ensures that D goes to zero smoothly as $\boldsymbol{\alpha}$ approaches $\boldsymbol{\alpha}^d$. C_D has a value of 0.10 in the current implementation in FLAC; while it is shown later that $C_D = 0.16$ in OpenSees provides a better match to FLAC results. Therefore the value of 0.16 is implemented in OpenSees. A detailed discussion on the choice of this value is presented in Chapter 4.

$$h_p = h_{po}\exp(-0.7 + 7.0(0.5 - \xi_R)^2) \quad for \quad \xi_R \leq 0.5\,, \tag{3.41}$$

$$h_p = h_{po}\exp(-0.7) \quad for \quad \xi_R > 0.5\,, \tag{3.42}$$

where the sate parameter ξ_R is defined in Eq. 3.15. An upper limit is imposed on the contraction rate, such that

$$D \leq 1.5 \cdot A_{do}\frac{(\boldsymbol{\alpha}^d - \boldsymbol{\alpha}) : \mathbf{n}}{(\boldsymbol{\alpha}^d - \boldsymbol{\alpha}) : \mathbf{n} + C_D}\,. \tag{3.43}$$

Effect of fabric

Following the idea proposed in MD, a fabric tensor $\mathbf{z}$ is used to account for strain accumulation based on previous strain history. The change of fabric is based on plastic volumetric strain during dilation,

$$\dot{\mathbf{z}} = \frac{c_z}{1 + \langle \frac{z_{cum}}{2z_{max}} - 1\rangle}\frac{\langle -\dot{\epsilon}_v^p\rangle}{D}(z_{max}\mathbf{n} + \mathbf{z})\,, \tag{3.44}$$

where the parameter c_z controls the rate of fabric accumulation and z_{max} controls the maximum value of $\mathbf{z}$. The scalar z_{cum} is the cumulative value of absolute change in $\mathbf{z}$ and its rate is,

$$\dot{z}_{cum} = |\dot{\mathbf{z}}|\ . \tag{3.45}$$

The greatest past peak value for $\mathbf{z}$, z_{peak}, is tracked as,

$$z_{peak} = max(\sqrt{\frac{\mathbf{z} : \mathbf{z}}{2}}, z_{peak})\,. \tag{3.46}$$

Similar to $\boldsymbol{\alpha}_{in}$, the initial fabric tensor, $\mathbf{z}_{in}$, at each loading branch is also tracked and updated when a loading direction reversal is detected. This term is used to describe the

degree of stress rotation and its effect on dilative plastic volumetric strain. The mean stress at which the fabric is formed, p_{zp}, along with zxp, defined as the product of $|\mathbf{z}|$ and p, are also tracked during loading. p_{zp} plays an important role in the plastic modulus and dilative plastic volumetric strain. It is used to address a couple of issues, including the issue of how fabric is formed during liquefaction and may be erased during reconsolidation. More details can be found in Boulanger and Ziotopoulou (2017). Note they are both positive in the current OpenSees implementation that is discussed later. p_{zp} and zxp are updated at the same time whenever the current p_{zp} and zxp values both exceed their previous peak value, respectively. It is also noted that in the current implementation in FLAC 8.0, p_{zp} is always updated at the first loading reversal even though no fabric is formed. In order to better match the material behavior from FLAC, this change in p_{zp} is also allowed in OpenSees using a flag called $m\_pzpFlag$, which is set as true initially and changes to false after the first change of p_{zp}.

Effect of fabric on plastic modulus

The plastic modulus K_p is expected to reduce as the fabric tensor grows. Therefore, Eq. 3.32 is modified to,

$$K_p = Gh_o \frac{[(\boldsymbol{\alpha}^b - \boldsymbol{\alpha}) : \mathbf{n}]^{0.5}}{[\exp[(\boldsymbol{\alpha} - \boldsymbol{\alpha}_{in}^{app}) : \mathbf{n}] - 1] + C_{\gamma 1}} C_{rev} \frac{C_{k\alpha}}{1 + C_{K_p}\left(\frac{z_{peak}}{z_{max}}\right)\langle(\boldsymbol{\alpha}^b - \boldsymbol{\alpha}) : \mathbf{n}\rangle\sqrt{1 - C_{zpk2}}}, \tag{3.47}$$

where,

$$C_{k_\alpha} = 1 + \frac{C_{k\alpha f}}{1 + \left(2.5 \cdot \langle(\boldsymbol{\alpha} - \boldsymbol{\alpha}_{in}^{true}) : \mathbf{n}\rangle\right)^2} \cdot C_{pzp2} \cdot C_{zpk1}\,, \tag{3.48}$$

$$C_{zpk1} = \frac{z_{peak}}{z_{cum} + \frac{z_{max}}{5}}\,, \tag{3.49}$$

$$C_{zpk2} = \frac{z_{peak}}{z_{cum} + \frac{z_{max}}{100}}\,, \tag{3.50}$$

$$C_{pzp2} = \frac{\langle pzp - p \rangle}{\langle pzp - p \rangle + p_{min}}\,, \tag{3.51}$$

and

$$G = G_o p_A (\frac{p}{p_A})^{1/2} C_{SR} (\frac{1 + \frac{z_{cum}}{z_{max}}}{1 + \frac{z_{cum}}{z_{max}} C_{GD}})\,. \tag{3.52}$$

Details on these additional terms can be found in Boulanger and Ziotopoulou (2017).

Effect of fabric on volumetric dilation

With the effect of fabric, the term A_{do} in Eq. 3.36 is modified to,

$$A_d = \frac{A_{do} C_{zin2}}{(\frac{z_{cum}^2}{z_{max}})\big(1 - \frac{\langle -\mathbf{z}:\mathbf{n} \rangle}{\sqrt{2} \cdot z_{peak}}\big)^3 C_\epsilon^2 C_{pzp} C_{pmin} C_{zin1} + 1}\,, \tag{3.53}$$

where C_ϵ is a constant that is used to control the rate of plastic shear strain accumulation and its default value varies with relative density as,

$$C_\epsilon = \begin{cases} = 0.2, & D_R > 0.75\,, \\ = 0.5 - (D_R - 0.55) \cdot 1.5 & 0.55 < D_R < 0.75\,, \\ = 0.5 & D_R < 0.55\,. \end{cases} \tag{3.54}$$

Note that Eq. 3.54 is different than what is presented in Boulanger and Ziotopoulou (2017). The equation presented here is the same as what is implemented in FLAC and it was confirmed by the model developers. C_{pzp} removes the effect of fabric on dilation when p is close to p_{zp}, and is defined as,

$$C_{pzp} = \frac{1}{1 + (\frac{2.5p}{p_{zp}})^5}\,. \tag{3.55}$$

C_{pmin} removes the effect of fabric on dilation when p is sufficiently small, and is defined as

$$C_{pmin} = \frac{1}{1 + (\frac{p_{min2}}{p})^2}\,. \tag{3.56}$$

The parameters p_{min2} and p_{min}(shown in later sections) are used to control the model behavior at small confining pressures and to get a better CRR curve slope. They are initialized

when *FirstCall* is activated and their values are taken as,

$$p_{min} = \frac{p}{200}\, and \tag{3.57}$$

$$p_{min2} = \frac{p}{20}\,. \tag{3.58}$$

The term C_{zin1} facilitates strain-hardening when stress reversals are not causing fabric changes and it is defined as,

$$C_{zin1} = 1.0 - \exp\Big(-2.0\Big|\frac{\mathbf{z}_{in} : \mathbf{n} - \mathbf{z} : \mathbf{n}}{z_{max}}\Big|\Big)\,. \tag{3.59}$$

The term C_{zin2} is used to decrease dilatancy by up to a factor of 3 under conditions of large strains and full stress reversals. It is defined as,

$$C_{zin2} = \frac{1 + C_{zin1}\dfrac{z_{cum} - z_{peak}}{3z_{max}}}{1 + 3\cdot C_{zin1}\dfrac{z_{cum} - z_{peak}}{3z_{max}}}\,. \tag{3.60}$$

During dilation at very low effective stresses, i.e., $p \leq 2p_{min}$, D is constrained to ensure soil at dense than critical states continue to be dilative. For this purpose,

$$D = -3.5A_{do}\langle M^b - M^d\rangle\frac{2p_{min} - p}{p_{min}}\,. \tag{3.61}$$

Effect of fabric on volumetric contraction

With the effect of fabric, Eq. 3.39 is extended to,

$$D = A_{dc}\cdot[(\boldsymbol{\alpha} - \boldsymbol{\alpha}_{in}^{app}) : \mathbf{n} + C_{in}]^2\frac{(\boldsymbol{\alpha}^d - \boldsymbol{\alpha}) : \mathbf{n}}{(\boldsymbol{\alpha}^d - \boldsymbol{\alpha}) : \mathbf{n} + C_D}C_{pmin2}\,. \tag{3.62}$$

where A_{dc} also evolves with fabric as,

$$A_{dc} = \frac{A_{do}(1 + \langle\mathbf{z} : \mathbf{n}\rangle)}{h_p C_{dz}}\,. \tag{3.63}$$

where the term C_{dz} is included to increase the rate of contraction as z_{peak} approaches z_{max} or a large amount of cumulative fabric formation/destruction has taken place. It is defined as,

$$C_{dz} = \Big(1 - C_{rot2}\cdot\frac{\sqrt{2}z_{peak}}{z_{max}}\Big)\Big(\frac{z_{max}}{z_{max} + C_{rot2}\cdot z_{cum}}\Big) \geq \frac{1}{1 + \dfrac{z_{max}}{2}}\quad. \tag{3.64}$$

where C_{rot2} is defined as,

$$C_{rot2} = 1 - \frac{z_{peak}}{z_{cum} + \frac{z_{max}}{100}} \ . \tag{3.65}$$

The term C_{in} is included to enhance the contraction rate at the start of an unloading cycle, and it is defined as,

$$C_{in} = \frac{2\langle \mathbf{z} : \mathbf{n} \rangle}{\sqrt{2} z_{max}} \, . \tag{3.66}$$

The term C_{pmin2} slows the rate of contraction when p is approaching to p_{min} and stops further contraction when p is less than twice p_{min}. A linear variation is defined as,

$$C_{pmin2} = \begin{cases} = 0, & p \leq 2p_{min} \, , \\ = \frac{p - 2p_{min}}{16 p_{min}} & 2p_{min} < p < 18p_{min} \, , \\ = 1 & p \geq 18p_{min} \, . \end{cases} \tag{3.67}$$

This term is used to improve stability of the model at small confining pressures. It has a significant effect on the variation of p and in turn on the stress dependent behavior of the model, especially in what it relates to shear strain accumulation.

Readers are encouraged to refer to the PM4Sand manual by Boulanger and Ziotopoulou (2017) for more details on these issues.

Post-shaking reconsolidation

Several studies (Ziotopoulou and Boulanger, 2013; Howell et al., 2014) have shown that predicted numerical volumetric strains tend to be much smaller than what is observed in experimental studies. To improve the estimation of post-shake reconsolidation settlement, PM4Sand incorporates a function the user can activate to reduce the value for the elastic shear and bulk modulus after a main shake. Then, the post-shaking elastic moduli can be determined by applying a reduction factor F_{sed} such that,

$$G_{post-shaking} = F_{sed} G \, , \tag{3.68}$$

$$K_{post-shaking} = F_{sed} K \, , \tag{3.69}$$

where F_{sed} is related to the accumulated fabric and the stress state at the end of the main shake, and it can be calculated as,

$$F_{sed} = F_{sed,min} + (1 - F_{sed,min})(\frac{p}{20p_{sed}})^2 \leq 1\,, \tag{3.70}$$

where p_{sed} is,

$$p_{sed} = p_{sed_o}(\frac{z_{cum}}{z_{cum} + z_{max}}) \left\langle 1 - \frac{M^{cur}}{M^d} \right\rangle^{0.25}\,, \tag{3.71}$$

and $F_{sed,min}$ is,

$$F_{sed,min} = 0.03 * \exp(2.6 * D_R) \leq 0.99\,, \tag{3.72}$$

and p_{sed_o} is,

$$p_{sed_o} = -\frac{P_{atm}}{5}\,. \tag{3.73}$$

Fig. 3.3 shows comparisons between results for a liquefied 1D level ground array obtained using OpenSees with and without *PostShake* activated after the main shake. The figure shows the increased predicted settlements due to the reduced stiffness that is meant to compensate for post shake reconsolidation. It also shows that the excess pore pressure dissipation rate is also affected due to the reduction in bulk modulus. Therefore, if dissipation of excess pore pressure is of interest, *PostShake* flag should be activated with care.

3.3 Brief Introduction of OpenSees

OpenSees (the Open System for Earthquake Engineering Simulation) is an open source finite element framework developed at the Pacific Earthquake Engineering Research Center (PEER). It is mainly written in C++ but also uses FORTRAN for solving systems of equations. Its brilliant architecture and efficient programming lead to fast performance and excellent expandability. Its functionality is ever-growing, and over the years, contributions from both industry and academic communities have led to the following advantages of OpenSees:

- Large selections of constitutive models for both structural and geotechnical applications.
- Capability for running static and transient analysis.

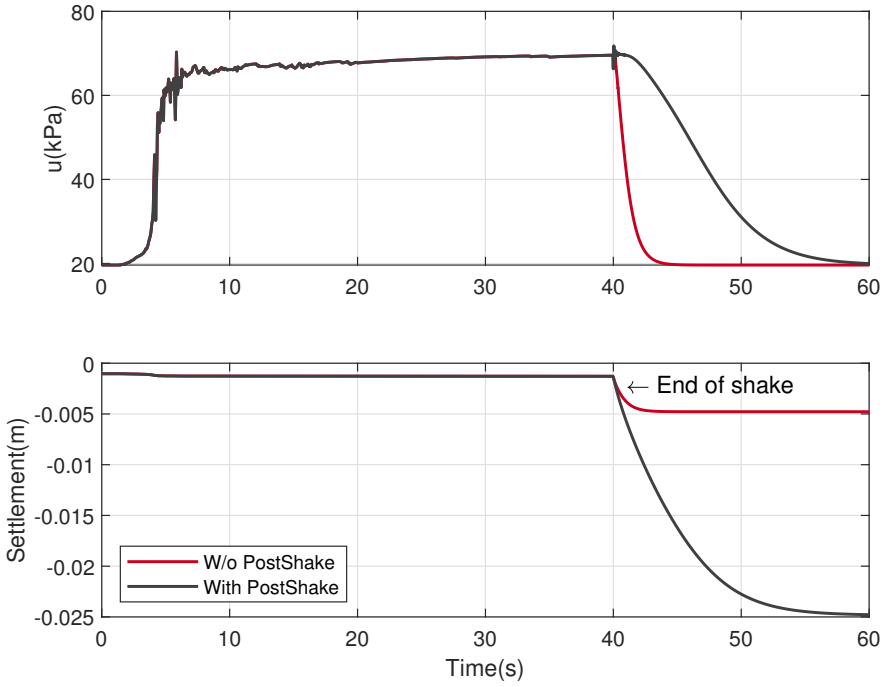

Figure 3.3: Comparison of excess pore pressure dissipation and settlement for cases with and without *PostShake* flag activated at the end of the main shake.

- Efficient fully coupled U-P elements for running effective stress analysis, that are suitable for liquefaction related analysis.
- Interface elements of varying complexity for modeling soil-structure interaction.
- Several high performance solvers, implicit or explicit, for fast computing.
- Thorough implementation of parallel computing: OpenSeesSP (single parallel), suitable for large models; and OpenSeesMP (multiple parallel), ideal for large scale parametric studies.
- Both Tcl and Python interpreters for direct execution of scripts. The newly implemented OpenSeesPy (Zhu et al., 2018) brings Python packages to the OpenSees community and enables using python packages, such as Jupyter Notebook and Matplotlib, directly with OpenSees.

- Powerful third-party pre- and post-processing tools available for mesh generation, model creation, and results visualization, e.g., STKO (ASDEA Software, 2020) and Gid+OpenSees (Kartalis-Kaounis and Papanikolaou, 2020).
- Light weight and great compatibility with different operating systems, i.e., Windows, Linux, and MacOS. Available on almost every high performance computing systems.

3.4 Implementation of PM4Sand in OpenSees

The implementation of PM4Sand in OpenSees closely followed the model's original formulations presented in Boulanger and Ziotopoulou (2017), with the only exception of Eq. 3.39, where the default value of C_d was modified, as discussed in the following chapter. Although the model's formulations were preserved to the most extent, integration schemes for nonlinear equations were implemented following OpenSees framework. Additional algorithms for improved accuracy, such as yield surface intersection detection and stresses drift correction, were also implemented.

3.4.1 Explicit integration schemes

The current implementation of PM4Sand in OpenSees includes three explicit integration schemes: Forward Euler, Modified (or two-step) Euler with substepping and 4^{th} order explicit Runge-Kutta method. During each strain subincrement, an algorithm that accounts for the transition from elastic to elasto-plastic states (yield surface intersection) and correction of stresses to the yield surface (yield surface drift), respectively, is used. Details on explicit schemes are presented by Sloan et al. (2001). Readers are encouraged to refer to the original paper by Sloan for more details while basic steps are presented here.

Yield surface intersection

At the beginning of each step, an elastic trial stress increment $\dot{\boldsymbol{\sigma}}_e$ is calculated using the strain increments $\dot{\boldsymbol{\epsilon}}$,

$$\dot{\boldsymbol{\sigma}}_e = \mathbb{C}_e : \dot{\boldsymbol{\epsilon}}\,, \tag{3.74}$$

where the stress-strain matrix $\mathbb{C}_e$ can be replaced by the secant elastic stiffness matrix $\overline{\mathbb{C}_e}$, defined in terms of the secant shear modulus G and bulk modulus K evaluated using the previous stress state, $\boldsymbol{\sigma}_0$, and total volumetric strain increment. The previous equation can be replaced by,

$$\dot{\boldsymbol{\sigma}}_e = \overline{\mathbb{C}_e}(K, G)\dot{\boldsymbol{\epsilon}} = \overline{\mathbb{C}_e}(\boldsymbol{\sigma}_0, \mathbb{C}_e\epsilon_v)\dot{\boldsymbol{\epsilon}} = \overline{\mathbb{C}_e}\dot{\boldsymbol{\epsilon}}\,. \tag{3.75}$$

The elastic trial stress increment is used in the formulation to check if the stress state has changed from elastic to elasto-plastic. Such a change occurs if $f(\boldsymbol{\sigma}_0, \boldsymbol{\alpha}) < 0$ and $f(\boldsymbol{\sigma}_0 + \dot{\boldsymbol{\sigma}}_e, \boldsymbol{\alpha}) > 0$. If this occurs, then it is necessary to check the fraction of $\dot{\boldsymbol{\epsilon}}$ that moves the stress state from $\boldsymbol{\sigma}_0$ to the stress state on the yield surface. The exact yield condition $f(\boldsymbol{\sigma}_0, \boldsymbol{\alpha}) = 0$ can be replaced by $|f(\boldsymbol{\sigma}_0, \boldsymbol{\alpha})| \leq FTOL$, where $FTOL$ is a small positive tolerance. This minimizes the effect of finite precision arithmetic and modifies the transition condition to $f(\boldsymbol{\sigma}_0, \boldsymbol{\alpha}) < -FTOL$ and $f(\boldsymbol{\sigma}_0 + \dot{\boldsymbol{\sigma}}_e, \boldsymbol{\alpha}) > FTOL$. Sloan et al. (2001) recommends suitable values for $FTOL$ in the range of 10^{-6} to 10^{-9}. 10^{-8} is set as the default value in the current OpenSees implementation. The problem of finding the stresses at the yield surface intersection point is equivalent to finding the scalar quantity elastic ratio e which satisfies the non-linear equation,

$$f(\boldsymbol{\sigma}_0 + e\dot{\boldsymbol{\sigma}}_e, \boldsymbol{\alpha}) = 0\,, \tag{3.76}$$

where $0 \leq e \leq 1$, and a value of 1 indicates purely elastic deformation and a value of 0 indicates purely elasto-plastic deformation. The Pegasus procedure of Dowell and Jarratt (1972) was implemented in this work to find the value of e.

Correction of stresses to yield surface

In the explicit integration process, at the end of each subincrement the stresses may diverge from the yield condition such that $f(\boldsymbol{\sigma}_0, \boldsymbol{\alpha}) > FTOL$. This violation is commonly known as yield surface drift and varies with the accuracy of the integration scheme and the non-linearity of the constitutive relations. The non-linearity of the PM4Sand constitutive relations leads to a small drift at each integration substep. This drift is cumulative and can cause model

instability. Therefore, it is pertinent to impose a yield surface correction at the end of each subincrement. Potts and Gens (1985) examined five methods for accounting for this drift. These involve correcting the stresses by projecting back along the plastic flow, the total strain increment, or the accumulated effective stress direction. In addition, a consistent correction method that preserves the total strain increment during the correction step, known as a consistent correction, is shown to be effective and successful by Potts and Gens (1985). Under certain conditions, however, the corrected stress state is further from the yield surface than the uncorrected stress state and the consistent correction may not converge. In these circumstances, the consistent return scheme may be abandoned for one iteration and replaced with a correction which is normal to the yield surface as the algorithm presented by Sloan et al. (2001). This correction is applied iteratively until $f(\boldsymbol{\sigma}_0, \boldsymbol{\alpha}) \leq FTOL$.

Forward Euler

The first order forward Euler method was first implemented in PM4Sand. This method is the most basic approximation method for the integration of ordinary differential equations of the form,

$$\dot{u} = u' = \frac{du}{dx} = f(x, u) \quad u(0) = u_0 \,. \tag{3.77}$$

Using Taylor's expansion, and neglecting $O(h^2)$ and higher terms,

$$\frac{u^{n+1} - u^n}{h} \approx f(x^n, u^n) \,. \tag{3.78}$$

resulting in a simple explicit approximation of the form,

$$u^{n+1} = u^n + hf(x^n, u^n) \,. \tag{3.79}$$

Although simple and straightforward, the forward Euler method is first order accurate and can be unstable. Hence when choosing forward Euler as the integration scheme, the time step should be carefully selected and a maximum strain increment scheme might need to be considered.

Modified Euler with substepping

The modified Euler scheme with substepping proposed in Sloan et al. (2001) was used in the implementation of PM4Sand in OpenSees to overcome the drawbacks of the forward Euler method. In this method, first a forward Euler step is calculated over half the time step and the differential function is evaluated at the resulting point. Then, this differential is used to calculate the next step in the solution.

- First Step (forward Euler): $\hat{u}^{n+\frac{1}{2}} = u^n + \frac{h}{2} f(u^n)$.
- Second Step: $u^{n+1} = u^n + h f(\hat{u}^{n+\frac{1}{2}})$.

A local error measurement is introduced by automatically subdividing the imposed strain increment. During each subincrement, the local error is found by taking the difference between stress solutions of a second order modified Euler and a first order accurate Euler. Once the local error has been computed for a given step, the size of the next step is determined using,

$$\begin{aligned} \Delta h^{k+1} &= q \Delta h^k \,, \\ q &= min\{0.9\sqrt{STOL/R_{h^k+\Delta h^{n+1}}}, 1.1\} \,, \end{aligned} \tag{3.80}$$

and h is a pseudo strain or pseudo time.

4th order Runge-Kutta

A classical 4^{th} order explicit Runge-Kutta method was also used in the implementation of PM4Sand in OpenSees. This method is reasonably simple and robust and is a good general candidate for numerical solution of differential equations. This method can also be paired with automatic error control with adaptive step-size routine for future work. The currently implemented four stages of this method are summarized below,

1. $\hat{u}^{n+\frac{1}{2}} = u^n + \frac{h}{2} f(u^n)$,
2. $\tilde{u}^{n+\frac{1}{2}} = u^n + \frac{h}{2} f(\hat{u}^{n+\frac{1}{2}})$,

3. $\tilde{u}^n = u^n + hf(\tilde{u}^{n+\frac{1}{2}})$,
4. $u^{n+1} = u^n + \frac{h}{6}(f(u^n) + 2\hat{u}^{n+\frac{1}{2}} + 2f(\tilde{u}^{n+\frac{1}{2}}) + f(\tilde{u}^n))$.

Maximum strain increments

A scheme to control the maximum strain increment that is sent to any of the Euler methods was also implemented in OpenSees. This method can be coupled with either one of the two Euler integration methods presented in previous sections. This scheme checks the trial strain that is being parsed to the integrator and subdivides it if a certain maximum strain increment is exceeded. In the current implementation, the maximum strain increment is set to be 10^{-6}.

The default and recommended integration scheme in the current implementation is the modified Euler that has also been optimized for performance. Nevertheless, the user is also able to switch to a different scheme by changing an input parameter at the time of material creation or using the built-in *setParameter* command during the analysis.

3.4.2 Tcl commands

OpenSees has both Tcl and Python interpreters for model building. Only commands using Tcl interpreter are discussed here. Information on the Python interpreter can be found at `https://openseespydoc.readthedocs.io/en/latest/`. In the current OpenSees implementation, the PM4Sand material can be created using the following Tcl command,

```
nDmaterial PM4Sand $matTag $Dr $Go $hpo $Den <$patm $h0 $emax $emin $nb \\
$nd $Ado $zmax $cz $ce $phic $nu $cgd $cdr $ckaf $Q $R $m $Fsed_min $p_sedo>
```

where *matTag* is an integer tag identifying the material. The other input are material parameters as discussed before. Secondary parameters are inside <> and are optional.

The integration scheme can be updated using *setParameter* command as,

```
setParameter -value $mScheme -eleRange $eleStart $eleEnd IntegrationScheme $matNum
```

where *mScheme* is an integer related to each integration scheme as shown below:

- $mScheme = \mathbf{1}$: Modified Euler with automatic substepping.
- $mScheme = \mathbf{2}$: Forward Euler.
- $mScheme = \mathbf{3}$: 4th Order Runge-Kutta.
- $mScheme = \mathbf{4}$: Forward Euler with manual maximum strain increment.
- $mScheme = \mathbf{5}$: Modified Euler with manual maximum strain increment.

The *PostShake* flag can be activated in OpenSees using:

```
setParameter -value 0 -eleRange $eleStart $eleEnd PostShake $matNum
setParameter -value 0 -ele $eleNum PostShake $matNum
```

where *$eleStart* and *$eleEnd* define the range of elements whose *PostShake* are going to be activated, and *$matNum* is the material tag assigned to the elements.

3.5 Parametric study on calibration of PM4Sand

The calibration procedure for PM4Sand is straight forward for general sand-like behavior as intended by the model developers. When detailed laboratory tests results are available, the apparent relative density D_R can be estimated using void ratio and measured e_{max} and e_{min}. However, as discussed in Boulanger and Ziotopoulou (2017), D_R is defined to bound the model response rather than a strict measured of relative density from maximum and minimum density tests. Therefore, the user can adjust its value as part of the calibration process, and the default critical state line might need to be re-positioned by adjusting secondary parameters Q and R, as well. Nevertheless, the estimated D_R provides a reasonable value, such that the resulting model response is also reasonable. G_o can be estimated using small-strain shear modulus estimation methods for different confining pressures. Once D_R and G_o are determined, h_{po} can be calibrated iteratively by matching: 1) excess pore pressure evolution for a range of individual laboratory tests, and/or 2) specific values of CRR. Additional secondary parameters can also be adjusted to fine tune the model response. For example, adjusting h_o can result in different modulus reduction curves.

On the other hand, when comprehensive laboratory tests are not available for specific sites, model calibration needs to be based on in-situ test data such as SPT blow count,

CPT penetration resistance, or shear wave velocity (V_s). For example, D_R can be estimated by correlations to penetration resistances. Idriss and Boulanger (2008) recommended the following correlation to SPT,

$$D_R = \sqrt{\frac{(N_1)_{60}}{C_d}}\,, \tag{3.81}$$

where C_d is recommended to be 46. For CPT, the following correlation can be used,

$$D_R = 0.465\Big(\frac{q_{c1N}}{C_{dq}}\Big)^{0.264} - 1.063\,, \tag{3.82}$$

where C_{dq} is recommended to be 0.9. The second primary input parameter G_o can also be estimated from in-situ data. Boulanger and Ziotopoulou (2017) modified the correlation by Andrus and Stokoe (2000) to constraint the extrapolation to very small $(N_1)_{60}$ values, as

$$V_{s1} = 85[(N_1)_{60} + 2.5]^{0.25}\,. \tag{3.83}$$

Alternatively, a simpler expression can be used when combined with a range of typical densities as,

$$G_o = 167\sqrt{(N_1)_{60} + 2.5}\,. \tag{3.84}$$

Subsequently, h_{po} can be calibrated to reproduce a specific value of CRR that can be computed using liquefaction triggering models. Numerous liquefaction triggering models incorporating the simplified cyclic stress approach have been proposed in the past such as Youd and Idriss (2001), Cetin et al. (2004), and Idriss and Boulanger (2008).

Once D_R, G_o, and CRR are chosen, the modeler should iteratively vary the value of h_{po} until the simulated CRR matches the targeted value. Interpolation and extrapolation are common when the variables are within or close to the range of existing calibrated sets of parameters. Secondary parameters are less common to be modified when only in-situ data are available. This calibration process can become cumbersome when in-situ data show a large degree of variability and calibration has to be performed for each soil unit.

To simplify the calibration process under these circumstances, a parametric study was conducted to establish a correlation among D_R, G_o, h_{po}, and CRR, i.e., $CRR = f(D_R, G_o, h_{po})$.

The function, f, should be solvable for h_{po} when the other variables are known and eventually yield $h_{po} = g(CRR, D_R, G_o)$. This correlation is intended to provide a preliminary estimation of h_{po} and simplify the iterative calibration process under selected D_R, G_o, and CRR, especially when both SPT and V_s data are available and the user wants to make G_o independent to D_R.

For this purpose, the Dakota (Adams et al., 2017) platform, run through the uqFEM (McKenna et al. (2018), now quoFEM) tool developed by the NHERI SimCenter, was used in this parametric study. The Dakota software provides advanced parametric analysis techniques enabling quantification of margins and uncertainty, risk analysis, model calibration, and design exploration with computational models. Its methods include optimization, uncertainty quantification, parameter estimation, and sensitivity analysis, which may be used individually or as components within surrogate-based and other advanced strategies. The uqFEM application is intended to advance the use of uncertainty quantification and optimization within the field of natural hazards engineering by combining existing finite element applications, e.g., OpenSees, with uncertainty quantification applications, i.e., Dakota, behind a simple user interface. In this study, uqFEM was modified to include our MixedDriver tool and all the simulations were performed on the Texas Advanced Computing Center (`http://www.tacc.utexas.edu`) Stampede2 supercomputer made available through DesignSafe-ci (Rathje et al., 2017).

Using this tool, D_R, G_o, and h_{po} were varied while all the secondary parameters were kept of their default values (predefined by primary parameters and initial stresses). The Latin Hypercube Sampling (LHS) method was used to generate near-random variables. Each of these three variables was assigned an independent uniform distribution between minimum and maximum values. The range of these variables was chosen to cover a reasonable range of scenarios and can be extended in future studies. D_R was set to be between 0.2 to 0.9, G_o between 250 to 1200, and h_{po} between 0.05 to 1.2. A total of one million samples were generated. For each set of parameters, Dakota ran MixedDriver to simulate undrained cyclic simple shear tests for 15 different CSRs ranging from 0.05 to 0.8 to produce smooth cyclic

strength curves (Fig. 3.6). A total of three initial conditions were considered: initial effective vertical stress $\sigma'_v = 1\ atm.$ with K_0 equal to 0.5 and 1.0, respectively, and $\sigma'_v = 2\ atm.$ with K_0 equal to 0.5. The analyses were capped at 350 uniform cycles. Once all 15 simulated CDSS tests were done, a python script was called by Dakota to calculate the number of cycles to reach liquefaction; which was defined as the number of cycles required to reach a single amplitude (SA) shear strain of 3% as recommended by Ishihara (1993). Number of cycles to reach 1% and 2% SA and the slope (-b) and intercept (a) of the CSR curves (Idriss and Boulanger, 2008) in logarithmic scale were also recorded. The number of cycles were rounded up to the nearest half. Then a cyclic strength curve was interpolated to calculate the Cyclic Resistance Ratio, CRR, which was determined as the CSR corresponding to 15 cycles. CRRs were bounded between 0.05 and 0.5 for interpolation accuracy. A sample of the the Dakota input file is shown below:

```
environment
tabular_data
tabular_data_file = 'dakotaTab.out'

method,
sampling
sample_type = lhs
samples = 1000000
seed = 215

variables,
uniform_uncertain = 3
lower_bounds = 0.2  200  0.05
upper_bounds = 0.95  1200  1.2
descriptors = 'dr'  'Go'  'hpo'

uncertain_correlation_matrix = 1.00000  0.00000  0.00000
                               0.00000  1.00000  0.00000
                               0.00000  0.00000  1.00000

interface,
fork
 asynchronous
analysis_driver = 'fem_driver'
```

```
parameters_file = 'params.in'
failure_capture = recover -1
results_file = 'results.out'
work_directory directory_tag
copy_files = 'templatedir/*'
named 'workdir'
aprepro

responses,
response_functions = 4
response_descriptors = 'a'
'b'
'crr'
'crr2'
'crr3'
no_gradients
no_hessians
```

Fig. 3.4 illustrates the histograms of all three input variables, D_R, G_o, and h_{po}, and one of the outputs, i.e., $CRR_{3\%}$ for the case with $K_0 = 0.5$ and $\sigma'_v = 1$ $atm.$. The input variable histograms generally show the predefined uniform distribution pattern, while the attained CRR histogram shows values concentrated near lower values, indicating higher CRR, such as 0.6, are highly unlikely to be achieved using the current ranges of input parameters. A small portion of the samples were discarded because no enough points were obtained to form a smooth CSR-N curve, meaning these sets of parameters produced 3% SA either under 1 cycle or beyond 350 cycles for a wide range of CSRs. This resulted in a slight reduction in the valid sample size from 1M to about 990k. Fig. 3.5 presents the pair-wise relationships between each of the three input parameters and $CRR_{3\%}$ for the same case. Positive correlations are shown in all three plots while more significant between D_R and $CRR_{3\%}$.

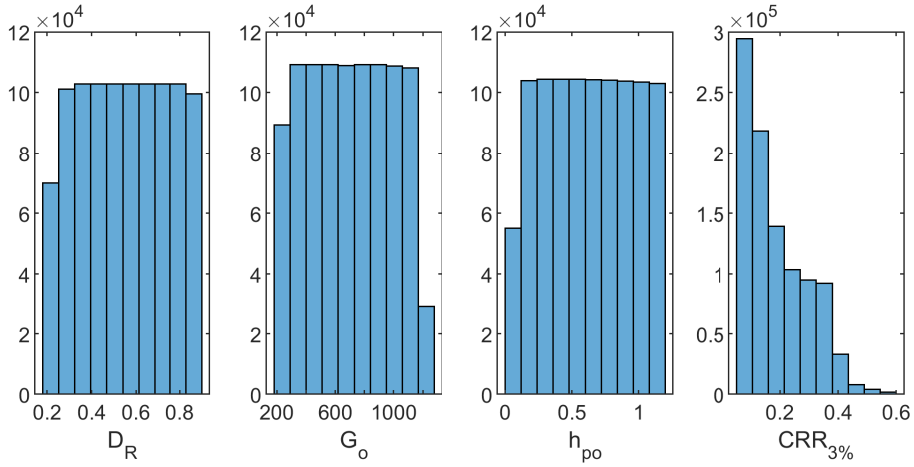

Figure 3.4: Pair-wise relationships between all inputs parameters and $CRR_{3\%}$, $K_0 = 0.5\,, and \sigma'_v = 1\ atm.$.

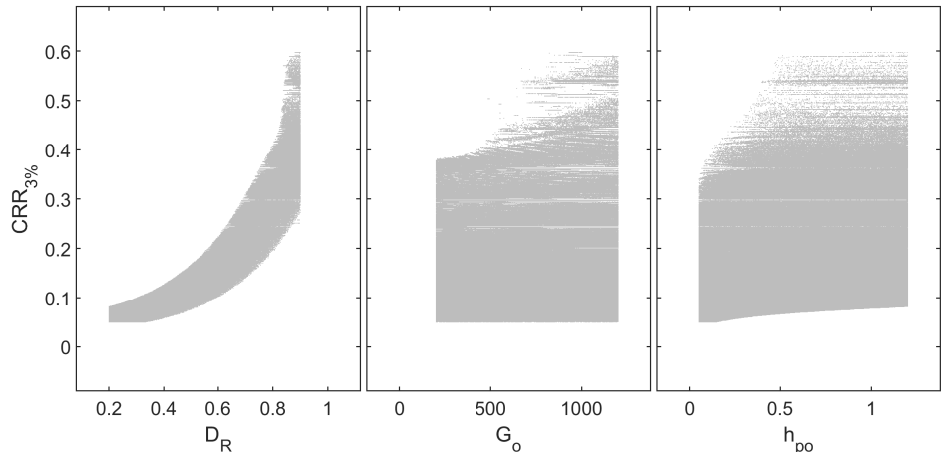

Figure 3.5: Pair-wise relationships between all the inputs and $CRR_{3\%}$, $K_0 = 0.5\,, and \sigma'_v = 1\ atm.$.

Table 3.1 presents partial rank correlation values between all inputs and outputs; with

larger values indicating greater correlation between input and output. The results echo the trend shown in Fig. 3.5, with both D_R and h_{po} having stronger influence on CRR as compared to G_o. This phenomenon echos PM4Sand's dependency on D_R which controls the state parameter and several other secondary parameters including fabric; and h_{po} which controls the rate of pore pressure accumulation during contraction. G_o has a stronger effect on CRR for larger strain criteria, i.e., 0.44 for 3% vs. 0.25 for 1%.

Table 3.1: Partial rank correlation matrix between inputs and outputs for $K_0 = 0.5, \sigma'_v = 1\ atm.$.

	$CRR_{1\%}$	$CRR_{2\%}$	$CRR_{3\%}$
D_R	0.990279	0.992808	0.993168
G_o	0.247524	0.308400	0.441622
h_{po}	0.879294	0.903305	0.901287

The results were processed through a linear regression analysis using *Matlab* to find the correlation between the input, D_R, h_{po} and G_o, and the output CRR. Different combination of terms were explored and the following format produced the largest R^2,

$$\begin{aligned} CRR_{3\%,K_0=0.5} =& 0.1282 - 0.4952 D_R - 5.0565 \times 10^{-5} G_o + 0.0749 h_{po} + 1.4665 \times 10^{-4} D_R G_o \\ &+ 0.1323 D_R h_{po} + 0.7252 D_R^2 - 0.0636 h_{po}^2 \,, \end{aligned} \tag{3.85}$$

with $R^2 = 0.989$. In this equation D_R is in fraction. CRRs using criteria of 1% and 2% SA as well as for other σ'_v and K_0 were also analyzed. All the estimated coefficients are summarized in Tables 3.2 and 3.3. It should be noted that the magnitude of these coefficients depends directly on the scale of the selected variables and smaller coefficients don't necessary imply less important features. For example, G_o is approximately three orders of magnitude larger than D_R, which leads to much smaller coefficients for it.

Table 3.2: Summary of estimated regression coefficients

	$\sigma'_v = 1\ atm.,\ K_0 = 0.5$			$\sigma'_v = 1\ atm.,\ K_0 = 1.0$		
	3%	2%	1%	3%	2%	1%
Intercept	0.1282	0.1127	0.1113	0.1262	0.1254	0.1279
D_R	-0.4952	-0.4437	-0.4186	-0.5038	-0.5002	-0.4727
G_o	-5.057×10^{-5}	-3.496×10^{-5}	-4.856×10^{-5}	-3.727×10^{-5}	-2.977×10^{-5}	-5.697×10^{-5}
h_{po}	0.07487	0.07790	0.08578	0.1090	0.1061	0.1163
$D_R G_o$	1.466×10^{-4}	9.953×10^{-5}	1.264×10^{-4}	1.148×10^{-4}	8.703×10^{-5}	1.491×10^{-4}
$D_R h_{po}$	0.1323	0.1282	0.1135	0.1483	0.1547	0.1301
D_R^2	0.7252	0.6962	0.6463	0.8485	0.8486	0.7729
h_{po}^2	-0.06362	-0.06437	-0.06568	-0.08380	-0.08349	-0.08379
R^2	0.989	0.993	0.987	0.995	0.995	0.987

Several visual-manual calibration studies presented in Chapter 4 and available in Boulanger and Ziotopoulou (2017) were revisited to evaluate the accuracy of the proposed correlation. These calibrations were done using the same initial conditions as in this study and the 3% SA criterion was used. Table 3.4 compares these results. As shown in the table, the predicted CRRs fall within a 5% range of the targeted CRRs. The correlation obtained from the regression showed good agreement with the calibrations.

Equ. 3.85 can be rearranged to isolate h_{po},

$$a h_{po}^2 + b h_{po} + c = 0\,, \tag{3.86}$$

where $a = 0.0636$, $b = -0.0749 - 0.1323 D_R$, and $c = -0.1282 + 0.4952 D_R + 5.0565 \times 10^{-5} G_o - 1.4665 \times 10^{-4} D_R G_o - 0.7252 D_R^2 + CRR_{3\%,K_0=0.5}$. This correlation becomes a quadratic equation for h_{po} that can be solved for two real roots for h_{po} when values of D_R, G_o, and CRR are given. The lesser root is the one that can be paired with D_R and G_o to yield the desired CRR in a calibration process. Using this equation, h_{po} values were calculated and compared with those obtained using the visual-manual calibration process. Table 3.5 summarizes these results. The observed error in h_{po} was larger than that observed

Table 3.3: Summary of estimated regression coefficients (continued)

	$\sigma'_v = 2\ atm.,\ K_0 = 0.5$		
	3%	2%	1%
Intercept	0.8540	0.8585	0.9228
D_R	-0.2928	-0.2942	-0.3060
G_o	-1.608×10^{-5}	-1.428×10^{-5}	-2.287×10^{-5}
h_{po}	0.02590	0.02587	0.02548
$D_R G_o$	5.285×10^{-5}	4.492×10^{-5}	6.921×10^{-5}
$D_R h_{po}$	0.03721	0.03748	0.03641
D_R^2	0.5971	0.5969	0.5807
h_{po}^2	-0.005031	-0.005042	-0.004916
R^2	0.990	0.989	0.987

in CRRs, especially for higher D_Rs, e.g., 0.75. However, no significant discrepancy was observed in the comparison of CSR-N curves obtained using the visual-manual calibrated and predicted h_{po}'s (Fig. 3.6). Two aspects possibly contributed: (1) The CRR obtained using PM4Sand is more sensitive to D_R, especially under higher D_Rs, thus a wider range of h_{po} can produce similar CRRs under these conditions. (2) The CRR obtained using a visual-manual calibration process is usually estimated using fewer number of points to form the CSR-N curve, thus larger uncertainty in obtained h_{po} at a given combination of CSR and N. Nevertheless, the results demonstrate the predictive equation can be used to provide good initial h_{po} values and speed up the calibration process.

Nonetheless, limitations exist in the predictive equation as real roots are not guaranteed for this quadratic equation under all combinations of D_R, G_o, and CRR. For example, when D_R, G_o, and CRR exceed the range of parameters considered in this parametric study, and when the resulting h_{po} is either larger than 1.2 or smaller than 0.05 depending on the CRR. Under these circumstances, manual calibration is required.

Fig. 3.7 shows all CRR (3%) calculated in this study plotted along with curves from

Table 3.4: Comparison of predicted and targeted $CRR_{3\%}$

N	D_R	G_o	h_{po}	CRR(Targeted)	CRR(Predicted)	error
5	0.330	354.0	0.533	0.086	0.088	2.2%
10	0.466	468.3	0.463	0.118	0.113	4.4%
20	0.659	651.0	0.425	0.206	0.207	0.7%
5*	0.35	476.0	0.53	0.090	0.090	0.8%
14*	0.55	677.0	0.40	0.148	0.144	2.3%
26*	0.75	890.0	0.63	0.312	0.302	4.4%

*From Boulanger and Ziotopoulou (2017)

empirical triggering models, where simulation $(N_1)_{60}$ was back-calculated from D_R using $C_d = 46$. Each simulation data point represents an unique combination of D_R, G_o, and h_{po}; and the data are bounded by h_{po} under a given D_R, since CRR is less sensitive to G_o (Table 3.1). The simulation data on the upper part of the plot correspond to h_{po} close to 1.2 while the data on lower part of the plot correspond to h_{po} close to 0.05. This figure shows that the general trend obtained from the simulation follows the empirical models closely, especially Idriss and Boulanger (2008), between approximately $(N_1)_{60}$ of 5 and 25. For higher $(N_1)_{60}$, both empirical models and the simulations show greater uncertainty. The maximum h_{po} value selected in this parametric study was not large enough to cover CRR for higher D_R ($(N_1)_{60}$).

Based on this observation, a series of additional simulations were performed using constant h_{po} ranging from 0.05 to 3.0, as shown in Fig. 3.8. Each additional h_{po} case represented 250k cases with all the other inputs remaining the same as in the previous study. The scatter plot in Fig. 3.8 illustrates all obtained CRR for each constant h_{po}, shown in different colors. A series of polynomials were then fitted through the data points to show the general trend between D_R and CRR for each h_{po}. These curves can be interpolated to provide an initial

Table 3.5: Comparison of predicted and targeted h_{po}

N	D_R	G_o	CRR (Targeted)	h_{po} (Visual-Manual calibration)	h_{po}(Predicted)	error
5	0.330	354	0.086	0.533	0.497	6.7%
10	0.466	468.3	0.118	0.463	0.534	15.4%
20	0.659	651	0.206	0.425	0.439	3.2%
5*	0.35	476	0.090	0.53	0.516	2.6%
14*	0.55	677	0.147	0.40	0.427	2.2%
26*	0.75	890	0.312	0.63	0.745	18.3%

*From Boulanger and Ziotopoulou (2017)

estimation of h_{po} for a given D_R.

The relationship between the CRR and N, within the range of cycles of interest for earthquake engineering, can generally be approximated with a power function as,

$$CRR = a \cdot N^{-b}\,, \tag{3.87}$$

where the parameters a and b are determined by regression against the simulated data. The parameter b for clean sands is typically about 0.34, whereas the parameter a depends on a wide range of factors. As shown in Fig. 3.9a, for relatively loose sand, i.e. D_R ranging from 0.2 to 0.6, the slope b is unlikely to go below 0.3 with changing primary parameters. Although laboratory tests conducted on Ottawa F-65 sand have shown b value of 0.08 (D_R = 20%) and 0.11 (D_R = 70%) using undrained simple shear tests (Bastidas, 2016). In this case, modifying only primary parameters is clearly not enough to reproduce the behavior observed in laboratory tests and change of secondary parameters becomes necessary.

Although the correlation proposed in this study can be used to calculate h_{po} automatically, it is only intended to provide a preliminary estimation. The stress-strain behavior attained

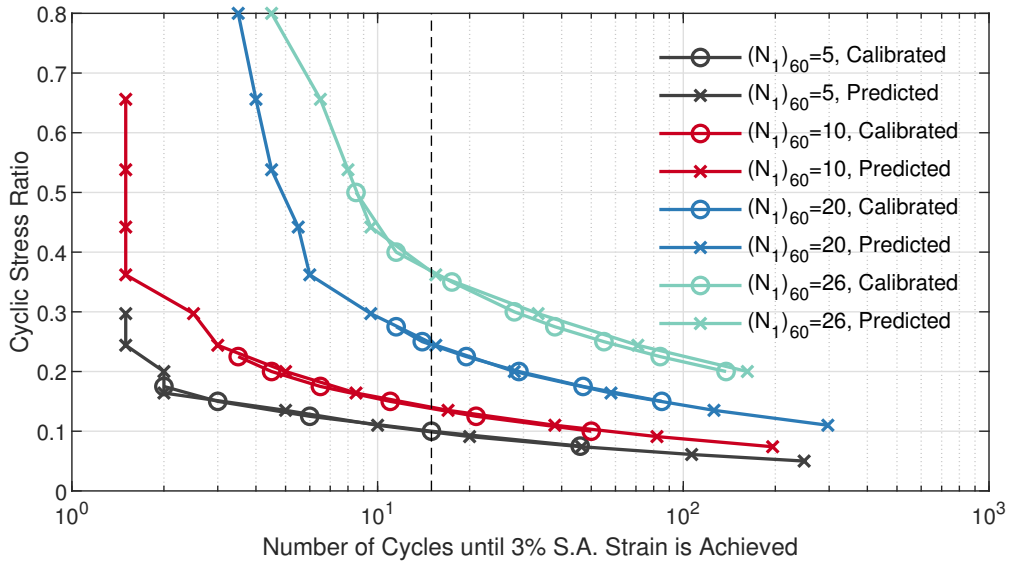

Figure 3.6: Comparison of CSR-N curves using visual-manual calibrated and predicted h_{po}.

with the model should always be examined against general soil behavior.

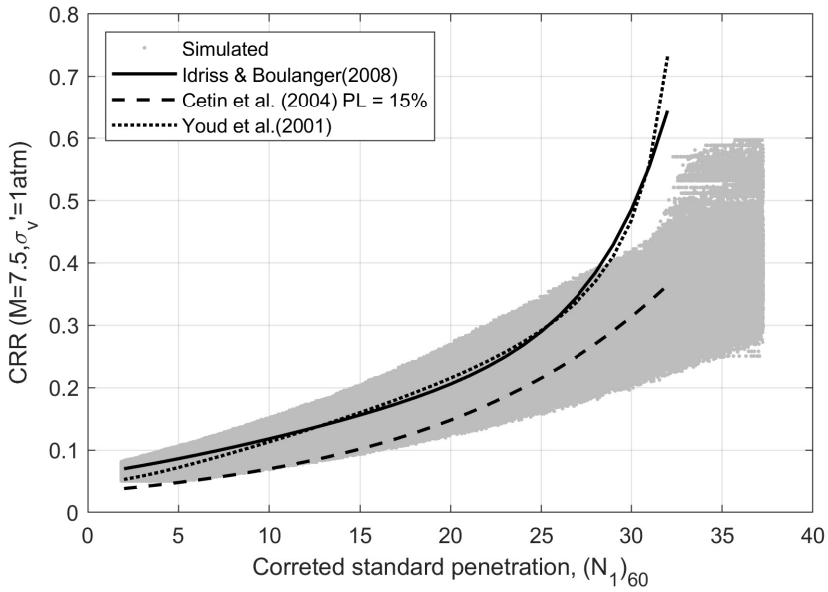

Figure 3.7: Comparison of CRR obtained using simulations with uniformly distributed h_{po} and using empirical models relating CRR to $(N_1)_{60}$ for clean sands with M = 7.5 and $\sigma'_{vc} = 1\ atm$..

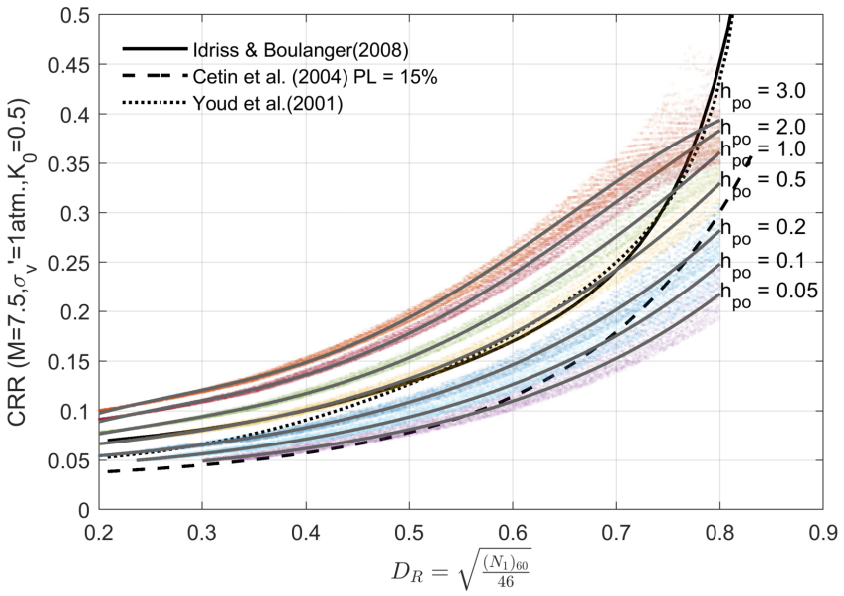

Figure 3.8: Comparison of CRR obtained using simulation with a series of constant h_{po} and using empirical models relating CRR to $(N_1)_{60}$ for clean sands with $M = 7.5$ and $\sigma'_{vc} = 1\ atm.$.

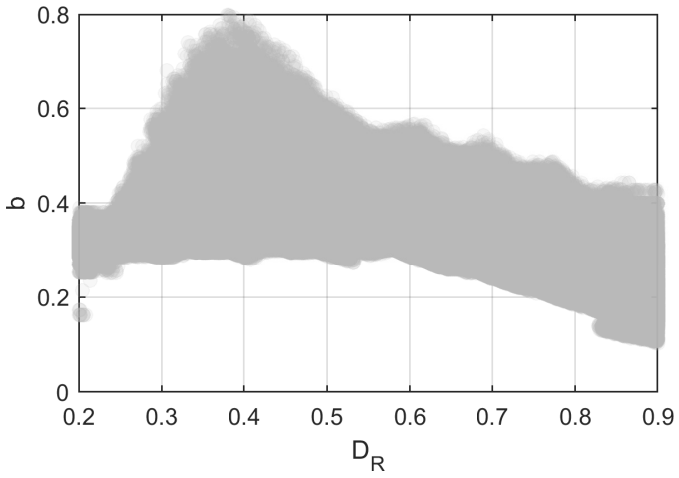

(a)

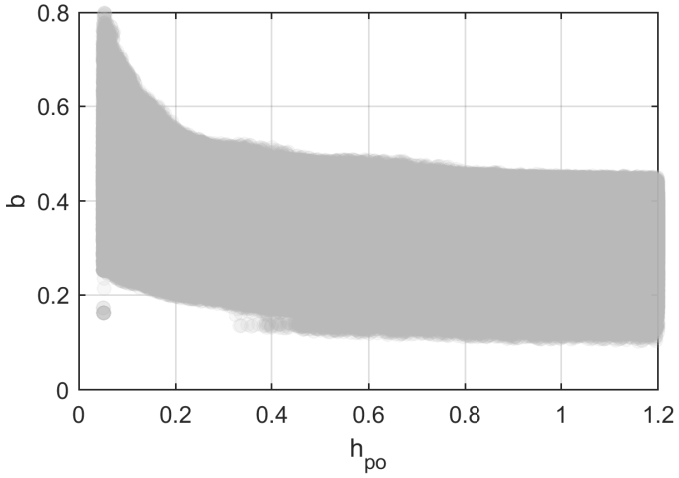

(b)

Figure 3.9: Correlation between the slope of CRR curves, b, and the primary parameters, D_R and h_{po}, respectively.

3.6 Summary

This chapter presents a brief introduction to the PM4Sand model and a discussion on key formulation aspects. Implementation details including stress correction strategies and integration schemes are also presented followed by a brief introduction to the OpenSees built-in commands that were considered in its implementation.

A parametric study was conducted to investigate PM4Sand's behavior under a large range of parameters to shed light on its calibration. Despite some limitation for representing dense sand behavior, a correlation was proposed from this study that provides a reasonable estimation of h_{po} for a given combination of D_R, G_o, and CRR, that can be used to speed up a calibration process when calibration has to be performed for each soil unit in a profile that shows large geological variability. The slope of the CRR curve, b, obtained using PM4Sand is also presented and was shown to be representative for clean sands. However, undrained CDSS tests performed on Ottawa F-65 sand (Bastidas, 2016) showed b values that are less than what would be expected indicating the limitation of just calibrating for primary parameters.

Chapter 4

VERIFICATION OF PM4SAND IN OPENSEES

4.1 Introduction

This chapter presents results of a verification study of the PM4Sand model implemented in OpenSees. Verification is meant to identify and remove programming errors in computer codes and verify numerical algorithms. The goal of this verification phase was to ensure OpenSees produced comparative results as the model's original implementation in FLAC. It was challenging since the comparison was between responses that were obtained using different numerical tools and systems, i.e., FEM and FDM. To address this issue, a series of stress point, single element, and 1D soil column analyses were considered such that system complexity was gradually increased and results were carefully examined to identify any inconsistency.

4.2 Verification of PM4Sand at an element level

4.2.1 Point level simulations using MixedDriver

Verification of the OpenSees PM4Sand implementation was first performed at a constitutive level using a constitutive driver conceived using the mixed control formulation proposed by Alawaji et al. (1992). This driver, refereed as *MixedDriver* hereafter, uses a mixed control formulation and was designed to include all necessary OpenSees libraries such that the same model implemented in OpenSees can be tested in the driver. Mixeddriver gives the user full control of strain and/or stress loading under drained or undrained conditions and represents a material point. In this context, it does not require definition of elements or boundary conditions as in standard OpenSees analyses. It is suitable for any verification study at an element level without bringing extra complexities related to the boundary value

solution framework. Using this driver, a series of drained and undrained monotonic and cyclic tests for three different relative densities, namely 35%, 55%, and 75%, were simulated using PM4sand and the example parameters published in Boulanger and Ziotopoulou (2017). These parameters are summarized in Table 4.1. All FLAC results presented in this section were obtained using the FLAC example drivers provided by Boulanger and Ziotopoulou (2017) on `https://pm4sand.engr.ucdavis.edu/pm4sand-files/`. PM4Sand model version 3.1 compiled for FLAC 8.0 was used.

Table 4.1: PM4Sand parameters for verification cases

$(N_1)_{60}$	V_{s1} using Andrus and Stokoe (2000)	$\text{CRR}_{M=7.5}$ using Idriss and Boulanger (2008)	D_R	G_o	h_{po}
6	144	0.090	0.35	476.0	0.53
14	171	0.147	0.55	677.0	0.40
26	196	0.312	0.75	890.0	0.63

*After Boulanger and Ziotopoulou (2017), all secondary input parameters were assigned default values.

Fig. 4.1 illustrates comparisons between MixedDriver and corresponding FLAC results for monotonic undrained tests under various initial consolidation pressures. In all these cases the lateral pressure coefficient, K_0, was set to 1.0. MixedDriver results matched well with FLAC results in terms of stress-strain behavior and change in pore pressure. Minor discrepancies were observed in post peak softening for higher confining pressures (Fig. 4.1a) and peak shear stress under sustained loading for a dense case (Fig. 4.1c).

The same tests were repeated using an initial $K_0 = 0.5$ and the results are presented in Fig. 4.2. It was shown that MixedDriver tends to over-predict the reduction in vertical effective stress, especially for loose cases (smaller relative density) under higher initial confining pressures (Fig. 4.2a). As shearing continues, the MixedDriver response tends to converge

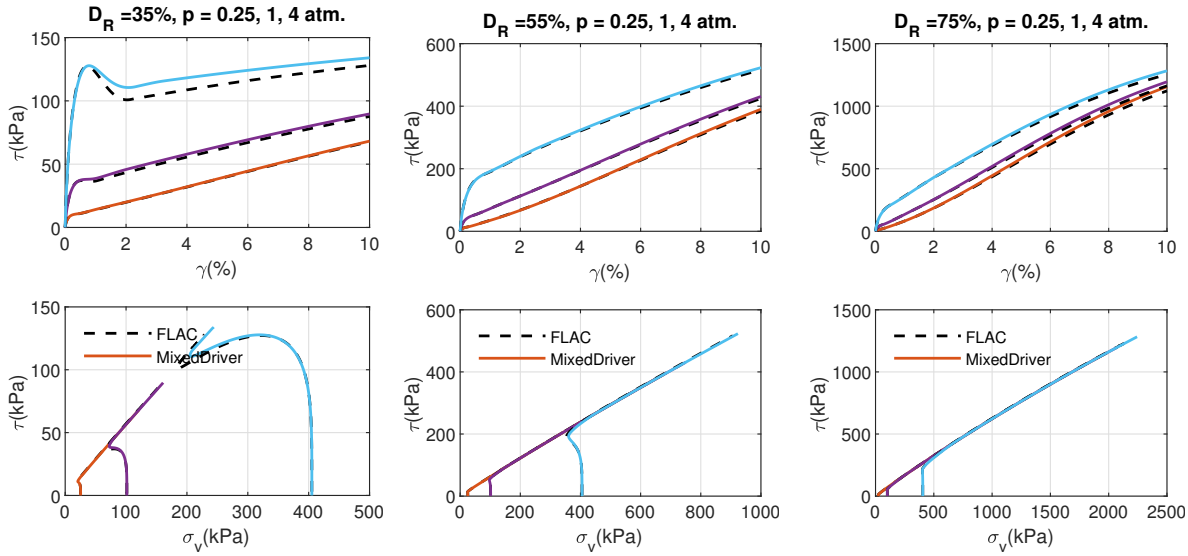

(a) (b) (c)

Figure 4.1: Comparison of responses obtained using MixedDriver (solid lines) and FLAC (dashed lines) for undrained monotonic DSS tests with (a) $D_R = 35\%$, (b) $D_R = 55\%$, (c) $D_R = 75\%$ under various initial vertical stresses of $\sigma_v = 0.25$, 1, and 4 atm., respectively, and $K_0 = 1.0$.

to the corresponding FLAC response. A detailed study was conducted to investigate the cause of this discrepancy. For this purpose, the strain history from FLAC was imported into MixedDriver and internal parameters were compared with FLAC step by step to identify any possible discrepancy in the formulation and implementation. Although no mistake was found, this discrepancy was narrowed down to be related to the method used for updating the back-stress ratio, $\boldsymbol{\alpha}$. As shown in Eq. 3.33, the increment $\dot{\boldsymbol{\alpha}}$ is proportional to $\boldsymbol{\alpha}^b - \boldsymbol{\alpha}$. Under a simple shear stress path, the loading direction, $\mathbf{n}$, written in vector form is,

$$\{\mathbf{n}\} = \begin{Bmatrix} 0 \\ 0 \\ \frac{\sqrt{2}}{2} \end{Bmatrix}. \tag{4.1}$$

Thus $\boldsymbol{\alpha}^b$ is in the form of,

$$\{\boldsymbol{\alpha}^b\} = \sqrt{1/2}[M^b - m]\{\mathbf{n}\} = \begin{Bmatrix} 0 \\ 0 \\ \alpha_{12}^b \end{Bmatrix}. \tag{4.2}$$

Assuming K_0 conditions with no initial static shear stress, the initial $\boldsymbol{\alpha}$ is,

$$\{\boldsymbol{\alpha}_o\} = \left\{\frac{\boldsymbol{\sigma} - p\mathbf{I}}{p}\right\} = \begin{Bmatrix} K_0\sigma_v \\ \sigma_v \\ 0 \end{Bmatrix}/p - \begin{Bmatrix} \frac{(K_0+1)\sigma_v}{2} \\ \frac{(K_0+1)\sigma_v}{2} \\ 0 \end{Bmatrix}/p = \begin{Bmatrix} \frac{(K_0-1)\sigma_v}{2} \\ \frac{(1-K_0)\sigma_v}{2} \\ 0 \end{Bmatrix}/p = \begin{Bmatrix} \frac{K_0-1}{K_0+1} \\ \frac{1-K_0}{K_0+1} \\ 0 \end{Bmatrix}, \tag{4.3}$$

where p is the mean effective stress. Recall that,

$$\dot{\boldsymbol{\alpha}} = \langle L \rangle \frac{2}{3} h(\boldsymbol{\alpha}_\sigma^b - \boldsymbol{\alpha}). \tag{4.4}$$

Therefore, under a simple shear stress path, $\boldsymbol{\alpha}$ will eventually converge to a state where $\alpha_{11} = \alpha_{22} = 0$ which is governed by $\boldsymbol{\alpha}^b$. The rate of this convergence was found to be related to the initial K_0. In FLAC's mixed discretization scheme, the zone (consisting of four subzones) averaged stresses are used to compute a new dilatancy D and plastic modulus K_p that are consistent with the average response of the zone over a time step. These values for D and K_p are then used by all four subzones in the next time step, i.e., lagging one step. In contrast, in OpenSees, the values of D and K_p are evaluated and used to update $\boldsymbol{\alpha}$ within the same step. The difference in calculated $\boldsymbol{\alpha}$ is cumulative and can lead to noticeable differences in the evolution of σ_v and σ_h at the beginning of loading when $K_0 \neq 0$. It can also lead to noticeable discrepancy in pore pressure evolution under sustained loading, e.g., cyclic tests continued for multiple cycles.

Because PM4Sand was calibrated for general soil behavior using FLAC, it was preferable to apply a slight modification to the model formulation to capture the general response obtained using FLAC. In this case, matching number of cycles to liquefaction instead of individual cycle's of pore pressure generation was emphasized. For this purpose, a parametric study was conducted to find out a reasonable implementation strategy to compensate the

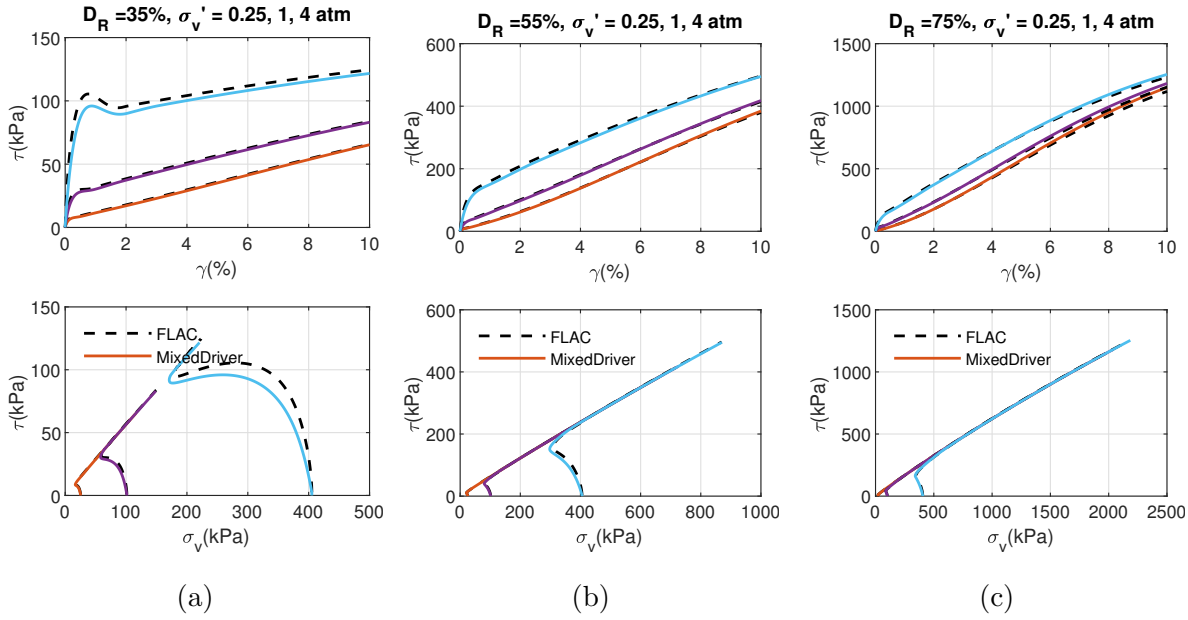

Figure 4.2: Comparison of responses obtained using MixedDriver (solid lines) and FLAC (dashed lines) for undrained monotonic DSS tests with (a) $D_R = 35\%$, (b) $D_R = 55\%$, (c) $D_R = 75\%$ under various initial vertical stresses of $\sigma_v = 0.25$, 1, and 4 atm., respectively, and $K_0 = 0.5$.

faster pore pressure buildup. In this context, the term C_D in Eq. 3.39, which is only for calibration purposes, and not related to any physical quantity, was chosen and modified from 0.10 to 0.16 in the OpenSees implementation. All the results presented hereafter were obtained using this new value.

Figs. 4.3 and 4.4 show comparisons between MixedDriver and corresponding FLAC results for cyclic direct simple shear (CDSS) tests using various D_Rs. The results show that the OpenSees implementation in MixedDriver was able to capture the general trends produced by FLAC. The tests were repeated for different vertical consolidation stresses to show the effect of overburden pressure. Comparison between MixedDriver and FLAC results for cyclic stress ratios vs. number of uniform loading cycles are illustrated in Fig. 4.5 and show good match.

Fig. 4.6 presents a comparison between the overburden correction factor K_σ calculated using these simulations and the relationship recommended by Boulanger and Idriss (2004). The good agreement observed in the figure verifies the model's capability to capture the effect of confining stress at stress point level.

The effect of initial static shear stress was also verified by simulations with various initial static shear stress ratios of 0.1, 0.2, and 0.3. These static shear stresses were applied during model initialization based on an effective vertical stress of 1 atm.. Fig. 4.7 illustrates the comparison between MixedDriver and corresponding FLAC results. The results are similar and agreeable indicating that the presence of an initial static shear stress results in lower cyclic strengths for loose sand and larger cyclic strengths for denser sands.

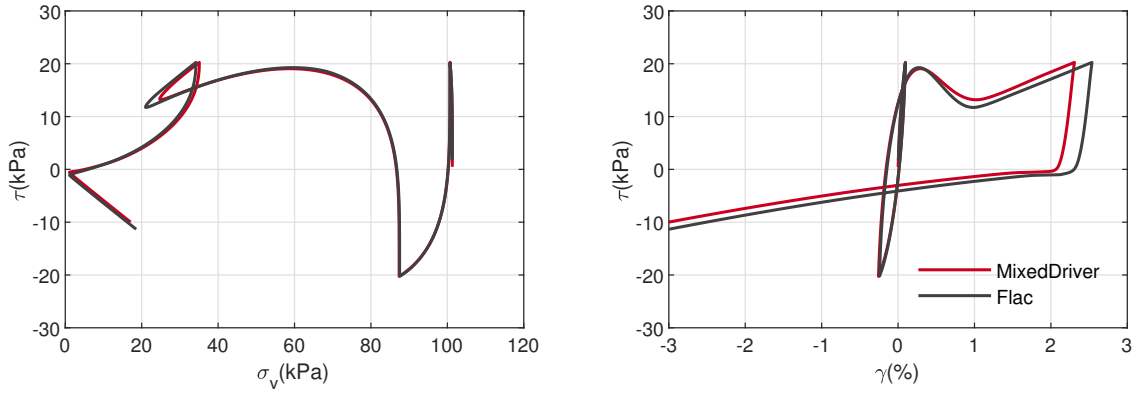

(a)

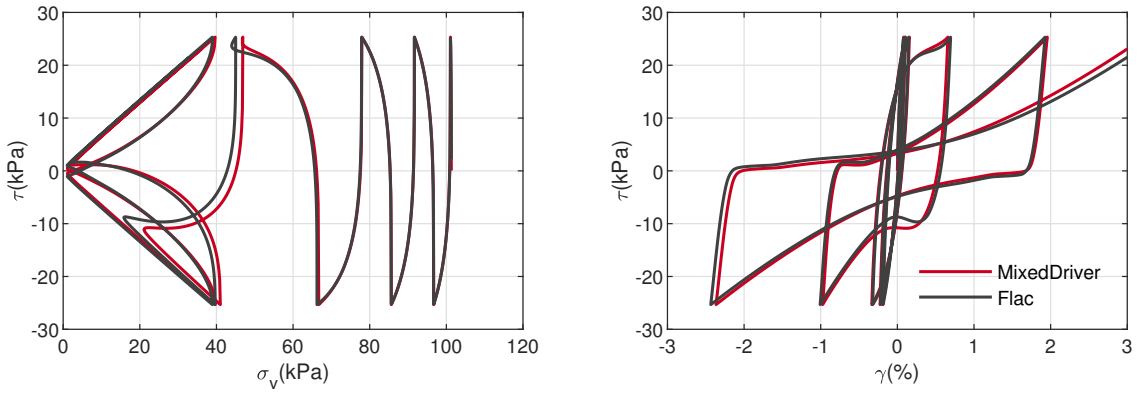

(b)

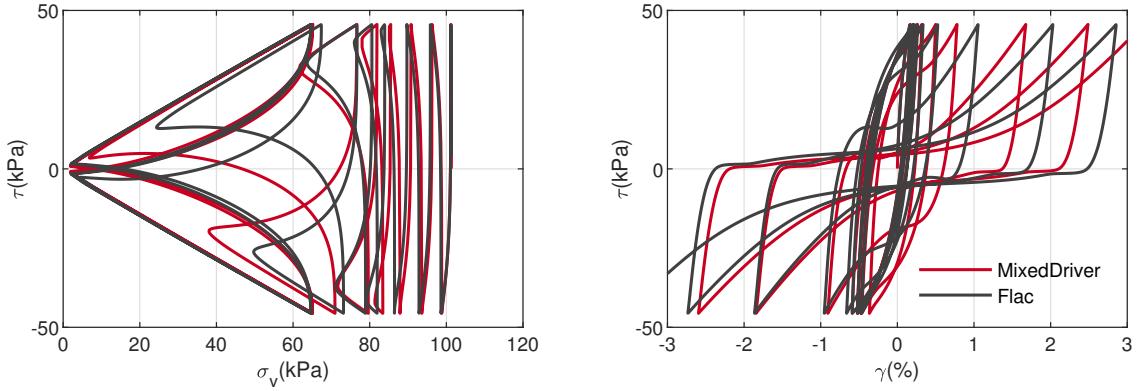

(c)

Figure 4.3: Comparison of results obtained using MixedDriver and FLAC for undrained CDSS tests for various D_Rs with an initial vertical stresses of 1 atm. and $K_0 = 1.0$. (a) D_R = 35%, (b) $D_R = 55\%$, (c) $D_R = 75\%$.

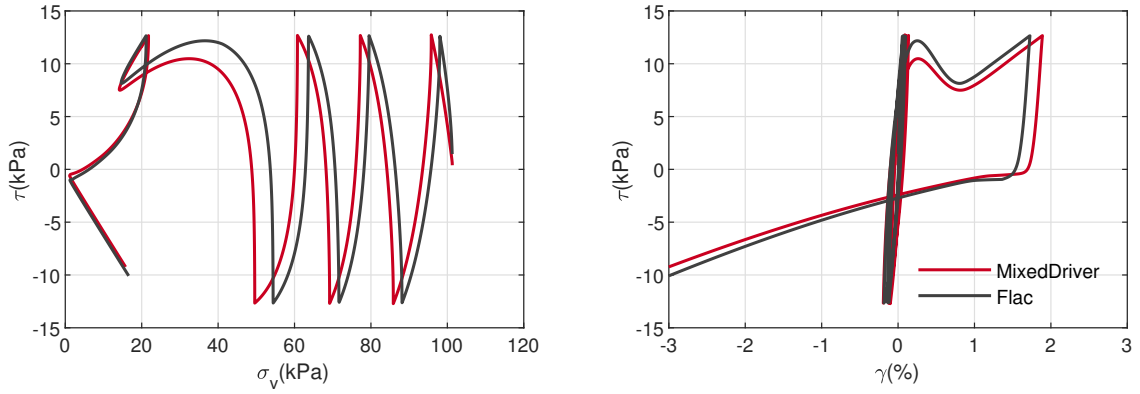

(a)

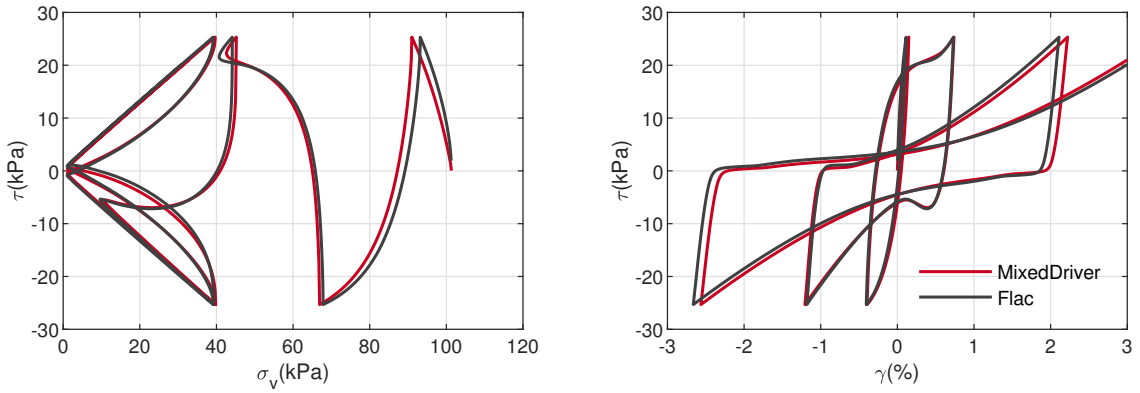

(b)

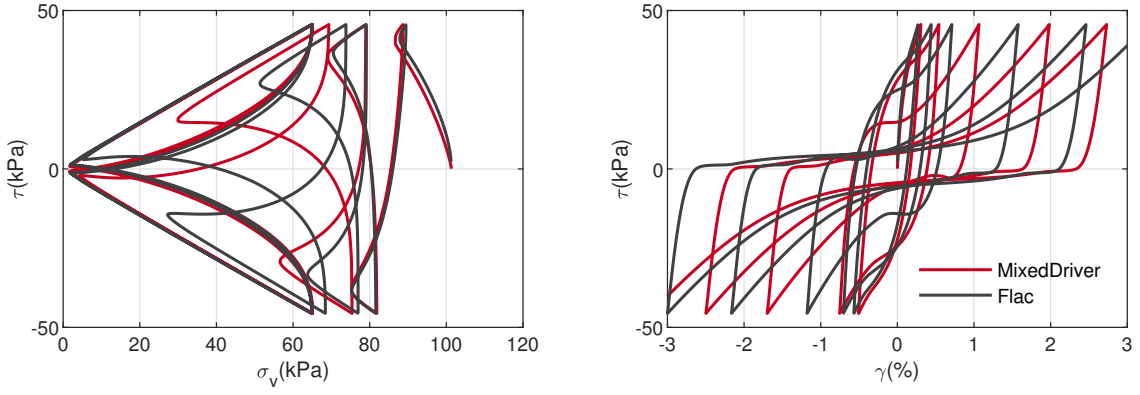

(c)

Figure 4.4: Comparison of results obtained using MixedDriver and FLAC for undrained CDSS tests for various D_Rs with an initial vertical stresses of 1 atm. and $K_0 = 0.5$. (a) $D_R = 35\%$, (b) $D_R = 55\%$, (c) $D_R = 75\%$.

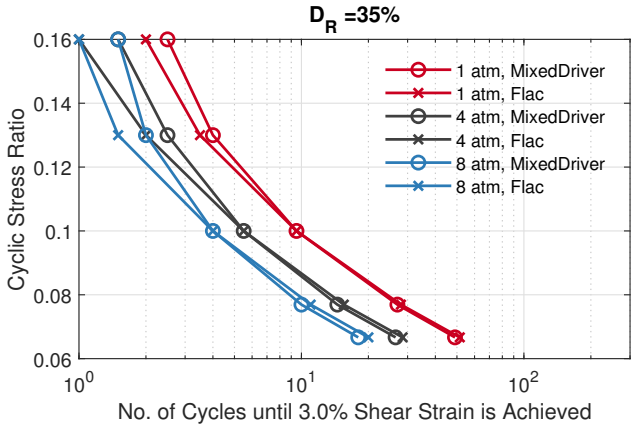

(a)

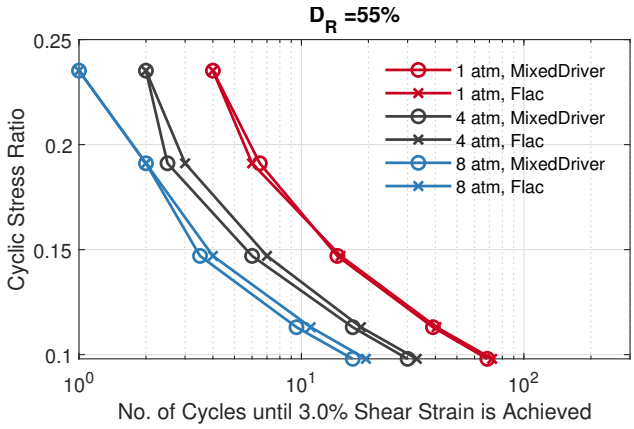

(b)

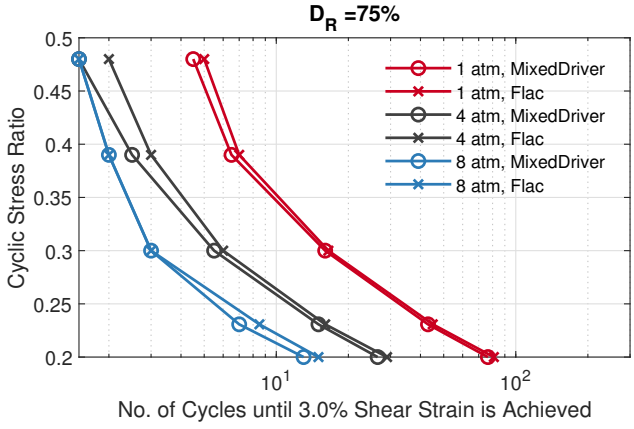

(c)

Figure 4.5: Cyclic stress ratios vs. number of cycles to reach 3% SA shear strain for (a) D_R = 35%, (b) D_R = 55%, (c) D_R = 75% with initial vertical consolidation stresses of σ_v = 1, 4, and 8 atm. and K_0 = 0.5.

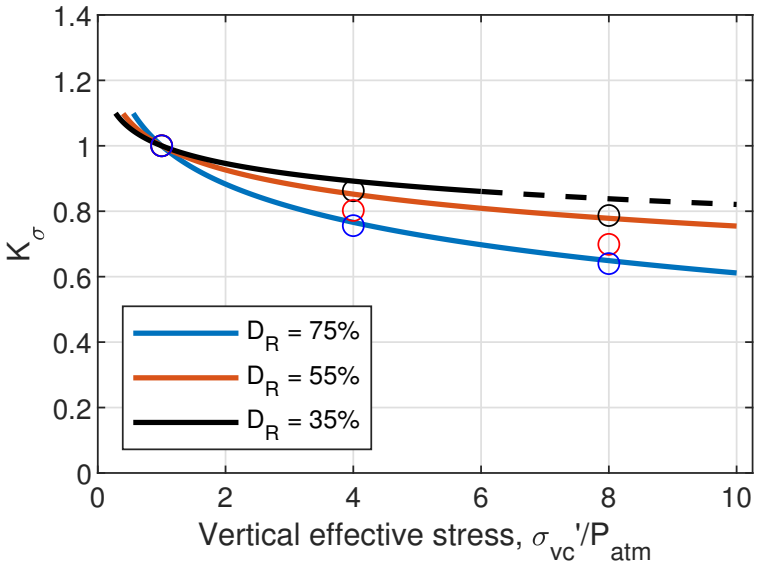

Figure 4.6: Comparison of simulated K_σ factors, determined at 15 uniform cycles to cause 3% SA shear strain, to relationships recommended by Idriss and Boulanger (2008).

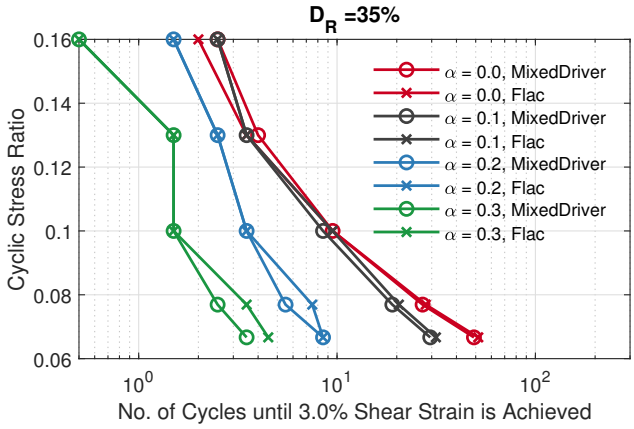

(a)

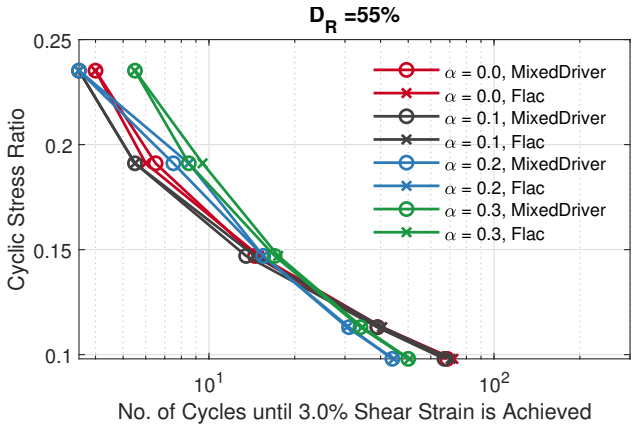

(b)

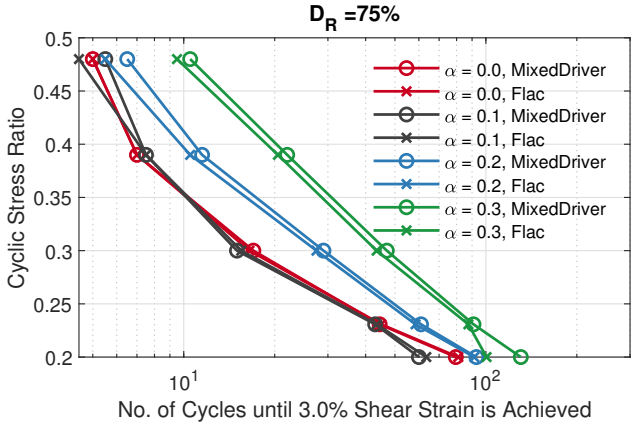

(c)

Figure 4.7: Cyclic stress ratios vs. number of cycles to reach 3% SA shear strain for (a) D_R = 35%, (b) D_R = 55%, (c) D_R = 75% with an initial static shear stress ratios (α) of 0.0, 0.1, 0.2, and 0.3, $\sigma_v = 1$ atm. and $K_0 = 0.5$.

4.2.2 Single-element simulations using OpenSees

After simulations using MixedDriver showed satisfactory results, the model was carried into OpenSees and its response in OpenSees was verified using single element analyses. The model was paired with coupled four-node quadrilateral elements in OpenSees, namely SSPquadUP (McGann et al., 2015) and QuadUp (Yang et al., 2003), respectively, to investigate the effective stress response under undrained conditions which is the most common application scenario for this model. The results using both elements showed good match with MixedDriver and FLAC simulations. For brevity, only results obtained using the SSPquadUP element are presented here. This element uses a single integration point and a stabilization method to prevent hour-glass locking modes. In addition to nodal displacements this element provides a pore water pressure degree of freedom. This pore water pressure is store in a velocity vector. Therefore, transient analyses are necessary in all undrained simulations. For this purpose, during the OpenSees simulation, the Newmark integration scheme was used to advance in time with parameters $\beta = \frac{5}{6}$ and $\gamma = \frac{4}{9}$. This pair of β and γ were chosen to introduce additional numerical damping and damp out any undesirable vibrations not included in MixedDriver results.

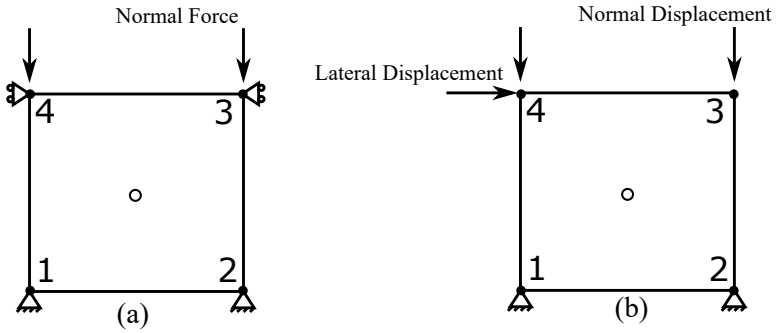

Figure 4.8: SSPquadUP element configuration for strain-controlled cyclic simple shear test during: (a) consolidation phase, and (b) shearing phase.

In contrast to MixedDriver, the OpenSees simulations require the application of forces

and/or displacements to impose initial conditions and shearing loads. In OpenSees, during the consolidation phase, the bottom of the element was fixed in all directions and the top nodes of the element were tied together in the horizontal direction (using *EqualDOF*). A normal pressure in the form of concentrated loads to the nodes, was applied to the top nodes to create a consolidation condition. Fig. 4.8a illustrates the test configuration during the consolidation stage. Normal forces were incrementally increased at the nodes until the desired consolidation pressure was reached in the element. During this phase a Poisson's ratio, $\nu = 0.33$ was used to produce an initial lateral stress that matched a $K_0 = 0.5$. The example OpenSees single element drivers can be found at `https://opensees.github.io/OpenSeesDocumentation/user/manual/material/ndMaterials/PM4Sand.html`.

Fig. 4.8b illustrates the test configuration during the shearing phase. During this phase, the normal forces were replaced by equivalent vertical nodal displacements to maintain the pressure. The material was re-initialized and ν was updated to 0.3 before applying a lateral displacement that was used to apply shearing. Figs. 4.9 and 4.10 compare results obtained using the OpenSees single element model and the corresponding results from the single point integration method using MixedDriver and FLAC single element model. The good match attained demonstrates the implementation of the constitutive model in OpenSees is accurate and reproduce the expected response.

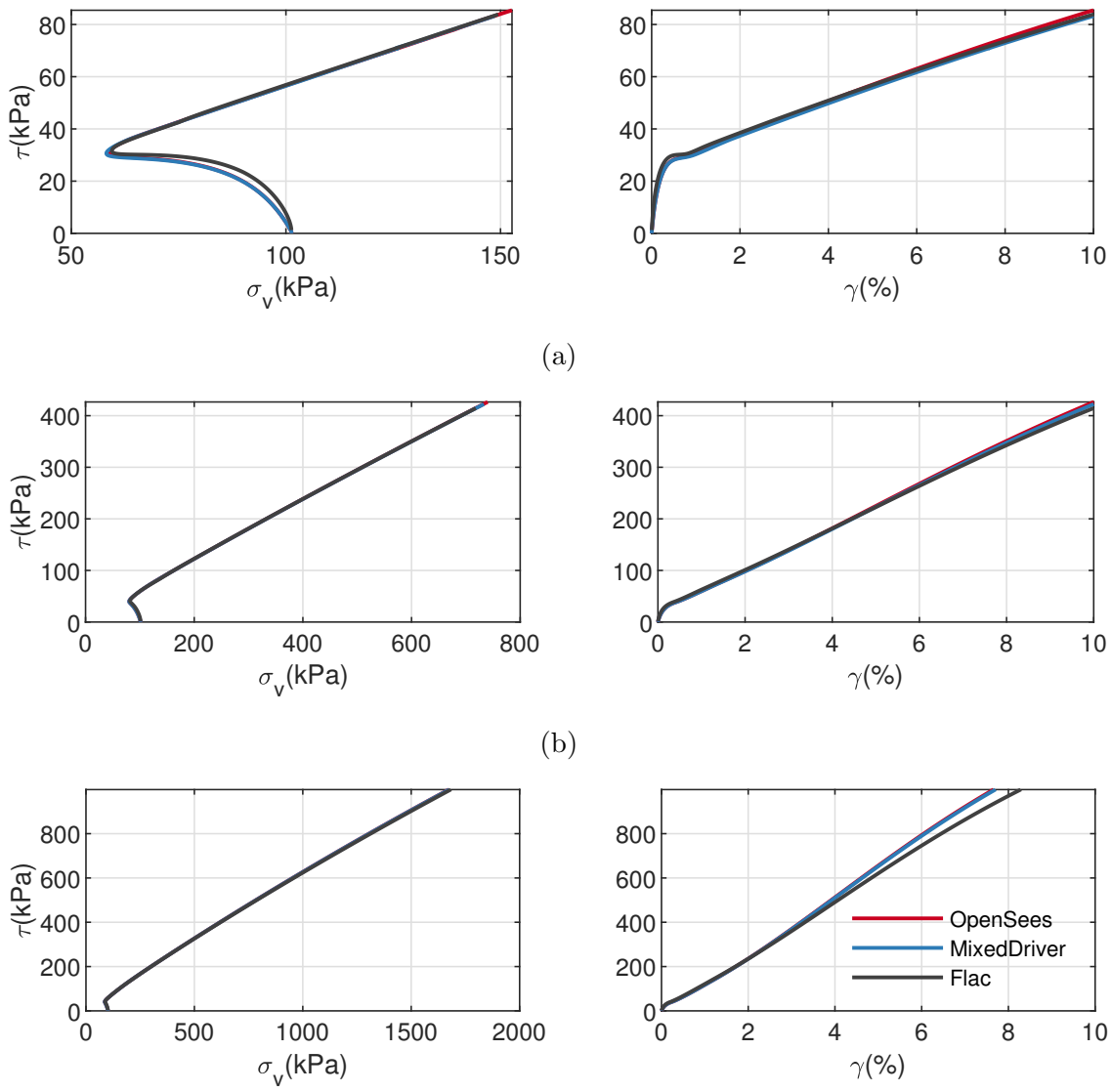

(a)

(b)

(c)

Figure 4.9: Comparison of results obtained using MixedDriver, OpenSees, and FLAC for an undrained monotonic DSS loading, initial vertical stress $\sigma_v = 1$ atm., and various D_R: (a) $D_R = 35\%$, (b) $D_R = 55\%$, (c) $D_R = 75\%$.

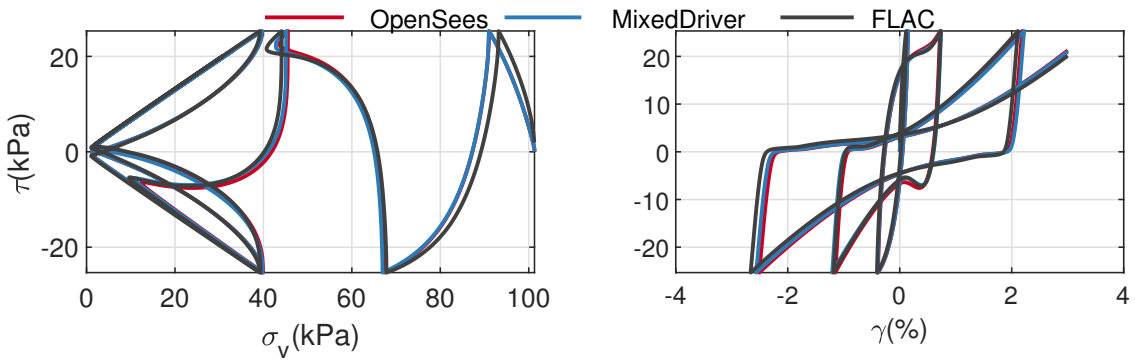

Figure 4.10: Comparison of results obtained using MixedDriver, OpenSees, and FLAC for an undrained cyclic DSS loading, initial vertical stress of 1 atm., and $D_R = 55\%$.

4.3 Verification of PM4Sand using 1D level ground site response analysis

Once verified at point and element levels, PM4Sand was verified using 1D soil columns. For this purpose, a group of 1D single columns of quadrilateral elements was used to simulate site response analysis using the OpenSees framework. The objective was to test the implementation and assess whether or not the model performed well in a more practical geotechnical scenario. The results were also compared with FLAC analyses performed by Andrew Makdisi at the University of Washington, and PLAXIS 2D analyses performed by Gregor Vilhar at PLAXIS, BV. This study offered the opportunity to directly compare the response of the same model (PM4Sand) implemented in three different frameworks and used by three different users. Among other things, this study provided the opportunity to assess variability associated with each framework, e.g., discretization scheme, solid-fluid coupling, and different implementation details. An independent verification study also showed good agreement between PLAXIS and FLAC at the element level (Vilhar et al., 2018).

4.3.1 Model building

Soil profile and material properties

For this verification study, six synthetic 1D soil profiles were created. As shown in Fig. 4.11, each profile had a layered soil configuration composing of a dry crust, a liquefiable layer, and a base layer. The dry crust and liquefiable layers had an uniform $(N_1)_{60}$. A total of three $(N_1)_{60}$ values, 5, 10, and 20, were considered to cover a wide range of soil conditions. The ground water table (GWT) was located at 2m below the surface for all three cases and the liquefiable layer was underlain by a 1m base layer. Both the liquefiable layer and dry crust were modeled using PM4Sand. The base layer was modeled using an elastic isotropic material that was available in all three programs. This layer was included only because, in FLAC, PM4Sand cannot be used in the bottom row of elements above a compliant base, which is not the case for OpenSees and PLAXIS. Thus, this layer can be omitted in practice when using OpenSees or PLAXIS. Two different thicknesses of liquefiable layer, 3m and

6m, were considered to study the effect of thickness of liquefiable layer on the response. As schematic of the soil column is illustrated in Fig. 4.11. All the simulated soil profiles are listed in Table 4.2.

Table 4.2: Summary of 1D soil profiles.

ID	Thickness of liquefiable layer(m)	$(N_1)_{60}$
N5T3	3	5
N5T6	6	5
N10T3	3	10
N10T6	6	10
N20T3	3	20
N20T6	6	20

The model calibration followed the procedure recommended by Boulanger and Ziotopoulou (2017) for a case where in-situ tests were available. D_R was estimated based on $(N_1)_{60}$ as,

$$D_R = \sqrt{\frac{(N_1)_{60}}{C_d}}\,, \tag{4.5}$$

where $c_d = 46$ (Idriss and Boulanger, 2008). The overburden stress-corrected shear wave velocity V_{s1} was estimated using the correlation proposed by Andrus and Stokoe (2000),

$$V_{s1} = 85[(N_1)_{60} + 2.5]^{0.25}\,, \tag{4.6}$$

and the small strain shear wave velocity V_s at each location was calculated using Robertson (1991),

$$V_s = \rho V_{s1}\Big(\frac{\sigma'_v}{p_A}\Big)^{0.25}\,, \tag{4.7}$$

where σ_v is the initial vertical effective stress and p_A is atmospheric pressure. The relationship for G_{max} in PM4Sand is based on mean in-plane effective stress, and the model input

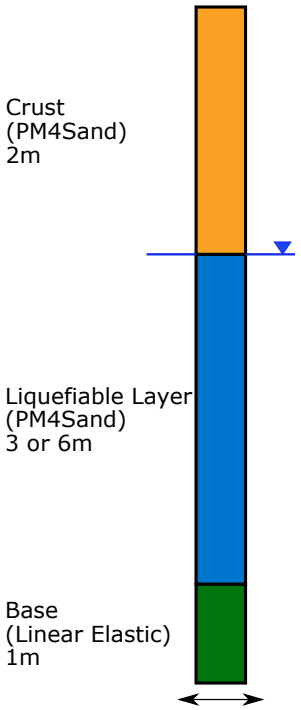

Figure 4.11: Illustration of the 1D level ground model.

parameter G_o was calculated from the following equation,

$$G_{max} = \rho V_s^2 = G_o p_A \left(\frac{p}{p_A}\right)^{0.5} = G_o p_A \left(\frac{1+K_0}{2}\frac{\sigma'_v}{p_A}\right)^{0.5}, \tag{4.8}$$

where $K_0 = 0.5$. ρ is the density of soil and it was computed using default values of $e_{max} = 0.8$ and $e_{min} = 0.5$, and specific gravity $G_s = 2.67$. Density was taken as the dry density above GWT and saturated density below. Target CRRs were calculated following the correlation proposed by Idriss and Boulanger (2008) using $(N_1)_{60}$. After determination of D_R, G_o, and CRR, h_{po} was calibrated iteratively to match CRR for a 3% single amplitude (SA) shear strain reached at 15 cycles in an undrained CDSS test. The cyclic strength curves obtained using the calibrated model parameters are presented in Fig. 4.12 and the resulting input material properties are summarized in Table 4.3. All secondary parameters were kept at their default values.

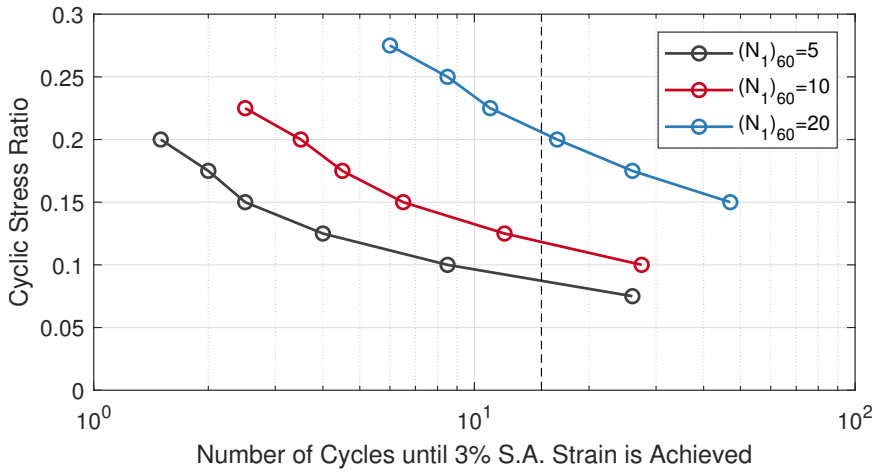

Figure 4.12: Number of cycles required to reach 3% SA shear strain in simulated undrained CSS tests with initial $K_0 = 0.5$ for three D_Rs.

The density of the isotropic elastic material was set to be same as the saturated density of the layer above, and its stiffness was chosen to produce a wave impedance ratio ($\rho_2 v_2/\rho_1 v_1$) = 1.3. The properties of the isotropic elastic material are summarized in Table 4.4. A small (10^{-10} m/s) permeability was chosen for all layers to minimize pore pressure migration and its effect on material response. It is worth mentioning that the so called *permeability* input parameter in FLAC and OpenSees is defined as the conventional hydraulic conductivity (units: [L/T] - e.g., m/sec) divided by unit weight of water (units: [F/V] - e.g., Pa/m). Some literature refers it as *dynamic permeability coefficient* (Jose Parra, 1996). In PLAXIS, the conventional hydraulic conductivity is directly input.

Input motions

Three outcrop motions were selected based on computed CRR so that their peak horizontal accelerations were high enough to induce factors of safety < 1 for liquefaction triggering

Table 4.3: Input parameters for PM4Sand

	N5T3 & N5T6		N10T3 & N10T6		N20T3 & N20T6	
	Dry	Saturated	Dry	Saturated	Dry	Saturated
D_R	0.330	0.330	0.466	0.466	0.659	0.659
G_o	354.0	447.0	468.3	584.1	651.0	798.0
h_{po}	0.533	0.533	0.463	0.450	0.425	0.388
$\gamma(kN/m^3)$	15.40	19.44	15.80	19.70	16.30	20.0
$CRR_{M=7.5}$	0.086	0.086	0.118	0.118	0.206	0.206

Table 4.4: Input parameters for isotropic elastic material

	N5T3	N5T6	N10T3	N10T6	N20T3	N20T6
$V_s(m/s)$	159.0	176.0	182.0	200.0	212.0	235.0
$E(kPa)$	1.30×10^5	1.60×10^5	1.73×10^5	2.09×10^5	2.38×10^5	2.93×10^5
ν	0.3					
$\gamma(kN/m^3)$	19.44	19.44	19.70	19.70	20.0	20.0

following the correlation proposed by Seed and Idriss (1971),

$$CSR = 0.65 \frac{\sigma_{vc}}{\sigma'_{vc}} \frac{a_{max}}{g} r_d \,, \tag{4.9}$$

where r_d is a shear stress reduction coefficient calculated using the correlation proposed by Idriss and Boulanger (2008).

Although a rigorous sensitivity study on the effect of input motion was not included in this study, attention was paid during motion selection so that the motions had different characteristics, including peak ground acceleration (PGA), duration, and predominant frequency. The selected motions were: RSN766, Gilroy #2 of 1989 Loma Prieta earthquake; RSN963, 1994 NorthRidge earthquake; and RSN1203, 1999 Chi-Chi earthquake. In this work they

are refereed by their ID number hereafter. Acceleration time histories and response spectra of each motion are presented in Fig. 4.13. Details of these motions are listed in Table 4.5. Note that a fourth motion was also included. This motion is a scaled version of RSN766 with PGA of 0.02g, and it was used to verify boundary and initial conditions of the soil columns and ensure consistency among different platforms. More information is given in the following section.

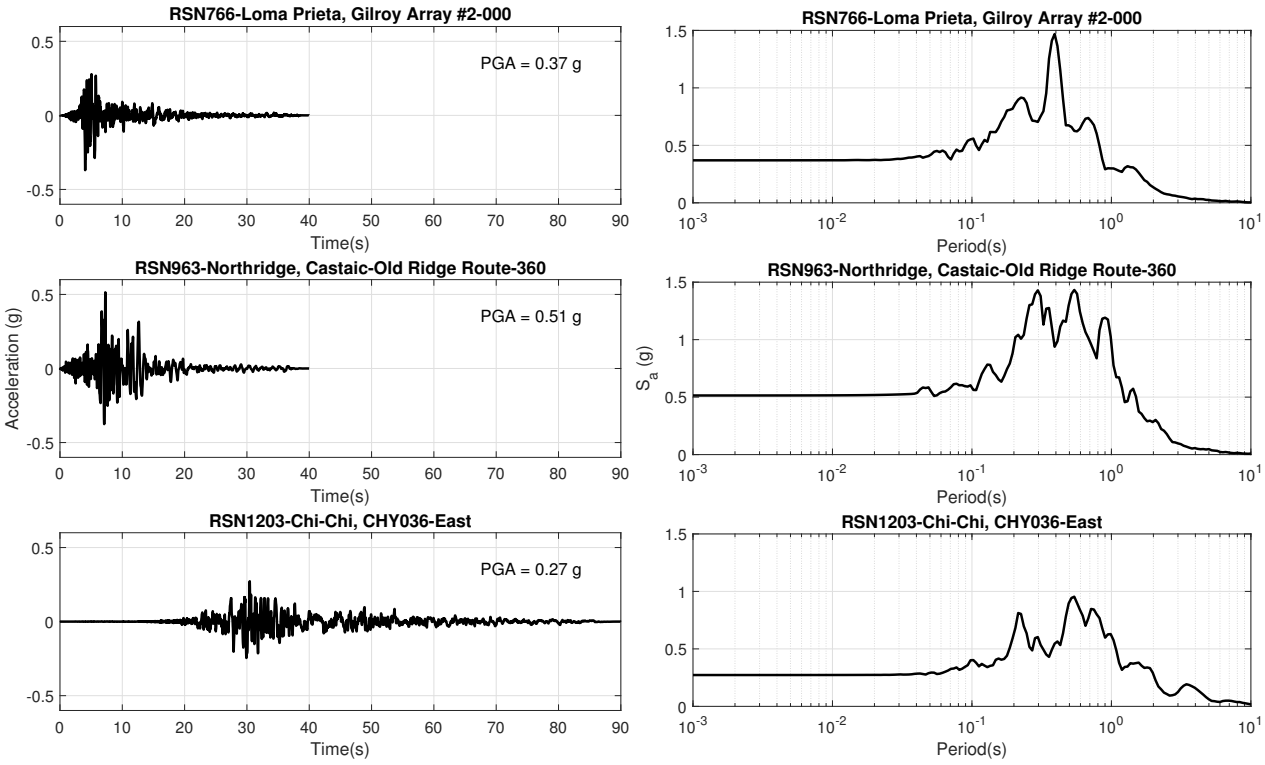

(a) (b)

Figure 4.13: Summary of selected input motions. (a) Acceleration time histories. (b) Acceleration response spectra with 5% damping.

Table 4.5: Details of selected input motions

Name	Duration(s)	Time Step(s)	PGA(g)
RSN766_G02_000(Loma Prieta)	39.99	0.005	0.37
RSN963_ORR_360(NorthRidge)	40	0.02	0.51
RSN1203_CHY036_E(Chi-Chi)	90	0.005	0.27
RSN766_G02_000_VEL_0p02g(Loma Prieta, scaled)	39.99	0.005	0.02

Boundary conditions

In OpenSees, simulation of the groundwater table (GWT) was achieved by fixing the nodal degrees of freedom for pore pressure at the selected GWT depth. Therefore, no pore water pressure was allowed to develop in the dry zone. In FLAC, the GWT was modeled by setting initial pore pressures to be zero above the GWT. However, these dry nodes could experience change in pore pressure due to dissipation of excess pore water pressure from underlain nodes. In PLAXIS, the dynamic-with-consolidation analysis type allows excess pore pressure development above the GWT. Thus, pore pressure migration to the dry layer above GWT was expected in FLAC as well as in PLAXIS results.

Displacement degrees of freedom were tied at the same elevation in all three programs. In this study, quadrilateral SSPquadUP elements were used in all OpenSees analyses. Quadrilateral zones with four overlapping triangular subzones were used in FLAC analyses. Therefore, the OpenSees and FLAC columns both had one element/zone at each level. On the other hand, there are no quadrilateral element available in PLAXIS, so higher order fifteen-node triangular elements were used. This led to more than one element at each level in the PLAXIS columns (Fig. 4.15). Therefore, although vertical side boundaries were tied together in all three models to represent a 1D free field wave propagation, some degree of two dimensional response might be present in PLAXIS model results.

The input motion was applied through a Lysmer dashpot (Lysmer and Kuhlemeyer, 1969)

and the stiffness of the dashpot was the same as the base elastic layer.

Analysis parameters

Rayleigh damping was added to compensate for small strain damping which is observed in lab tests results, and not captured by the model in its elastic range. FLAC uses a single frequency formulation for Rayleigh damping and f_{min} and ξ_{min} are the required input parameters, while OpenSees and PLAXIS use a two frequency formulation, where α and β are the required input parameters. f_{min} and ξ_{min} can be related to α and β through:

$$\begin{aligned} \alpha &= \frac{2\xi_c \omega_1 \omega_2}{\omega_1 + \omega_2}\,, \\ \beta &= \frac{2\xi_c}{\omega_1 + \omega_2}\,, \end{aligned} \tag{4.10}$$

$$\begin{aligned} \alpha &= \xi_{min}\omega_{min}\,, \\ \beta &= \xi_{min}/\omega_{min}\,, \end{aligned} \tag{4.11}$$

and

$$\xi_{min} = 2\pi f_{min}\,, \tag{4.12}$$

where ξ_{min} is the minimum damping ratio and f_{min} is the corresponding frequency. Fig. 4.14 depicts a comparison of the attained Rayleigh damping in both cases. The two frequencies were selected as the natural frequency of the soil column ($\frac{V_s}{4H}$, where V_s is the average shear wave velocity and H is the total thickness of the soil column) and five times the natural frequency of the soil column. This follows recommendations by Kwok et al. (2007).

Hourglass locking is a well-known problem when reduced integration schemes are used. To mitigate for this effect, the PM4Sand implementation in FLAC includes an elasto-plastic material parallel to PM4Sand that inserts artificial stiffness to the hourglass deformation modes. In OpenSees, this effect is mitigated in the SSP-family elements that use a stabilization algorithm (McGann et al., 2012) resulting in an element that is free from volumetric and shear locking. In this study, the SSPquadUP with a stabilization parameter α of 10^{-6}

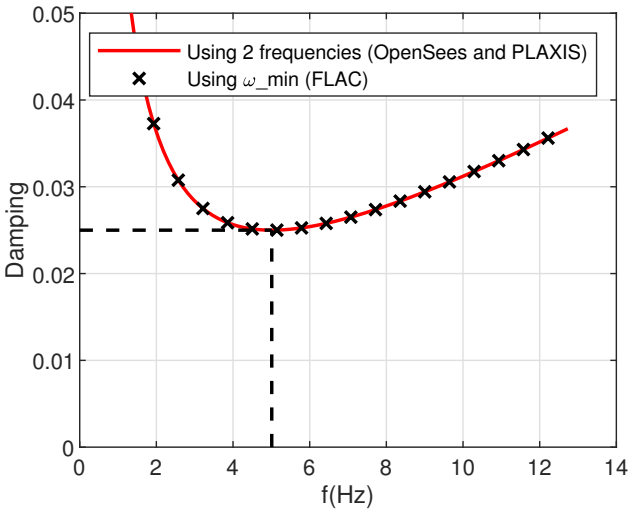

Figure 4.14: Comparison of Rayleigh damping in FLAC, OpenSees, and PLAXIS.

Table 4.6: OpenSees analysis parameters

Rayleigh Damping	α	0.786969	f_{min}	5.01
	β	0.000794	ξ_{min}	0.025
Element Size	0.25m			
Time Step	0.0001s			

was used. Since PLAXIS utilizes higher order elements and a more refined mesh, it does not require additional consideration for locking.

The selected model discretization for each platform is illustrated in Fig. 4.15. The figure clearly shows that due to different discretization schemes, the meshes were different in all three numerical models. Therefore, a verification study was required to check sensitivity of results with mesh refinement.

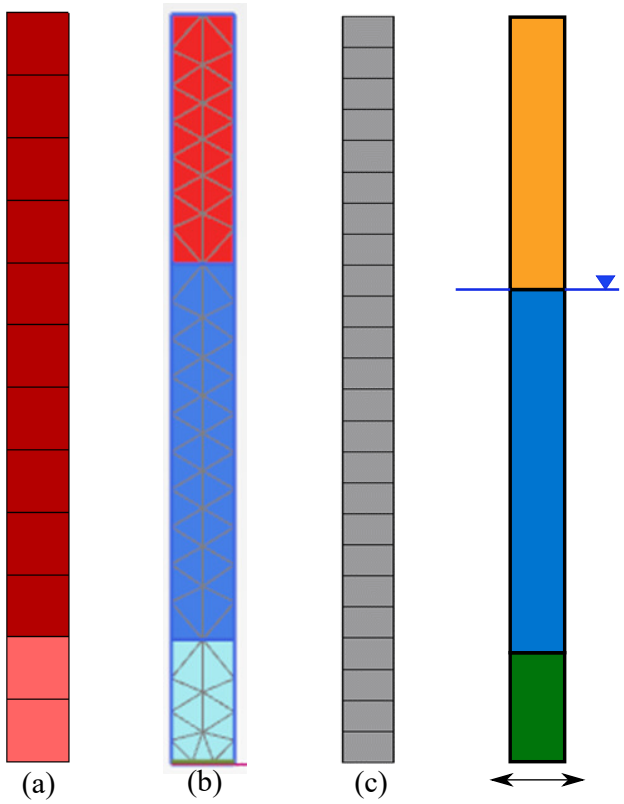

Figure 4.15: Comparison of model discretization for N10T3 case. (a) FLAC model with 12 quadrilateral zones with four triangles each, (b) PLAXIS model with 72 15-node triangular elements, and (c) OpenSees model with 24 four-node quadrilateral elements.

4.3.2 Analysis metrics

For the level ground case, peak horizontal acceleration (PHA), maximum horizontal displacement, maximum shear strain (γ_{max}), maximum excess pore pressure ratio (r_u), and maximum cyclic stress ratio (CSR) along the soil profile were used as metrics for comparison purposes and to assess the model behavior. The acceleration response at the surface was also used in this comparison.

r_u can be computed using excess pore pressure as,

$$r_u = \frac{\Delta u}{\sigma'_{v,0}}\,, \tag{4.13}$$

where Δu is the change in pore pressure and $\sigma'_{v,0}$ is the initial vertical effective stress at that location, or using the change in effective vertical stress,

$$r_u = 1.0 - \frac{\sigma'_v}{\sigma'_{v,0}}\,, \tag{4.14}$$

In this study r_u was computed using both definitions and the results were consistent within the saturated layer. In the dry layer, the stress state tends to converge to $K_0 = 1$ and σ'_v tends to change for the reason discussed in the previous section. This can lead to unrealistic r_u. Hence only the excess pore pressure based r_u results are presented.

Cyclic stress ratio (CSR) was calculated as:

$$CSR = 0.65\frac{\tau_{max}}{\sigma'_{v,0}}\,, \tag{4.15}$$

where the factor 0.65 is included for liquefaction evaluation procedures, and τ_{max} is the maximum shear stress observed during analysis at a certain location.

Arias intensity was used to measure the strength of each ground motion and it was computed as,

$$I_A = \frac{\pi}{2g}\int_0^{T_d} a(t)^2 dt\,, \tag{4.16}$$

where T_d is the duration of the motion.

4.3.3 Model verification

As a first step in this study, the soil columns were verified in the elastic range using a weak motion to ensure consistency among models and modelers. Motion RSN766 was scaled down to 0.02g so the new motion was weak enough to induce an almost pure elastic response and avoid possible discrepancies caused by material nonlinearity. By mostly staying in an elastic regime, any small strain damping, including damping induced by the integration scheme and Rayleigh damping, could be verified as well as the wave propagation based on the low strain

stiffness. Mesh refinement and boundary conditions were also verified by checking simulated acceleration responses.

Secondary parameters for PM4Sand were computed during the time of material initialization using the existing stress state. The stress state could be applied directly in FLAC, while in PLAXIS the so called K_0 procedure was used. In OpenSees a gravity analysis phase using an elastic material was applied. The elastic material had the same unit weight and low strain stiffness as the corresponding nonlinear material. It is also worth mentioning other differences required for computing the initial stress state between the three programs: In OpenSees, and for the SSPquadUP element, density and a vector describing the gravitational acceleration are required. In PLAXIS the unit weight of the material has to be specified, while in FLAC, the user specifies dry density and void ratio. In order to avoid inconsistencies in the initial stress state, and in turn in secondary parameters, initial stress fields were carefully compared and examined. For added confidence, the same analysis was also performed using ProShake (EduPro Civil Systems (2017), here referred as PS) and DeepSoil (Hashash et al. (2016), here referred as DS).

As shown in Figs. 4.16 to 4.18, all five programs produced very similar results in terms of PHA, γ_{max}, and CSR along the column, as well as acceleration time history and Arias intensity at the surface. Note that a constant 2% damping instead of Rayleigh damping was used in PS and DS analyses, therefore, all the other three programs showed slightly smaller PHA in the profile plots and weaker Arias intensity in Fig. 4.17 due to extra frequency dependent damping. γ_{max} and CSR profiles in Fig. 4.16 also showed good agreement in spite of PLAXIS results showing the effect of discretization. Location of γ_{max} from PLAXIS was slightly shifted and contributed to its more refined mesh and higher density of stress points.

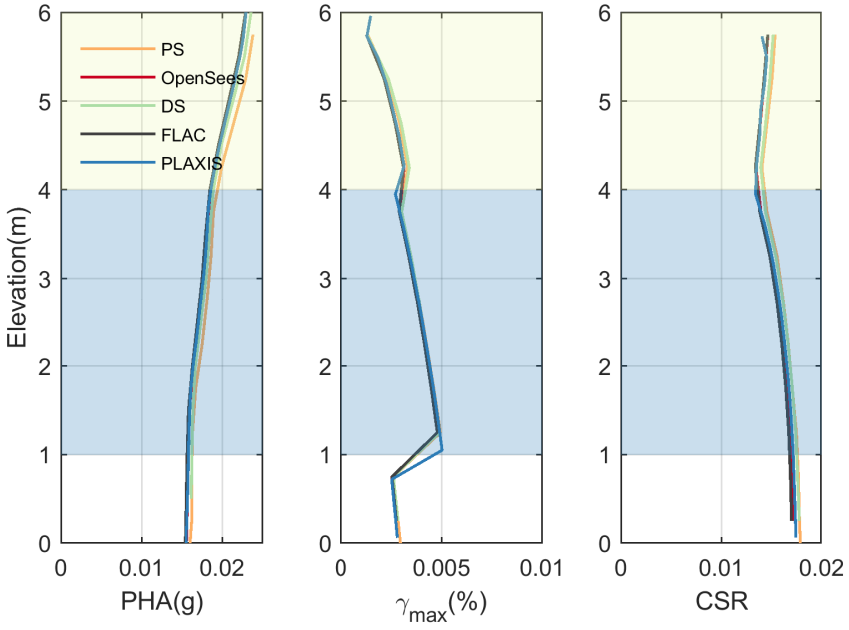

Figure 4.16: Comparison of PHA, γ_{max}, and CSR from PS, OpenSees, DS, FLAC, and PLAXIS.

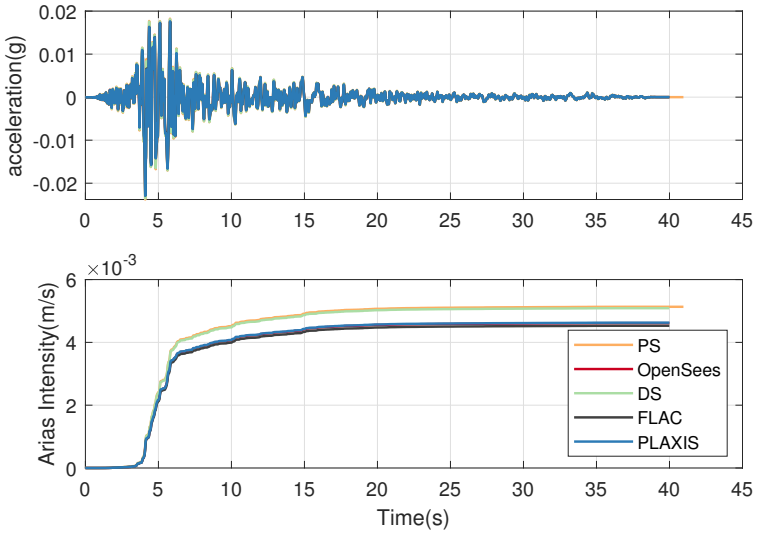

Figure 4.17: Comparison of simulated acceleration time histories and Arias intensity at the surface from PS, OpenSees, DS, FLAC, and PLAXIS.

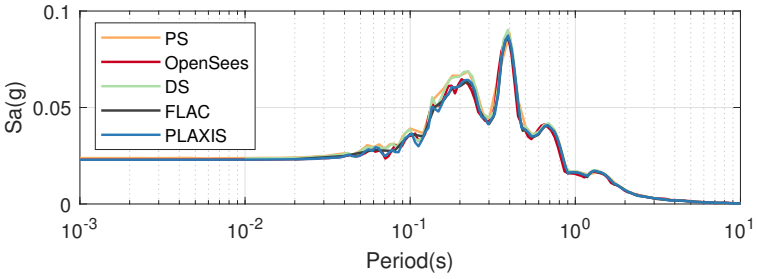

Figure 4.18: Comparison of simulated acceleration response spectra (5%) at the surface from PS, OpenSees, DS, FLAC, and PLAXIS.

4.3.4 Free field verification results

Once the model was verified, the complete set of free-field analysis was done using OpenSees, FLAC, and PLAXIS and results were compared. Due to space constraints, only N10T3 results are presented here. Results for all other five cases can be found in Appendix A. Figs. 4.19 through 4.21 depict comparisons of simulated PHA, γ_{max}, maximum displacement, CSR, and max r_u along the soil column. In general, all three programs produced similar results and liquefaction was triggered as expected. Presence of higher PHA coincided with large γ_{max} and max $r_u = 1$, which indicates the presence of dilation spikes after fully liquefaction of the soil. However, the predicted PHA from FLAC was noticeably higher than from OpenSees and PLAXIS. Comparison of acceleration time histories at those locations (not shown here) revealed that FLAC tended to produce higher magnitudes of dilation spikes compared to OpenSees and PLAXIS, but all three programs predicted similar times of triggering of these spikes and the overall acceleration responses were similar. Comparison of the acceleration response at the surface (Figs. 4.22 through 4.27) also show the same trend. In terms of CSR, FLAC also tended to predict slightly larger values which also coincided with higher PHA values. As discussed before, excess pore pressure could be generated within the dry layer in FLAC and PLAXIS analyses. This phenomenon was observed in maximum r_u response even when small permeability was assigned to minimize pore pressure migration. Nevertheless, the results clearly demonstrate that, when carefully performed, PM4Sand in all three programs can produce consistent results. Moreover, the PM4Sand in OpenSees and PLAXIS can be used in site response analysis to study liquefaction triggering.

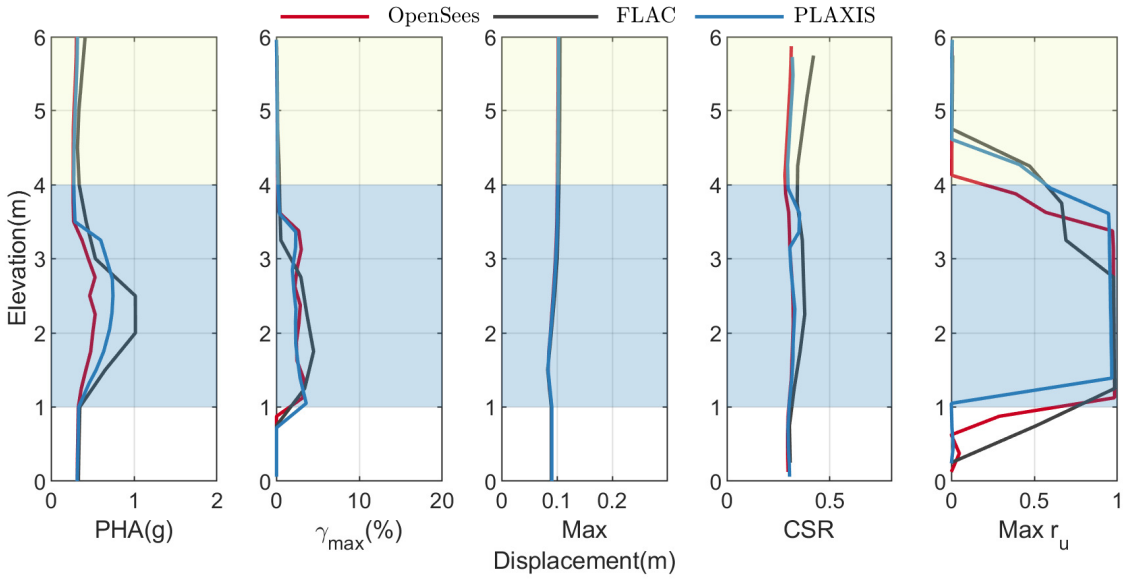

Figure 4.19: Comparison of PHA, γ_{max}, maximum displacement, CSR, and max r_u obtained using OpenSees, FLAC and PLAXIS for motion RSN766.

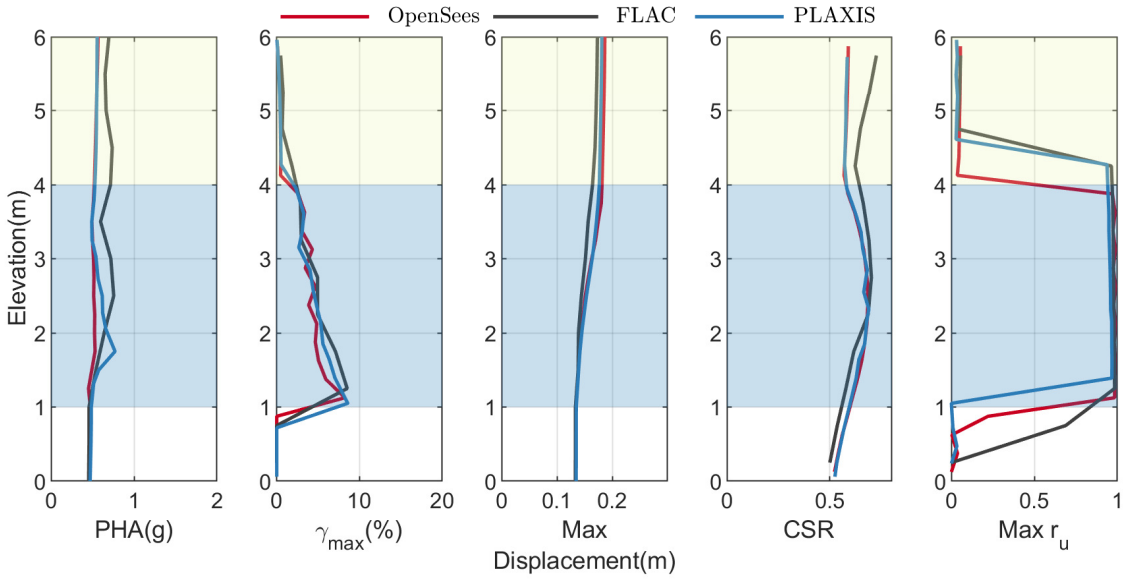

Figure 4.20: Comparison of PHA, γ_{max}, maximum displacement, CSR, and max r_u obtained using OpenSees, FLAC and PLAXIS for motion RSN963.

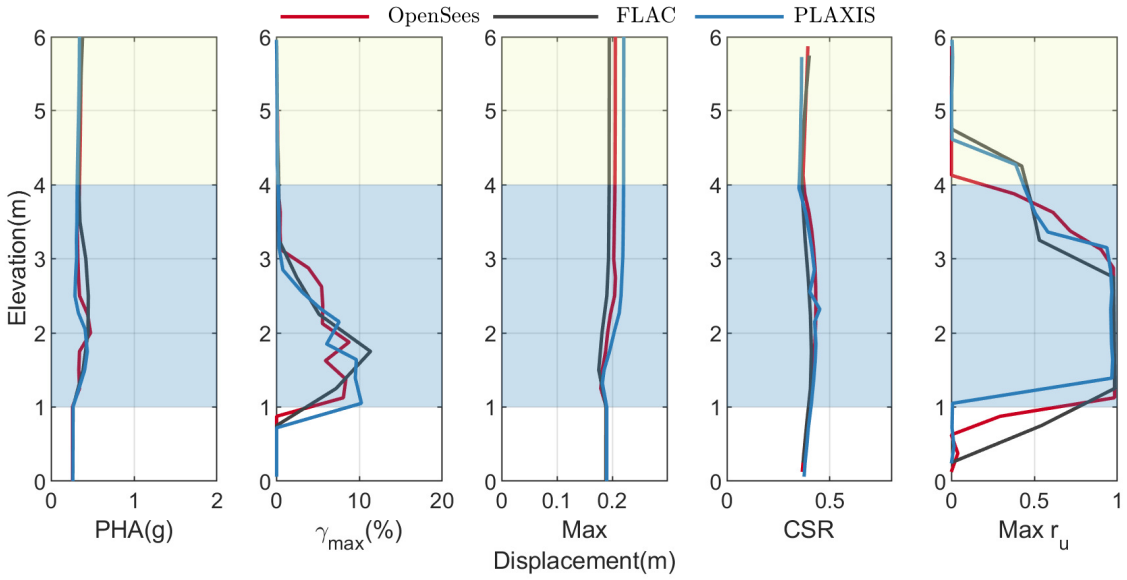

Figure 4.21: Comparison of PHA, γ_{max}, maximum displacement, CSR, and max r_u obtained using OpenSees, FLAC and PLAXIS for motion RSN1203.

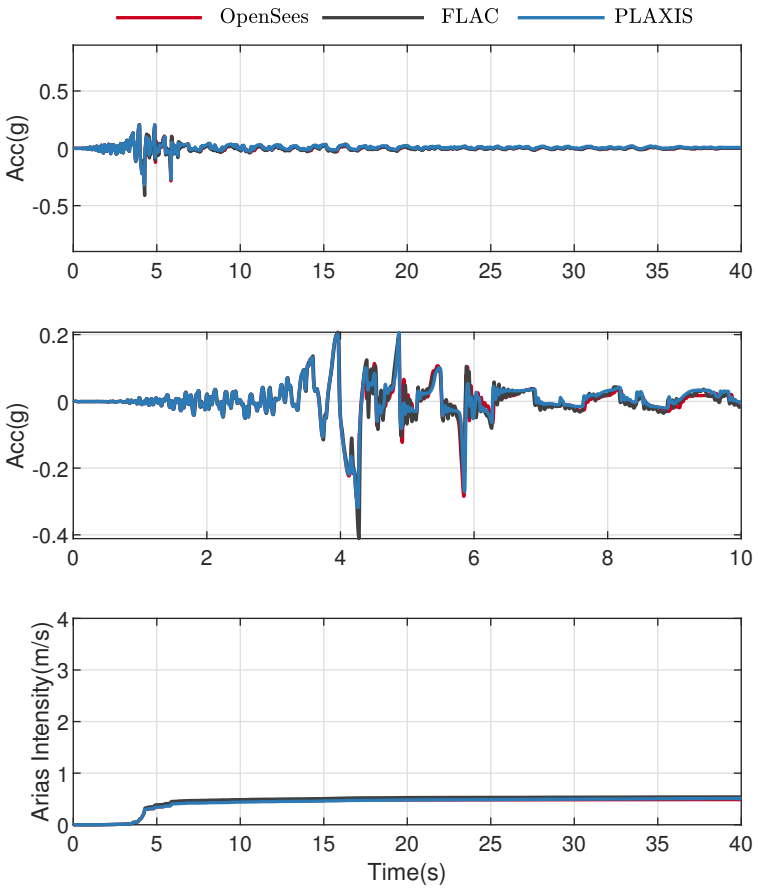

Figure 4.22: Comparison of acceleration time history at the surface obtained using OpenSees, FLAC and PLAXIS for motion RSN766. From top to bottom: acceleration time history, close up of acceleration time history, and Arias intensity.

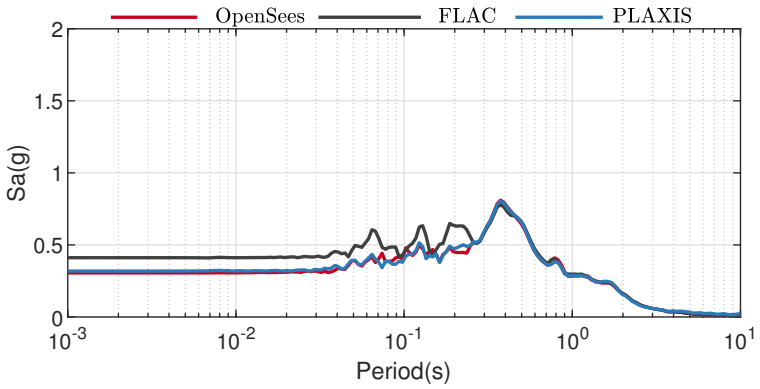

Figure 4.23: Comparison of acceleration response spectra (5%) at the surface obtained using OpenSees, FLAC, and PLAXIS for motion RSN766.

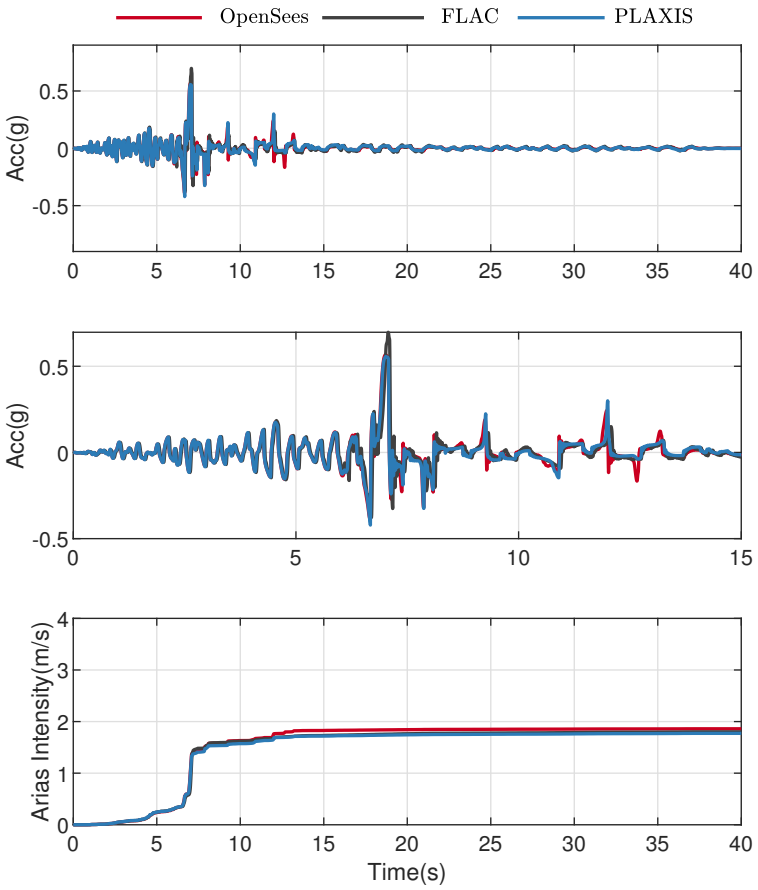

Figure 4.24: Comparison of acceleration time history at the surface obtained using OpenSees, FLAC and PLAXIS for motion RSN963. From top to bottom: acceleration time history, close up of acceleration time history, and Arias intensity.

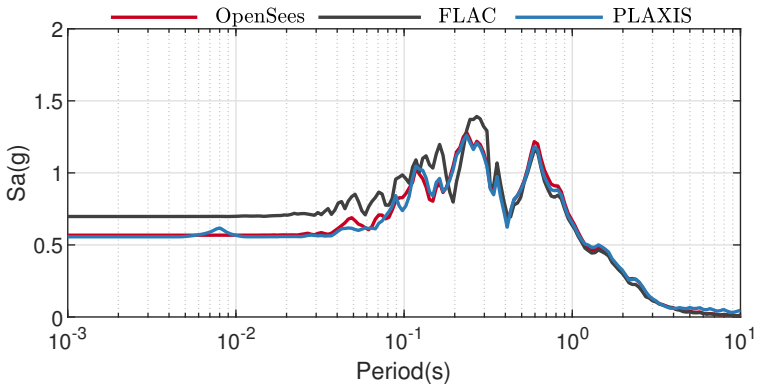

Figure 4.25: Comparison of acceleration response spectra (5%) at the surface obtained using OpenSees, FLAC, and PLAXIS for motion RSN963.

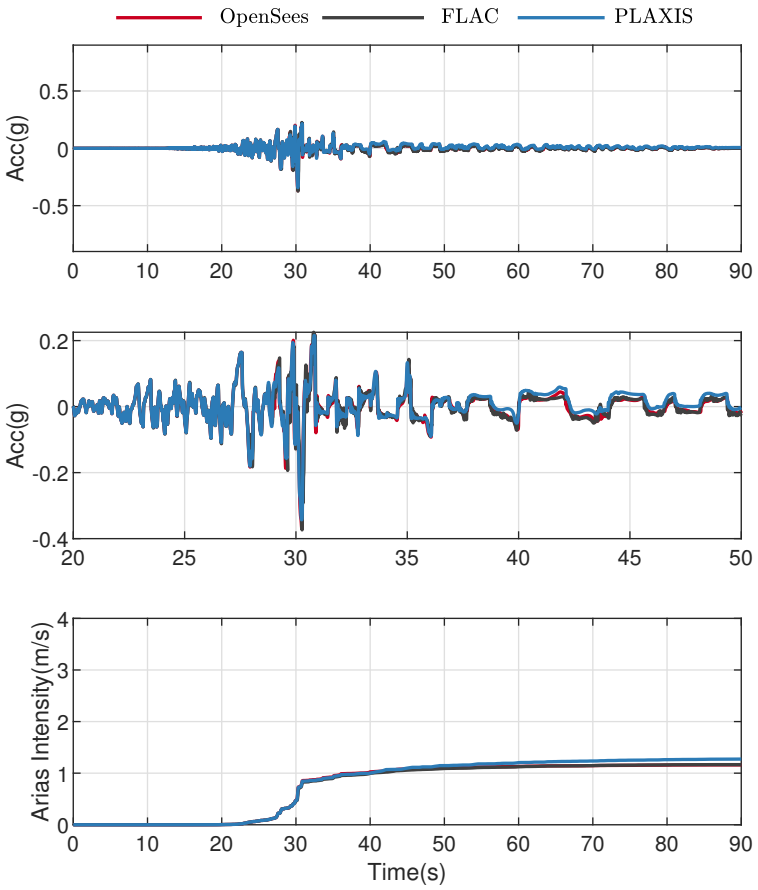

Figure 4.26: Comparison of acceleration time history at the surface obtained using OpenSees, FLAC and PLAXIS for motion RSN1203. From top to bottom: acceleration time history, close up of acceleration time history, and Arias intensity.

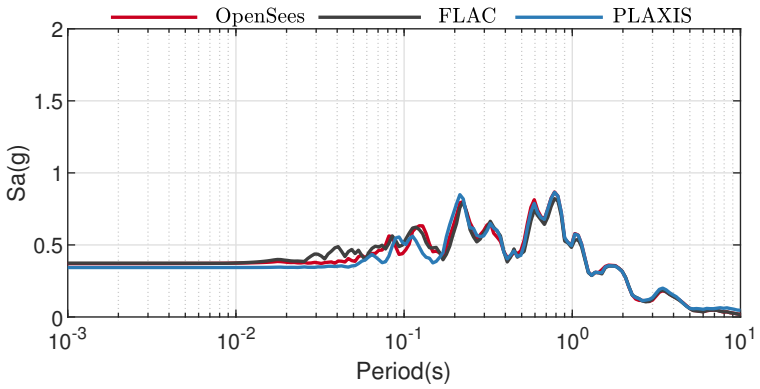

Figure 4.27: Comparison of acceleration response spectra (5%) at the surface obtained using OpenSees, FLAC, and PLAXIS for motion RSN1203.

4.4 1D sloping ground site response analysis

PM4Sand has already been used in nonlinear effective stress analyses to study earthquake-induced deformation in gently sloped ground (e.g., embankment dams Montgomery (2012) and infinite slopes Ziotopoulou (2017)). Although the effect of static shear stress on liquefaction resistance (K_α) of the PM4Sand model OpenSees implementation was verified as shown in Fig. 4.7, it was still important to verify the model response within the OpenSees numerical framework. For this purpose, the 1D soil columns presented in the previous section were slightly modified to represent gentle (3%) infinite slopes as shown in Fig. 4.28. Instead of modifying the geometry of the column, the slope was simulated by changing the direction of the gravitational field such that a constant additional horizontal acceleration component representing the slope was applied to the entire column during the dynamic analysis. This case represents a constant infinite slope with no rotational behavior. All three programs (OpenSees, FLAC, PLAXIS) allowed changes of the gravitational field so modifications were trivial. The three motions presented in the previous section were scaled to three PGA levels, namely 0.1g, 0.2g, and 0.3g in this study. All the material properties and analysis parameters stayed the same.

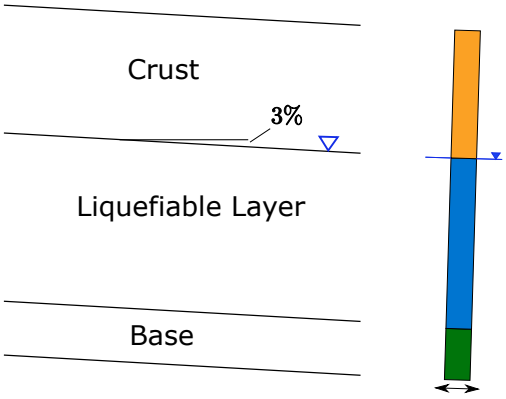

Figure 4.28: Illustration of 1D sloping ground model in terms of soil layering.

Simulation results using 0.3g motions are presented in Figs. 4.29 to 4.34. For brevity, all other results are included in Appendix A.6. All three programs produced consistent results and showed similar liquefaction trends as observed in the level ground case. FLAC tended to predict higher PHA values. In terms of lateral displacements, all three programs showed the same trend. Only after fully liquefaction of the material, the programs showed evidence of significant and different shear strain magnitudes that lead to different lateral displacement magnitudes. In contrast to PLAXIS, OpenSees tended to predict slightly higher magnitudes than FLAC. This is again related to the domain discretization and algorithmic conditions for small confining pressures. Nevertheless, the observed good agreement verifies the OpenSees and PLAXIS implementations of PM4Sand and shows the models are capable of predicting reasonable results. It is important to note, the predicted shear strains were not in the small-strain range; for example Fig. 4.33 showed γ_{max} over 50%. Therefore, the PM4Sand model formulation, as well as any other small strain constitutive model formulation, may not be valid under these circumstances and results must be interpreted with caution. In addition to an appropriate formulation, more comprehensive 2D models might be needed for large deformation analyses.

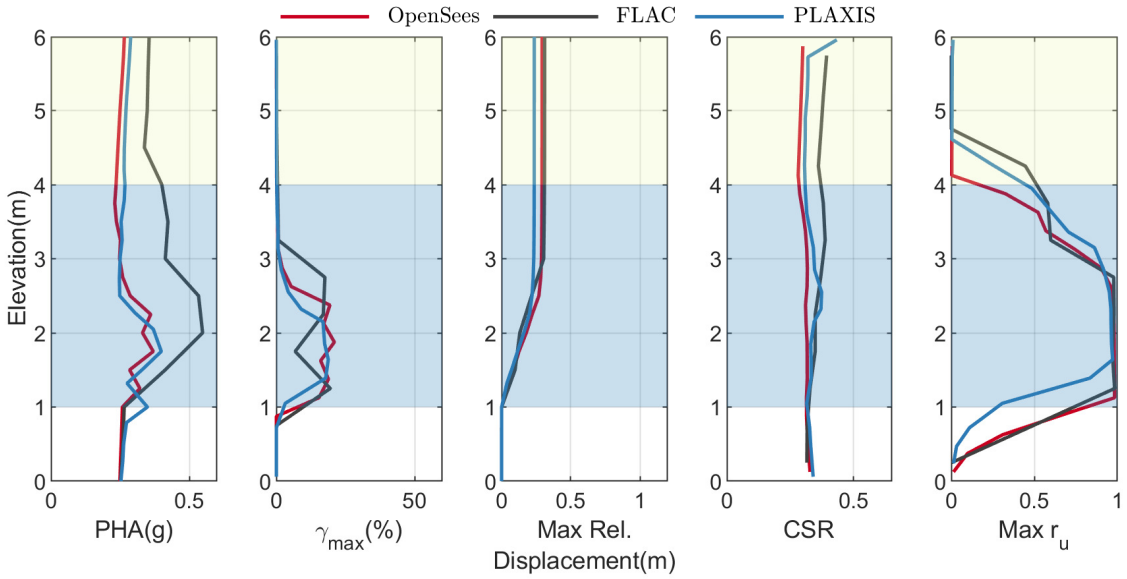

Figure 4.29: Comparison of PHA, γ_{max}, maximum displacement, CSR, and max r_u obtained using OpenSees, FLAC, and PLAXIS for motion RSN766 and $a_{max} = 0.3$g.

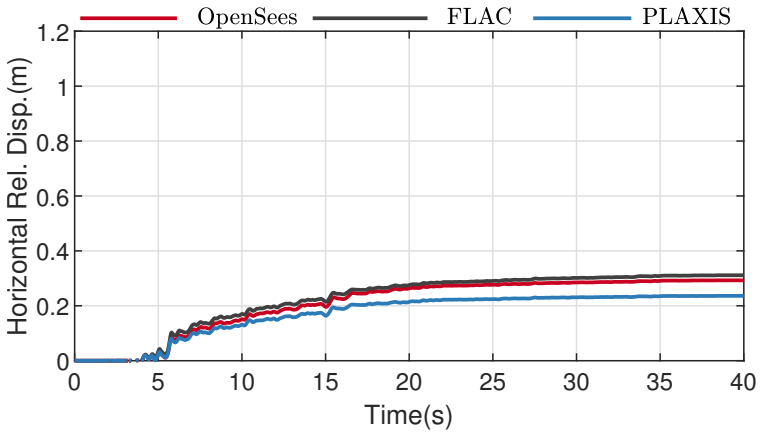

Figure 4.30: Comparison of horizontal displacement at the surface obtained using OpenSees, FLAC, and PLAXIS for motion RSN766 and $a_{max} = 0.3$g.

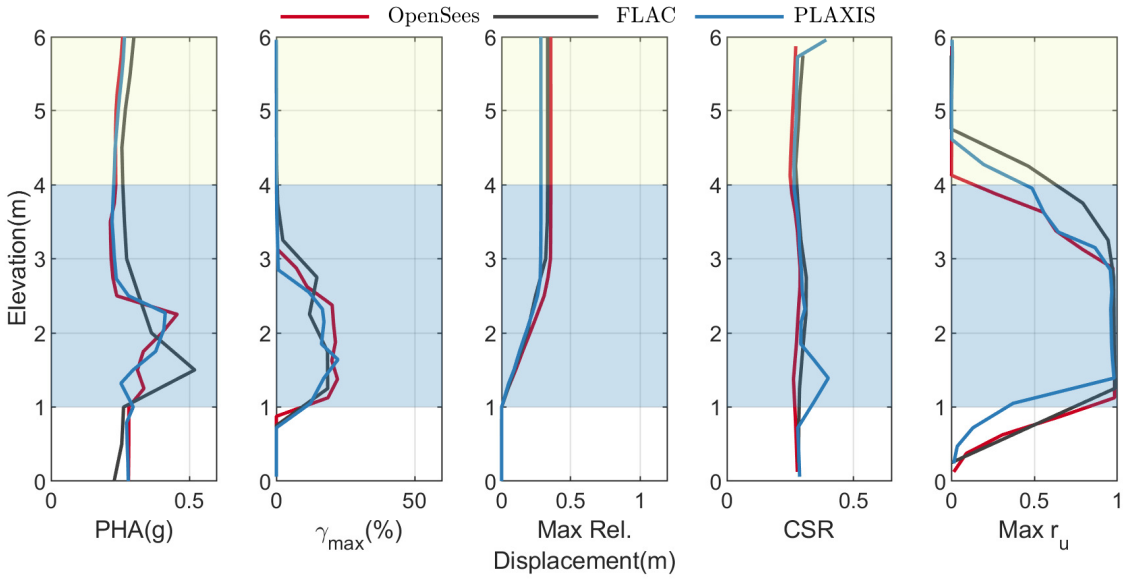

Figure 4.31: Comparison of PHA, γ_{max}, maximum displacement, CSR, and max r_u obtained using OpenSees, FLAC, and PLAXIS for motion RSN963 and $a_{max} = 0.3$g.

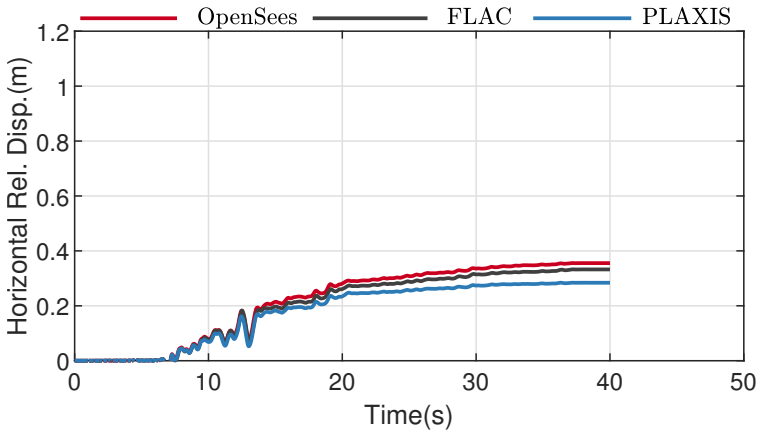

Figure 4.32: Comparison of horizontal displacement at the surface obtained using OpenSees, FLAC, and PLAXIS for motion RSN963 and $a_{max} = 0.3$g.

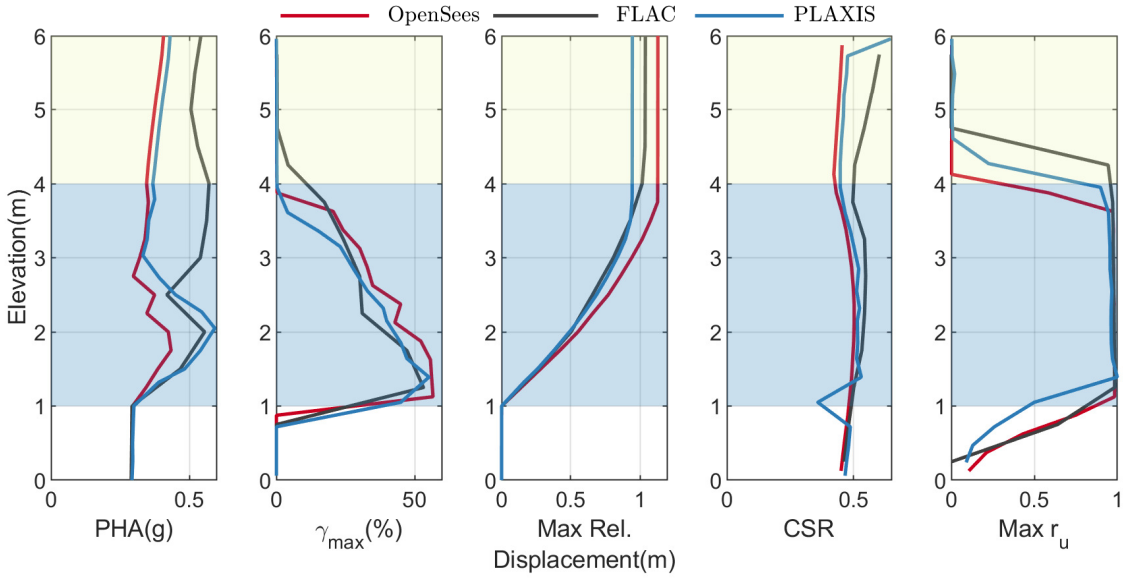

Figure 4.33: Comparison of PHA, γ_{max}, maximum displacement, CSR, and max r_u obtained using OpenSees, FLAC, and PLAXIS for motion RSN1203 and a_{max} = 0.3g.

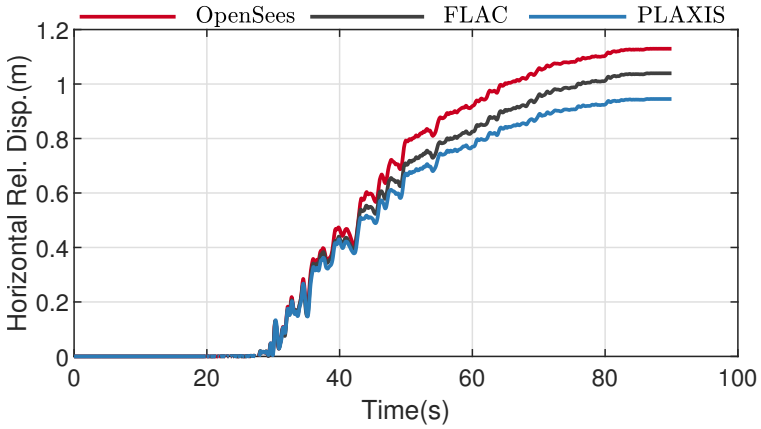

Figure 4.34: Comparison of horizontal displacement at the surface obtained using OpenSees, FLAC, and PLAXIS for motion RSN1203 and a_{max} = 0.3g..

4.5 Summary

This chapter presents results of a verification study for PM4Sand as implemented in OpenSees using point, single element, and 1D soil column analyses. The results show that, despite discrepancies due to platform differences, i.e., FEM vs. FDM and different model discretization, that the OpenSees implementation produce consistent results to FLAC and PLAXIS.

Chapter 5

IMPLEMENTATION AND VERIFICATION OF PM4SILT IN OPENSEES

5.1 Introduction

During the 2010-2011 Canterbury earthquake sequence, liquefaction was triggered throughout the city of Christchurch causing vast damage. However, a significant number of cases, for which the simplified methods predicted heavy ground damage, exhibited no ground damage during the earthquakes. Among several factors, the presence of low plasticity silt layers, not properly accounted for, were deemed the reason for such conservative predictions.

Unlike sands, low-plasticity silts and clays can exhibit behavior that range from sand-like (liquefaction) to clay-like (cyclic softening) in a narrow range of Atterberg limits (Boulanger and Idriss, 2006). Clay-like materials typically can not reach excess pore pressure ratios of 100% and dissipate more hysteretic energy than their sand counterparts, but can still develop large shear strains, which can certainly be manifested as ground deformations in a field situation. The PM4Sand model discussed in previous chapters is suitable for capturing sand-like behavior but was not developed to represent clay-like behavior. Therefore, a material constitutive model capable of capturing clay-like cyclic softening behavior is an essential tool for researchers who are trying to perform numerical simulation to study sites containing low-plasticity silts and clays. The PM4Silt model proposed by Boulanger and Ziotopoulou (2018) fits this need. This model follows the framework of PM4Sand (version 3.1) presented by Boulanger and Ziotopoulou (2017) with modifications that were developed to improve its ability to approximate undrained monotonic and cyclic loading responses of low-plasticity silts and clays, as opposed to those for purely nonplastic silts or sands. Similar to PM4Sand, PM4Silt uses three primary input parameters, namely the undrained shear strength at critical

state (S_u) or undrained shear strength ratio ($S_{u,rat} = \frac{S_u}{\sigma'_{vc}}$), shear modulus coefficient (G_o), and contraction rate parameter (h_{po}), and 20 secondary parameters, that the user can use to further fine-tune the response.

This chapter presents a brief introduction to PM4Silt and implementation details of its most current version in OpenSees. Results of a verification study of the PM4Sand model implemented in OpenSees are also presented here.

5.2 Introduction to PM4Silt

Due to its similarity to the PM4Sand model, only differentiating aspects are discussed in following sections. Interested readers are referred to Boulanger and Ziotopoulou (2018) for more details.

5.2.1 Elastic response and yield surface

The stress and strain tensors are the same as for the PM4Sand model. The shear modulus, G, is modified to,

$$G = G_o p_A (\frac{p}{p_A})^{n_G} C_{SR}\,, \tag{5.1}$$

where n_G is a shear modulus exponent controlling how the shear modulus varies with confining pressure and its default value is 0.75.

5.2.2 Critical state surface

The PM4Silt model incorporates the critical state concept defined by Schofield and Wroth (1968) and Muir Wood (1990) and uses the state parameter ξ proposed by Been and Jefferies (1985),

$$\xi = e - e_{cs}\,, \tag{5.2}$$

where e is the current void ratio and e_{cs} is the void ratio at critical state for the current mean effective stress,

$$e_{cs} = \Gamma - \lambda \cdot \ln\left(\frac{p}{1kPa}\right). \tag{5.3}$$

The critical line is linear in the $e - \ln p$ space, with a slope λ and intercept Γ for $p' = 1kPa$. During initialization, the critical state line is positioned using the primary input S_u such that,

$$\Gamma = e + \lambda \ln\left(101.3\frac{p_{cs}}{p_A}\right) = e + \lambda \ln\left(101.3\frac{2S_u}{Mp_A}\right). \tag{5.4}$$

5.2.3 Bounding surface and dilatancy surface

The model simplifies the bounding, dilatancy and critical state surfaces presented by Dafalias and Manzari (2004) by removing the Lode angle dependency. The dilatancy ratio, M^d, is related to the critical stress ratio by,

$$M^d = M \cdot \exp(n^d \frac{\xi_R}{\lambda}), \tag{5.5}$$

where M is set to be $\leq 2sin(45°)$ and a default value of n^d is 0.3. The bounding ratio, M^b, has different forms for dense and loose of critical states, respectively. For loose of critical states, i.e., the "wet" side, M^b is related to M by,

$$M^b = M \cdot \exp(-n^{b,wet} \frac{\xi_R}{\lambda}), \tag{5.6}$$

where $n^{b,wet}$ is a positive number with a default value of 0.80 such that M^b is always smaller than M on the loose of critical side. For dense of critical states, i.e., the "dry" side, M^b is related to M by,

$$M^b = M \cdot \left(\frac{1 + C_{MB}}{\frac{p}{p_{cs}} + C_{MB}}\right)^{n^{b,dry}}, \tag{5.7}$$

where

$$C_{MB} = \frac{1}{\left(\frac{M^{b,max}}{M}\right)^{1/n^{b,dry}} - 1}, \tag{5.8}$$

and

$$M^{b,max} = 2 \cdot \sin(\phi_{max}). \tag{5.9}$$

The default value of $n^{b,dry}$ is 0.5. These formulations ensure that values of M^b vary from M at critical state to a maximum value $M^{b,max}$ when p approaches 0. Finally, the value of $M^{b,max}$ is limited by an arbitrary maximum friction angle than can be mobilized near the origin, with $\phi_{max} = 60°$.

5.2.4 Dilatancy and effects of fabric

The PM4Silt equations for evaluating plastic volumetric dilation, including the effect of fabric, remain the same as for PM4Sand. On the other hand, several modifications are included in the evaluation of plastic volumetric contraction. Dilatancy D during contraction is modified to,

$$D = A_{dc}[(\boldsymbol{\alpha} - \boldsymbol{\alpha}_{in}^{app}) : \mathbf{n}]^2 \frac{(\boldsymbol{\alpha}^d - \boldsymbol{\alpha}) : \mathbf{n}}{(\boldsymbol{\alpha}^d - \boldsymbol{\alpha}) : \mathbf{n} + C_D} C_{pmin} \leq A_{do} \frac{(\boldsymbol{\alpha}^d - \boldsymbol{\alpha}) : \mathbf{n}}{(\boldsymbol{\alpha}^d - \boldsymbol{\alpha}) : \mathbf{n} + C_D} C_{pmin}\,, \quad (5.10)$$

and a new term C_{wet} is added to the formulation of A_{dc} such that,

$$A_{dc} = \frac{A_{do}(1 + \langle \mathbf{z} : \mathbf{n} \rangle)}{h_p C_{dz} C_{wet}}\,, \quad (5.11)$$

where

$$C_{wet} = \frac{1}{1 + \left(\frac{C_{w1}}{(\boldsymbol{\alpha}^b - \boldsymbol{\alpha}) : \mathbf{n}}\right)^4} + \frac{1}{1 + \left(\frac{\xi/\lambda}{C_{wc}}\right)^2} \leq 1\,, \quad (5.12)$$

$$C_{w1} = 0.02\,,$$

$$C_{w2} = 0.1\,.$$

The dependency of the contraction rate on the state is incorporated through h_p that varies with the scaled state parameter, ξ/λ, as,

$$h_p = h_{po} \cdot \exp\Big(-0.7 + 0.2 \left\langle 3 - \frac{\xi}{\lambda} \right\rangle^2 \Big) \quad for \quad \frac{\xi}{\lambda} \leq 3\,, \quad (5.13)$$

$$h_p = h_{po} \cdot \exp(-0.7) \quad for \quad \frac{\xi}{\lambda} > 3\,. \quad (5.14)$$

Thus, the primary input parameter, h_{po}, provides a linear scaling of contraction rates and can be calibrated to achieve a desired CRR. Given the nature of exponential function and the small value of the denominator, λ, this formula for $\frac{\xi}{\lambda} \leq 3$ is highly sensitive to the

value of ξ as a minor change on the state parameter could lead to a significant change in the computed h_p.

The minimum admissible effective stress is limited by the term C_{pmin} in Equ. 5.10 and is modified as,

$$C_{pmin} = \begin{cases} = 0, & p \leq 2p_{min}\,, \\ = \frac{p-2p_{min}}{6p_{min}} & 2p_{min} < p < 8p_{min}\,, \\ = 1 & p \geq 8p_{min}\,. \end{cases} \tag{5.15}$$

The parameter p_{min} can either be set manually by setting the secondary parameter $r_{u,max}$ such that,

$$p_{min} = (1 - r_{u,max})\frac{p}{2}\,, \tag{5.16}$$

where $r_{u,max}$ should be between 0 and 0.99; or automatically calculated when FirstCall is called and no $r_{u,max}$ is specified by user as,

$$p_{min} = \frac{p_{cs}}{8} = \frac{2S_u}{8M}\,. \tag{5.17}$$

This value is limited to be no greater than the p_{min} calculated using $r_{u,max} = 0$. For either case, an additional minimum limit of 0.5 kPa is imposed on p_{min}.

5.2.5 Post-shaking undrained shear strength

A new functionality was added to PM4Silt to enable reducing S_u by a factor of F_{su} at a specific time during an analysis. This is useful when the undrained shear strength needs to be updated before evaluating static stability after strong shaking. As discussed in Boulanger and Ziotopoulou (2018), the S_u that should be used after strong shaking is often smaller than its value during dynamic excitation. This is due to: (1) the change of loading rate, and/or, (2) cyclic degradation or remolding during shaking. F_{su} is used to shift the critical state line leftward relative to its initial position as,

$$\xi = e - \left[\Gamma - \lambda \cdot \ln\left(\frac{p}{F_{su} \cdot 1kPa}\right)\right]. \tag{5.18}$$

Subsequently, the undrained shear strength at critical state is reduced by the same factor. The default value for F_{su} is 1.0, and its value can be changed using the following command:

```
setParameter -value 0 -eleRange $eleStart $eleEnd Su_factor $matNum
setParameter -value 0 -ele $eleNum Su_factor $matNum
```

where *$eleStart* and *$eleEnd* define the range of elements for which *PostShake* is going to be activated, and *$matNum* is the material tag assigned to the elements. Fig. 5.1 shows the effect of F_{su} on an undrained monotonic DSS test with $S_{u,rat} = 0.25$ and $\sigma'_{vc} = 1\,atm.$. With an updated F_{su}, PM4Silt captures softening behavior towards its new critical state undrained strength. However, since this command alters critical state line and subsequently affects all the model's behaviors that are tied to the critical state, it is not intended to be used during shaking and should be used with care.

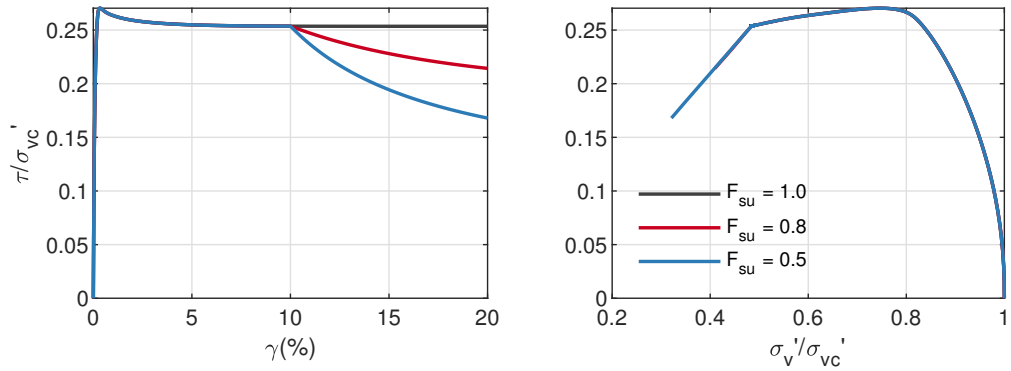

Figure 5.1: Effect of setting $F_{su} = 0.8$ or 0.5 at $\gamma = 10\%$ on the response of PM4Silt under sustained monotonic DSS loading with $S_{u,rat} = 0.25$.

5.2.6 Post-shaking reconsolidation

Similar to PM4Sand, after shaking the Elastic moduli G and K can be reduced to increase volumetric strains, and hence improve the attained post-shaking reconsolidation settlement. The post-shaking elastic moduli are determined by applying a reduction factor F_{sed} to the

conventional elastic moduli as,

$$G_{post-shaking} = F_{consol} G \,, \tag{5.19}$$

$$K_{post-shaking} = F_{consol} K \,, \tag{5.20}$$

wehre F_{consol} is related to the accumulated fabric and the stress state at the end of the main shake, and it can be calculated as,

$$F_{consol} = 1 - \Big(1 - \frac{G_{c,min}}{G}\Big)\Big\langle 1 - \frac{M^{cur}}{M^d}\Big\rangle^{0.25} \,, \tag{5.21}$$

$$G_{c,min} = \big(\frac{8p}{\lambda}\big)\Big(\frac{1}{1 + (C_{GC} - 1)\big(\frac{z_{cum}}{z_{cum} + z_{max}}\big)}\Big) \,, \tag{5.22}$$

where C_{GC} determines how much the elastic moduli will be degraded if z_{cum} becomes larger than z_{max}. If z_{cum} is small, the value of $G_{c,min}$ corresponds to an elastic modulus consistent with one dimensional recompression stiffness estimated based on p and λ. The term $\big\langle 1 - \frac{M^{cur}}{M^d}\big\rangle^{0.25}$ allows $G_{post-shaking}$ to become close to $G_{c,min}$ if the loading is well within the dilatancy surface, i.e. $M^{cur} << M^d$, and close to G if the loading is near the dilatancy surface,i.e. $M^{cur} \approx M^d$. In OpenSees, post shake reconsolidation is activated using the following command:

```
setParameter -value 0 -eleRange $eleStart $eleEnd PostShake $matNum
setParameter -value 0 -ele $eleNum PostShake $matNum
```

It should be noted that PM4Silt does not include a cap, and therefore is not suited for simulating consolidation settlements or strength evolution with consolidation stress history.

5.3 Implementation of PM4Silt in OpenSees

The implementation of PM4Silt in OpenSees uses the same components of PM4Sand; including stress correction and explicit integration schemes. Thus, these details will not be discussed here. The default and recommended integration scheme in the current implementation is the Modified Euler with maximum strain increment control. The user can switch it to a different scheme using:

```
setParameter -value $mScheme -eleRange $eleStart $eleEnd IntegrationScheme $matNum
```

where *mScheme* are integers IDs that associate to each integration scheme:

- *mScheme* = **1**: Modified Euler with automatic substepping.
- *mScheme* = **2**: Forward Euler.
- *mScheme* = **3**: 4th Order Runge-Kutta.
- *mScheme* = **4**: Forward Euler with manual maximum strain increment.
- *mScheme* = **5**: Modified Euler with manual maximum strain increment (Default).

5.4 Verification of PM4Silt in OpenSees

The verification study of PM4Silt performed in this study follows the same procedure used for PM4Sand; which consisted in comparing simulation results obtained using point and 1D column analyses using OpenSees and FLAC. PM4Silt model version 1.0 paired with FLAC version 8.1 was used for this purpose. Three sets of input parameters, adopted from Boulanger and Ziotopoulou (2018), were considered in this study, and are presented in Table 5.1 and include three different undrained shear strength ratios, $S_{u,rat}$, of 0.25, 0.5, and 0.75.

Table 5.1: Input parameters for verification cases

$S_{u,rat}$	G_o	h_{po}	Implied V_{s1} (m/s)
0.25	588.0	20.0	177
0.50	776.0	50.0	204
0.75	913.0	60.0	221

*After Boulanger and Ziotopoulou (2018), all secondary input parameters were assigned default values.

5.4.1 Verification of PM4Silt implementation at element level

Verification of the OpenSees PM4Silt implementation was first performed at a constitutive level (point) using MixedDriver. All FLAC results presented in this section were obtained using the FLAC example drivers provided by Boulanger and Ziotopoulou (2018) on `https://pm4silt.engr.ucdavis.edu/pm4silt-files/`.

Monotonic loading

Figs. 5.2 to 5.4 illustrate comparisons between MixedDriver and corresponding FLAC results for monotonic undrained tests under various initial consolidation pressures. In all these cases the lateral pressure coefficient, K_0, was set to 1.0. MixedDriver results matched well with FLAC results in terms of stress-strain behavior and change in pore pressure.

The same tests were repeated using an initial $K_0 = 0.5$ and the results are presented in Figs. 5.5 to 5.7. The figures show that MixedDriver tended to slightly over-predict the reduction in vertical effective stress. As shearing continued, the MixedDriver response tended to converge to the corresponding FLAC response.

Cyclic loading

Fig. 5.8 illustrates comparisons between MixedDriver and corresponding FLAC results for cyclic direct simple shear (CDSS) tests using various $S_{u,rat}$. Again, MixedDriver tended to over-predict the accumulation of pore pressure (contraction rate). The results show that the OpenSees implementation in MixedDriver was able to capture the general trends produced by FLAC.

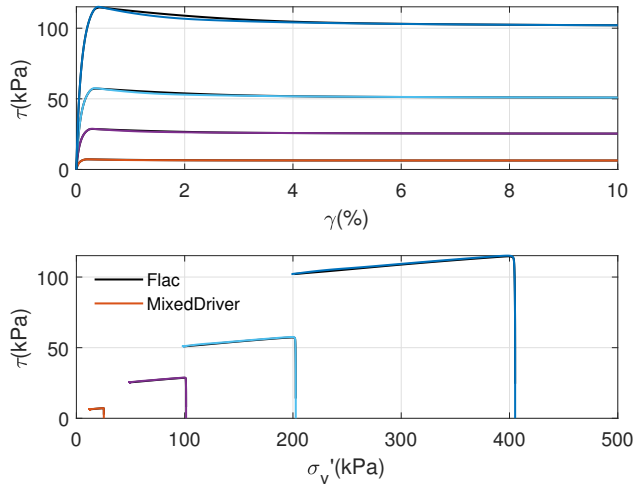

Figure 5.2: Comparison of responses from MixedDriver and FLAC for undrained monotonic DSS tests with $S_{u,rat} = 0.25$ under various initial vertical effective stresses of $\sigma_v = 0.25$, 1, 2, and 4 atm., respectively, and $K_0 = 1.0$.

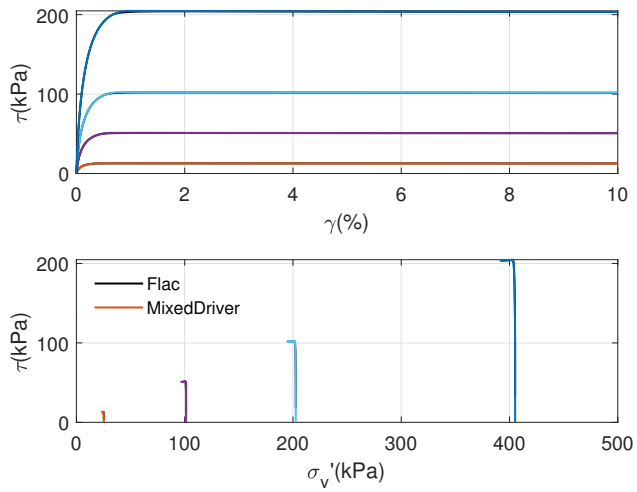

Figure 5.3: Comparison of responses from MixedDriver and FLAC for undrained monotonic DSS tests with $S_{u,rat} = 0.50$ under various initial vertical effective stresses of $\sigma_v = 0.25$, 1, 2, and 4 atm., respectively, and $K_0 = 1.0$.

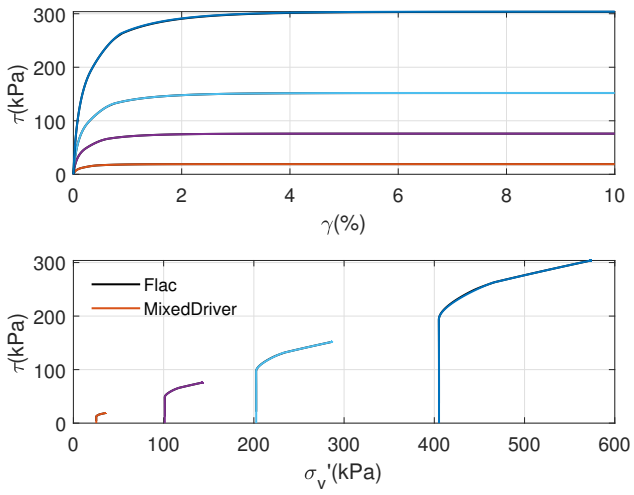

Figure 5.4: Comparison of responses from MixedDriver and FLAC for undrained monotonic DSS tests with $S_{u,rat} = 0.75$ under various initial vertical effective stresses of $\sigma_v = 0.25$, 1, 2, and 4 atm., respectively, and $K_0 = 1.0$.

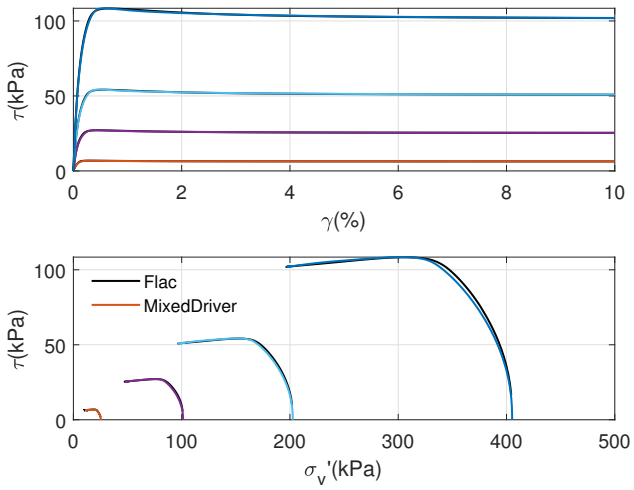

Figure 5.5: Comparison of responses from MixedDriver and FLAC for undrained monotonic DSS tests with $S_{u,rat} = 0.25$ under various initial vertical effective stresses of $\sigma_v = 0.25$, 1, 2, and 4 atm., respectively, and $K_0 = 0.5$.

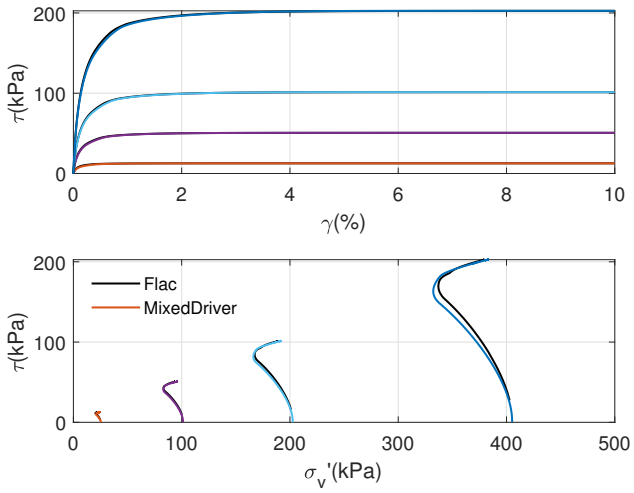

Figure 5.6: Comparison of responses from MixedDriver and FLAC for undrained monotonic DSS tests with $S_{u,rat} = 0.50$ under various initial vertical effective stresses of $\sigma_v = 0.25$, 1, 2, and 4 atm., respectively, and $K_0 = 0.5$.

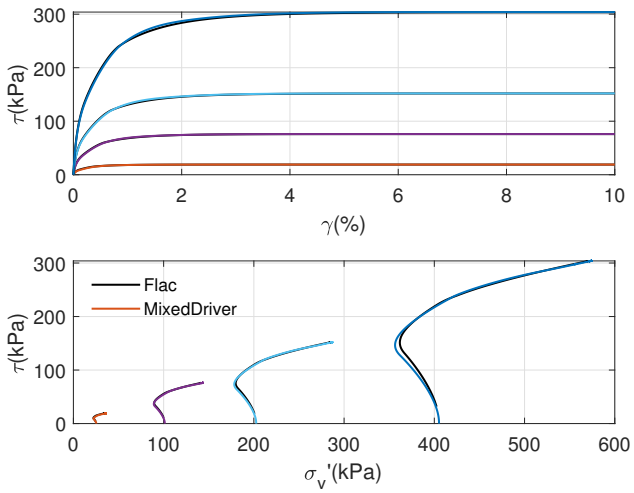

Figure 5.7: Comparison of responses from MixedDriver and FLAC for undrained monotonic DSS tests with $S_{u,rat} = 0.75$ under various initial vertical effective stresses of $\sigma_v = 0.25$, 1, 2, and 4 atm., respectively, and $K_0 = 0.5$.

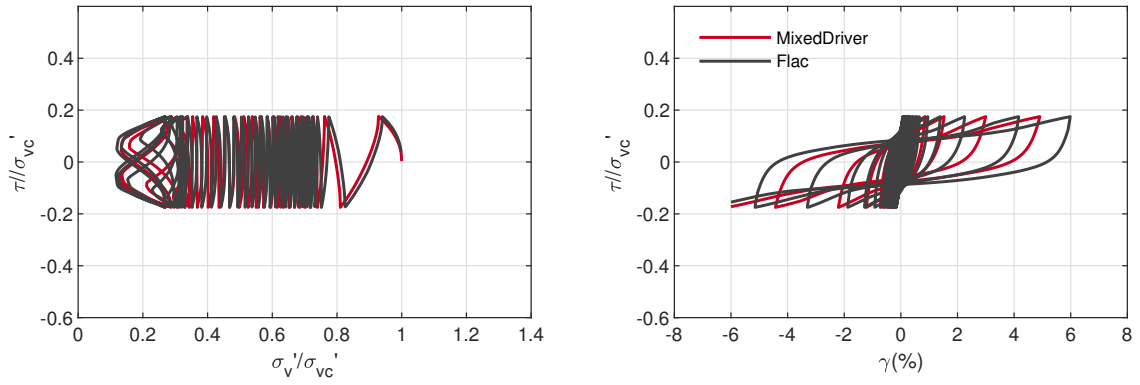

(a)

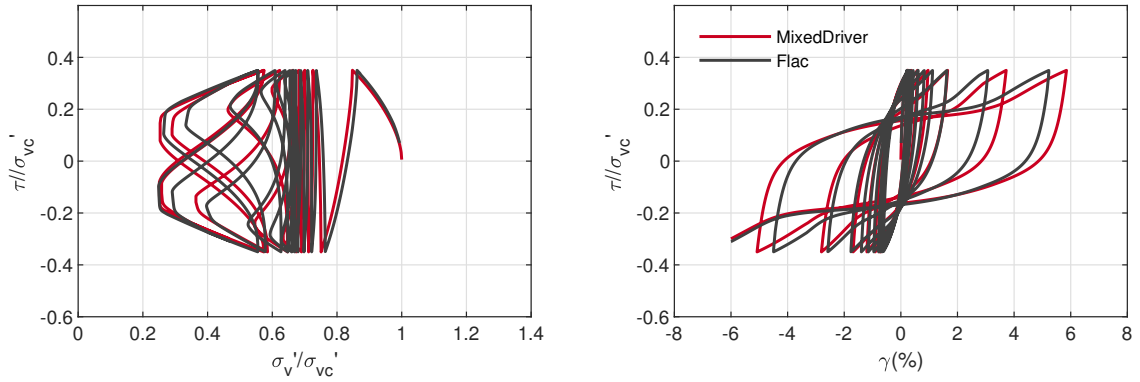

(b)

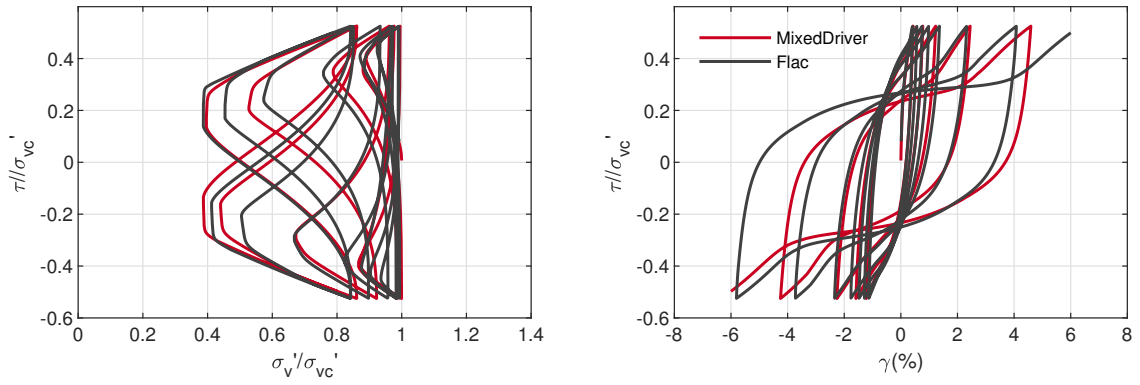

(c)

Figure 5.8: Comparison of results obtained using MixedDriver and FLAC for undrained CDSS tests for various $S_{u,rat}$ with an initial vertical stress of 1 atm. and $K_0 = 0.5$. (a) $S_{u,rat} = 0.25$, (b) $S_{u,rat} = 0.50$, (c) $S_{u,rat} = 0.75$.

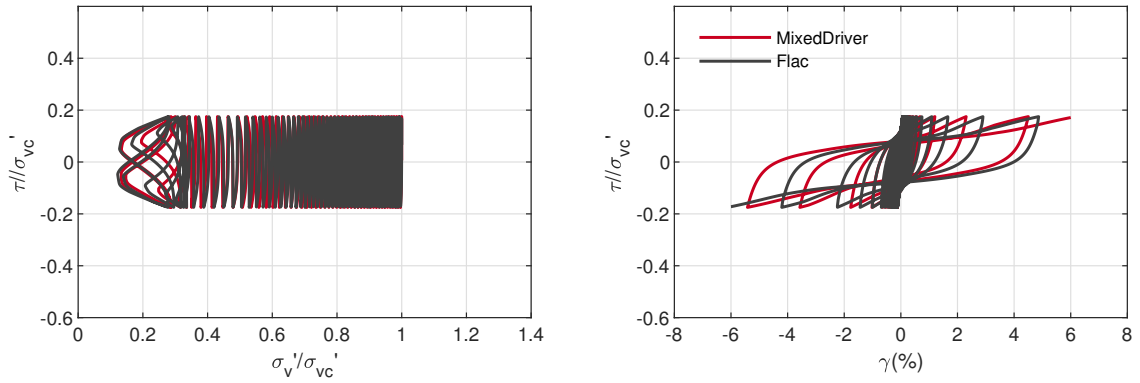

(a)

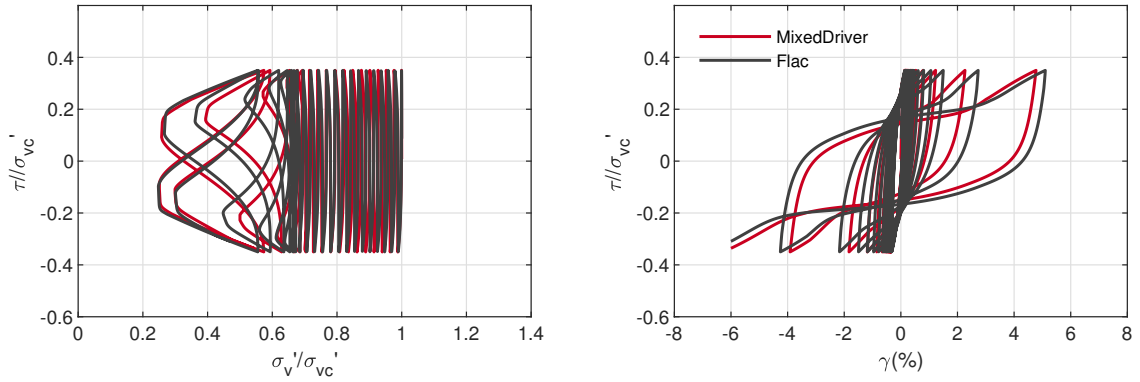

(b)

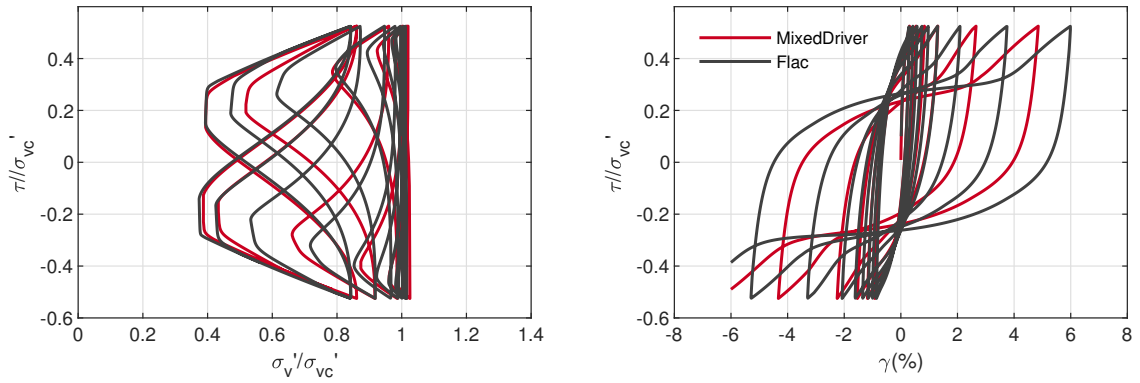

(c)

Figure 5.9: Comparison of results obtained using MixedDriver and FLAC for undrained CDSS tests for various D_R with an initial vertical stress of 1 atm. and $K_0 = 1.0$. (a) $S_{u,rat} = 0.25$, (b) $S_{u,rat} = 0.50$, (c) $S_{u,rat} = 0.75$.

5.4.2 1D level ground site response analysis

Once the model was verified at the element level, PM4Silt was then verified using 1D soil columns. For this purpose, a group of 1D single columns of quadrilateral elements similar to the ones presented in Chapter 4 was used to simulate site response analysis using the OpenSees framework. The results were also compared with FLAC analyses. The three motions, namely, RSN766, RSN963, and RSN1203, listed in Table 4.5 were also used here.

Three synthetic 1D soil profiles similar to the profiles used in the PM4Sand verification study were created. Each profile had a layered soil configuration composing of a dry crust, a liquefiable layer, and a base layer. The dry crust and liquefiable layers had an uniform $S_{u,rat}$. A total of three $S_{u,rat}$ values, 0.25, 0.50, and 0.75, were considered and the input parameters are summarized in Table 5.2. In addition to the primary parameters, the secondary parameter shear modulus exponent, n_G, was modified to 0.5. The density of the isotropic elastic material was set to be same as the saturated density of the layer above, and its stiffness was chosen to produce a wave impedance ratio $(\rho_2 v_2/\rho_1 v_1) = 1.3$. The properties of the isotropic elastic material are summarized in Table 5.3. A frequency dependent Rayleigh damping was applied to account for the lack of small strain damping. Rayleigh damping coefficients are summarized in Table 5.4.

Figs. 5.10 through 5.18 show comparisons of simulated PHA, γ_{max}, maximum displacement, CSR, and maximum r_u along the soil column. r_u was calculated using the change in effective vertical stress, and the associated elevation was taken at the center of each element/zone. In general, OpenSees and FLAC produced similar results. However, discrepancies were observed at locations where CSR exceeded the input $S_{u,rat}$, such as the $S_{u,rat} = 0.25$ case for motion RSN766 shown in Fig. 5.10. At the interface between the PM4Silt layer and elastic bedrock, large shear strains were produced by both OpenSees and FLAC models indicating the PM4Silt layer was shearing off. Since PM4Silt does not exhibit stress hardening, large strains tend to develop under sustained loading after failure. Base isolation followed and its effect is clearly observed in the comparison of PHAs (Fig. 5.11). Nevertheless, the

results clearly demonstrate that, when carefully performed, PM4Silt in all three programs can produce consistent results.

Table 5.2: Summary of PM4Silt input parameters

	$S_{u,rat} = 0.25$		$S_{u,rat} = 0.50$		$S_{u,rat} = 0.75$	
	Dry	Saturated	Dry	Saturated	Dry	Saturated
$S_{u,rat}$	0.25	0.25	0.50	0.50	0.75	0.75
G_o	501.8	671.0	666.6	891.3	782.4	1046.1
h_{po}	20.0	20.0	50.0	50.0	60.0	60.0
$\gamma(kN/m^3)$	13.8	18.4	13.8	18.4	13.8	18.4
Implied V_{s1} (m/s)	177	177	204	204	221	221

Table 5.3: Summary of input parameters for isotropic elastic material

	$S_{u,rat} = 0.25$	$S_{u,rat} = 0.50$	$S_{u,rat} = 0.75$
$V_s(m/s)$	194.1	223.7	242.3
$E(kPa)$	1.84×10^5	2.44×10^5	2.87×10^5
ν	0.3		
$\gamma(kN/m^3)$	18.4		

Table 5.4: Rayleigh damping parameters

	$S_{u,rat} = 0.25$	$S_{u,rat} = 0.50$	$S_{u,rat} = 0.75$
f_{min}	6.03	6.95	7.53
ξ_{min}	0.025	0.025	0.025
α	0.947	1.092	1.183
β	0.0006598	0.0005725	0.0005284

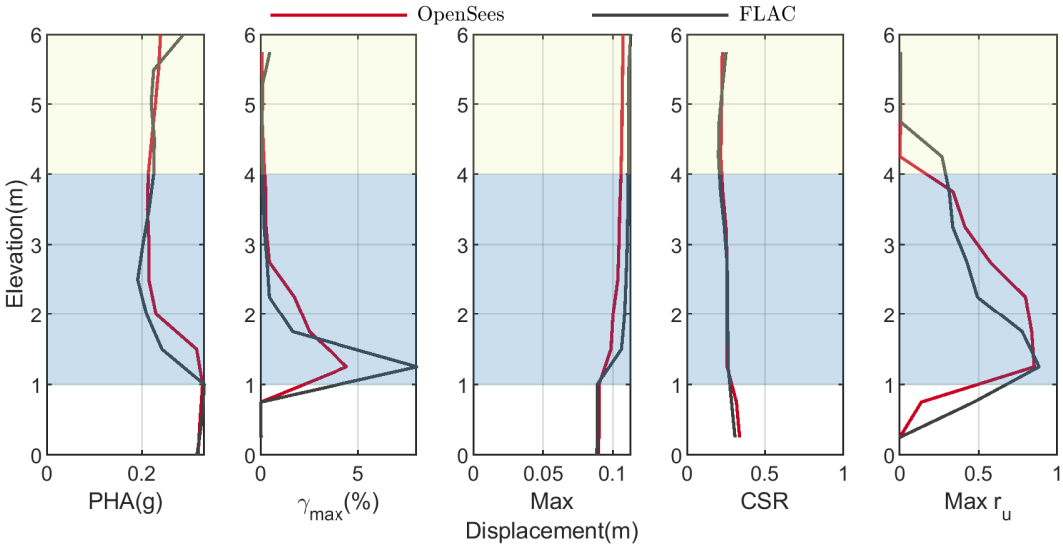

Figure 5.10: Comparison of PHA, γ_{max}, maximum displacement, CSR, and max r_u obtained using OpenSees and FLAC for motion RSN766. $S_{u,rat} = 0.25$.

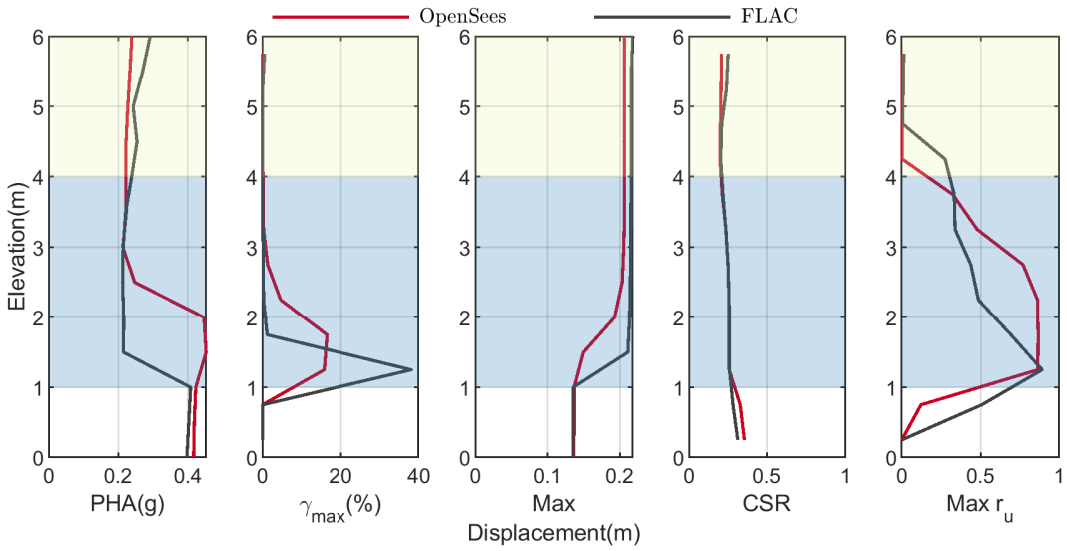

Figure 5.11: Comparison of PHA, γ_{max}, maximum displacement, CSR, and max r_u obtained using OpenSees and FLAC for motion RSN963. $S_{u,rat} = 0.25$.

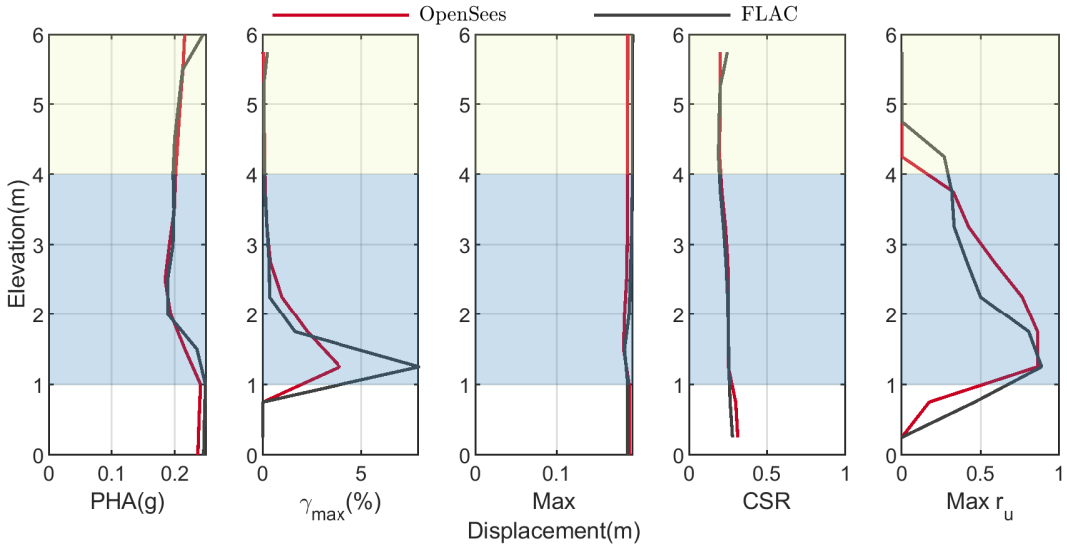

Figure 5.12: Comparison of PHA, γ_{max}, maximum displacement, CSR, and max r_u obtained using OpenSees and FLAC for motion RSN1203. $S_{u,rat} = 0.25$.

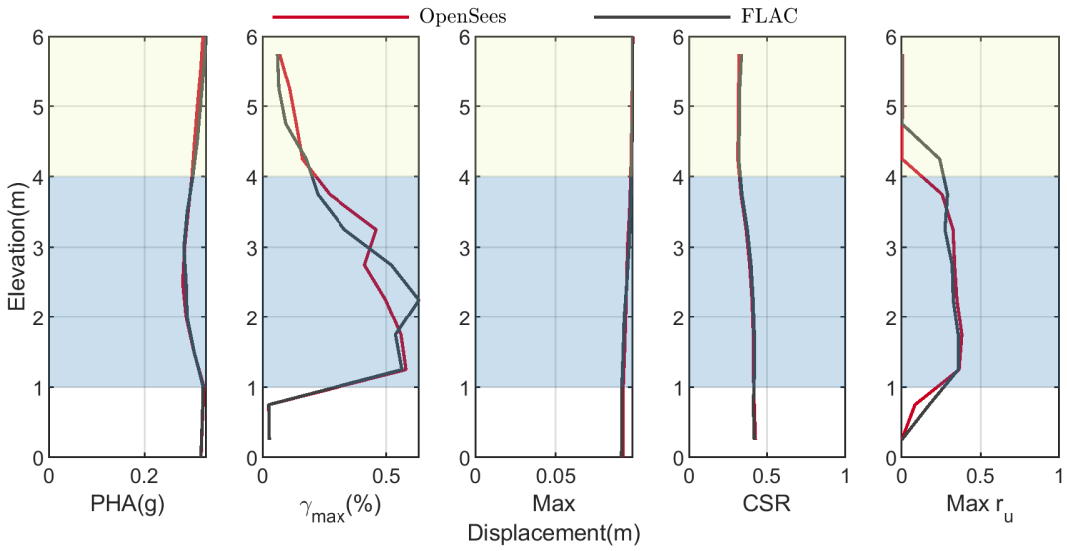

Figure 5.13: Comparison of PHA, γ_{max}, maximum displacement, CSR, and max r_u obtained using OpenSees and FLAC for motion RSN766. $S_{u,rat} = 0.50$.

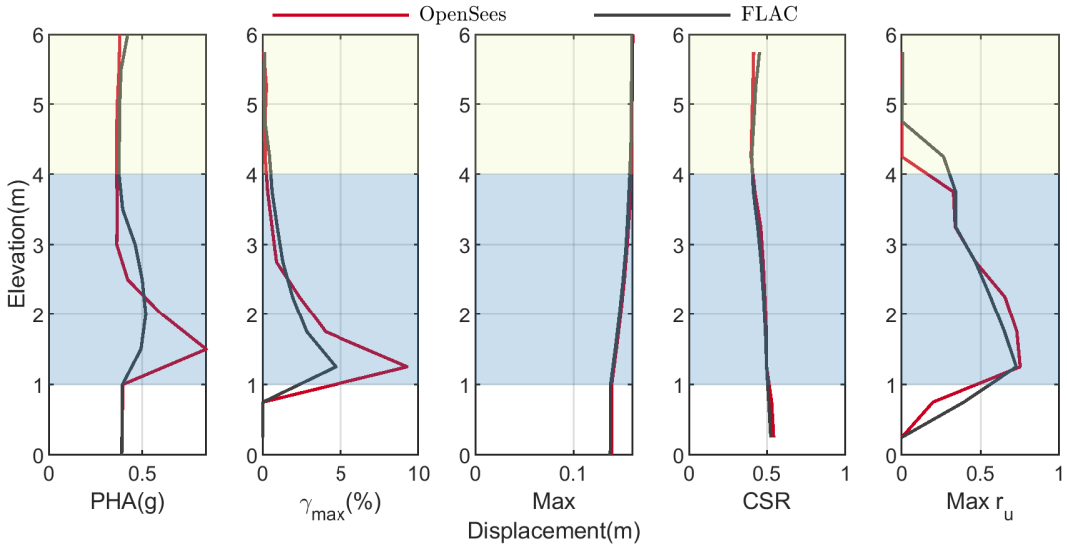

Figure 5.14: Comparison of PHA, γ_{max}, maximum displacement, CSR, and max r_u obtained using OpenSees and FLAC for motion RSN963. $S_{u,rat} = 0.50$.

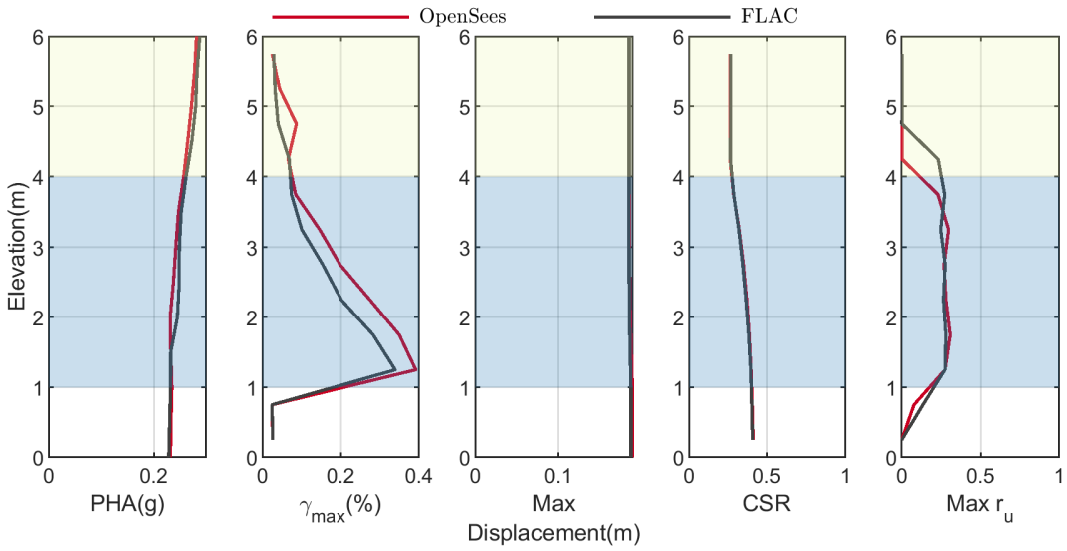

Figure 5.15: Comparison of PHA, γ_{max}, maximum displacement, CSR, and max r_u obtained using OpenSees and FLAC for motion RSN1203.$S_{u,rat} = 0.50$.

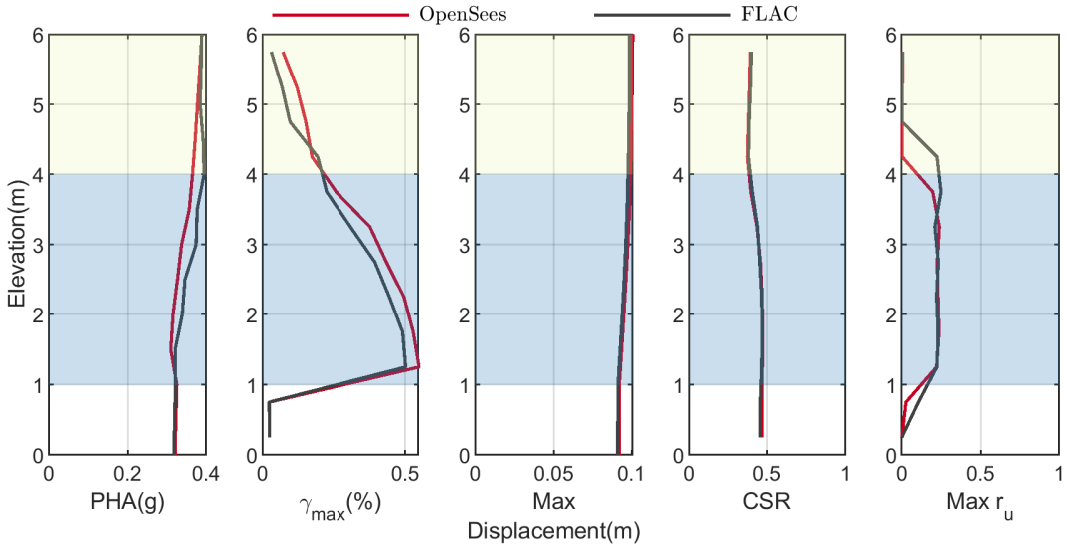

Figure 5.16: Comparison of PHA, γ_{max}, maximum displacement, CSR, and max r_u obtained using OpenSees and FLAC for motion RSN766. $S_{u,rat} = 0.75$.

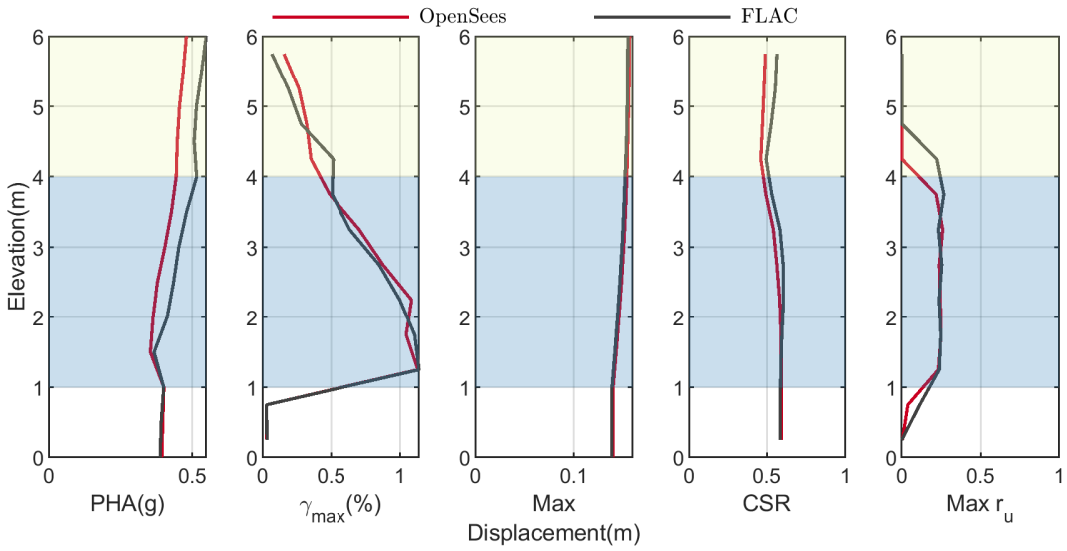

Figure 5.17: Comparison of PHA, γ_{max}, maximum displacement, CSR, and max r_u obtained using OpenSees and FLAC for motion RSN963. $S_{u,rat} = 0.75$.

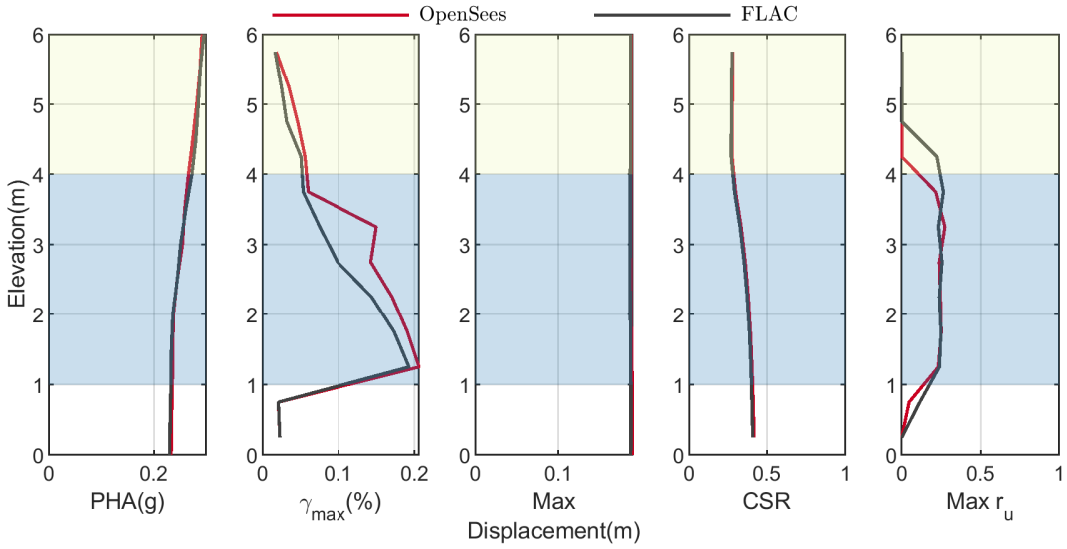

Figure 5.18: Comparison of PHA, γ_{max}, maximum displacement, CSR, and max r_u obtained using OpenSees and FLAC for motion RSN1203. $S_{u,rat} = 0.75$.

5.5 Summary

This chapter presents a brief introduction to the PM4Silt constitutive model including key formulation aspects, implementation details followed by a brief introduction to the OpenSees built-in commands that were considered during its implementation.

Results of a verification study for PM4Silt as implemented in OpenSees, using stress points and 1D soil columns are also presented in this chapter. The results show that, despite discrepancies in results observed due to inherent differences between these platforms, i.e., FEM vs. FDM and different model discretization, the OpenSees implementation produced consistent results to FLAC.

Chapter 6

VALIDATION OF PM4SAND AND PM4SILT IN OPENSEES

6.1 Introduction

This chapter presents results of a validation study of the PM4Sand and PM4Silt models implemented in OpenSees. Ever since the model publication, the FLAC version has been used in a wide range of studies, including 1D site response analysis of liquefiable soil deposit (Ziotopoulou et al., 2012), 2D deformation analysis of embankments underlain by liquefied soils (Armstrong et al., 2013), analysis of spatial variability on liquefaction-induced settlement and lateral spreading (Montgomery and Boulanger, 2017; Boulanger et al., 2019), and prediction of centrifuge tests that represent 2D sloping ground (Ziotopoulou, 2017) just to name a few. These results have proven the model to be satisfactory and provide valuable insight on various problems related to liquefaction. In the same line of thought, the PM4Sand model implemented in OpenSees has also been used in various research projects and shown its capability in capturing soil behavior during liquefaction. In this context, and to complement the aforementioned studies, a study on two well-known case histories as well as blind prediction of a large-scale shake table experiment are presented in this chapter. Accompanying studies by the authors on type-B and type-C prediction results of centrifuge experiments that represent a liquefying ground are presented in Part II of this document.

6.2 Site response analysis of WildLife Array

This section describes simulation results for a vertical array installed in liquefiable soil profiles that in the past have captured strong motion events, and is widely regarded as one of the best available in-situ measurements of a liquefiable soil response to earthquake loading. This array, known as the Wildlife Liquefaction Array (WLA), has been studied extensively by

different researchers (Youd et al., 2004; Holzer and Youd, 2007; Sideras, 2011; Ziotopoulou et al., 2012; Kramer et al., 2018). These field recordings provide excellent information to validate liquefiable soil models.

WLA is a ground motion-monitoring and liquefaction research site located at the southern most terminus of the San Andreas Fault system. WLA is situated in California's Imperial Valley on the west bank of the Alamo River 13 km north of Brawley, California and 160 km east of San Diego. This site is instrumented with six piezometers and two accelerometers. One of the piezometers, P5, is buried near the top of a sandy silt layer and accelerometers are located at 0m and 7.5m, respectively. The WLA field site records numerous earthquakes daily in this seismically active area. Among these events, two significant events have drawn researchers attention: the M6.2 Elmore Ranch event on November 23rd, 1987 (Holzer and Youd (2007)) and its aftershock M6.6 Superstition Hills Earthquake that occurred the following day. Instruments were triggered and acceleration and pore pressure time histories were recorded at this site during both events. Liquefaction was not triggered during the Elmore Ranch event however was triggered during the latter one with evidence, i.e., sand boils and ground cracks, observed at the site. Although questions have been raised regarding the reliability of measured pore pressure during the Superstition Hills event (Kramer et al., 2018), the recorded ground motion (Fig. 6.1) clearly showed dilation pulses and shift of frequency contents after liquefaction triggering. In this study, only the North-South (NS) record was considered.

In terms of soil conditions, the WLA soil profile consists of four general soil layers: the upper 2.5 m consists of lean clay/silt (CL-ML), underlain by 1 m of sandy silt (ML). Extending 3.3 m below this is a silty-sand (SM) layer, which is liquefiable. This layer is underlain by a 0.7 m deposit of high plastic clay (CH). The water table is at a depth of 1 m below the ground surface. The soil profile along with SPT, CPT, and V_s measurements is shown in Fig. 6.2.

For modeling purposes, the profile was divided into five layers as shown in Table 6.1. Within these five layers, layer 1, 2, and 5 were modeled using the *PresusreIndepenedMulti-*

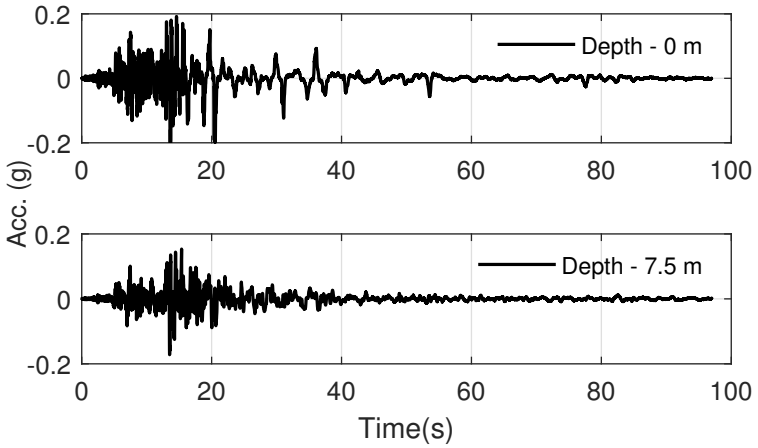

Figure 6.1: Recorded N-S horizontal acceleration time histories at various depths for WLA.

Yield (PIMY) model available in OpenSees that is appropriate for clayey type soils. The shear modulus G for each layer was calculated using V_s, and the bulk modulus, K, was calculated from G with an assumed $\nu = 0.3$. Modulus reduction (G/G_{max}) curves proposed by Darendeli (2001) were used to define the yield surfaces in the PIMY model. Darendeli (2001) curves are based on a hyperbolic model and are derived from cyclic laboratory tests; often not run to failure. Consequently, these curves do not necessarily provide an accurate representation of soil strength at large shear strains. In some cases, the shear strength can be grossly inaccurate, which may result in significant errors for analyses involving shear stress levels at or near failure (Gingery and Elgamal, 2013). In this study, a method proposed by Alborz Ghofrani (personal communication, 2016) was used to correct G/G_{max} curves to match shear strength of soil at failure strain. Fig. 6.3 illustrates the difference between the original Darendeli (2001) curves and the strength corrected ones. The dash line in the shear stress-strain plots depicts the shear strength of the soil obtained from laboratory tests. The figure clearly shows the original curves under-predicted the strength of the shallow layer while over-predicted the strength of the deep layer in this case. The correction algorithm can smoothly transform the original curve from a desired strain to match real shear strength

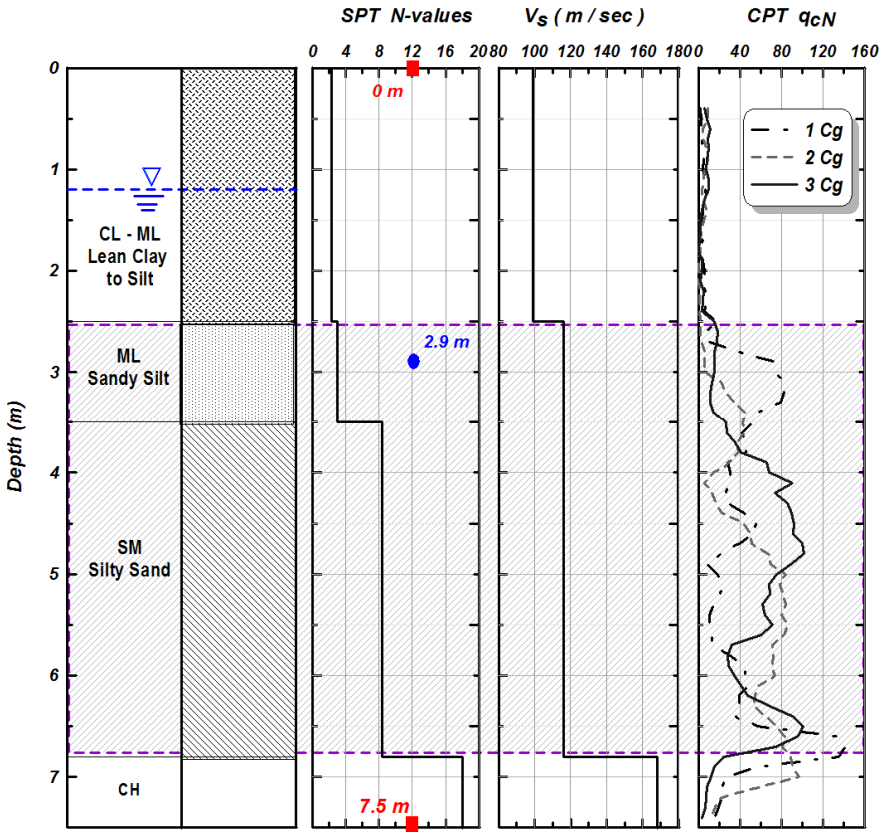

Figure 6.2: Soil profile for WLA site showing SPT N-values, and shear value velocities (reproduced from Ziotopoulou et al. (2012)).

at large strain. In this study, correction was applied at strain where 50% of shear strength implied by the original G/G_{max} curve was reached.

Layer 3 and 4 were modeled using the PM4Sand model. Material properties for PM4Sand are presented in Table 6.2. CRR and D_R values were adopted from Ziotopoulou (2010). G_o was computed based on V_s. Then, h_{po} was calibrated iteratively to match the targeted CRRs. All secondary parameters were kept as default values. The soil column was modeled using 15 SSPquadUP elements. *Uniform Excitation* was used to apply the acceleration time history recorded in the downhole array. Other boundary conditions and analysis parameters

Table 6.1: Layering and material models used in OpenSees to simulate WLA site and adopted soil properties. Soil properties are adopted from Youd et al. (2004)

.

Layer #	Thickness (m)	Material Model	Hydraulic Conductivity(m/s)	γ_{Dry} (kN/m^3)	γ_{Sat} (kN/m^3)	OCR	PI	Su(kPa)
1	1.0	PIMY	10^{-5}	14.13	-	4	8	36.0
2	1.5	PIMY	10^{-5}	-	18.63	4	8	36.0
3	1.0	PM4Sand	10^{-4}	-	18.82			
4	3.5	PM4Sand	10^{-4}	-	18.82			
5	0.5	PIMY	10^{-5}	-	19.18	2	29	30.5

Table 6.2: Input parameters for PM4Sand for WLA.

Layer #	Material Model	$CRR_{M7.5}$	Primary Parameters		
			D_R	G_o	h_{po}
3	PM4Sand	0.115	0.38	525.0	1.2
4	PM4Sand	0.155	0.58	410.0	0.44

*All secondary input parameters were assigned the default values.

were similar to those used in the 1D soil column analyses described in the verification study section.

From the simulations and comparison with field recordings several findings are of interest. First, as indicated by the simulated pore water pressure evolution plot, shown in Fig. 6.5, liquefaction was triggered during this event. Fig. 6.4 shows the comparison between simulated and recorded acceleration response at the surface. The simulations were able to capture the general trend of recorded acceleration response, but, simulations under-estimated long period components associated with post liquefaction softening and intermittent higher frequencies associated with dilation pulses. This indicates the material parameters should be modified

to produce more dilative soil behavior than what is shown in Fig. 6.6. Simulations using the original and corrected G/G_{max} curves produced similar results as shown in Fig. 6.4 which indicates the shear stress-strain behavior of those layers during this motion was still within the unaffected portion of the original curves.

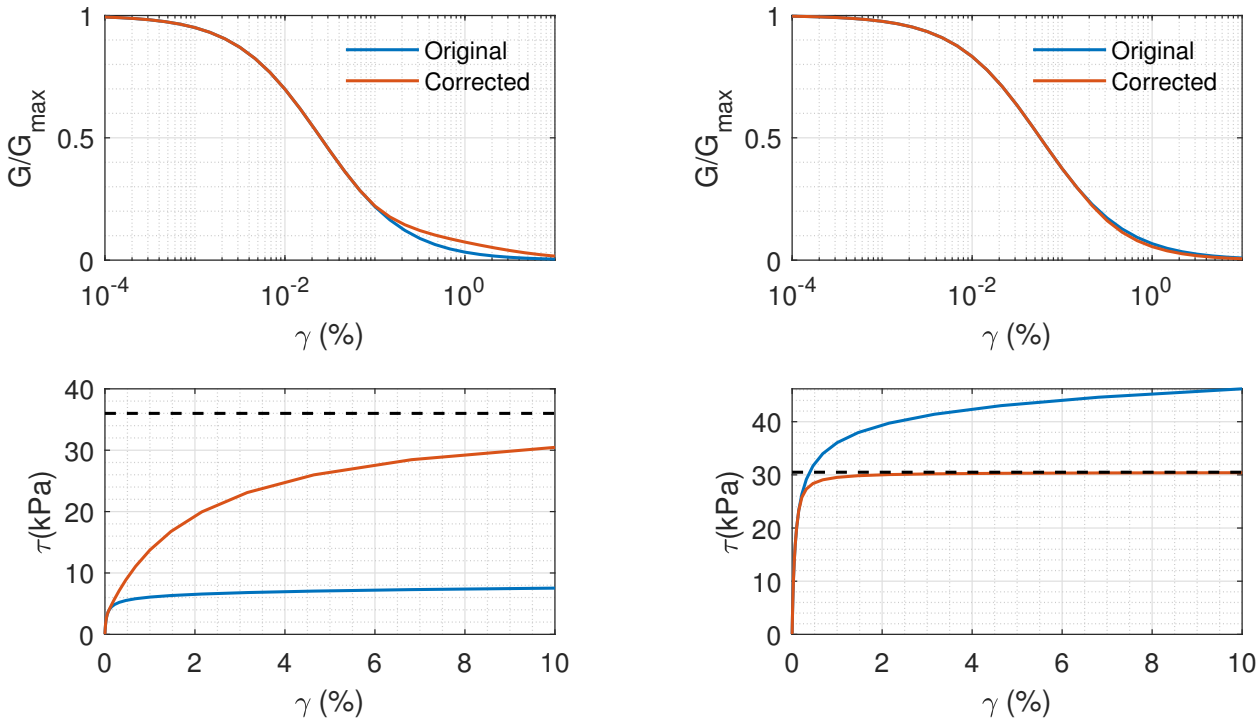

Figure 6.3: Comparison of strength corrected and original Darendeli (2001) shear modulus reduction curves and computed shear stress-shear strain curves for: (a) Layer 2 and (b) Layer 5.

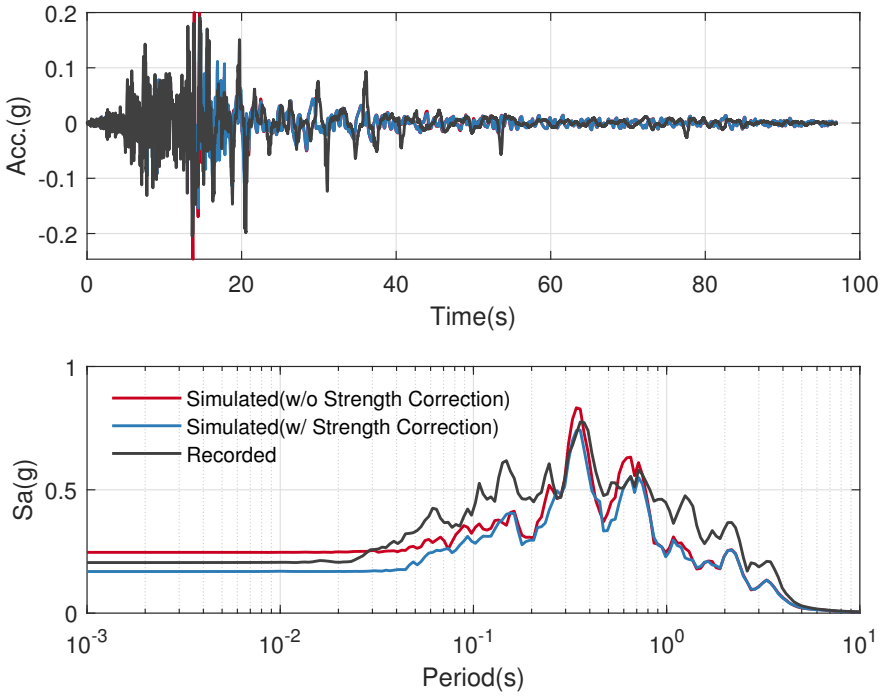

Figure 6.4: Comparison of time history and response spectra of simulated and recorded motions at surface.

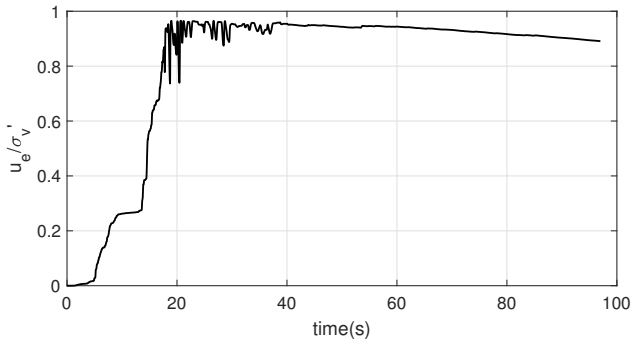

Figure 6.5: Evolution of excess pore pressure at the top of sandy silt layer.

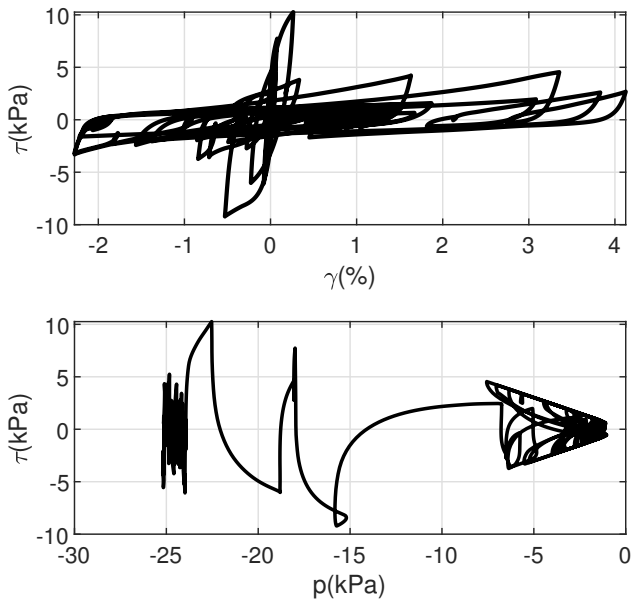

Figure 6.6: Stress-strain loop and stress path for PM4Sand model at a depth of 4 m for WLA.

6.3 Site response analysis of Port Island Array

The second case investigated in this study is the Port Island array. This array is located in Kobe Port Island, Japan, a man-made island that suffered substantial damage during the 1995 Kobe earthquake (Hyogoken-Nambu earthquake). This array has been studied by different researchers in the past (Ishihara et al., 1996; Cubrinovski et al., 1996, 1999; Ziotopoulou et al., 2012; Sideras, 2011). The array consists of four sets of strong motion accelerometers positioned at the ground surface and at depths of 16, 32, and 83 m (Cubrinovski et al., 1996). No piezometers were installed, unlike WLA. Shown in Fig. 6.7, the soil profile consists of roughly five layers: a 18 m thick reclaimed Masado soil (well-graded and containing a fairly large portion of gravel) at surface, a 10 m thick alluvial clay layer, a 9 m thick alluvial gravelly sand layer, a 22 m thick diluvial gravelly sand layer, and a 22 m thick diluvial clay layer. The water table oscillates at around 3 m depth approximately.

During the Kobe earthquake massive liquefaction was triggered in the area of this site resulting in settlements and sand boils. Fig. 6.8 illustrates the North-South horizontal acceleration recorded by the downhole arrays. The records show evolution of frequency content possibly due to softening of soils during strong shake.

Only the top 32 m of this profile was simulated in this study. Thus the motion recorded at 32 m in the downhole was applied as a within motion using the *Uniform Excitation* pattern in OpenSees. The profile was divided into 6 sublayers as listed in Table 6.3 for modeling purposes. The soil column was modeled using a total of 64 SSPquadUP elements with average size of 0.5 m. The material properties for PM4Sand was adopted from Ziotopoulou et al. (2012) and are listed in Table 6.4.

The silty clay and top of the gravelly sand and silt layer were expected to show clay-like behavior and hence were simulated using the PM4Silt model. In this study, G_o was calculated from measured shear wave velocity values at this site (Fig. 6.7). The other two primary parameters were selected for medium and stiff clays, respectively, based on SPT blow counts as presented in Table 6.4.

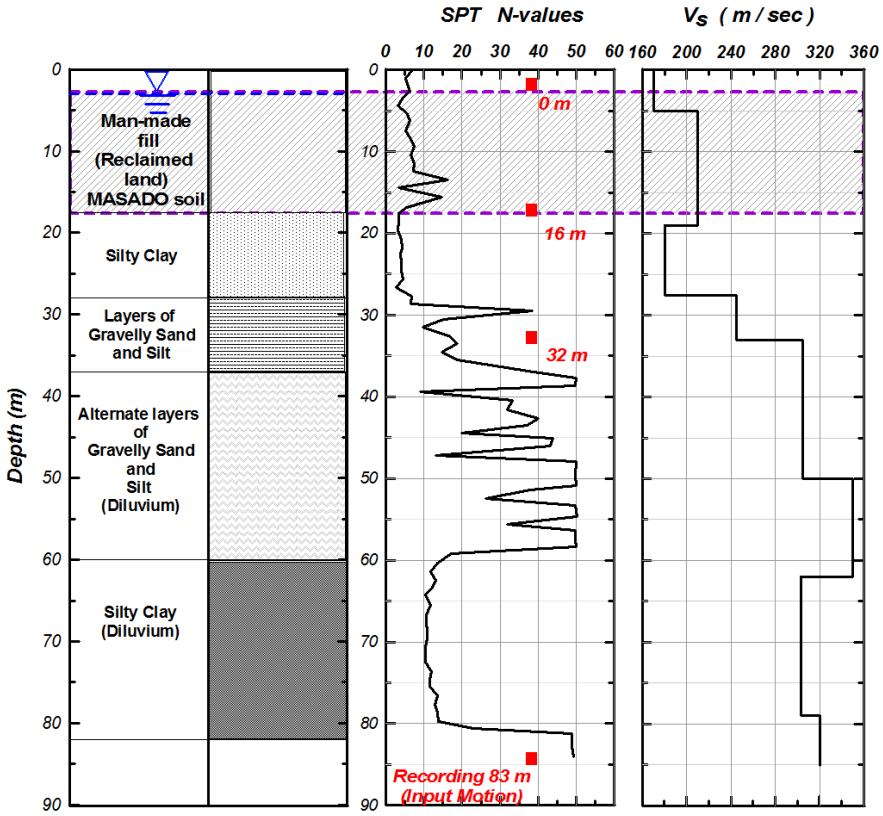

Figure 6.7: Soil profile for Port Island site showing SPT N-values and shear wave velocities (reproduced from Ziotopoulou et al. (2012)).

Fig. 6.9 illustrates the simulated soil behavior obtained using PM4Sand at a depth of 10 m. As indicated by the pore water pressure evolution plot, liquefaction was triggered at around 14 sec. and PM4Sand was able to capture the general behavior of the sand and liquefaction triggered by the earthquake. Figs. 6.10 and 6.11 depict the comparison between simulated and recorded acceleration response at the surface and a depth of 16 m, respectively. The simulations were able to capture the general trend of recorded acceleration response.

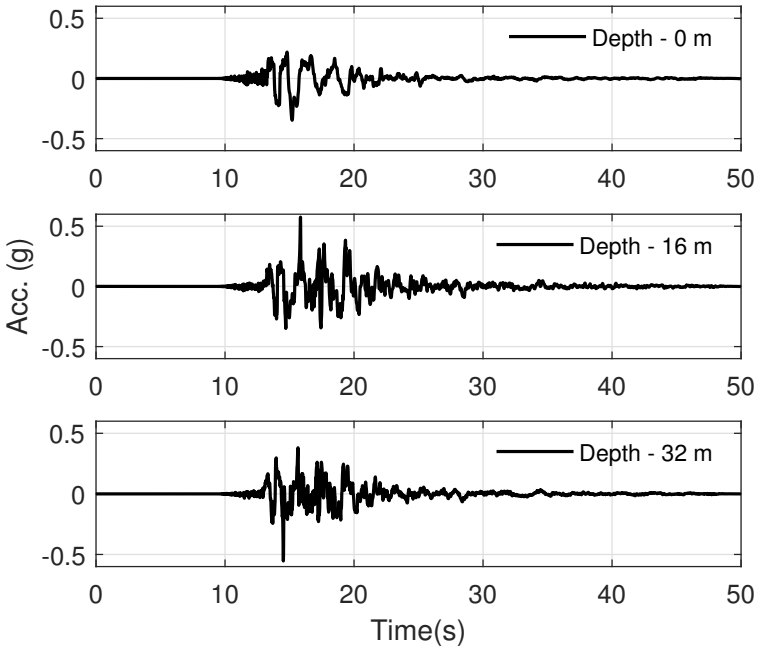

Figure 6.8: Recorded N-S horizontal acceleration time histories at various depths for Port Island array.

Table 6.3: Layering and material models used in OpenSees to simulate Port Island array and adopted soil properties.

Layer #	Thickness(m)	Material Model	Hydraulic Conductivity(m/s)
1	3.0	PM4Sand	10^{-4}
2	2.0	PM4Sand	10^{-4}
3	9.0	PM4Sand	10^{-4}
4	3.5	PM4Sand	10^{-4}
5	10.5	PM4Silt	10^{-6}
6	4.0	PM4Silt	10^{-6}

Table 6.4: Input parameters for PM4Sand for the Port Island array.

Layer #	Material Model	Primary Parameters			
		D_R	S_u/σ'_v	G_o	h_{po}
1	PM4Sand	0.47		729.0	0.7
2	PM4Sand	0.47		729.0	0.7
3	PM4Sand	0.39		695.51	0.8
4	PM4Sand	0.47		507.53	0.9
5	PM4Silt		0.5	465.0	50.0
6	PM4Silt		0.75	686.0	60.0

*All secondary input parameters were assigned the default values.

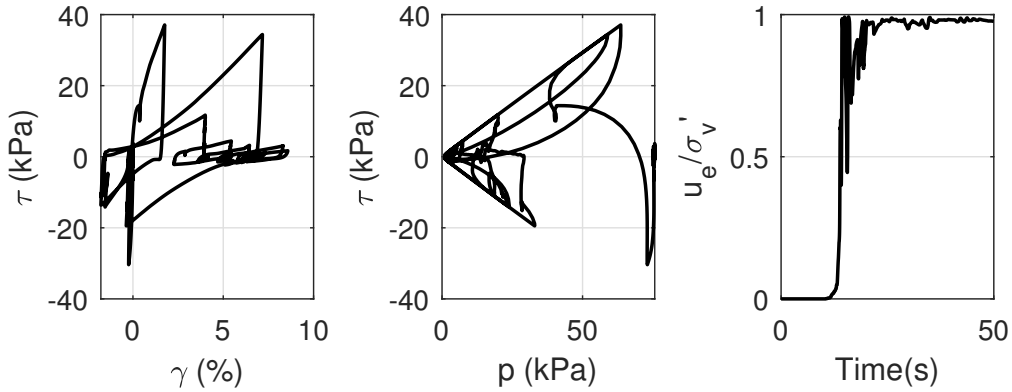

Figure 6.9: Stress-strain loop, stress path, and excess pore-pressure evolution at the depth of 10 m obtained using PM4Sand.

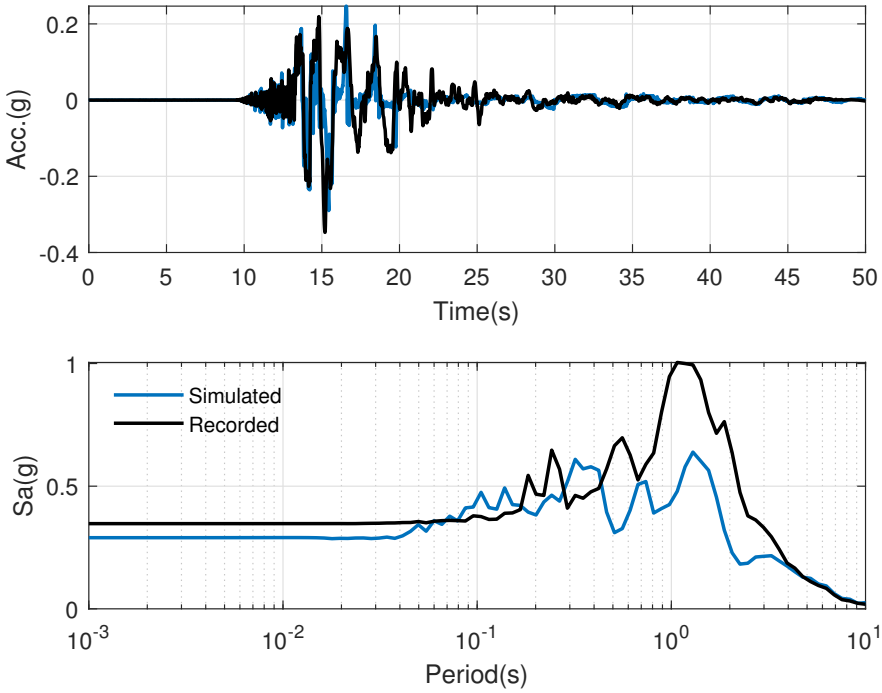

Figure 6.10: Comparison of acceleration time history and response spectra of simulated and recorded motions at the surface.

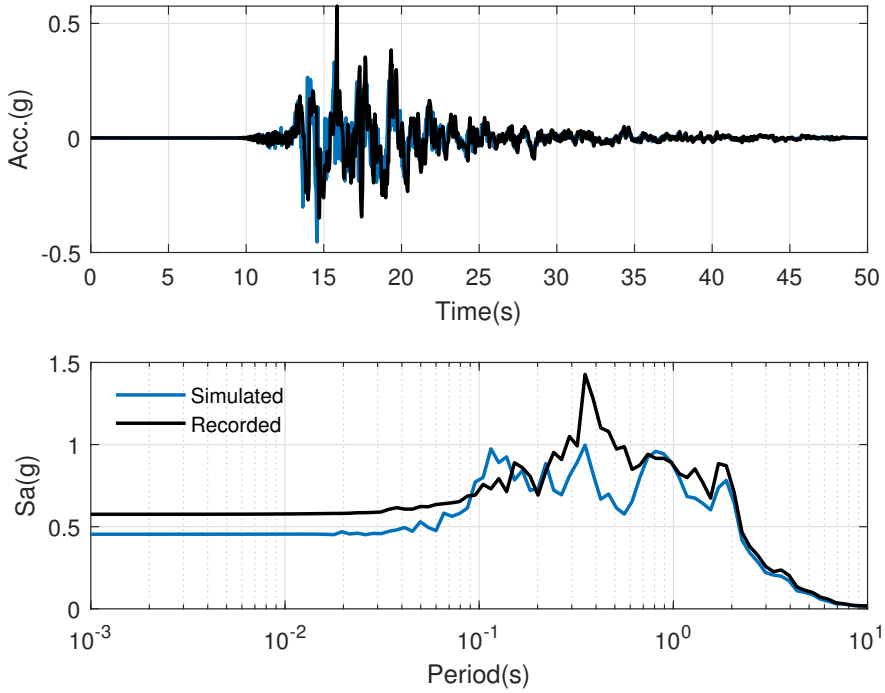

Figure 6.11: Comparison of acceleration time history and response spectra of simulated and recorded motions at a depth of 16m.

6.4 Blind prediction of a large-scale liquefaction shake table experiment

This section presents details on the modeling strategy of a large-scale shake table test that focused on shallow foundations in liquefied soils and was completed at University of California San Diego (UCSD) (Motamed et al., 2020). This test was performed as a benchmark test in which no mitigation methods were adopted to reduce liquefaction induced settlement of a shallow foundation. Extensive liquefaction and sand ejecta were observed and it was chosen as the 2018 annual blind prediction contest organized by the Pacific Earthquake Engineering Research Center (PEER). Each participant was required to predict permanent settlements at multiple locations shown in Fig. 6.12. The accuracy of blind prediction submissions was evaluated in terms of Root-Mean-Square Error (RMSE) and the team with the lowest RMSE was ranked 1st and declared as the winner of the blind prediction. The top three teams were announced and acknowledged during the 2019 PEER Annual Meeting which was held at UCLA, during January 17-18 2019 and their information can be accessed through PEER website (`https://peer.berkeley.edu/news/congratulations-2018-peer-blind-prediction-contest-and-phi-challenge-winners`). The University of Washington team used PM4Sand implemented in OpenSees in this prediction and was ranked at 2nd place.

6.4.1 Model configuration

The experiment model was built inside a large-scale laminar soil shear box which had a height of 2.9 m, length of 3.9 m, and width of 1.8 m and consists of 43 steel laminar frames to allow unidirectional movements. The weight of the steel frame was approximately 10 to 13 percent of the soil weight, depending on the density of soil. The model ground consisted of three layers of Ottawa F-65 sand: a dense non-liquefiable layer of at the base ($D_R = 90\%$) with a thickness of 1.0 m overlain by a medium liquefiable sand ($D_R = 50\%$) with a thickness of 1.3 m. The liquefiable layer was overlain by a medium dense sand crust layer with a thickness of 0.6 m. The model ground configuration is presented in Fig. 6.13. Three methods were

used to calculate relative density: sand cone test, volume and weight, and dynamic cone penetrometer (DCP) test. The calculated relative densities are presented in Table 6.5. The water table was at the depth of 0.6 m. The contact pressure between footing and underlain soil was 41.6 kPa, which was achieved by placing additional weights on the top of the footing as shown in Fig. 6.14. The density of concrete used to construct the footing was 2616 kg/m^3. A harmonic input motion with PGA of 0.15 g, frequency of 2 Hz, and duration of 18 seconds was targeted. The achieved motion is shown in Fig. 6.16 and it was later used in as the input of numerical simulation. The test was displacement controlled and large acceleration pikes as high as 0.5 g were observed in the achieved motion.

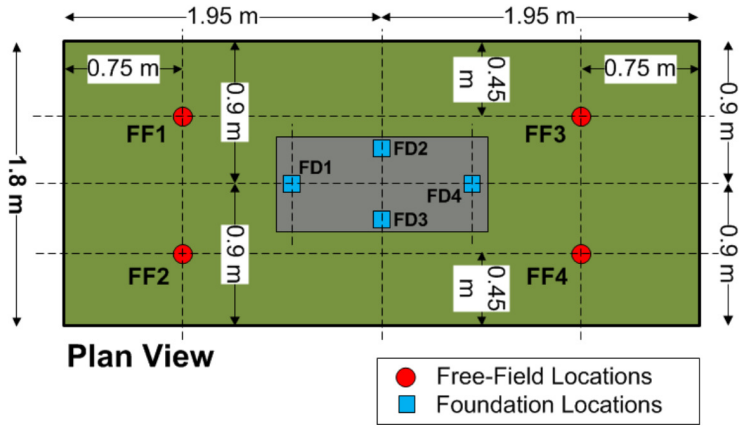

Figure 6.12: Locations of points for settlement prediction, all points are located on surface (z=0).

6.4.2 Numerical model

PM4Sand model was used to represent the behavior of soil layers. The material properties (Table 6.6) were adopted from author's previous calibration on Ottawa sand during LEAP-UCD-2017 project(Chen et al., 2019). Since PM4Sand was developed for plane-strain

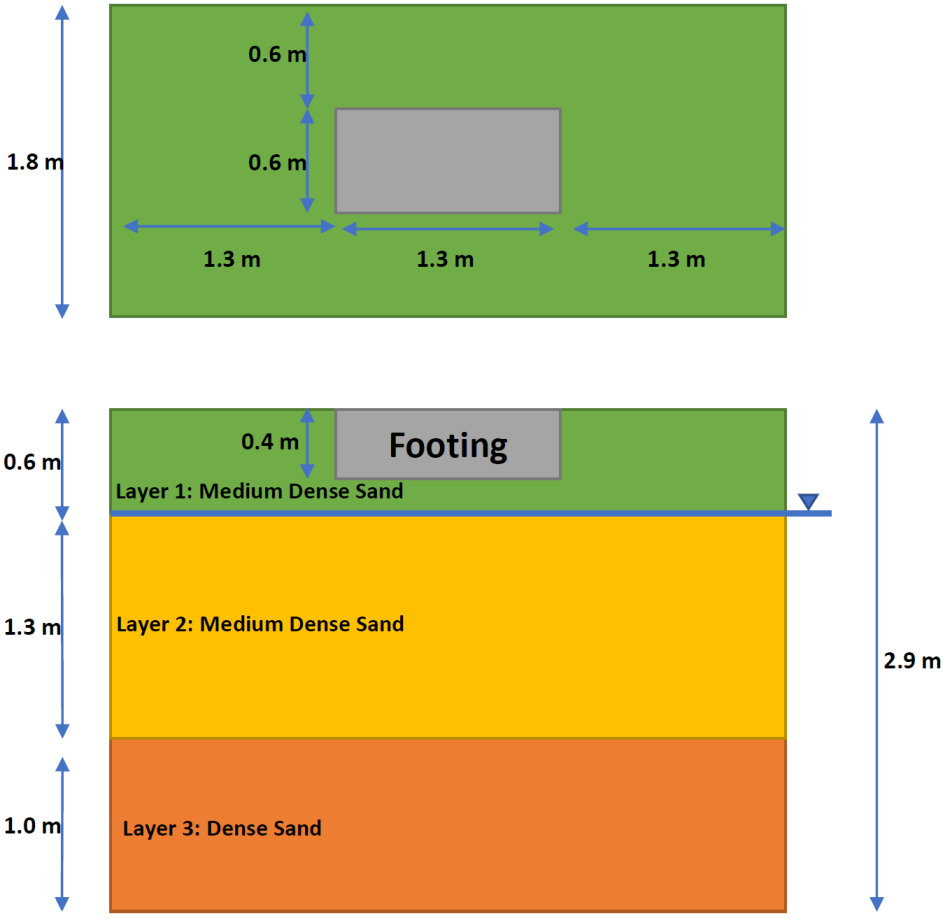

Figure 6.13: Model configuration.

Table 6.5: Measured relative density prior to shaking.

Layer	D_R % (Sand cone)	D_R % (Weight)	D_R % (DCP)
Crust	52	53	-
Medium Dense Sand	-	41	-
Dense Sand	90	87	83

Figure 6.14: Model footing prior to placement and steel weights to replicate target contact pressure (from Motamed et al. (2020)).

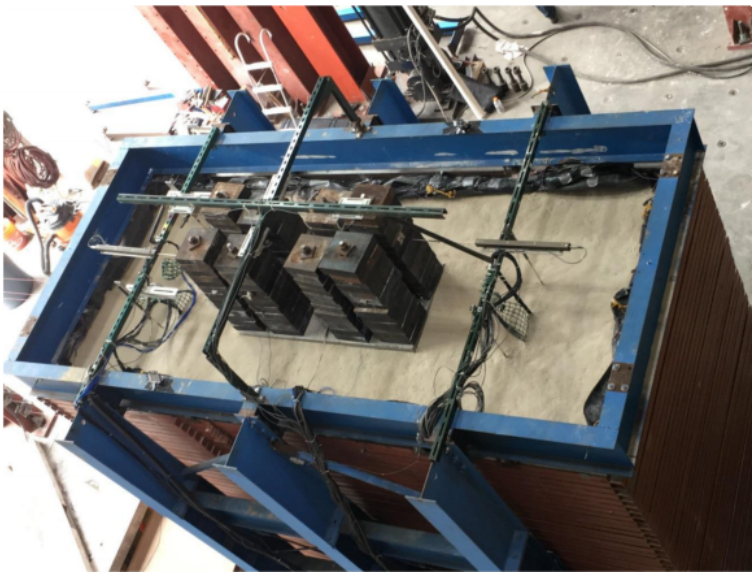

Figure 6.15: Model ground prior to shaking (from Motamed et al. (2020)).

conditions, a 2D plane-strain representation of the problem was adopted and numerical models were built using OpenSees. SSPquadUP element was used to capture the effective stress response of the shake table test.

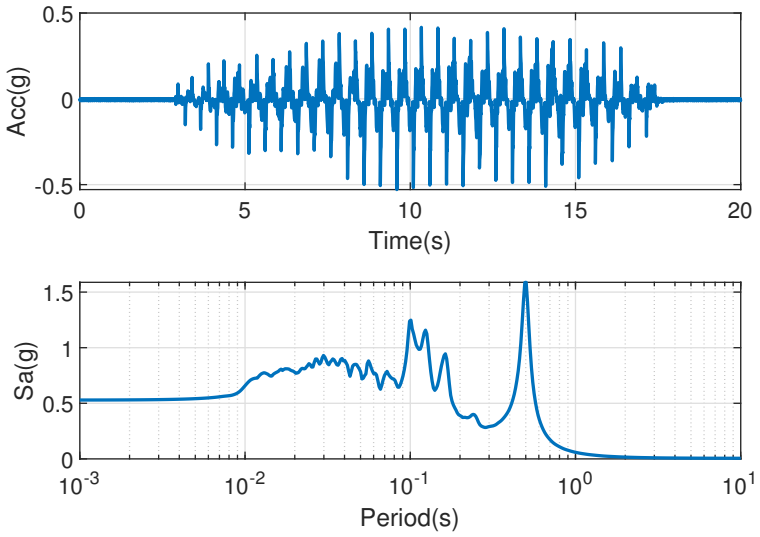

Figure 6.16: Achieved input motion recorded during experiment.

Table 6.6: Input parameters for PM4Sand, all other secondary parameters were kept as default values.

		Dense Layer	Medium Dense Layer	Crust
Primary Parameters	D_R	87%	41%	53%
	G_o	600.0	350.0	350.0
	h_{po}	0.0	0.07	0.07
Secondary Parameters	e_{max}	0.74	0.74	0.74
	e_{min}	0.49	0.49	0.49
	ϕ_{cv}	35.6	35.6	35.6
	c_z	200.0	200.0	200.0
	$\rho(kg/m^3)$	2.08	2.00	1.65

Two cases were considered in this study and the results were compared:

- Case 1: Only the contact load due to weight of footing and steel plates to underlain soil was considered. The rigidity of buried footing was ensured by attaching both vertical sides of soil that contacting footing together for horizontal movement.

- Case 2: Footing and steel plates were modeled using elastic isotropic material with self weight. Hence the inertial effect of footing and steel plates was considered in this case. Densities of concrete and steel was 2.616 and 7.5 kg/m^3, respectively. The interface between footing and soil was modeled using *zeroLength* elements with uniaxial *Elastic-No Tension* material. The stiffness of material is chosen to be same as the stiffness of the elastic material used to model concrete.

A schematic of the mesh used in this work is depicted in Fig. 6.17. Appropriate mesh refinement was chosen to properly resolve the propagation of shear waves of up to 50 Hz in the soil domain. The bottom boundary was fixed against both horizontal and vertical movements. The acceleration time history was applied to the base of the model using the so called *UniformExcitation* loading pattern in OpenSees. The vertical boundaries are tied together using *equalDOF* to simulate the shear box. Pore pressure degree of freedom of nodes above water table (-0.6 m) were set to be zero during the analysis to ensure drainage and avoid generation of excess pore pressures. The soil was assumed to be always in contact with the shear box. A frequency dependent Rayleigh damping was applied for the lack of small strain damping; which PM4Sand model lacks in its formulation. The Rayleigh damping coefficients were chosen such that a 2% damping was obtained at 0.2 Hz and 20 Hz. The hydraulic conductivity for element was set to be 3.0×10^{-4} m/s.

To apply gravity, the soil materials were set to be linear elastic and elemental body force was increased gradually to reduce numerical instabilities in the model. The self weight of footing and steel plates was not activated in case 2. Once gravity was in place, the materials were switched to have *elasto-plastic* behavior and enough extra steps were run to adjust their

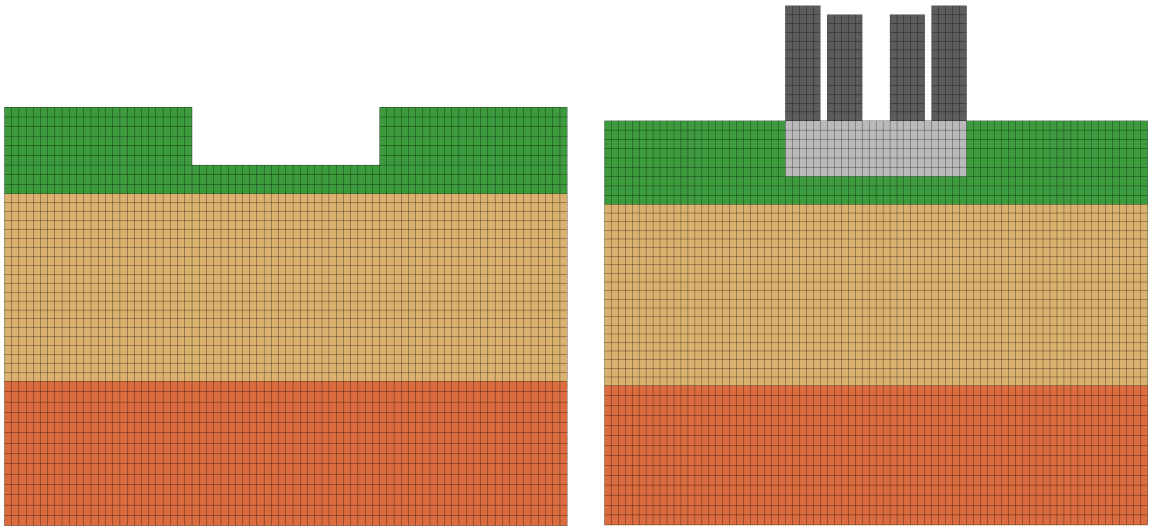

(a) Case 1 (b) Case 2

Figure 6.17: FEM meshes used in simulation for case 1 and 2, respectively.

internal variables to any plastic behavior and maintain equilibrium. A Poisson's ratio of 0.3 was assumed to generate the initial stress state. This Poisson's ratio yielded a lateral earth pressure coefficient K_0 of 0.43 under level ground plane-strain conditions. Figs. 6.18 to 6.20 present the imposed initial state of stress in terms of vertical, horizontal, and shear stresses. For case 1, the equivalent contact load was increased gradually until the final contact stress of 41.6 kPa was achieved. For case 2, the self weight of footing and steel plates were gradually increased until full weight was achieved. Figs. 6.21 to 6.23 show the imposed initial state of stress in terms of vertical, horizontal, and shear stresses after this phase. Noticeably, the reaction of soil underlying footing in case 1 and 2 represented a flexible and rigid footing condition, receptively, which caused discrepancy in achieved initial stress states of the two cases. Along with the boundary conditions discussed above, stress concentration was shown around the corner of the footing, especially in case 2.

After reaching the desired initial stress state, the acceleration time history was applied to the rigid bottom boundary. The constant average acceleration Newmark method ($\beta = 0.25$,

$\gamma = 0.5$) was used in order to resolve the integration in time. To account for the material nonlinearity both models used explicit modified Euler integration schemes with sub-stepping error control (Sloan et al., 2001). After shaking, PM4Sand's *PostShake* flag was turned on and additional dynamic analysis steps were executed to dissipate any excess pore pressure generated during the shaking and to simulate post-shake consolidation.

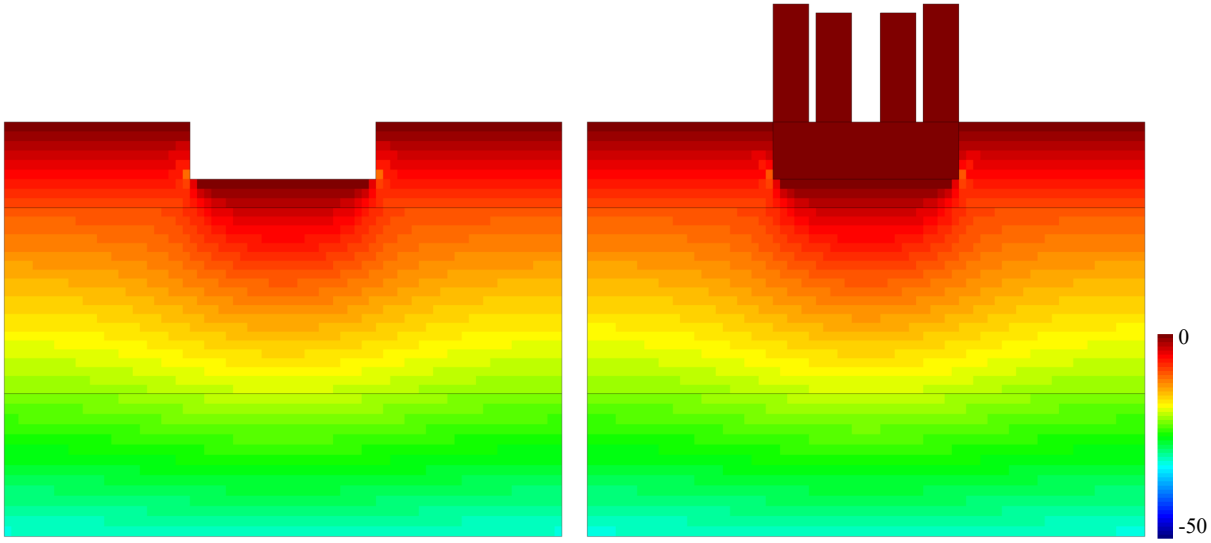

(a) Case 1 (b) Case 2

Figure 6.18: Initial vertical effective stress field after applying the weight of soil. Weight of superstructure was not applied. Unit in kPa.

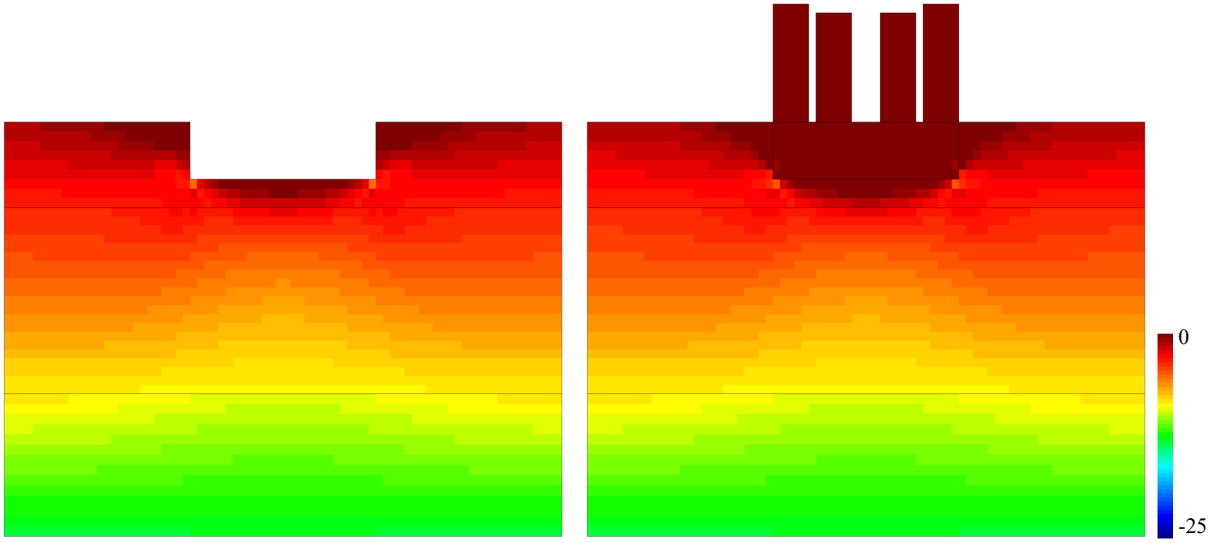

(a) Case 1 (b) Case 2

Figure 6.19: Initial horizontal stress field after applying the weight of soil. Weight of superstructure was not applied. Unit in kPa.

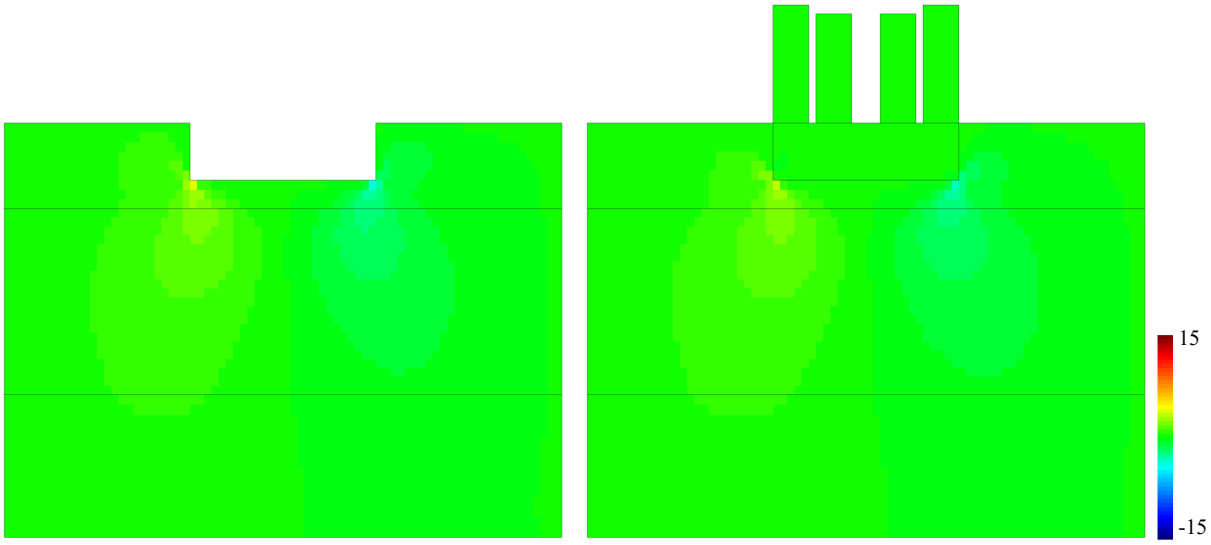

(a) Case 1 (b) Case 2

Figure 6.20: Initial shear stress field after applying the weight of soil. Weight of superstructure was not applied. Unit in kPa.

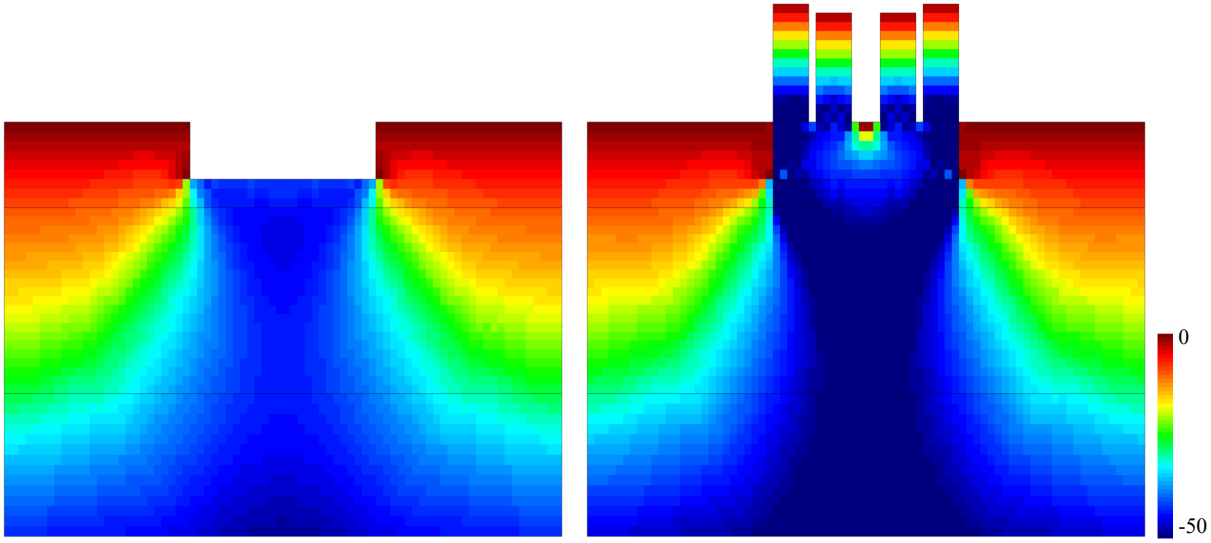

(a) Case 1 (b) Case 2

Figure 6.21: Final vertical effective stress field before shaking. Equivalent load and weight of superstructure was applied for case 1 and 2, respectively. Unit in kPa.

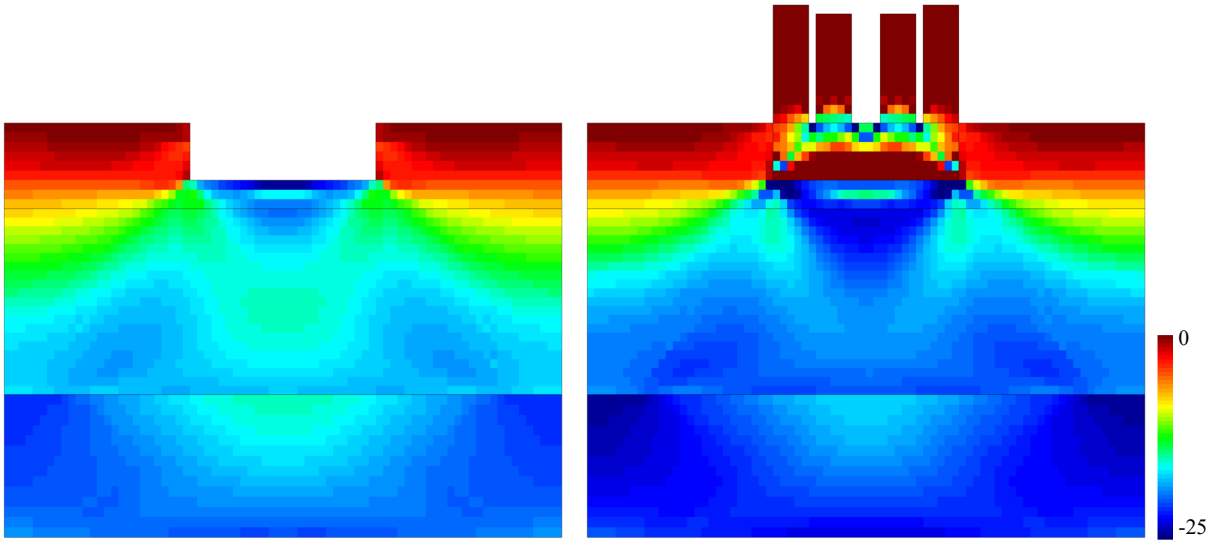

(a) Case 1 (b) Case 2

Figure 6.22: Final horizontal effective stress field before shaking. Equivalent load and weight of superstructure was applied for case 1 and 2, respectively. Unit in kPa.

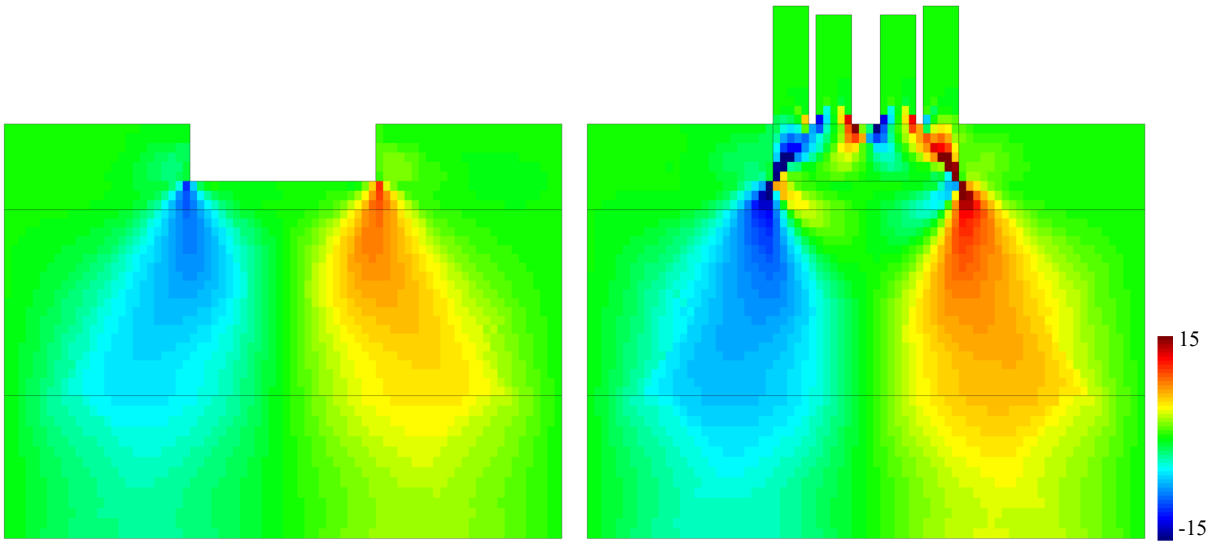

(a) Case 1 (b) Case 2

Figure 6.23: Final shear stress field before shaking. Equivalent load and weight of superstructure was applied for case 1 and 2, respectively. Unit in kPa.

6.4.3 Results

Comparison between two numerical cases

Fig. 6.24 depicts the final absolute displacement contours plotted on the final deformed shape of models. Both cases showed punching shear failure but with great difference and case 2 showed much larger magnitude of deformation. The results from case 2 also showed slip surface as well as soil heaving close to the surface. Fig. 6.26 illustrates the displacement time histories obtained from both cases. A total of 5 sets (FF1/2, FF3/4, FD1, FD2/3, and FD4 shown in 6.12) of displacement time histories were obtained from this 2D model.

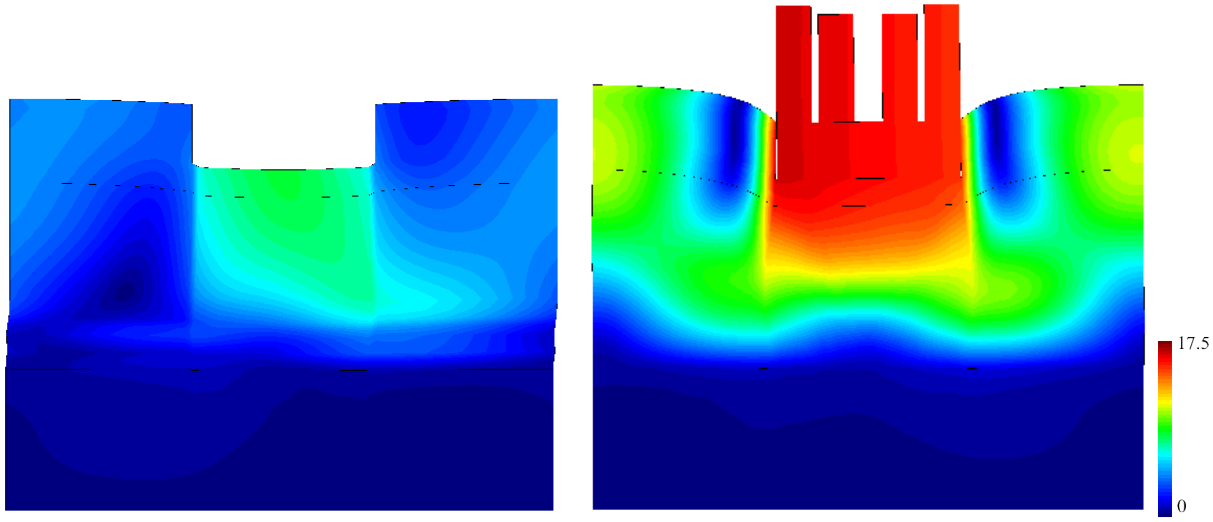

(a) Case 1 (b) Case 2

Figure 6.24: Final absolute displacement contour with deformed shape. Unit in cm.

Note that the displacement histories at FD1, FD3, and FD4 of case 1 were taken within the soil domain at the the base of the virtual footing. Displacement time histories from case 2 also showed ratcheting effect that is recognized in the study by Bray and Dashti (2014). Fig. 6.25 depicts the evolution of pore water pressure ratio from both cases. Although both cases demonstrated soil liquefaction beneath the footing, the trend was rather different.

Results obtained from Case 2 showed more dilative behavior, that coincides with ratcheting of the footing. Case 2 results showed better agreement with general behavior observed from previous studies. Thus, this set of results was submitted to the contest.

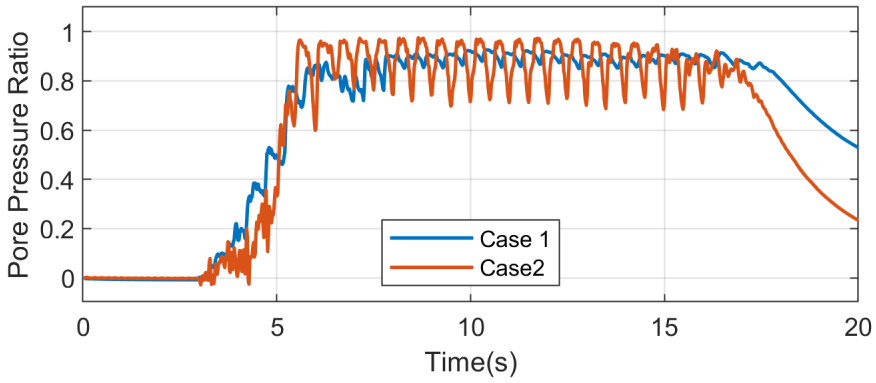

Figure 6.25: Comparison of pore pressure ratio evolution at center of loose layer underneath left corner of the footing obtained from case 1 and case 2.

Comparison between numerical and experimental results

Currently, only settlement time histories at sensor locations FF1 and FD1 have been published by the experimentalists and were compared with results from Case 2. Presented in Fig 6.27, predicated results obtained using numerical simulation was able to capture the general trend shown in experimental results, especially the developmental of settlement under foundation. However, simulation underpredicted the magnitude of ultimate settlement under foundation, while overpredicted the magnitude of heave at freefield location. PM4Sand greatly underestimated volumetric strain within the soil domain. Soil densification, as shown in recorded FF1 displacement from about 5 to 10 seconds (Fig. 6.27), was not captured in the numerical model.

Permanent settlements, recorded at 80 s, at both freefield and foundation locations were used to define the prediction bias,

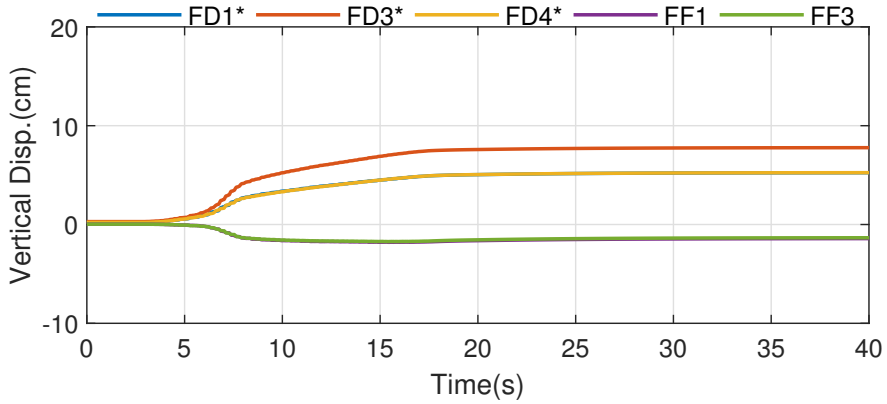

(a) Case 1

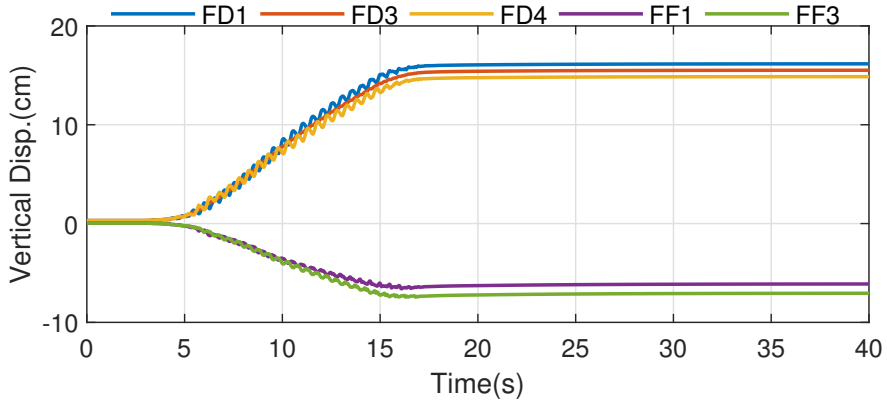

(b) Case 2

Figure 6.26: Comparison of displacement time histories recorded at various locations along surface obtained from (a) case 1 and (b) case 2. Positive value means downwards movement.

$$Bias(\%) = \frac{x_i - x}{x} \times 100 \tag{6.1}$$

where x_i is the predicted settlement and x is the measured settlement. Positive bias values indicate overestimation of numerical predictions whereas negative bias values show underestimation of the settlements. Table 6.7 shows calculated bias from all participants as well as UW team. Results obtained at UW were in line with other teams: majority of the teams overestimates the freefield heave and underestimates the settlement under foundation.

Prediction of deformation remain a challenge for numerical modelers.

Table 6.7: Bias in predicted settlements.

Settlement at	Average bias (All participants)	UW Team
FF1	227%	368%
FD1	-43%	-34%

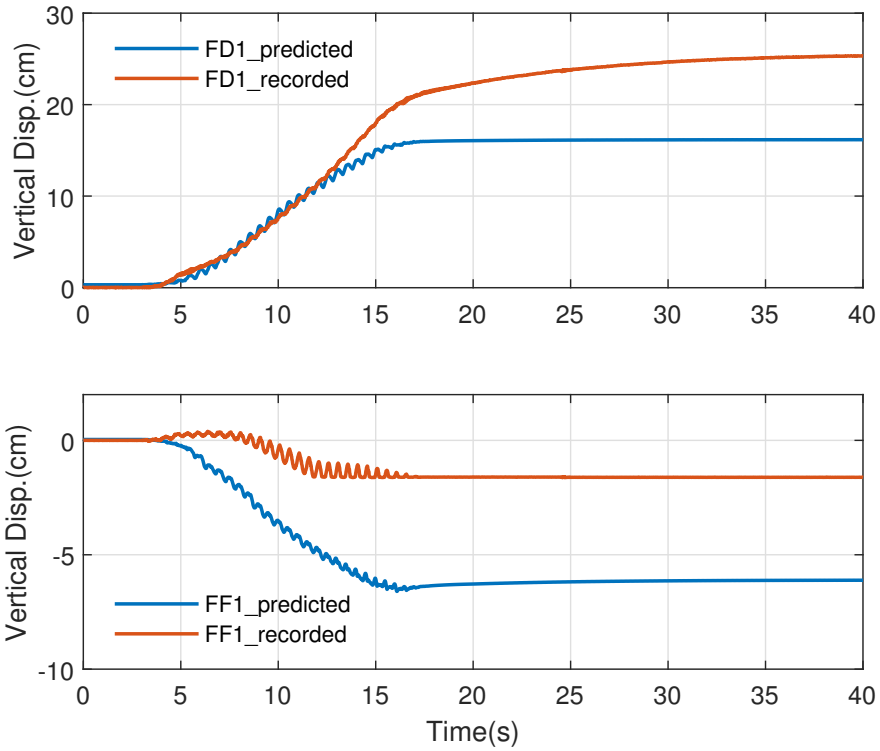

Figure 6.27: Comparison of recorded and predicted displacement time histories at FD1 and FF1. Positive value means downwards movement.

In this study, PM4Sand was able to capture the general trend shown in the shake-table experiment, however, further refinement of input parameters are required to better capture

permanent deformation under shallow foundation due to failure of liquefied ground. This observation reflects the limitation of model calibration during this blind prediction, that was based on liquefaction triggering instead of permanent deformation after failure. There were also possible limitations in using FEM tool, since it was not able to capture some phenomenon like void redistribution that existed in experiment.

6.5 Summary

This chapter presents a series of validation studies for PM4Sand including a 1D analysis of two liquefaction array case-histories (WLA and Port Island) and blind prediction of a large-scale shake table experiment. These studies illustrate capabilities and limitations of simulation of liquefaction sites using PM4Sand. The results obtained using PM4Sand for the liquefiable layers provided realistic and reasonable responses for all three cases with limited soil information, although further refinement of input parameters were warranted for better predictions.

Part II

LIQUEFACTION EXPERIMENTS AND ANALYSIS PROJECTS (LEAP)

The second part of the dissertation presents the work related to LEAP. Three projects, LEAP-UCD-2017, LEAP-Asia-2019, and LEAP-RPI-2020, are discussed. Three types of prediction, A, B, and C, are considered in these projects. Prediction type definitions are modified from Lambe (1973) and listed as follows:

- Type-A prediction: type-A prediction is performed toward a planned experiment, not targeted at an actual experiment. Thus, it is a true prediction of an event made prior to the event.

- Type-B prediction: type-B prediction is targeted at an actual experiment after the experiment is conducted. The predictors can get information on as-built properties and measured input data, but no knowledge of the results is available.

- Type-C prediction: type-C prediction is performed after the experiment is completed and results are disclosed. Thus, model parameters can be adjusted to enhance the quality of simulation results.

Archival journal papers and proceedings published by the author and coworkers as a result of this part of the research include:

– *Liquefaction Experiment and Analysis Projects (LEAP)*

1. Chen, L., Ghofrani, A., and Arduino, P. (2020, accepted). "Remarks on numerical simulation of the LEAP-Asia-2019 centrifuge tests"." *Soil dynamics and earthquake engineering*

2. Chen, L., Ghofrani, A., and Arduino, P. (2019). "Prediction of LEAP-UCD-2017 centrifuge test results using two advanced plasticity sand models." *Model Tests and Numerical Simulations of Liquefaction and Lateral Spreading: LEAP-UCD-2017*, B. L. Kutter, M. Manzari, and M. Zeghal, eds., Springer, 405–420

3. Chen, L., Ghofrani, A., and Arduino, P. (2020). "Prediction of LEAP-Asia-2019 centrifuge test results using prototype- and physical-scale models". LEAP-Asia-2019 Proceedings - Submitted, under review

4. Manzari, M. T., Ghoraiby, M. E., Zeghal, M., Kutter, B. L., Arduino, P., Barrero, A. R., Bilotta, E., Chen, L., Chen, R., Chiaradonna, A., Elgamal, A., Fasano, G., Fukutake, K., Fuentes, W., Ghofrani, A., Haigh, S., Hung, W.-Y., Ichii, K., Kim, D. S., Kiriyama, T., Lascarro, C., Madabhushi, G. S., Mercado, V., Montgomery, J., Okamura, M., Ozutsumi, O., Qiu, Z., Taiebat, M., Tobita, T., Travasarou, T., Tsiaousi, D., Ueda, K., Ugalde, J., Wada, T., Wang, R., Yang, M., Zhang, J.-M., Zhou, Y.-G., and Ziotopoulou, K. (2019). "LEAP 2017: Comparison of the type B numerical simulations with centrifuge test results." *Model Tests and Numerical Simulations of Liquefaction and Lateral Spreading: LEAP-UCD-2017*, B. Kutter, M. Manzari, and M. Zeghal, eds., Davis, California, Springer, 175–207

5. Manzari, M. T., El Ghoraiby, M., Zeghal, M., Kutter, B. L., Arduino, P., Barrero, A. R., Bilotta, E., Chen, L., Chen, R., Chiaradonna, A., Elgamal, A., Fasano, G., Fukutake, K., Fuentes, W., Ghofrani, A., Ichii, K., Kiriyama, T., Lascarro, C., Mercado, V., Montgomery, J., Ozutsumi, O., Qiu, Z., Taiebat, M., Travasarou, T., Tsiaousi, D., Ueda, K., Ugalde, J., Wada, T., Wang, R., Yang, M., Zhang, J.-M., and Ziotopoulou, K. (2020). "LEAP-2017 simulation exercise: Calibration of constitutive models and simulation of the element tests." *Model Tests and Numerical Simulations of Liquefaction and Lateral Spreading*, B. L. Kutter, M. T. Manzari, and M. Zeghal, eds., Cham, Springer International Publishing, 165–185

6. Kutter, B. L., Manzari, M. T., Zeghal, M., Arduino, P., Barrero, A. R., Carey,

T. J., Chen, L., Elgamal, A., Ghofrani, A., Montgomery, J., Ozutsumi, O., Qiu, Z., Taiebat, M., Tobita, T., Travasarou, T., Tsiaousi, D., Ueda, K., Ugalde, J., Yang, M., Zheng, B. L., and Ziotopoulou, K. (2020). "Numerical sensitivity study compared to trend of experiments for LEAP-UCD-2017." *Model Tests and Numerical Simulations of Liquefaction and Lateral Spreading*, B. L. Kutter, M. T. Manzari, and M. Zeghal, eds., Cham, Springer International Publishing, 219–236

– *Miscellaneous Projects*

6. Ramirez, J., Barrero, A., Chen, L., Dashti, S., Ghofrani, A., Taiebat, M., and Arduino, P. (2018a). "Site response in a layered liquefiable deposit: Evaluation of different numerical tools and methodologies with centrifuge experimental results." *Journal of Geotechnical and Geoenvironmental Engineering*, 144(10), 04018073

7. Ramirez, J., Barrero, A., Chen, L., Ghofrani, A., Dashti, S., Taiebat, M., and Arduino, P. (2018b). "Capabilities and limitations of different numerical tools in capturing seismic site performance in a layered liquefiable site." *Geotechnical Earthquake Engineering and Soil Dynamics V: Numerical Modeling and Soil Structure Interaction*, S. J. Brandenberg and M. T. Manzari, eds., number GSP 292

Chapter 7

LEAP-UCD-2017 SIMULATION EXERCISE

7.1 Introduction

Liquefaction induced lateral spreading causes significant economic and human life losses every year (Mason et al., 2019). Nonlinear dynamic effective stress analysis is an effective method for predicting the onset and consequences of lateral spreading. Case history measurements and laboratory test results are commonly used to calibrate such models. Several aspects of these models require attention, particularly, the calibration of the constitutive model parameters. Other important aspects necessary for a successful simulation consist of appropriate model boundary conditions, initial conditions, in particular the initial stress state of the model, and analysis parameters used for integrating the equation of motion in time and nonlinear differential equations of the constitutive model. In terms of calibrating the constitutive model, it is essential to validate the implementation of the model at different levels, i.e., element test level, where the constitutive differential equations are integrated mathematically, and progressively larger scale models representing more realistic conditions where other complexities of numerical modeling come into play and their effects are considered and evaluated. Centrifuge tests are commonly used to generate realistic stress levels in a soil mass using much smaller scales than the actual prototype. Properly configured and instrumented, these experiments are proven useful to capture realistic full-scale soil behavior in smaller scale models. These tests provide valuable data that can be complemented with case histories. In this context, LEAP (Liquefaction Experiments and Analysis Projects) (Manzari et al., 2017) is an effort to produce a well maintained database of clean centrifuge experimental data, validated using numerical models.

7.2 Background

LEAP consists of a series of projects that aim to provide high quality experimental data to extend our understanding on the behavior of saturated granular soils subjected to seismic loading and evaluate the capability of constitutive models to reproduce soil behavior related to liquefaction. Four phases of the project have been completed so far. LEAP-GWU-2015 (Kutter et al., 2017) was a preliminary phase that demonstrated that an international collaboration project aiming at validating numerical modeling techniques using high quality laboratory tests on liquefiable soils was feasible. This phase lead to LEAP-UCD-2017 that focused on repeatability, variability, and sensitivity of both experimental and numerical simulation studies. During this second phase, a large number of experiments were conducted using identical test configurations. The relatively large number of centrifuge tests helped define the test-to-test and facility-to-facility sensitivity and variability of centrifuge tests. In this chapter, comparisons between experimental results and numerical simulations obtained using two different constitutive models, i.e., Manzari-Dafalias (Dafalias and Manzari, 2004) and PM4Sand implemented in OpenSees are presented and discussed. The other two phases, 2019 and 2020, will be discussed in the following chapters.

The experiments of LEAP-UCD-2017 were conducted at nine centrifuge facilities around the world, namely Cambridge University(CU), Ehime University (Ehime), Korea Advanced Institute of Science and Technology (KAIST), Kyoto University (KyU), Taiwan National Central University (NCU), University of California Davis (UCD) and Zhejiang University (ZJU). Blind simulations were completed and submitted to the LEAP organizers and a second workshop (LEAP-UCD-2017) was organized at Davis at the end of 2017.

In all these studies, the well-characterized Ottawa F-65 sand (Bastidas, 2016; Vasko, 2015) was used. During this second set of experiments the sand was deposited uniformly in an instrumented 5-degree slope. All centrifuge experiments used a rigid box container to eliminate complexities in boundary conditions. With small variations, depending on the configuration of each centrifuge facility, all models were prepared to represent a unique proto-

type size 20 m in length, 4 m in height at the midpoint and width greater than 9 m to reduce the effects of frictional boundary conditions on the container sidewalls. Four accelerometers (AH1-AH4) and four pore pressure transducers (P1-P4) were positioned along the centerline. A series of four 1 Hz ramped sine motions were imposed on each model. Motions 2 and 3 with $PGA = 0.15$ g and 0.25 g, respectively, were considered strong enough to represent a destructive event. Motion 2 acceleration time history is shown in Fig. 7.1 and was used in all the type-B predictions presented in this chapter.

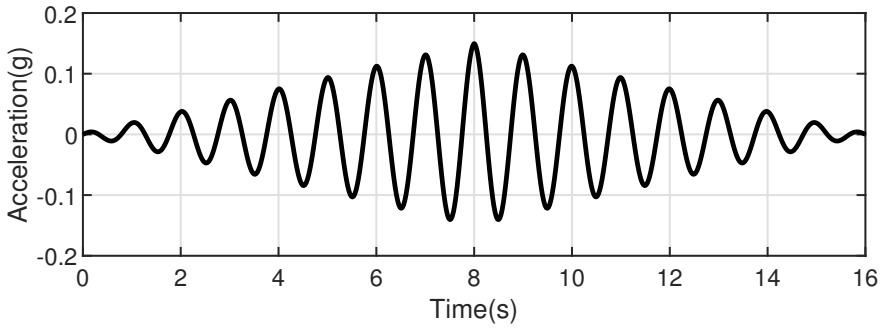

Figure 7.1: Target input motion 2 acceleration time history.

7.3 FE model development

In this work a 2D plane-strain representation of the problem was adopted and numerical models were built in prototype scale using OpenSees. The models consisted of 3125 four-node quadrilateral elements with an average size of $0.16\,m \times 0.16\,m$. The physically stabilized single-point integration and mixed displacement-pressure (u-p) element (SSPquadUP, see McGann et al. (2015)) was used to capture the effective stress response of each simulated centrifuge test. A schematic of the mesh used in this work along with the location of recorded responses are depicted in Fig. 7.2. Appropriate mesh refinement was chosen to properly resolve the propagation of shear waves of up to 50 Hz in the soil domain.

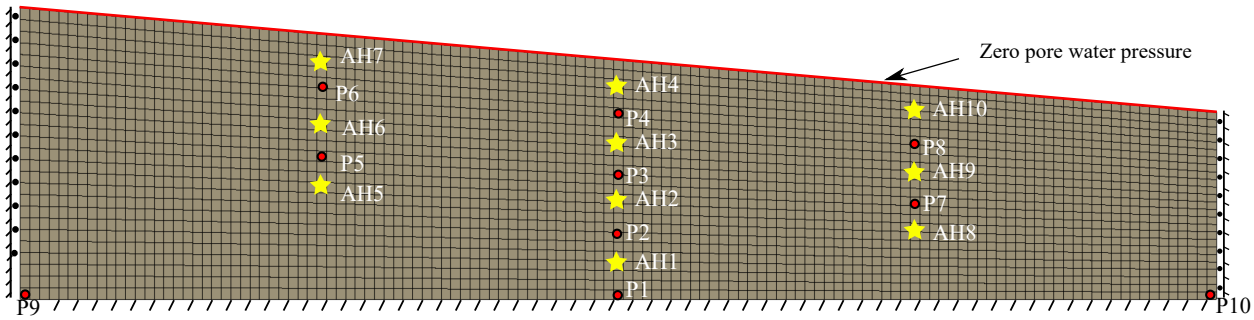

Figure 7.2: Finite element mesh and location of recorded pore water pressures (P) and accelerations (AH).

7.3.1 Boundary and loading conditions

The bottom boundary was fixed against vertical movement. The acceleration time history was applied to both vertical boundaries as well as the base of the model using the so called *UniformExcitation* loading pattern in OpenSees. This was done to account for a rigid container. Pore pressures at the slope surface nodes were set to be zero during the analysis to ensure drainage and avoid generation of excess pore pressures at the surface. The free water on the slope was not modeled and effects of water sloshing (if any) were not considered. The soil was assumed to be always in contact with the container. A frequency dependent Rayleigh damping was applied to compensate for small strain damping; which both MD and PM4Sand models lack in their formulation. The Rayleigh damping coefficients were chosen such that a 2% damping was obtained at 0.2 Hz and 20 Hz. The permeability was adopted from Ghofrani and Arduino (2017) and set to be $3.0 \times 10^{-5}\, m/s$.

To apply gravity, the materials were set to be linear elastic and elemental body forces were increased gradually to reduce numerical instabilities in the model. Once gravity was in place, the materials were switched to *elasto-plastic* and enough extra steps were run to adjust their internal variables to any plastic behavior and maintain equilibrium. A Poisson's ratio $\nu = 0.3$ was assumed to generate the initial stress state. This Poisson's ratio yielded a lateral

earth pressure coefficient $K_0 = 0.43$ under level ground plane-strain conditions. Figure 7.3 shows the imposed initial state of stress in terms of vertical, horizontal, and shear stresses. After reaching the desired initial stress state, the acceleration time history was applied to the rigid boundaries. The constant average acceleration Newmark method ($\beta = 0.25$, $\gamma = 0.5$) was used in order to resolve the integration in time. To account for material nonlinearity both models used explicit modified Euler integration schemes with sub-stepping error control (Sloan et al., 2001). After the main shake portion of the motion, additional dynamic analysis steps were executed to dissipate any excess pore pressures generated during the shake.

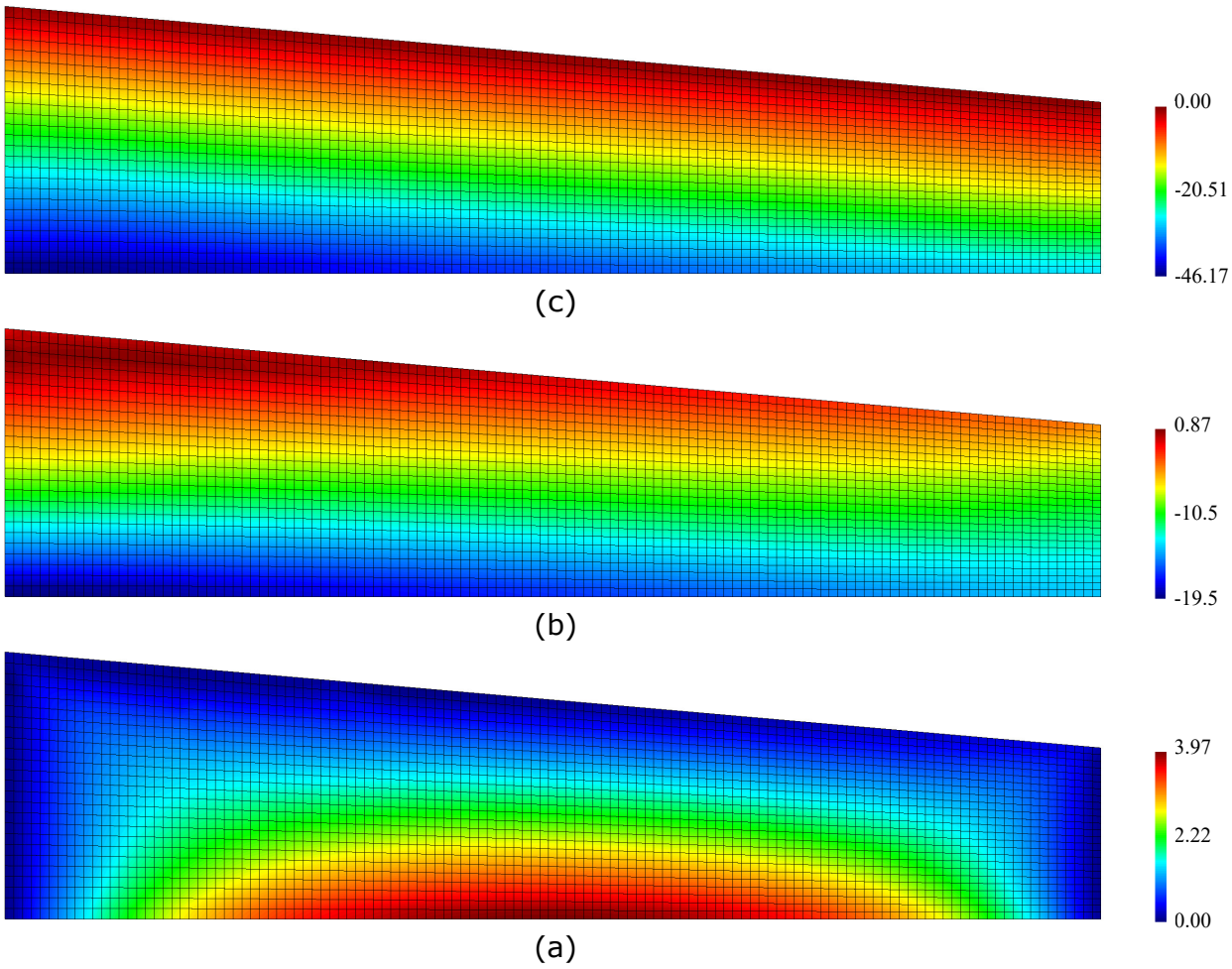

Figure 7.3: Initial stress field after gravity. (a) Vertical effective stress distribution. (b) Horizontal effective stress distribution. (c) Shear stress distribution. All units in kPa.

7.3.2 Material constitutive models

The bounding surface constitutive models developed by Dafalias and Manzari (2004)(referred as *MD* henceforth for brevity) and PM4Sand were used for comparison purposes. Both models follow critical state soil mechanics concepts and are capable of capturing stress-strain relationships for denser-than-critical and looser-than-critical sands under different drainage and loading conditions.

7.3.3 Calibration

In order to predict the response of centrifuge tests, material parameters were calibrated using available laboratory tests data. Several drained and undrained cyclic triaxial as well as cyclic simple shear tests were used for this purpose (El Ghoraiby et al., 2017, 2019). To calibrate the model parameters, the constitutive evolution equations were integrated independently of the FE framework using MixedDriver.

MD parameter calibration

Some of the MD constitutive model parameters can be estimated directly from drained and undrained monotonic triaxial tests. These parameters include G_o, Mc, c, λ_c, e_0, ξ, n^b and n^d. These parameters, in particular the last three, play an essential role in the response obtained from the MD model as the whole framework is built upon the critical state surface concept. From the experimental stand point, however, it is very difficult to obtain reliable data to represent the critical state of a soil. This has important implications in the MD model. Therefore, emphasis should be given to laboratory specimen sheared enough to reach critical state. The rest of the parameters can be calibrated using either trial and error or optimization techniques. Since the authors had experience working with Ottawa F65 sand from the previous LEAP 2015 exercise (Ghofrani and Arduino, 2017), as well as few other projects (e.g., Ramirez et al. (2018b)), some of the same parameters used in previous calibration efforts were used for this study. Although it would have been ideal to calibrate the model for all the characteristics revealed by the lab results at hand, due to intrinsic characteristics of the constitutive model, a few specific response patterns could not be achieved. In this context, the trend of number of cycles to reach liquefaction is one example. Based on experience, number of cycles to liquefaction at smaller cyclic stress ratios do not play an important role in centrifuge experiments of this size and in particular are not observed with the loading conditions used in LEAP. Therefore, during calibration attention was given to achieving a reasonable range of excess pore water pressure in cyclic tests as well as accu-

mulation of shear strains, rather than trying to achieve perfect match between the number of cycles to reach liquefaction at different cyclic stress ratios. Table 7.1 summarizes the calibrated parameters for this phase of LEAP 2017.

Table 7.1: Calibrated MD parameters and their values

Parameter		Value	Typical Range
Elastic	G_o	82.35	Variable
	μ	0.01	Variable
Critical State	M	1.35	1.1 - 1.7
	c	0.70	0.3 - 1.0
	λ_c	0.055	0.01 - 0.1
	e_0	0.80	Variable
	ξ	0.50	0.4 - 1.0
Yield Surface	m	0.02	0.01 - 0.05
Plastic Modulus	h_0	16.18	5.0 - 16.0
	c_h	0.996	0.8 - 1.05
	n^b	0.64	0.5 - 2.6
Dilatancy	A_0	0.75	0.4 - 1.6
	n^d	1.50	0.5 - 5.5
Fabric Tensor	z_{max}	12.50	2.0 - 40.0
	c_z	500.0	500.0 - 2500.0

PM4Sand parameter calibration

The biggest advantage in using PM4Sand is that the calibration process is relatively straightforward. As mentioned before, only three primary parameters and four secondary parameters

(out of 21) are necessary and were used for calibration in this study. The remaining secondary parameters were kept at their default values, previously calibrated by Boulanger and Ziotopoulou to represent typical soil behavior.

Since PM4Sand was developed for plane-strain conditions, undrained cyclic plane strain compression (PSC) conditions were used for calibration purposes. Initially three sets of parameters were calibrated for three void ratios, namely 0.515 ($D_R = 90.5\%$), 0.542 ($D_R = 79.6\%$) and 0.585 ($D_R = 62.2\%$), in accordance with LEAP phase 1 guidelines. Maximum and minimum void ratios for the Ottawa F65 sand were adopted from previous tests and used to calculate relative densities. The critical state effective friction angle $\phi_{cv}$was evaluated using shear and normal stresses at which the soil reached critical state during monotonic drained triaxial tests. The shear modulus coefficient G_o was calibrated by matching the initial slope of the stress-strain curves in undrained cyclic tests. h_{po}, which controls the rate of pore pressure generation between contraction and dilation, and c_z, which controls the strain level at which fabric becomes relevant, were calibrated iteratively to match the liquefaction strength curves. In contrast to the MD model, calibration of the PM4Sand model was done to capture the number of cycles to liquefaction observed in the triaxial tests. Table 7.2 summarizes the calibrated parameters for this phase of LEAP 2017.

Fig. 7.4 depicts the case of a cyclic stress-controlled undrained triaxial test (El Ghoraiby et al. 2017 and 2019) along with simulations obtained using MD and PM4Sand. The MD model was able to capture the asymmetry of the cyclic triaxial test and showed that axial strains accumulate in the extension direction, while the PM4Sand model results were symmetrical in compression and extension. Both the PM4Sand and MD models underpredicted excess pore pressure during the first cycle while overpredicted overall the rate of excess pore pressure generation. Fig. 7.5 depicts comparisons between simulations using both models and laboratory test data in terms of number of cycles to initial liquefaction for different cyclic stress ratios (CSR). The number of cycles to liquefaction was evaluated counting the number of cycles necessary to reach a 2.5% single amplitude axial strain. In general, both models

Table 7.2: Calibrated PM4Sand parameters and their values

Primary Parameters	D_R	62.2%	Modified to 65% for Type-B prediction
	G_o	350.0	
	h_{po}	0.07	
Secondary Parameters	emax	0.7389	Modified to match 65% relative density for type-B prediction
	emin	0.4915	
	ϕ_{cv}	35.6	
	c_z	200.0	

predicted fewer number of cycles to trigger liquefaction than the experiment and this became more significant under smaller CSRs, especially for the MD model. However, both models behaved consistently for CSRs larger than 0.2. This is an important consideration since, as will be explained later, most of the simulated and estimated-from-experiments CSRs in the centrifuge experiments were higher than 0.2.

7.4 Type-B prediction results

By definition type-B predictions are done with limited amount of data from completed experiments. In this study, the calibrated single set of parameters for MD was used without modification. For PM4Sand, the set of parameters calibrated for the void ratio of 0.585 was chosen and the primary parameter D_R was modified to 65%. The minimum void ratio achieved in the triaxial experiments was used in all cases while the maximum void ratio was back calculated using the achieved void ratio in each centrifuge test to match the 65% relative density. In the following subsections results and comparisons are presented in term

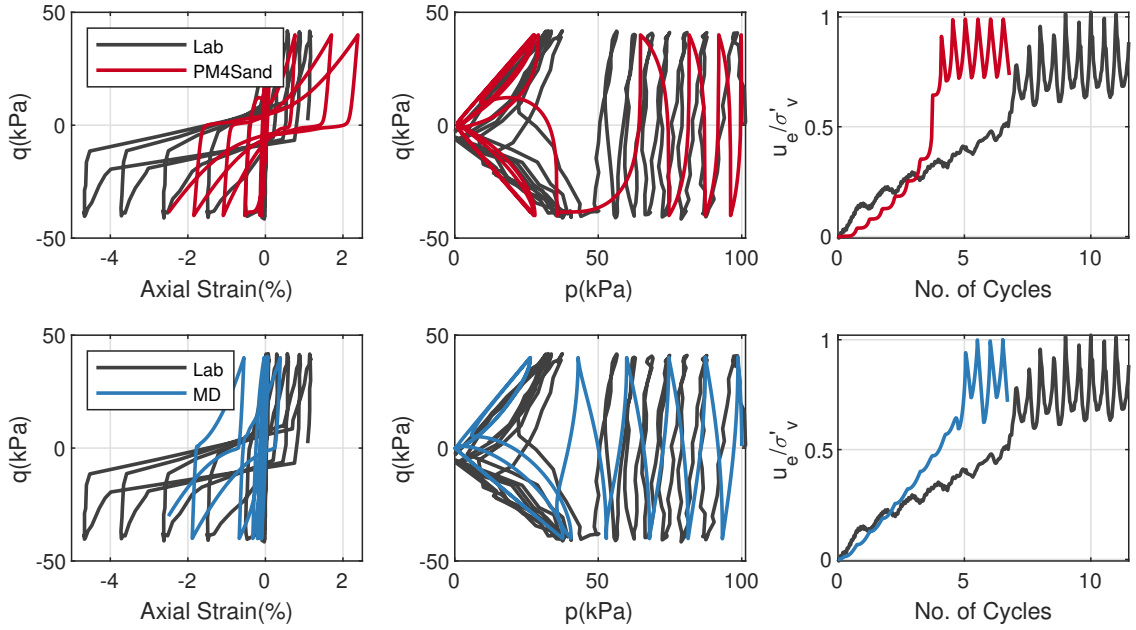

Figure 7.4: Elemental level calibration: Comparison between simulations and experimental results. The results are presented in terms of deviatoric stress, q, vs. axial strain, deviatoric stress, q, vs. mean effective stress, p, and excess pore pressure ratio vs. number of cycles.

of acceleration response, pore pressure response, and surface displacement.

7.4.1 Acceleration response

Figs. 7.6 to 7.9 show recorded and predicted acceleration response for all centrifuge experiments in terms of 5% damping response spectra at the AH1-AH4 sensors (see Fig. 7.2 for sensor location). The plots show the simulation results predicted the recorded experimental results very well at the intended input motion frequency of 1 Hz. PM4Sand predicted higher PGAs for the Ehime2 experiment and generally produced results with higher frequency content. This was most likely due to material overprediction of the soil stiffness under dilation which leads to stronger dilation pulses.

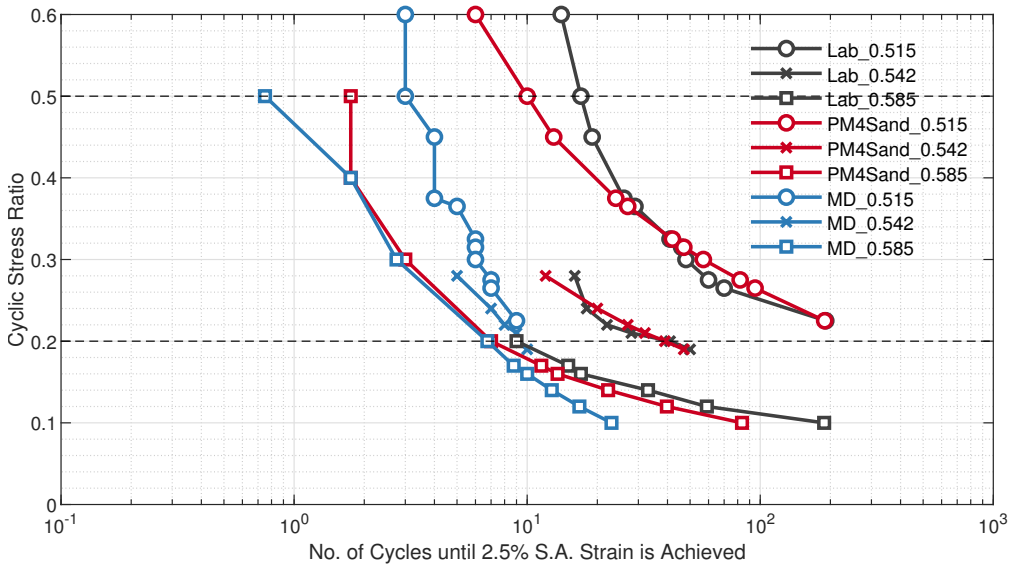

Figure 7.5: Element level calibration: Comparison of number of cycles required to reach 2.5% single amplitude shear strain in simulations and laboratory tests.

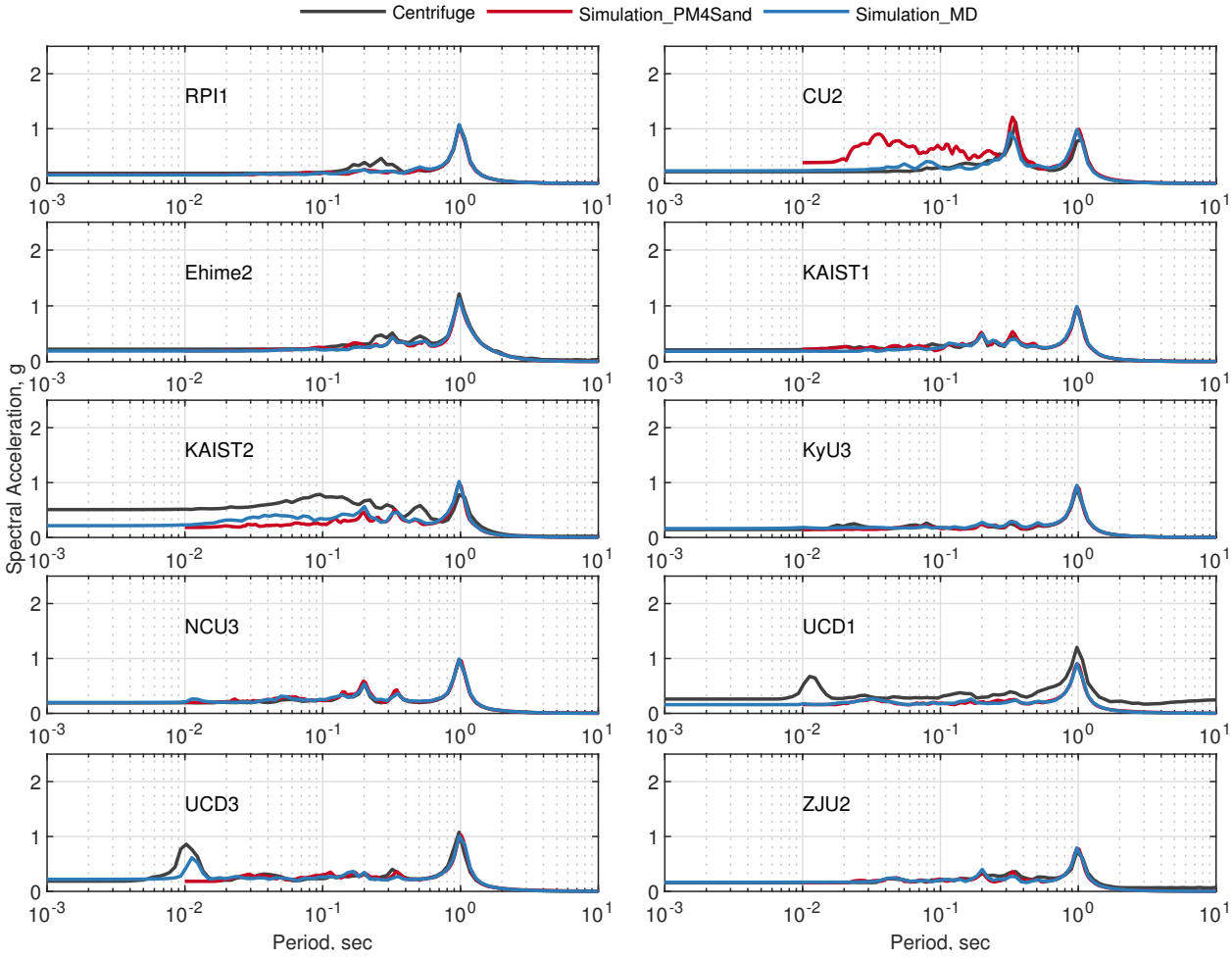

Figure 7.6: Type-B prediction results: Comparison of acceleration response spectra (5% damping) at AH1 in simulations and centrifuge tests.

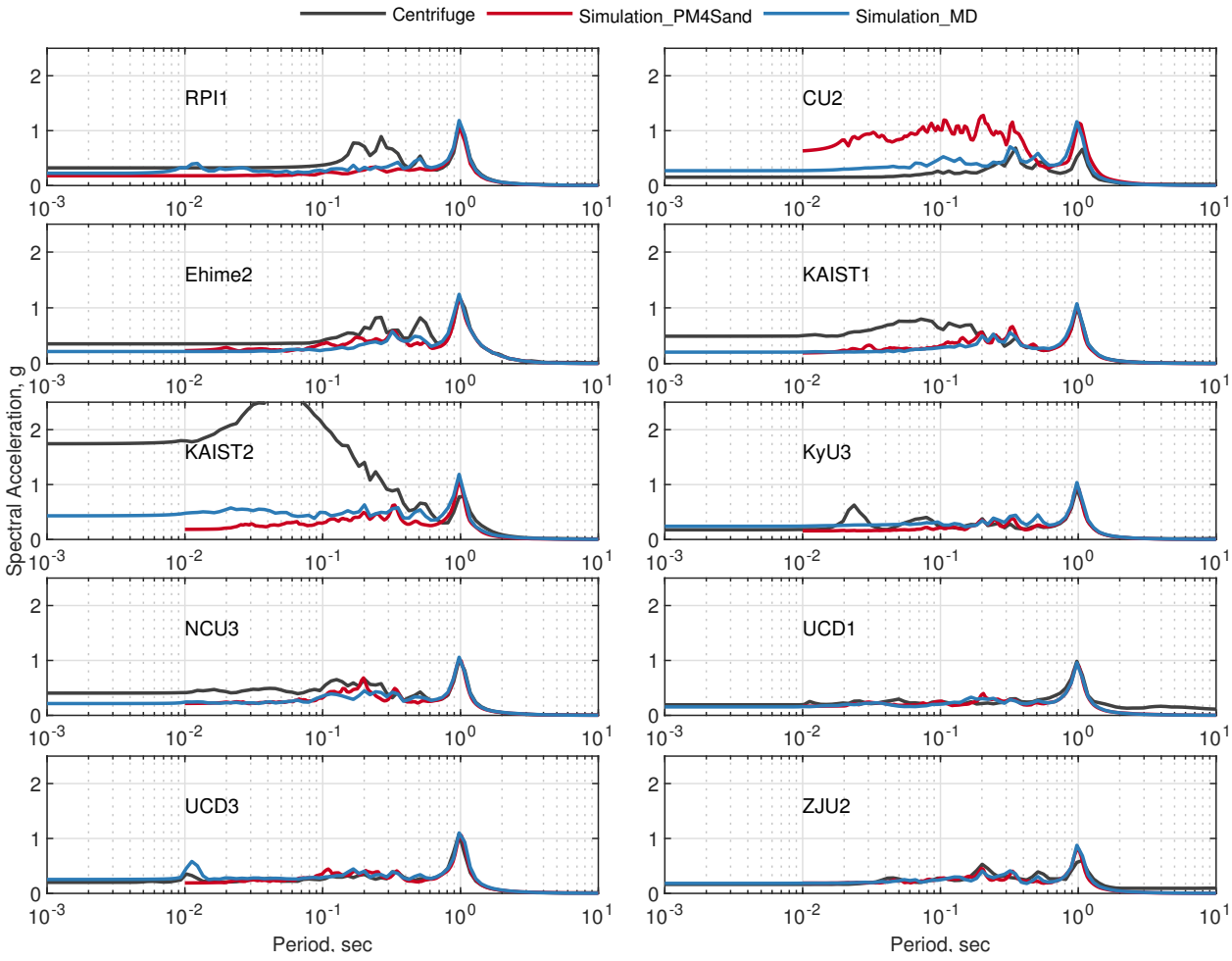

Figure 7.7: Type-B prediction results: Comparison of acceleration response spectra (5% damping) at AH2 in simulations and centrifuge tests.

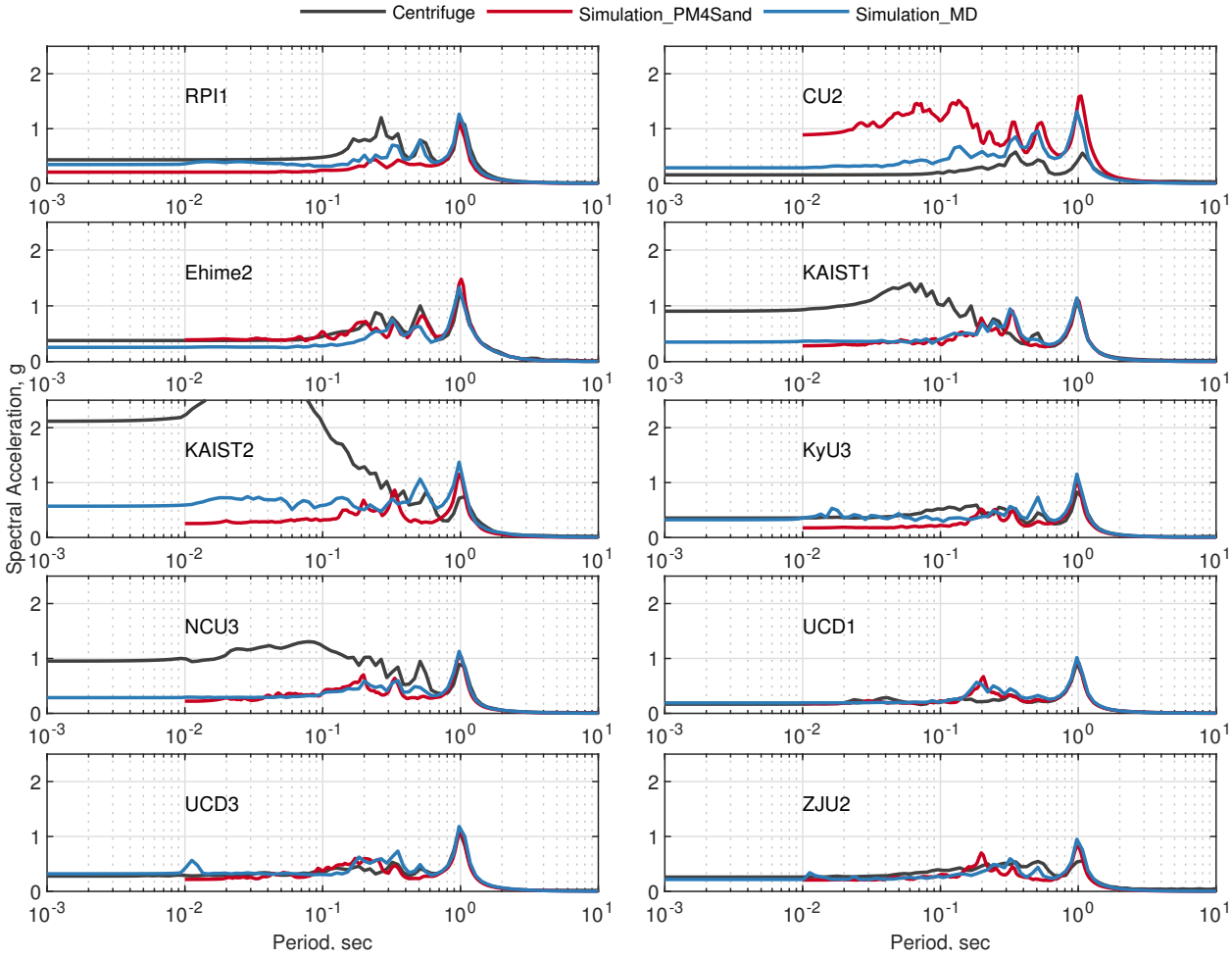

Figure 7.8: Type-B prediction results: Comparison of acceleration response spectra (5% damping) at AH3 in simulations and centrifuge tests.

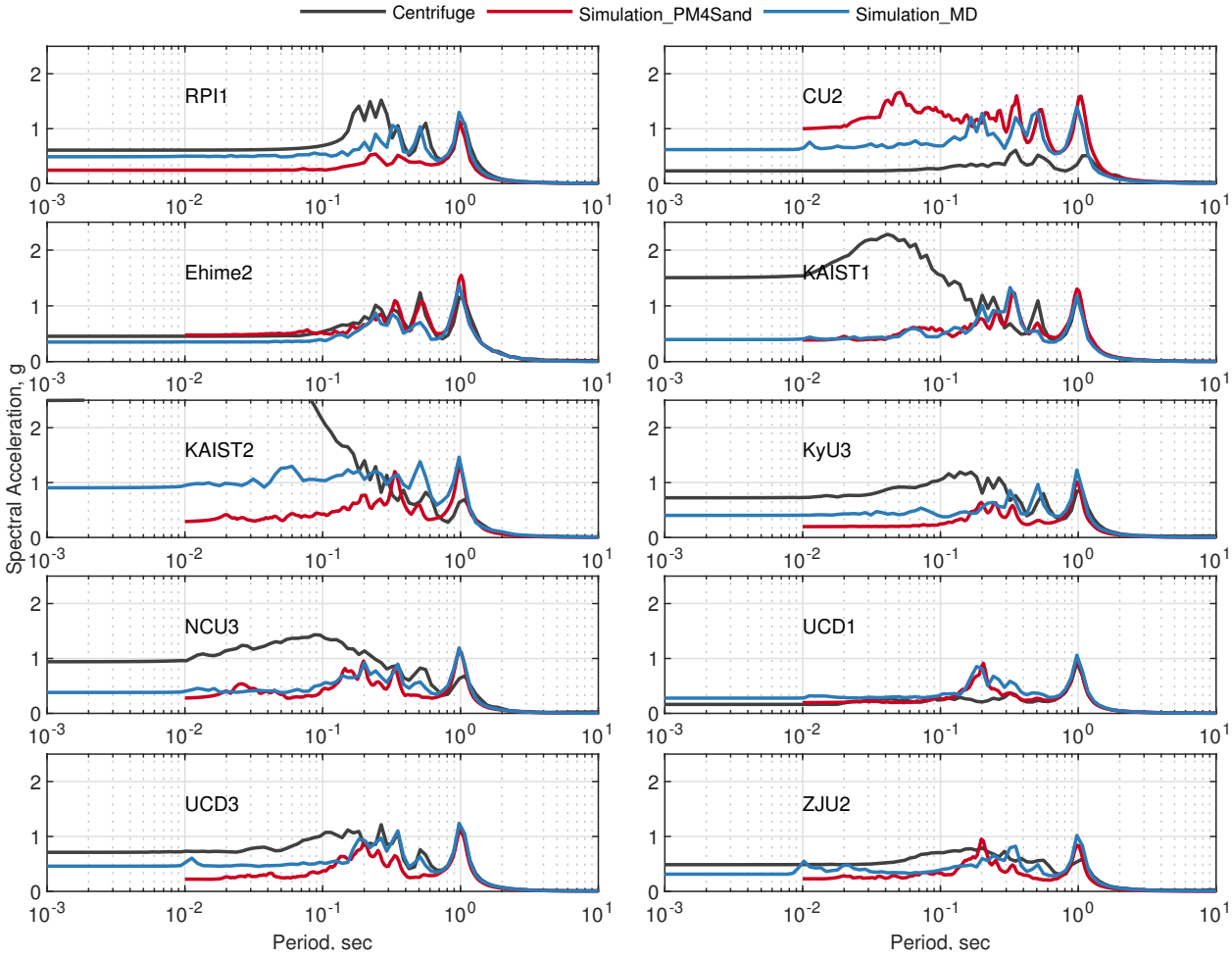

Figure 7.9: Type-B prediction results: Comparison of acceleration response spectra (5% damping) at AH4 in simulations and centrifuge tests.

7.4.2 Stress strain response

Figs. 7.10 to 7.11 depict comparisons between shear stress-strain histories predicted by PM4Sand and MD at pore pressure sensor locations along the center line profile (see Fig. 7.2 for sensor location). The simulation results were consistent with the model behavior observed at the element level and presented in the calibration section. PM4Sand model results showed higher cyclic resistance at deeper sensor locations, e.g., P1, with higher initial effective stresses and subject to lower maximum shear stress ratio. Closer to the surface, both models predicted similar cyclic mobility with PM4Sand showing higher stiffness under dilation.

Fig. 7.12 depicts simulated and estimated-from-experiments profiles of maximum shear stress ratio (CSR_{max}) along the centerline (see Fig. 7.2 for sensor location). In the absence of 2017 stress-strain responses from experiments, and given that the same model configuration, soil properties and targeted input motion were used in both LEAP-UCD-2017 and LEAP-GWU-2015 projects, LEAP-2015 data interpreted from Zeghal et al. (2017) were used here to compare with numerical predictions. The centrifuge test data was calculated using maximum absolute ratios of shear stress and initial effective vertical stresses estimated from Fig. 17 and 18 in Zeghal et al. (2017), respectively. The experimental data showed large variability, while the numerical predictions showed a general trend with maximum stress ratios reducing with increasing depth. This is shown in Fig. 7.12. From these results it is clear a maximum shear stress ratio of 0.5 was very likely exceeded in all experiments. This value is considerably higher than the maximum cyclic stress ratio achieved in the laboratory and used for calibration purposes; which only goes up to $CSR = 0.2$ as shown in Fig. 7.5. It should be note that although some laboratory experiments were performed at CSR values as high as 0.6, they were performed on samples which had a void ratio of around 0.505 and an estimated relative density of 90%, which is larger than the targeted $D_R = 65\%$ used in the centrifuge experiments. As was presented in the calibration section, the PM4Sand model results showed higher cyclic resistance and could better match CRR curves from the lab tests

compared to the MD model. But at CSRs larger than 0.3, PM4Sand and MD showed almost the same CRR behavior. Therefore, although the trend of number of cycles to reach liquefaction was not the main target in the MD calibration, the MD model adequately predicted the experiments, or produced similar results compared to the PM4Sand model for which a different calibration strategy was used. This is in agreement with the authors' previous experience modeling similar centrifuge tests.

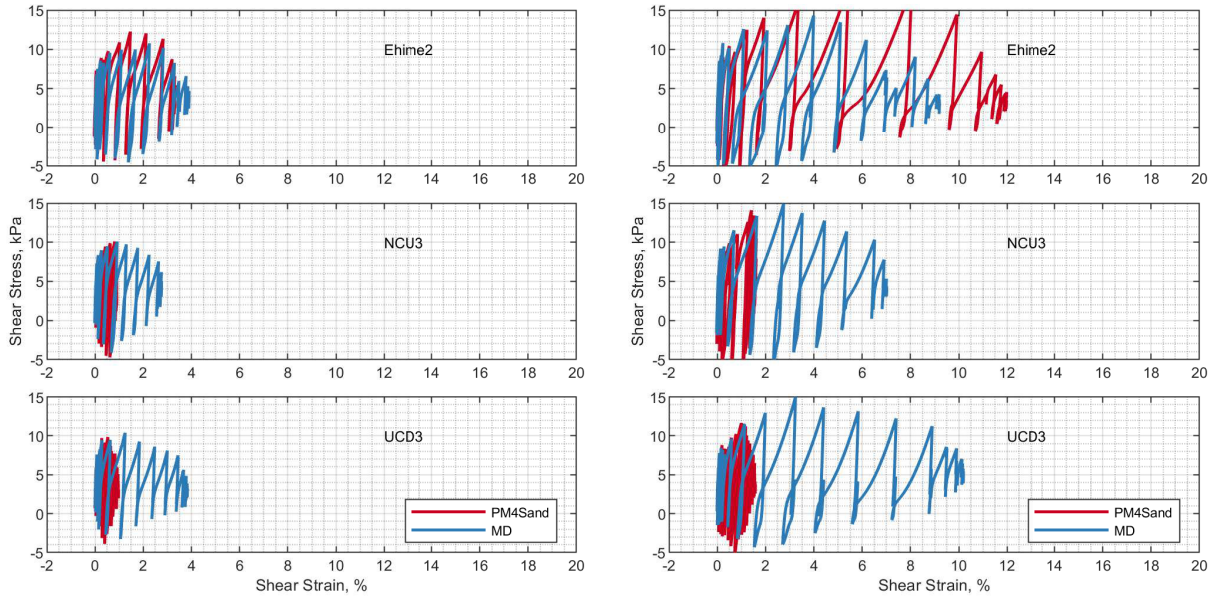

Figure 7.10: Type-B prediction results: Comparison of shear stress-strain histories at P1 & P2 in simulations and centrifuge tests.

7.4.3 Pore pressure response

All centrifuge tests showed similar trends in pore pressure response. Comparisons of predicted and recorded pore pressure response at pore pressure sensors along center line are depicted in Figs. 7.13 to 7.16. The figures show both models could capture the trend of

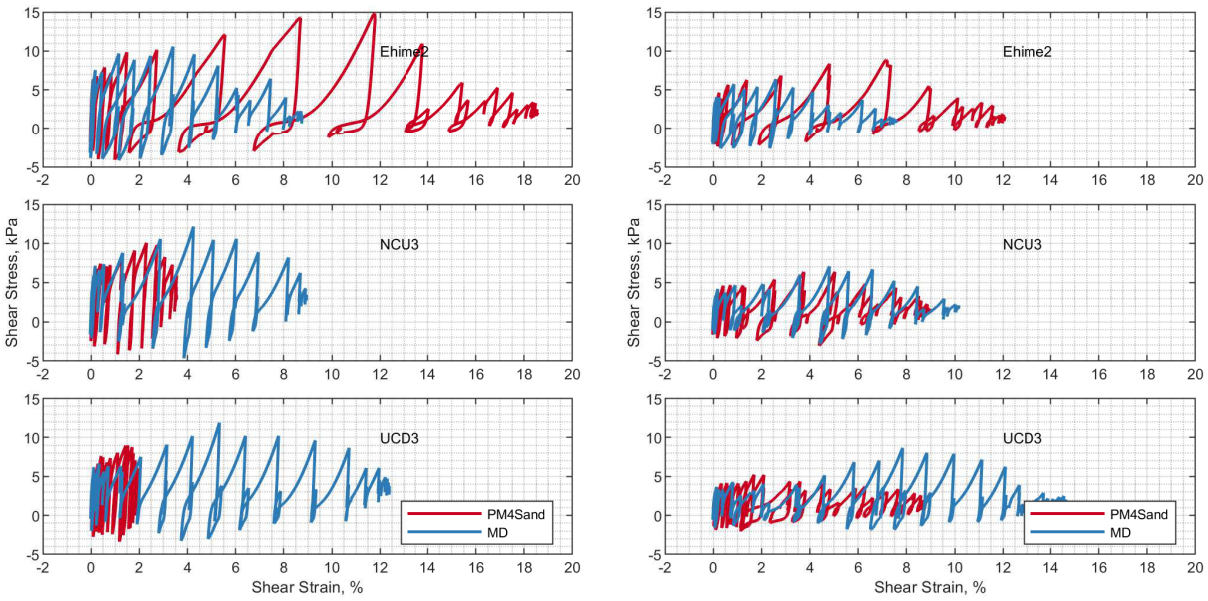

Figure 7.11: Type-B prediction results: Comparison of shear stress-strain histories at P3 & P4 in simulations and centrifuge tests.

pore pressure generation observed in the experiments, however, PM4Sand was only able to match recorded excess pore pressure in limited cases, e.g., CU2 and Ehime2, meaning model parameters need to be revised for future simulation exercises. As shown in Fig. 7.5, the MD model exhibited lower cyclic resistance under lower CSRs compared to the PM4Sand model. This manifested itself in different predicted response of pore pressure for both models. Both models showed the same excess pore pressure dissipation pattern after the main shake and until 25 seconds. A slower dissipation rate of excess pore pressure shown in the simulation results after the main shake suggests that the permeability used in the numerical simulations was possibly larger than the actual value. It should be mentioned that after 25 seconds, the *"PostShake"* flag in PM4Sand model was turned "on" to achieve better post shake settlements. Moreover, in PM4Sand the bulk modulus of the material was modified using the accumulated fabric history at each element. Details about PM4Sand can be found

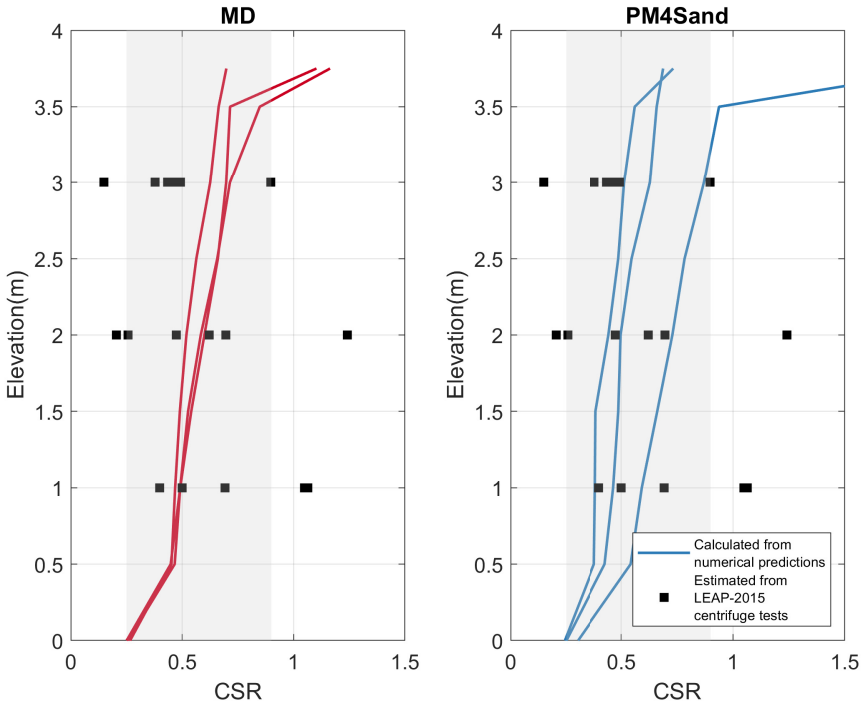

Figure 7.12: Type-B prediction results: Comparison of maximum shear stress ratio.

in Boulanger and Ziotopoulou (2017).

7.4.4 Surface displacement response

Fig. 7.17 depicts nodal displacements contours at the end of shaking. As expected the up-slope part of the soil settled and the down-slope part heaved resulting in flattening of the slope. Fig. 7.18 depicts the evolution of recorded horizontal displacements for a surface point at the center compared to simulated results. Large variability in both centrifuge experiments and numerical simulations are observed indicating that estimation of surface displacement continues to be a challenge for both physical and numerical models.

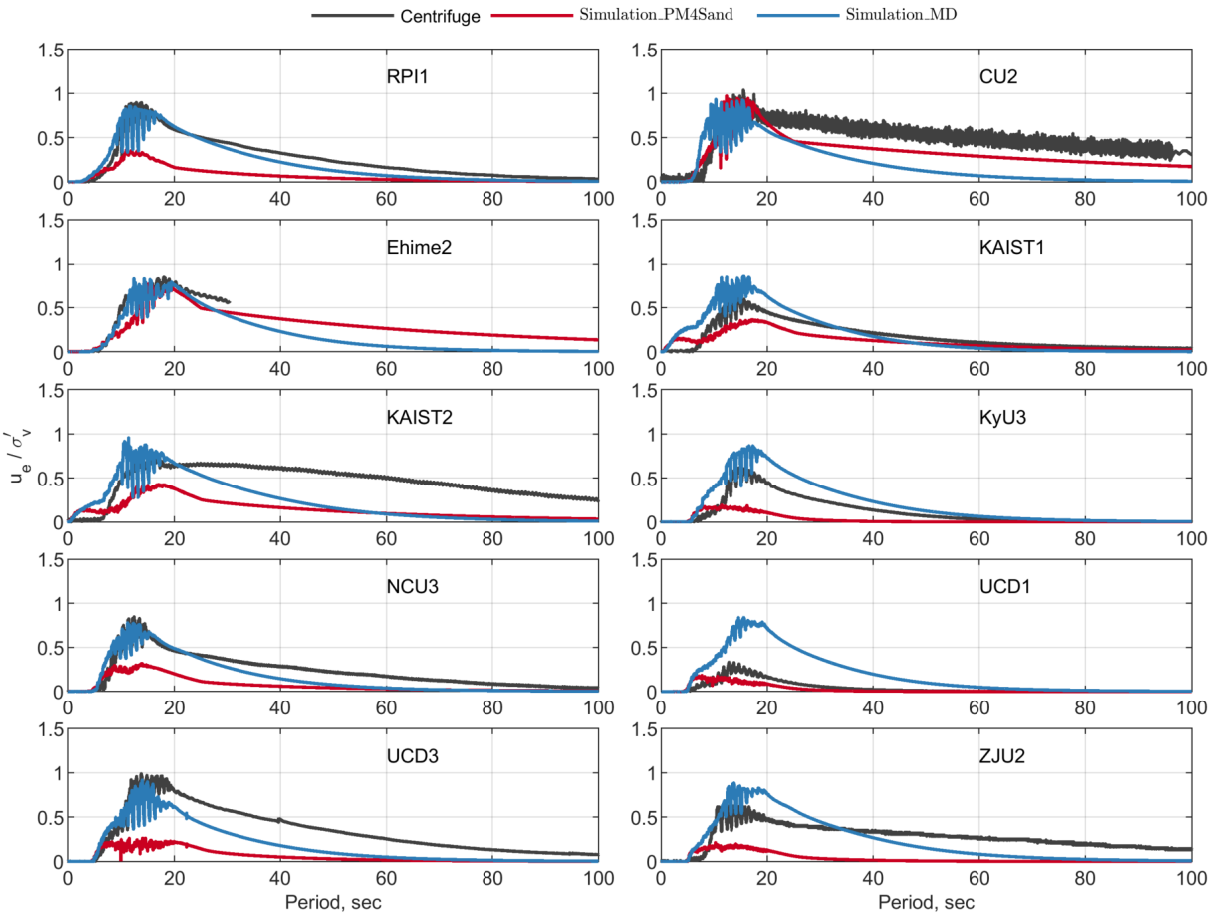

Figure 7.13: Type-B prediction results: Comparison of excess pore water pressures at P1 in simulations and centrifuge tests.

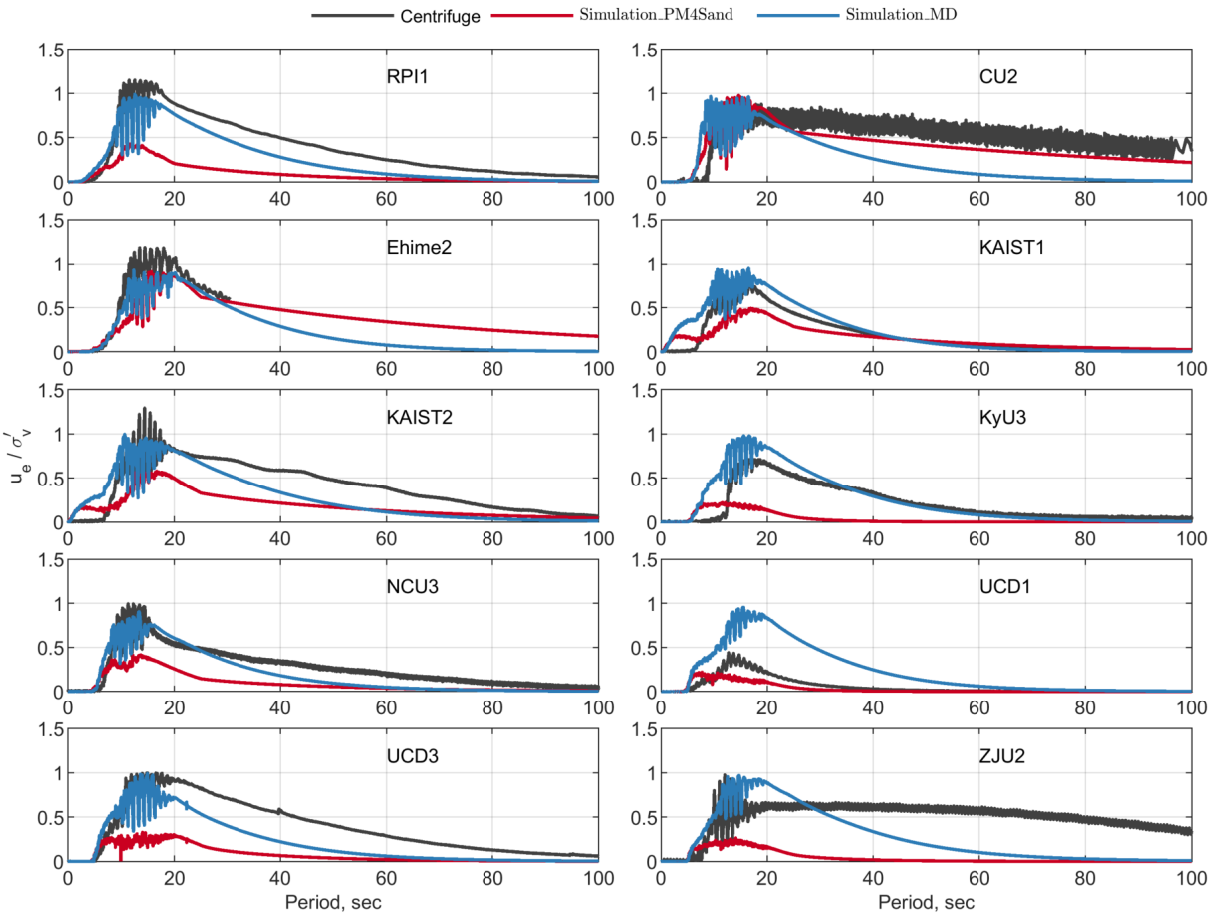

Figure 7.14: Type-B prediction results: Comparison of excess pore water pressures at P2 in simulations and centrifuge tests.

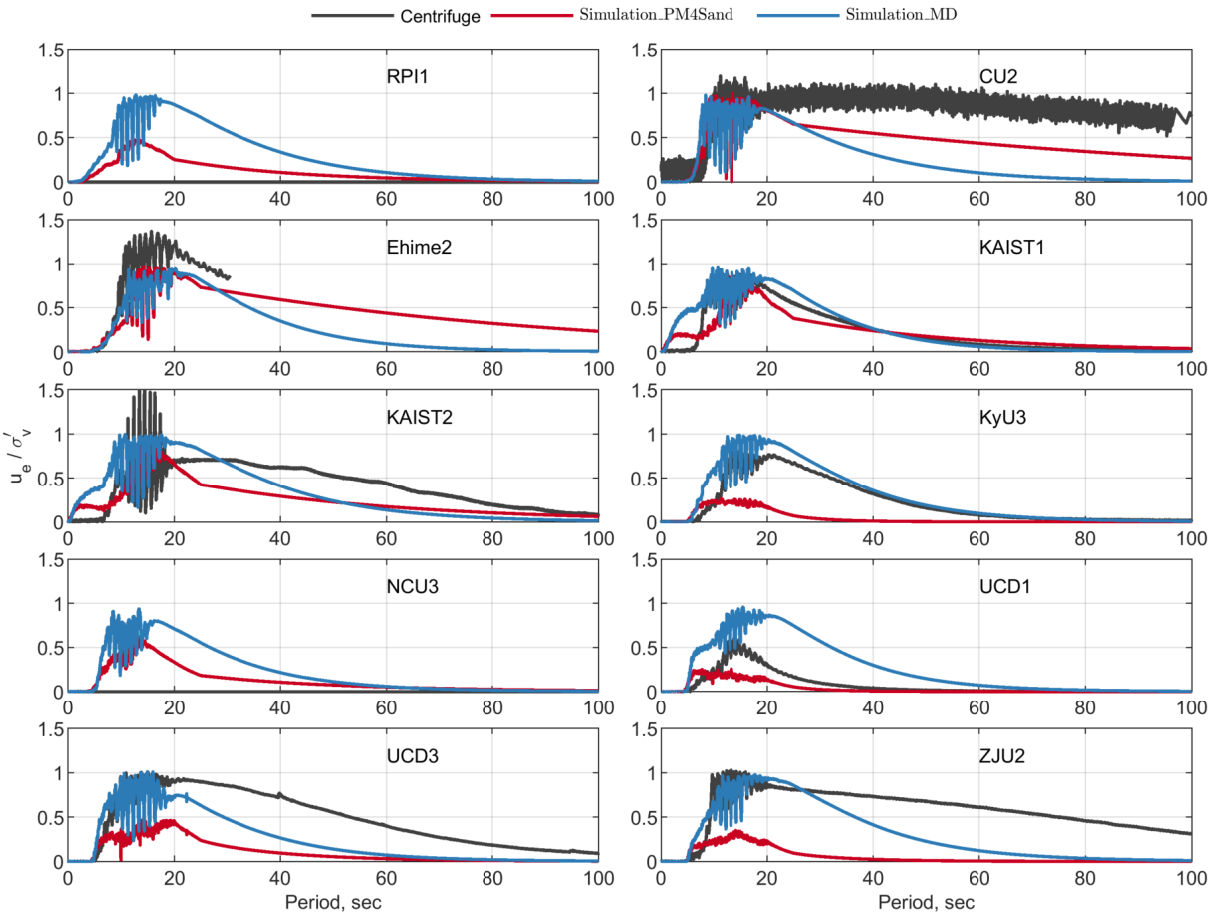

Figure 7.15: Type-B prediction results: Comparison of excess pore water pressures at P4 in simulations and centrifuge tests.

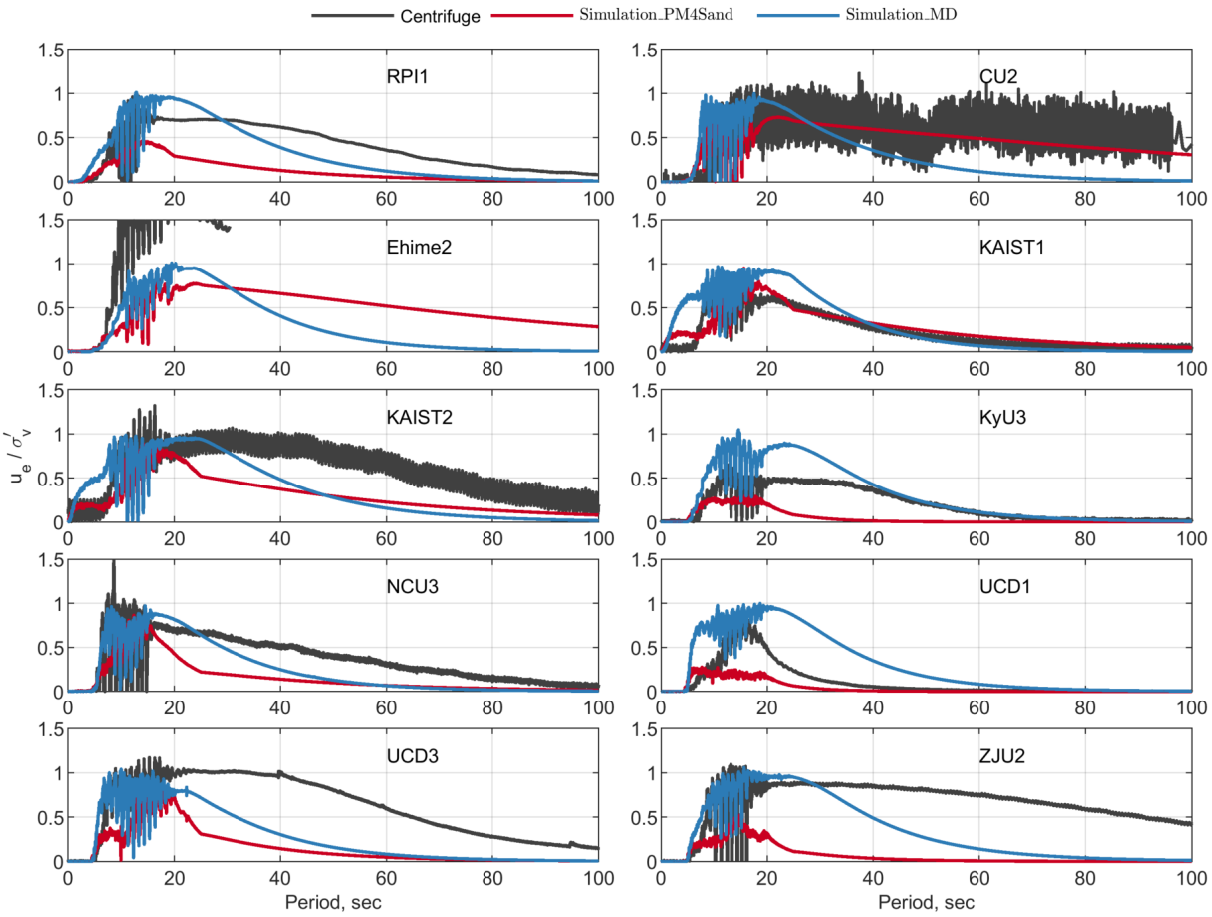

Figure 7.16: Type-B prediction results: Comparison of excess pore water pressures at P4 in simulations and centrifuge tests.

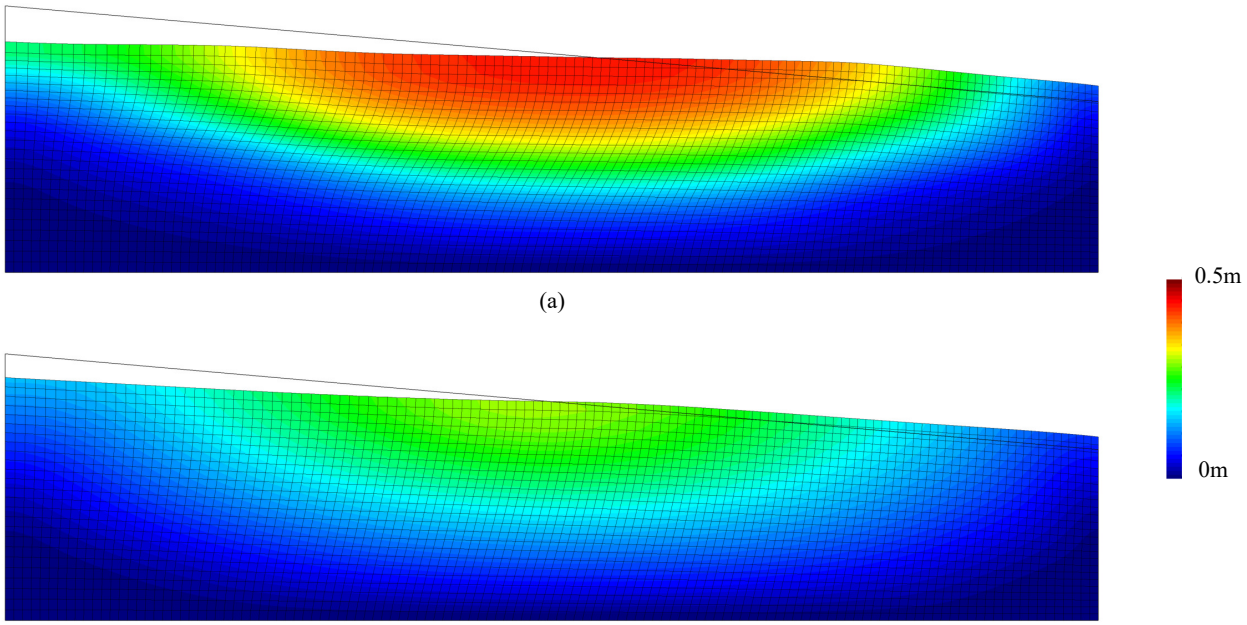

Figure 7.17: Type-B prediction results: Contour plot of absolute displacement (Ehime2). (a) PM4Sand (b) MD.

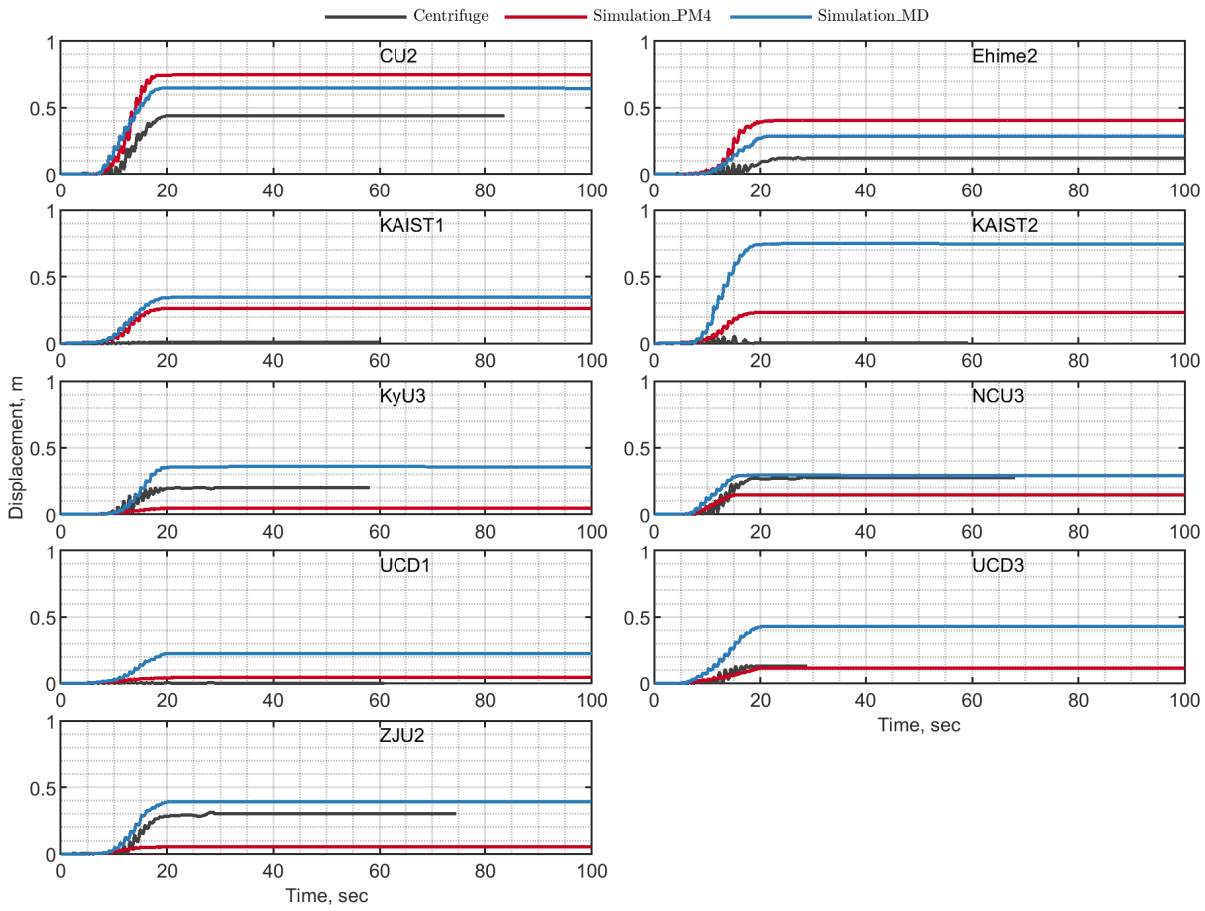

Figure 7.18: Type-B prediction results: Comparison of simulated and centrifuge horizontal displacements for a surface point located at the center of the model.

7.5 Summary

Two constitutive models based on critical state soil mechanics and bounding surface plasticity, MD and PM4Sand, were calibrated independently to simulate the behavior of Ottawa-F65 sand in accordance with the LEAP-UCD-2017 project guidelines. The calibrated models were then used to model the response of a boundary value problem representing a slopping ground using OpenSees. Besides using different material models, the same exact finite element model was used in all simulations. Type-B predictions were completed and simulations compared to recorded data from centrifuge experiments at several facilities around the world.

The MD model was calibrated for general soil behavior, and number of loading cycles to trigger liquefaction under small CSR was not prioritized. In the calibration of PM4Sand, the number of cycles to liquefaction observed in the laboratory tests results was emphasized and used as a calibration criterion. The models' behavior at element level was compared and PM4Sand showed higher, and better, cyclic resistances to smaller CSRs than MD, while the two models showed very similar cyclic resistance at CSRs larger than 0.2.

Type-B prediction results showed that although calibrated using different methods, both models were able to predict the results from centrifuge experiments, especially the acceleration response at the frequency of the input motion. The evolution of excess pore pressures predicted by PM4Sand and MD were comparable and showed the similarity and differences in calibration process. The predicted horizontal displacements were in the range of the recorded displacements at each facility.

Chapter 8

LEAP-ASIA-2019 SIMULATION EXERCISE

8.1 Introduction

This chapter presents results from numerical simulations of centrifuge experiments using prototype and physical centrifuge scale models in accordance with LEAP-Asia-2019 numerical simulation guidelines using PM4Sand. For this purpose, type-C predictions were completed and compared to recorded data from centrifuge experiments. The results were compared for prototype and physical centrifuge models as well as between Model-A (1-step scaling) and Model-B (2-step scaling) based on the similitude laws proposed by Iai et al. (2005). Finally the importance of properly considering Cyclic Stress Ratios (CSR) in the calibration of constitutive model parameters is discussed.

8.2 Background

Built on the success of the previous two phases (LEAP-GWU-2015 and LEAP-UCD-2017), LEAP-Asia-2019 provided a third set of experiments conducted at nine centrifuge facilities around the world, namely Cambridge University (CU), Ehime University (Ehime), French Institute of Science and Technology for Transport (IFSTTAR), Korea Advanced Institute of Science and Technology (KAIST), Kyoto University (KyU), Taiwan National Central University (NCU), Rensselaer Polytechnic Institute (RPI), University of California Davis (UCD) and Zhejiang University (ZJU). Type-C simulations of these experiments were completed and submitted to the LEAP organizers and a workshop was organized at Osaka, Japan during March of 2019.

One of LEAP-Asia-2019 main goals was to verify the generalized scaling laws proposed by Iai et al. (2005). In these laws a similitude concept was proposed by Iai et al. for shaking

table tests on saturated soil-structure-fluid models in 1G gravitational acceleration fields. It was shown that stress-strain behavior of soils experiencing intermediate strain levels, i.e., under 10%, can be produced irrespective of confining pressure if appropriate scaling factors (shown in Table 8.1) are used. This concept allows scaling of a potentially large prototype model into a smaller virtual intermediate model in 1G scale before scaling to the subsequent actual physical centrifuge scale used in centrifuge experiments; whose maximum size is often governed by centrifuge specifications, i.e., maximum centrifugal acceleration and bucket area. This allows modeling of large prototype models using reasonable scales in the centrifuge. Since its introduction, these generalized scaling laws have been validated in several studies, e.g., Tobita and Iai (2011) and Ueda et al. (2019). These results have demonstrated that the generalized scaling laws are applicable to the fully nonlinear regime of soil-structure systems subject to cumulative shear strains in the order of 10% due to cyclic mobility of sands during earthquakes. LEAP-Asia-2019 aimed, and this study contributes to, this effort to shed light on the similitude's application to lateral spreading problems.

Table 8.1: Summary of scaling factors for various measurements.

	Scaling factors for 1G test	Scaling factors for centrifuge test	Generalized scaling factors (Iai et al., 2005)
Length	μ	η	$\mu\eta$
Density	1	1	1
Time	$\mu^{0.75}$	η	$\mu^{0.75}\eta$
Frequency	$\mu^{0.75}$	$1/\eta$	$\mu^{0.75}/\eta$
Acceleration	1	$1/\eta$	$1/\eta$
Velocity	$\mu^{0.75}$	1	$\mu^{0.75}$
Displacement	$\mu^{1.5}$	η	$\mu^{1.5}\eta$
Stress, Pore pressure	μ	1	μ
Strain, Stiffness	$\mu^{0.5}$	1	$\mu^{0.5}$
Permeability	$\mu^{0.75}$	η	$\mu^{0.75}\eta$

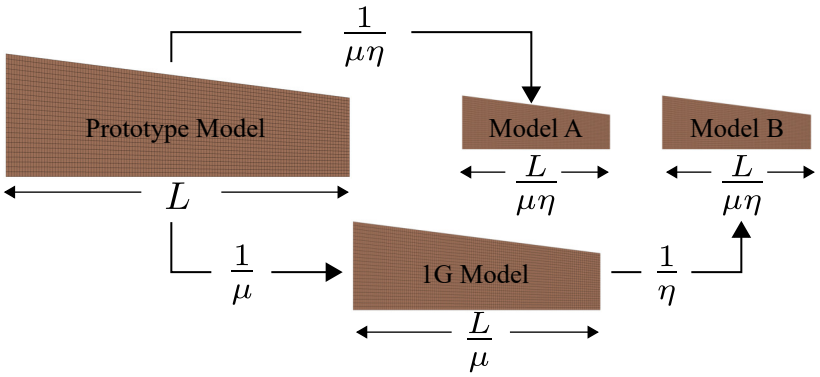

Figure 8.1: Relationship between prototype, virtual 1G model and centrifuge Model-A and Model-B (μ: 1G scaling factor, η: centrifuge scaling factor).

All LEAP centrifuge tests have used Ottawa F-65. This sand has been thoroughly characterized by many researchers (Vasko, 2015; Bastidas, 2016; El Ghoraiby et al., 2019; Ueda, 2018; Manzari, 2018). In all LEAP-Asia-2019 centrifuge tests the sand was deposited uniformly in an instrumented 5-degree slope with different target densities and a rigid box container was used to eliminate complexities in boundary conditions. The dimension of the prototype model is the same as the one used in LEAP-UCD-2017. Although all models were prepared to represent a unique prototype size, true physical centrifuge models varied to accommodate restrictions dictated by specifications of each centrifuge facility, including: rotation direction, effective radius, and applied centrifugal acceleration. With small variations in height, four accelerometers (AH1-AH4) and four pore pressure transducers (P1-P4) were positioned along the centerline of the model. This is shown in Fig. 8.3. Two different models were studied: Model-A or 1-step scaling model using the scaling law from prototype to physical centrifuge scale model, and Model-B or 2-step scaling model based on a virtual intermediate 1G scale model using generalized scaling laws. Fig. 8.1 illustrates the scaling procedure followed for Model-A and Model-B, respectively. Multiple experiments were made available to numerical simulation teams for type-C predictions, of which, three for Model-A and two for Model-B are indicated in Table 8.2 and were considered in this study. As noted

in the table, the KyU and RPI experiments examined the scaling guidelines in different directions. While KyU targeted a combined scale $\mu\eta = 44.4$ with $\mu = 2$, RPI targeted a combined scale $\mu\eta = 23.0$ with $\mu = 0.5$. A series of 1 Hz ramped sine motions were imposed on each model. Fig. 8.2 shows the target as well as the achieved input acceleration time histories for each experiment and facility. RPI experiments showed good consistency in the achieved motions and measurements and therefore results from these experiments were chosen for further numerical simulation. The two KyU experiment motions, although only showed 7% difference in effective peak ground motion (PGA_{1Hz}+0.5$PGA_{HighFrequency}$), showed 34% and 28% differences in Arias intensity and cumulative absolute velocity (CAV_5), respectively. In terms of evolutionary intensity measures (IM), the KyU motion B was significantly more demanding than motion A, and direct comparison between measured results from these two experiments need to be carried out carefully since other researchers have shown excess pore pressure generation in potentially liquefiable soils is closely related to these IMs (Kramer and Mitchell, 2006).

Table 8.2: Summary of centrifuge experiments required for type-C simulations in LEAP-Asia-2019 (case and motion numbers were omitted for simplicity)

	Density (kg/m^3)	Relative Density D_R(%)	Virtual 1G, μ	Centrifuge, η	PGAeff (g)	Arias Intensity (m/s)	CAV_5 (m/s)	Shaking direction
KyU_A	1628.0	56	1	44.4	0.118	0.618	6.304	Tangential
RPI_A	1651.0	64	1	23.0	0.143	0.822	7.025	Axial
UCD_A	1658.1	67	1	43.75	0.134	0.610	6.055	Tangential
KyU_B	1633.0	58	2	22.2	0.126	0.790	8.417	Tangential
RPI_B	1644.0	62	0.5	46.0	0.151	0.872	7.136	Axial

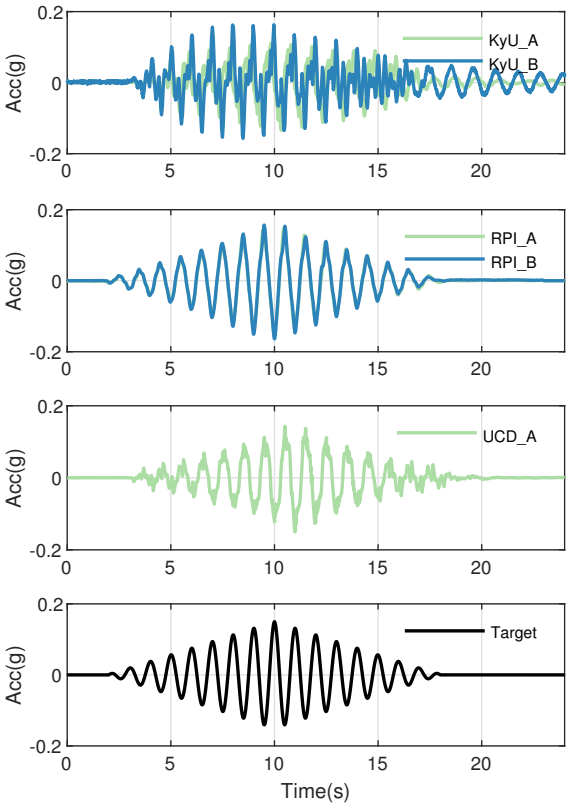

Figure 8.2: Acceleration time histories of LEAP-Asia-2019 simulation input motions.

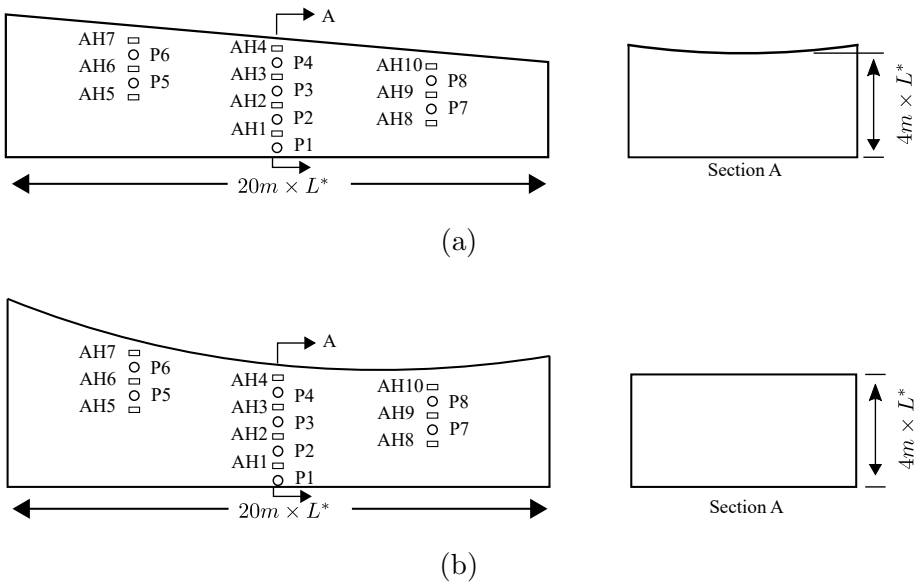

Figure 8.3: Baseline schematic for LEAP-Asia-2019 experiment (Kutter et al., 2017) for: (a) shaking parallel to the axis of the centrifuge (axial shaking cases, e.g., RPI). (b) shaking in the circumferential direction of the centrifuge (tangential shaking cases, e.g., UCD, KyU). L* in the figure corresponds to $1/\mu\eta$.

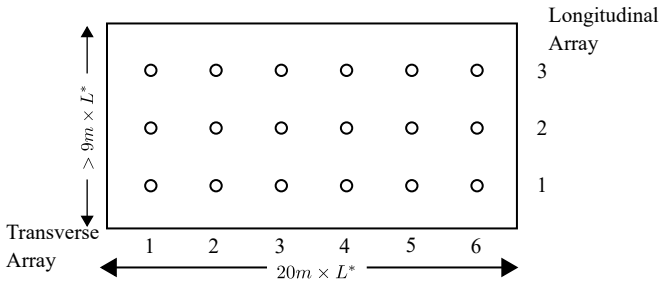

Figure 8.4: Surface marker locations for displacement measurement (top view). Numerical simulation results of lateral displacements time histories were reported along the longitudinal array 2 at locations 2-2, 2-3, 2-4, and 2-5.

8.3 FE model development

A 2D plane-strain numerical representation of the problem was adopted and numerical models were built in both prototype and physical scales using the OpenSees. Prototype scale models, without any scaling, were considered first for convenience. Physical scale models were considered next. These models varied from facility to facility and required consideration of proper scaling of geometry and other measurements for analysis. Depending on shaking direction with respect to the axis of the centrifuge, the surface of the physical centrifuge scale models were curved in the rotation direction as shown in Fig. 8.3. The curvature was calculated based on effective radius and the slope of the surface in prototype scale. In the tangential shaking case, e.g., KyU, the surface was a logarithmic-spiral curve to simulate a constant 5 degree slope. Fig. 8.5 compares three possible geometries for the tangential shaking case: (a) prototype model, commonly used by numerical modelers, (b) physical centrifuge scale model, obtained in centrifuge experiments, and (c) ideal scaled prototype model in a centrifugal acceleration field, implied by geometry (a). Comparison between geometries (b) and (c) shows the differences in vertical and bottom boundary conditions as well as implied shaking direction. These differences became significant for facilities with smaller effective radius. In this study, models for both physical centrifuge and prototype scales (Figs. 8.5a

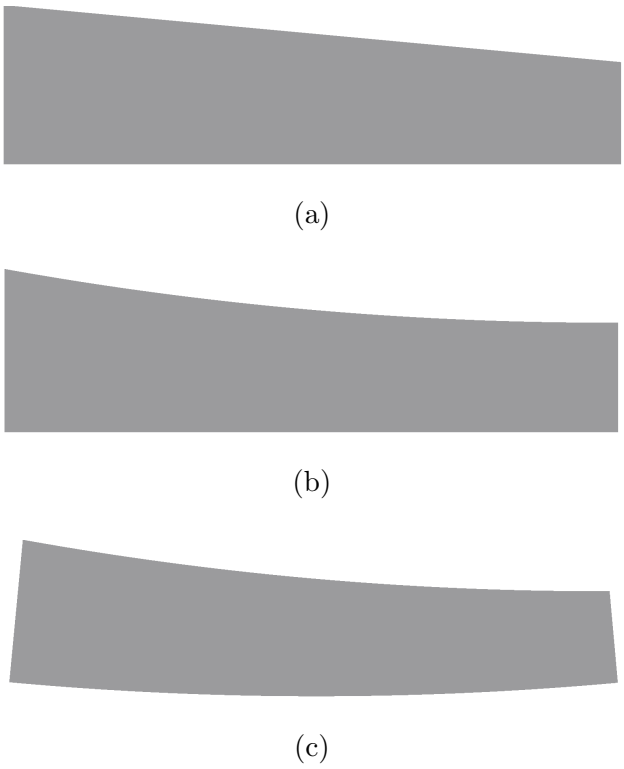

Figure 8.5: Three possible geometries for the tangential shaking case: (a) prototype model, (b) physical centrifuge scale model, (c) ideal scaled prototype model in a centrifugal acceleration field. Length of each geometry in the figure corresponds to $1/\mu\eta$.

and 8.5b) were developed to investigate discrepancies caused by geometrical differences, if any.

All models consisted of 3125 four-node quadrilateral elements with an equivalent average size of $0.16\,m \times 0.16\,m$ in prototype scale. The size of the elements depends on the scaling factor of each experiment. The stabilized single-point integration and mixed displacement-pressure (u-p) element (SSPquadUP, see McGann et al. (2015)) was used to capture the effective stress response of each simulated centrifuge test. This level of mesh refinement was chosen to properly resolve the propagation of shear waves of up to 50 Hz in the soil domain.

8.3.1 Boundary and loading conditions

The boundary and loading conditions remained unchanged from authors' previous LEAP exercises (Ghofrani and Arduino, 2017; Chen et al., 2019): the bottom boundary was fixed against vertical movement and the acceleration time history was applied to both vertical boundaries as well as the base of the model using the so called *UniformExcitation* loading pattern in OpenSees. This ensured a rigid container condition. Pore pressures at the slope surface nodes were set to be zero during the analysis to ensure drainage and avoid generation of excess pore pressures at the surface. The free water on the slope was not modeled and the effect of water sloshing (if any) was not considered. The soil was assumed to be in contact with the rigid container at all times and no gap was allowed. Hydraulic conductivity (K) was modified to be $10^{-5}m/s$ to better match the observed excess pore water pressure (pwp) dissipation trends. It is worth mentioning that the SSPquadUP element in OpenSees utilizes a *dynamic permeability coefficient*, which is defined as $k = \frac{K}{\rho_f g}$, where ρ_f is the density of fluid and g is the gravitational acceleration. This parameter was carefully adjusted following scaling laws.

To apply gravity, the material was set to be linear elastic and elemental body forces were increased gradually to reduce numerical instabilities in the model. The direction of centrifugal acceleration was applied in the radial orientation for the tangential physical centrifuge scale models; hence horizontal components of gravity existed. The material was then switched to *elasto-plastic* and new equilibrium was achieved by allowing enough extra analysis steps to adjust constitutive model internal variables to any plastic behavior. A Poisson's ratio of 0.3, which yielded a lateral earth pressure coefficient $K_0 = 0.43$ under level ground plane-strain conditions, was assumed to generate the initial stress state. Fig. 8.6 shows the imposed initial state of stress in terms of vertical, horizontal, and shear stresses for prototype and physical centrifuge scale models, respectively. The difference in initial stress state, due to different boundary conditions, model geometry, and gravity direction, is noticeable especially near the vertical boundaries. After reaching the desired initial stress state, the

acceleration time history was applied to the rigid boundaries horizontally. After the main shake, additional dynamic analysis steps were executed to dissipate any excess pore pressure.

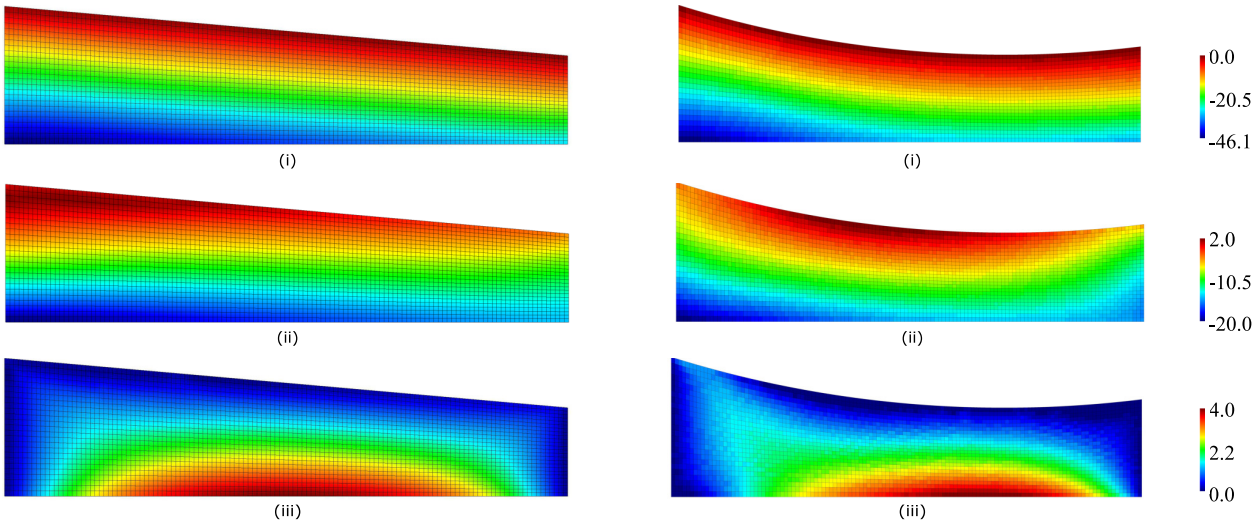

Figure 8.6: Initial stress state for prototype scale and physical centrifuge scale models after applying gravity for UCD Model-A: (i) Vertical effective stress distribution, (ii) Horizontal effective stress distribution, (iii) Shear stress distribution. All units in kPa and length of each figure corresponding to $1/\mu\eta$.

8.3.2 Solution algorithm

The constant average acceleration Newmark method ($\beta = 0.25$, $\gamma = 0.5$) was used in order to resolve the integration in time. A frequency dependent Rayleigh damping was applied to account for lack of small strain damping. The Rayleigh damping coefficients were chosen such that a 2% damping ratio was obtained at 0.2 Hz and 20 Hz. This damping was scaled based on the generalized scaling laws when appropriate. To account for material nonlinearity, the PM4Sand model implemented in OpenSees was used. In OpenSees the constitutive equations for this model are integrated using an explicit modified Euler integration schemes with sub-stepping error control (Sloan et al., 2001) and a maximum strain increment limit.

8.3.3 Constitutive model and calibration

PM4Sand was calibrated using available laboratory test data on Ottawa F-65 sand from previous LEAP projects (Ziotopoulou et al., 2018; Chen et al., 2019). During this phase of LEAP, a previous set of calibrated model parameters was carried over with minor modifications based on newly available torsional shear tests performed at Kyoto University Ueda (2018). In a first round of simulations, two sets of parameters summarized in Table 8.3, were calibrated for two relative densities, $D_R = 50\%$ and $D_R = 60.0\%$, in accordance with LEAP guidelines. Figs. 8.8a and 8.8b illustrate the case of a cyclic stress-controlled undrained torsional simple shear experiment along with simulations obtained using PM4Sand. In both cases, PM4Sand underpredicts the excess pore pressure during the first cycle while overpredicts the overall rate of excess pore pressure generation. This was observed in all element tests using PM4Sand under $K_0 = 1$. Nevertheless, PM4Sand captures well the shape of stress-strain loops and maximum shear strains. Fig. 8.7 illustrates comparisons between simulation results and laboratory experiments for both relative densities in terms of number of cycles to initial liquefaction, defined as 3.0% double amplitude (DA) shear strain, for different cyclic stress ratios (CSR). In general, the PM4Sand predictions follow the observed slope of cyclic strength curve but with fewer number of cycles to trigger liquefaction. This difference becomes more significant for smaller CSRs. Simulations were also performed for CSRs larger than 0.2 based on observations made from previous LEAP phases that indicated that most of the simulated and estimated-from-experiments stress ratios in the centrifuge experiments were higher than 0.2.

The PM4Sand primary parameter D_R was modified for each experiment based on reported sand relative density. As expected, the simulated centrifuge response showed great dependency and sensitivity on this parameter. This is natural for sand models based on critical state concepts, and certainly true for PM4Sand, as many of its secondary parameters (that were assigned their default values during calibration) are closely related to D_R. In addition to D_R, h_{po}, that controls contraction rate through a power function, was also changed

to better match the recorded experimental results. Final PM4Sand calibrated parameters are shown in Table 8.4.

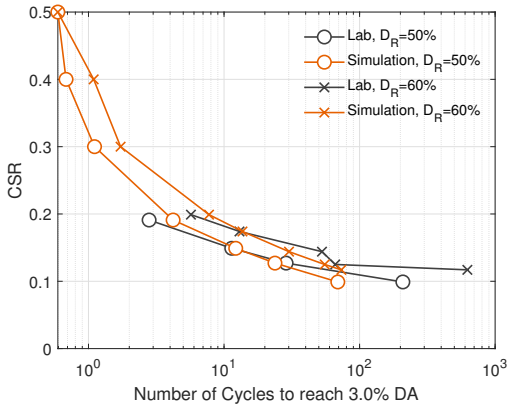

Figure 8.7: PM4Sand calibration: Comparison of number of cycles required to reach 3.0% DA shear strain in simulations and laboratory tests.

Table 8.3: Calibrated PM4Sand parameters and their values

Primary Parameters	D_R	50.0%	60.0%
	G_o	350.0	350.0
	h_{po}	0.275	0.175
Secondary Parameters	ϕ_{cv}	35.6	35.6
	c_z	200.0	200.0

8.4 Results

8.4.1 Model-A simulation results

Results from Model-A simulations, which applies scaling factors without introducing a virtual intermediate 1G model, are presented here for both prototype and physical centrifuge scale

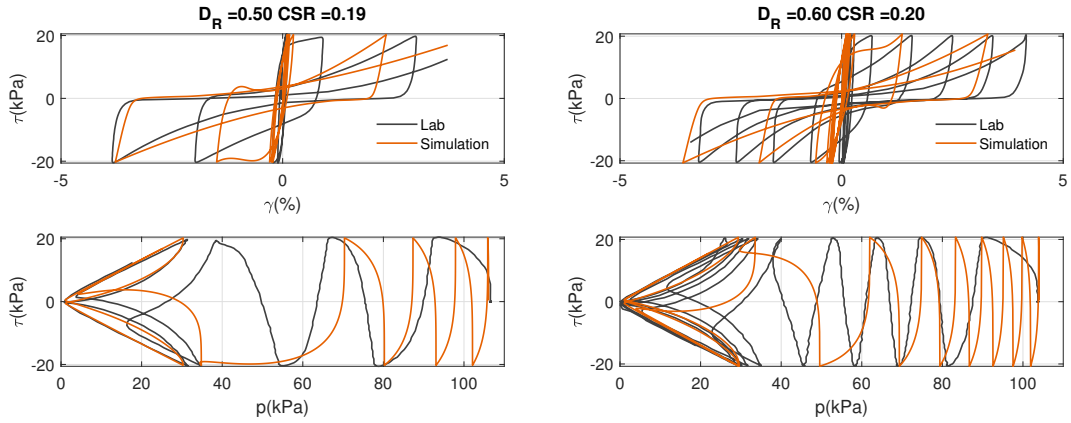

Figure 8.8: PM4Sand calibration: Comparison between simulations and experimental results obtained using element test and torsional shear test, respectively, for two combinations of D_R and CSR. The results are presented in terms of shear stress, τ, vs. shear strain, and shear stress, τ, vs. mean effective stress, p.

Table 8.4: Input parameters for PM4Sand for each centrifuge case

	KyU_A	RPI_A	UCD_A	KyU_B	RPI_B
D_R	56%	64.0%	67.0%	58.0%	62.0%
G_o	350.0				
h_{po}	0.275	0.07	0.02	0.275	0.07

models. RPI Model-A served as a verification case for proper scaling because its spinning direction relative to its shaking direction lead to identical geometries between prototype and centrifuge scale models for 2D plane-strain model; and for which the simulation results showed insignificant difference. KyU and UCD Model-A experiments, on the other hand, showed different degrees of discrepancy between prototype and physical centrifuge scale models due to differences in geometry as illustrated in Fig. 8.5 for tangential shaking cases.

With shorter centrifuge arm length compared to KyU case (1.09 m vs. 2.5 m), UCD centrifuge model scaled to the actual prototype size implies a greater curvature in the base boundary and more inclined side boundaries. Thus more difference is implied in the geometry between the prototype scale of the two experiments, as manifested in the obtained simulation results.

Fig. 8.9 illustrates recorded and predicted acceleration response for all Model-A cases in terms of 5% damping acceleration response spectra at the AH1-AH4 sensors (see Fig. 8.3 for sensor location). The plots show the simulation results predicted the recorded experimental results very well at the intended input motion frequency of 1Hz. The responses were consistent between the prototype and centrifuge scale models except in the UCD case, where the prototype scale model showed higher PGA at shallower sensor locations.

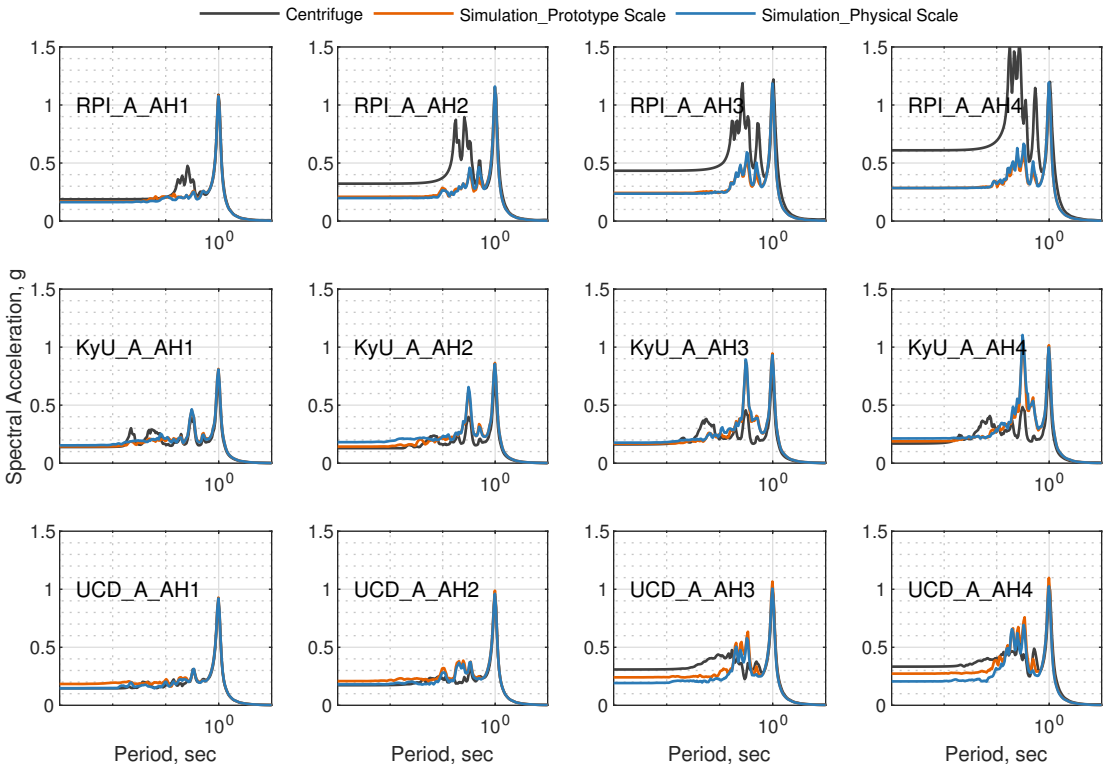

Figure 8.9: Comparison of acceleration response spectra (5% damping) between centrifuge and simulation results at accelerometers AH1 - AH4. - see Fig. 8.3 for location of the sensors.

All centrifuge tests showed similar trends in pore pressure response, except for the KyU case where full liquefaction was not triggered despite having the loosest condition ($D_R = 56\%$) among all centrifuge tests. Comparison of predicted and recorded pore pressure response at pore pressure sensors along the center line and other locations is illustrated in Figs. 8.10 and 8.11, respectively. The figures show PM4Sand could capture the trend of pore pressure generation observed in the experiments. The plots show that the response obtained from prototype and physical centrifuge scale models was consistent along the centerline, i.e., P1-P4, while it was slightly different at locations closer to the boundaries, i.e., P5-P8.

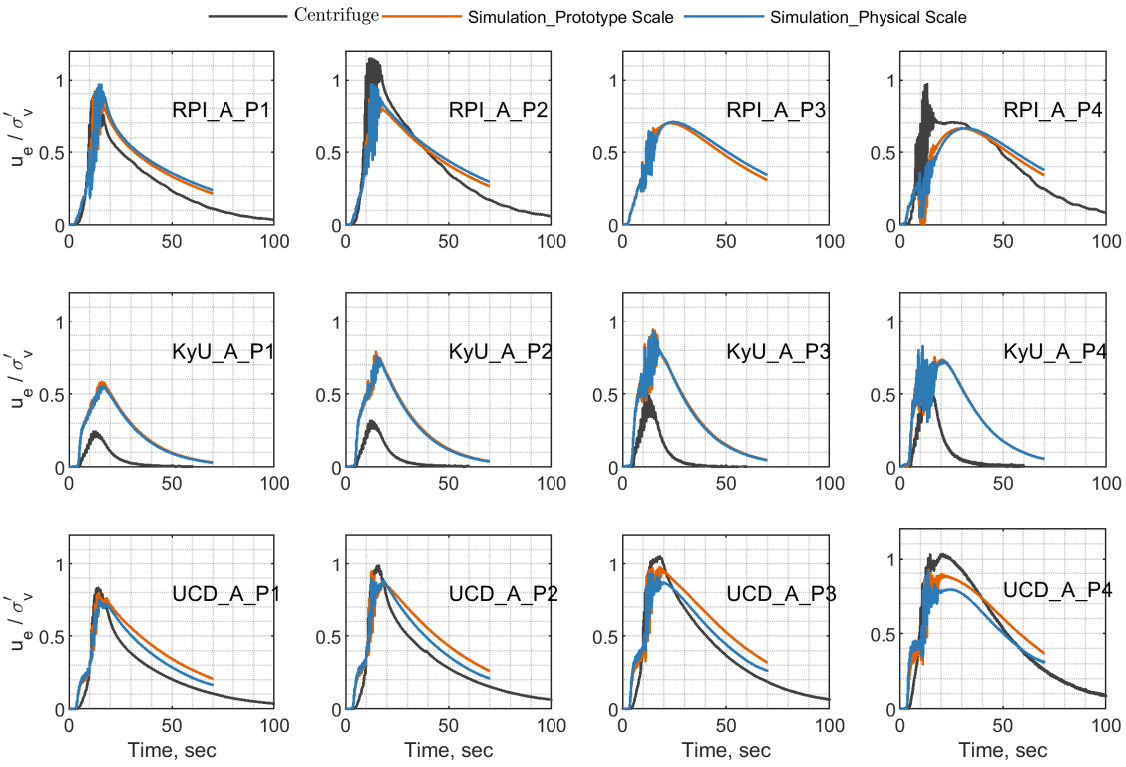

Figure 8.10: Comparison of evolution of pwp between centrifuge, prototype scale model, and physical centrifuge scale model at transducers P1-P4. - see Fig. 8.3 for location of the sensors.

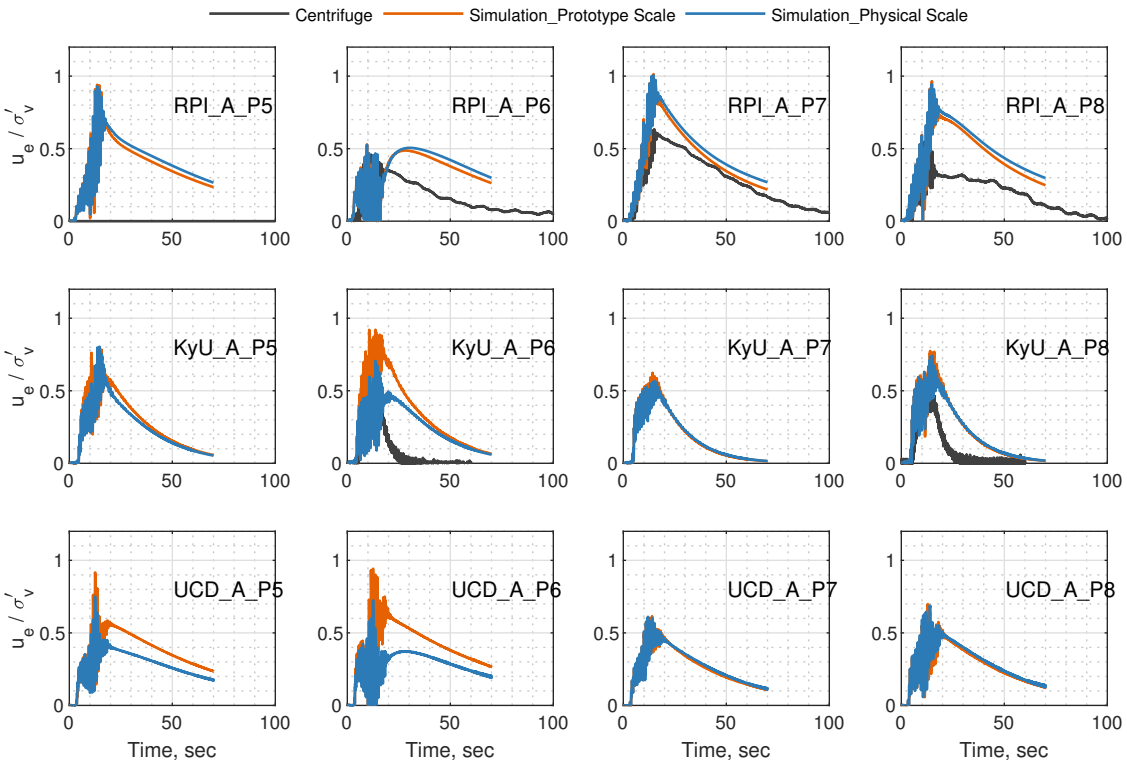

Figure 8.11: Comparison of evolution of pwp between centrifuge, prototype scale model, and physical centrifuge scale model at transducers P5-P8. - see Fig. 8.3 for location of the sensors.

Prediction of lateral displacements continues to be a challenge for both experimentalists and numerical modelers (Manzari et al., 2019; Chen et al., 2019). General trends of simulated soil deformation at the end of shaking are illustrated in Fig. 8.12. The figure shows contours of nodal displacements for three physical centrifuge scale models. The figure shows the expected discrepancies in total horizontal displacement due to differences in physical geometry and input motion. The figure also indicates the up-slope part of the soil settled and the down-slope part heaved resulting in the flattening of the slope, which was expected. Comparison of horizontal displacement time histories between experiments and numerical simulations reinforce these findings and are presented in Fig. 8.13. The displacements recorded at the

surface marker locations are shown in Fig. 8.4. The PM4Sand model was able to capture the evolution of displacements reasonably well for RPI and UCD cases, while overpredicted the magnitude of displacements for the KyU case. The results were fairly consistent between the two numerical simulation approaches, i.e., prototype scale and centrifuge physical scale models, with the exception of the tangential shaking cases, i.e., KyU and UCD, where the prototype scale results showed larger lateral displacements when compared to the physical centrifuge scale models; and the difference was larger at up-slope locations. Many factors, including geometry, boundary conditions, direction of applied input motion, and horizontal gravity component presented in physical centrifuge scale models, can be attributed to the cause of this observation.

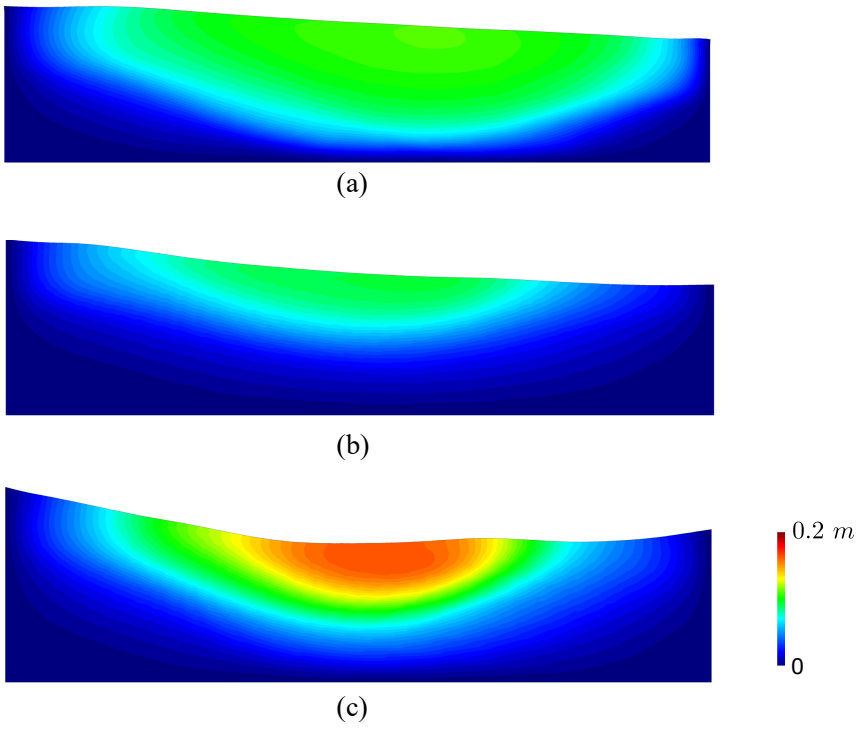

Figure 8.12: Contours of final horizontal displacement from three simulated physical centrifuge scale models: (a) RPI Model-A, (b) KyU Model-A, and (c) UCD Model-A. Geometries are presented in prototype scale.

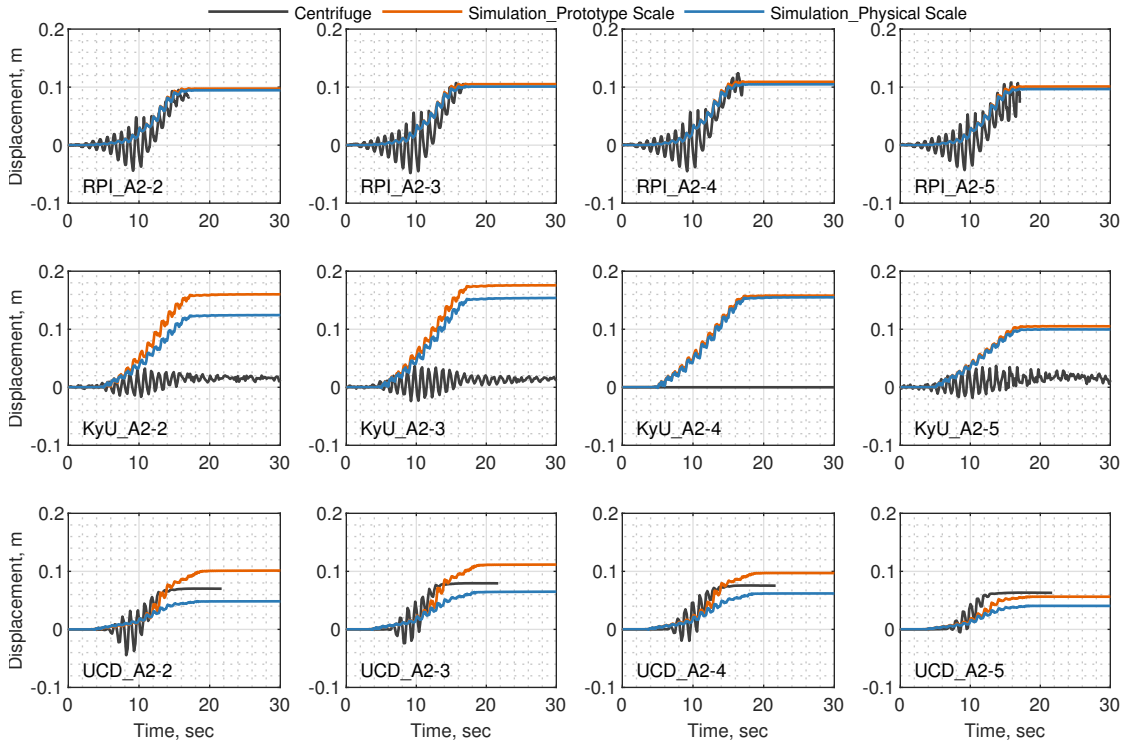

Figure 8.13: Simulated and recorded lateral displacement located at surface marker locations. - see Fig. 8.4 for location of the markers.

8.4.2 Model-B simulation results

In Model-B (2-step scaling), a virtual intermediate 1G model was introduced and an additional scaling step was considered compared to Model-A. Both RPI and KyU's Model-A and Model-B achieved similar relative density in the experiments. That is 64% vs. 62% and 56% vs. 58%, respectively. Simulation results for Model-B are presented and compared to centrifuge records as well as Model-A simulation results. All the results are presented in prototype scale. Figs. 8.14 and 8.15 illustrate recorded lateral displacements at several surface locations obtained from both simulations and experiments for RPI and KyU, respectively. RPI cases show good match between simulation and experimental responses for both Model-A and B, while KyU cases show simulations over-predicted lateral displacements in both Model-A and B. It is noted that even though opposite scales were used in the RPI and KyU experiments, both simulations and experiments showed the same trend. That is, Models-B produced larger lateral displacements than Models-A. Two aspects are important to consider here: (a) the effect of the virtual scale on overburden stresses, and (b) the effect of motion discrepancies on recorded lateral deformations. RPI and KyU's virtual intermediate models were scaled in opposite ways, and therefore, the initial stress state in RPI Model-B was twice as large as in RPI Model-A, while it was halved from KyU Model-A to KyU Model-B. Due to the K_σ effect it was expected to observe larger displacements for larger initial stresses and smaller values for smaller initial stresses. The opposite was observed in the KyU case. One contributing factor to this discrepancy is likely the differences in input motion achieved in the KyU Model-B, which unlike RPI, was stronger than Model-A's (Fig. 8.2). To eliminate the effect of different input motions, one additional KyU Model-A2 numerical analysis was examined using the input motion recorded in Model-B and the results are also included in Fig. 8.15. KyU Model-A2 simulations showed lateral displacements trends consistent with the trend observed in the RPI cases. In both cases, models with higher initial stresses predicted larger lateral displacements when similar input motions and relative densities were achieved. Finally, Fig. 8.16 presents recorded stress-strain responses from the simulations

showing significant differences between Model-A and Model-B in terms of maximum shear strains obtained in each case. At transducers P2 and P3, maximum shear strains obtained from the RPI Model-B exceeded the so called intermediate strain level of 10% used in Iai et al. Iai et al. (2005) to validate the generalized scaling law proposed.

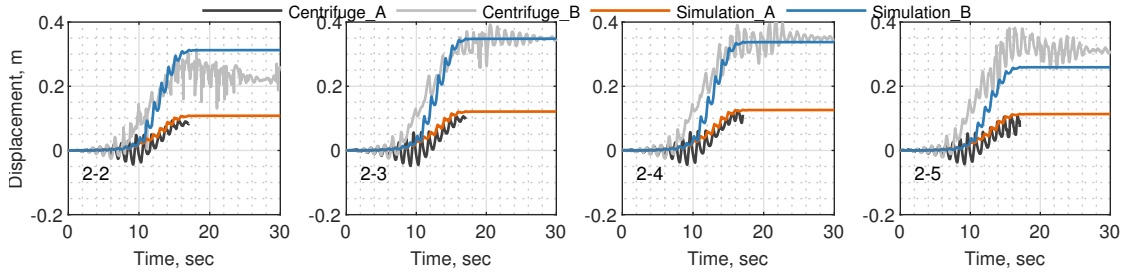

Figure 8.14: Comparison of lateral displacement recorded at surface marker locations in simulations and experiments (RPI). - see Fig. 8.4 for marker location.

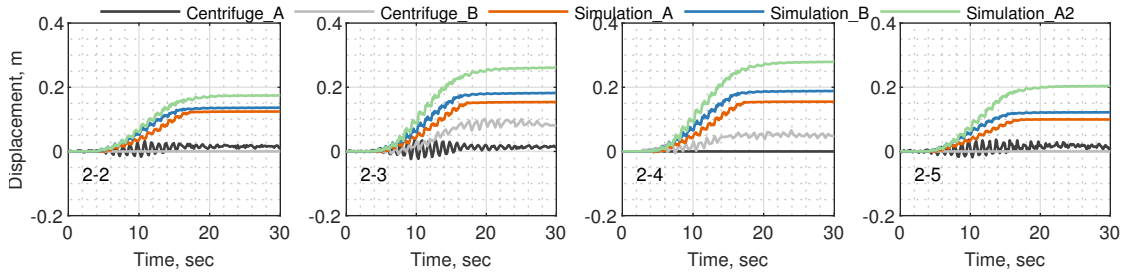

Figure 8.15: Simulated and recorded lateral displacements at surface marker locations for (KyU) experiment. - see Fig. 8.4 for marker location.

Lastly, by examining cyclic resistance and strain accumulation under simplified loading conditions, fundamental behavior of PM4Sand can be assessed to understand the aforementioned discrepancy in accumulated permanent deformations between Model-A and Model-B simulations. For this purpose, additional single element simulations were performed on sensitivity of PM4Sand responses under different initial vertical stresses and loading conditions. A first series of results were obtained from undrained CDSS simulations under uniform

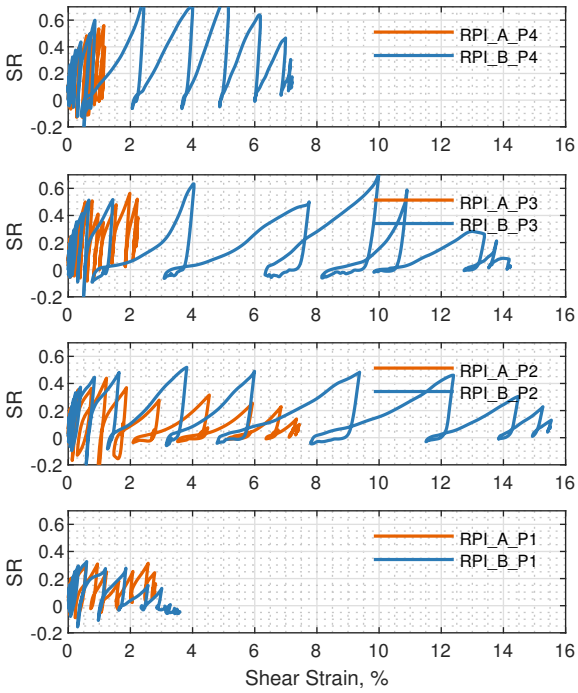

Figure 8.16: Comparison of simulated stress-strain responses from RPI Model-A and Model-B at transducers P1-P4.

CSR and three initial vertical stresses within the range of values found in the experiments. Fig. 8.17 shows cyclic strength curves obtained using calibrated PM4Sand parameters for the RPI_A case. At 15 cycles, PM4Sand results show 10% increase in CRR as initial vertical stress, σ'_v, changed from 100 kPa to 40 kPa, which is consistent with the trend presented in Idriss and Boulanger Idriss and Boulanger (2008). However, due to limitation of PM4Sand, CRR shows 30% increase as σ'_v changed from 100 kPa to 20 kPa. This behavior does not follow the limit on K_σ under lower stresses, which was set to be 1.1 by Idriss and Boulanger because the dependence of K_σ on σ'_v has not been measured or validated for very low effective stresses. This limit on K_σ is not accounted in PM4Sand and model parameters might need to be revised when laboratory tests under lower stresses, e.g., 20 kPa, become available.

Furthermore, a second series of results were obtained using undrained CDSS simulations under ramped CSR with initial static shear stress, a stress condition that is similar to LEAP

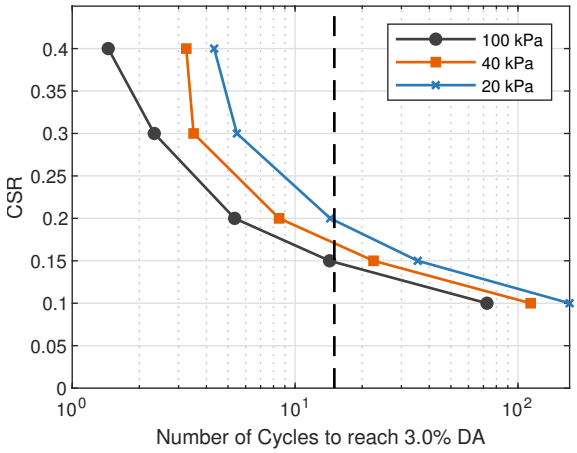

Figure 8.17: Comparison of number of cycles required to reach 3.0% DA shear strain in simulations under different initial vertical stresses, σ'_v.

centrifuge experiments. Fig. 8.18 shows that strain accumulation in PM4Sand after liquefaction triggering is sensitive to initial vertical stresses under LEAP loading conditions. It is worth mentioning that PM4Sand formulations, that incorporate K_σ effect, were calibrated for cyclic resistance, and not necessarily to account for permanent deformations after liquefaction triggering. More studies are needed to refine the calibrated PM4Sand parameters to better capture the effect of initial vertical and shear stresses on post liquefaction permanent deformations.

Nevertheless, observed trends are consistent between simulations and experiments. These findings suggest that initial stress state has an important effect on permanent deformation and the generalized scaling law should be used with care. Soil condition, e.g., relative density, should be further studied and adjusted to account for the change in initial stress state and its effect on liquefaction triggering and permanent deformation in both centrifuge test and numerical model calibration.

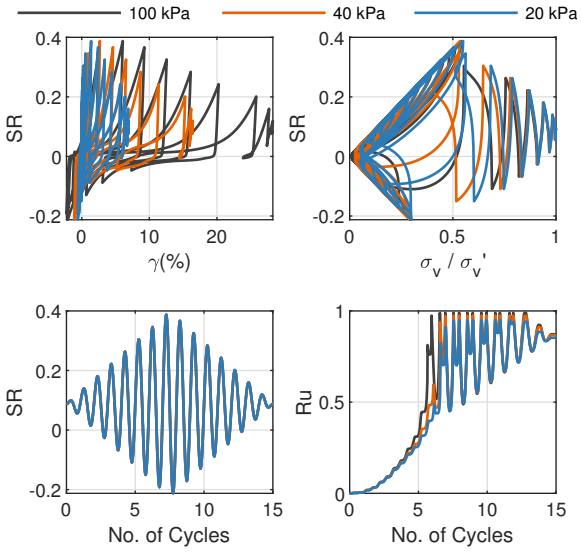

Figure 8.18: Comparison of simulated stress-strain responses using single element test under ramped cyclic stress ratio and different initial vertical stresses.

8.4.3 Discussion on cyclic stress ratio

Previous sections indicate initial overburden stresses and imposed cyclcic stress ratio have important consequences in the observed model response. In this context, Fig. 8.19 illustrates simulated and estimated (from experiments) profiles of maximum shear stress ratio along the centerline (P1-P4). In the absence of 2019 stress-strain responses from experiments, and given that the same model configuration, soil properties and targeted input motion were used in all the LEAP projects, LEAP-2015 data extracted from Zeghal et al. (Zeghal et al., 2017) was used here for comparison with numerical predictions. Centrifuge test data were evaluated using maximum absolute ratios of shear stress and initial effective vertical stresses extracted from Figs. 17 and 18 in Zeghal et al. (Zeghal et al., 2017), respectively. The experimental data showed large variability, while the numerical predictions showed a general trend with maximum stress ratios reducing with increasing depth. This is shown in Figs. 8.19 and 8.20. From these results it is clear a maximum shear stress ratio of 0.5 was very likely to be exceeded in all experiments. This value is considerably higher than the

maximum cyclic stress ratios used in the laboratory tests and used for calibration purposes; which only went up to $CSR = 0.2$ for $D_R = 60\%$ as shown in Fig. 8.7. Cyclic simple shear tests conducted at George Washington University (GWU) (Manzari, 2018) considered two different overburden stresses, 40 and 100 kPa, and CSR ranges from 0.08 to 0.14 and 0.075 to 0.15, respectively. It should be noted that although some laboratory experiments were performed at CSR values as high as 0.6 during LEAP-UCD-2017, they were performed on samples that had a void ratio of around 0.505, which is smaller than measured values (ranges from 0.558 to 0.664) in the centrifuge experiments.

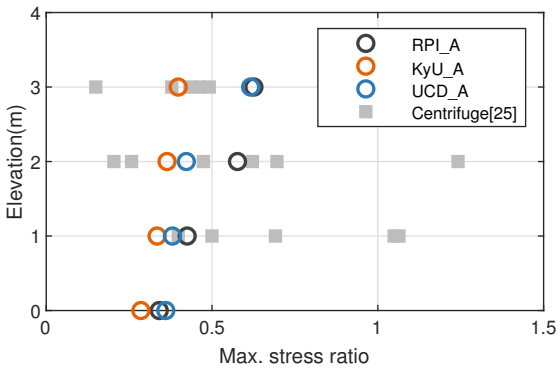

Figure 8.19: Comparison of maximum shear stress ratio between LEAP-Asia-2019 simulation and LEAP-GWU-2015 experiments extracted from Zeghal et al. (Zeghal et al., 2017).

As a side note, in a previous LEAP exercise the authors used two constitutive models, PM4Sand and MD. PM4Sand showed the capability of reproducing the cyclic strength curve observed from lab tests, while MD underpredicted the number of cycles to liquefaction under smaller CSRs, i.e., 0.3, and the slope of cyclic strength curve was much steeper. However, at CSRs larger than 0.3, PM4Sand and MD showed almost the same cyclic resistance behavior. Therefore, although the trend in number of cycles to reach liquefaction was not the main target in the MD calibration, the MD model adequately predicted the experiments and produced better results compared to the PM4Sand model for which a different calibration strategy was used (Manzari et al., 2019). This indicates the importance to calibrate

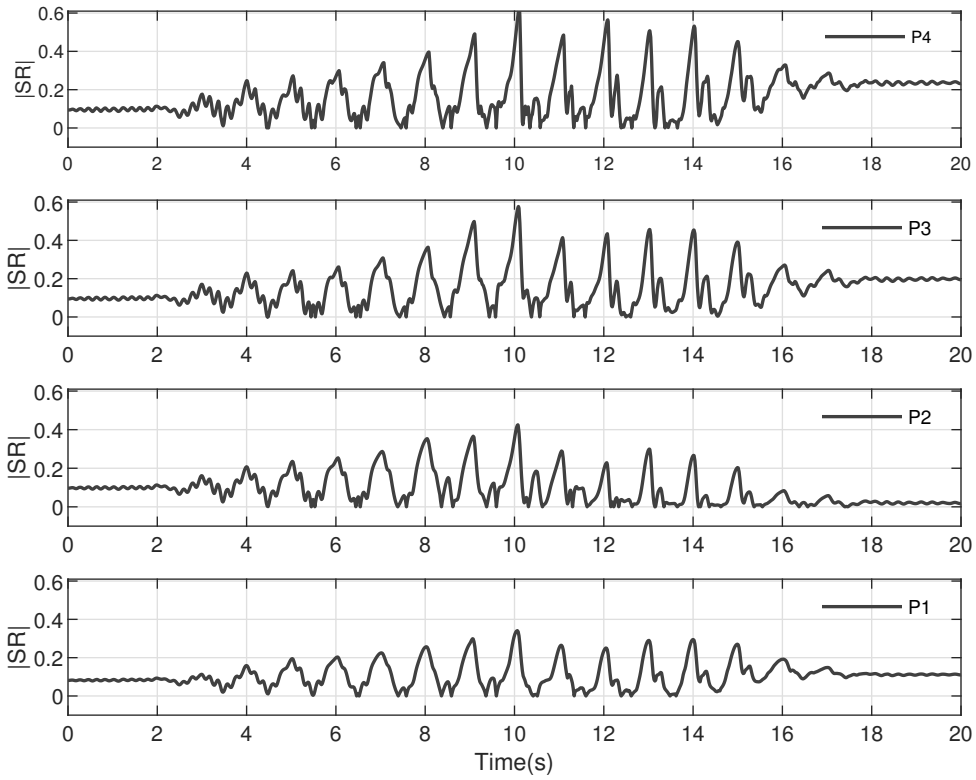

Figure 8.20: Histories of calculated shear stress ratio from simulations at various locations along the centerline.

constitutive parameters at appropriate CSR levels.

The large stress ratio observed in both simulation and experiment was associated with the existence of initial static shear stresses, especially near the surface of the model. Its effect on cyclic resistance of soil, known as K_α effect (Idriss and Boulanger, 2008), may be different for different D_Rs and should be considered in model calibration procedures. It is understandably complicated to perform laboratory tests at small confining pressures, high CSRs, and initial static shear stress. More detailed experimental and numerical studies are warranted on the effect of K_α and K_σ under various stress paths and using different constitutive models. This will be beneficial to our understanding of fundamental soil behavior and fine tune the results obtained from numerical models.

8.5 Summary

Both prototype and physical centrifuge scale models were built in OpenSees to simulate the response of Ottawa F-65 sand in accordance with LEAP-Asia-2019 numerical simulation guidelines using the bounding surface plasticity constitutive model PM4Sand, calibrated using high quality laboratory test data. Type-C predictions were obtained and compared to recorded data from centrifuge experiments. The results were compared between prototype and physical centrifuge models as well as between Model-A (1-step scaling) and Model-B (2-step scaling).

In general, type-C prediction results showed PM4Sand was able to predict the results from centrifuge experiments, especially the acceleration response at the frequency of the input motion. The evolution of excess pore pressures predicted by PM4Sand was also comparable to experiments. The amount of predicted horizontal displacement was in the range of the recorded displacements for RPI and UCD cases but showed over-predication for the KyU case.

Comparison between prototype and physical centrifuge scale models generally showed consistent acceleration and pore pressure response along the centerline. However, it was shown that for the tangential shaking cases, i.e., KyU and UCD, the prototype scale models tended to predict higher lateral displacements compared to the physical centrifuge scale model results. Many factors, including geometry, boundary conditions, direction of applied input motion, and horizontal gravity component presented in physical centrifuge scale models, were related to this phenomenon.

Comparison between Model-A and Model-B demonstrates that close attention should be paid to the effect of initial stress state when generalized scaling laws are adopted. Numerical simulations showed that changes in initial stress state affected magnitudes of lateral displacements. In this study, models with higher initial stresses typically predicted larger lateral displacement for similar relative density and input motion. More studies, both centrifuge tests and numerical simulations, are needed in order to establish appropriate soil properties

guidelines, e.g., relative density or soil fabric, to account for the effect of initial overburden pressure on liquefaction triggering and soil residual stress-strain behavior such that virtual intermediate scale results can be used to represent the interested prototype model response.

Higher CSRs and initial static shear stresses were found to be important for calibration of the constitutive model for this specific centrifuge experiment. It appears that in order to capture the behavior of the soil in the centrifuge experiment, appropriate CSR levels should be used. As such, current LEAP model calibration guidelines might not be using element tests representing the real conditions achieved in LEAP centrifuge experiments.

Chapter 9

LEAP-RPI-2020 SIMULATION EXERCISE

9.1 Introduction

The LEAP project included a final set of centrifuge experiments and simulation exercises and a workshop to be held at Rensselaer Polytechnic Institute (LEAP-RPI-2020). As part of this phase a series of centrifuge experiments were performed at 10 different centrifuge facilities across the world to investigate the seismic response of a sheet pile retaining structure supporting liquefiable soils (LEAP-RPI-2020 Organizing Team, 2020). This chapter presents simulation results performed as part of this exercise.

Fig. 9.1 illustrates the baseline schematic of the centrifuge model experiments. The model consisted of a (top) layer of Ottawa F-65 sand supported by a sheet pile wall made of aluminum. Behind the sheet pile, the soil layer had a thickness of 4 m and a length of about 13 m in prototype scale. In front of the sheet pile, the layer had a thickness of 1 m and a length of about 7 m. The reference relative density for this layer ranged from 55% to 75% as presented in Table 9.1. This layer of soil was underlain by a dense soil layer with 90% relative density and 1 m thickness. The total length of the model was about 20 m. The tip of the wall was initially located at mid-depth of the dense layer before the centrifuge acceleration was applied.

In addition to varying initial relative densities, the tests were conducted with different base excitations. The target motion was a ramped sine wave with dominant frequency $f = 1$ Hz and 5 consecutive uniform cycles at the PGA. In addition to the 1 Hz cycles, the base motions included higher frequency harmonics (3 to 6 Hz) that were either included intentionally in the target motion or obtained as a result of the dynamic characteristics of the shaking system. Of primary interest in these tests was the lateral displacement of the

soil surface behind the wall, the deflection of the sheet pile and the general dynamic response of the soil deposit.

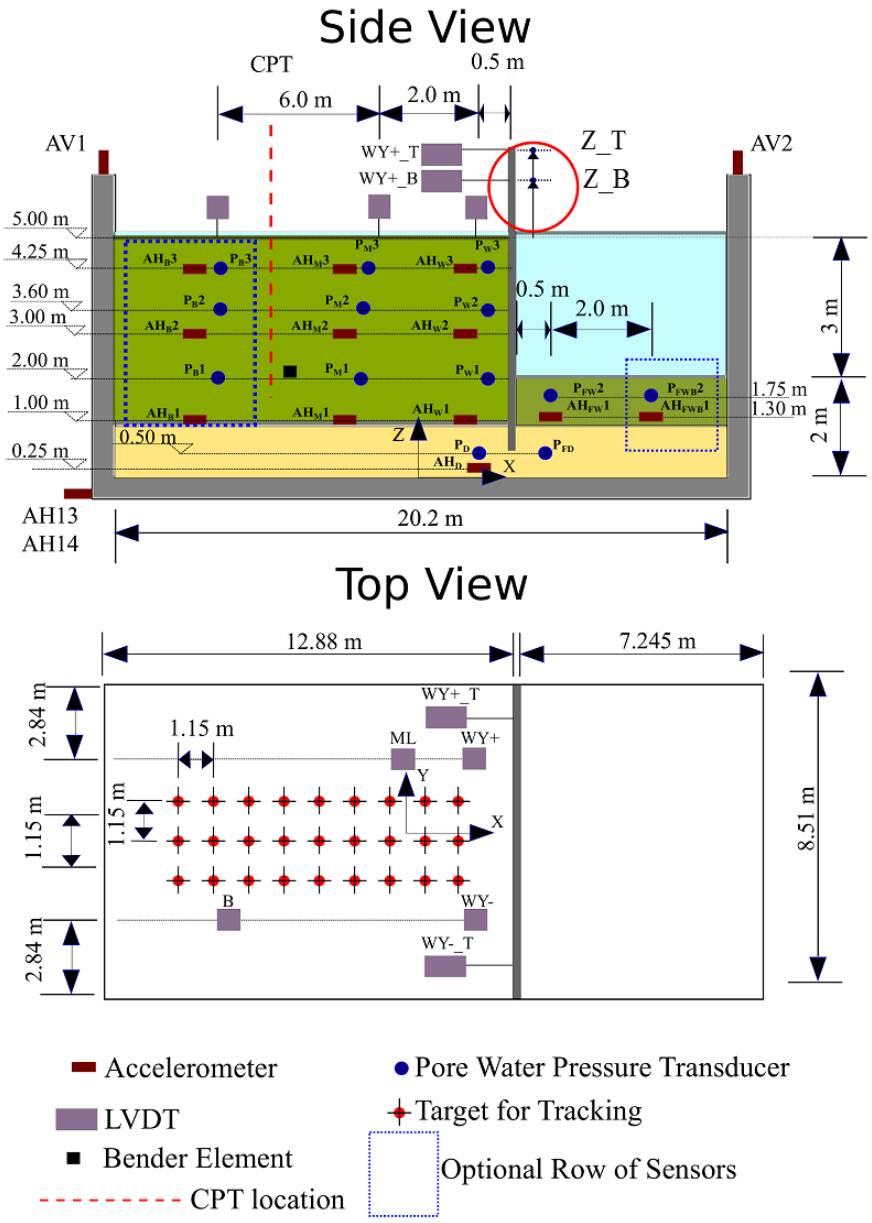

Figure 9.1: Experimental setup and instrumentation for LEAP-2020 centrifuge tests (after LEAP-RPI-2020 Organizing Team (2020)).

Table 9.1: Reported density achieved in each centrifuge test

	Density (Mg/m^3)	Relative Density
Ehime-2	1650	65%
KAIST-2	1649	65%
KyU-1	1627 ± 10	55%
KyU-3	1650 ± 10	65%
RPI-9	1650	65%
RPI-10	1650	65%
RPI-11	1660	66%
RPI-12	1630	55%
RPI-13	1684	75%
UCD-1	1650	65%
ZJU-1	1679	75%

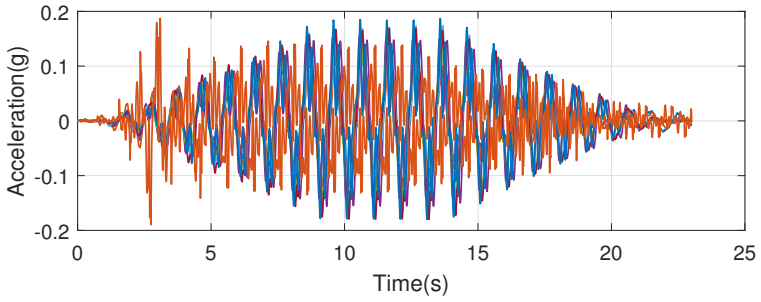

(a)

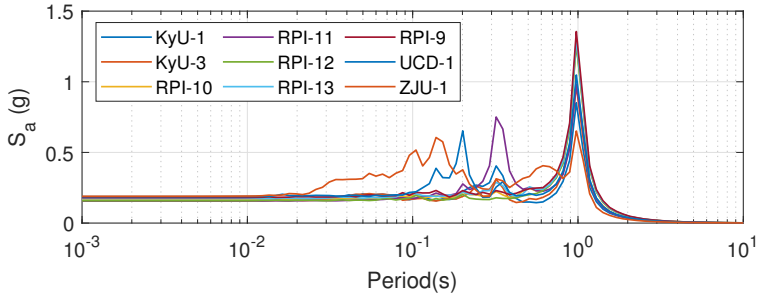

(b)

Figure 9.2: Excitations for LEAP-2020 centrifuge experiments, (a) achieved base acceleration time histories and (b) response spectra (5% damping)

The specimen was built in a container with rigid walls. Three arrays of sensors ("B", "M", and "W" shown in Fig. 9.1) were used to monitor the soil response behind the wall. Two arrays were used for the soil in front of the wall. Additional sensors were also installed within the dense base layer. Each location included an accelerometer and/or a pore pressure transducer. The middle "M" array was installed aiming to capture the soil response close to an hypothetical failure prism behind the wall, while the "W" array was intended to capture the soil-structure interaction response.

As of April 2020, two phases were completed for LEAP-RPI-2020: (1) model calibration and type-A prediction of element tests, and (2) type-B prediction of centrifuge experiments. The University of Washington simulation effort included analyses using two bounding surface plasticity constitutive models, (i.e., MD and PM4Sand) and comparison with experimental results. Both models follow critical state soil mechanics concepts and were deemed capable of capturing the stress-strain relationships for loose to dense sands, and varying drainage and loading conditions present in these experiments.

9.2 Model calibration

The PM4Sand model was calibrated using data from available laboratory tests on Ottawa F-65 sand from previous LEAP projects (Ziotopoulou et al., 2018; Chen et al., 2019). During this phase of LEAP, a previous set of calibrated model parameters was carried over with minor modifications to match new results from direct simple shear tests performed at George Washington University. The calibrated input parameters are summarized in Table 9.2. Input parameters for MD remained unchanged from previous LEAP-UCD-2017 practice and can be found in Table 7.1.

Fig. 9.3 shows comparisons of experimental and simulated soil response for an undrained CDSS test with $\sigma'_v = 40kPa$ and uniform $CSR = 0.16$. Both MD and PM4Sand underestimated soil contraction in the initial loading cycle while overestimated pore pressure generation afterwards. It was also noted that MD showed cyclic strain "stalling" as continued cyclic loading did not induce further accumulation of shear strain after R_u reached

Table 9.2: Calibrated PM4Sand parameters and their values

Primary Parameters	D_R	Varies based on recorded relative density
	G_o	350.0
	h_{po}	0.07
Secondary Parameters	ϕ_{cv}	35.6
	e_{max}	0.74
	e_{min}	0.49
	c_z	200.0

0.95. On the other hand, PMSand showed continuing accumulation of shear strain. This was a typical response observed in all tests. A complete set of simulations and comparisons with experimental results can be found in LEAP 2020 simulation exercise - phase I: model calibration report.

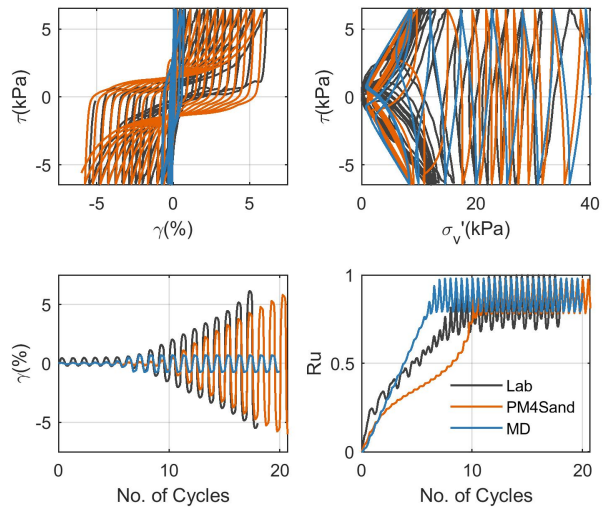

Figure 9.3: Comparison of calibration and laboratory test results. $\sigma'_v = 40\,kPa$, CSR = 0.16.

9.3 Type-A prediction of element tests

As discussed in Chapter 8, previous LEAP exercises showed it was not sufficient to use results from low CSR uniform tests to calibrate the model parameters. This was acknowledged by the organizing team. Therefore, after the calibration process was complete, the simulation teams were asked to use the calibrated parameters to simulate the stress-strain response of CDSS soil specimens subjected non-uniform stress cycles with higher stress ratios. The goal of this phase was to examine the response of the constitutive models to loading conditions similar to those achieved in LEAP-UCD-2017 and LEAP-Asia-2019 experiments and expected in LEAP-RPI-2020 tests. Therefore, a non-uniform shear stress input was proposed in the form of a ramped sinusoidal wave reaching a maximum cyclic stress ratio (CSR_{max}) and ramping down to zero. A constant static shear stress bias (α) of 0.087, as a result of the 5° constant slope simulated in previous LEAP projects, was imposed onto the non-uniform shear stress histories as shown in Fig. 9.4. Two initial vertical stresses, 30 and 40 kPa were considered. CSR_{max} ranged from 0.22 to 0.42. The soil relative density of 66.7% ($e_0 = 0.6$) was used in all simulations.

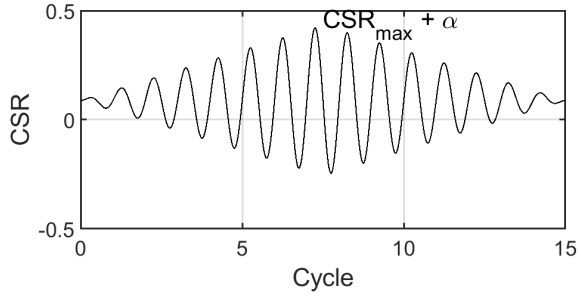

Figure 9.4: Non-uniform cyclic stress ratio input.

For this purpose, a stress controlled element test script was developed and simulation results were obtained using OpenSees. Figs. 9.5 and 9.6 present results obtained using the calibrated PM4Sand and MD parameters for non-uniform CDSS tests under $\sigma'_v = 40\,kPa$

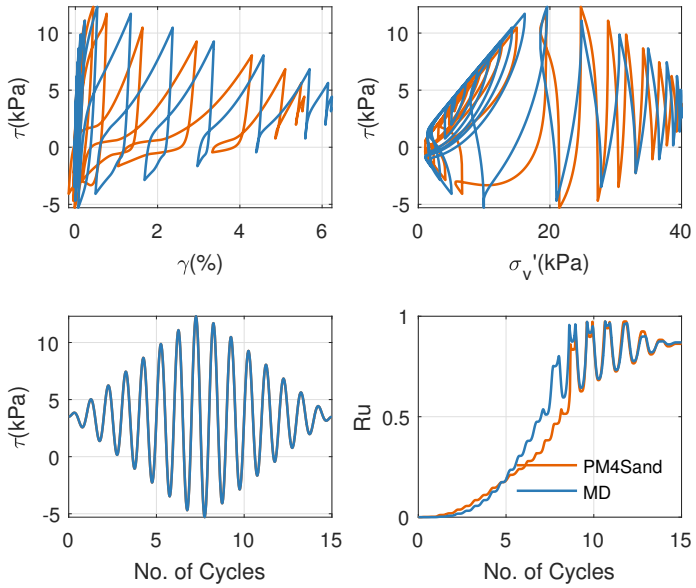

Figure 9.5: Type-A prediction results for $\sigma'_v = 40\,kPa$ and $CSR_{max} = 0.22$.

and $CSR_{max} = 0.22$ and 0.38, respectively. A complete set of simulation results can be found in Appendix B. Similar to what was observed in the calibration phase, the results showed larger shear strain accumulation in PM4Sand than MD and faster PWP build-up (between $R_u = 0.2$ to 0.5) in MD than PM4Sand. However, these differences were much less significant than for low CSR_{max} as shown in Fig. 9.3. The presence of the static shear bias had a profound affect on the MD responses, and it is believed to be the cause for obtaining reasonable predictions of the centrifuge experiments presented in Chapter 7, despite the limitation of shear strain "stalling" indicated above.

9.4 Type-B prediction of centrifuge experiments

The second phase of LEAP-RPI-2020 was a type-B prediction of centrifuge experiments. Following LEAP-RPI-2020 guidelines, a 2D plane-strain model was built using the FEM tool OpenSees (OpenSees, 2007), and GiD pre-post processor (CIMNE, 2020). In these analyses a prototype scale model was considered. This work was facilitated through the use

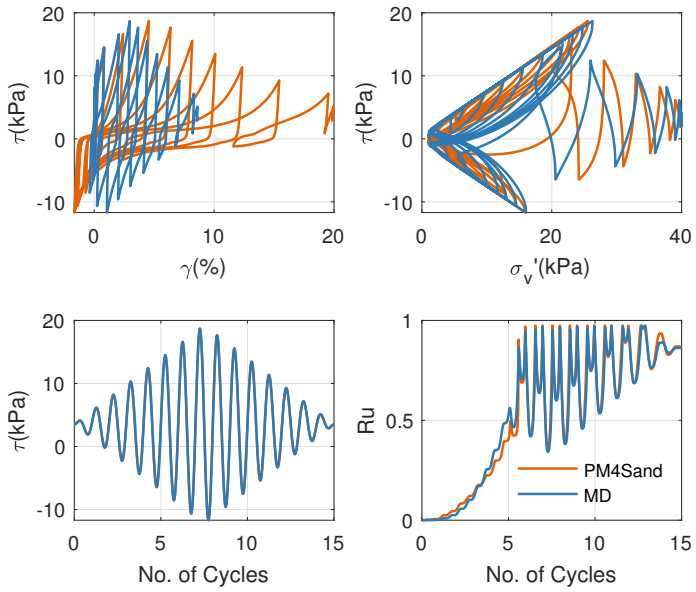

Figure 9.6: Type-A prediction results for $\sigma'_v = 40\,kPa$ and $CSR_{max} = 0.38$.

of advanced computational, storage, and networking infrastructure provided by the Hyak supercomputer system at the University of Washington (Hyak, 2020).

9.4.1 Model building

Soil domain

Similar to other LEAP exercises, the medium dense liquefiable layer ($D_R = 55\% - 75\%$) was modeled using PM4Sand and MD, and the underlying dense layer ($D_R = 90\%$) using an elastic material. The PM4Sand primary parameter D_R was modified to match reported relative densities for each centrifuge experiment. The initial void ratio e_{init} used in MD was also modified to match reported relative densities. The base dense layer elastic modulus was calculated using previously calibrated PM4Sand parameters for Ottawa F-65 sand with relative density $D_R = 90\%$. Other properties are listed in Table 9.3. A constant permeability $k = 3 \times 10^{-5}\ m/s$ was applied to all soils based on reported values and author's previous

experience with LEAP experiments (Chen et al., 2019).

Table 9.3: Input parameters for dense layer

Elastic Modulus (kPa)	40000
Poisson's ratio	0.3
Density (Mg/m^3)	1.73

The FEM model of the soil domain consisted of 2544 elements and 2683 nodes, with vertical element size of 0.125 m, as shown in Fig. 9.7. The mesh was refined horizontally around the sheet pile wall. The stabilized single point quadrilateral element with mixed displacement-pressure formulation (SSPquadUP) proposed by McGann et al. (2015) was used in all simulations.

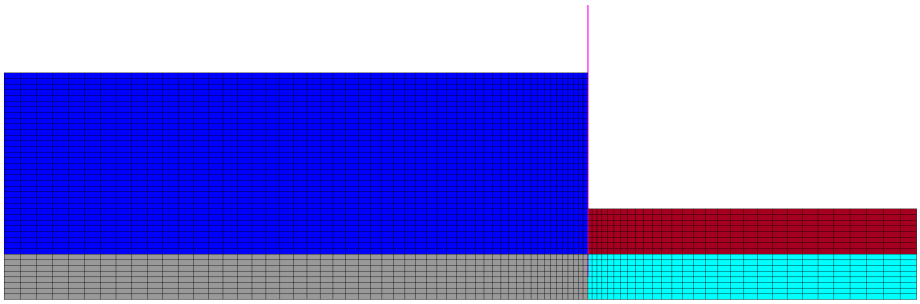

Figure 9.7: 2D OpenSees mesh developed in prototype scale.

The nodes at the base of the model were fixed in the horizontal and vertical directions. Side nodes were fixed in the horizontal directions. Pore pressure degrees of freedom were fixed along the horizontal free surfaces to ensure zero pore water pressures at all times. The free water level on the right side of the wall was not simulated. Consequently, the static pore water pressures calculated using UP elements on nodes behind and in front of the wall

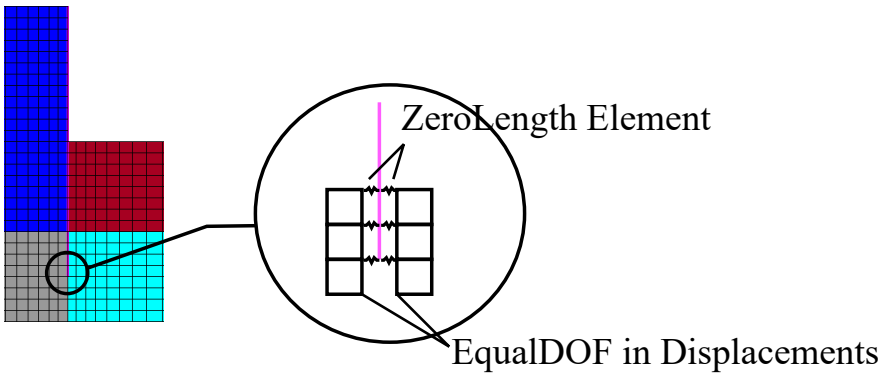

Figure 9.8: Boundary condition around the toe of the embedded wall.

were different. To ensure correct initial static pore pressures, the soil domain on both sides of the wall were separated. As shown in Fig. 9.8, there are three nodes located at the same location along the embedded portion of the wall: two soil nodes and one beam node that represents the wall. Each soil node was connected to the wall through zero length elements with elastic no tension (ENT) materials such that no drag forces were generated when the wall was moving away from the soil while lateral support was provided by the wall. The same ENT springs were applied to the left side of the cantilever portion of the wall. The stiffness of the ENT springs was set to be ten times stronger than the wall.

Wall

Aluminum sheet pile walls were used in all experiments; with minor variations in stiffness as listed in Table 9.4. All walls had similar geometry as shown in Fig. 9.9; although exact dimensions varied from facility to facility (Table 9.4). In OpenSees, the 6 m sheet pile wall was located 0.5 m above the base of the model and was modeled using elastic beam column elements 0.125 m in size. The bottom of the wall was fixed in rotation and vertical direction and free to move in the horizontal direction. No additional constraints were applied to other wall nodes during dynamic analysis. The thickness and stiffness of the wall was adopted

from reported values and varied from site to site.

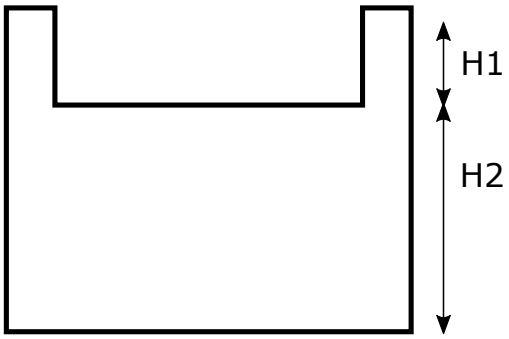

Figure 9.9: Typical geometry of the sheet pile wall used in centrifuge experiment.

Table 9.4: Information of sheet pile wall used in each centrifuge experiment (dimensions in prototype scale)

	Aluminum Grade	E(GPa)	Density (Mg/m^3)	Thickness (m)	I (m^4)	H1 (m, Fig 9.9)	H2 (m, Fig 9.9)
RPI	6061	68.9	2.74	0.109	1.08×10^{-4}	1.73	5.89
Ehime	5052	69.3	2.68	0.12	1.44×10^{-4}	4.46	4.78
ZJU	6063	68.3	2.8	0.104	9.37×10^{-5}	1.74	5.90
KAIST	6061	68.9	2.72	0.112	1.17×10^{-4}	2.40	5.88
KyU-1	6000?	68.9	2.71	0.08	4.27×10^{-5}	3.46	5.46
KyU-3	6000?	68.9	2.71	0.12	1.08×10^{-4}	3.46	5.46
UCD	6061	68.9	2.72	0.0948	7.10×10^{-5}	1.39	5.22

9.4.2 Solution algorithm and assumptions

Kinematic constraints were applied using the Penalty method and time integration was performed using the Newmark integration scheme. To solve the nonlinear system of equations,

the Newton method was used with Mumps solver. The entire analysis was divided into three phases: gravity, dynamic shaking, and post-shaking dissipation. Rayleigh damping was applied to account for the lack of small strain damping or to enforce additional damping when necessary. Newmark and Rayleigh damping parameters are summarized in Table 9.5. Note that additional damping was applied during gravity and post-shaking dissipation.

Table 9.5: Analysis parameters

Rayleigh Damping	ξ	0.1 (Dissipation Phase) 0.02 (Dynamic Phase)
	f_1	0.2
	f_2	20.0
Newmark Integration Parameters	γ	5/6 (Gravity Phase) 0.5 (Dynamic & Dissipation Phase)
	β	4/9 (Gravity Phase) 0.25 (Dynamic & Dissipation Phase)
Constraints	Penalty	10^{15}

Gravity phase

The goal of the gravity phase was to generate a realistic initial stress field for subsequent dynamic analysis. During this phase, both MD and PM4Sand were first set to behave elastic and the soil permeability was set very high ($k = 1\ m/s$); to facilitate the dissipation of artificial excess pore water pressures generated due to gravity loading. A Poisson's ratio of 0.3 was used and time integration was performed with Newmark parameters $\gamma = 5/6$, and $\beta = 4/9$ to damp out (numerically) the waves generated due to the sudden application of gravity. It is important to note that when UP elements are used in OpenSees transient analysis is required for the static application of gravity. This is due to the fact that pore pressure degrees of freedom are stored (for computational efficiency) in the velocity array;

which only exists in a transient analysis.

The lateral movement of the wall was initially prevented by adding a series of virtual stiff springs along the wall to enforce a nearly K_0 condition as illustrated in Fig 9.10. These springs were in addition to the ENT springs discussed earlier. Stress concentrations were observed around the toe of the wall located in the elastic layer. Then the MD/PM4Sand model was switched to *elasto-plastic* and the stiffness of these springs was reduced gradually while additional analysis steps were performed to minimize the shock to the system after each stiffness reduction. Enough iterations were performed until the stiffness of the springs was low enough and the springs could be removed completely. The achieved final stress field is shown in Fig 9.11. Fig. 9.12 presents contours of nodal displacement before and after allowing lateral movement of the wall. Notice small displacements were observed after releasing the virtual springs and before the dynamic loading. Fig 9.13 illustrates the achieved initial static pore pressures.

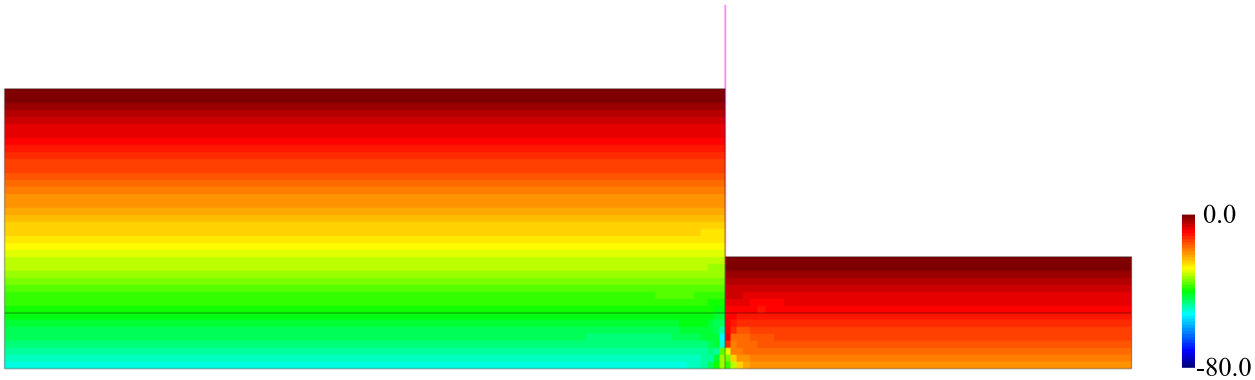

(a)

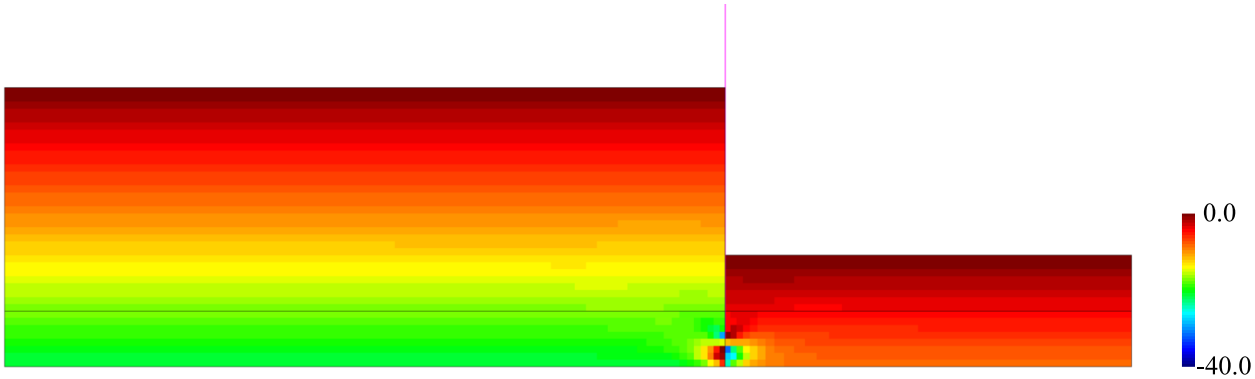

(b)

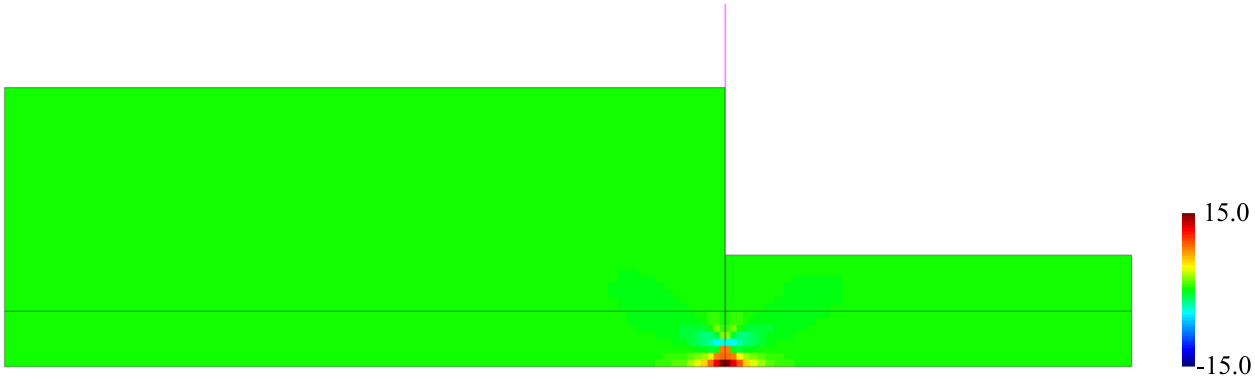

(c)

Figure 9.10: Initial stresses (kPa) before releasing the horizontal constraints on the sheet pile wall: (a) vertical stress, (b) horizontal stress, and (c) shear stress.

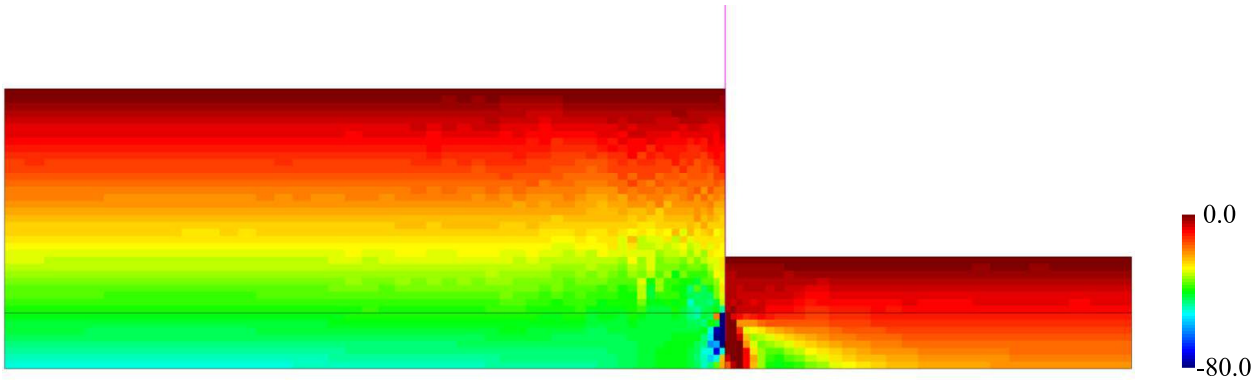

(a)

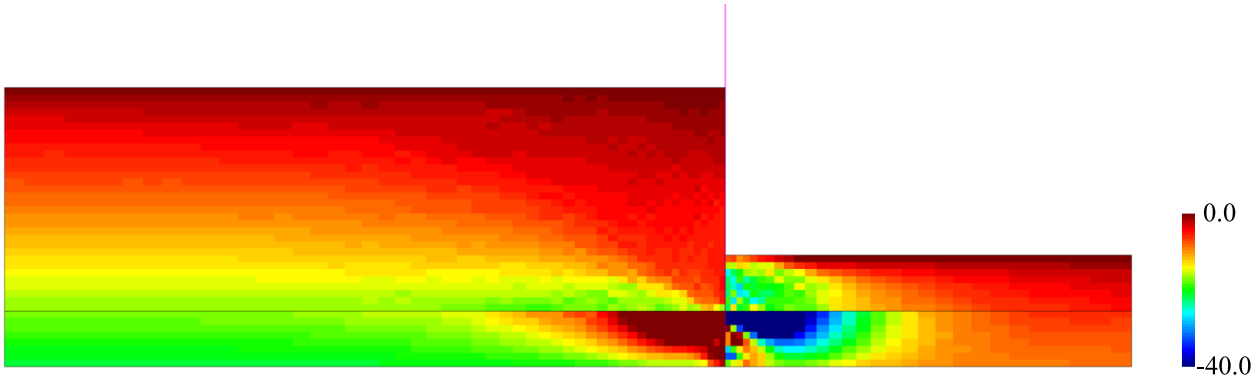

(b)

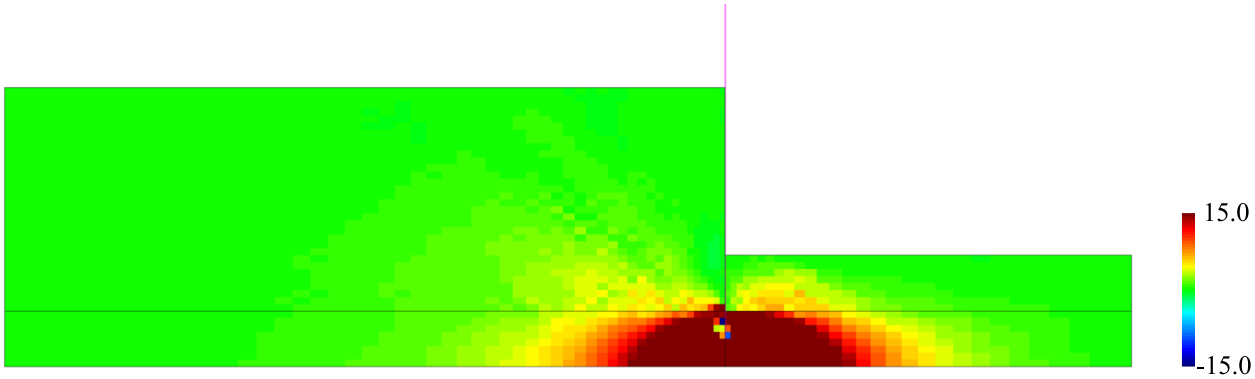

(c)

Figure 9.11: Initial stresses (kPa) after releasing the sheet pile wall: (a) vertical stress, (b) horizontal stress, and (c) shear stress.

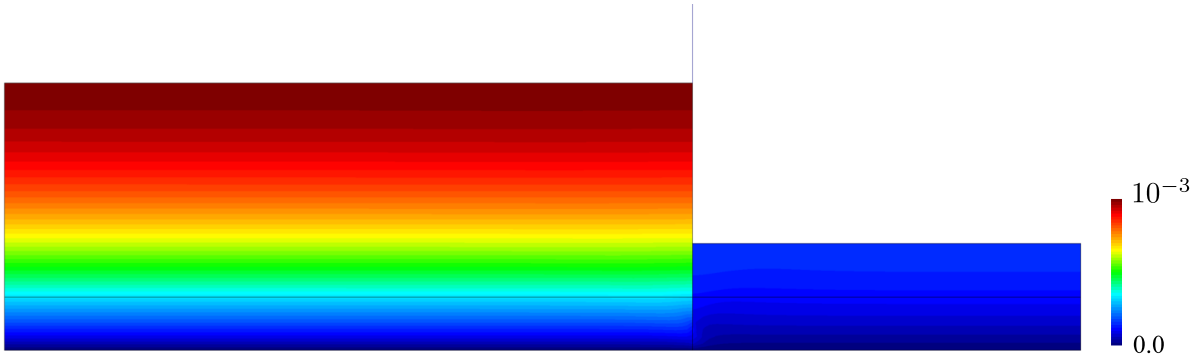

(a)

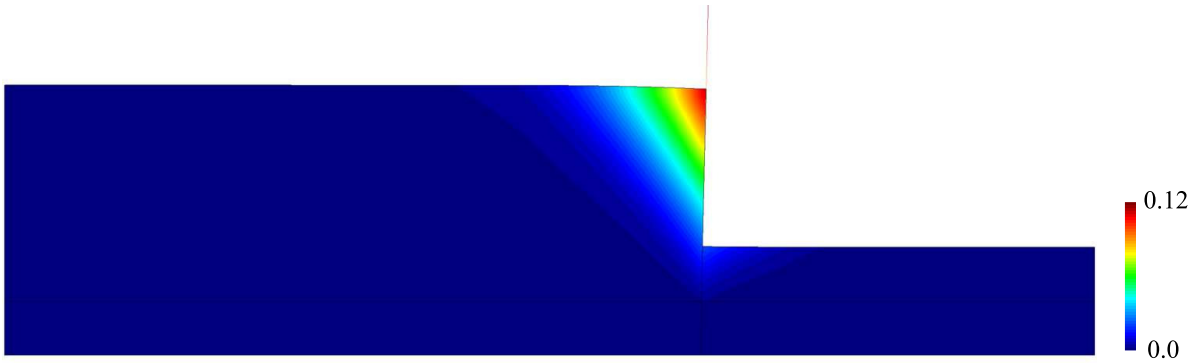

(b)

Figure 9.12: Nodal displacement contours (m): (a) before and (b) after releasing the sheet pile wall.

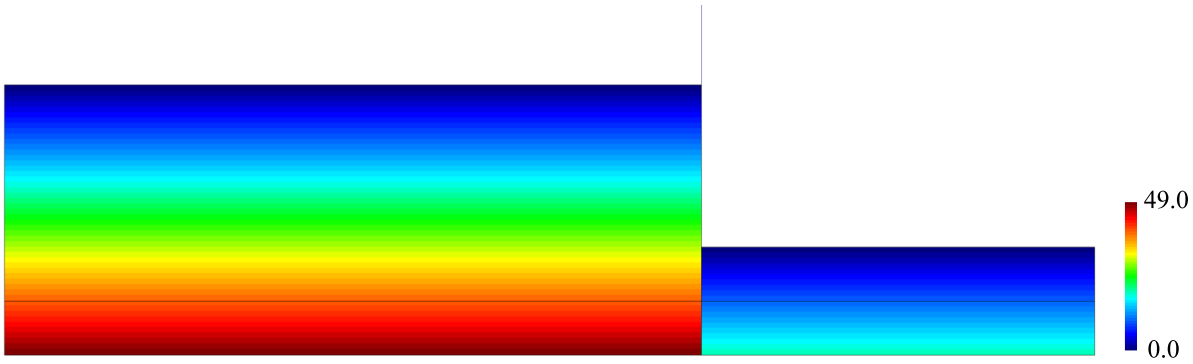

Figure 9.13: Initial pore water pressure (kPa) after gravity phase.

Dynamic phase

The acceleration time history recorded at each centrifuge site, representing the target motion, was applied to all nodes with fixed horizontal DOFs, i.e., the base and vertical boundaries of the model, using *Uniform Excitation* to simulate a rigid container.

Dissipation phase

After primary shaking, simulations were run up to 100 seconds to simulate the dissipation of excess pore pressures generated during shaking. For this purpose a *zero* motion was appended to the original input motion. During this phase (i.e., after shaking) high frequency vibrations were observed in the numerical model, especially at locations close to the wall, and dissipation of pore water pressure was affected. Therefore, to improve the simulated dissipation trend, additional Rayleigh damping was applied to reduce noise. The post shaking reconsolidation was not turned on when using PM4Sand because this functionality affects dissipation.

9.4.3 Results

On May 2020, selected centrifuge data was revealed to predictors and preliminary comparisons were made between simulation predictions and experimental results. Fig. 9.14 illustrates lateral displacements of the wall at the soil surface. During the experiments, only minor lateral displacement was observed during centrifuge spin-up, while 5 to 20 cm of lateral displacements, depending on relative density and wall thickness, were predicted in OpenSees after releasing constrains on the wall at the beginning of shaking. These initial displacements were included in Fig. 9.14 to compare final wall displacements. Great variability is observed in both experiment and simulations with simulations underestimating lateral displacements in most cases. However, the simulations successfully captured the correct wall movement trend, e.g., in KyU-1 and KyU-3 cases, where both experiment and simulation results showed larger displacements for KyU-1, due to a thinner wall thickness, compared to KyU-3 (Table 9.4). In terms of numerical results, models using PM4Sand showed larger

amplitudes in the evolution of lateral displacements than those using MD. This is consistent with what was observed at element level. Stress strain responses at sensor location P_B1 obtained using PM4Sand and MD are presented in Fig. 9.15. PM4Sand showed much larger shear strain amplitudes after liquefaction.

In terms of acceleration and pore water pressure only data for the RPI-9 test is presented here and all other simulation results are included in Appendix C as they all show trends similar to the RPI-9 case. Figs. 9.16 and 9.17 show recorded and predicted acceleration response for RPI-9 experiment in terms of time history and 5% damping response spectra at array sensor locations B-W (see Fig. 9.1 for sensor location). The plots show the simulation results predicted very well the recorded experimental data at the intended 1 Hz input motion frequency. Both simulated and recorded results show higher frequency content near the surface as well as near the wall. PM4Sand and MD predicted very similar responses despite PM4Sand showing higher PGAs at most sensor locations. This observation was most likely related to PM4Sand material over prediction of soil stiffness during dilation cycles leading to stronger simulated dilation pulses.

Comparisons of predicted and recorded pore pressure response at pore pressure sensor arrays B-W are depicted in Fig. 9.18. The plots show both models could capture the trend of pore pressure generation observed in the experiments. As shown in Figs. 9.5 and 9.6, the MD model exhibited slower pore pressure generation compared to the PM4Sand model. PM4Sand showed more significant dilative cycles that matched better the experimental results.

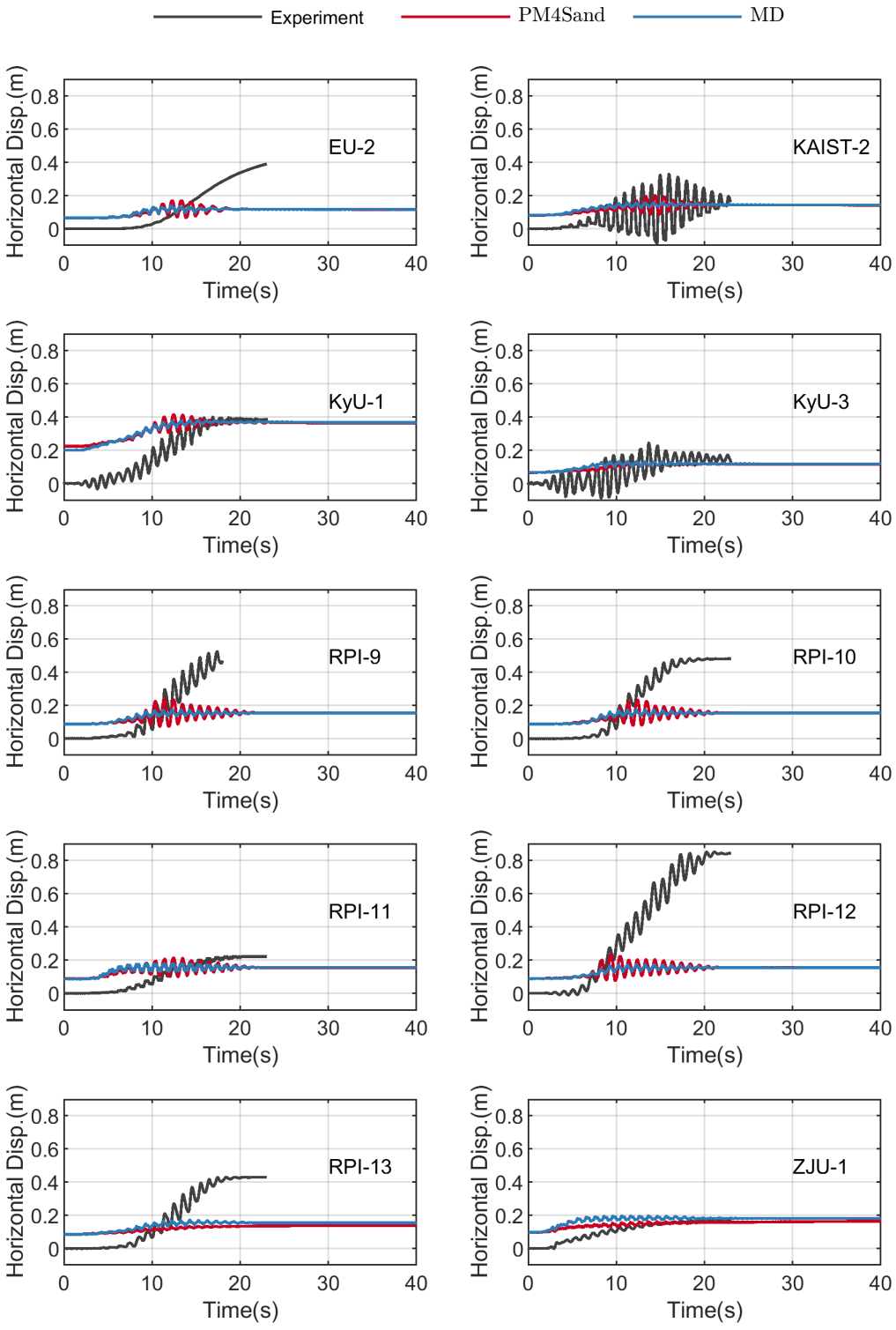

Figure 9.14: Comparison of simulated and recorded sheet pile wall lateral displacement at the soil surface.

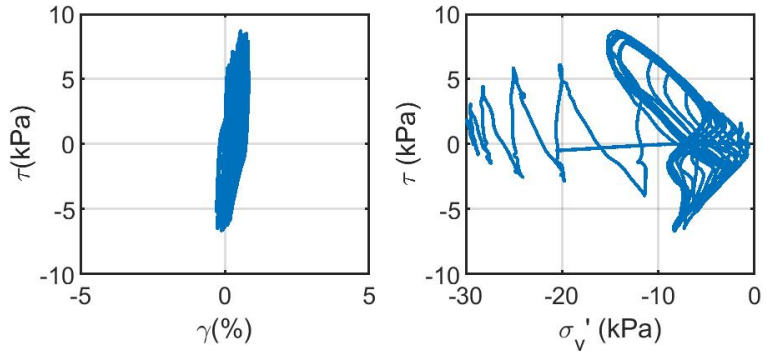

(a)

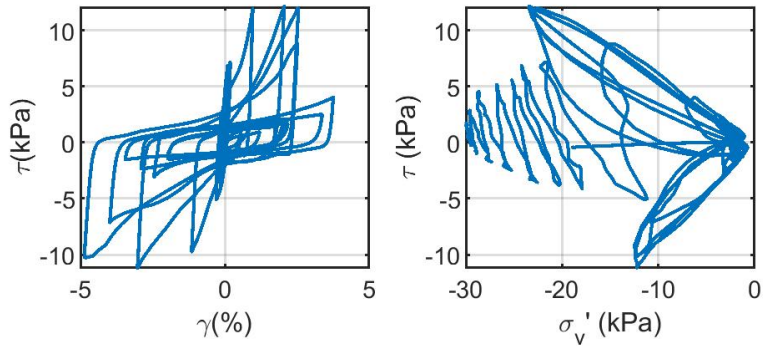

(b)

Figure 9.15: Stress strain responses at transducer location P_B1 obtained using: (a) MD and (b) PM4Sand material.

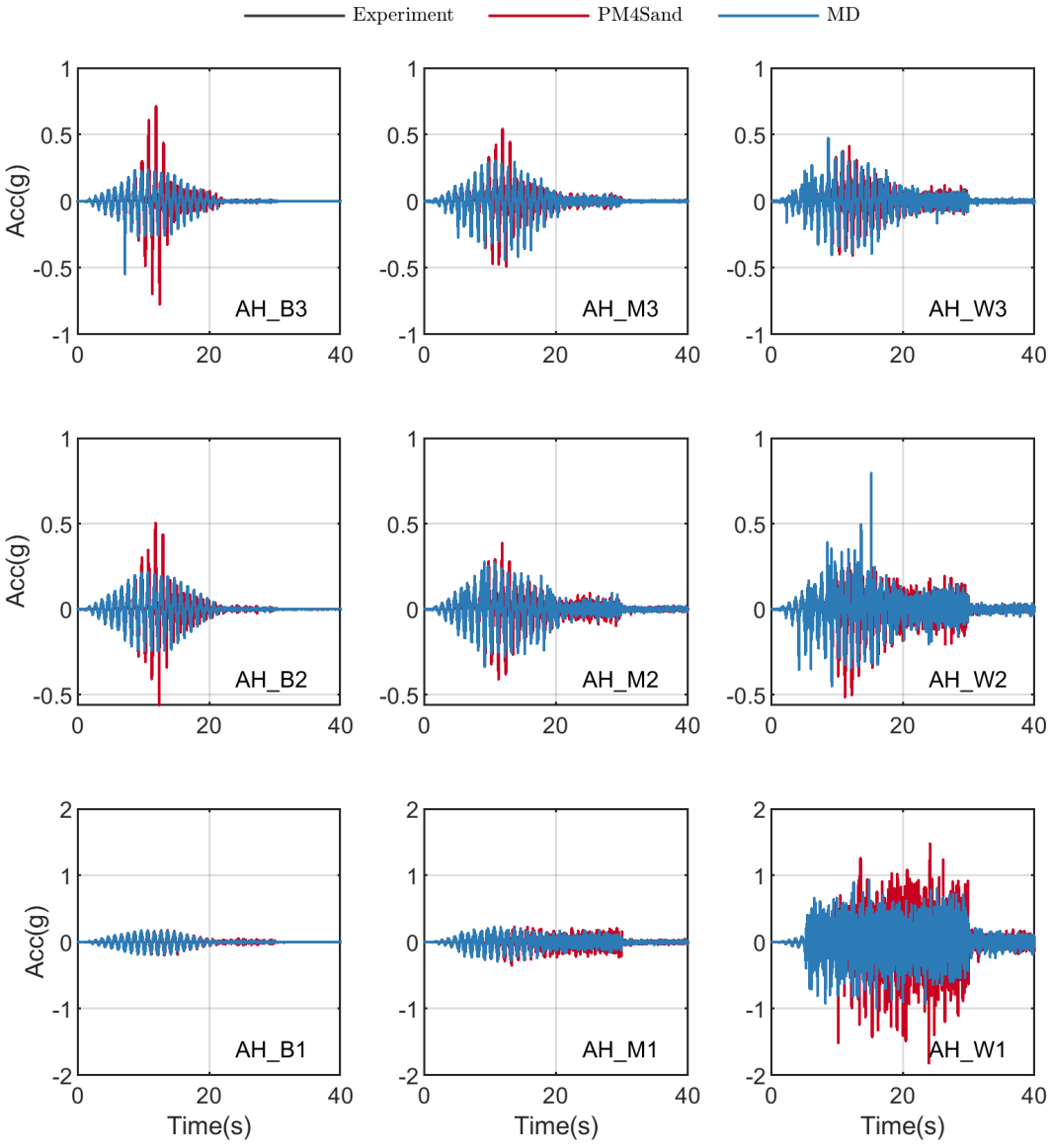

Figure 9.16: Comparison of simulated and recorded acceleration time histories for RPI9 case at accelerometer arrays B-W. - see Fig. 9.1 for location of sensors.

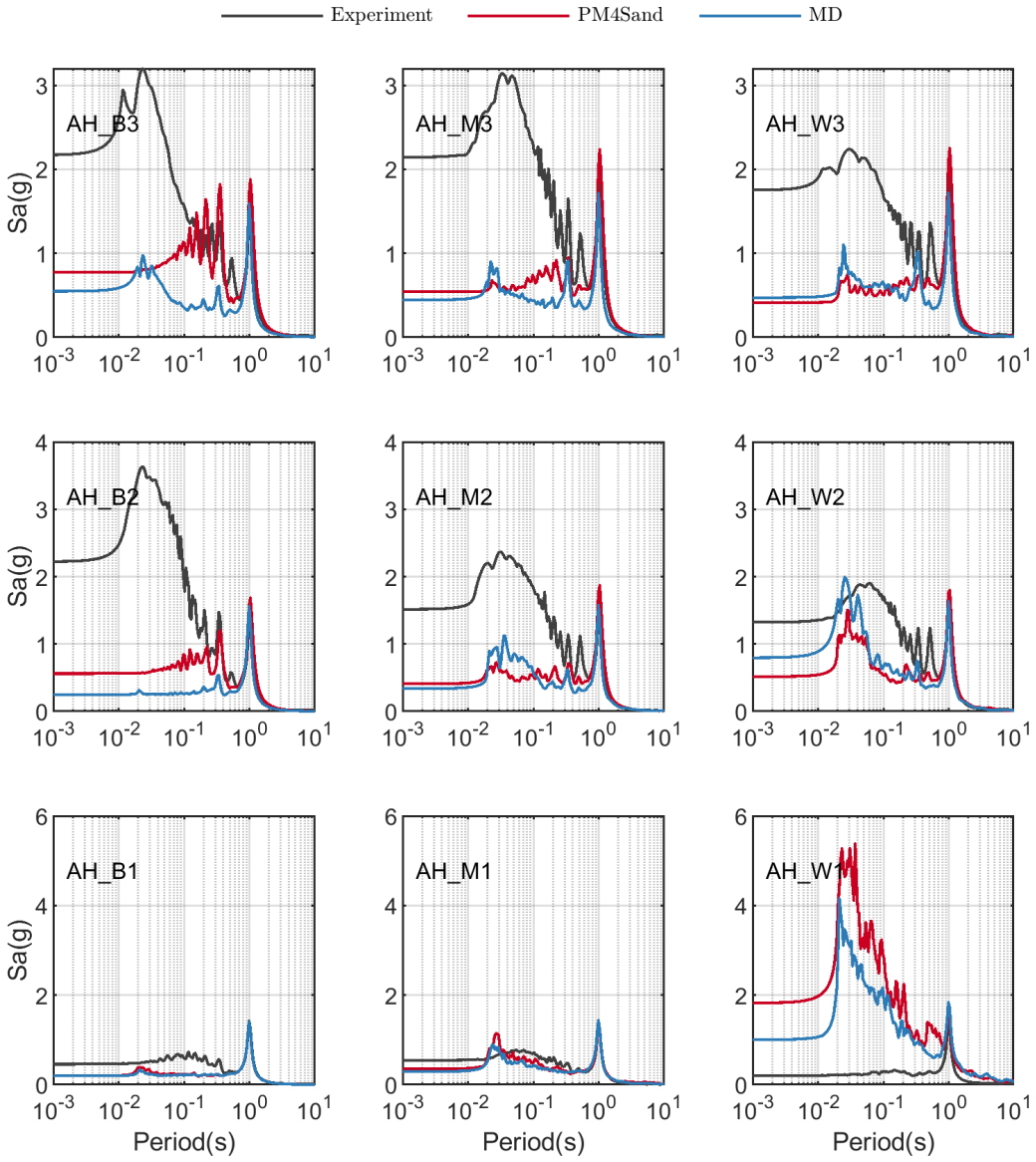

Figure 9.17: Comparison of simulated and recorded acceleration response spectra (5% damping) for RPI-9 case at accelerometer arrays B-W. - see Fig. 9.1 for location of sensors.

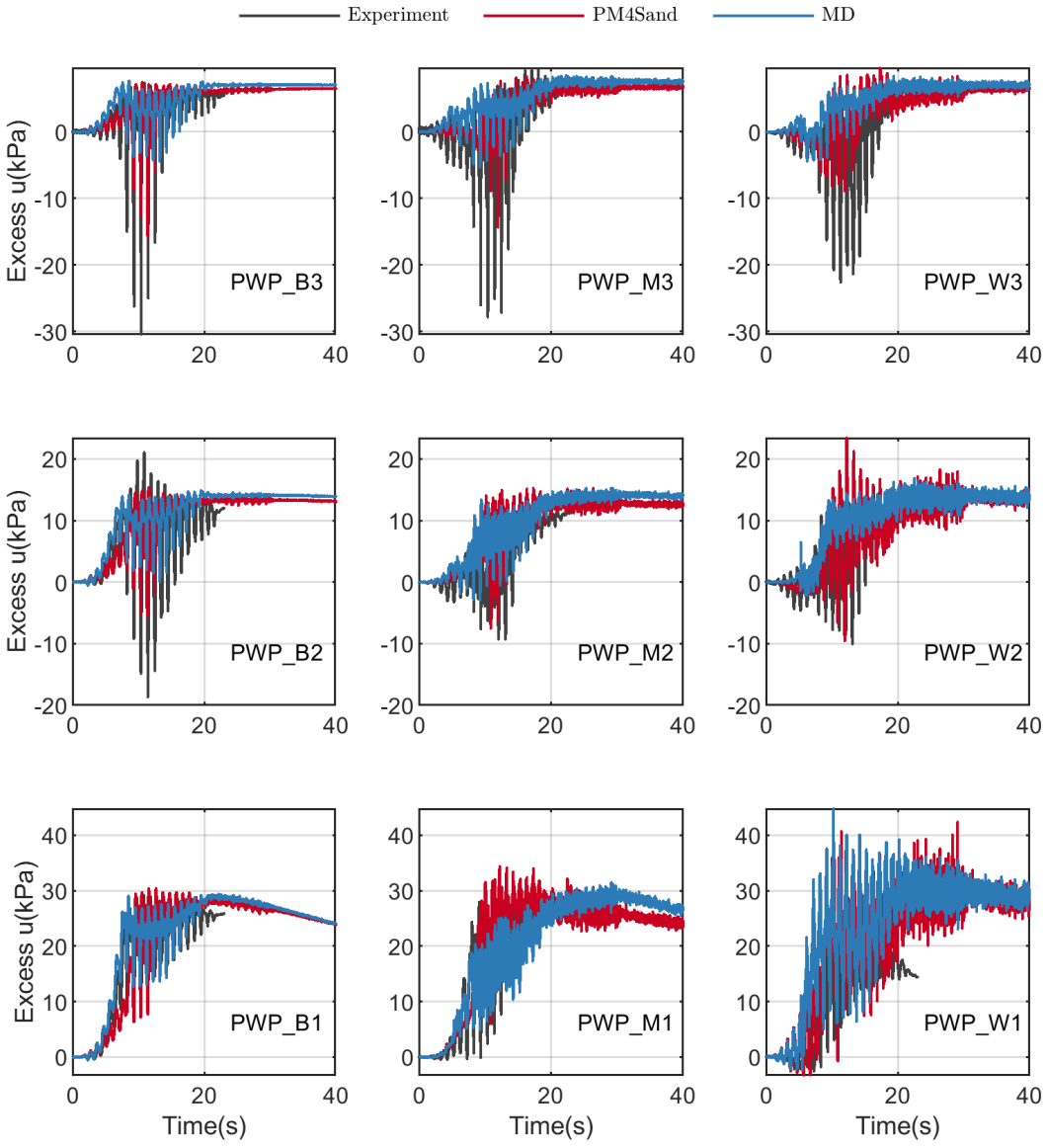

Figure 9.18: Comparison of evolution of pwp between centrifuge and simulation results of RPI-9 case at transducer arrays B-W. - see Fig. 9.1 for location of the sensors.

9.5 Summary

This chapter presents simulation results and comparison with experiments for the LEAP-RPI-2020 project. MD and PM4Sand were calibrated independently to simulate the behavior of Ottawa F-65 sand in accordance with LEAP-RPI-2020 project guidelines. The calibrated models were then used in a type-A element test predictions using non-uniform cyclic loading and type-B prediction of liquefiable soils supported by a sheet pile wall. A 2D model was developed in OpenSees with special consideration to modeling soil structure interaction and achieving reasonable initial stress states.

Besides using different material models, the same exact FEM model was used in all simulations. Type-B predictions were obtained and simulations compared to recorded data from centrifuge experiments from several facilities around the world. Type-B prediction results showed that although limitations existed in the numerical model, both constitutive models were able to predict the results from centrifuge experiments such as lateral displacements of sheet pile wall, acceleration response, and evolution of excess pore pressures.

Part III

POTENTIAL FOR LIQUEFACTION-INDUCED LATERAL SPREADING CONSIDERING SPATIAL VARIABILITY: TWO CASE STUDIES

The third part of this dissertation addresses two case studies using PM4Sand and PM4Silt to shed light on their application for analyzing lateral spreading induced by liquefaction. The first case focuses on a typical highway bridge embankment and investigates the efficiency of different intensity measures for estimating lateral displacement. The second case focuses on a real case study that showed zero-displacement lateral spreading during a recent earthquake event due, possibly, to interbedded sand and clay deposits.

A Poster was presented by the author and coworkers as a result of this part of the research:

- Chen, L. and Arduino, P. (2020a). "Application of PM4Sand and PM4Silt models to study effect of spatial variability in liquefiable soil." Poster presented at PEER Annual Meeting, Berkeley, CA

Chapter 10

EVALUATION OF IM EFFICIENCY FOR A TYPICAL HIGHWAY BRIDGE EMBANKMENT

10.1 Introduction

Estimation of the seismic performance of bridge embankments is an important application of advanced soil constitute models to evaluate the potential damage to the bridge systems caused by earthquake induced liquefaction. The Pacific Earthquake Engineering Research Center (PEER) has developed a probabilistic framework for Performance Based Earthquake Engineering (PBEE) to evaluate the risk associated with earthquake shaking at a particular site (Deierlein et al., 2003). The risk, expressed in terms of economic loss, fatalities or other measures, is computed as a function of ground shaking through a series of intermediate steps: (1) seismic hazard, (2) demand hazard, and (3) damage hazard. The seismic hazard is characterized in terms of an Intensity Measures, IM, which describe the level of ground shaking. The demand hazard is some form of response, characterized in terms of an Engineering Demand Parameter, EDP, at the site of interest. The damage hazard that results from this EDP contributes to the overall risk.

The study presented in this chapter revisits a typical highway bridge embankment investigated by Shin (2007) and Ledezma and Bray (2008) but using the newly implemented PM4Sand and PM4Silt constitutive models in OpenSees to study the efficiency of various IMs. For the PBEE analysis performed in this study, four different hazard levels of near-fault motions were considered and used in OpenSees simulations. Besides record-to-record uncertainty, spatial variability uncertainty was also considered. Using OpenSees simulations, the relative efficiency of several IMs were investigated with the hope of reducing demand parameter uncertainty.

10.2 Brief review of performance based earthquake engineering

Performance-based earthquake engineering (PBEE) refers to an emerging paradigm in which the "performance" of a system of interest can be quantified and predicted on a discrete or continuous basis. The notion of performance means different things to different stakeholders, and an important goal of PBEE is to allow performance to be expressed using terms and quantities that are of interest and meaning to a wide range of earthquake professionals and decision-makers.

The PBEE framework developed by PEER computes risk as a function of ground shaking through the use of several intermediate variables. The ground motion is characterized by an intensity measure, IM, which could be any one of a number of ground motion parameters (e.g., PGA, Arias intensity, Sa, magnitude corrected PGA, etc.). The effects of the IM on a system of interest are expressed in terms that make sense to engineers such as drifts, accelerations, ground failure, or other engineering demand parameters (EDP). The physical effects associated with the EDPs are expressed in terms of damage measures, or DM. Finally, the risk associated with the DM is expressed in a form that is useful to decision-makers by means of decision variables, DV (e.g., repair cost). The mean annual rate of exceedance of various DV levels, λ_{DV}, can be expressed in terms of the other variables as

$$\lambda_{DV} = \sum^{N_{DM}} \sum^{N_{EDP}} \sum^{N_{IM}} P[DV|DM] \cdot P[DM|EDP] \cdot P[EDP|IM] \cdot \Delta\lambda_{IM}\,, \tag{10.1}$$

where $P[a|b]$ describes the probability of exceeding a given b, and where N_{DM}, N_{EDP}, and N_{IM} are the number of increments of DM, EDP, and IM, respectively; with accuracy increasing with increasing number of increments.

For a liquefiable site, the geotechnical engineer's initial contribution to this process for evaluating liquefaction hazards comes primarily in the evaluation of $P[EDP|IM]$ (Kramer and Mayfield, 2007). It is important to choose an IM with the best possible ability to predict liquefaction: it should have high predictability to reduce uncertainty in IM hazard curve, and high efficiency and sufficiency to reduce uncertainty in IM-EDP fragility curves. The

response model must be able to predict the probability distribution of an EDP for a given IM value. Improving the accuracy in EDP|IM relationships can have a pronounced and beneficial effect on EDP hazard levels (Mayfield, 2007).

10.3 Application of PBEE to a typical highway bridge embankment

The foundation of a typical Caltrans highway bridge underlain by liquafiable soil susceptible to lateral ground movement was considered in this study to investigate efficiency of several popular IMs. The studied soil profile was adopted from Ledezma and Bray (2008) and previously investigated by Shin (2007) using *PressureDependMultiYield* (PDMY) and *PressureIndependMultiYield* (PIMY) constitutive models. Previous studies included a five-span bridge as superstructure to study soil-structure interaction. This study focused on the behavior of the liquefying soils but represented by the newly implemented PM4Sand and PM4Silt constitutive models. Therefore, the bridge was excluded from these analysis.

The soil below the left embankment (Fig. 10.1) consists of a medium stiff clay crust underlain by a thin, loose to medium dense sand, a layer of stiff clay, and a dense sand layer. The lower clay layer becomes thinner toward the center of the profile and does not extend to the right embankment (Fig. 10.2). The embankments are 8.5 m (28 ft) high and have a slope of 2:1. The groundwater is located at the bottom of the surface clay layer. The properties of the loose and medium sand layers across the profile were chosen by Ledezma and Bray (2008) such that liquefaction could be triggered under moderate ground shaking. Lateral ground displacement, especially in the vicinity of the right embankment, were expected to be induced.

10.3.1 Model building

All numerical simulations were performed using OpenSees. Fig. 10.3 illustrates the mesh developed for this study. The 2D FEM model consisted of 8587 elements and 8900 nodes. The model was extended 150 m (492 ft) outward from the slope crest to reduce possible boundary effects. The outer-most soil column elements were modified to generate a free-field

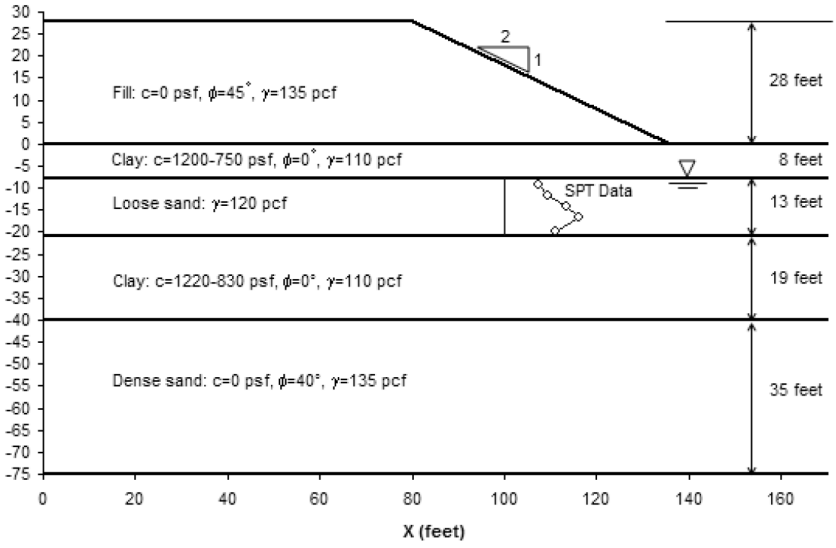

SPT Data

Depth (feet)	N1,60-CS
9.3	15
11.7	19
14.2	27
16.8	32
19.7	22

Figure 10.1: Soil profile and dimensions of left embankment (after Ledezma and Bray (2008)).

response by increasing their out-of-plane thicknesses and constraining the outer-most soil column element nodes at the same elevation to have the same horizontal movement using *equalDOF*. The stabilized single-point integration and mixed displacement-pressure (u-p) element (SSPquadUP), proposed by McGann et al. (McGann et al., 2015)) was used to capture the effective stress response. Pore pressures above the groundwater table were set to be zero during the analysis to ensure drainage and avoid generation of excess pore pressures in the dry layers. In the FEM model, the groundwater table, that was originally located at the bottom of the surface clay layer per prior studies, was slightly raised to be one element above the sand layer. This ensured the impedance of excess pore pressure dissipation due to surface clay layer's low hydraulic conductivity. The bottom boundary was fixed against vertical and horizontal movements and the acceleration time history was applied to the base of the model using the so called *UniformExcitation* loading pattern in OpenSees. This loading pattern applies uniform shaking to all the nodes with fixed horizontal DOF.

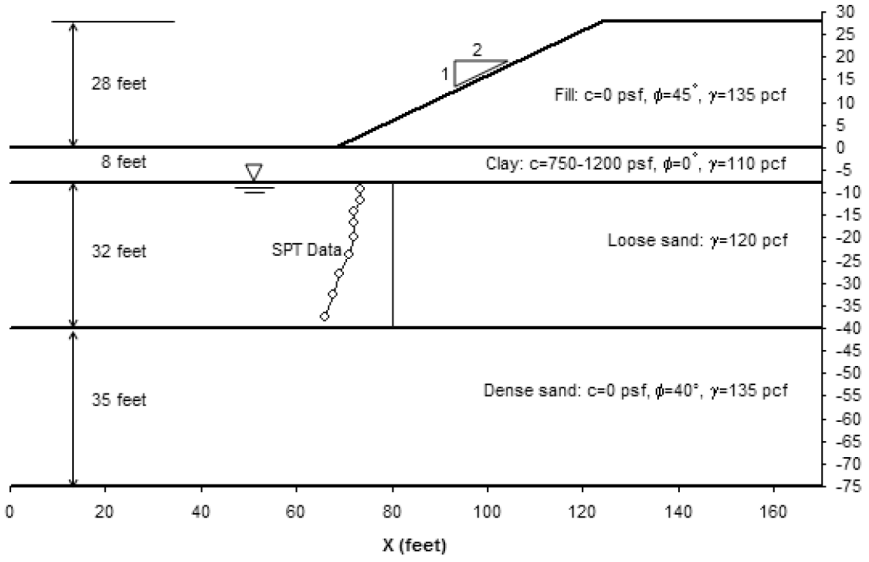

SPT Data

Depth (feet)	N1,60-CS
9.3	13
11.7	13
14.2	16
16.8	16
19.7	16
23.6	18
28.0	22
32.5	25
37.5	28

Figure 10.2: Soil profile and dimensions of right embankment (after Ledezma and Bray (2008)).

To apply gravity, the material was set to be linear elastic and elemental body forces were increased gradually to reduce numerical instabilities in the model. This elastic initial stress state was then used to calculate material parameters that are stress-dependent at each element. The attained material properties were subsequently used to regenerate the initial stress state. The material was then switched to *elasto-plastic* and a new equilibrium was achieved by allowing enough extra analysis steps to adjust constitutive model internal variables to any plastic behavior. A Poisson's ratio of 0.3, which yielded a lateral earth pressure coefficient $K_0 = 0.43$ under level ground plane-strain conditions, was assumed for PM4Sand and PM4Silt to generate the initial stress state.

The constant average acceleration Newmark method ($\beta = 0.25$, $\gamma = 0.5$) was used in order to resolve the integration in time. A frequency dependent Rayleigh damping was applied to account for the lack of small strain damping. The Rayleigh damping coefficients

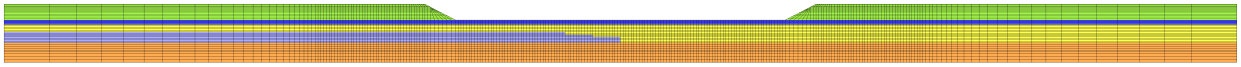

Figure 10.3: 2D FEM mesh created for the studied site. Different colors indicate major soil layers.

were chosen such that a 2% damping ratio was obtained at 0.2 Hz and 20 Hz.

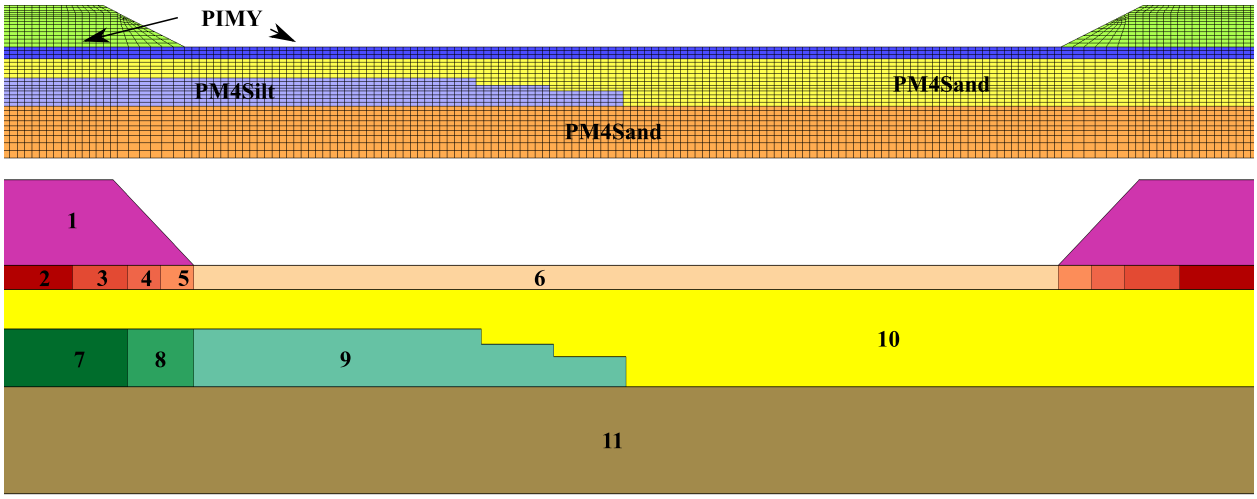

Figure 10.4: Layer definition for material assignment purposes.

Three constitutive models, PM4Sand, PM4Silt, and PIMY were used to represent the soil response. As shown in Fig. 10.4, PM4Sand was assigned to the base dense sand layer (zone 11) as well as the liquefiable layer (zone 10). PM4Silt was assigned to the clay layer (zones 7-9) under the left embankment to represent clay-like behavior. PIMY model was assigned to all other layers above the ground water table (zones 1-6).

The calibration process for PM4Sand and PM4Silt was relatively straightforward. The PM4Sand D_R was estimated using correlations to penetration resistance as recommended by

Idriss and Boulanger (2008),

$$D_R = \sqrt{\frac{(N_1)_{60}}{C_d}}\,, \tag{10.2}$$

where C_d was chosen to be 46. G_o was estimated using the correlation used in Boulanger and Ziotopoulou (2017),

$$G_o = 167\sqrt{(N_1)_{60} + 2.5}\,. \tag{10.3}$$

A target CRR was computed using the SPT-based correlation proposed by Idriss and Boulanger (2008),

$$CRR_{M=7.5,\sigma'_v=1} = \exp\left(\frac{(N_1)_{60cs}}{14.1} + \left(\frac{(N_1)_{60cs}}{126}\right)^2 - \left(\frac{(N_1)_{60cs}}{23.6}\right)^3 + \left(\frac{(N_1)_{60cs}}{25.4}\right)^4 - 2.8\right). \tag{10.4}$$

Then h_{po} was calculated using the correlation obtained from the parametric study presented in Chapter 3. For the base case model, SPT values were obtained by interpolating between the SPT profiles at left and right embankments.

The primary input parameters S_u and G_o of PM4Silt for the deep clay layer were computed from the undrained shear strength and shear modulus data adopted from Shin (2007). Then h_{po} was calibrated iteratively to match the target CRR (required to trigger peak shear strains of approximately 3% in 30 uniform cycles of undrained loading) computed by the procedure proposed by Boulanger and Idriss (2007),

$$CRR_{M=7.5} = 0.8 \cdot \frac{S_u}{\sigma'_{vc}}\,. \tag{10.5}$$

The cyclic strength curves obtained using the calibrated model parameters are presented in Fig. 10.5 and the resulting input material properties are summarized in Table 10.1.

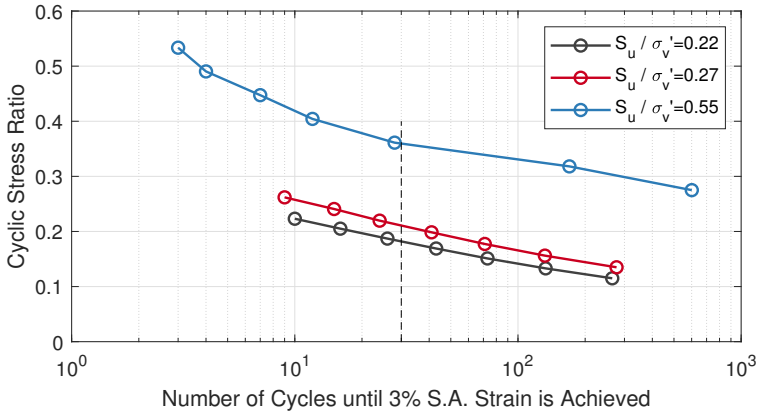

Figure 10.5: Number of cycles required to reach 3% SA shear strain in simulated undrained CSS tests with initial $K_0 = 0.5$ for three $S_{u,rat}$s.

Table 10.1: Calibrated PM4Silt parameters and their values

soil	layer number	$S_{u,rat}$	G_o	h_{po}	rho (Mg/m^3)
Deep Clay	7	0.23	546.7	20.0	1.67
	8	0.27	668.9	30.0	1.65
	9	0.55	841.5	150.0	1.52

The PIMY material parameters for clay were adopted from Shin (2007) and listed in Table 10.2. The hydraulic conductivity of the clay layer and silt layers was set to be 10^{-5} cm/s. The hydraulic conductivity of the sand layer was assumed to vary proportionally to the square of $(N_1)_{60cs}$ such that the permeability was 10^{-3} cm/s for a $(N_1)_{60cs} = 15$ and decreased to 4.4×10^{-4} cm/s for a $(N_1)_{60cs} = 10$ and increased to 1.8×10^{-3} cm/s for a $(N_1)_{60cs} = 20$ (adopted from Montgomery (2012)).

Table 10.2: Summary of PIMY material parameter values used for cohesive soil

soil	layer number	Su (kPa)	rho (Mg/m^3)	Gr (kPa)	Br (kPa)
Dry Layer	1	calculated using $\phi = 39°$	2.26	155000	279000
Surface Clay (PIMY)	2	57.5	1.662	108553	542763
	3	53.9	1.633	100026	500131
	4	46.7	1.577	82974	414868
	5	39.5	1.520	65921	329605
	6	35.9	1.488	57279	286394

10.3.2 Input motions and intensity measures

To apply the PEER PBEE framework, four sets of input motions corresponding to return periods of 15, 72, 475, and 2475 years (i.e., 97 %, 50 %, 10 %, and 2 % in 50 years) selected by Somerville and Collins (2002) were considered. The motions were originally selected for a PEER testbed study for a I-880 viaduct in Oakland, CA (Kunnath, 2006). Near-fault ground motions were used. Near-fault ground motions are different from ordinary ground motions since they are often dominated by strong, long period pulses, which result from rupture directivity effects. Details on the characteristics of the selected near-fault ground motions are described by Kunnath (2006) and Shin (2007). Characteristics of the 40 motions are summarized in Table 10.3. Since the scaled motions were based on rock outcrop conditions, the motions were corrected by Shin (2007) using the computer program *Proshake* to remove free surface effects prior to their use as rigid base input motions in OpenSees.

Uncertainty in estimated EDP vs. IM relationships is different for different EDPs and IMs. An efficient IM is one for which an EDP of interest is closely related; i.e. one for which a plot of EDP vs. IM exhibits little scatter. The use of efficient IMs leads to more accurate and less conservative performance estimation in PBEE evaluation procedures.

For a situation influenced by the occurrence of liquefaction, the estimated response should be closely related to an IM that reflects the liquefaction response. For example, Kramer and Mitchell (2006) have shown that excess pore pressure generation in potentially liquefiable soils is considerably more closely related to CAV_5 than to other intensity measures and therefore was considered in this study. Other common IMs also considered in this study were: peak ground acceleration (PGA), peak ground velocity (PGV), Arias intensity (I_a), and spectral acceleration at 0.5 and 1 second, respectively.

Recently , Sideras (2019) found a modified $PGA_m = PGA/MSF$ to be the most efficient predictor of pore pressure generation and the initiation of liquefaction. In here MSF is a Magnitude Scaling Factor developed to account for the effect of duration; quantified as the number of equivalent cycles at the reference stress level, N. Based on this definition MSF can be expressed as,

$$MSF = \frac{CSR_{M=m}}{CSR_{M=7.5}}\,, \tag{10.6}$$

where $CSR_{M=7.5}$ is the CSR corresponding to a magnitude 7.5 event, and $CSR_{M=m}$ is the CSR corresponding to a magnitude m event. Two procedures to compute MSF, proposed by Boulanger and Idriss (2014) and Liu et al. (2001), were considered in Sideras (2019) giving origin to two possible definitions of PGA_m, i.e., PGA_{mB} and PGA_{mL}. The MSF from Boulanger and Idriss (2014) is expressed as,

$$MSF = \frac{CSR_{M=m}}{CSR_{M=7.5}} = \frac{aN_{M=m}^{-b}}{aN_{M=7.5}^{-b}} = \big(\frac{N_{M=7.5}}{N_{M=m}}\big)^b\,, \tag{10.7}$$

where the exponent b varies with relative density of the soil. In the framework proposed by Boulanger and Idriss (2014), the maximum value that the MSF can obtain for a small magnitude earthquake (MSF_{max}) corresponds to a single strong acceleration pulse, that corresponds to 3/4 of a cycle at its peak stress. Then the equivalent number of uniform cycles at 65% of the peak stress would be (Idriss and Boulanger, 2008),

$$N_{min} = \big(\frac{1.0}{0.65}\big)^{\frac{1}{b}}\big(\frac{3}{4}\,cycle\big)\,, \tag{10.8}$$

then

$$MSF_{max} = \left(\frac{N_{M=7.5}}{N_{min}}\right)^{b}. \tag{10.9}$$

The $\mathrm{MSF_{max}}$ can also be expressed as a function of penetration resistance of soil,

$$MSF_{max} = 1.09 + \left(\frac{(N_1)_{60cs}}{31.5}\right)^{2} \leq 2.2\,. \tag{10.10}$$

When using $N_{M=7.5} = 15$ and $(N_1)_{60cs} = 15$ in Equs. 10.8 to 10.10, $b = 0.236$ can be obtained. This value is used in this study.

The MSF from Liu et al. (2001) is expressed as,

$$\ln MSF = a_1 + a_2 \ln N\,, \tag{10.11}$$

where a_1 and a_2 were determined based on regressions with field and laboratory liquefaction observations. Liu et al. (2001) recommended averaged weighting factors $a_1 = 1.3$ and $a_2 = -0.41$. A comparison between these two MSF functions is presented in Fig. 10.6. The weighting scheme used in this study to compute equivalent number of cycles from a_{max} is presented in Table 10.4.

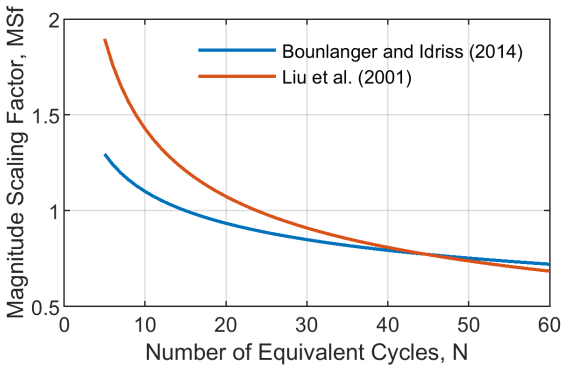

Figure 10.6: Comparison of MSF using procedures proposed by Liu et al. (2001) and Boulanger and Idriss (2004).

A complete list of all IMs considered in this study is summarized in Table 10.5. Fig. 10.7 shows the range of IMs for each hazard level considered in this study.

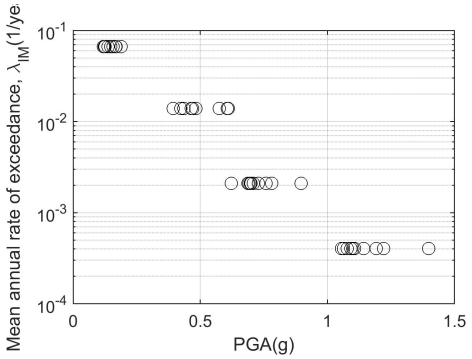

(a) IM = PGA

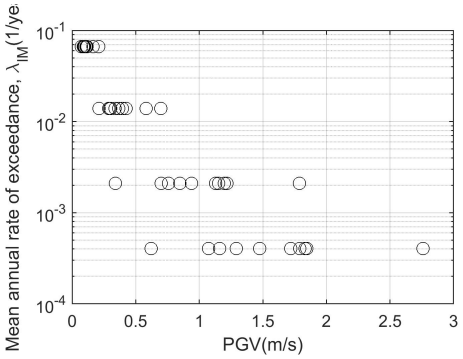

(b) IM = PGV

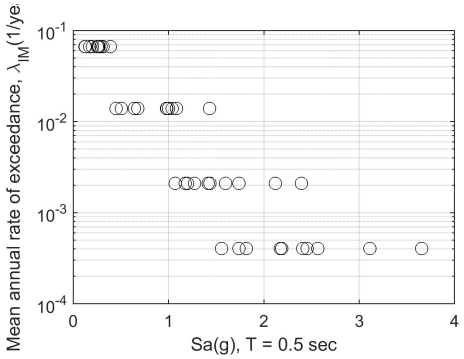

(c) IM = $Sa\,(T = 0.5\,s)$

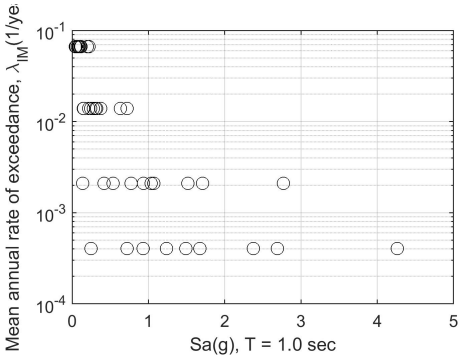

(d) IM = $Sa\,(T = 1.0\,s)$

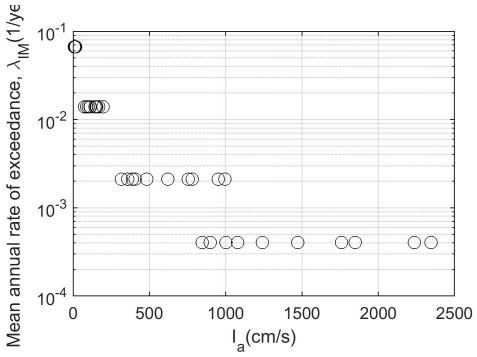

(e) IM = I_a

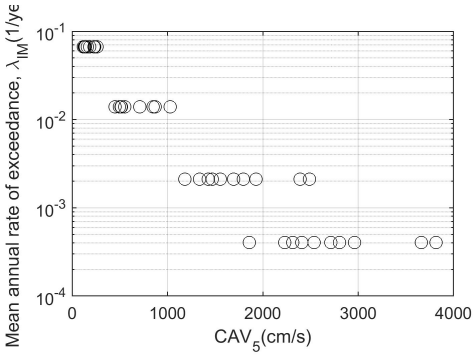

(f) IM = CAV_5

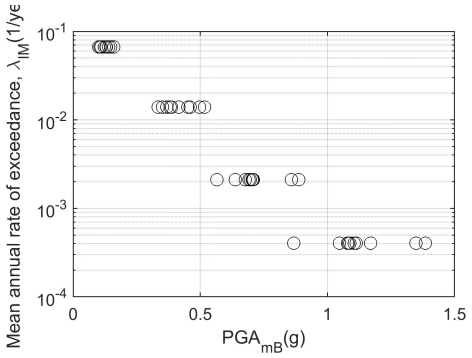

(g) IM = PGA_{mB}

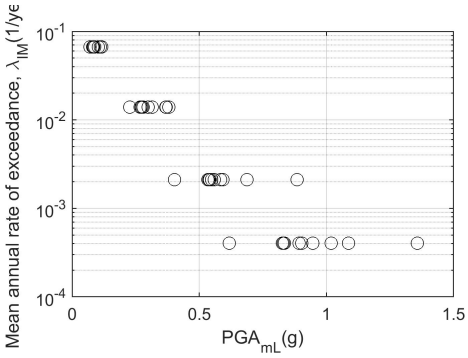

(h) IM = PGA_{mL}

Figure 10.7: IM harzard curves.

Table 10.3: Input motion characteristics (four hazards)

hazard	Record (station)	File	Earthquake	Magnitude	MSF	PGA_M	dt	PGA	duration
	Coyote Lake Dam abutment	A01	Coyote Lake	5.7	2.247	0.211	0.005	0.168	40.96
	Gilroy #6	A02	(6/ 8/1979)				0.005	0.167	40.96
return	Temblor	A03	Parkfield	6.0	1.931	0.182	0.010	0.157	40.96
period	Array #5	A04	(6/27/1966)				0.010	0.137	81.92
	Array #8	A05					0.010	0.119	40.96
15 yrs	Fagundes Ranch	A06	Livermore	5.5	2.497	0.235	0.005	0.189	20.48
	Morgan Territory Park	A07	(6/27/1980)				0.005	0.148	40.96
target	Coyote Lake Dam abutment	A08	Morgan Hill	6.2	1.753	0.165	0.005	0.122	40.96
PGA_M	Anderson Dam DS	A09	(4/24/1984)				0.005	0.126	40.96
= 0.094g	Halls Valley	A10					0.005	0.124	40.96
	Coyote Lake Dam abutment	B01	Coyote Lake	5.7	2.247	0.672	0.005	0.574	40.96
	Gilroy #6	B02	(6/ 8/1979)				0.005	0.610	40.96
return	Temblor	B03	Parkfield	6.0	1.931	0.578	0.010	0.469	40.96
period	Array #5	B04	(6/27/1966)				0.010	0.470	81.92
72 yrs	Array #8	B05					0.010	0.394	40.96
	Fagundes Ranch	B06	Livermore	5.5	2.497	0.747	0.005	0.606	20.48
target	Morgan Territory Park	B07	(6/27/1980)				0.005	0.483	40.96
PGA_M	Coyote Lake Dam abutment	B08	Morgan Hill	6.2	1.753	0.524	0.005	0.423	40.96
= 0.299g	Anderson Dam DS	B09	(4/24/1984)				0.005	0.435	40.96
	Halls Valley	B10					0.005	0.464	40.96
	Los Gatos Presentation Ctr	C01	Loma Prieta	7.0	1.226	0.799	0.005	0.687	40.96
	Saratoga Aloha Avenue	C02	(10/17/1989)				0.005	0.728	40.96
return	Corralitos	C03					0.005	0.709	40.96
period	Gavilan College	C04					0.005	0.699	40.96
	Gilroy Historic	C05					0.005	0.691	40.96
475 yrs	Lexington Dam abutment	C06					0.020	0.759	40.96
	Kobe JMA	C07	Kobe, Japan	6.9	1.279	0.834	0.020	0.781	81.92
			(1/17/1995)						
target	Kofu	C08	Tottori, Japan	6.6	1.458	0.951	0.010	0.622	40.96
PGA_M	Hino	C09	(10/6/2000)				0.005	0.897	81.92
= 0.652g	Erzincan	C10	Erzincan	6.7	1.395	0.909	0.005	0.696	40.96
			(3/13/1992)						
	Los Gatos Presentation Ctr	D01	Loma Prieta	7.0	1.226	1.228	0.005	1.101	40.96
	Saratoga Aloha Avenue	D02	(10/17/1989)				0.005	1.141	40.96
return	Corralitos	D03					0.005	1.078	40.96
period	Gavilan College	D04					0.005	1.055	40.96
	Gilroy Historic	D05					0.005	1.063	40.96
2475 yrs	Lexington Dam abutment	D06					0.020	1.191	40.96
	Kobe JMA	D07	Kobe, Japan	6.9	1.279	1.282	0.020	1.221	81.92
			(1/17/1995)						
target	Kofu	D08	Tottori, Japan	6.6	1.458	1.461	0.010	1.092	40.96
PGA_M	Hino	D09	(10/6/2000)				0.005	1.399	81.92
= 1.002g	Erzincan	D10	Erzincan,Turkey	6.7	1.395	1.398	0.005	1.107	40.96
			(3/13/1992)						

Table 10.4: Equivalent number of cycles from Seed et al. (1975) (after Greenfield (2017))

Cyclic Amplitude a/a_{max}	Number of Equivalent Cycles	Cyclic Amplitude a/a_{max}	Number of Equivalent Cycles
1	3	0.6	0.7
0.95	2.7	0.55	0.4
0.9	2.4	0.5	0.2
0.85	2.05	0.45	0.1
0.8	1.7	0.4	0.04
0.75	1.4	0.35	0.02
0.7	1.2	0.3	0
0.65	1		

Table 10.5: Intensity Measures

IM name	Definition	Units
Peak ground acceleration	$PGA = \max\|a(t)\|$	g
Peak ground velocity	$PGV = \max\|v(t)\|$	m/s
Arias intensity	$I_a = \frac{\pi}{2g} \int_0^{T_d} [a(t)]^2 \, dt$	cm/s
Cumulative absolute velocity	$CAV_5 = \int_0^{T_d} \langle\chi\rangle \, \|a(t)\| \, dt$ where T_d = earthquake duration $\langle\chi\rangle = 0$, if $\|a(t)\| < 5$ cm/s^2 $\langle\chi\rangle = 1$, if $\|a(t)\| \geq 5$ cm/s^2	cm/s
Spectral acceleration	$Sa(T_1) = Sa(T_1)$	g
Evolutionary PGA_{mL}	$PGA_m(t) = PGA(t)/MSF(t)$ where $PGA(t)$ is the absolute peak acceleration of the acceleration time history up to time t, and $MSF(t)$ is an evolutionary magnitude scaling factor, as defined by Liu et al. (2001) in Equ.10.11 and the number of cycles is evaluated using the scaling factors listed in Table 10.4.	g
Evolutionary PGA_{mB}	$PGA_m(t) = PGA(t)/MSF_L(t)$ where $MSF_L(t)$ is computed using Equ. 10.7 with $N_{ref} = 15$ and b = 0.236.	g

10.3.3 EDPs

In this study, the permanent lateral displacement at toe of the left and right embankments, H_L and H_R as shown in Fig. 10.8, were identified as the EDPs of interest .

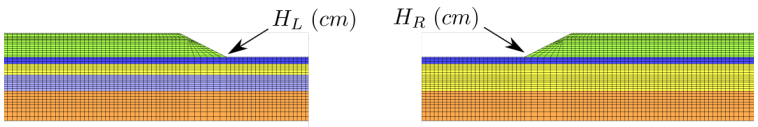

Figure 10.8: Horizontal displacements at the toe of embankments were taken as EDPs.

10.3.4 Modeling spatial variability uncertainty of soil

Spatial variability can also alter the EDP-IM relationship. To investigate the effect of spatial variability, Gaussian stochastic random fields were generated for the liquefiable soil layer (zone 10 only as shown in Fig. 10.4) by randomizing the assigned soil strength parameter over the soil layers with a certain spatial probability density.

Physical properties of soils vary from place to place within a soil deposit due to varying geologic formation and loading histories such as sedimentation, erosion, transportation, and weathering processes. This spatial variability in the soil properties cannot be simply described by a mean and variance since the estimation of the two statistic values does not account for the spatial variation of the soil property data in the soil profile. Spatial variability is often modeled using two separated components: a known deterministic trend and a residual variability about the trend. These components are illustrated in Fig. 10.9.

This simplified spatial variability proposed by Phoon and Kulhawy (1999) can be expressed as,

$$\xi(z) = t(z) \; + \; w(z)\,, \tag{10.12}$$

where $\xi(z)$ = soil property at location z, $t(z)$ = deterministic trend at z, and $w(z)$ = residual variation. The trend is a smooth deterministic function that can be obtained from a

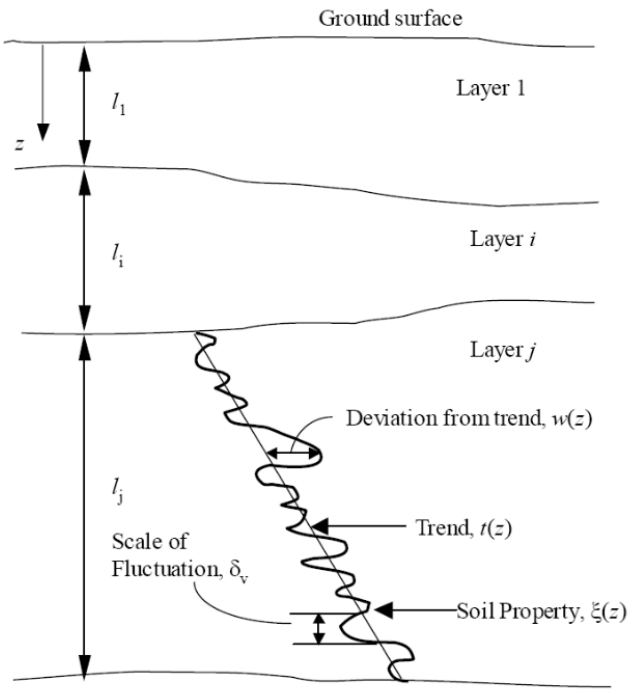

Figure 10.9: Inherent soil variability (after Phoon and Kulhawy (1999)).

regression analysis of measured data. The residuals are characterized statistically as random variables, usually with zero mean and non-zero variance. The pattern of the residuals depends on the local spatial variability of a property. The residual about a trend does not change erratically in a probabilistically independent way. Rather, similar property values (positive or negative residuals around a trend) occur together in adjacent locations characterizing the scale of fluctuation (or wave length of a residual along the trend) as shown in Fig. 10.9.

Shin (2007) introduced a procedure for generating stochastic random field based on the method outlined in Yamazaki and Shinozuka (1988) considering uncertainties in soil properties. The spatial variability within the SPT blow count was accounted in this study. The trend field ($t(z)$) represents the deterministic mean field interpolated using the SPT profiles at left and right embankments. To obtain the residual field ($w(z)$), a Gaussian random field was generated using the algorithm proposed by Yamazaki and Shinozuka (1988). A lognor-

mal distribution with coefficient of variation $COV = 0.3$ was assigned for SPT. Currently, the method for generating a random field mesh adopted from Yamazaki and Shinozuka (1988) can only assign an equal value of scale of fluctuation in both the vertical and horizontal directions. In order to simulate the anisotropic characteristics in SPT resistance, the size of the mesh was scaled in the vertical direction when sampling random numbers to fit the correct scale of fluctuation. The scale of fluctuation in the horizontal direction was set to be 10 times larger than in the vertical direction.

The generated Gaussian field could not be directly used in the simulation since values in the field were calculated for uniform incremental positions in the horizontal and vertical direction, whereas the soil mesh in the OpenSees model did not have uniform element size. Therefore, the values obtained using Yamazaki and Shinozuka (1988)'s method were interpolated according to the soil element center locations. Examples of generated stochastic fields are presented in Fig. 10.10.

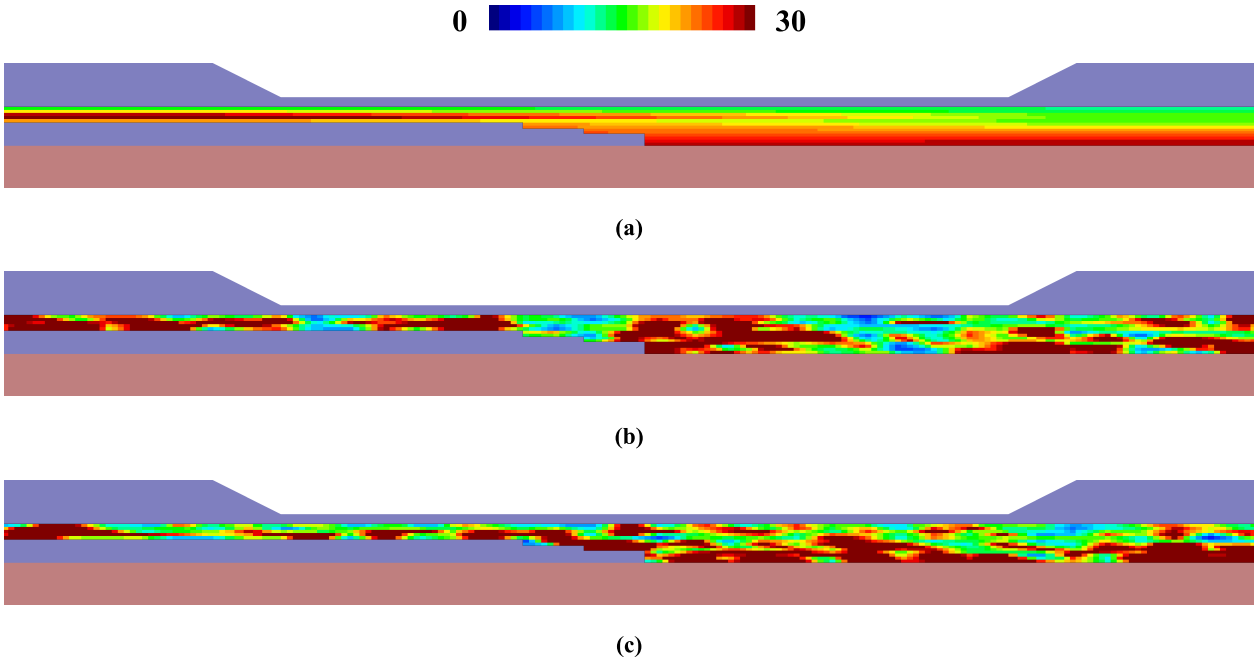

Figure 10.10: Stochastic $(N_1)_{60cs}$ field in loose sand layer: (a) case 0 or deterministic mean field, (b) realization 1, (c) realization 2.

10.4 Record-to-record uncertainty

Results obtained from the deterministic case (realization 0) are presented in this section to investigate record-to-record uncertainty. Significant lateral spreading was observed with most input motions except the lowest hazard level. For example, permanent horizontal displacement contours from four motions belonging to each hazard level, namely A01, B01, C01, and D01, are presented in Fig. 10.11. As expected, results obtained from A01 case showed the smallest permanent displacements while the D01 case showed the largest. Transient absolute maximum horizontal displacements were also recorded during shaking and their contours are presented in Fig. 10.12 for the same four motions. It should be noted that during wave propagation, each node could reach their maximum horizontal displacement at different times. It was shown the maximum horizontal displacement obtained from D01 case was significantly larger than the C01 case, although similar magnitudes of permanent horizontal displacements were observed between these two cases as shown in Fig. 10.11.

Using simulation results for all four hazard levels, several EDP-IM relationships and uncertainty parameters were obtained for each IM. From the EDP-IM relationships, linear regressions in log-log space were obtained to estimate record-to-record uncertainties assuming a constant lognormal probability distribution of EDP conditional upon IM.

Based on these results, efficient IMs were identified for different EDPs. For example, Fig. 10.13 shows permanent horizontal displacement in the left abutment slope as a function of the eight different IMs. This figure also shows the standard deviation of $\ln EDP$ residual and median relationship with median $\pm$ standard deviation lines. Fig. 10.14 shows the same information for permanent horizontal displacement in the right abutment. For the right abutment horizontal displacement, CAV_5 appeared to be the most efficient IM (smallest $\sigma_{\ln EDP}$, meaning least dispersion in EDP-IM) among the IMs considered in Table 10.5. For the left abutment horizontal displacement, all the IMs showed large standard derivation while PGA_{mB} and CAV_5 showed slightly better efficiency. Fig. 10.15 compares the efficiency of IMs for the two EDPs. These results showed that the most efficient IMs depends on

the EDP being considered and soil conditions. In this deterministic case, the sand layer under left embankment had higher blow counts (Fig. 10.10a) and liquefaction was unlikely to be triggered. And the relatively weaker underlain clay layer showed cyclic softening and dissipated significant amount of energy. All the IMs showed less efficiency in predicting the deformation caused by the softened clay layer. On the other hand, evolutionary IMs showed better efficiency in predicting deformation in the right embankment, where lower blow counts and larger thickness warranted liquefaction in the sand layer.

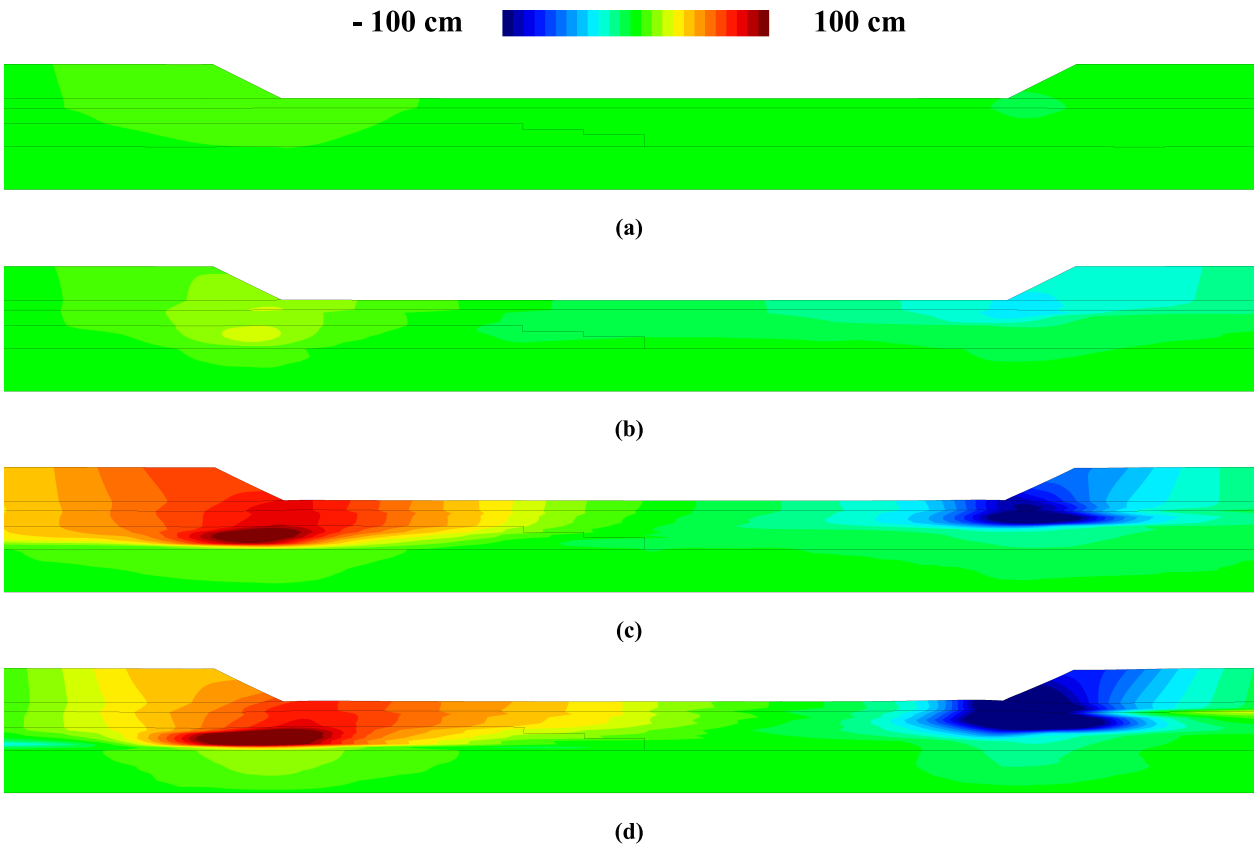

Figure 10.11: Contours of final horizontal displacement obtained using four motions: (a) A01, (b) B01, (c) C01, and (d) D01.

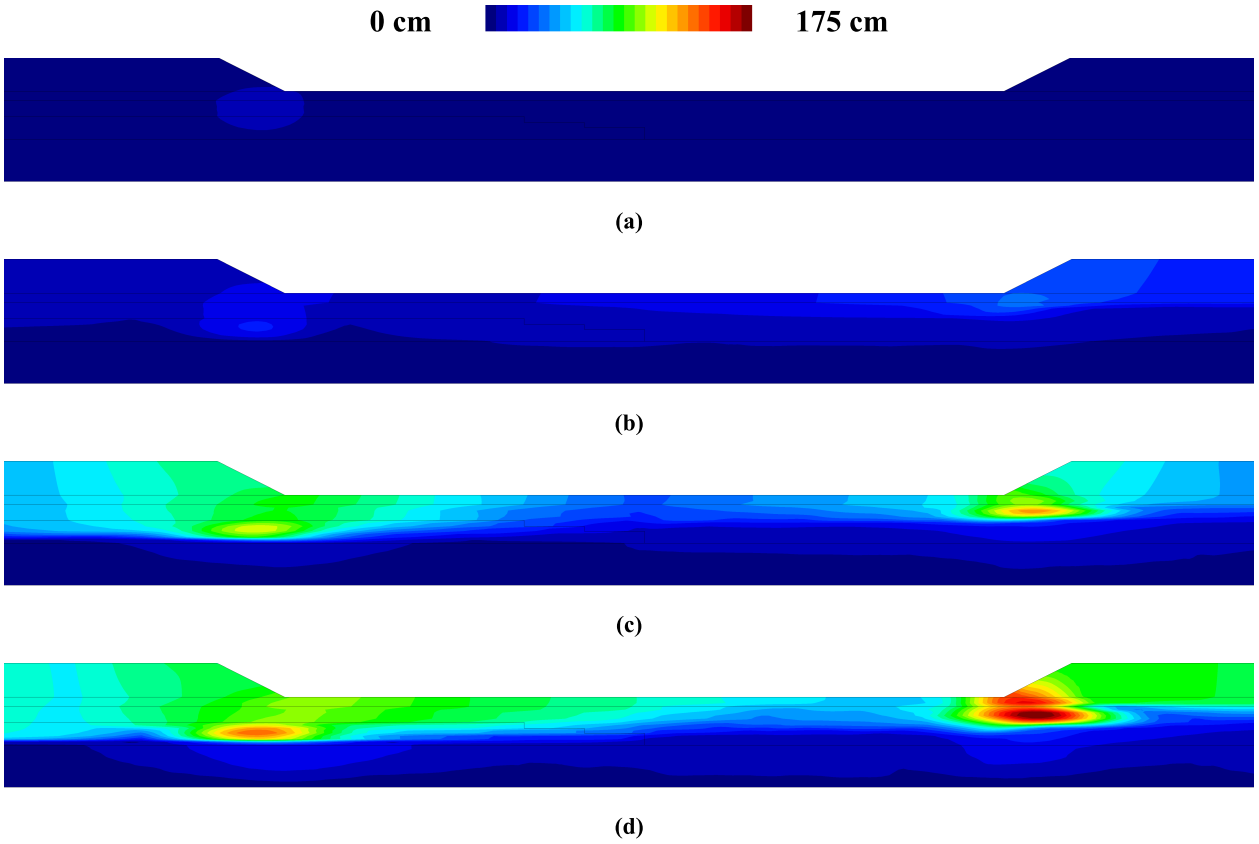

Figure 10.12: Contours of max. horizontal displacement during shaking obtained using four motions: (a) A01, (b) B01, (c) C01, and (d) D01.

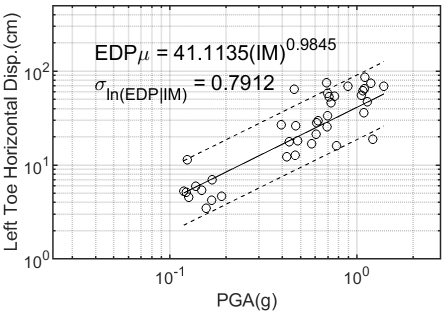

(a) IM = PGA

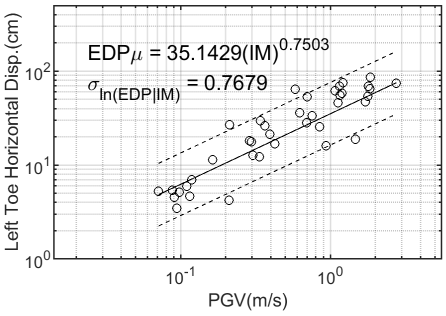

(b) IM = PGV

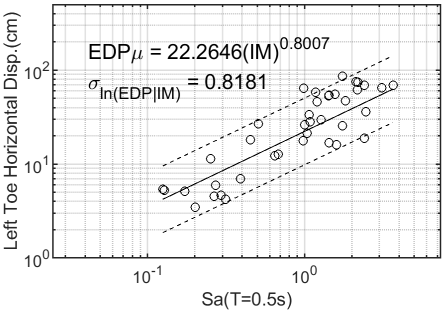

(c) IM = S_a ($T = 1.0s$)

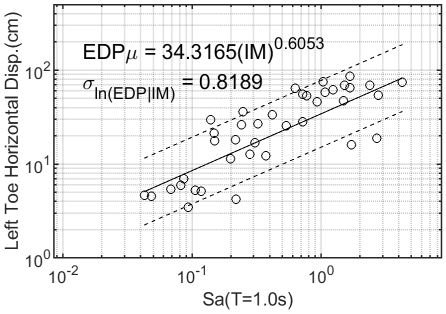

(d) IM = S_a ($T = 1.0s$)

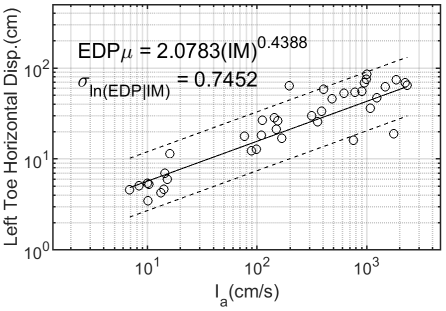

(e) IM = I_a

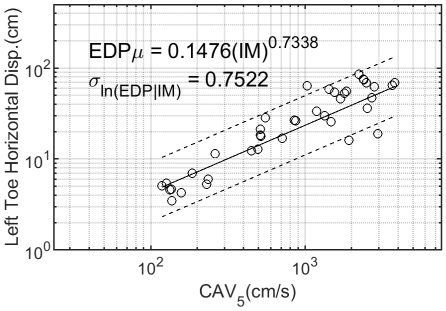

(f) IM = CAV_5

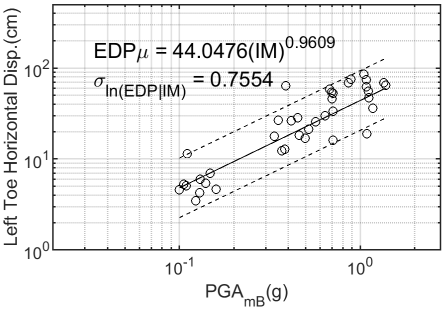

(g) IM = PGA_{mB}

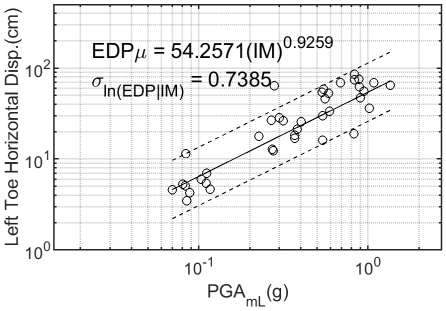

(h) IM = PGA_{mL}

Figure 10.13: EDP-IM relationships for left toe horizontal displacement.

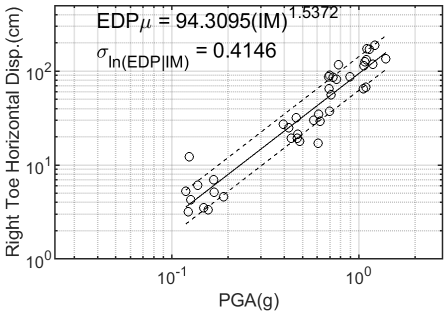

(a) IM = PGA

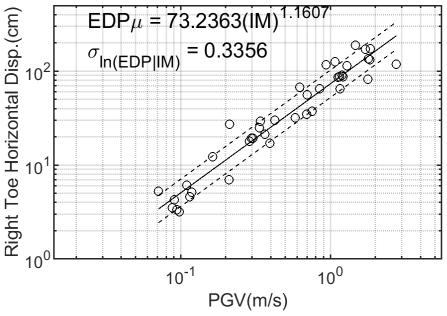

(b) IM = PGV

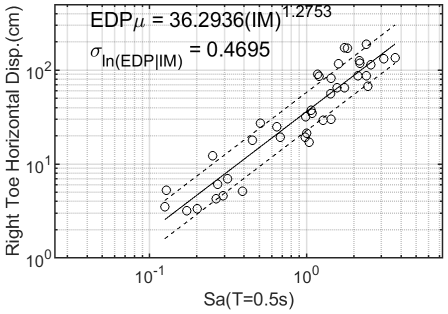

(c) IM = S_a ($T = 1.0s$)

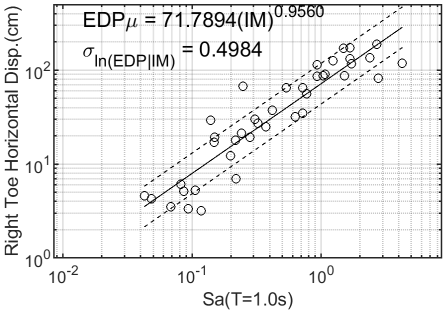

(d) IM = S_a ($T = 1.0s$)

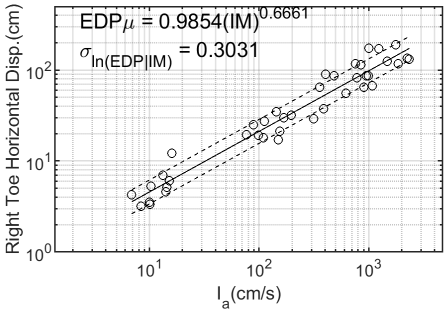

(e) IM = I_a

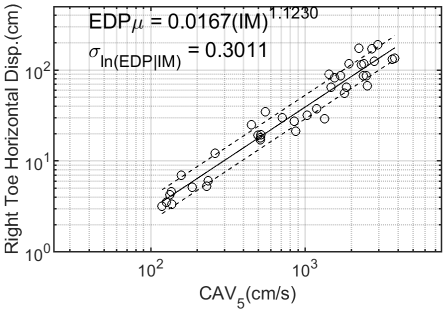

(f) IM = CAV_5

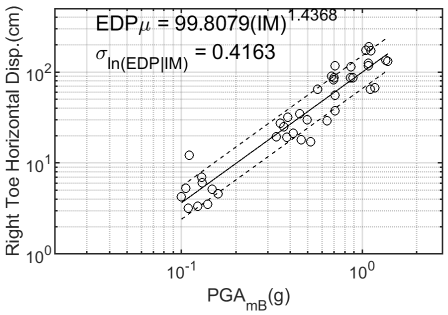

(g) IM = PGA_{mB}

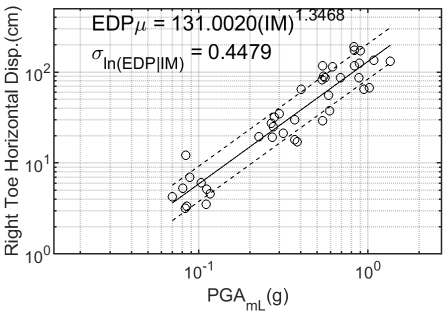

(h) IM = PGA_{mL}

Figure 10.14: EDP-IM relationships for right toe horizontal displacement.

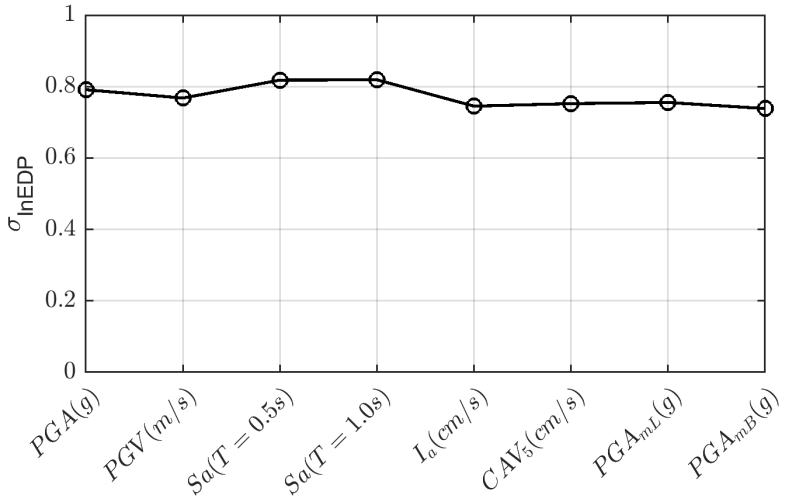

(a) $EDP = H_L$.

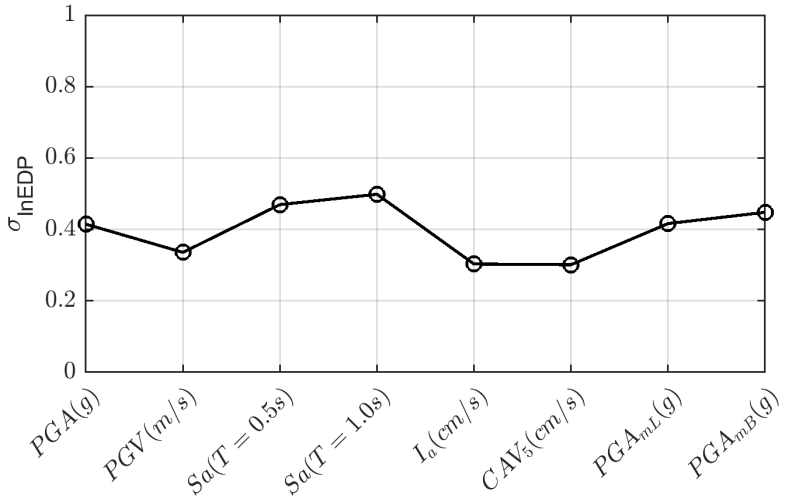

(b) $EDP = H_R$.

Figure 10.15: IM efficiency for evaluating left and right toe horizontal displacement, respectively.

10.5 Realization-to-realization uncertainty

Uncertainty due to spatial variability was investigated by simulating 25 stochastic fields with the considered 40 motions (1,000 cases total). Fig. 10.16 illustrates contours of final horizontal displacement obtained from realizations 0 to 2 using motion C01 showing large variability in displacement magnitudes. Figs. 10.17 and 10.18 illustrate contours of maximum horizontal displacement and maximum pore pressure ratio, respectively, obtained for the same cases. The pore pressure ratio was calculated using change in effective vertical stresses and some elements above the groundwater table showed non-zero values due to rotation of stress states. The results reflected the distribution of loose sand lenses in the generated stochastic $(N_1)_{60cs}$ fields as shown in Fig. 10.10b and c. For example, in realization 2, the sand layer under the left embankment had generally lower blow counts comparing to the deterministic case and realization 1. Extensive liquefaction was observed under the left embankment and resulted in larger permanent and transient maximum horizontal displacements.

Using the simulation results for all the 26 cases, one deterministic case and 25 stochastic cases, a series of EDP-IM relationships and uncertainty parameters were obtained for different IMs. Fig. 10.19 compares the efficiency of IMs for the two EDPs for all the cases. Large variability was shown for H_L for all realizations. Liquefaction triggering under the left embankment, where the sand layer was thinner with higher mean $(N_1)_{60cs}$ values, was closely related to the existence and distribution of loose sand lenses that varied realization to realization. Therefore, large uncertainty was shown from realization to realization. All the evolutionary IMs, i.e., CAV_5, I_a and PGA_m showed very similar efficiency for predicting H_L. The efficiency of PGA_m was improved comparing to the deterministic case (Fig. 10.15), reflecting their ability in predicting liquefaction triggering. On the other hand, the H_R and IMs relationships presented less uncertainty due to spatial variability. This was likely due to the soil condition under the right embankment, where the liquefiable layer was thicker and had smaller mean $(N_1)_{60cs}$ values, warranting liquefaction triggering in almost all realizations. Overall, CAV_5 appeared to be the most efficient IM in predicting liquefaction induced

lateral displacements in the studied case.

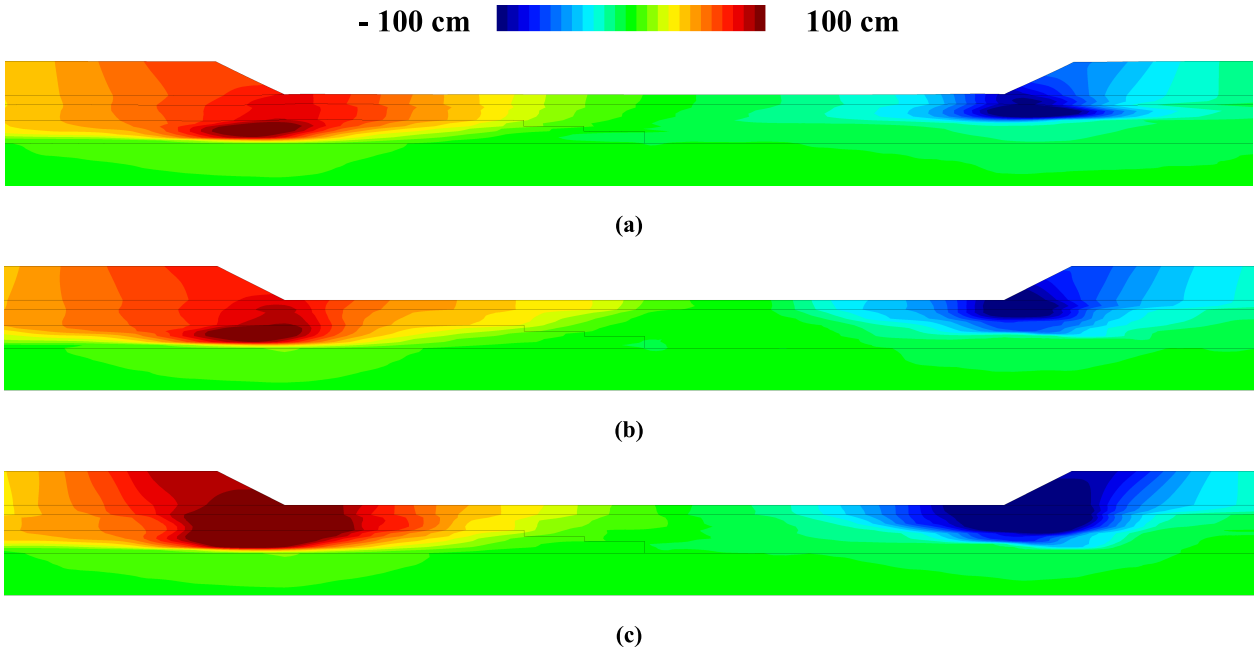

Figure 10.16: Contours of final horizontal displacement obtained using motion C01 from three realizations: (a) realization 0, (b) realization 1, (c) realization 2. See Fig. 10.10 for stochastic $(N_1)_{60cs}$ field.

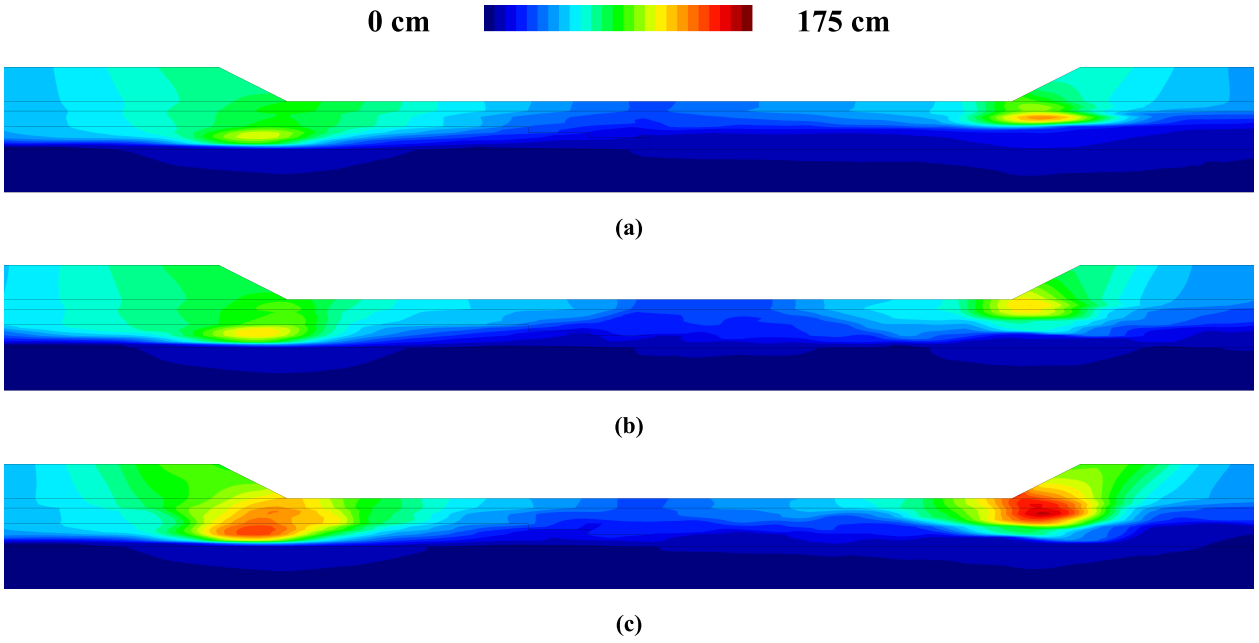

Figure 10.17: Contours of max. horizontal displacement during shaking obtained using motion C01 from three realizations: (a) realization 0, (b) realization 1, (c) realization 2. See Fig. 10.10 for stochastic $(N_1)_{60cs}$ field.

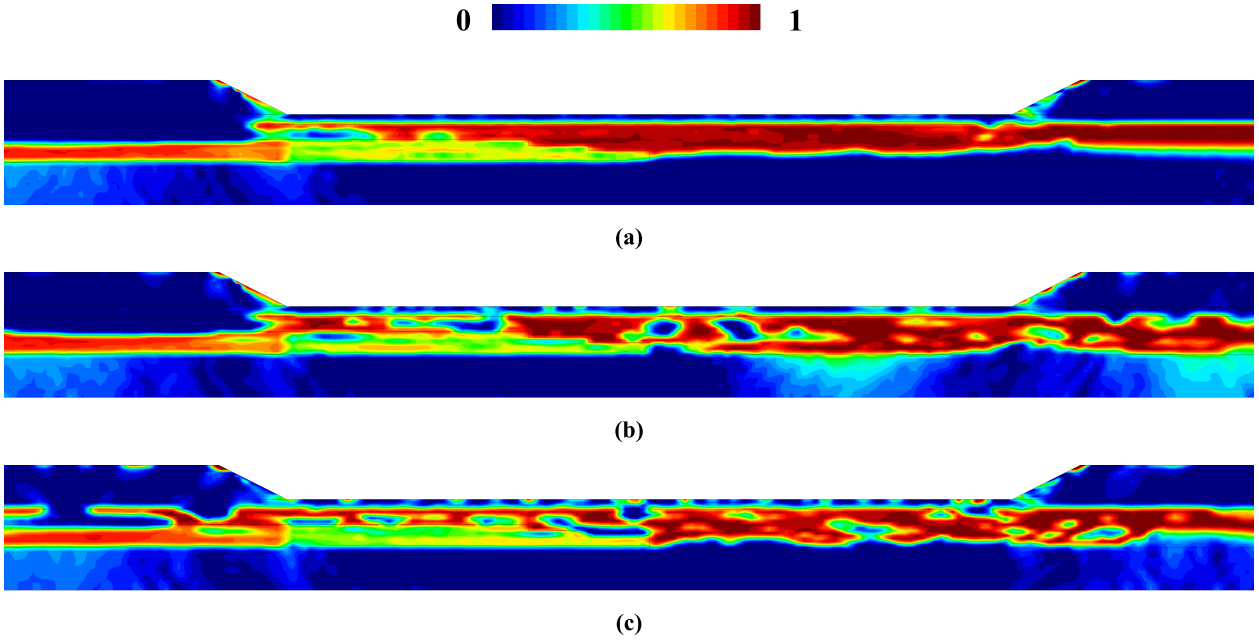

Figure 10.18: Contours of pore pressure ratio, Ru, defined as change in σ'_v and obtained using motion C01 from three realizations: (a) realization 0, (b) realization 1, (c) realization 2. See Fig. 10.10 for stochastic $(N_1)_{60cs}$ field.

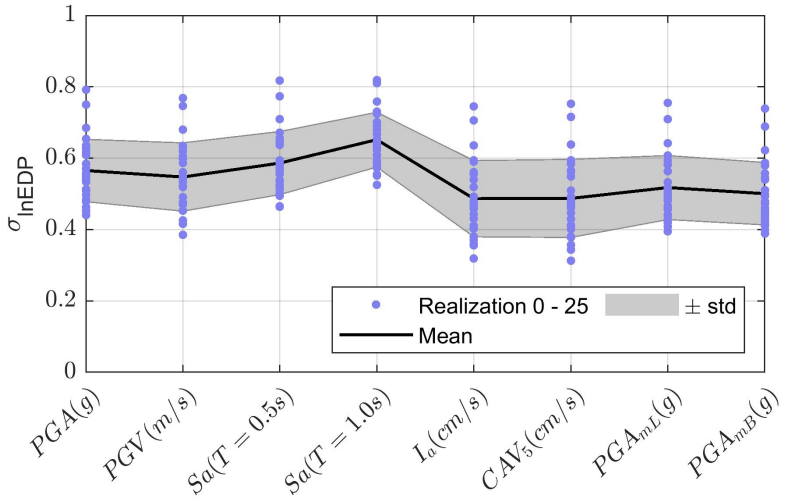

(a) $EDP = H_L$.

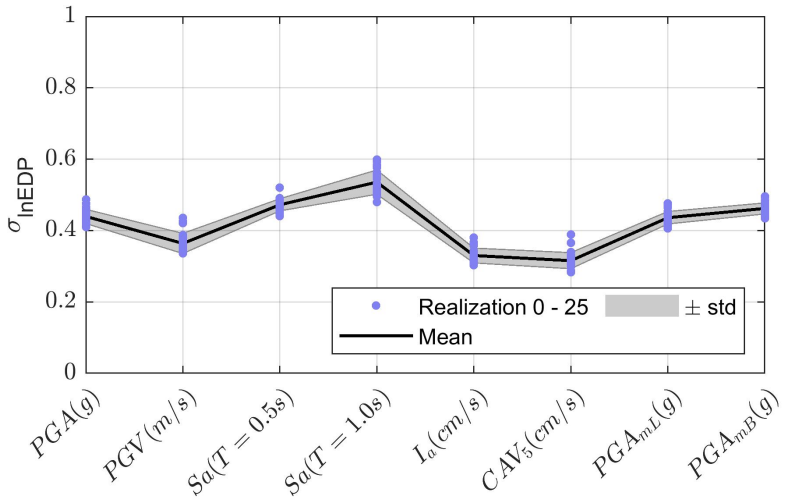

(b) $EDP = H_R$.

Figure 10.19: IM Efficiency for evaluating left and right toe horizontal displacement, respectively, from all 26 cases.

10.6 Summary

Using newly implemented PM4Sand and PM4Silt models in OpenSees, the foundation of a typical highway bridge underlain by liquefiable soil susceptible to lateral ground movement was investigated to study efficiency of several IMs. Following the PEER Performance Based Earthquake Engineering (PBEE) framework, a total of 40 earthquake motions representing four different hazard levels were applied to study record-to-record uncertainty. Spatial variability uncertainty was also investigated using generalized stochastic fields.

Soil behavior, including lateral soil displacement and soil liquefaction, were investigated for different motions. At most hazard levels except the lowest hazard level, most of the loose sand layer was liquefied, which resulted in lateral spreading beneath the embankments. EDP-IM relationships were obtained and efficiency of IMs was examined. The results showed that the most efficient IMs depends on the EDP being considered and soil conditions. Overall, CAV_5 appeared to be the most efficient IM in predicting liquefaction induced lateral displacements in the studied case.

Chapter 11

LIQUEFACTION EVALUATION OF INTERBEDDED SOIL DEPOSIT: A CASE STUDY USING PM4SAND AND PM4SILT

11.1 Introduction

In-situ tests have been widely used in liquefaction potential assessment and liquefaction induced ground deformation prediction (Idriss and Boulanger, 2008; Youd et al., 2002). However, case history studies have shown that empirical regression models tend to over-estimate earthquake induced liquefaction deformation in interbedded deposits of sands, silts, and clays. Youd et al. studied three sites in Turkey, where potential lateral spreading was predicted using current predictive procedure but exhibited negligible displacements during the August 17, 1999 Kocaeli earthquake (M_w = 7.5). Among them, the Çark Canal site, located at Adapazari, Turkey, showed no surface evidence of ground displacement near the canal, despite multiple linear regression procedures predicted between 0.7 m and 2.6 m of lateral displacements (Youd et al., 2009). The over-estimation was thought to be related to interbedded deposits of sand, silt, and clay encountered at this site. In an evaluation of the Liquefaction Potential Index (LPI) for assessing liquefaction hazard in Christchurch, New Zealand, during the 2010-2011 Canterbury earthquake sequence, Maurer et al. (2014) also identified a relation between overprediction of liquefaction severity and soils with inferred elevated silt or clay fractions. The effect of plastic soils limiting propagation of liquefied soil to the ground surface was identified as a likely contributor to this trend.

This and similar case histories have attracted the attention from researchers. Several studies have tried to provide insight into the possible factors contributing to the overestimation of ground deformations in interbedded deposits. Among them, Boulanger et al. (2019) performed nonlinear effective stress analyses using FLAC to study the Çark Canal

site. The sand-like and clay-like portions of the interbedded stratum were modeled using PM4Sand and PM4Silt, respectively. A transition probability approach was used to generate stochastic realizations for the interbedded layer. Binomial classification of sand-like and clay-like soils was used and uniform material parameters based on CPT data were assigned to each category. Soil behavior was not transitioned gradually between these two categories, i.e., soil elements in two adjacent zones could have distinctly different behaviors. Hydraulic conductivity was assigned uniformly and a single input motion (east–west Kocaeli outcrop recording nearby Sakarya station) was used in all simulations.

The study presented in this thesis examines the same case study using a simple workflow for model selection and calibration, aiming to represent the gradual transition of soil properties within interbedded layer and shed light on the application of PM4Sand and PM4Silt models. This workflow was inspired by the work of Boulanger and Idriss (2007) and Bray and Sancio (2006). The effect of spatial variability within the interbedded layer based on variation of fines content (FC) and plasticity index (PI) was examined. Uncertainty in input motions and sensitivity to motion polarity, correlation length, undrained shear strength, and hydraulic conductivity was also investigated.

11.2 Site condition

The Çark Canal site (referred as the site hereafter) is located over recent Holocene alluvial sediments created by the meandering and frequently flooding of the Sakarya and Çark rivers. Youd et al. (2009) reported the canal as 6.5 m deep with 1H:1V side slopes while Munter et al. (2017) analyzed several photographs of the site taken during reconnaissance that led to an updated geometry with a channel depth of 4.6 m, water depth of 1 m, and side slopes of 1.8H:1V. The latter geometry was adopted in this study and Fig. 11.1 shows a simplified cross section.

Fig. 11.2 illustrates the location of detailed in-situ tests performed by Youd et al. (2000) to characterize the soils. These tests included five CPT soundings (Fig. 11.3), two SPT borings (Figs. 11.4 and 11.5), and Spectral Analysis of Surface Waves (SASW) down to 15

m (Fig. 11.3).

At the selected locations the surficial fill had a thickness of 1 m and was underlain by a layer of interbedded sands, silts, and clays of thickness of 6 m. For the nonsandy sediments, liquid limits (LL) ranged from 25 to 45 with one exception of 61 in a high plasticity clay (CH) layer (Fig. 11.4); PI ranged from 8 to 24 with an exception of 35 in the CH layer. FC from low plasticity clay (CL) and low plasticity silt (ML) specimens ranged from 51% to 98%. Based on SPT borings, the east bank of the site showed more sands and silts within the interbedded layer compared to the west bank. Beneath this layer was a stratum of dense sands. The ground water table depth was likely between 2.6 and 3.3 m (Youd et al., 2009) at the time of the earthquake.

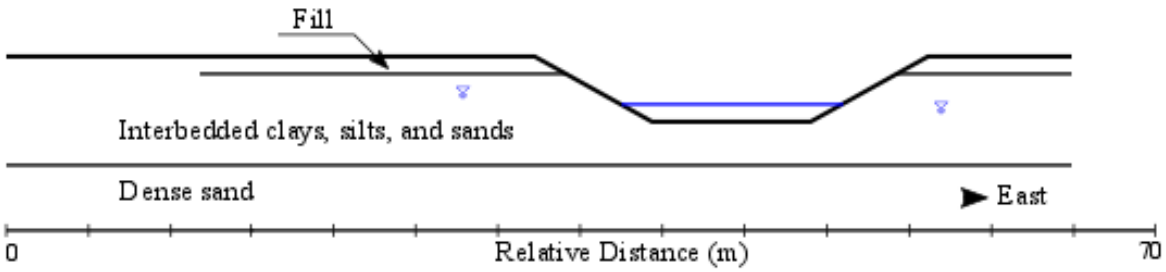

Figure 11.1: Cross section of Çark Canal site (data from Youd et al. (2009) and Boulanger et al. (2019)).

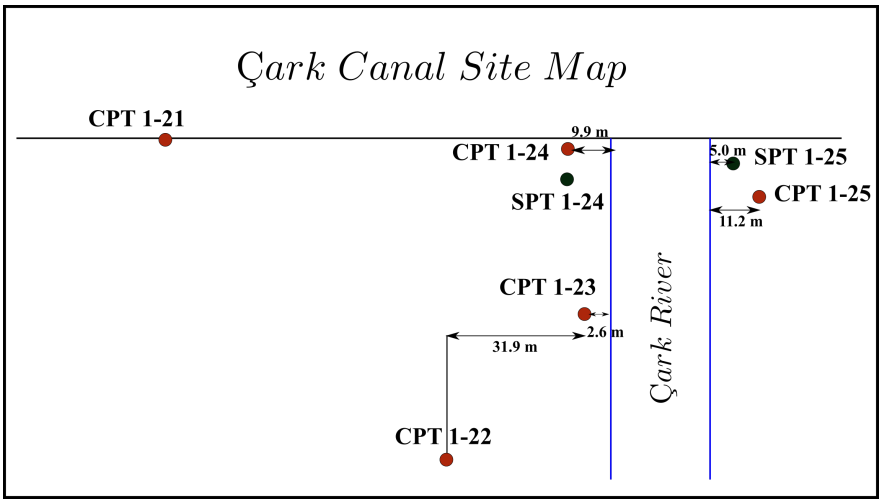

Figure 11.2: Plan view and in-situ tests locations (after Youd et al. (2000)).

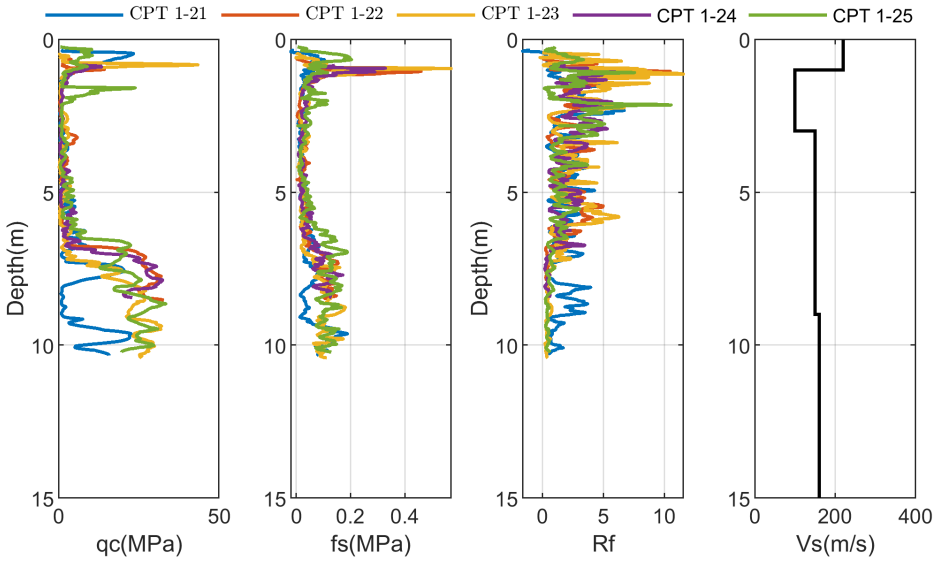

Figure 11.3: CPT sounding profiles (after Youd et al. (2000)) and measured shear wave velocity profiles at Çark site using SASW (after Bay and Cox (2001)).

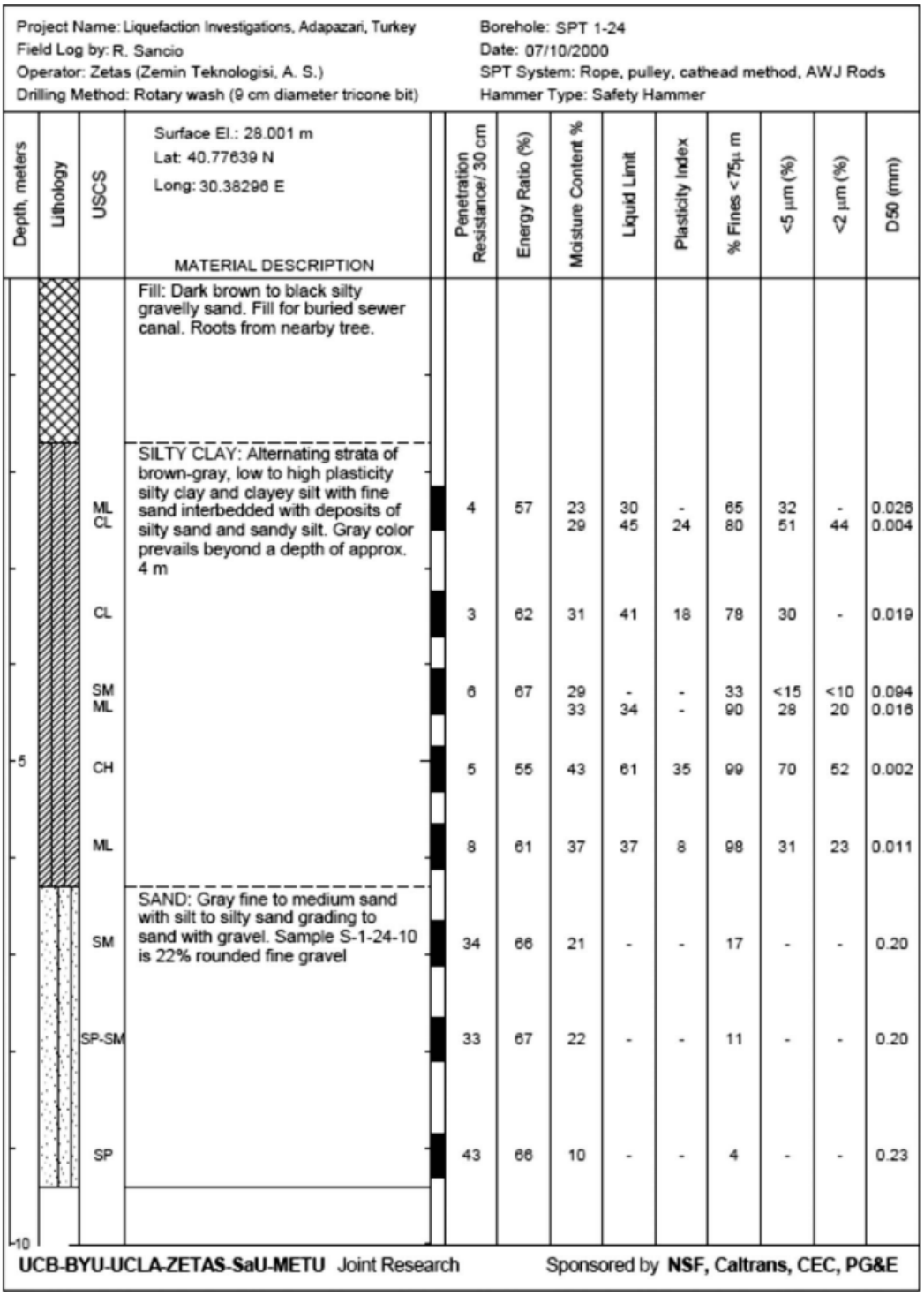

Figure 11.4: Log and laboratory data for Borehole 1-24 drilled on the west side of Çark Canal (from Youd et al. (2009)).

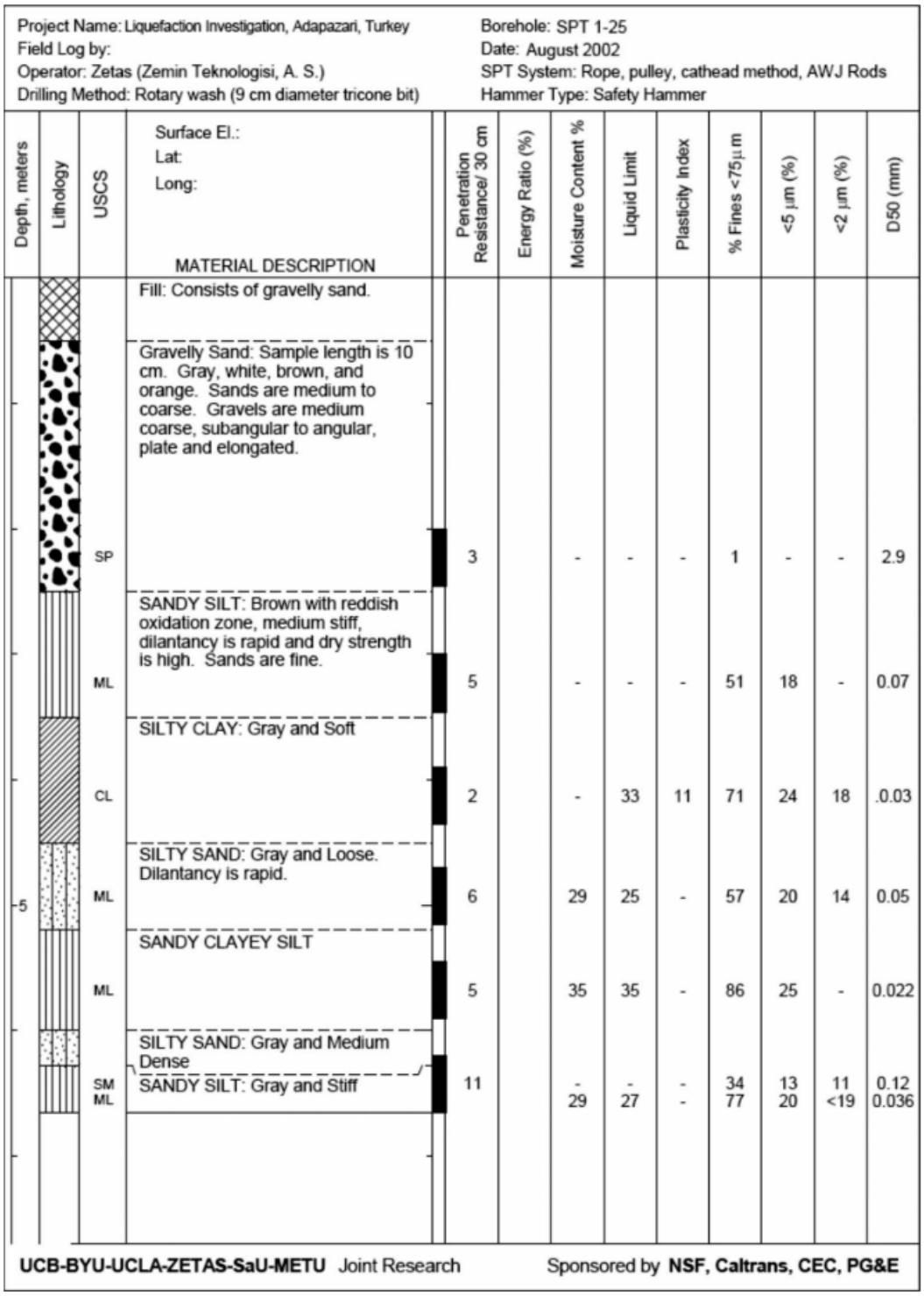

Figure 11.5: Log and laboratory data for Borehole 1-25 drilled on the east side of Çark Canal (from Youd et al. (2009)).

11.3 Input motions

The motion recorded at the Sakarya station (ID: AI_005_SKR), and closest to the site, was used in previous simulation studies. However, this station, referred as SKR hereafter, is located more than 4 km away from the site (Fig. 11.6) and failed to record the north-south (fault-normal) component of the main event. In the Engineering Strong Motion Database, this record was deemed to be of poor quality (Luzi et al., 2016). Therefore, in this study it was deemed necessary to complement this motion with additional motions obtained using a predictive model suitable for the site.

Figure 11.6: Relative location of Çark Canal site to SKR station.

Kale et al. (2015) proposed a predictive model for 5% damped horizontal spectral acceleration between $0\,s \leq T \leq 4\,s$ for seismic-hazard assessment of shallow active crustal regions in Iran and Turkey. Their proposed GMPE was developed from a recently compiled

strong-motion database for the Earthquake Model of the Middle East Region project (Zare et al., 2014), which consisted of 670 Turkish accelerograms and 528 Iranian accelerograms. The applicability range of the predictions was bounded for distances up to 200 km, between $4 \leq M_w \leq 8$ and $150\,m/s \leq V_{s30} \leq 1200\,m/s$. The emphasis of the proposed model was the consideration of regional differences in the variations of estimated ground motions in terms of magnitude and distance scaling, as well as spectral shapes. Using this model, a target spectrum was computed and ten motions were subsequently selected from the NGA-West database by spectra matching. Target spectrum and 5% damping response spectra of selected input motions are presented in Fig. 11.7. Characteristics of these ten motions are summarized in Table 11.1 and more information is available in Appendix D.

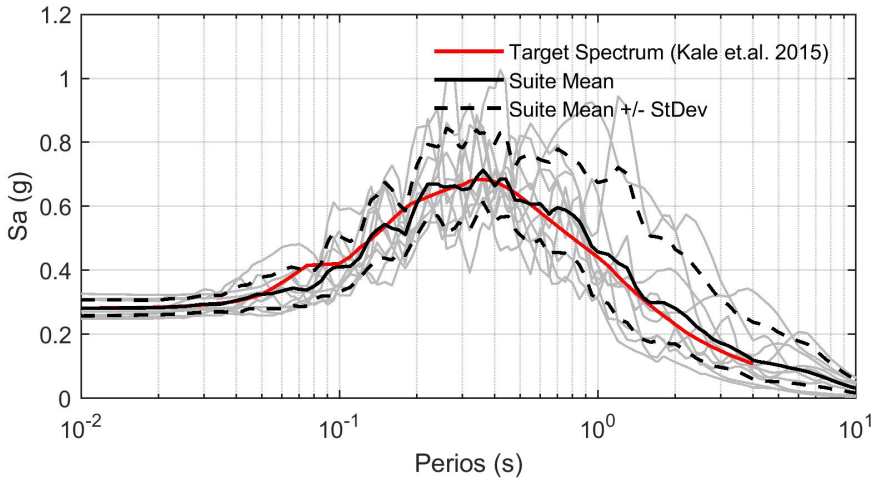

Figure 11.7: Target spectrum and 5% damping response spectra of selected input motions.

Table 11.1: List of additional records considered in this study

Motion ID	Record Sequence Number	Scale Factor	Tp-Pulse Period (s)	5-75% Duration (s)	Scaled Arias Intensity (m/s)	Magni-tude	Rjb (km)	Rrup (km)	Vs30 (m/s)
1	1106	0.354	1.09	4.3	2.97	6.9	0.94	0.96	312.0
2	1119	0.461	1.81	2.2	1.80	6.9	0	0.27	312.0
3	1120	0.453	1.55	6.0	3.94	6.9	1.46	1.47	256.0
4	1176	1.114	4.95	7.0	1.45	7.51	1.38	4.83	297.0
5	1602	0.409	0.88	2.6	1.51	7.14	12.02	12.04	293.6
6	2114	0.934	3.16	9.1	1.78	7.9	0.18	2.74	329.4
7	6887	1.654	12.62	11.0	1.49	7	18.05	18.05	187.0
8	6897	1.042	7.83	13.0	2.19	7	5.28	8.46	295.7
9	6906	0.473	6.23	5.6	2.22	7	1.22	1.22	344.0
10	6911	0.617	9.92	7.0	1.98	7	7.29	7.29	326.0

11.4 Approach to modeling the interbedded layer

This study utilized three constitutive models, PM4Sand, PM4Silt, and PIMY, to simulate different soil behaviors within the interbedded layer. Out of these three models, PM4Sand and PM4Silt are two constitutive models for earthquake engineering applications proposed by Boulanger and Ziotopoulou (2017, 2018) to represent stress dependent sand-like and clay-like soil behavior (Boulanger and Idriss, 2006), respectively. PIMY (*PressureIndepend-MultiYield*, Yang (2000)) material, on the other hand, is an elastic-plastic material in which plasticity is only exhibited in the deviatoric direction. The volumetric stress-strain response is linear-elastic and independent of the deviatoric response. This material was implemented to simulate monotonic or cyclic response of materials whose shear behavior is insensitive to mean stress (confinement) changes.

As shown in Fig. 11.8, these three models can capture different aspects of soil behavior under cyclic loading, such as liquefaction, cyclic softening, and modulus reduction. The PM4Sand and PM4Silt responses presented here were obtained using the input parameters adopted from Boulanger et al. (2019) as shown in Table 11.2. The PIMY response was

obtained using input parameters that represent a medium clay. As shown in Fig. 11.8a, as cyclic loading progressed on PM4Sand, σ'_v gradually decreased until temporarily approached zero ($R_u \approx 100\%$). The shear strain remained relatively small until R_u neared 100%, after which the strains grew rapidly with each additional cycle of loading. After this point, PM4Sand developed hardening at the end of each subsequent loading cycle and developed enough shear strength to resist the peak applied shear load. On the other hand, PM4Silt under the same loading showed a slower progressive increase in excess pore water pressure reaching a limiting level ($R_u = 60\%$ shown in Fig. 11.8b). The achieved maximum R_u can be controlled using PM4Silt's secondary parameter $R_{u,max}$ whose default value is tied to S_u. After approaching $R_{u,max}$, the material developed rapidly increasing strains, although slower compared to PM4Sand, with each subsequent loading cycle. The stress-strain loops after this limiting R_u had been reached dissipated considerably more energy than in equivalent PM4Sand cycles (i.e., the hysteretic loops were broader). Further, the stress-strain loops for PM4Silt did not develop the very flat middle portions, where the shear stiffness was essentially zero, that were observed in PM4Sand after it temporarily developed $R_u \approx 100\%$. The PIMY model, in which plasticity exhibits only in a deviatoric stress-strain response, did not develop significant pore pressure and shear strains.

Table 11.2: Input parameters for PM4Sand and PM4Silt (from Boulanger et al. (2019))

Input Parameter	Sand-like portion of interbedded layer	Clay-like portion of interbedded layer	Underlying dense stratum
D_R	61%	-	99%
S_u (kPa)	-	55	-
G_o	585	585	600
h_{po}	0.28	100.0	1.0

*All secondary input parameters were assigned default values as listed in Boulanger and Ziotopoulou (2017, 2018). h_{po} for PM4Sand and PM4Silt should not be compared directly.

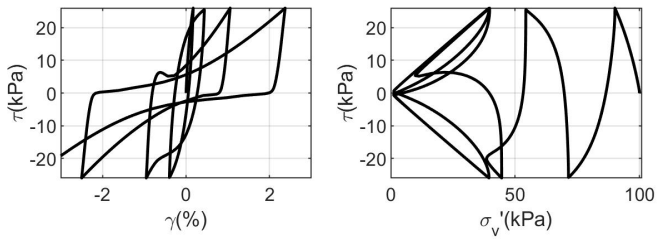

(a) PM4Sand

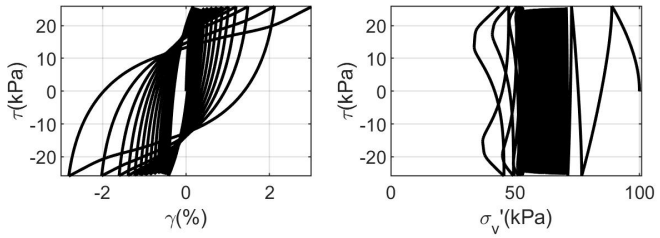

(b) PM4Silt

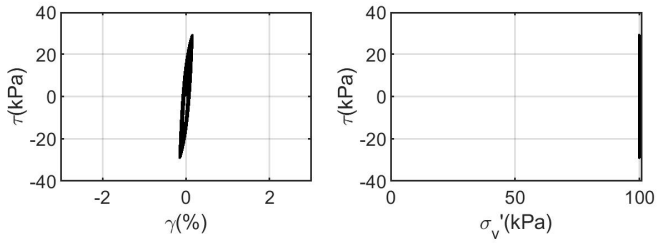

(c) PIMY

Figure 11.8: Typical behavior of models used in this study under undrained CSS loading. (a) PM4Sand, (b) PM4Silt, (c) PIMY.

The selection of constitutive model at each location was based on FC and PI; since numerous studies have shown dependency of soil behavior, such as cyclic resistance, on FC and PI. In 2001 Polito and Martin (2001) conducted a laboratory parametric study to clarify the effects which varying fines content and plasticity have upon the liquefaction resistance of sandy sands using cyclic triaxial tests. If the silt content was greater than a limiting silt content, which appeared to be predominately between 25 and 45% for most sands (Polito,

1999), the specimen's structure consisted predominately of sand grains suspended within a silt matrix with little sand grain to sand grain contact. Above the limiting silt content, the amounts of sand presented in the soil and its soil specific relative density had little effect on its cyclic resistance. The mixed soil then behaved more like pure clay or silt. The deformation behavior then became more clay/silt dominated, and the coarser particles may or may not contribute to the strength properties.

Bray and Sancio (2006) evaluated the performance of fine-grained soils in Adapazari, Turkey during the 1999 Kocaeli earthquake to understand their susceptibility to liquefaction and response under cyclic loading. Cyclic testing of a wide range of soils, found to liquefy in Adapazari during the Kocaeli earthquake, confirmed that these fine-grained soils were susceptible to liquefaction. It was not the amount of "clay-size" particles in the soil, rather, it was the amount and type of clay minerals in the soil that best indicated liquefaction susceptibility. Thus PI was deemed a better indicator of liquefaction susceptibility. Loose soils with $PI < 12$ and $w_c/LL > 0.85$ were susceptible to liquefaction, and loose soils with $12 < PI < 18$ and $w_c/LL > 0.8$ were systematically more resistant to liquefaction. Soils with $PI > 18$ and tested at low effective confining stresses were not susceptible to liquefaction.

Boulanger and Idriss (2006) compiled a wide range of data of Atterberg Limits for fine-grained soils that have exhibited clay-like, intermediate, and sand-like soil behavior and recommended that: fine-grained soils can confidently be expected to exhibit clay-like behavior if they have $PI \geq 7$ and fine-grained soils with PI values between 3 - 6 may exhibit intermediate behavior. The schematic illustration of the transition from sand-like to clay-like behavior for fine-grained soils with increasing PI, and the recommended guideline for practice is presented in Fig. 11.9.

Other properties of soil are also affected by FC and PI. Increasing FC tends to decrease minimum void ratio thus increasing the maximum dry density and also decreasing hydraulic conductivity substantially. Gomez et al. (2014) studied the effects of FC on hydraulic conductivity of granular structural Backfill. For the soils investigated, the measured hydraulic conductivity for 0%, 5%, and 10% fines contents were quite close to each other. Hydraulic

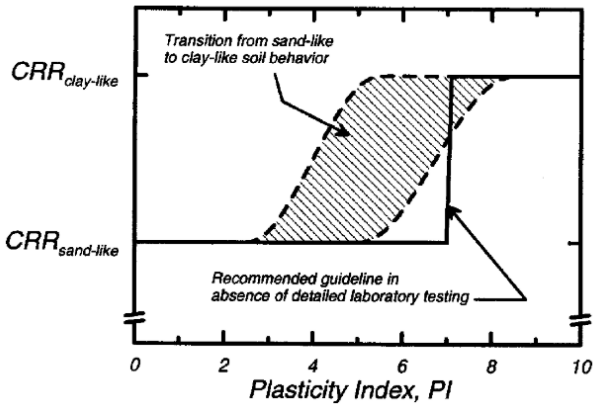

Figure 11.9: Schematic illustration of the transition from sand-like to clay-like behavior for fine-grained soils with increasing PI, and the recommended guideline for practice (from Boulanger and Idriss (2006)).

conductivity was significantly lower for fines content in excess of 15%. A varying function of hydraulic conductivity was fitted based on data presented by Gomez et al. (2014) and it is shown in Fig. 11.10. PI can alter the shear modulus reduction behavior of a soil. As shown by Darendeli (2001), under the same confining pressure, increasing PI can lead to slower reduction of shear modulus.

Based on this information, a workflow based on a combination of FC and PI was proposed to select the most representative constitutive model to be used in all numerical simulations. The effect of w_c/LL was omitted since information regarding moisture content at the site was not complete. The PM4Sand model was assigned to elements where, (1) FC was less than 15% regardless of PI, or (2) FC was in the range of 15% to 35% and PI was less than 7, or (3) FC was larger than 35% and PI was less than 3. PM4Silt was assigned to elements where, (1) FC was in the range of 15% to 35% and PI was lager or equal to 7, or (2) FC was larger than 35% and PI was in the range of 3 to 18. PIMY was assigned to elements located where FC was larger than 35% and PI was larger than 18. Fig. 11.11 illustrates the

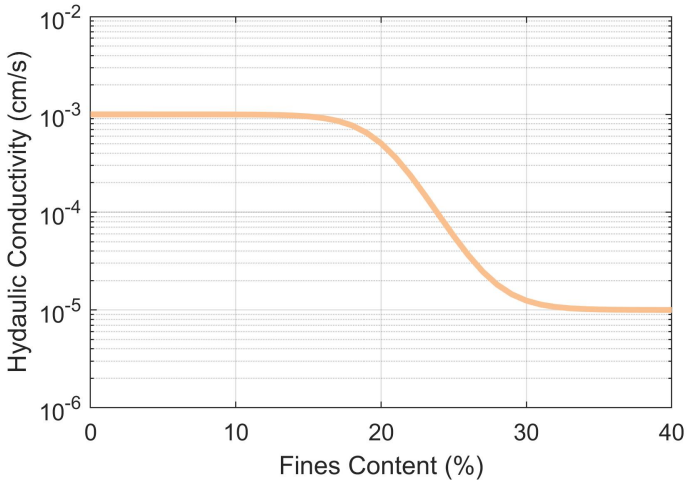

Figure 11.10: Change of hydraulic conductivity based on FC. This relationship was based on a study conducted by (Gomez et al., 2014) on effects of FC on hydraulic conductivity of granular structural backfill.

flowchart that represents the process of model selection based on combination of FC and PI.

Stochastic fields of FC and PI were generated for this site using the approach presented in Chapter 10. This method requires to define correlation lengths L_z and L_x in two directions. Boulanger et al. (2019) found the mean correlation length in the vertical direction, L_z, was 0.26 m for this site, and estimated mean correlation length in the horizontal direction, L_x, based on the site's sedimentary setting. Three values of L_x, 5, 10, and 40 m were examined, however, the difference in observed results was not significant. Therefore, L_z of 0.26 m and L_x of 10 m was adopted as the base case in this study. The other two correlation lengths were also considered in a sensitivity study. A total of 20 realizations were generated for each scenario and analyzed for all motions. A lognormal distribution with coefficient of variation (COV) of 0.3 was assigned to both PI and FC. Mean fields for PI and FC were obtained interpolating laboratory testing results from samples obtained at SPT borings 1-24 and 1-25 and reported by Youd et al. (2000). Stochastic fields for FC and PI were generated

independently. At the centroid of each element, a random combination of FC and PI was then obtained and a proper constitutive model was subsequently assigned based on the flowchart shown in Fig. 11.11. This proposed workflow can be further refined when more laboratory tests become available. Figs. 11.12 and 11.13 illustrate two realizations of FC and PI and selected constitutive models based on the workflow. Realization 7 consisted of more sand-like materials close to the river.

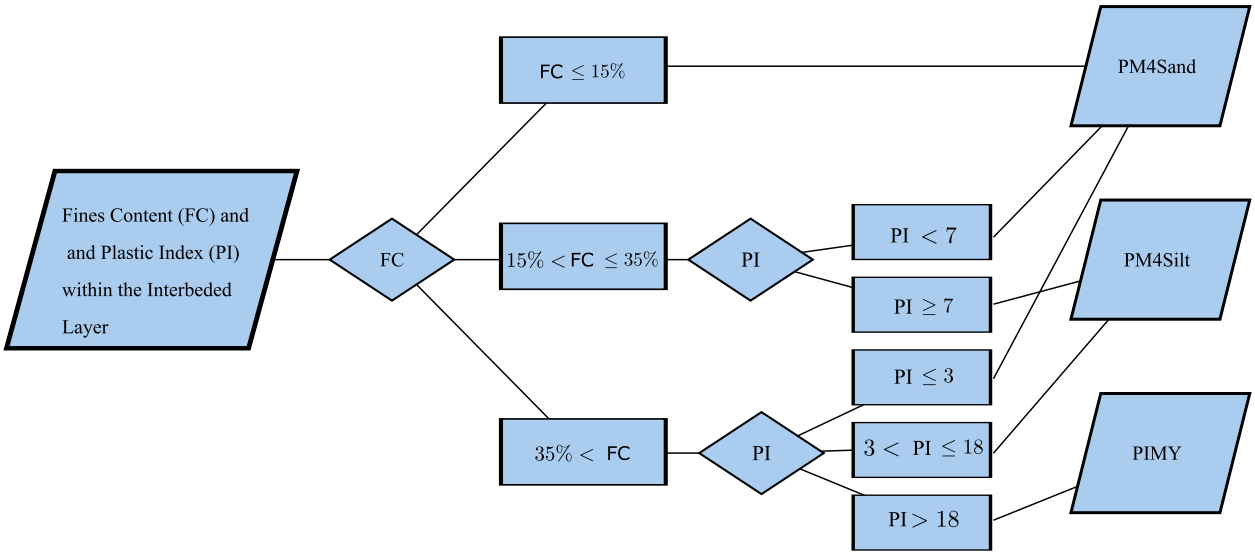

Figure 11.11: Flowchart for assigning constitutive model based on FC and PI.

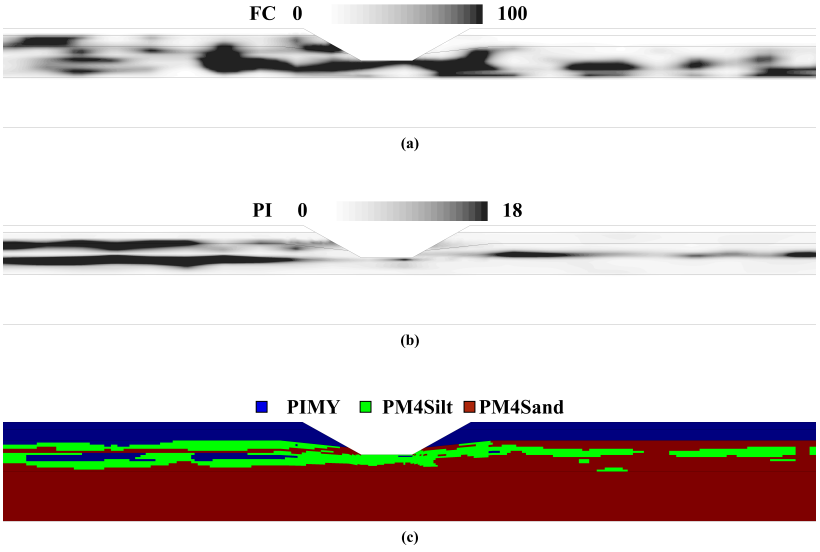

Figure 11.12: Constitutive models used in realization 1 based on stochastic field of FC and PI.

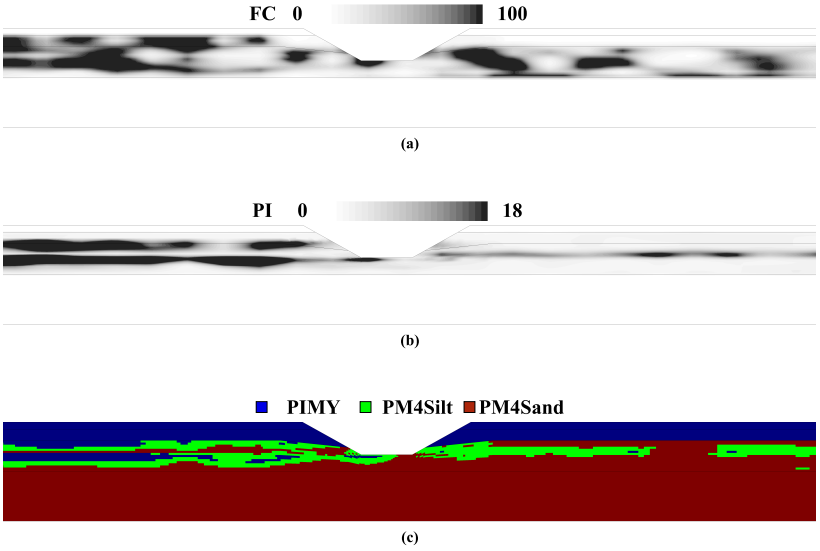

Figure 11.13: Constitutive models used in realization 7 based on stochastic field of FC and PI.

11.4.1 Constitutive model parameter calibration

In addition to FC and PI, other in-situ tests data, i.e., CPT resistance and shear wave velocity (V_s), were also considered to determine model parameters. Measured tip resistances were interpolated between soundings at the centroid of each element and later used to estimate undrained shear strength, relative density, and cyclic resistance ratio (CRR). V_s was used to estimated parameters related to shear modulus, i.e., shear modulus coefficient, G_o, for PM4Sand/PM4Silt and reference low-strain shear modulus, G_r, for PIMY. All input parameters are summarized in Table 11.3. Constant densities were assigned to each layer.

Table 11.3: Input parameters for the constitutive models

Input Parameter	Surficial fill	Sand-like portion of interbedded layer	Clay-like portion of interbedded layer ($PI < 18$)	Clay-like portion of interbedded layer ($PI > 18$)	Underlying dense stratum
Material	PIMY	PM4Sand	PM4Silt	PIMY	PM4Sand
D_R	-	Variable	-	-	90%
$G_r(kPa)$	84700	-	-	39375	-
G_o	-	585	585	-	630
h_{po}	-	Variable	100.0	-	1.0
S_u	Variable	-	Variable	Variable	-
$\rho(Mg/m^3)$	1.75	1.75	1.75	1.75	2.0

*All secondary input parameters of PM4Sand and PM4Silt were assigned default values as listed in Boulanger and Ziotopoulou (2017, 2018).

For PM4Silt, its first primary input parameter undrained shear strength, S_u, was estimated using the CPT data with a constant cone bearing factor (N_{kt}) of 15,

$$S_u = \frac{q_t - \sigma_v}{N_{kt}}\,. \tag{11.1}$$

It should be noted that typically N_{kt} varies from 10 to 18 and tends to increase with increasing plasticity and decrease with increasing soil sensitivity (Robertson and Cabal, 2015). Clay-

like soils also tend to show different S_u under different strain rates. A simple sensitivity study was performed on S_u and results are discussed later. Similar to Boulanger et al. (2019), the shear modulus coefficient (G_o) was set to 585 for PM4Silt and assigned to the interbedded layer to match the in-situ V_s at the middle of the stratum. The third primary input parameter of PM4Silt, h_{po}, remained unchanged from Table 11.2.

In terms of PIMY, G_r was computed as ρV_s^2. The reference bulk modulus, K_r, was calculated from G_r with an assumed $\nu = 0.33$. Modulus reduction (G/G_{max}) curves proposed by Darendeli (2001) were used to define the yield surfaces in the PIMY model. Darendeli (2001) curves are based on a hyperbolic model and are derived from cyclic laboratory tests; often not run to failure. Consequently, these curves do not necessarily provide an accurate representation of soil strength at large shear strains. In some cases, the shear strength can be grossly inaccurate, which may result in significant errors for analyses involving shear stress levels at or near failure (Gingery and Elgamal, 2013). In this study, a method proposed by Alborz Ghofrani (personal communication, 2016) was used to correct G/G_{max} curves to match shear strength of soil at failure strain.

G_o was set to 585 for PM4Sand. In order to obtain other input parameters for PM4Sand, overburden corrected tip resistance, q_{c1}, was computed at the centroid of each element. The attained q_{c1} was then used to calculate FC corrected tip resistances, q_{c1Ncs} following Boulanger and Idriss (2014) such that,

$$q_{c1Ncs} = q_{c1N} + \Delta q_{c1N}\,, \tag{11.2}$$

$$\Delta q_{c1N} = \left(11.9 + \frac{q_{c1N}}{14.6}\right) \cdot \exp\left(1.63 - \frac{9.7}{FC+2} - \left(\frac{15.7}{FC+2}\right)^2\right). \tag{11.3}$$

Relatice density, D_R, was then estimated based on q_{c1Ncs} as recommended by Idriss and Boulanger (2008),

$$D_R = 0.465\left(\frac{q_{c1Ncs}}{C_{dq}}\right)^{0.264} - 1.063\,. \tag{11.4}$$

where C_{dq} was taken as 0.9 (Idriss and Boulanger, 2008).

The target CRR was computed using the CPT-based correlation proposed by Boulanger

and Idriss (2014),

$$CRR_{M=7.5,\sigma'_v=1} = \exp\left(\frac{q_{c1Ncs}}{113} + \left(\frac{q_{c1Ncs}}{1000}\right)^2 - \left(\frac{q_{c1Ncs}}{140}\right)^3 + \left(\frac{q_{c1Ncs}}{137}\right)^4 - 2.8\right), \quad (11.5)$$

h_{po} was subsequently calculated using the correlation proposed in Chapter 3. h_{po} was bounded between 0.05 and 1.0. Increasing FC tends to increase both D_R and h_{po}, implying higher cyclic resistance under the same tip resistance.

Other than the interbedded layer, the layers above the ground water table were modeled using PIMY model. The underlain dense layer was modeled using PM4Sand after Boulanger et al. (2019) with D_R slightly modified to 0.9.

Hydraulic conductivity plays an important role in dynamic effective stress analysis. Variable hydraulic conductivity was assigned to each element based on FC following the work by Gomez et al. (2014) as shown in Fig. 11.10. Other hydraulic conductivity schemes were also considered to examine its sensitivity and are discussed later in this chapter.

11.5 FE model development

All numerical simulations were performed using OpenSees. Figs. 11.14 and 11.15 depict the mesh developed for this study. The 2D FEM model consisted of 8758 elements and 9080 nodes, with extra refinement near the river bed. The model was extended 100 m outward from the slope crest to reduce possible boundary effects. The outer-most soil column elements were modified to generate a free-field response by increasing their out-of-plane thicknesses and constraining the outer-most soil column element nodes at the same elevation to have the same horizontal movement using *equalDOF*. The stabilized single-point integration and mixed displacement-pressure (u-p) element (SSPquadUP, see McGann et al. (McGann et al., 2015)) was used to capture the effective stress response of each realization. Pore pressures above groundwater table were set to be zero during the analysis to ensure drainage and avoid generation of excess pore pressures in the dry layers. The bottom boundary was fixed against vertical movement and tied in the horizontal direction using *EqualDOF*. The velocity time history was applied to the base of the model as a stress history through a Lysmer dashpot

(Lysmer and Kuhlemeyer, 1969). The coefficient of the dashpot was calculated using the thickness, stiffness, and density of the base layer.

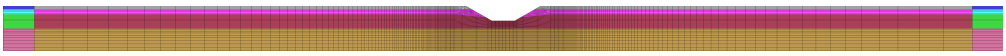

Figure 11.14: 2D FEM mesh developed for the site.

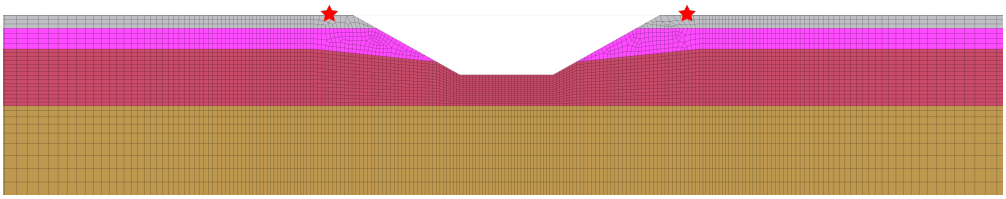

Figure 11.15: FEM mesh (enlarged). Locations of interested lateral displacement are highlighted on west (left) and east (right) banks.

Two iterations were required to apply gravity since some material properties were stress-dependent as discussed above. Uniform material properties listed in Table 11.2 were assigned during the first iteration. To apply gravity, the material was set to be linear elastic and elemental body forces were increased gradually to reduce numerical instabilities in the model. This elastic initial stress state was then used to calculate stress dependent material properties at each element. After the second iteration, the material was then switched to *elasto-plastic* and new equilibrium was achieved by allowing enough extra analysis steps to adjust constitutive model internal variables to any plastic behavior. A Poisson's ratio of 0.3, which yielded a lateral earth pressure coefficient $K_0 = 0.43$ under level ground plane-strain conditions, was assumed for PM4Sand and PM4Silt to generate the initial stress state.

The constant average acceleration Newmark method ($\beta = 0.25$, $\gamma = 0.5$) was used in order to resolve the integration in time. A frequency dependent Rayleigh damping was

applied to account for the lack of small strain damping. The Rayleigh damping coefficients were chosen such that a 2% damping ratio was obtained at 0.2 Hz and 20 Hz.

11.6 Simulation results

Lateral ground surface displacements at points located 2 m from the head of each slope (shown in Fig. 11.15) were obtained from 20 realizations and all motions. Fig 11.16 illustrates the results grouped by each motion along with their logarithmic means (log-mean) and standard derivations. Large variability was observed from record-to-record (input motion characteristics) and realization-to-realization (stratigraphy near the slopes). Histograms of these results are presented in Fig. 11.17 and show generally log-normal distribution. Overall, the predicted lateral displacements were consistent with the range associated with minor to no surface manifestation as the log-mean was 6.74 cm and 6.46 cm on west and east bank, respectively. It is worth mentioning that although the lateral displacements obtained on the east bank, which consisted of more sand-like portions, showed a slightly lower log-mean, large values existed under certain combination of realization and motion. When combined with results obtained using reversed polarity motions (discussed in the following section), the east bank tended to produce larger lateral displacements overall. This observation reflects the same trend shown in the calculation performed by Youd et al. (2009). Using revised liquefaction susceptibility criteria (Bray and Sancio, 2006), Youd et al. predicted displacements west of the canal of 0 m due to the high FC of 94%, while on the east bank, the predicted displacements were between 0.35 m and 1.4 m with a mean predicted displacement of 0.7 m. Similar trends were obtained by Boulanger et al. (2019) and results are shown in red in Fig 11.16 for comparisson purposes.

Input motion had a profound effect in predicted lateral displacements, although all the motions were scaled based on the target spectrum. Fig. 11.18 a and b illustrate permanent horizontal displacements for realization 1 using motions SKR and 3, respectively. Information about this realization is depicted in Fig. 11.12. Both cases showed lateral displacements were greatest near the canal and decreased with distance from the canal. Larger perma-

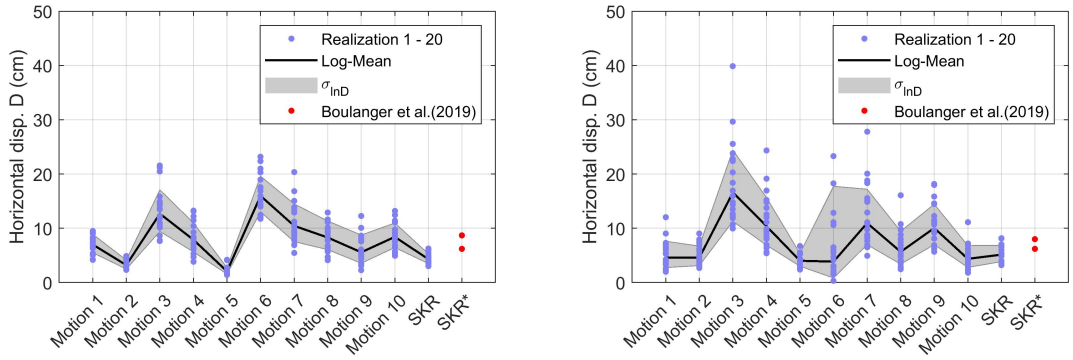

(a) West (b) East

Figure 11.16: Horizontal displacement toward the canal on the west and east banks from all realizations (lines) and motions (x axis).

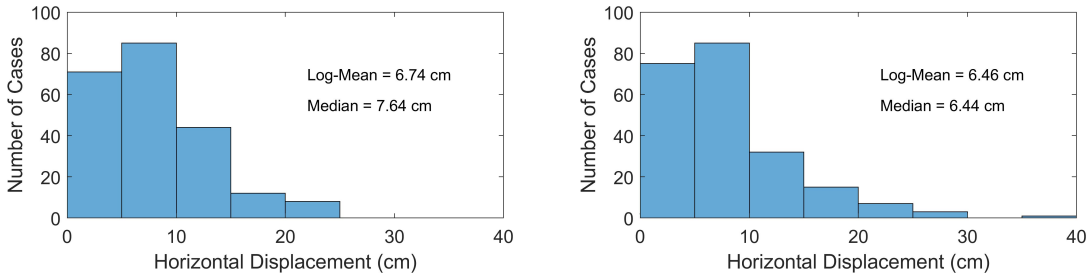

(a) West (b) East

Figure 11.17: Histograms of horizontal displacement toward the canal on the west and east banks from all realizations and motions.

nent horizontal displacements were shown in the case of motion 3 when compared to those corresponding to motion SKR. Fig. 11.19 a and b illustrate maximum pore pressure ratio obtained for the same two cases. Wide-distributed liquefaction was trigger within the sand-like portions of the interbedded layer, however, pore pressure generation was limited within the clay-like portions. Pore water pressure ratios for motion SKR were less pronounced than

for motion 3, in conformity with lateral displacements.

Different degrees of realization-to-realization variability were shown with different motions with motion 3 showing the greatest variability. Fig. 11.18 b and c illustrate permanent horizontal displacements for realizations 1 and 7 using motions 3, respectively. Fig. 11.19 b and c illustrate maximum pore pressure ratio obtained from the same two cases. The large differences observed may be attributed to differences in stratigraphy near the slopes as shown in Figs. 11.12 and 11.13. OpenSees results for motion SKR showed lateral displacements ranging from 3.0 cm to 6.3 cm with a log-mean of 4.3 cm on the west bank; and 3.2 cm to 8.2 cm with a log-mean of 5.1 cm on the east bank. The results match the results obtained by Boulanger et al. (2019) using FLAC; with 8.7 cm and 6.8 cm on the west side and 6.2 cm and 8.0 cm on the east side as reported for the SKR motion with both polarities. Large dispersion in OpenSees results was observed between realizations as a result of varying input parameters within each material type.

Additional sensitivity analyses were performed on motion polarity, untrained shear strength, and hydraulic conductivity. The results are presented and discussed in the following sections.

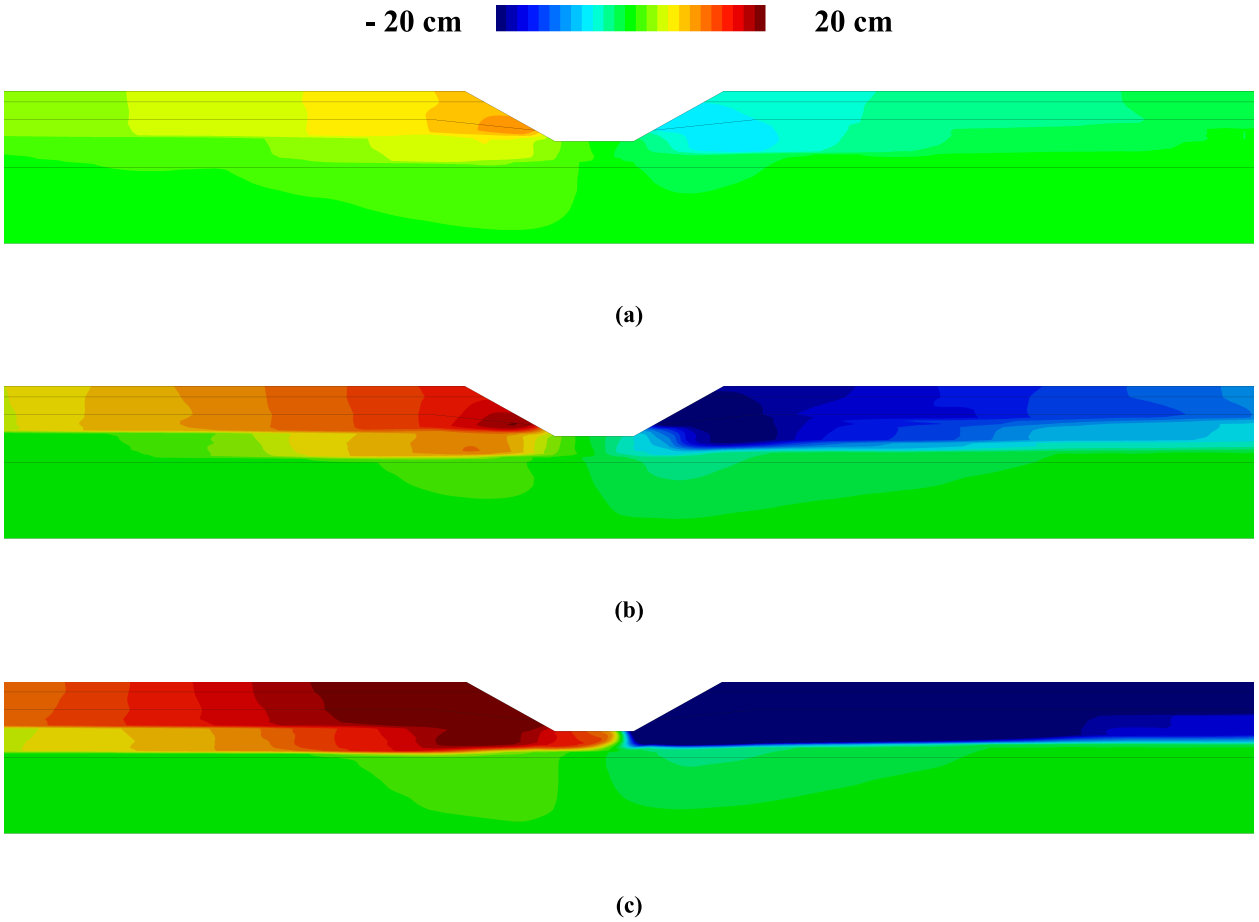

Figure 11.18: Contours of final horizontal displacement obtained from three cases: (a) realization 1 with SKR motion, (b) realization 1 with motion 3 (RSN1120), and (c) realization 7 with motion 3 (RSN1120).

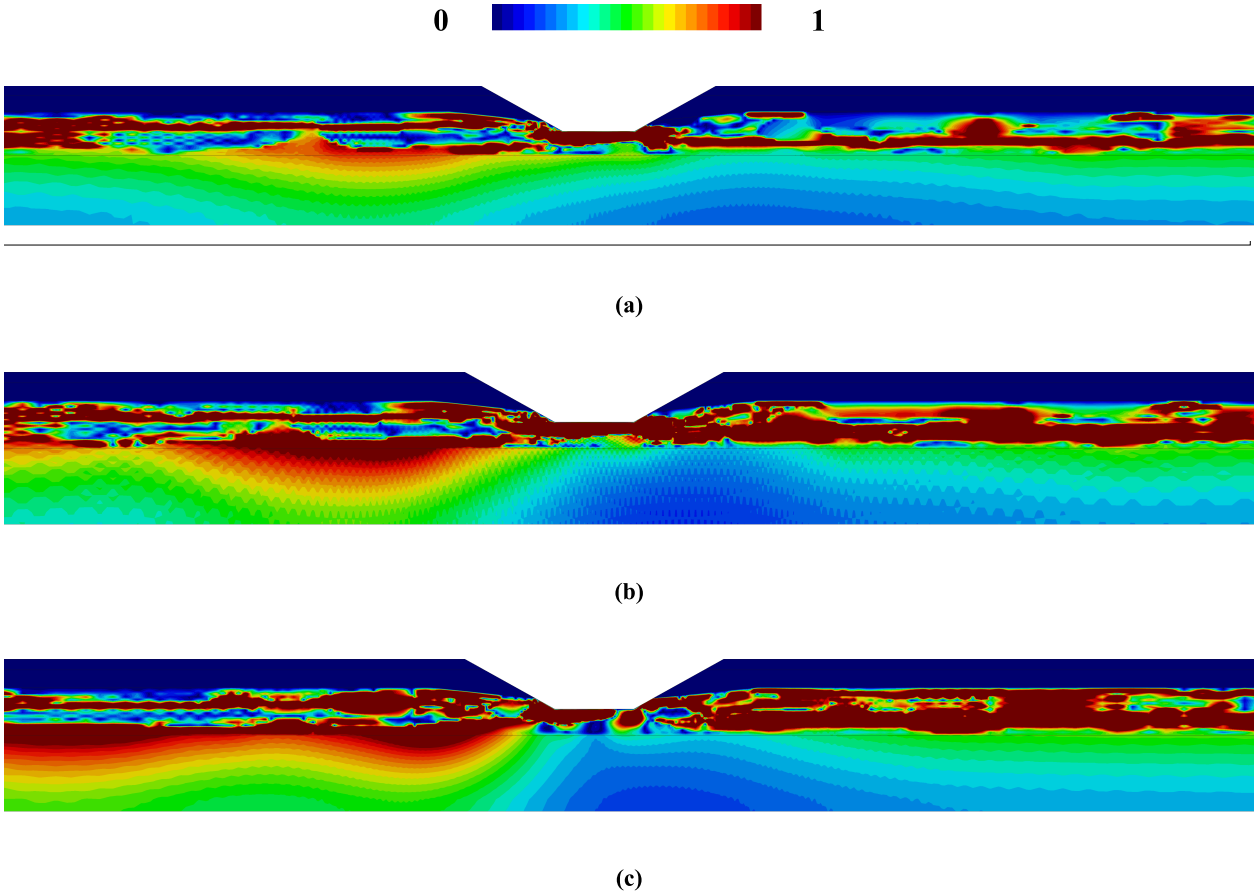

Figure 11.19: Contours of maximum R_u obtained from three cases: (a) realization 1 with SKR motion, (b) realization 1 with motion 3 (RSN1120), and (c) realization 7 with motion 3 (RSN1120).

11.6.1 Motion polarity

The analyses were repeated with motions' polarity reversed and the results are illustrated in Figs. 11.20 and 11.21. New log-means were obtained for each motion for 20 realizations each. The ratios between new and original log-means were computed and listed in Table 11.4. The effect of motion polarity was significantly different for different motions as shown in the Table. Considering the west bank for example, motions 6, 9, and SKR showed ratio of 0.3, 2.6, and 1, respectively, meaning motions 6 and 9 show larger dependency on motion polarity. However, after combing results for all 11 motions, insignificant change was shown in predicted lateral displacements. The results obtained using reversed polarity motions showed log-means of, 5.95 cm (vs. 6.74 cm), 6.80 cm (vs. 6.46 cm), for the west and east bank, respectively, meaning using multiple motions can likely average the effect of motion polarity, and therefore reduce the uncertainty associated with polarity.

Table 11.4: Ratio between log-means of horizontal displacement obtained using motions with original and reversed polarity

	$\text{log-mean}_{\text{Original}}$ / $\text{log-mean}_{\text{Reversed}}$										
Motion	1	2	3	4	5	6	7	8	9	10	SKR
West bank	0.8	1.1	1.5	1.3	1.5	0.3	1.3	0.6	2.6	0.5	1.0
East bank	1.2	0.8	0.8	0.8	0.8	5.4	1.0	1.4	0.6	1.5	1.1

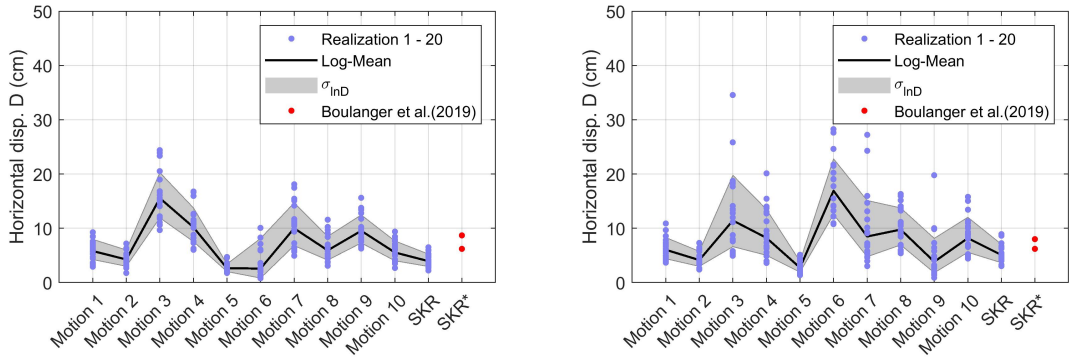

(a) West (b) East

Figure 11.20: Horizontal displacement toward the canal on the west and east banks from all realizations (lines) and motions (x axis), obtained using motions with reversed polarity.

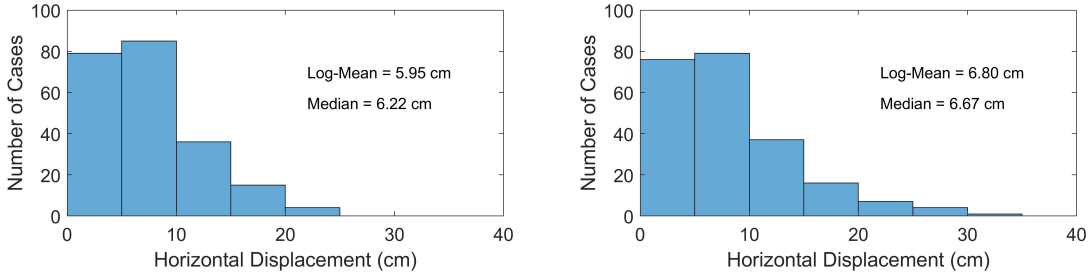

(a) West (b) East

Figure 11.21: Histograms of horizontal displacement toward the canal on the west and east banks from all realizations and motions, obtained using motions with reversed polarity.

11.6.2 Correlation length

Two additional sets of realizations (20 each) were generated and analyzed using horizontal correlation lengths, $L_x = 5\ m$ and $40\ m$, respectively, to study its sensitivity. Fig. 11.22 compares one realization using each L_x clearly showing differences in stratum continuity. The results obtained using these two new cases are illustrated in Figs. 11.23 and 11.24 for the case of $L_x = 5\ m$ and Figs. 11.25 and 11.26 for the case of $L_x = 40\ m$. The $L_x = 5\ m$ case produced lateral displacements of 6.45 cm and 5.29 cm for the west and east banks, respectively. The $L_x = 40\ m$ case produced lateral displacements of 5.43 cm and 4.76 cm for west and east banks, respectively. Both showed smaller values compared to the base $L_x = 10\ m$ case. This seemed to be related to the fact that sand-like portions showed limited continuity in the $L_x = 5\ m$ case, while clay-like portions showed extensive distribution of clay in the $L_x = 40\ m$ case (Fig. 11.22).

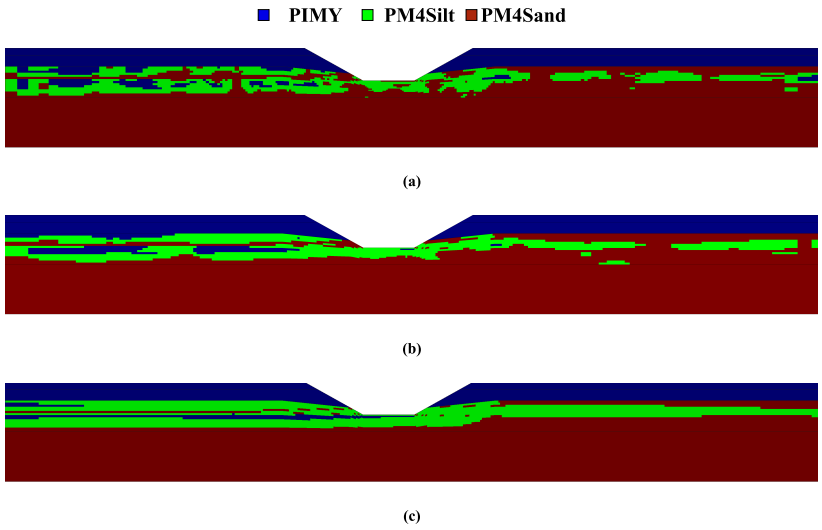

Figure 11.22: Constitutive models utilized in three realizations with different horizontal correlation lengths: (a) $L_x = 5\ m$, (b) $L_x = 10\ m$, (c) $L_x = 40\ m$.

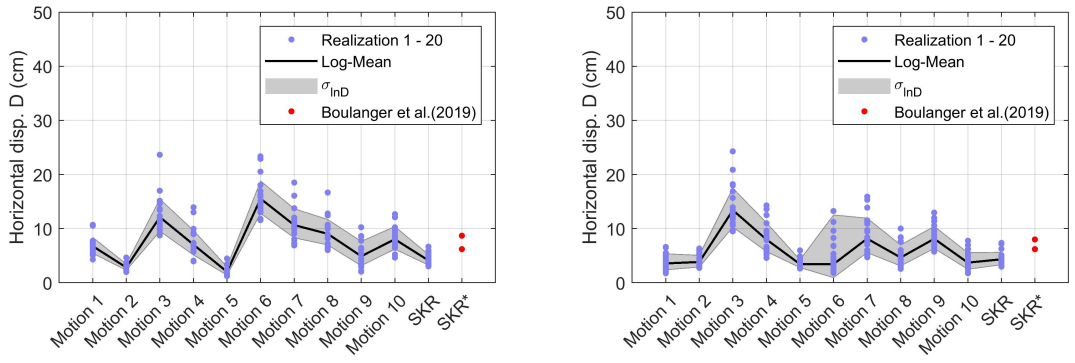

(a) West (b) East

Figure 11.23: Horizontal displacement toward the canal on the west and east banks from all realizations (lines) and motions (x axis), obtained using horizontal correlation length $L_x = 5\ m$.

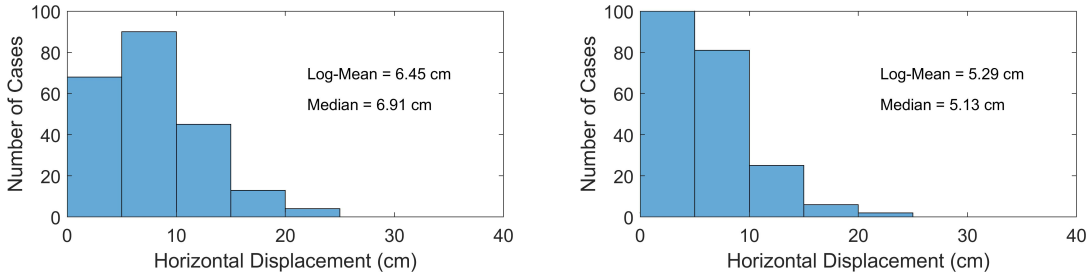

(a) West (b) East

Figure 11.24: Histograms of horizontal displacement toward the canal on the west and east banks from all realizations and motions, obtained using horizontal correlation length $L_x = 5\ m$.

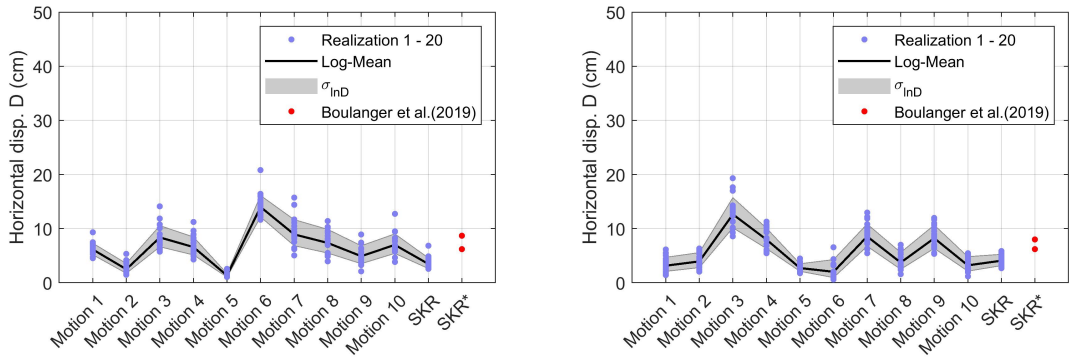

(a) West (b) East

Figure 11.25: Horizontal displacement toward the canal on the west and east banks from all realizations (lines) and motions (x axis), obtained using horizontal correlation length $L_x = 40\ m$.

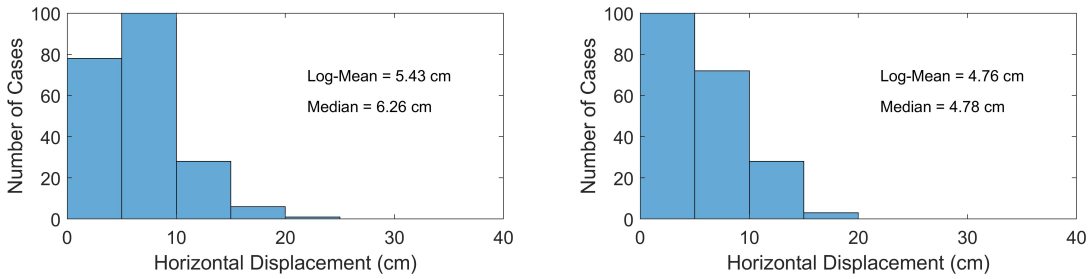

(a) West (b) East

Figure 11.26: Histograms of horizontal displacement toward the canal on the west and east banks from all realizations and motions, obtained using horizontal correlation length $L_x = 40\ m$.

11.6.3 Undrained shear strength

In the analysis performed by Boulanger et al. (2019), the S_u values computed using Equ. 11.1 were only applicable for static loading applications, whereas for dynamic analyses the PM4Silt S_u was increased to represent critical states representative for earthquake loading rates. Accordingly, in this study the analysis were repeated with the values obtained using Equ. 11.1 increased by 25% to account for strain rate effects relative to the CPT-derived S_u values. The results showed insignificant change in predicted lateral displacements when compared to the base case, with 6.16 cm (vs. 6.74 cm), and 6.06 (vs. 6.46 cm), for west and east bank, respectively. The small effect obtained by increasing S_u was attributed to the fact that the shear strength of clay-like portions was not fully mobilized and failure was mainly associated to sand-like portions.

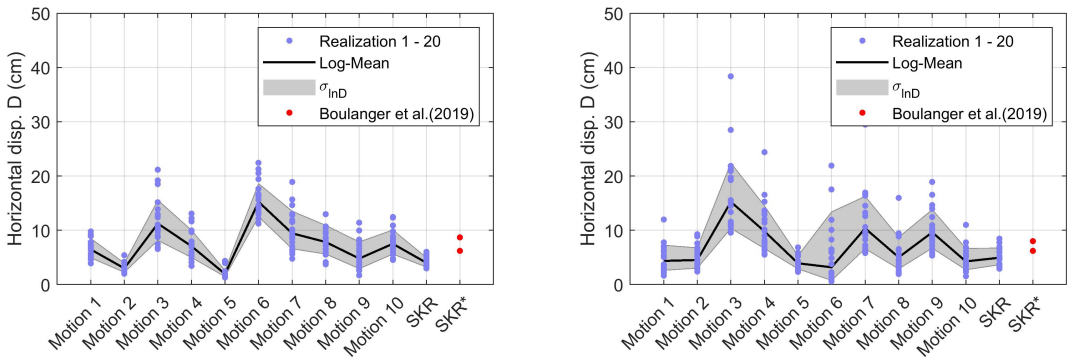

(a) West (b) East

Figure 11.27: Horizontal displacement toward the canal on the west and east banks from all realizations (lines) and motions (x axis), obtained using increased S_u.

11.6.4 Hydraulic conductivity

Greenfield (2017) underscored the need to consider the potential for pore pressure dissipation or redistribution during shaking, particularly during long-duration ground motions. To shed

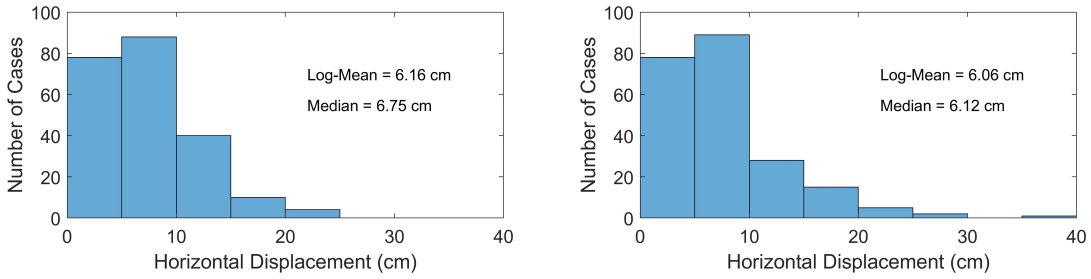

(a) West (b) East

Figure 11.28: Histograms of horizontal displacement toward the canal on the west and east banks from all realizations and motions, obtained using increased S_u.

light on the sensitivity of results due to hydraulic conductivity, the analyses were repeated with three additional hydraulic conductivity configurations for the interbedded layer:

- Case 2: variable hydraulic conductivity based on soil type as listed in Table 11.5.
- Case 3: constant hydraulic conductivity of 10^{-3} cm/s throughout the interbedded layer.
- Case 4: constant hydraulic conductivity of 10^{-5} cm/s throughout the interbedded layer.

Figs. 11.29 to 11.31 depict results obtained using these three new cases. Histograms of obtained lateral displacements from these three cases are compared in Figs. 11.32 and 11.33 to the base case, that utilized variable hydraulic conductivity based on FC as shown in Fig. 11.10, . As expected, case 3, that utilized the largest hydraulic conductivity, produced the smallest lateral displacements, 5.11 cm and 5.61 cm for west and east banks, respectively. While case 4, that utilized the smallest hydraulic conductivity, produced largest lateral displacements, with 6.85 cm and 6.37 cm for west and east banks, respectively.

The case using larger hydraulic conductivity showed less realization-to-realization variability, i.e., grey band shown in Fig. 11.30, indicating narrower variability compared to case 3 shown in Fig. 11.30. The difference, however, was not significant.

Table 11.5: Uniform hydraulic conductivity assigned to each constitutive model for case 2

Constitutive Model	Hydraulic Conductivity (cm/s)
PM4Sand	10^{-3}
PM4Silt	10^{-4}
PIMY	10^{-5}

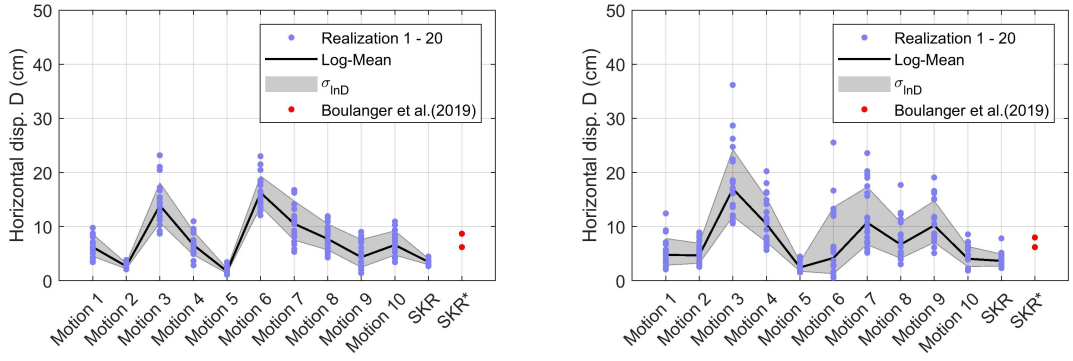

(a) West (b) East

Figure 11.29: Horizontal displacement toward the canal on the west and east banks from all realizations (lines) and motions (x axis), obtained from case 2, that utilized uniform hydraulic conductivity listed in Table 11.5.

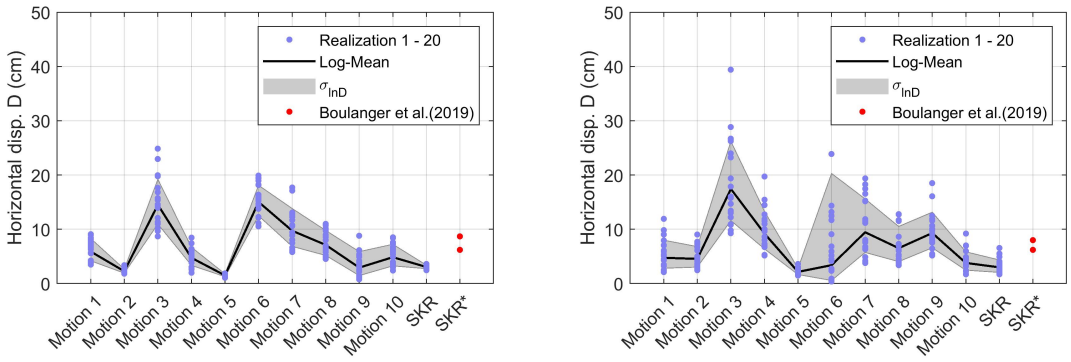

(a) West (b) East

Figure 11.30: Horizontal displacement toward the canal on the west and east banks from all realizations (lines) and motions (x axis), obtained from case 3, that utilized constant hydraulic conductivity of 10^{-3} cm/s throughout the interbedded layer.

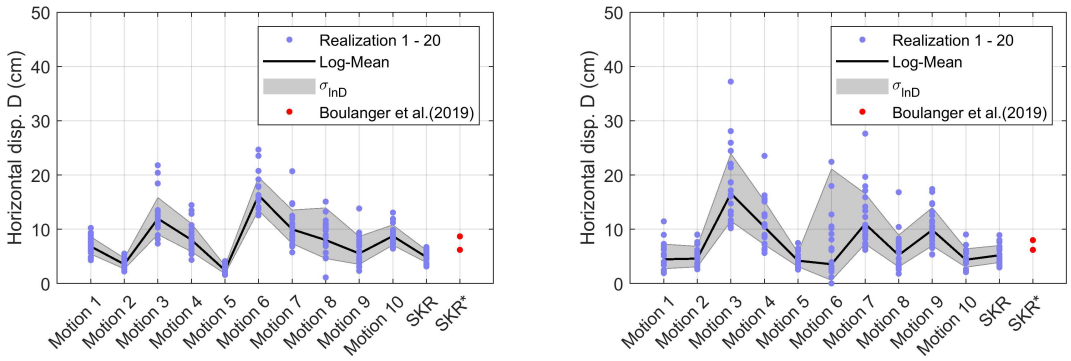

(a) West (b) East

Figure 11.31: Horizontal displacement toward the canal on the west and east banks from all realizations (lines) and motions (x axis), obtained from case 4, that utilized constant hydraulic conductivity of 10^{-5} cm/s throughout the interbedded layer.

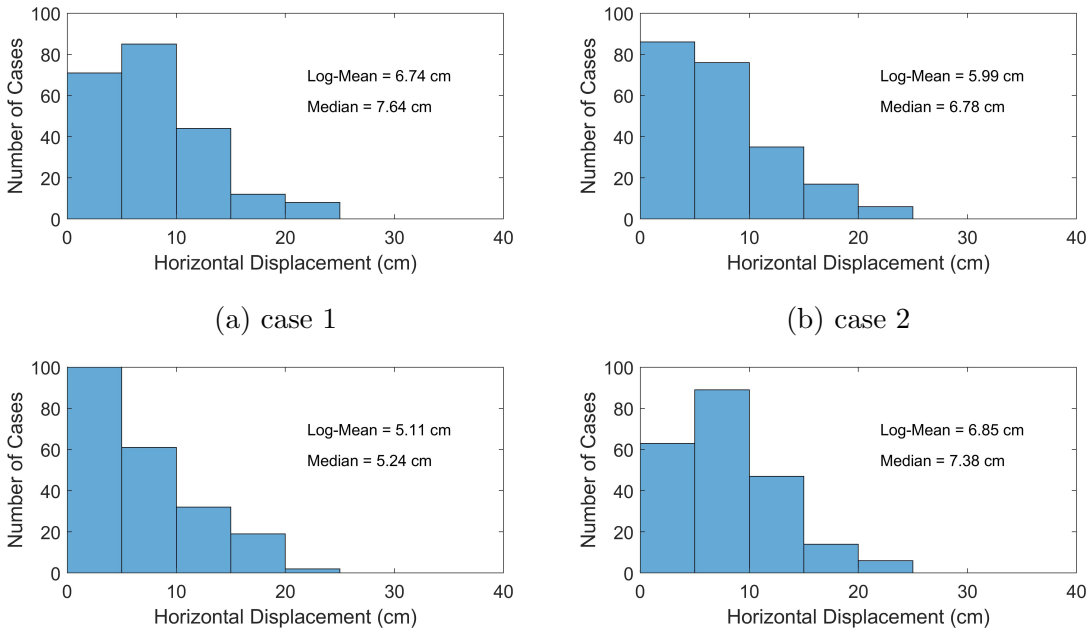

(a) case 1

(b) case 2

(c) case 3

(d) case 4

Figure 11.32: Comparison of horizontal displacement toward west bank obtained from simulations using four hydraulic conductivity configurations.

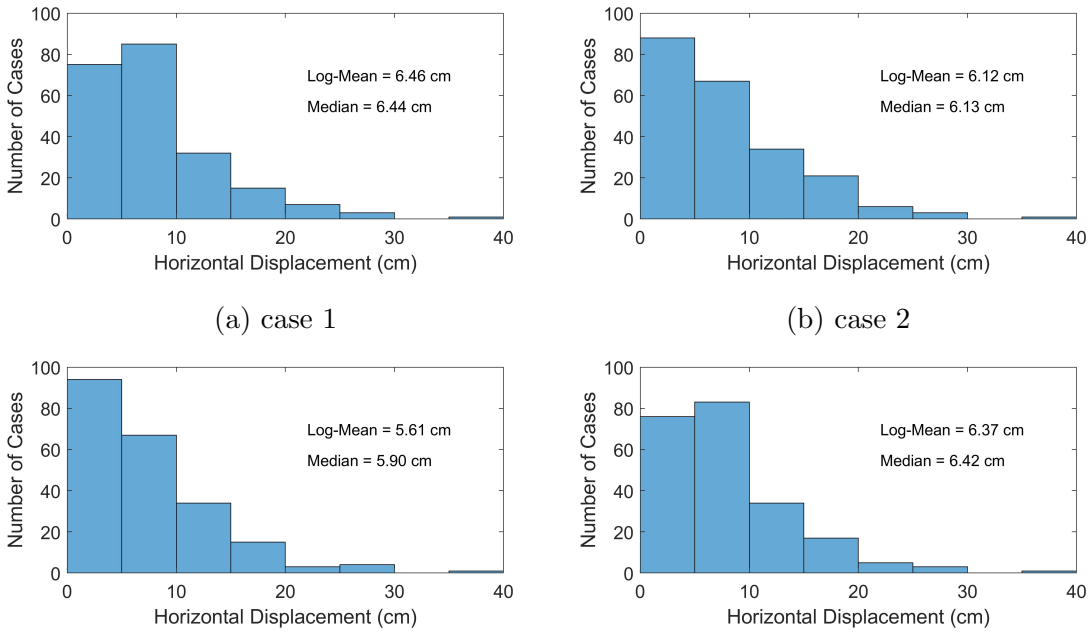

(a) case 1

(b) case 2

(c) case 3

(d) case 4

Figure 11.33: Comparison of horizontal displacement toward east bank obtained from simulations using four hydraulic conductivity configurations.

11.7 Summary

The seismic performance of the Çark Canal in the 1999 M = 7.5 Kocaeli earthquake was evaluated using effective stress analyses performed using PM4Sand and PM4Silt and OpenSees. These analyses complemented previous analyses by Youd et al. (2009) and Boulanger et al. (2019). In this study a new workflow for model selection and calibration was proposed. A numerical model was created using randomized FC and PI stochastic fields and simulations were complemented using additional motions. The obtained results were consistent with field observations and the results obtained using FLAC by Boulanger et al. (2019). Furthermore, this study provides the following improvements:

- The smooth transition of soil behavior within the interbedded layers was modeled. Following the workflow proposed in this study, soil behavior can vary among liquefiable sand-like, liquefiable clay-like, and non-liquefiable behavior in the developed FEM model. The assignment and calibration of the constitutive model parameters (PM4Sand, PM4Silt, and PIMY) was performed automatically to ensure smooth spatial variation of cyclic resistance of soil. This was enabled by a large scale parametric study ($\tilde{1}$5 million samples, presented in Chapter 3) using a constitutive driver developed for PM4Sand based on the OpenSees framework and UQ software Dakota.
- In addition to variability associated with input motion characteristics and spatial variability, sensitivity to motion polarity, undrained shear strength, and hydraulic conductivity were investigated. These analyses were achieved using OpenSees with parallel computing. During this process, the OpenSees implementation of PMSand and PM4Silt was extensively optimized for performance and stability. The SSPquadUP element was improved for parallelization and the PIMY material was extended to include strength corrected modulus reduction (G/G_{max}) curves. Compilation of OpenSees was also optimized on HPC systems. As a result, the computational performance was improved significantly.

In summary, the overall variability is presented in Fig. 11.34 as a tornado plot. Greatest variability was observed from record-to-record, followed by spatial variability. Some combina-

tion of realization and motion lead to overly conservative estimates of ground displacement. In general, the workflow yielded satisfactory results and shed light on the application of PM4Sand and PM4Silt to the numerical analysis of lateral spreading.

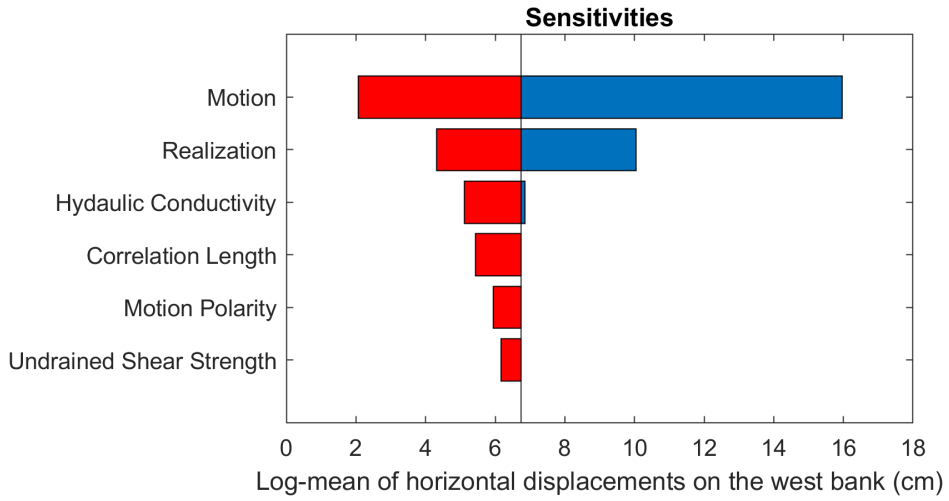

(a) West

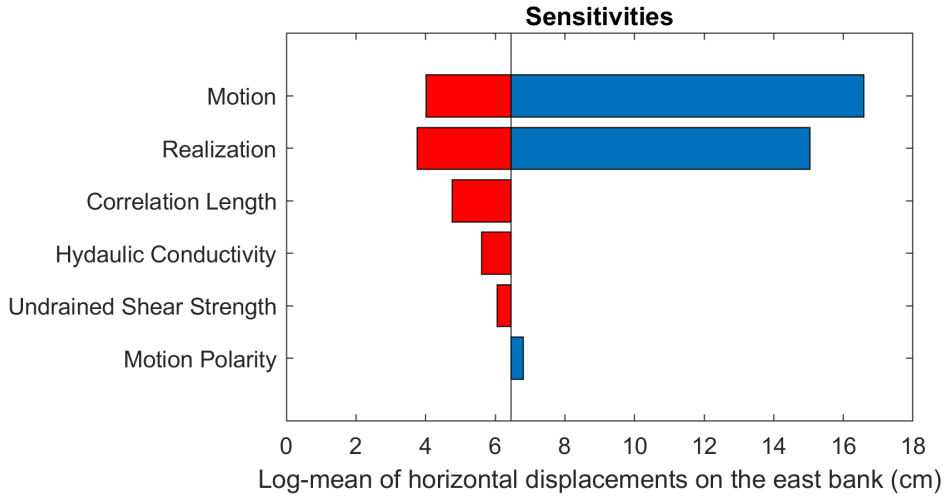

(b) East

Figure 11.34: Sensitivity (Tornado) plots for the log-mean of predicted lateral displacement toward the canal on the west and east banks, respectively.

Chapter 12

RESEARCH OUTCOMES AND RECOMMENDATIONS FOR FUTURE RESEARCH

This dissertation presents the implementation, verification, validation, and application of two advanced bounding surface constitutive models, PM4Sand and PM4Silt, in the OpenSees FEM framework. Specifically, this work concentrates on advanced constitutive modeling for the analysis of liquefaction induced lateral spreading in geotechnical earthquake engineering problems. The thesis includes a brief introduction to the PM4Sand and PM4Silt models and details about their implementation in OpenSees. A series of verification studies are performed at different levels. A validation study is also performed using 1D case histories, a large scale shake table test, and centrifuge experiments. Lastly, two application case-studies on the potential for liquefaction-induced lateral spreading considering spatial variability are presented.

12.1 Summary and conclusions

This section presents a summary of the work completed as part of this research. Basic aspects of each part are reiterated and conclusions drawn from these studies are emphasized.

12.1.1 Implementation of PM4Sand and PM4Silt in OpenSees

PM4Sand and PM4Silt are two constitutive models for earthquake engineering applications proposed by Boulanger and Ziotopoulou (2017, 2018) to represent sand-like and clay-like soil behavior (Boulanger and Idriss, 2006), respectively. In this study, both constitutive models were implemented in the OpenSees framework. Their implementation included bounding surface and yield surface stress correction strategies and several different integration schemes,

e.g., modified Euler method with automatic error control. The implementation was optimized for performance with built-in commands for users' choices.

A parametric study was conducted to investigate PM4Sand's behavior under a large range of parameters to shed light on its calibration. A correlation was proposed for h_{po} for a given combination of D_R, G_o, and CRR, that can be used to speed up a calibration process when calibration has to be performed for each soil unit in a profile that shows large geological variability. The slope of the CRR curve, b, obtained using PM4Sand was also presented and was shown to be representative for clean sands. The correlation appeared to be very useful for calibration purposes despite some limitation for representing dense sand behavior, and problems capturing the response observed in undrained CDSS tests performed on Ottawa F-65 sand (Bastidas, 2016) which showed b values that are less than what would be expected. This showed the limitation of just calibrating for primary parameters.

12.1.2 Verification of PM4Sand and PM4Silt in OpenSees

A verification study was presented for the PM4Sand and PM4Silt models implemented in OpenSees, which was meant to identify and remove programming errors in computer codes and verify numerical algorithms. The goal of this verification phase was to ensure OpenSees produced comparative results as the model's original implementation in FLAC. This was challenging since comparisons were between responses that were obtained using different numerical tools and systems, i.e., FEM and FDM. To address this issue, a series of stress point, single element, and 1D soil column analyses were performed such that system complexity was gradually increased and results were carefully examined to identify any inconsistency. The results showed that, despite discrepancies due to platform differences, i.e., FEM vs. FDM and different model discretization, that the OpenSees implementation produce consistent results to FLAC and PLAXIS.

12.1.3 Validation of PM4Sand and PM4Silt in OpenSees

A series of validation studies for PM4Sand and PM4Silt models implemented in OpenSees were performed, including a 1D analysis of two liquefaction array case-histories (WLA and Port Island) and a blind prediction of a large-scale shake table experiment. These studies illustrated capabilities and limitations of simulation of liquefaction sites using PM4Sand. The results obtained using PM4Sand for the liquefiable layers provided realistic and reasonable responses for all three cases with limited soil information, although further refinement of input parameters were warranted for better predictions.

12.1.4 Liquefaction Experiments and Analysis Projects (LEAP)

During the progression of this study, the author participated in a series of LEAP projects. LEAP (Liquefaction Experiments and Analysis Projects) (Manzari et al., 2017) is a new effort to validate liquefaction numerical models using centrifuge tests. In this thesis, three projects, LEAP-UCD-2017, LEAP-Asia-2019, and LEAP-RPI-2020, were presented and discussed.

LEAP-UCD-2017

In this LEAP project two constitutive models based on critical state soil mechanics and bounding surface plasticity, Manzari-Dafalias (Dafalias and Manzari, 2004) and PM4Sand, were calibrated independently to simulate the behavior of Ottawa-F65 sand in accordance with LEAP-UCD-2017 project guidelines. The calibrated models were then used to model the response of a boundary value problem using OpenSees. Besides using different material models, the same exact finite element model was used in all simulations. Type-B predictions were obtained and simulations compared to recorded data from centrifuge experiments at several facilities around the world.

The MD model was calibrated for general soil behavior, and number of loading cycles to trigger liquefaction under small CSR was not prioritized. In the calibration of PM4Sand, number of cycles to liquefaction observed in the laboratory tests results was emphasized and

used as a calibration criterion. The models' behavior at element level was compared and PM4Sand showed higher, and better, cyclic resistances to smaller CSRs than MD, while the two models showed very similar cyclic resistance at CSRs larger than 0.2.

Type-B prediction results showed that although calibrated using different methods, both models were able to predict the results from centrifuge experiments, especially the acceleration response at the frequency of the input motion. The evolution of excess pore pressures predicted by PM4Sand and MD were comparable and showed the similarity and differences in calibration process. The amount of predicted horizontal displacement was in the range of the recorded displacements at each facility.

LEAP-Asia-2018

For this phase of LEAP, type-C predictions were completed and compared to recorded data from centrifuge experiments. Both prototype and physical centrifuge scale models were built in the FEM framework OpenSees to simulate the response of Ottawa F65 sand in accordance with LEAP-Asia-2019 guidelines using the bounding surface plasticity constitutive model PM4Sand; calibrated using high quality laboratory test data. Type-C predictions were obtained and compared to recorded data from centrifuge experiments. The results were compared between prototype and physical centrifuge models as well as between Model-A (1-step scaling) and Model-B (2-step scaling).

In general, these type-C predictions showed PM4Sand was able to predict the results from centrifuge experiments, especially the acceleration response at the frequency of the input motion. The evolution of excess pore pressures predicted by PM4Sand was also comparable to experiments. The amount of predicted horizontal displacement was in the range of the recorded displacements for RPI and UCD cases but showed over-predication for the KyU case.

Comparison between prototype and physical centrifuge scale models showed consistent acceleration and pore pressure response along the centerline. However, it was shown that for the tangential shaking cases (i.e., KyU and UCD) the prototype scale models tended to

predict higher lateral displacements compared to the physical centrifuge scale model results. Many factors, including geometry, boundary conditions, direction of applied input motion, and horizontal gravity component presented in physical centrifuge scale models, were considered to be related to this phenomenon.

Comparison between Model-A and Model-B demonstrated that close attention should be given to the effect of initial stress state when generalized scaling laws are adopted. Numerical simulations showed that changes in initial stress state affected magnitudes of lateral displacements. In this study, models with higher initial stresses typically predicted larger lateral displacement for similar relative density and input motion. More studies, both centrifuge tests and numerical simulations, are needed in order to establish appropriate soil properties guidelines, e.g., relative density or soil fabric, to account for the effect of initial overburden pressure on liquefaction triggering and soil residual stress-strain behavior such that virtual intermediate scale results can be used to represent the interested prototype model response.

Higher CSRs and initial static shear stresses were found to be important for calibration of the constitutive model for this specific centrifuge experiment. It appears that in order to capture the behavior of the soil in the centrifuge experiment, appropriate CSR levels should be used. As such, current LEAP model calibration guidelines might not be using element tests representing the real conditions achieved in LEAP centrifuge experiments.

LEAP-RPI-2020

Simulations were performed to investigate the seismic response of a sheet pile retaining structure supporting liquefiable soils. MD and PM4Sand were calibrated independently to simulate the behavior of Ottawa-F65 sand in accordance with LEAP-RPI-2020 guidelines. The calibrated models were then used in a type-A prediction of element tests subjected to non-uniform cyclic loading and a Type-B prediction of liquefiable soils supported by a sheet pile wall. A 2D model was developed in OpenSees giving special consideration to modeling soil structure interaction and achieving a reasonable initial stress state.

Type-B predictions were obtained and simulations compared to recorded data from cen-

trifuge experiments at several facilities around the world. Type-B prediction results showed that although limitations existed in the numerical model, both constitutive models were able to predict the results from centrifuge experiments such as lateral displacements of the sheet pile wall, acceleration response, and evolution of excess pore pressures.

12.1.5 Potential for liquefaction-induced lateral spreading considering spatial variability: two case studies

As a final phase of this study, two application case-studies were considered to shed light on the capabilities of PM4Sand and PM4Silt implemented in OpenSees to address liquefaction related problems. The intention was to consider problems that are challenging using conventional methods and require advanced modeling, including large number of large models that require HPC resources. A summary of results for the to case-studies are presented next.

Estimation of EDP-IM relationships for a typical highway bridge embankment

As a first case, a typical highway bridge embankment was investigated with newly implemented PM4Sand and PM4Silt constitutive models in OpenSees to study the efficiency of IMs for performance based earthquake engineering (PBEE) analysis and selected demand parameters. For the PBEE analysis performed in this study, four different hazard levels of near-fault motions were considered in OpenSees simulations. Using OpenSees results, record-to-record uncertainties were estimated. In this estimation, relative efficiencies of several IMs were investigated to reduce the demand model uncertainties. Besides the record-to-record uncertainty, spatial variability uncertainty was also investigated using generalized stochastic fields.

The soil response, including lateral soil displacement and soil liquefaction, was investigated for different motions. At most hazard levels, except the lowest hazard level, most of the loose sand layer was liquefied, which resulted in lateral spreading beneath the embankments. EDP-IM relationships were obtained and efficiency of IMs was examined. These results showed that the most efficient IMs depends on the EDP being considered and soil

conditions. Overall, CAV_5 appeared to be the most efficient IM in predicting liquefaction induced lateral displacements in the studied case.

Liquefaction evaluation of interbedded soil deposit: a case study using PM4Sand and PM4Silt

As a second case, the seismic performance of Çark Canal in the 1999 M = 7.5 Kocaeli earthquake was evaluated using effective stress analyses performed using PM4Sand and PM4Silt models implemented in OpenSees. This analyses complements previous analyses by Youd et al. (2009) and Boulanger et al. (2019). A simple workflow for model selection and calibration was presented. This workflow was inspired by the work of Boulanger and Idriss (2007) and Bray and Sancio (2006) and aimed to represent the gradual transition of soil properties within interbedded layers and shed light on the application of PM4Sand and PM4Silt models. The effect of spatial variability within the interbedded layer based on variation of fines content (FC) and plasticity index (PI) was examined. Uncertainty in input motions and sensitivity in motion polarity, undrained shear strength, and hydraulic conductivity was also investigated.

The obtained results were consistent with field observations and the results obtained using FLAC by Boulanger et al. (2019). In addition to variability due to input motion characteristics and spatial variability, sensitivity to motion polarity, undrained shear strength, and hydraulic conductivity were investigated and the overall variability presented in the form of a tornado diagram. Greatest variability was observed from record-to-record, followed by spatial variability. Some combination of realization and motion lead to overly conservative estimates of ground displacement. Nevertheless, the workflow yielded satisfactory results and shed light on the application of PM4Sand and PM4Silt models to the numerical analysis of lateral spreading.

12.2 Summary of contributions

Based on the summary above, this dissertation provides the following contributions for numerical analysis of earthquake induced soil liquefaction:

- A complete new implementation of PM4Sand and PM4Silt models in OpenSees was conducted, which included implementation of parallelization method and optimization for performance and stability. The models' original formulations were preserved to the most extent, while several improvements, such as higher order integertors and yield surface correction, were added.
- Extensive verification studies were performed on both PM4Sand and PM4Silt using stress point, element, and 1D (level and sloped ground) models in OpenSees, FLAC, and PLAXIS. This step ensured consistency in results between these three software.
- A constitutive driver (MixedDriver) was developed for each model following the OpenSees framework. This customized driver allowed convenient control of initial and loading conditions at the stress point level and enabled a large scale parametric study to simplify the calibration of PM4Sand using the UQ software Dakota. This parametric study paved the road for selection of model parameters for the later case studies considering spatial variability.
- Other than these two constitutive models, several other improvements were introduced to OpenSees. The SSPquadUP element was improved for parallelization and the PIMY material was extended to include strength corrected modulus reduction (G/G_{max}) curves. Compilation of OpenSees was also optimized on HPC systems. As a result, the computational performance of OpenSees was improved significantly.
- Validation studies were performed using 1D case histories, a large scale shake table test, and centrifuge experiments. The two classical liquefaction array case studies, WLA and Port Island, were revisited with updated model parameters and material assignment. The blind prediction of a large scale shake table test was performed using two different modeling strategies and the results showed the importance of soil-structure interaction on liquefaction induced settlement. Participation on three LEAP projects provided high quality data that include model calibration, FEM model creation, and comparisons between constitutive models. Success and fallout of various modeling strategies were examined and presented. These LEAP projects shed light on the advantages and limitations of PM4Sand.

- Two case studies on embankments were performed to assess the models' applicability to simulate liquefaction induced lateral spreading. The first case focused on the evaluation of the efficiency of intensity measures, while the second case focused on the proper modeling of interbedded layers. The smooth transition of soil behavior within the interbedded layers was modeled. Following the workflow proposed in this study, soil behavior can be varied among liquefiable sand-like, liquefiable clay-like, and non-liquefiable behaviors in the developed FEM model. The assignment and calibration of the constitutive model parameters (PM4Sand, PM4Silt, and PIMY) was performed automatically to ensure smooth spatial variation of cyclic resistance of soil. In addition to variability associated with input motion characteristics and spatial variability, sensitivity on motion polarity, undrained shear strength, and hydraulic conductivity were investigated. With the optimized PM4Sand and PM4Silt in OpenSees, large amount of 2D analyses were able to be performed in the timely manner.

12.3 Recommendations for future research

The research performed in this dissertation reflects the latest development of advanced constitutive models for geotechnical earthquake engineering purposes and liquefaction. Several specific studies that would improve the understanding in numerical simulation of liquefaction hazards are summarized here.

12.3.1 Constitutive model

This study emphasized the calibration of PM4Sand and included a preliminary parametric studies on its calibration. Using the tools discussed in this document, this parametric study can be extended by including the secondary parameters. The effect of K_σ and K_α on cyclic resistance and strain accumulation should also be included. A similar parametric study can also be conducted for the calibration of PM4Silt.

PM4Sand and PM4Silt models can also be extended. They were developed only for 2D plane strain cases and extension of these models to 3D multiaxial cases would be very useful

yet challenging.

12.3.2 Standalone site response tool

The architecture of the OpenSees framework leads to its advantages such as efficiency and flexibility. However, learning OpenSees could be challenging for first time users giving its enormous available functionalities. Using OpenSees libraries, lighter and simpler specialized site response tools can be developed. And the implemented PM4Sand and PM4Silt models can be easily transplanted into these tools. For example, a tool providing a friendly interface for model generation, analysis, and results postprocessing and visualization could be very useful.

12.3.3 Additional case studies

The workflow presented in this study included only one possibility for model assignation based on FC and PI. Other indexes, such as soil behavior type index I_c, can also be used for this purpose and the workflow can be modified accordingly. The Çark canal case provides a case history showed insignificant lateral spreading related to interbedded soil layer. Additional case histories showing different degrees of ground movements can provide additional quantitative information to help improve the workflow presented in this document and better understand the effect of interbedded deposits on lateral spreading.

BIBLIOGRAPHY

Adams, B. M., Ebeida, M. S., Eldred, M. S., Jakeman, J. D., Swiler, L. P., and Eddy, J. P. (2017). "Dakota, a multilevel parallel object-oriented framework for design optimization, parameter estimation, uncertainty quantification, and sensitivity analysis: Version 6.7 reference manual.." *Report No. SAND2014-5015*, Sandia National Laboratories, Albuquerque, NM.

Alawaji, H., Runesson, K., Sture, S., and Axelsson, K. (1992). "Implicit integration in soil plasticity under mixed control for drained and undrained response." *International journal for numerical and analytical methods in geomechanics*, 16(10), 737–756.

Andrus, R. D. and Stokoe, K. H. (2000). "Liquefaction resistance of soils from shear wave velocity." *Journal of Geotechnical and Geoenvironmental Engineering*, 126(11), 1015–1025.

Armstrong, R. J., Boulanger, R. W., and Beaty, M. H. (2013). "Liquefaction effects on piled bridge abutments: Centrifuge tests and numerical analyses." *Journal of Geotechnical and Geoenvironmental Engineering*, 139(3), 433–443.

ASDEA Software (2020). *Scientific ToolKit for OpenSees*. `http://www.asdeasoft.net/stko?product-stko`. ASDEA Software, Pescara, Italy.

Bastidas, A. M. P. (2016). "Ottawa F-65 sand characterization." Ph.D. thesis, University of California, Davis, Davis, CA.

Been, K. and Jefferies, M. G. (1985). "A state parameter for sands." *Géotechnique*, 35(2), 99–112.

Bolton, M. D. (1986). "The strength and dilatancy of sands." *Géotechnique*, 36(1), 65–78.

Borja, R. I. and Amies, A. P. (1994). "Multiaxial cyclic plasticity model for clays." *Journal of Geotechnical Engineering*, 120(6), 1051–1070.

Boulanger, R. W. (2003). "Relating k_α to relative state parameter index." *Journal of Geotechnical and Geoenvironmental Engineering*, 770–773.

Boulanger, R. W. and Idriss, I. M. (2004). "State normalization of penetration resistance and the effect of overburden stress on liquefaction resistance." *11th International Conference on Soil Dynamics and Earthquake Engineering, and 3rd International Conference on Earthquake Geotechnical Engineering*, University of California, Berkeley.

Boulanger, R. W. and Idriss, I. M. (2006). "Liquefaction susceptibility criteria for silts and clays." *Journal of Geotechnical and Geoenvironmental Engineering*, 132(11), 1413–1426.

Boulanger, R. W. and Idriss, I. M. (2007). "Evaluation of cyclic softening in silts and clays." *Journal of Geotechnical and Geoenvironmental Engineering*, 133(6), 641–652.

Boulanger, R. W. and Idriss, I. M. (2014). "CPT and SPT based liquefaction triggering procedures." *Report No. UCD/CGM-14/01*, Department of Civil & Environmental Engineering, College of Engineering, University of California at Davis.

Boulanger, R. W., Munter, S. K., Krage, C. P., and Dejong, J. T. (2019). "Liquefaction evaluation of interbedded soil deposit: Çark Canal in 1999 m7.5 Kocaeli earthquake." *Journal of Geotechnical and Geoenvironmental Engineering*, 145(9), 1–16.

Boulanger, R. W. and Ziotopoulou, K. (2015). "PM4Sand (Version 3): a sand plasticity model for earthquake engineering applications." *Report No. UCD/CGM-15/01*, Center for Geotechnical Modeling, University of California at Davis.

Boulanger, R. W. and Ziotopoulou, K. (2017). "PM4Sand (Version 3.1): a sand plasticity model for earthquake engineering applications." *Report No. UCD/CGM-17/01*, Center for Geotechnical Modeling, University of California at Davis.

Boulanger, R. W. and Ziotopoulou, K. (2018). "PM4SILT (Version 1): a silt plasticity model for earthquake engineering applications." *Report No. UCD/CGM-18/01*, Center for Geotechnical Modeling, University of California at Davis.

Bray, J. D. and Dashti, S. (2014). "Liquefaction-induced building movements." *Bulletin of Earthquake Engineering*.

Bray, J. D. and Sancio, R. B. (2006). "Assessment of the liquefaction susceptibility of fine-grained soils." *Journal of Geotechnical and Geoenvironmental Engineering*, 132(9), 1165–1177.

Cetin, K. O., Tokimatsu, K., Harder, L. F., Moss, R. E. S., Kayen, R. E., Der Kiureghian, A., and Seed, R. B. (2004). "Standard penetration test-based probabilistic and deterministic assessment of seismic soil liquefaction potential." *Journal of Geotechnical and Geoenvironmental Engineering*, 130(12), 1314–1340.

Chen, L. and Arduino, P. (2020a). "Application of PM4Sand and PM4Silt models to study effect of spatial variability in liquefiable soil." Poster presented at PEER Annual Meeting, Berkeley, CA.

Chen, L. and Arduino, P. (2020b). "Implementation, verification, and validation of PM4Sand model in OpenSees". PEER Report - Submitted, under review.

Chen, L., Ghofrani, A., and Arduino, P. (2019). "Prediction of LEAP-UCD-2017 centrifuge test results using two advanced plasticity sand models." *Model Tests and Numerical Simulations of Liquefaction and Lateral Spreading: LEAP-UCD-2017*, B. L. Kutter, M. Manzari, and M. Zeghal, eds., Springer, 405–420.

Chen, L., Ghofrani, A., and Arduino, P. (2020). "Prediction of LEAP-Asia-2019 centrifuge test results using prototype- and physical-scale models". LEAP-Asia-2019 Proceedings - Submitted, under review.

Chen, L., Ghofrani, A., and Arduino, P. (2020, accepted). "Remarks on numerical simulation of the LEAP-Asia-2019 centrifuge tests"." *Soil dynamics and earthquake engineering*.

CIMNE (2020). *GiD, The universal, adaptative and user friendly pre and postprocessing system for computer analysis in science and engineering*. `https://www.gidhome.com/`. International Center for Numerical Methods in Engineering (CIMNE), Barcelona , Spain.

Cubrinovski, M. and Ishihara, K. (1998). "Modelling of sand behaviour based on state concept." *soils and foundations*, 38(3), 115–12.

Cubrinovski, M., Ishihara, K., and Furukawazono, K. (1999). "Analysis of two case histories on liquefaction of reclaimed deposits." *Proceedings of the Twelfth World Conference on Earthquake Engineering*, Auckland, New Zealand.

Cubrinovski, M., Ishihara, K., and Tanizawa, F. (1996). "Numerical simulation of the Kobe Port Island liquefaction." *Eleventh World Conference on Earthquake Engineering*, number 330, Acapulco, Mexico.

Dafalias, Y. (1986). "Bounding surface plasticity. i: mathematical foundation and hypoplasticity." *Journal of Engineering Mechanics*, 112(9), 966–987.

Dafalias, Y. F. (1980). "The concept and application of the bounding surface in plasticity theory." *Physical Non-Linearities in Structural Analysis*, J. Hult and J. Lemaitre, eds., Berlin, Heidelberg, Springer Berlin Heidelberg, 56–63.

Dafalias, Y. F. and Manzari, M. T. (2004). "Simple plasticity sand model accounting for fabric change effects." *Journal of Engineering Mechanics*, 130(6), 622–634.

Dafalias, Y. F. and Popov, E. P. (1977). "Cyclic loading for materials with a vanishing elastic region." *Nuclear Engineering and Design*, 41(2), 293–302.

Darendeli, M. B. (2001). "Development of a new family of normalized modulus reduction and material damping curves." Ph.D. thesis, University of Texas at Austin, Austin, TX.

Deierlein, G. G., Krawinkler, H., and Cornell, C. A. (2003). "A framework for performance-based earthquake engineering." *Proceedings of the 2003 Pacific Conference on Earthquake Engineering*, 273(140), 140–148.

Dowell, M. and Jarratt, P. (1972). "The "pegasus" method for computing the root of an equation." *BIT Numerical Mathematics*, 12(4), 503–508.

EduPro Civil Systems, I. (2017). *ProShake*. `http://www.proshake.com/`. EduPro Civil Systems, Inc., Sammamish, WA.

El Ghoraiby, M., Park, H., and Manzari, M. (2017). "Leap 2017: Soil characterization and element tests for ottawa f65 sand." *Report no.*, The George Washington University, Washington, DC.

El Ghoraiby, M., Park, H., and Manzari, M. (2019). "Physical and mechanical properties of ottawa f65 sand." *Model Tests and Numerical Simulations of Liquefaction and Lateral Spreading: LEAP-UCD-2017*, B. L. Kutter, M. Manzari, and M. Zeghal, eds., Springer.

Elgamal, A., Yang, Z., Parra, E., and Ragheb, A. (2003). "Modeling of cyclic mobility in saturated cohesionless soils." *International Journal of Plasticity*, 19(6), 883 – 905.

Ghofrani, A. (2018). "Development of numerical tools for the evaluation of pile response to laterally spreading soil." Ph.D. thesis, University of Washington, Seattle, WA.

Ghofrani, A. and Arduino, P. (2017). "Prediction of leap centrifuge test results using a pressure-dependent bounding surface constitutive model." *Soil Dynamics and Earthquake Engineering*, 113(August 2016), 758–770.

Gingery, J. R. and Elgamal, A. (2013). "Shear stress-strain curves based on the G/G_{max} logic: A procedure for strength compatibility." *IACGE 2013: Challenges and Recent Advances in Geotechnical and Seismic Research and Practices*, 721–729.

Gomez, B. W., Dewoolkar, M. M., Lens, J. E., and Benda, C. (2014). "Effects of fines content on hydraulic conductivity and shear strength of granular structural backfill." *Transportation Research Record*, 2462, 1–6.

Greenfield, M. (2017). "Effects of long-duration ground motions on liquefaction hazards." Ph.D. thesis, University of Washington, Seattle, WA.

Hashash, Y., Musgrove, M., Harmon, J., Groholski, D., Phillips, C., and Park, D. (2016). *DEEPSOIL 6.1, User Manual*. `http://deepsoil.cee.illinois.edu/`. Board of Trustees of University of Illinois at Urbana-Champaign, Urbana, IL.

Holzer, T. L. and Youd, T. L. (2007). "Liquefaction, ground oscillation, and soil deformation at the wildlife array, california." *Bulletin of the Seismological Society of America*, 97, 961–976.

Howell, R., Rathje, E. M., and Boulanger, R. W. (2014). "Evaluation of simulation models of lateral spread sites treated with prefabricated vertical drains." *Journal of Geotechnical and Geoenvironmental Engineering*.

Hyak (2020). *Hyak: A Shared Scalable Compute Cluster for Research*. `https://wiki.cac.washington.edu/display/hyakusers/WIKI+for+Hyak+users`. University of Washington, Seattle, WA.

Iai, S., Tobita, T., and Nakahara, T. (2005). "Generalised scaling relations for dynamic centrifuge tests." *Géotechnique*, 55(5), 355–362.

Idriss, I. M. and Boulanger, R. W. (2008). *Soil liquefaction during earthquakes*. MNO-12. Earthquake Engineering Research Institute, Oakland, Calif.

Ishihara, K. (1993). "Liquefaction and flow failure during earthquakes." *Géotechnique*, 43(3), 351–451.

Ishihara, K., Yasuda, S., and Nagase, H. (1996). "Soil characteristics and ground damage." *soils and foundations*, 109–118.

Itasca (2016). *FLAC - Fast Lagrangian Analysis of Continua, Version 8.0*. Itasca Consulting Group, Inc., Minneapolis, Minnesota.

Jose Parra, E. (1996). "Numerical modeling of liquefaction and lateral ground deformation including cyclic mobility and dilation response in soil systems." Ph.D. thesis, Rensselaer Polytechnic Institute, Troy, NY.

Kale, Ö., Akkar, S., Ansari, A., and Hamzehloo, H. (2015). "A ground-motion predictive model for iran and turkey for horizontal PGA, PGV, and 5% damped response spectrum: Investigation of possible regional effects." *Bulletin of the Seismological Society of America*, 105(2), 963–980.

Kartalis-Kaounis, T. and Papanikolaou, V. (2020). *GiD + OpenSees Interface*. `https://github.com/rclab-auth/gidopensees`. Aristotle University of Thessaloniki, Thessaloniki, Greece.

Khosravifar, A., Elgamal, A., Lu, J., and Li, J. (2018). "A 3d model for earthquake-induced liquefaction triggering and post-liquefaction response." *Soil Dynamics and Earthquake Engineering*, 110(March), 43–52.

Kramer, S. L. (1996). *Geotechnical Earthquake Engineering*. Pearson.

Kramer, S. L. and Mayfield, R. T. (2007). "Return period of soil liquefaction." *Journal of Geotechnical and Geoenvironmental Engineering*, 133(7), 802–813.

Kramer, S. L. and Mitchell, R. A. (2006). "Ground motion intensity measures for liquefaction hazard evaluation." *Earthquake Spectra*, 22(2), 413–438.

Kramer, S. L., Sideras, S. S., Greenfield, M., and Hushmand, B. (2018). "Liquefaction, ground motions, and pore pressures at the wildlife liquefaction array in the 1987 su-

perstition hills earthquake." *Geotechnical Earthquake Engineering and Soil Dynamics V*, 384–402.

Kunnath, S. K. (2006). "Application of the PEER PBEE Methodology to the I-880 Viaduct." *PEER Report 2006/10*, (february), 1–118.

Kutter, B. L., Carey, T. J., Hashimoto, T., Zeghal, M., Abdoun, T., Kokkali, P., Madabhushi, G., Haigh, S. K., D'Arezzo, F. B., Madabhushi, S., Hung, W.-Y., Lee, C.-J., Cheng, H.-C., Iai, S., Tobita, T., Ashino, T., Ren, J., Zhou, Y.-G., Chen, Y.-M., Sun, Z.-B., and Manzari, M. T. (2017). "LEAP-GWU-2015 experiment specifications, results, and comparisons." *Soil Dynamics and Earthquake Engineering*.

Kutter, B. L., Manzari, M. T., Zeghal, M., Arduino, P., Barrero, A. R., Carey, T. J., Chen, L., Elgamal, A., Ghofrani, A., Montgomery, J., Ozutsumi, O., Qiu, Z., Taiebat, M., Tobita, T., Travasarou, T., Tsiaousi, D., Ueda, K., Ugalde, J., Yang, M., Zheng, B. L., and Ziotopoulou, K. (2020). "Numerical sensitivity study compared to trend of experiments for LEAP-UCD-2017." *Model Tests and Numerical Simulations of Liquefaction and Lateral Spreading*, B. L. Kutter, M. T. Manzari, and M. Zeghal, eds., Cham, Springer International Publishing, 219–236.

Kwok, A. O. L., Stewart, J. P., Hashash, Y. M. a., Matasovic, N., Pyke, R., Wang, Z., and Yang, Z. (2007). "Use of exact solutions of wave propagation problems to guide implementation of nonlinear seismic ground response analysis procedures." *Journal of Geotechnical and Geoenvironmental Engineering*, 133(11), 1385–1398.

Lambe, T. W. (1973). "Predictions in soil engineering." *Geotechnique*, 23(2), 151–202.

LEAP-RPI-2020 Organizing Team (2020). "LEAP 2020 simulation exercise." *Guidelines for submission of the numerical simulations*, George Washington University, University of California, Davis, Rensselaer Polytechnic Institute, Cambridge University, Ehime University,

IFSTTAR, Kyoto University, KAIST, National Central University of Taiwan, Zhejiang University, Tokyo Institute of Technology.

Ledezma, C. A. and Bray, J. D. (2008). "Performance-based earthquake engineering design evaluation procedure for bridge foundations undergoing liquefaction-induced lateral ground displacement." *Report No. PEER Report 2008/05*, Pacific Earthquake Engineering Research Center.

Liu, A. H., Stewart, J. P., Abrahamson, N. A., and Moriwaki, Y. (2001). "Equivalent number of uniform stress cycles for soil liquefaction analysis." *Journal of Geotechnical and Geoenvironmental Engineering*, 127(12).

Luzi, L., Puglia, R., Russo, E., and ORFEUS WG5 (2016). *Engineering Strong Motion Database, Version 1.0*. Istituto Nazionale di Geofisica e Vulcanologia, Observatories & Research Facilities for European Seismology.

Lysmer, J. and Kuhlemeyer, A. M. (1969). "Finite dynamic model for infinite media." *Journal of the Engineering Mechanics Division, ASCE*, 95, 859–877.

Manzari, M. (2018). "LEAP-2019 - stress-strain response of Ottawa F65 sand in cyclic simple shear. doi:10.17603/DS2HX3H.

Manzari, M. T. and Dafalias, Y. F. (1997). "A critical state two-surface plasticity model for sands." *Géotechnique*, 47(2), 255–272.

Manzari, M. T., El Ghoraiby, M., Zeghal, M., Kutter, B. L., Arduino, P., Barrero, A. R., Bilotta, E., Chen, L., Chen, R., Chiaradonna, A., Elgamal, A., Fasano, G., Fukutake, K., Fuentes, W., Ghofrani, A., Ichii, K., Kiriyama, T., Lascarro, C., Mercado, V., Montgomery, J., Ozutsumi, O., Qiu, Z., Taiebat, M., Travasarou, T., Tsiaousi, D., Ueda, K., Ugalde, J., Wada, T., Wang, R., Yang, M., Zhang, J.-M., and Ziotopoulou, K. (2020). "LEAP-2017 simulation exercise: Calibration of constitutive models and simulation of the element tests." *Model Tests and Numerical Simulations of Liquefaction and Lateral*

Spreading, B. L. Kutter, M. T. Manzari, and M. Zeghal, eds., Cham, Springer International Publishing, 165–185.

Manzari, M. T., Ghoraiby, M. E., Kutter, B. L., Zeghal, M., Abdoun, T., Arduino, P., Armstrong, R. J., Beaty, M., Carey, T., Chen, Y., Ghofrani, A., Gutierrez, D., Goswami, N., Haigh, S. K., Hung, W.-Y., Iai, S., Kokkali, P., Lee, C.-J., Madabhushi, S. P. G., Mejia, L., Sharp, M., Tobita, T., Ueda, K., Zhou, Y., and Ziotopoulou, K. (2017). "Liquefaction Experiment and Analysis Projects (LEAP): Summary of observations from the planning phase." *Soil Dynamics and Earthquake Engineering*.

Manzari, M. T., Ghoraiby, M. E., Zeghal, M., Kutter, B. L., Arduino, P., Barrero, A. R., Bilotta, E., Chen, L., Chen, R., Chiaradonna, A., Elgamal, A., Fasano, G., Fukutake, K., Fuentes, W., Ghofrani, A., Haigh, S., Hung, W.-Y., Ichii, K., Kim, D. S., Kiriyama, T., Lascarro, C., Madabhushi, G. S., Mercado, V., Montgomery, J., Okamura, M., Ozutsumi, O., Qiu, Z., Taiebat, M., Tobita, T., Travasarou, T., Tsiaousi, D., Ueda, K., Ugalde, J., Wada, T., Wang, R., Yang, M., Zhang, J.-M., Zhou, Y.-G., and Ziotopoulou, K. (2019). "LEAP 2017: Comparison of the type B numerical simulations with centrifuge test results." *Model Tests and Numerical Simulations of Liquefaction and Lateral Spreading: LEAP-UCD-2017*, B. Kutter, M. Manzari, and M. Zeghal, eds., Davis, California, Springer, 175–207.

Martin, P. and Seed, H. B. (1982). "One-dimensional dynamic ground response analyses." *Journal of Geotechnical Engineering Division*, 108(7), 935–952.

Mason, H., Gallant, A. P., Hutabarat, D., Montgomery, J., Reed, N., and Wartman, J. (2019). "Geotechnical reconnaissance: the 28 September 2018 M7.5 Palu-Donggala, Indonesia Earthquake." *Report No. April 2019*, The Geotechnical Extreme Events Reconnaissance (GEER) Association.

Maurer, B. W., Green, R. A., Cubrinovski, M., and Bradley, B. A. (2014). "Evaluation

of the liquefaction potential index for assessing liquefaction hazard in christchurch , new zealand." *J. Geotech. Geoenviron. Eng*, 140(7), 1–11.

Mayfield, R. T. (2007). "Return period of soil liquefaction." Ph.D. thesis, University of Washington, Seattle, WA.

McGann, C. R., Arduino, P., and Mackenzie-Helnwein, P. (2012). "Stabilized single-point 4-node quadrilateral element for dynamic analysis of fluid saturated porous media." *Acta Geotechnica*, 7(4), 297–311.

McGann, C. R., Arduino, P., and Mackenzie-Helnwein, P. (2015). "A stabilized single-point finite element formulation for three-dimensional dynamic analysis of saturated soils." *Computers and Geotechnics*, 66(0), 126–141.

McKenna, F., Padhye, N., Wang, C., Mackenzie-Helnwein, P., and Gardner, M. (2018). *NHERI-SimCenter/uqFEM: Release V1.1.0* (oct).

Menq, F.-Y. (2003). "Dynamic properties of sandy and gravelly soils." Ph.D. thesis, The University of Texas at Austin, Austin, TX.

Montgomery, J. (2012). "Issues in nonlinear deformation analyses of embankment dams affected by liquefaction." Ph.D. thesis, University of California Davis, Davis, CA.

Montgomery, J. and Boulanger, R. W. (2017). "Effects of spatial variability on liquefaction-induced settlement and lateral spreading." *Journal of Geotechnical and Geoenvironmental Engineering*, 143(1), 04016086.

Moss, R. E., Seed, R. B., Kayen, R. E., Stewart, J. P., Der Kiureghian, A., and Cetin, K. O. (2006). "CPT-based probabilistic and deterministic assessment of in situ seismic soil liquefaction potential." *Journal of Geotechnical and Geoenvironmental Engineering*, 132(8), 1032–1051.

Motamed, R., Orang, M. J., Parayancode, A., and Elgamal, A. (2020). "Results of a Class C blind prediction competition on the numerical simulation of a large-scale liquefaction shaking table test." *Geo-Congress 2020*, J. Hambleton, R. Makhnenko, and A. Budge, eds., number GSP 315, Minneapolis, Minnesota, 334–342.

Muir Wood, D. (1990). *Soil Behaviour and Critical State Soil Mechanics*. Cambridge University Press.

Munter, S. K., Boulanger, R. W., Krage, C. P., and DeJong, J. T. (2017). "Evaluation of liquefaction-induced lateral spreading procedures for interbedded deposits: Çark Canal in the 1999 M7.5 Kocaeli earthquake." *Geotechnical Special Publication*, number GSP 281, American Society of Civil Engineers (ASCE), 254–266.

OpenSees (2007). *Open System for Earthquake Engineering Simulation*. `http://opensees.berkeley.edu`. Pacific Earthquake Engineering Research Center (PEER), University of California, Berkeley.

Phoon, K. K. and Kulhawy, F. H. (1999). "Characterization of geotechnical variability." *Canadian Geotechnical Journal*, 36(4), 612–624.

Plaxis.B.V (2018). *PLAXIS 2D*. `https://www.plaxis.com/product/plaxis-2d/`. Plaxis.B.V, Delft, Netherlands.

Polito, C. P. (1999). "The effects of non-plastic and plastic fines on the liquefaction of sandy soils." Ph.D. thesis, Virginia Polytechnic Institute and State University, Blacksburg, VA.

Polito, C. P. and Martin, J. R. (2001). "Effects of non-plastic fines on the liquefaction resistance of sands." *Journal of Geotechnical and Geoenvironmental Engineering*, 127(5), 408–415.

Potts, D. M. and Gens, A. (1985). "A critical assessment of methods of correcting for drift from the yield surface in elasto-plastic finite element analysis." *International Journal for Numerical and Analytical Methods in Geomechanics*, 9(2), 149–159.

Ramirez, J., Barrero, A., Chen, L., Dashti, S., Ghofrani, A., Taiebat, M., and Arduino, P. (2018a). "Site response in a layered liquefiable deposit: Evaluation of different numerical tools and methodologies with centrifuge experimental results." *Journal of Geotechnical and Geoenvironmental Engineering*, 144(10), 04018073.

Ramirez, J., Barrero, A., Chen, L., Ghofrani, A., Dashti, S., Taiebat, M., and Arduino, P. (2018b). "Capabilities and limitations of different numerical tools in capturing seismic site performance in a layered liquefiable site." *Geotechnical Earthquake Engineering and Soil Dynamics V: Numerical Modeling and Soil Structure Interaction*, S. J. Brandenberg and M. T. Manzari, eds., number GSP 292.

Ramos, A. (2010). "Instabilities in sands." Ph.D. thesis, Universidad de los Andes, Bogotá, Colombia.

Rathje, E., Clint, D., E., P. J., Jean-Paul, P., Dan, S., Ashley, A., Pedro, A., J., B. S., Tim, C., Charlie, D., Maria, E., L., H. F., Matthew, H., Ahsan, K., Laura, L., Stephen, M., and Gilberto, M. (2017). "Designsafe: New cyberinfrastructure for natural hazards engineering." *Natural Hazards Review*, 18(3), 6017001.

Régnier, J., Bonilla, L. F., Bard, P. Y., Bertrand, E., Hollender, F., Kawase, H., Sicilia, D., Arduino, P., Amorosi, A., Asimaki, D., Boldini, D., Chen, L., Chiaradonna, A., Demartin, F., Ebrille, M., Elgamal, A., Falcone, G., Foerster, E., Foti, S., Garini, E., Gazetas, G., Gélis, C., Ghofrani, A., Giannakou, A., Gingery, J. R., Glinsky, N., Harmon, J., Hashash, Y., Iai, S., Jeremić, B., Kramer, S., Kontoe, S., Kristek, J., Lanzo, G., Di Lernia, A., Lopez-Caballero, F., Marot, M., McAllister, G., Mercerat, E. D., Moczo, P., Montoya-Noguera, S., Musgrove, M., Nieto-Ferro, A., Pagliaroli, A., Pisanò, F., Richterova, A., Sajana, S., Santisi D'avila, M. P., Shi, J., Silvestri, F., Taiebat, M., Tropeano, G., Verrucci, L., and Watanabe, K. (2016). "International benchmark on numerical simulations for 1d, nonlinear site response (prenolin): Verification phase based on canonical cases." *Bulletin of the Seismological Society of America*, 106(5), 2112–2135.

Régnier, J., Bonilla, L. F., Bard, P. Y., Bertrand, E., Hollender, F., Kawase, H., Sicilia, D., Arduino, P., Amorosi, A., Asimaki, D., Boldini, D., Chen, L., Chiaradonna, A., Demartin, F., Elgamal, A., Falcone, G., Foerster, E., Foti, S., Garini, E., Gazetas, G., Gélis, C., Ghofrani, A., Giannakou, A., Gingery, J., Glinsky, N., Harmon, J., Hashash, Y., Iai, S., Kramer, S., Kontoe, S., Kristek, J., Lanzo, G., Lernia, A. D., Lopez-Caballero, F., Marot, M., McAllister, G., Mercerat, E. D., Moczo, P., Montoya-Noguera, S., Musgrove, M., Nieto-Ferro, A., Pagliaroli, A., Passeri, F., Richterova, A., Sajana, S., Santisi D'Avila, M. P., Shi, J., Silvestri, F., Taiebat, M., Tropeano, G., Vandeputte, D., and Verrucci, L. (2018). "Prenolin: International benchmark on 1d nonlinear: Site-response analysis-validation phase exercise." *Bulletin of the Seismological Society of America*, 108(2), 876–900.

Robertson, P. K. (1991). "Soil classification using the cone penetration test." *Canadian Geotechnical Journal*, 28(1), 176–178.

Robertson, P. K. and Cabal, K. L. (2015). *Guide to cone penetration testing for geotechnical engineering*.

Robertson, P. K. and Wride, C. (1998). "Evaluating cyclic liquefaction potential using the cone penetration test." *Canadian Geotechnical Journal*, 35(3), 442–459.

Schofield, A. and Wroth, C. (1968). "Critical state soil mechanics." *Soil Use and Management*, 228.

Seed, H. B. and Idriss, I. M. (1971). "Simplified procedure for evaluating soil liquefaction potential." *ASCE J Soil Mech Found Div*, 97(9), 1249–1273.

Seed, H. B., Martin, P., and Lysmer, J. (1975). *The Generation and Dissipation of Pore Water Pressures During Soil Liquefaction*. College of Engineering, University of California.

Shin, H. (2007). "Numerical modeling of a bridge system & its application for performance-based earthquake engineering." Ph.D. thesis, University of Washington, Seattle, WA.

Sideras, S. S. (2011). "Response of liquefiable soil deposits to earthquake loading"." Master's thesis, University of Washington, Seattle, WA.

Sideras, S. S. (2019). "Evolutionary intensity measures for more accurate and informative evaluation of liquefaction triggering." Ph.D. thesis, University of Washington, Seattle, WA.

Sloan, S. W., Abbo, A. J., and Sheng, D. (2001). "Refined explicit integration of elastoplastic models with automatic error control." *Engineering Computations*, 18(1/2), 121–194.

Somerville, P. G. and Collins, N. (2002). "Ground motion time histories for the I880 Bridge-Oakland." *Report to PEER methodology testbeds projects, URS Corporation.*

Taiebat, M. and Dafalias, Y. F. (2008). "Sanisand: Simple anisotropic sand plasticity model." *International Journal for Numerical and Analytical Methods in Geomechanics*, 32(8), 915–948.

Taiebat, M., Jeremić, B., Dafalias, Y. F., Kaynia, A. M., and Cheng, Z. (2010). "Propagation of seismic waves through liquefied soils." *Soil Dynamics and Earthquake Engineering*, 30(4), 236–257.

Tobita, T. and Iai, S. (2011). "Application of the generalized scaling law to liquefiable model ground." *Annual Report of Disaster Prevention Research Institute*, (54), 225 – 236.

Ueda, K. (2018). "LEAP-Asia-2018: Stress-strain response of ottawa sand in cyclic torsional shear tests. doi:10.17603/DS2D40H.

Ueda, K., Sawada, K., Wada, T., Tobita, T., and Iai, S. (2019). "Applicability of the generalized scaling law to a pile-inclined ground system subject to liquefaction-induced lateral spreading." *Soils and Foundations.*

Vasko, A. (2015). "An investigation into the behavior of Ottawa sand through monotonic and cyclic shear tests." Ph.D. thesis, The George Washington University, Washington, D.C.

Vilhar, G., Laera, A., Foria, F., Gupta, A., and Brinkgreve, R. (2018). "Implementation, validation and application of PM4Sand model in PLAXIS." *Geotechnical Earthquake Engineering and Soil Dynamics V*, 200–211.

Wang, G. and Sitar, N. (2006). "Nonlinear analysis of a soil-drilled pier system under static and dynamic axial loading." *Report No. PEER 2006/06*, Pacific Earthquake Engineering Research Center.

Yamazaki, F. and Shinozuka, M. (1988). "Digital generation of Non-Gaussian stochastic fields." *Journal of Engineering Mechanics*, 114(7), 1183–1197.

Yang, Z. (2000). "Numerical modeling of earthquake site response including dilation and liquefaction." Ph.D. thesis, Columbia University, New York, NY.

Yang, Z., Elgamal, A., and Parra, E. (2003). "Computational model for cyclic mobility and associated shear deformation." *Journal of Geotechnical and Geoenvironmental Engineering*, 129(12), 1119–1127.

Yang, Z., Lu, J., and Elgamal, A. (2008). "OpenSees soil models and solid-fluid fully coupled elements." *Report No. October*, University of California, San Diego.

Youd, T. L., Bartholomew, H. A. J., and Proctor, J. S. (2004). "Geotechnical logs and data from permanently instrumented field sites: Garner Valley Downhole Array (GVDA) and Wildlife Liquefaction Array (WLA)." *Report no.*, Brigham Young University.

Youd, T. L., DeDen, D. W., Bray, J. D., Sancio, R., Cetin, K. O., and Gerber, T. M. (2009). "Zero-displacement lateral spreads, 1999 Kocaeli, Turkey, earthquake." *Journal of Geotechnical and Geoenvironmental Engineering*.

Youd, T. L., Çetin, K., Bray, J., R., S., Durgunoglu, H., and Önalp, A. (2000). *Geotechnical Site Investigation at Lateral Spread Sites*. `https://apps.peer.berkeley.edu/publications/turkey/adapazari/phase4/cark/index.html`. Collaborative Research

by U.C. Berkeley, Brigham Young Univ., and UCLA with ZETAS, Sakarya Univ., and Middle East Technical Univ., University of California, Berkeley.

Youd, T. L., Hansen, C. M., and Bartlett, S. F. (2002). "Revised multilinear regression equations for prediction of lateral spread displacement." *Journal of Geotechnical and Geoenvironmental Engineering*, 128(12), 1007–1017.

Youd, T. L. and Idriss, I. M. (2001). "Liquefaction resistance of soils: Summary report from the 1996 nceer and 1998 nceer/nsf workshops on evaluation of liquefaction resistance of soils." *Journal of Geotechnical and Geoenvironmental Engineering*, 127(4), 297–313.

Zare, M., Amini, H., Yazdi, P., Sesetyan, K., Demircioglu, M. B., Kalafat, D., Erdik, M., Giardini, D., Khan, M. A., and Tsereteli, N. (2014). "Recent developments of the Middle East catalog." *Journal of Seismology*, 18(4), 749–772.

Zeghal, M., Goswami, N., Kutter, B. L., Manzari, M. T., Abdoun, T., Arduino, P., Armstrong, R., Beaty, M., Chen, Y.-M., Ghofrani, A., Haigh, S., Hung, W.-Y., Iai, S., Kokkali, P., Lee, C.-J., Madabhushi, G., Tobita, T., Ueda, K., Zhou, Y.-G., and Ziotopoulou, K. (2017). "Stress-strain response of the LEAP-2015 centrifuge tests and numerical predictions." *Soil Dynamics and Earthquake Engineering*.

Zhu, M., McKenna, F., and Scott, M. H. (2018). "OpenSeesPy: Python library for the OpenSees finite element framework." *SoftwareX*, 7, 6–11.

Ziotopoulou, K. (2010). "Evaluating model uncertainty against strong motion records at liquefiable sites." M.S. thesis, University of California, Davis, Davis, CA.

Ziotopoulou, K. (2017). "Seismic response of liquefiable sloping ground: Class A and C numerical predictions of centrifuge model responses." *Soil Dynamics and Earthquake Engineering*.

Ziotopoulou, K. and Boulanger, R. W. (2013). "Calibration and implementation of a sand plasticity plane-strain model for earthquake engineering applications." *Soil Dynamics and Earthquake Engineering*, 53, 268–280.

Ziotopoulou, K., Boulanger, R. W., Kramer, S. L., and S.L., K. (2012). "Site response analysis of liquefying sites." *Geo-Congress 2012: State of the art and practice in Geotechnical engineering*, number March 2012, 1799–1808.

Ziotopoulou, K., Montgomery, J., Bastidas, A., and Morales, B. (2018). "Cyclic strength of Ottawa F-65 sand: Laboratory testing and constitutive model calibration." *Geotechnical Earthquake Engineering and Soil Dynamics V: Slope Stability and Landslides, Laboratory Testing, and In Situ Testing*, S. J. Brandenberg and M. T. Manzari, eds., number GSP 293, 394–403.

Appendix A

ADDITIONAL PM4SAND VERIFICATION RESULTS

A.1 N5T3

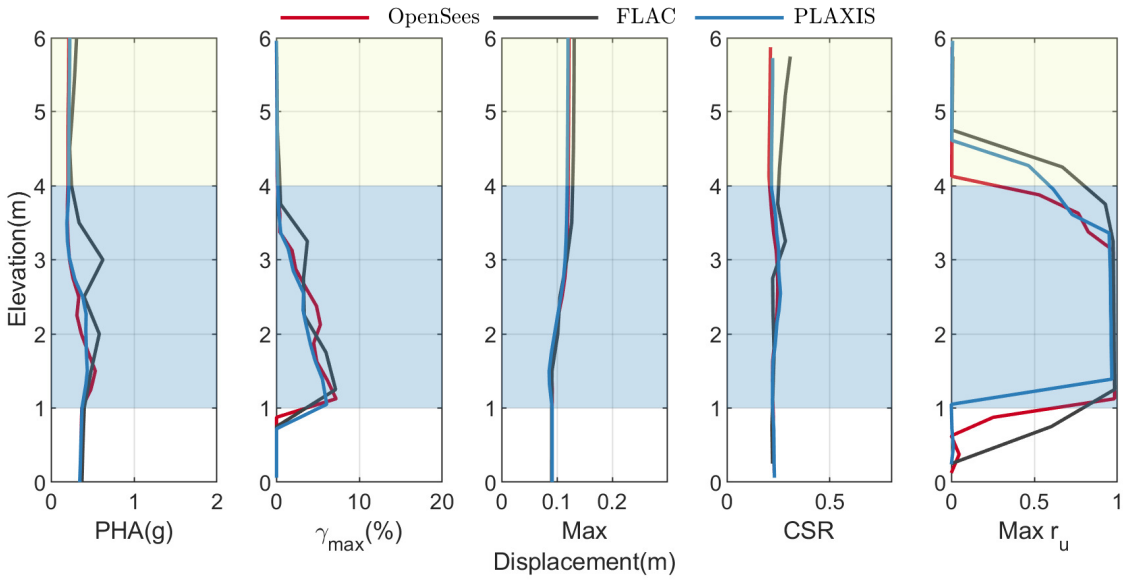

Figure A.1: Comparison of profile of PHA, γ_{max}, maximum displacement, CSR, and max r_u obtained using OpenSees, FLAC, and PLAXIS for motion RSN766.

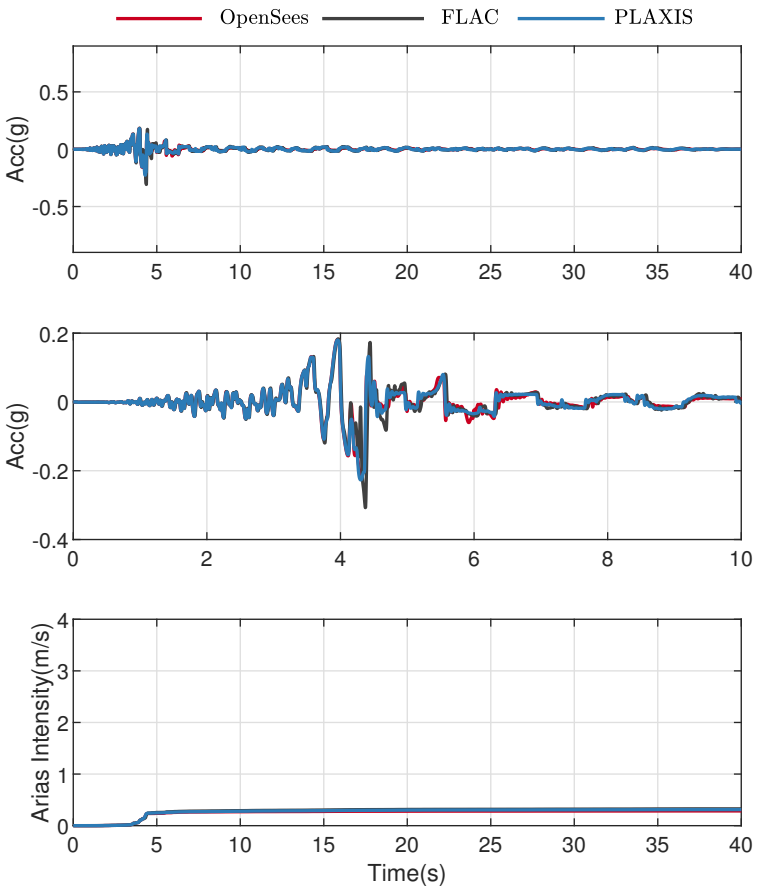

Figure A.2: Comparison of acceleration time histories at surface obtained using OpenSees, FLAC, and PLAXIS for motion RSN766.

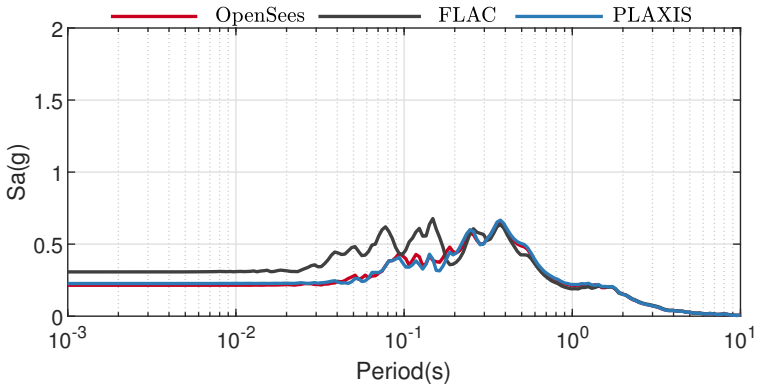

Figure A.3: Comparison of acceleration response spectra at surface obtained using OpenSees, FLAC, and PLAXIS for motion RSN766.

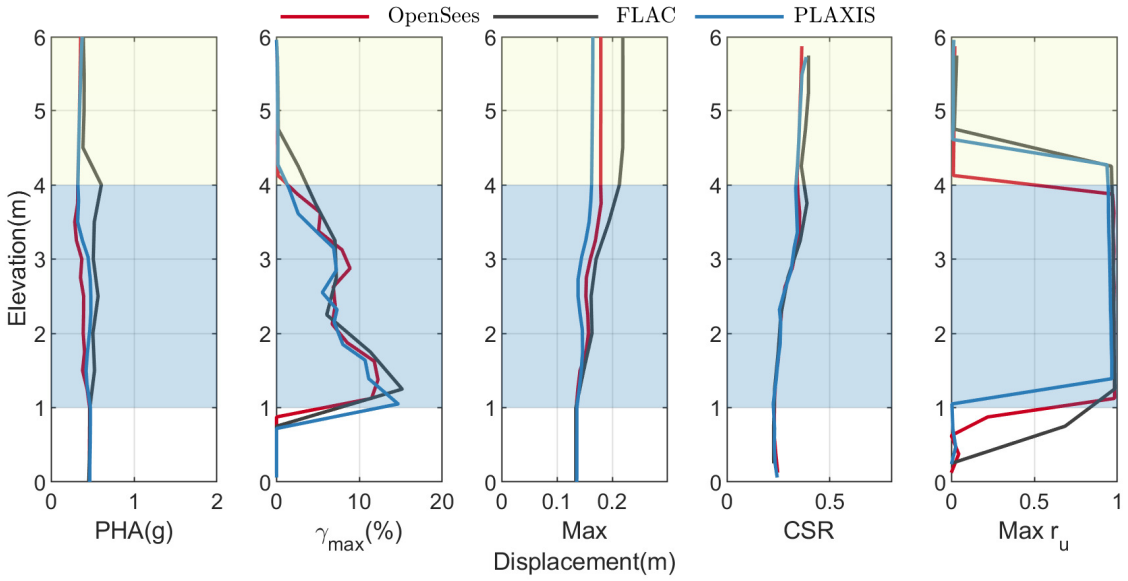

Figure A.4: Comparison of profile of PHA, γ_{max}, maximum displacement, CSR, and max r_u obtained using OpenSees, FLAC, and PLAXIS for motion RSN963.

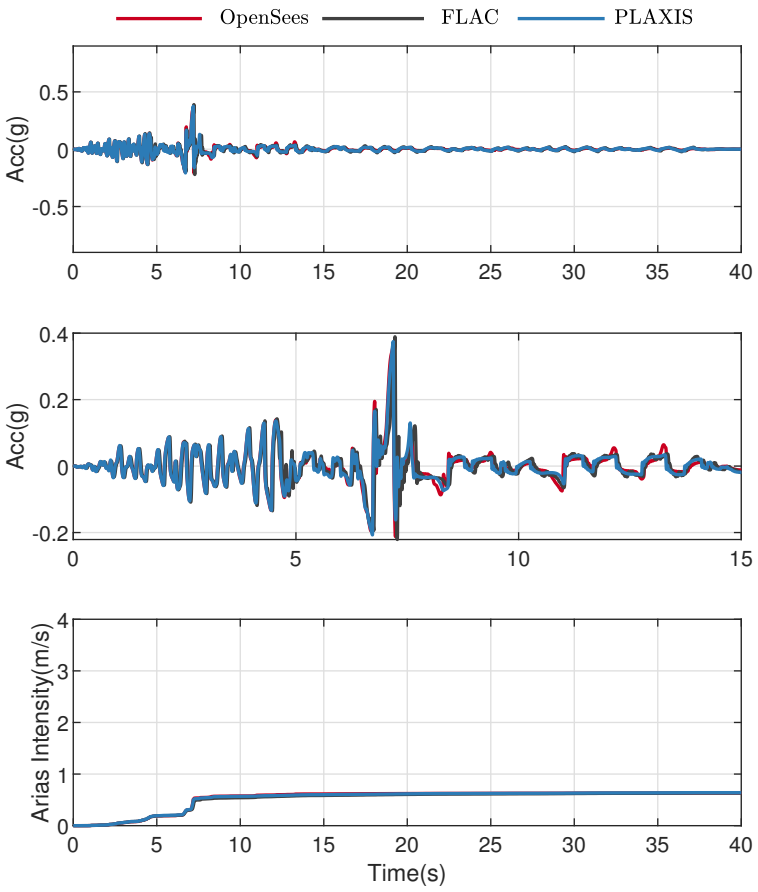

Figure A.5: Comparison of acceleration time histories at surface obtained using OpenSees, FLAC, and PLAXIS for motion RSN963.

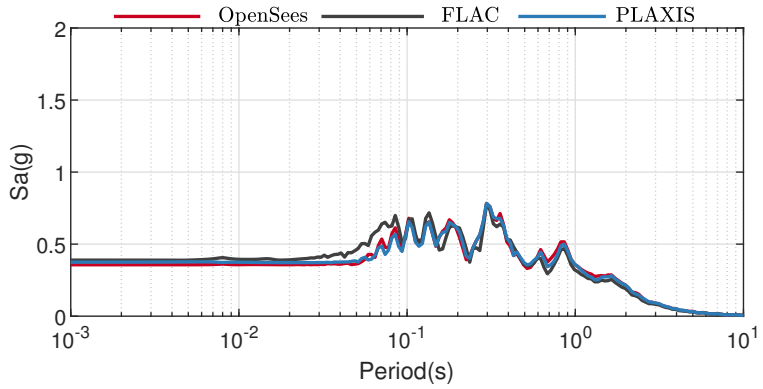

Figure A.6: Comparison of acceleration response spectra at surface obtained using OpenSees, FLAC, and PLAXIS for motion RSN963.

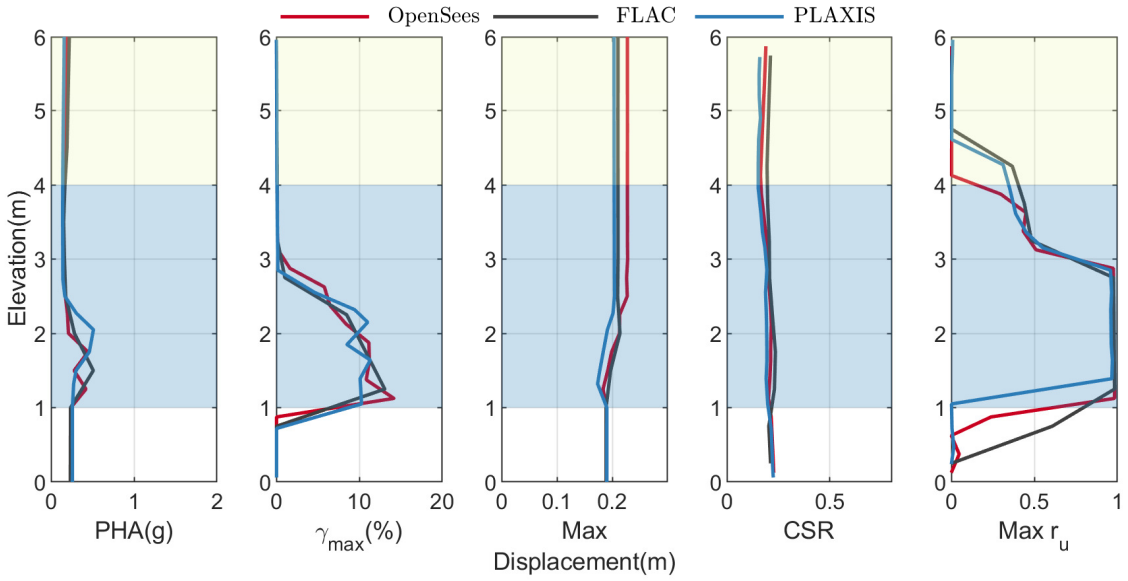

Figure A.7: Comparison of profile of PHA, γ_{max}, maximum displacement, CSR, and max r_u obtained using OpenSees, FLAC, and PLAXIS for motion RSN1203.

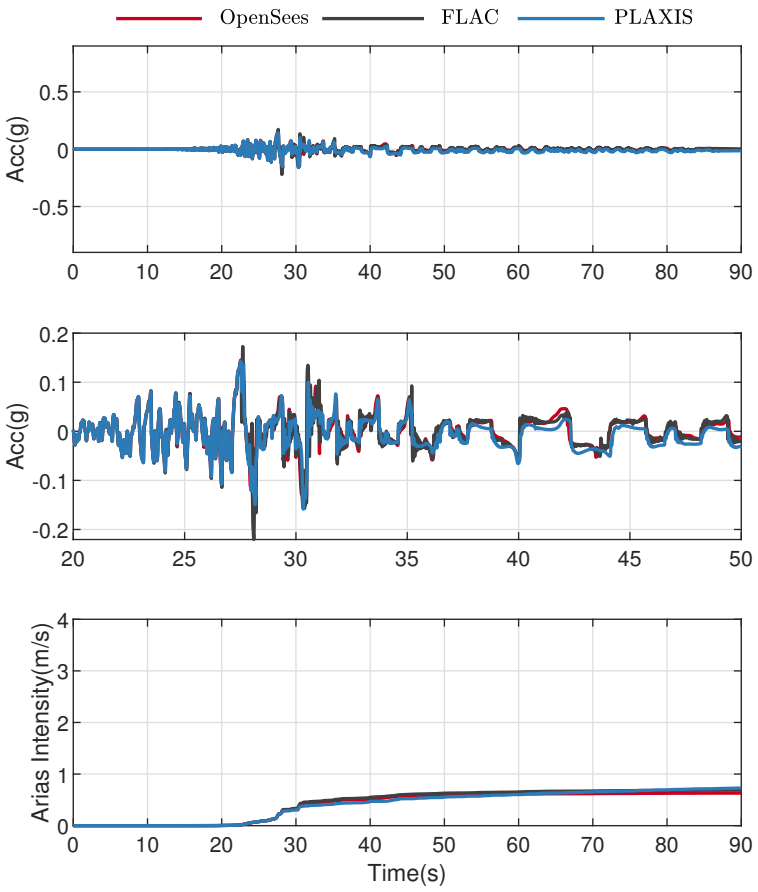

Figure A.8: Comparison of acceleration time histories at surface obtained using OpenSees, FLAC, and PLAXIS for motion RSN1203.

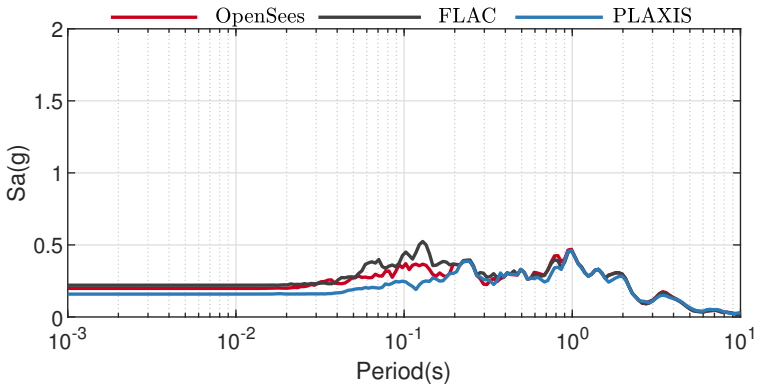

Figure A.9: Comparison of acceleration response spectra at surface obtained using OpenSees, FLAC, and PLAXIS for motion RSN1203.

A.2 N5T6

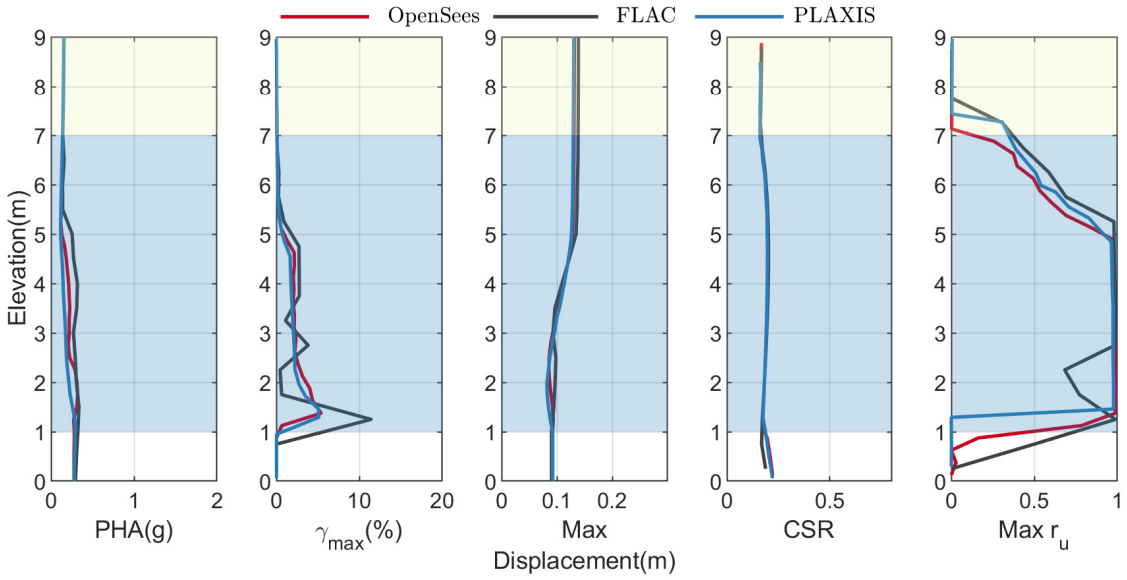

Figure A.10: Comparison of profile of PHA, γ_{max}, maximum displacement, CSR, and max r_u obtained using OpenSees, FLAC, and PLAXIS for motion RSN766.

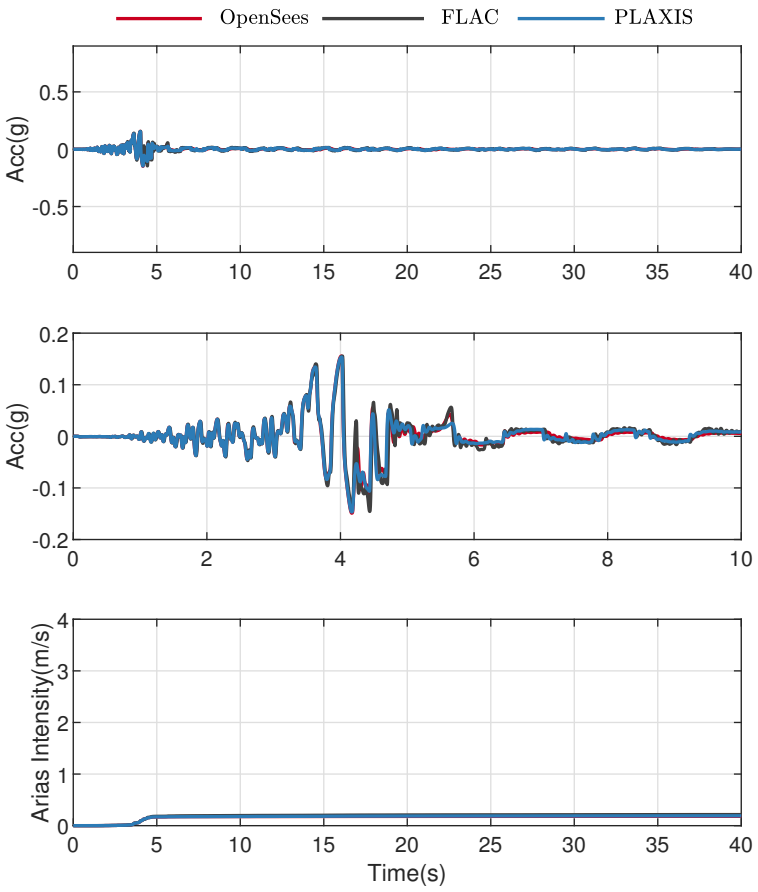

Figure A.11: Comparison of acceleration time histories at surface obtained using OpenSees, FLAC, and PLAXIS for motion RSN766.

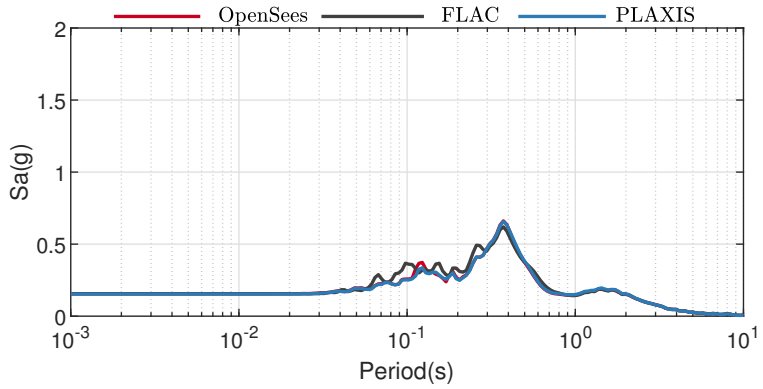

Figure A.12: Comparison of acceleration response spectra at surface obtained using OpenSees, FLAC, and PLAXIS for motion RSN766.

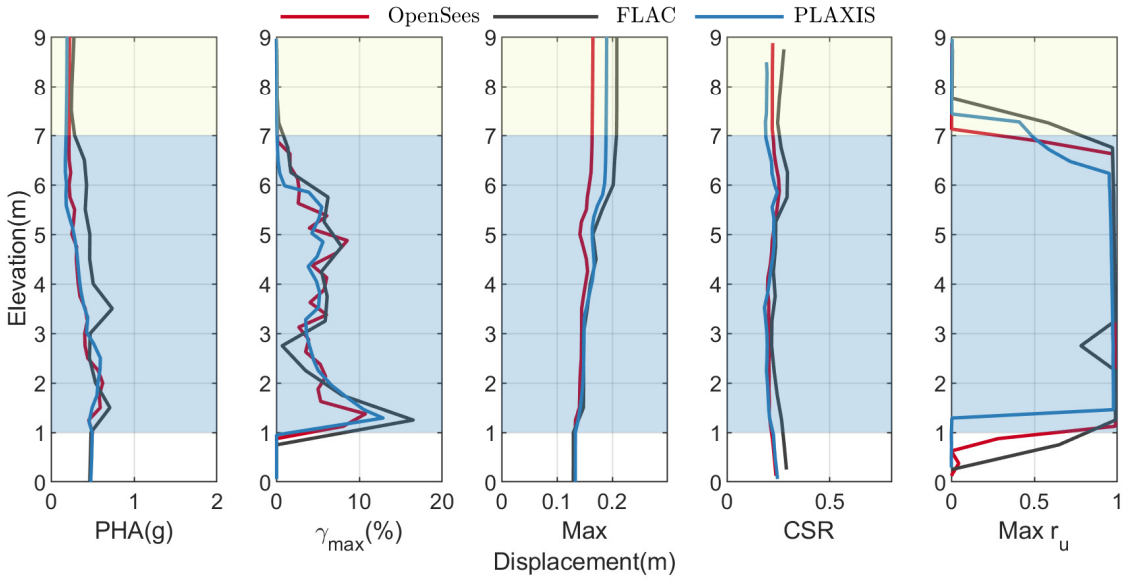

Figure A.13: Comparison of profile of PHA, γ_{max}, maximum displacement, CSR, and max r_u obtained using OpenSees, FLAC, and PLAXIS for motion RSN963.

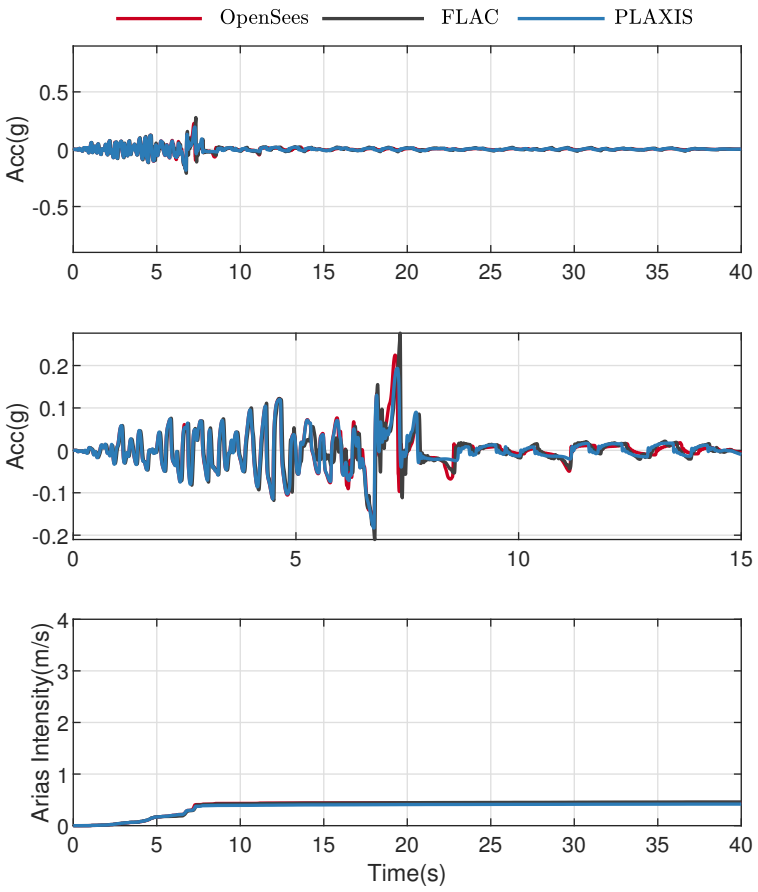

Figure A.14: Comparison of acceleration time histories at surface obtained using OpenSees, FLAC, and PLAXIS for motion RSN963.

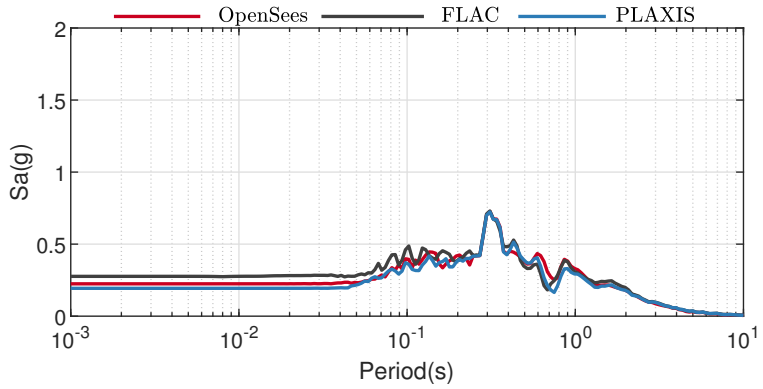

Figure A.15: Comparison of acceleration response spectra at surface obtained using OpenSees, FLAC, and PLAXIS for motion RSN963.

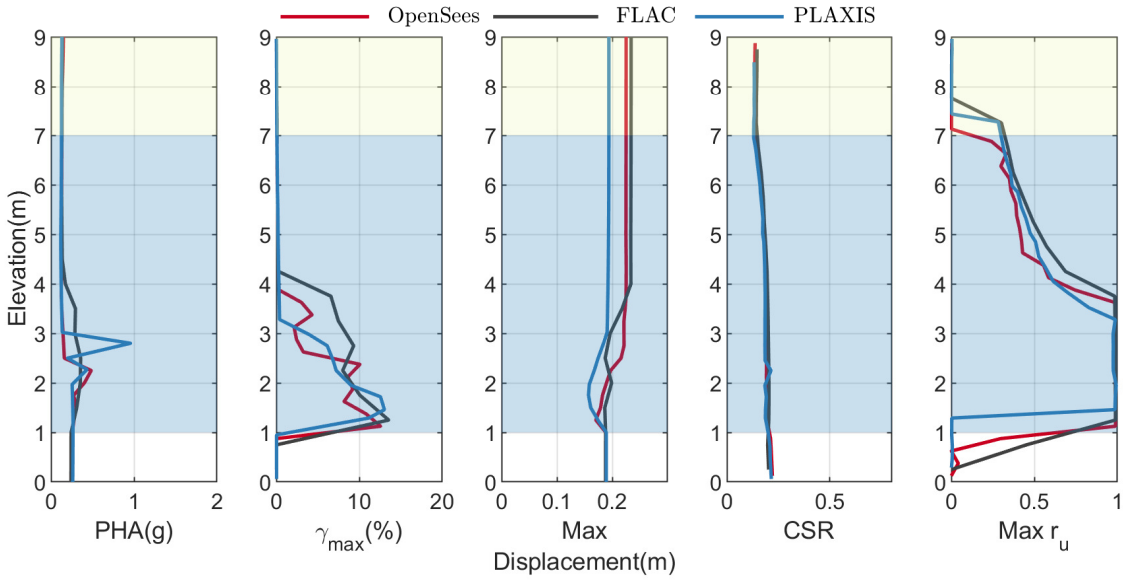

Figure A.16: Comparison of profile of PHA, γ_{max}, maximum displacement, CSR, and max r_u obtained using OpenSees, FLAC, and PLAXIS for motion RSN1203.

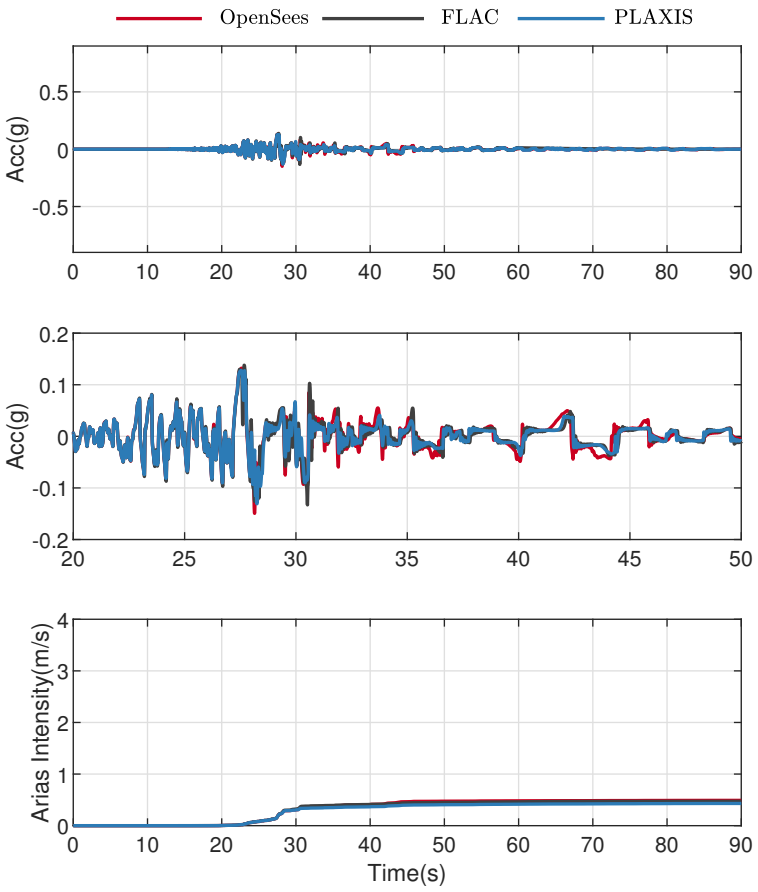

Figure A.17: Comparison of acceleration time histories at surface obtained using OpenSees, FLAC, and PLAXIS for motion RSN1203.

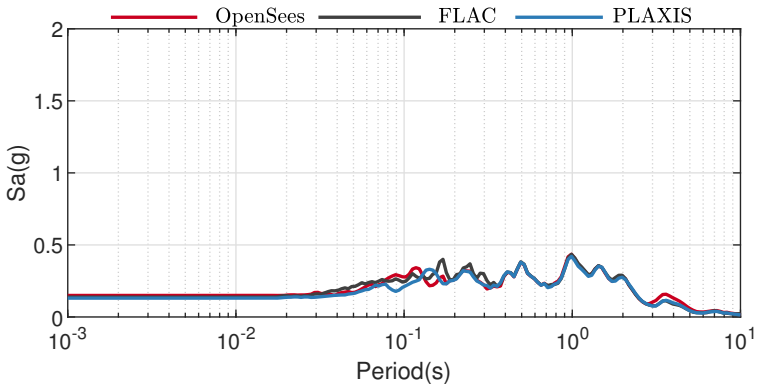

Figure A.18: Comparison of acceleration response spectra at surface obtained using OpenSees, FLAC, and PLAXIS for motion RSN1203.

A.3 N10T6

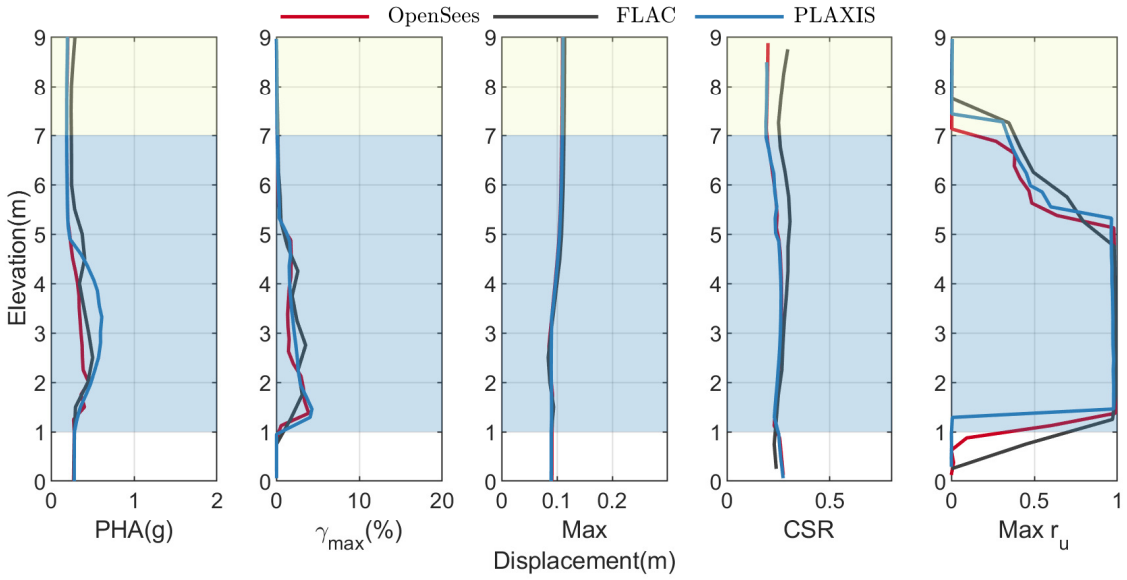

Figure A.19: Comparison of profile of PHA, γ_{max}, maximum displacement, CSR, and max r_u obtained using OpenSees, FLAC, and PLAXIS for motion RSN766.

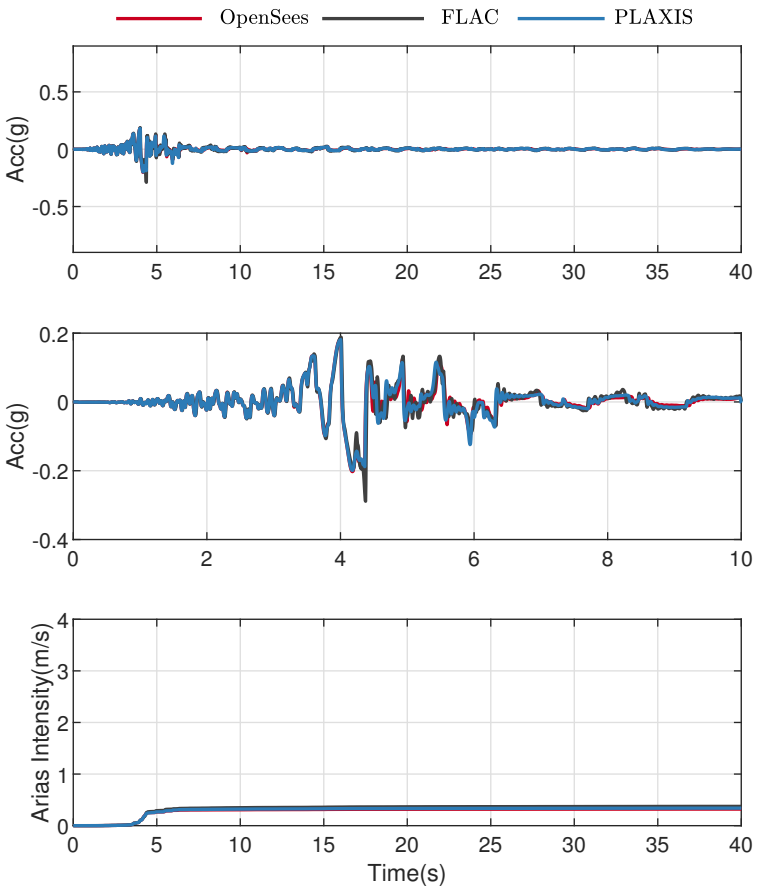

Figure A.20: Comparison of acceleration time histories at surface obtained using OpenSees, FLAC, and PLAXIS for motion RSN766.

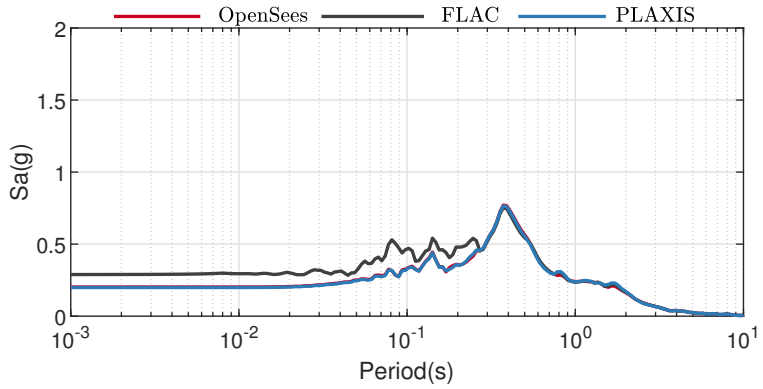

Figure A.21: Comparison of acceleration response spectra at surface obtained using OpenSees, FLAC, and PLAXIS for motion RSN766.

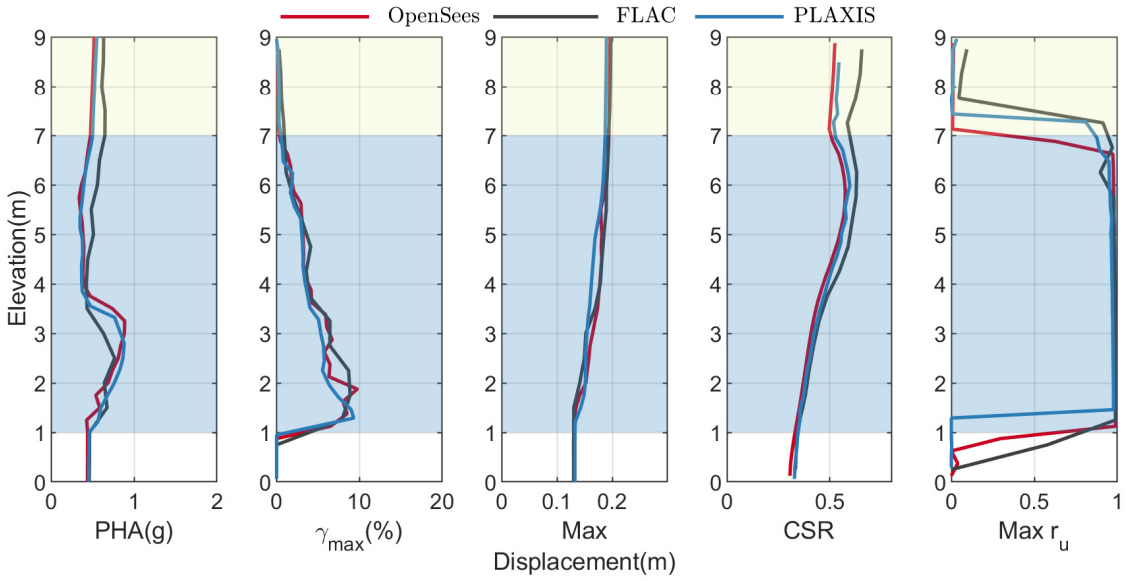

Figure A.22: Comparison of profile of PHA, γ_{max}, maximum displacement, CSR, and max r_u obtained using OpenSees, FLAC, and PLAXIS for motion RSN963.

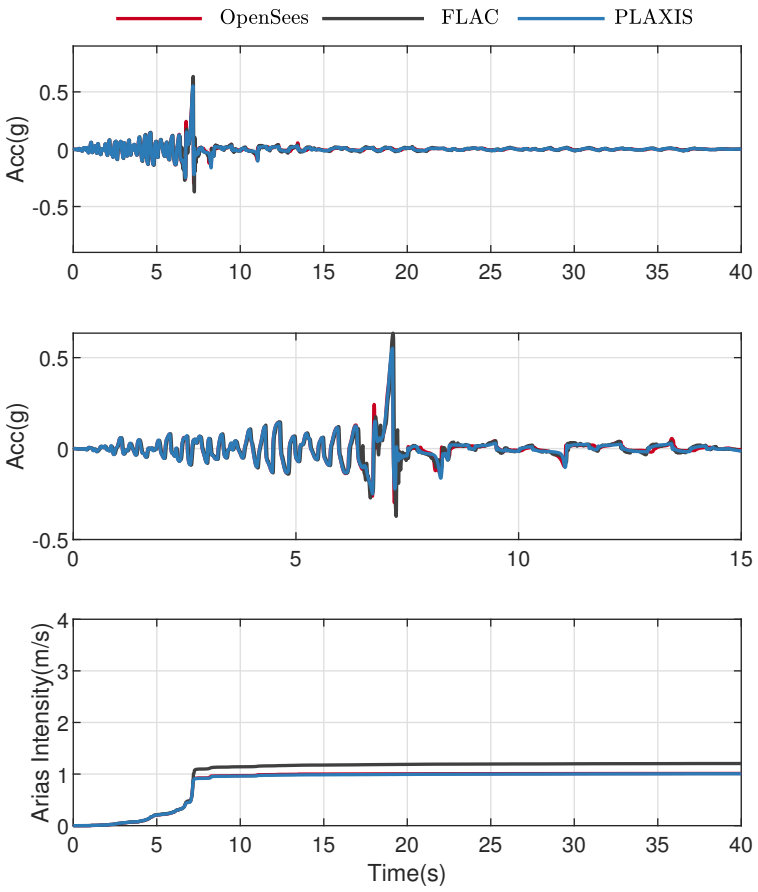

Figure A.23: Comparison of acceleration time histories at surface obtained using OpenSees, FLAC, and PLAXIS for motion RSN963.

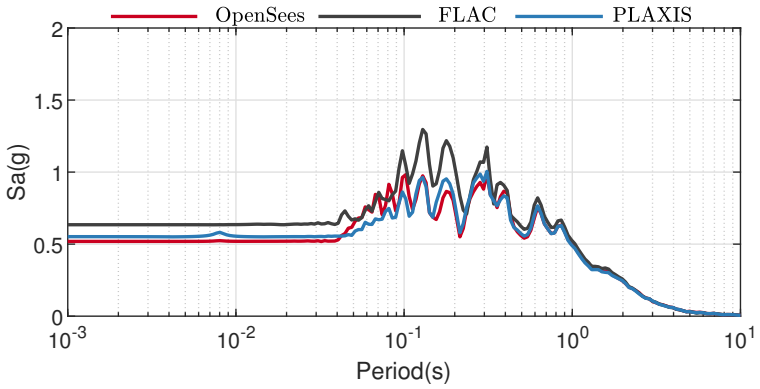

Figure A.24: Comparison of acceleration response spectra at surface obtained using OpenSees, FLAC, and PLAXIS for motion RSN963.

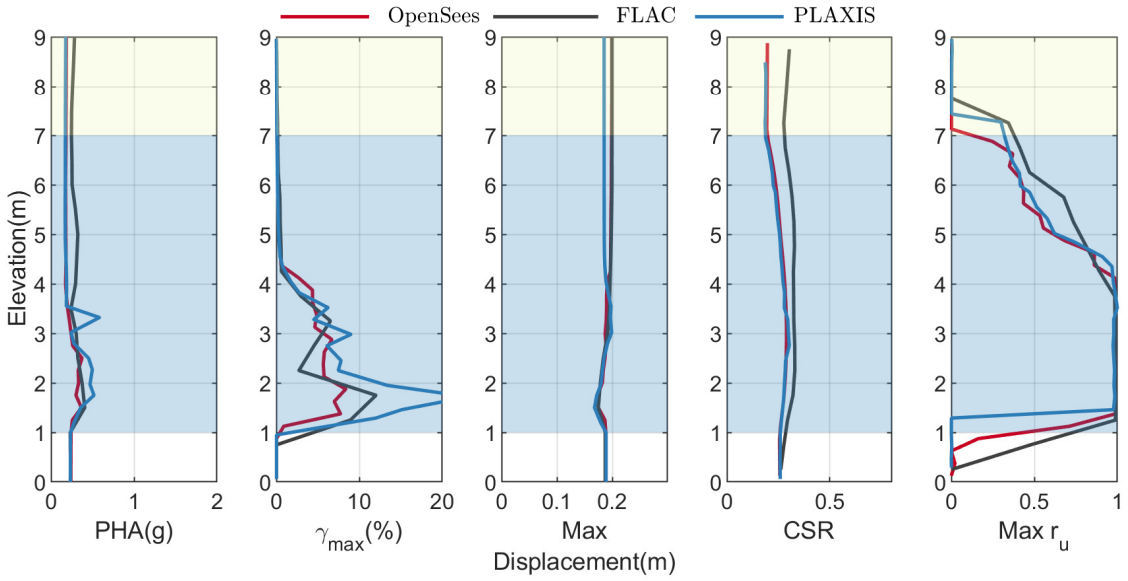

Figure A.25: Comparison of profile of PHA, γ_{max}, maximum displacement, CSR, and max r_u obtained using OpenSees, FLAC, and PLAXIS for motion RSN1203.

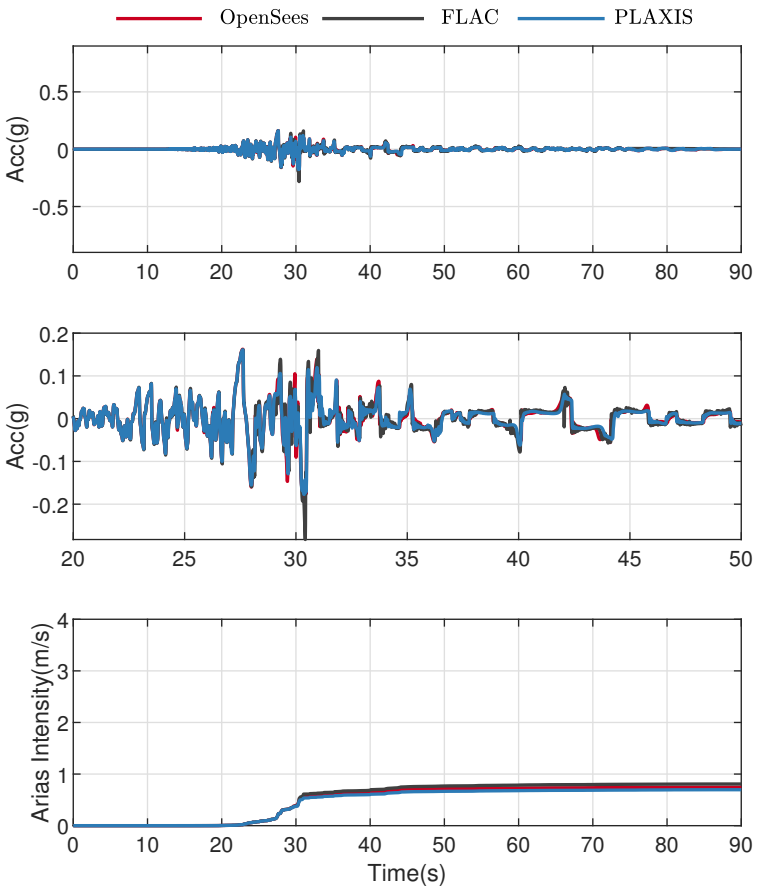

Figure A.26: Comparison of acceleration time histories at surface obtained using OpenSees, FLAC, and PLAXIS for motion RSN1203.

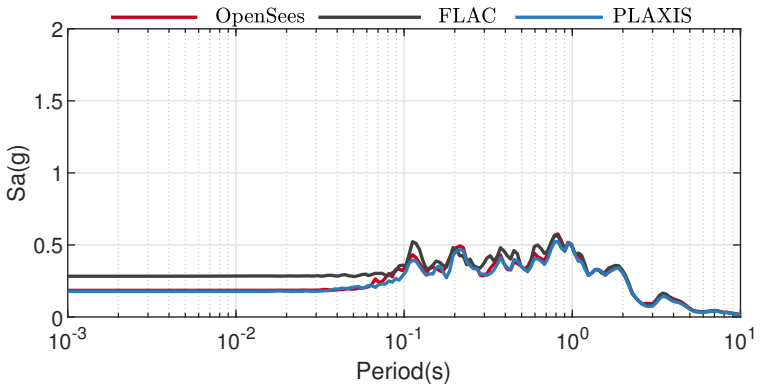

Figure A.27: Comparison of acceleration response spectra at surface obtained using OpenSees, FLAC, and PLAXIS for motion RSN1203.

A.4 N20T3

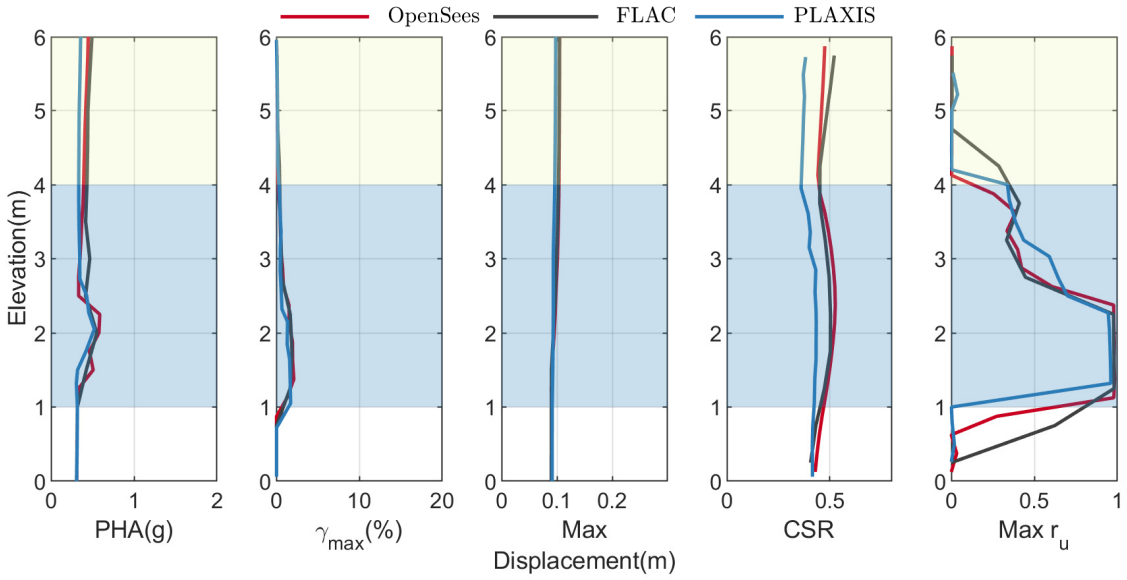

Figure A.28: Comparison of profile of PHA, γ_{max}, maximum displacement, CSR, and max r_u obtained using OpenSees, FLAC, and PLAXIS for motion RSN766.

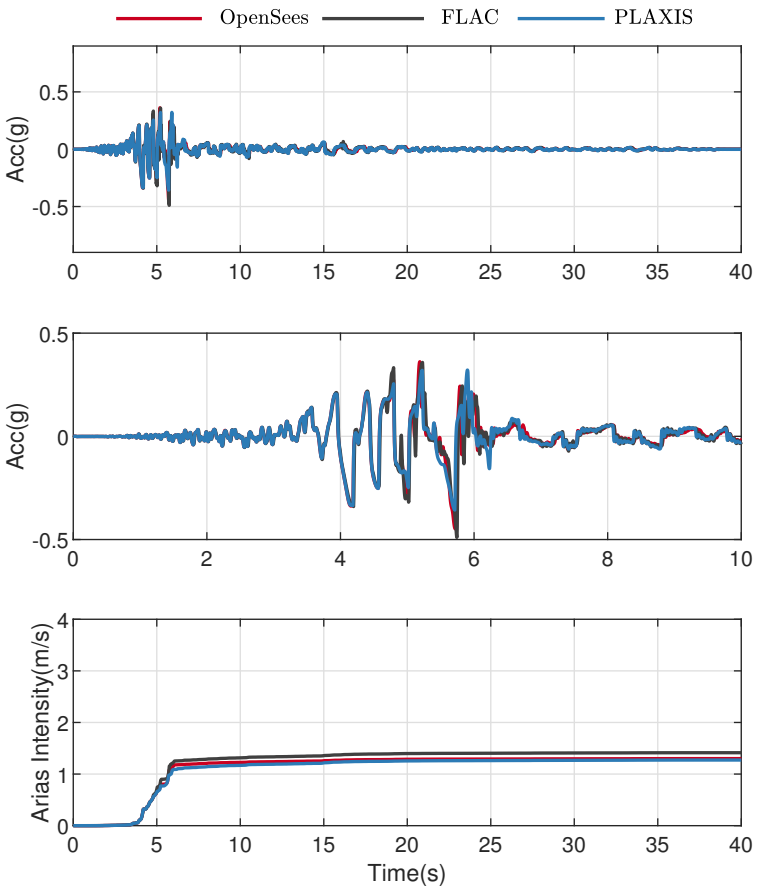

Figure A.29: Comparison of acceleration time histories at surface obtained using OpenSees, FLAC, and PLAXIS for motion RSN766.

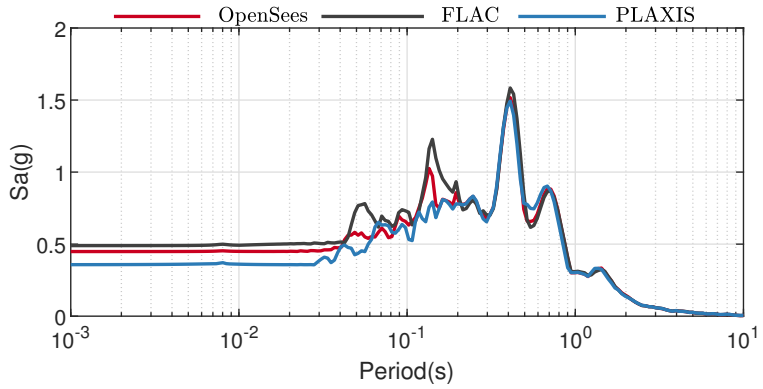

Figure A.30: Comparison of acceleration response spectra at surface obtained using OpenSees, FLAC, and PLAXIS for motion RSN766.

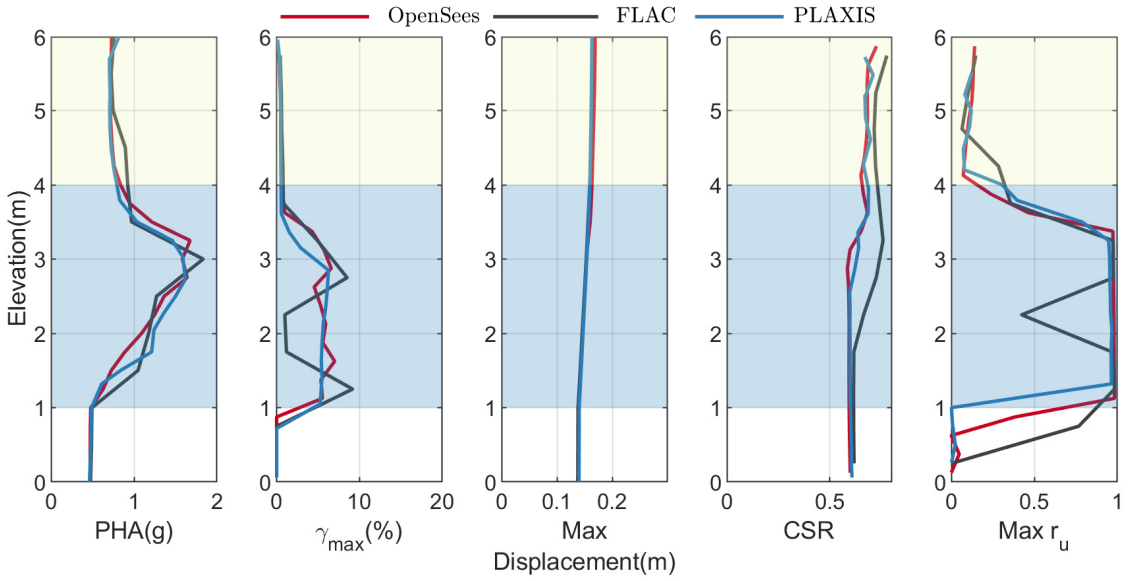

Figure A.31: Comparison of profile of PHA, γ_{max}, maximum displacement, CSR, and max r_u obtained using OpenSees, FLAC, and PLAXIS for motion RSN963.

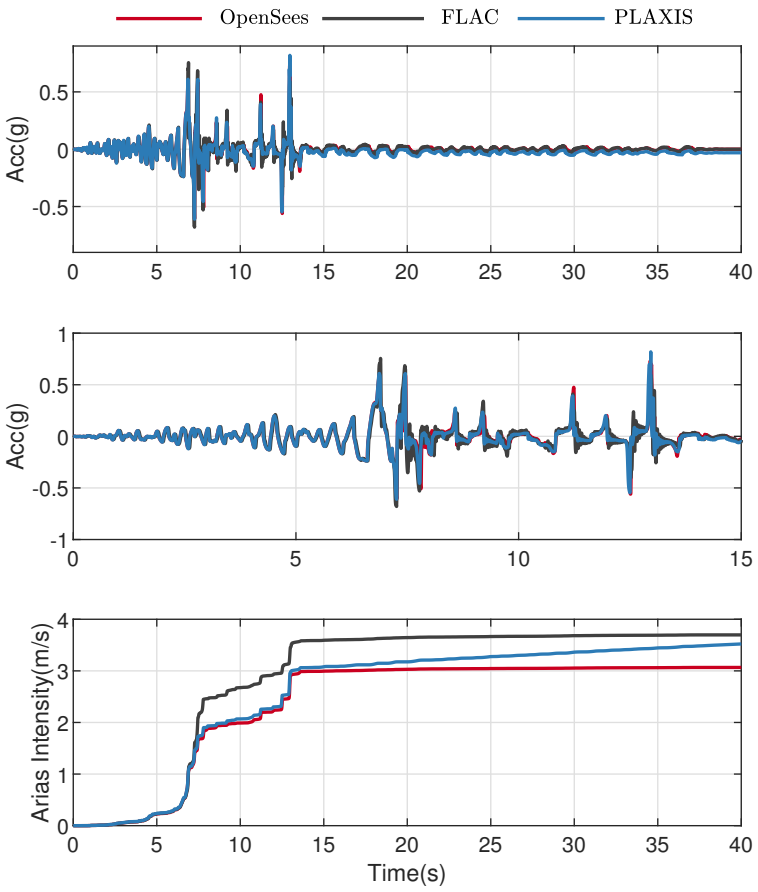

Figure A.32: Comparison of acceleration time histories at surface obtained using OpenSees, FLAC, and PLAXIS for motion RSN963.

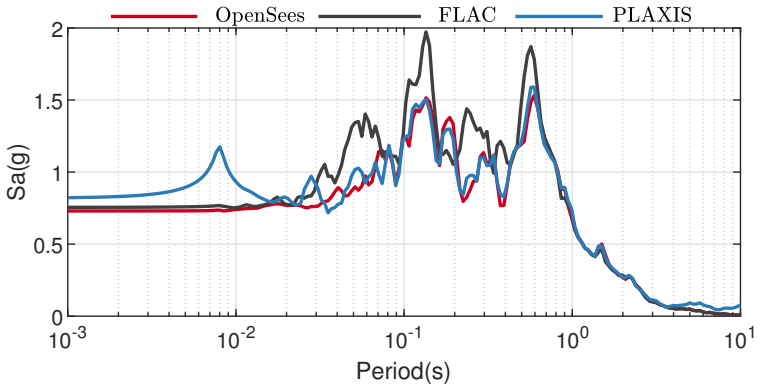

Figure A.33: Comparison of acceleration response spectra at surface obtained using OpenSees, FLAC, and PLAXIS for motion RSN963.

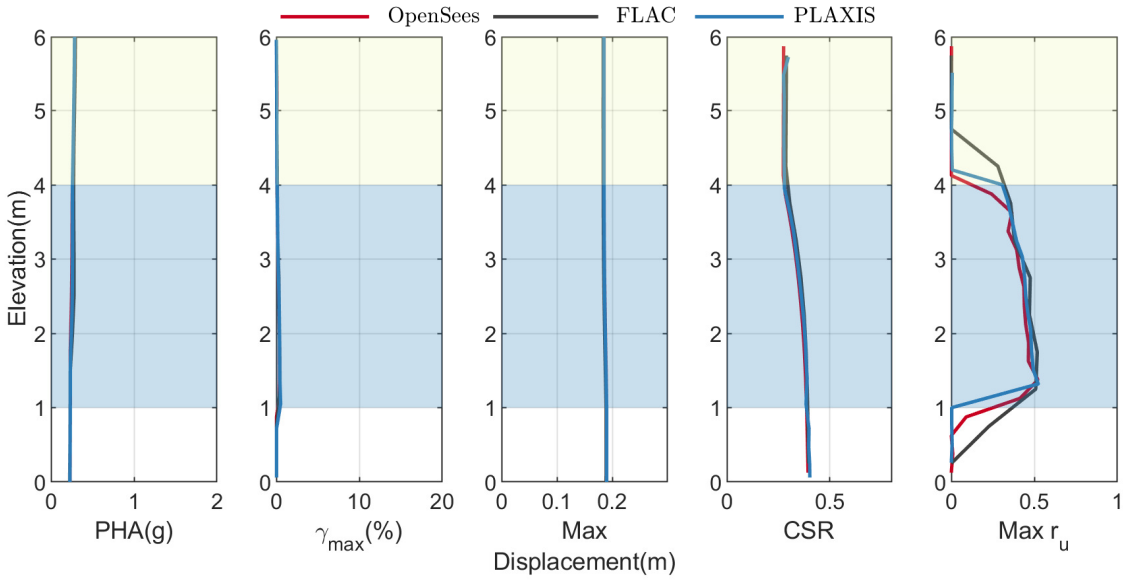

Figure A.34: Comparison of profile of PHA, γ_{max}, maximum displacement, CSR, and max r_u obtained using OpenSees, FLAC, and PLAXIS for motion RSN1203.

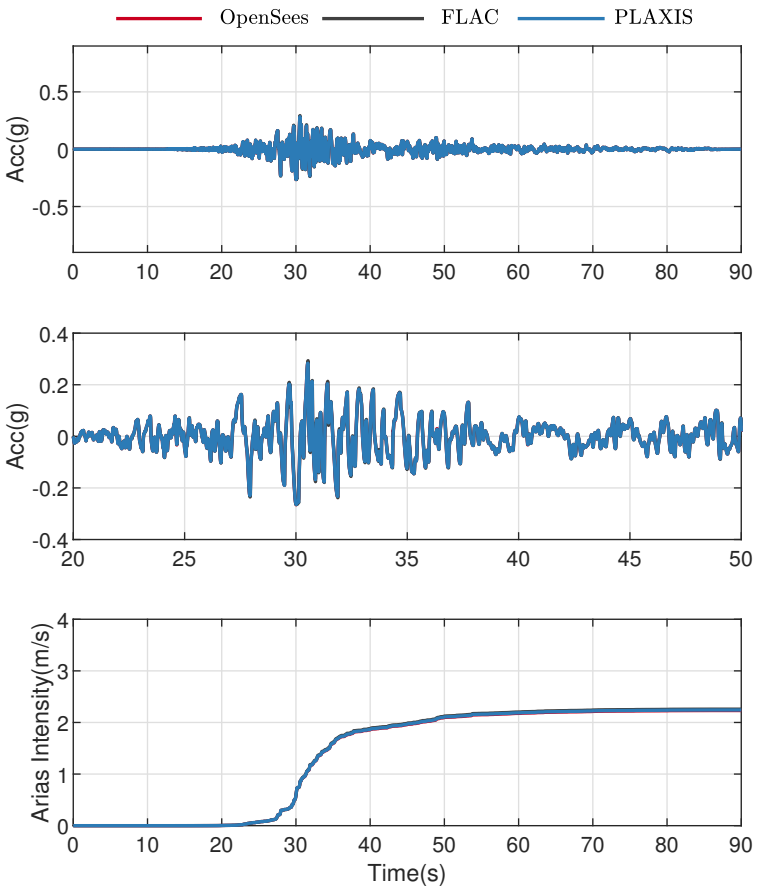

Figure A.35: Comparison of acceleration time histories at surface obtained using OpenSees, FLAC, and PLAXIS for motion RSN1203.

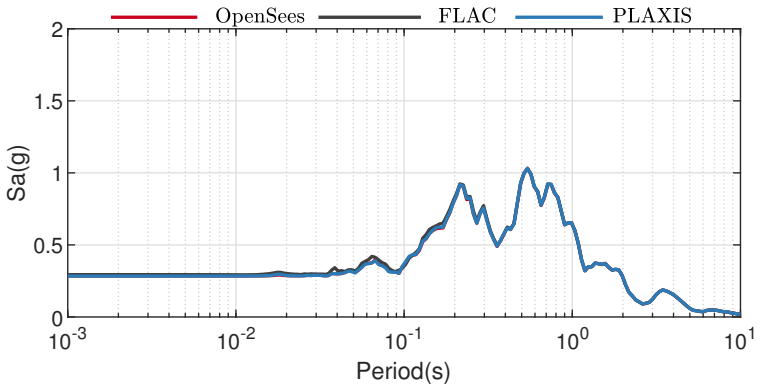

Figure A.36: Comparison of acceleration response spectra at surface obtained using OpenSees, FLAC, and PLAXIS for motion RSN1203.

A.5 N20T6

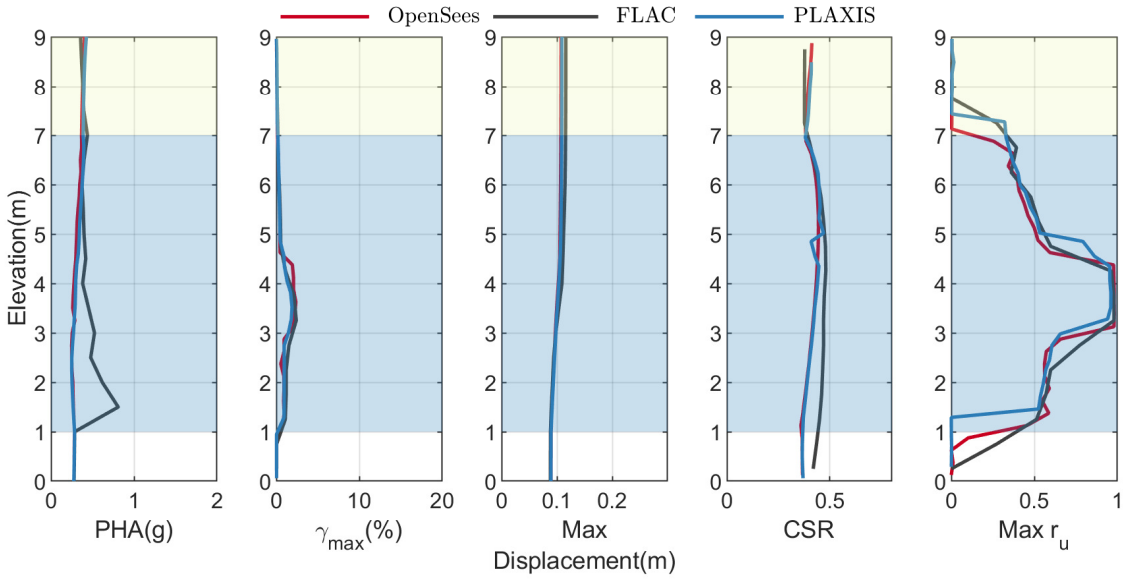

Figure A.37: Comparison of profile of PHA, γ_{max}, maximum displacement, CSR, and max r_u obtained using OpenSees, FLAC, and PLAXIS for motion RSN766.

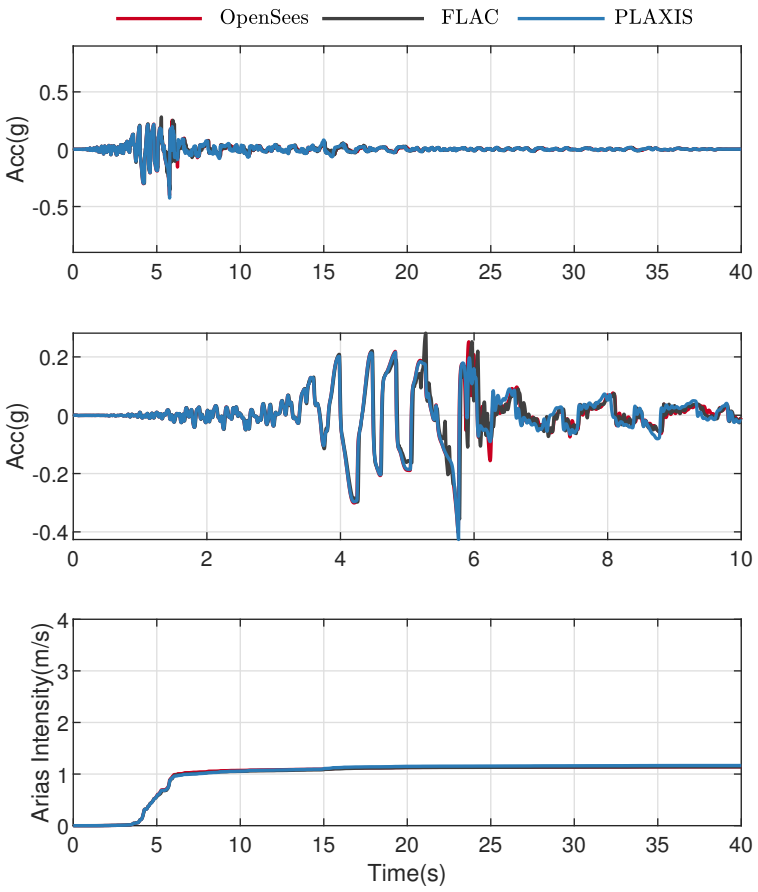

Figure A.38: Comparison of acceleration time histories at surface obtained using OpenSees, FLAC, and PLAXIS for motion RSN766.

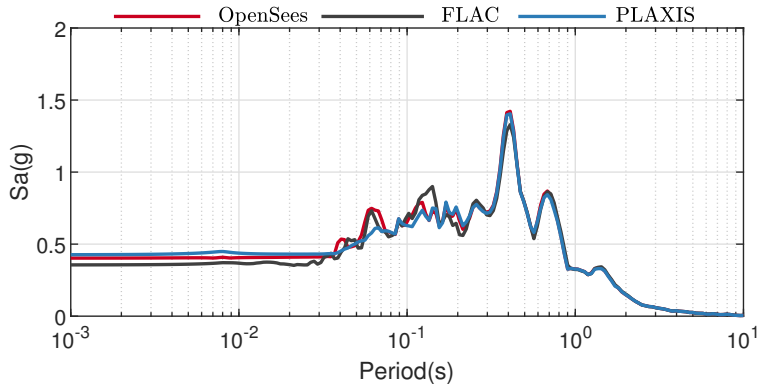

Figure A.39: Comparison of acceleration response spectra at surface obtained using OpenSees, FLAC, and PLAXIS for motion RSN766.

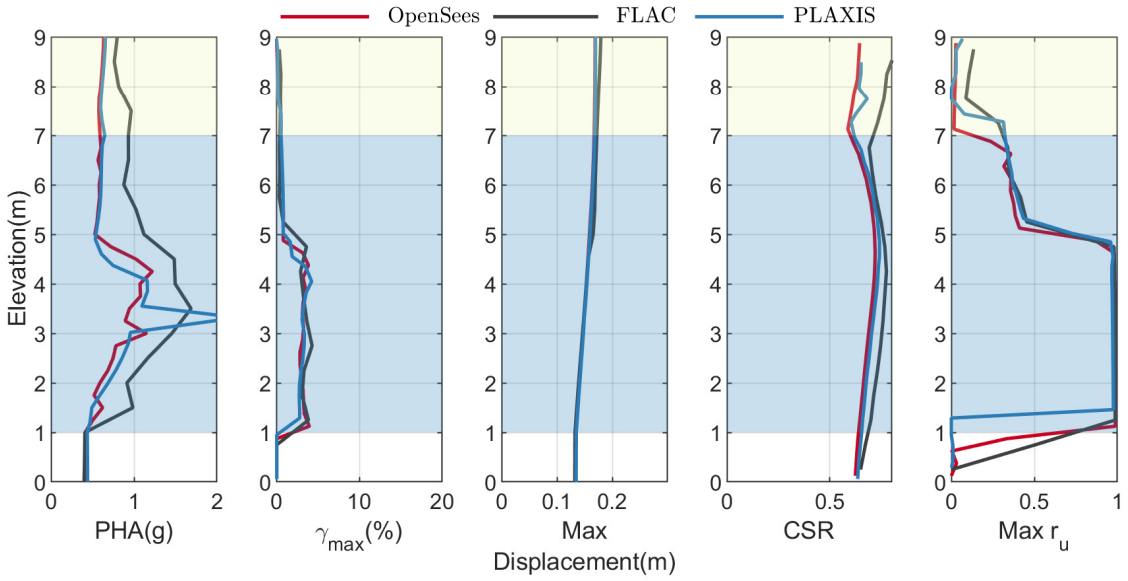

Figure A.40: Comparison of profile of PHA, γ_{max}, maximum displacement, CSR, and max r_u obtained using OpenSees, FLAC, and PLAXIS for motion RSN963.

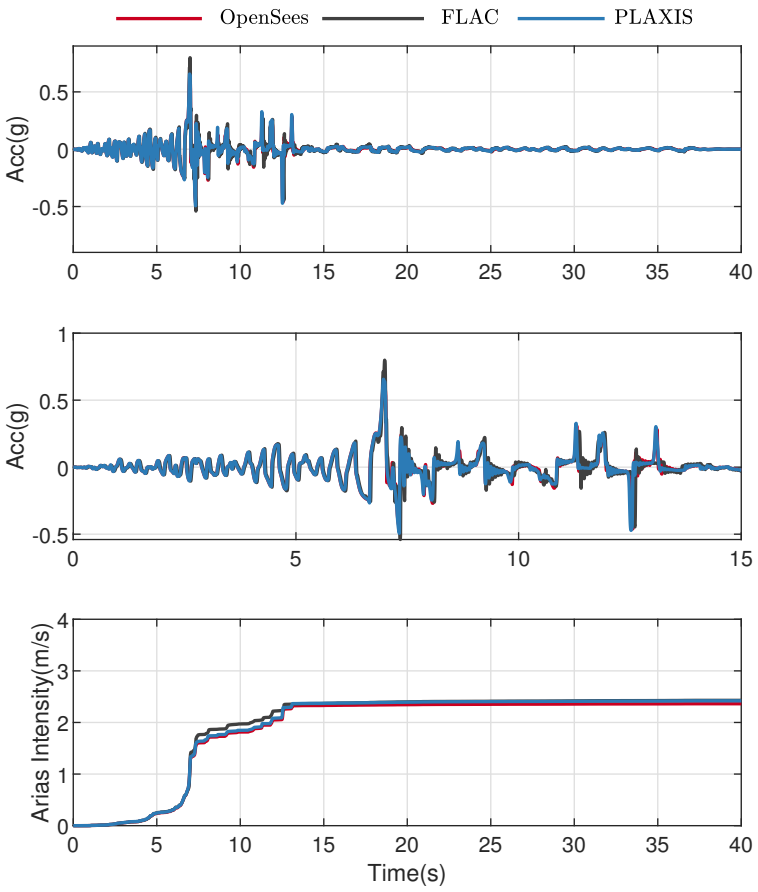

Figure A.41: Comparison of acceleration time histories at surface obtained using OpenSees, FLAC, and PLAXIS for motion RSN963.

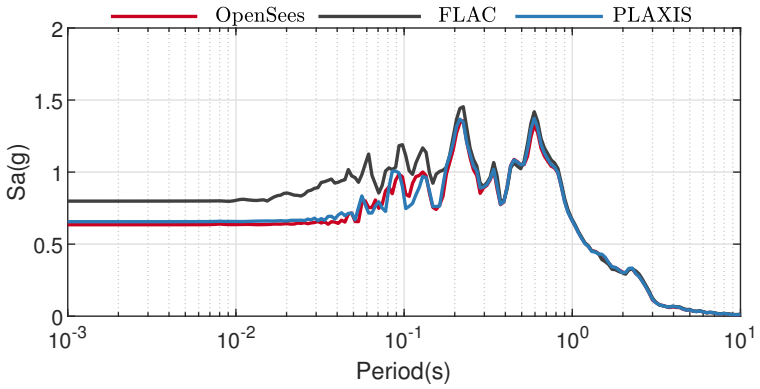

Figure A.42: Comparison of acceleration response spectra at surface obtained using OpenSees, FLAC, and PLAXIS for motion RSN963.

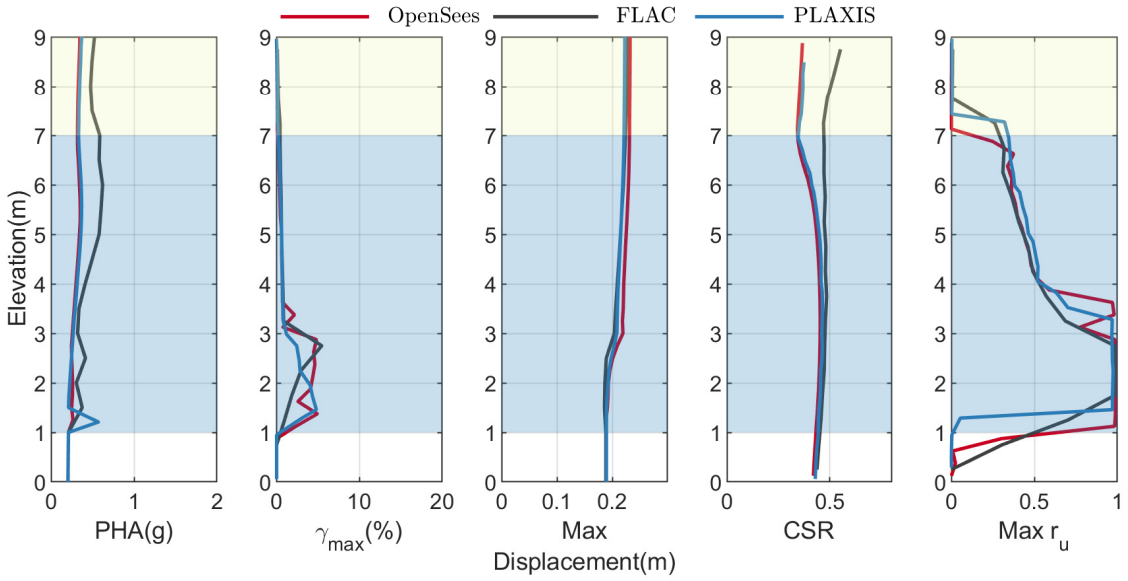

Figure A.43: Comparison of profile of PHA, γ_{max}, maximum displacement, CSR, and max r_u obtained using OpenSees, FLAC, and PLAXIS for motion RSN1203.

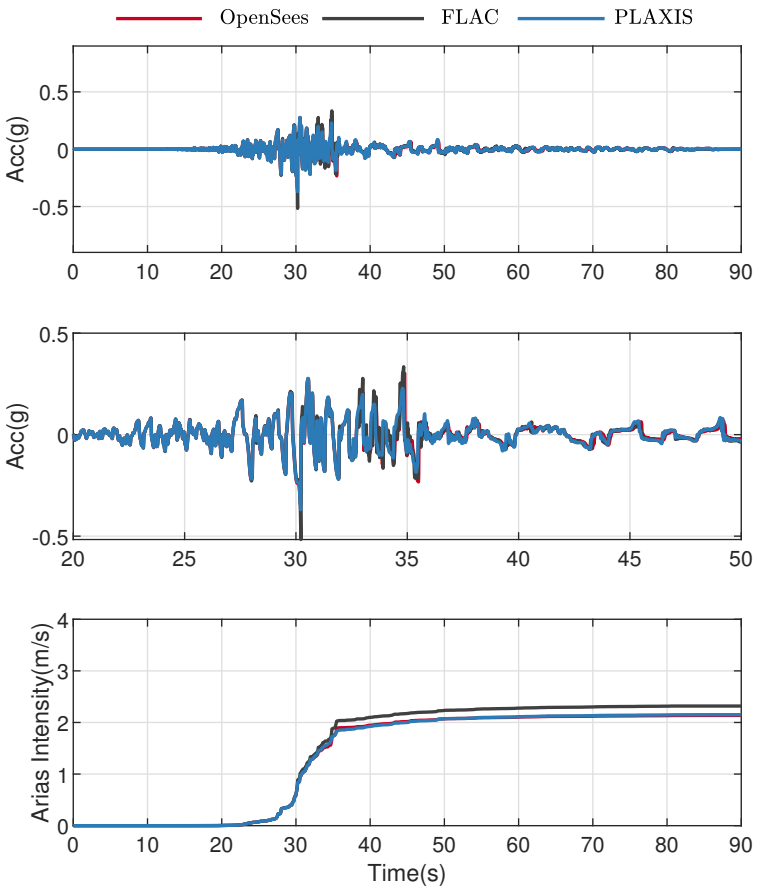

Figure A.44: Comparison of acceleration time histories at surface obtained using OpenSees, FLAC, and PLAXIS for motion RSN1203.

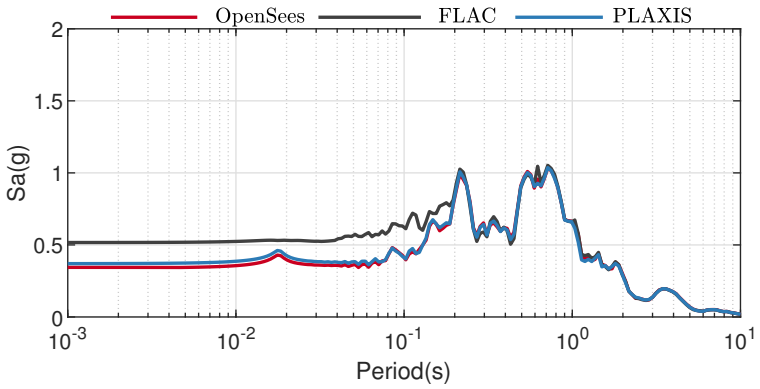

Figure A.45: Comparison of acceleration response spectra at surface obtained using OpenSees, FLAC, and PLAXIS for motion RSN1203.

A.6 Additional Sloping Ground Results

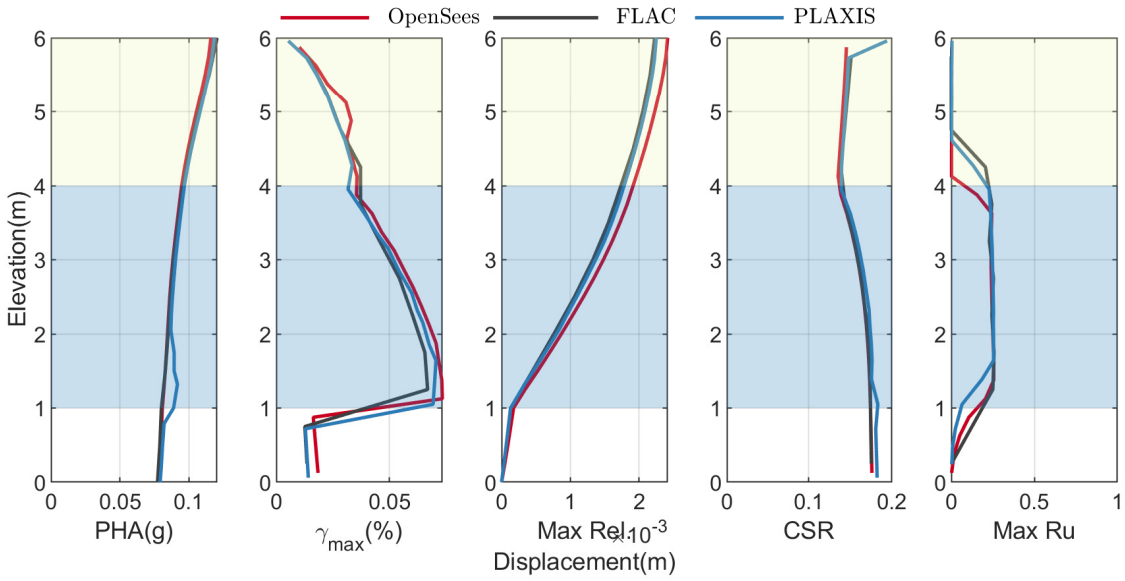

Figure A.46: Comparison of PHA, γ_{max}, maximum displacement, CSR, and max r_u obtained using OpenSees, FLAC and PLAXIS for Motion RSN766 and $a_{max} = 0.1$g.

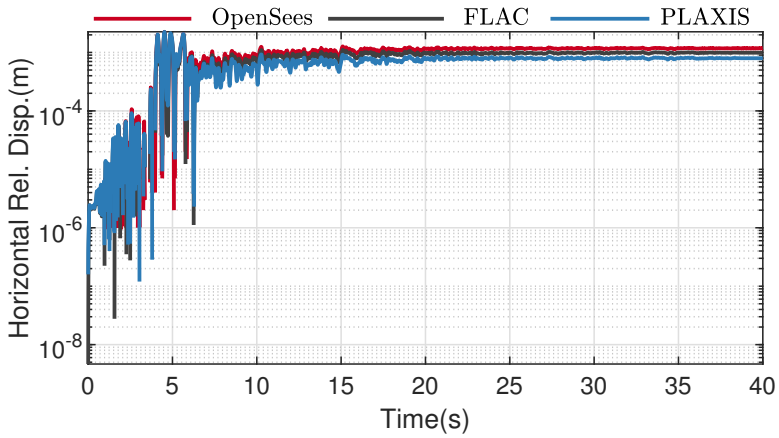

Figure A.47: Comparison of horizontal displacement at the surface obtained using OpenSees, FLAC, and PLAXIS for Motion RSN766 and a_{max} =0.1g.

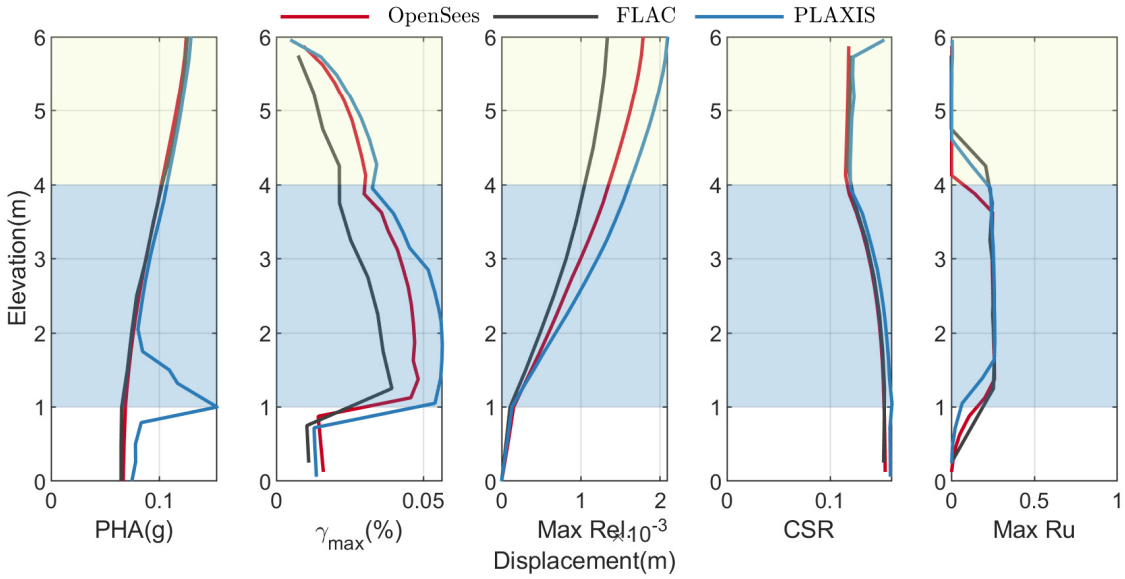

Figure A.48: Comparison of PHA, γ_{max}, maximum displacement, CSR, and max r_u obtained using OpenSees, FLAC and PLAXIS for Motion RSN963 and a_{max} = 0.1g.

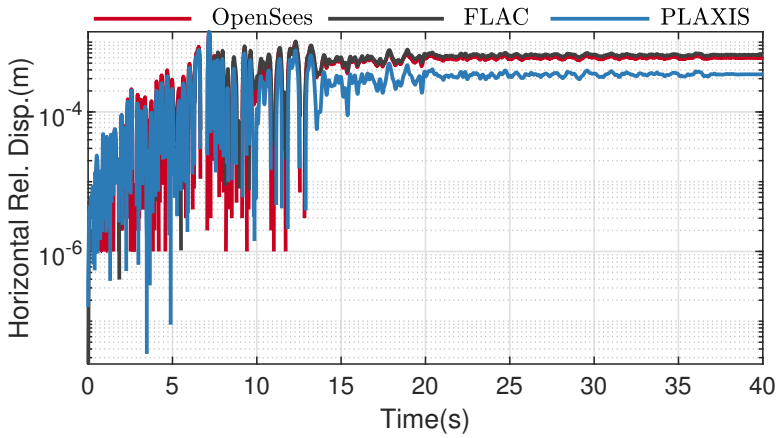

Figure A.49: Comparison of horizontal displacement at the surface obtained using OpenSees, FLAC, and PLAXIS for Motion RSN963 and a_{max} =0.1g.

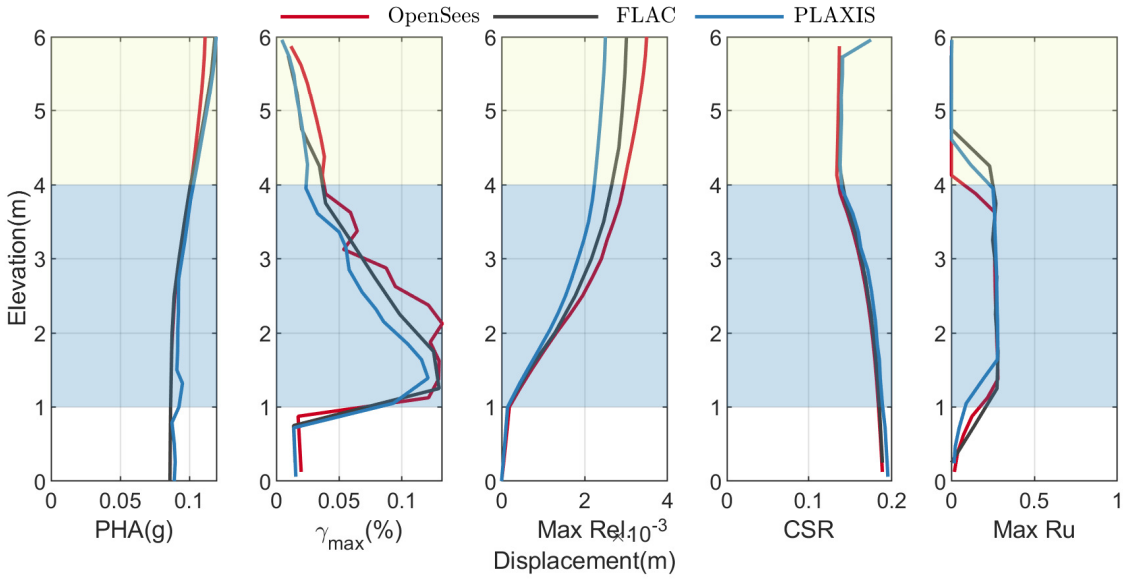

Figure A.50: Comparison of PHA, γ_{max}, maximum displacement, CSR, and max r_u obtained using OpenSees, FLAC and PLAXIS for Motion RSN1203 and a_{max} = 0.1g.

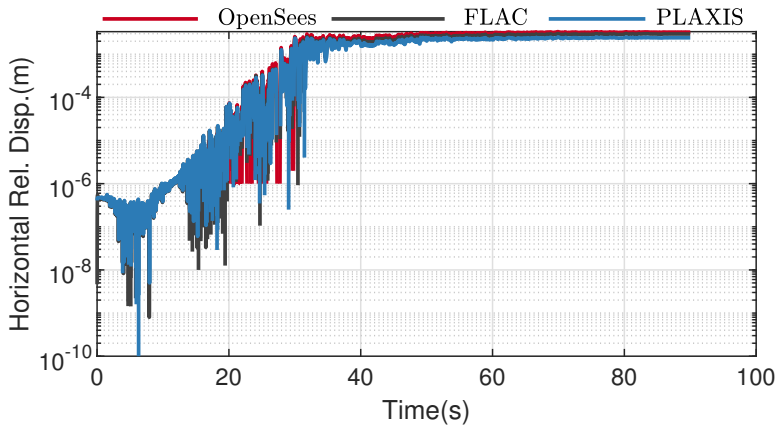

Figure A.51: Comparison of horizontal displacement at the surface obtained using OpenSees, FLAC, and PLAXIS for Motion RSN1203 and $a_{max} = 0.1$g.

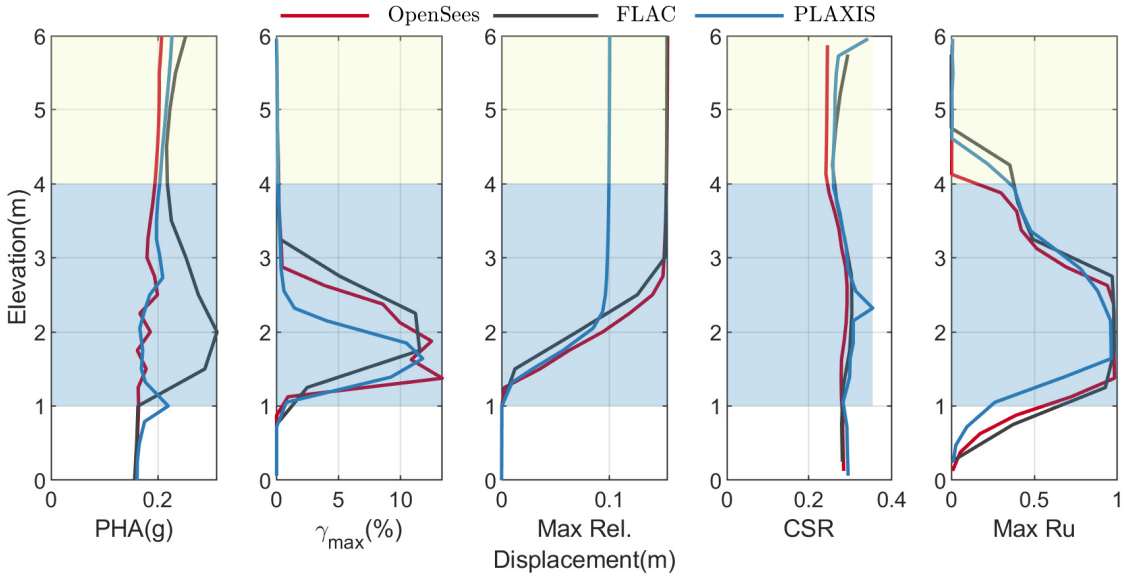

Figure A.52: Comparison of PHA, γ_{max}, maximum displacement, CSR, and max r_u obtained using OpenSees, FLAC and PLAXIS for Motion RSN766 and $a_{max} = 0.2$g.

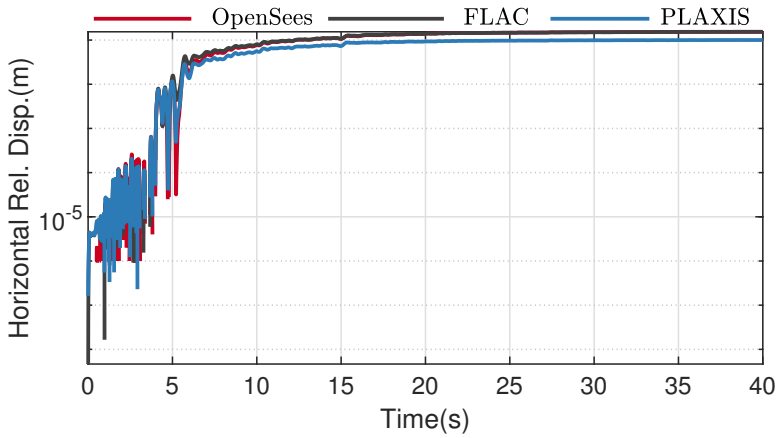

Figure A.53: Comparison of horizontal displacement at the surface obtained using OpenSees, FLAC, and PLAXIS for Motion RSN766 and a_{max} =0.2g.

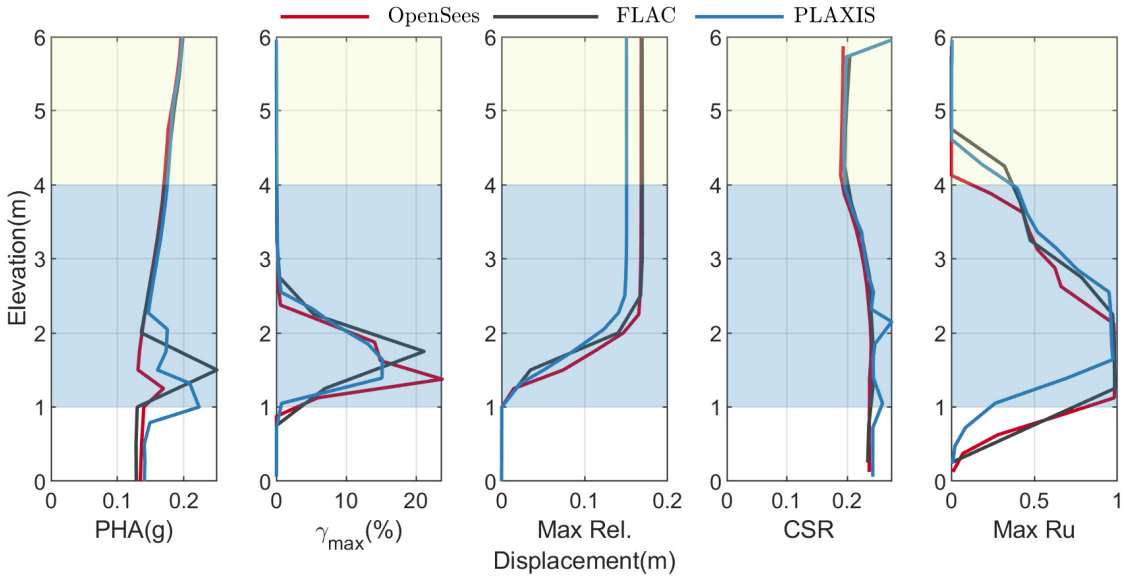

Figure A.54: Comparison of PHA, γ_{max}, maximum displacement, CSR, and max r_u obtained using OpenSees, FLAC and PLAXIS for Motion RSN963 and a_{max} = 0.2g.

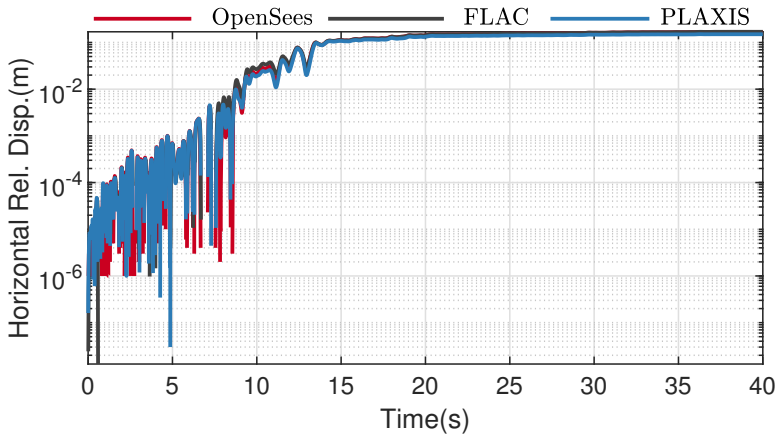

Figure A.55: Comparison of horizontal displacement at the surface obtained using OpenSees, FLAC, and PLAXIS for Motion RSN963 and a_{max} =0.2g.

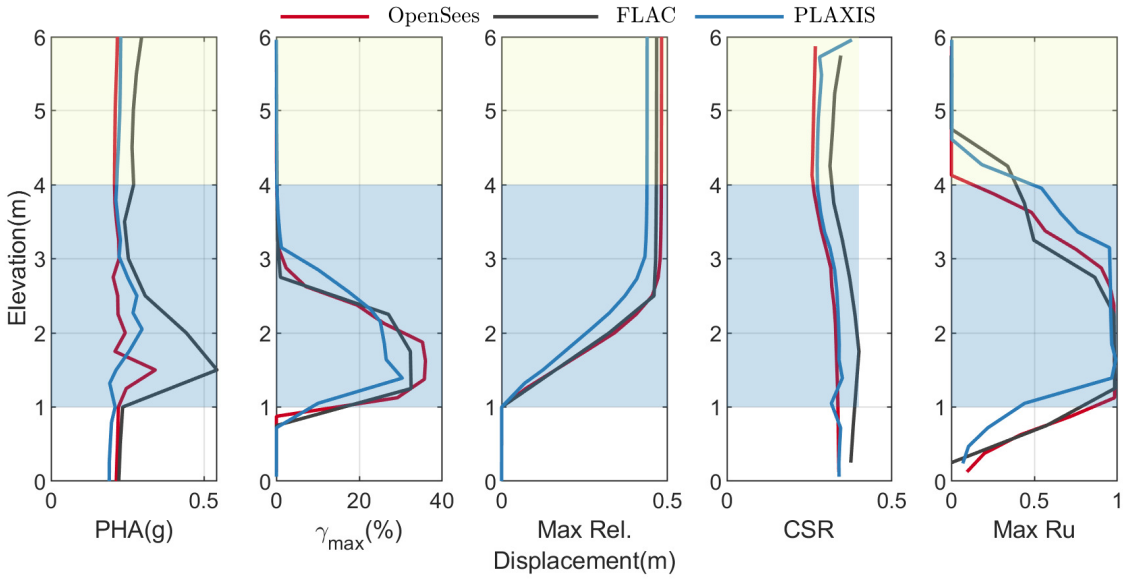

Figure A.56: Comparison of PHA, γ_{max}, maximum displacement, CSR, and max r_u obtained using OpenSees, FLAC and PLAXIS for Motion RSN1203 and a_{max} = 0.2g.

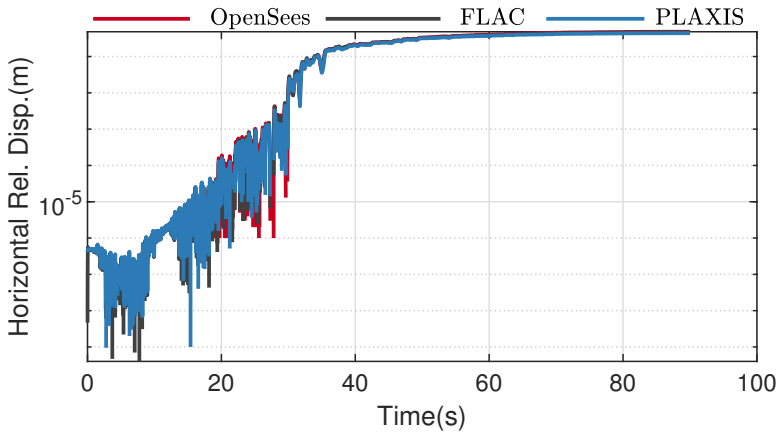

Figure A.57: Comparison of horizontal displacement at the surface obtained using OpenSees, FLAC, and PLAXIS for Motion RSN1203 and $a_{max} = 0.2$g.

Appendix B

ADDITIONAL LEAP2020 PHASE A PREDICTION RESULTS

Additional simulations of non-uniform CSR simple shear tests were performed using OpenSees and the results are presented in Figs. B.1 to B.17. The physically stabilized single-point integration and mixed displacement-pressure(u-p) element (SSPquadUP, see McGann et al. (2015)) was used to capture the effective stress response of each simulated element test.

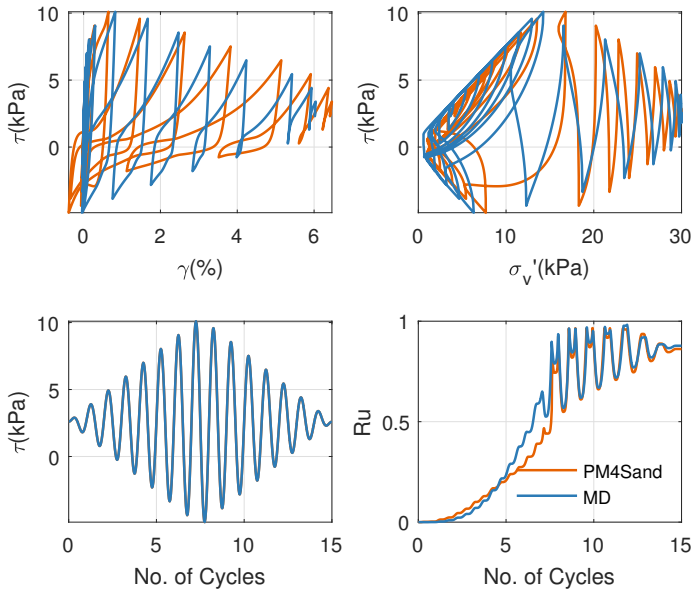

Figure B.1: Type-A prediction results for $\sigma'_v = 30\,kPa$ and $CSR = 0.25$.

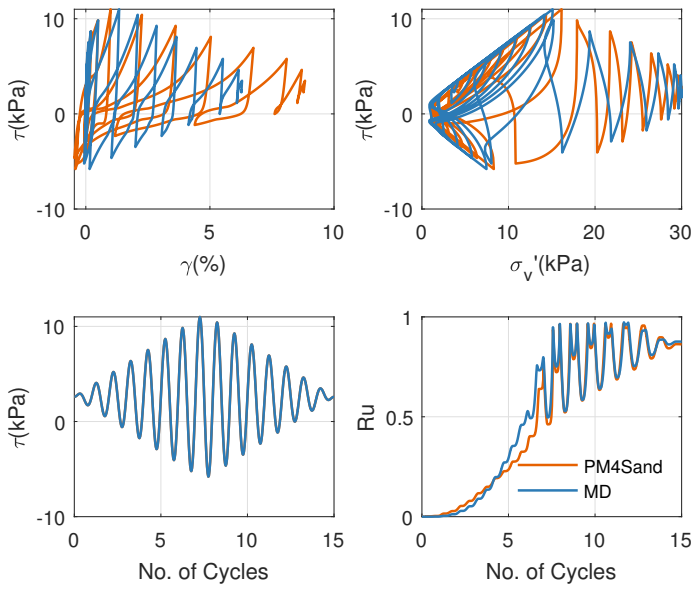

Figure B.2: Type-A prediction results for $\sigma'_v = 30\,kPa$ and $CSR = 0.28$.

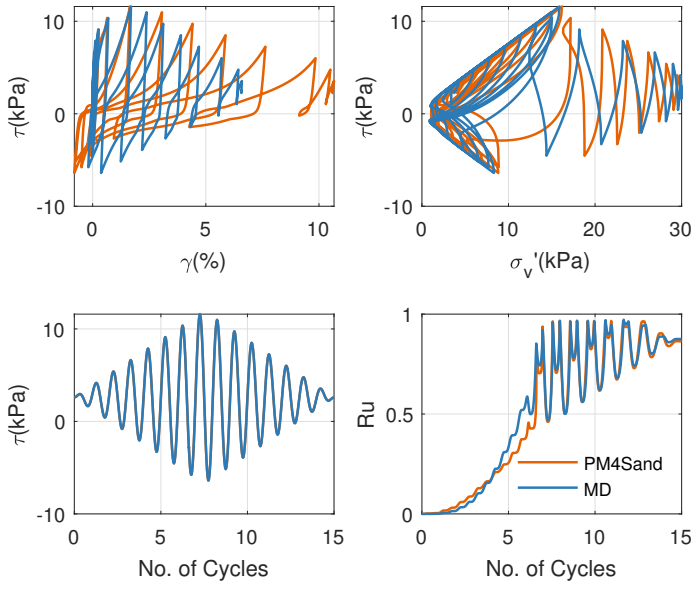

Figure B.3: Type-A prediction results for $\sigma'_v = 30\,kPa$ and $CSR = 0.30$.

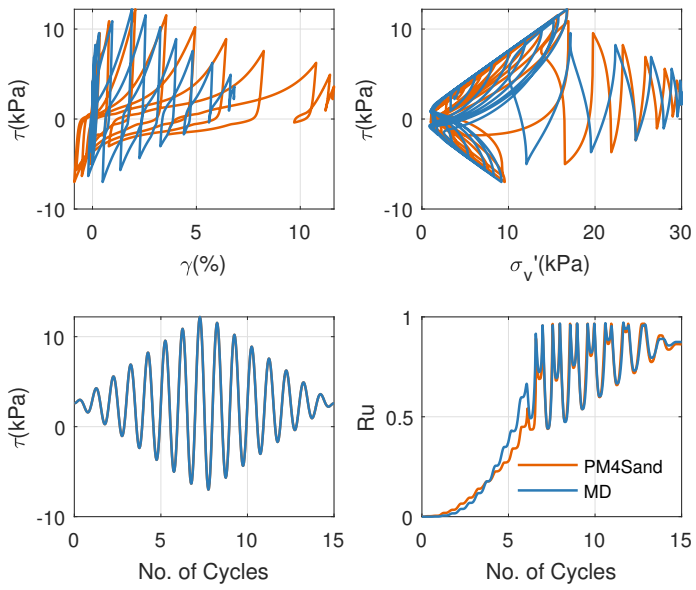

Figure B.4: Type-A prediction results for $\sigma'_v = 30\,kPa$ and $CSR = 0.32$.

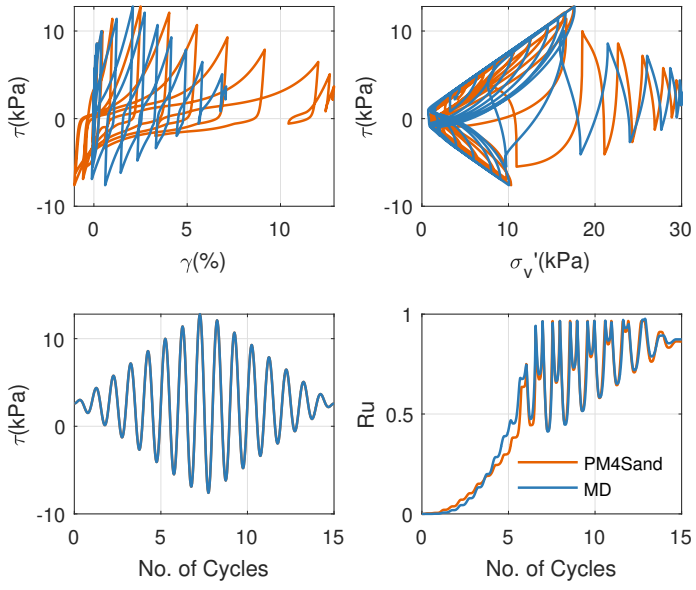

Figure B.5: Type-A prediction results for $\sigma'_v = 30\,kPa$ and $CSR = 0.34$.

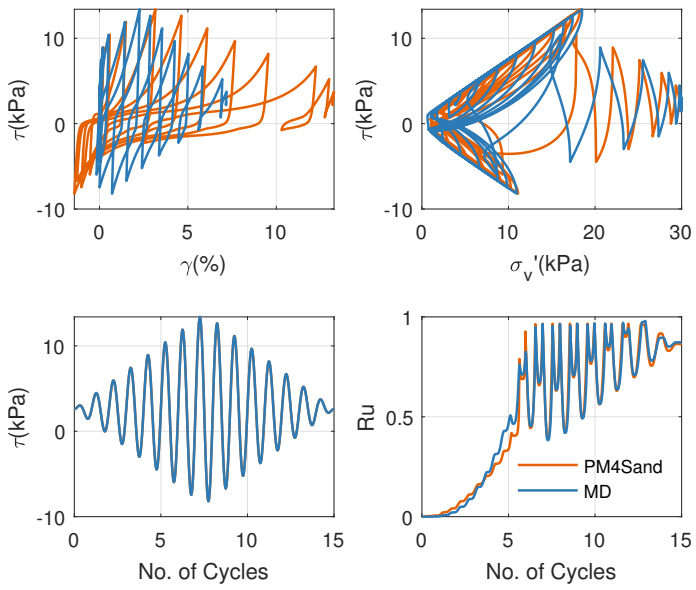

Figure B.6: Type-A prediction results for $\sigma'_v = 30\,kPa$ and $CSR = 0.36$.

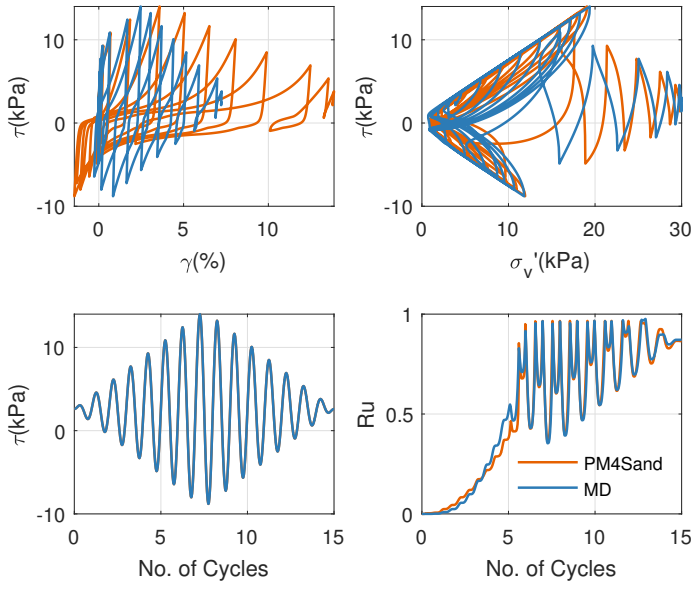

Figure B.7: Type-A prediction results for $\sigma'_v = 30\,kPa$ and $CSR = 0.38$.

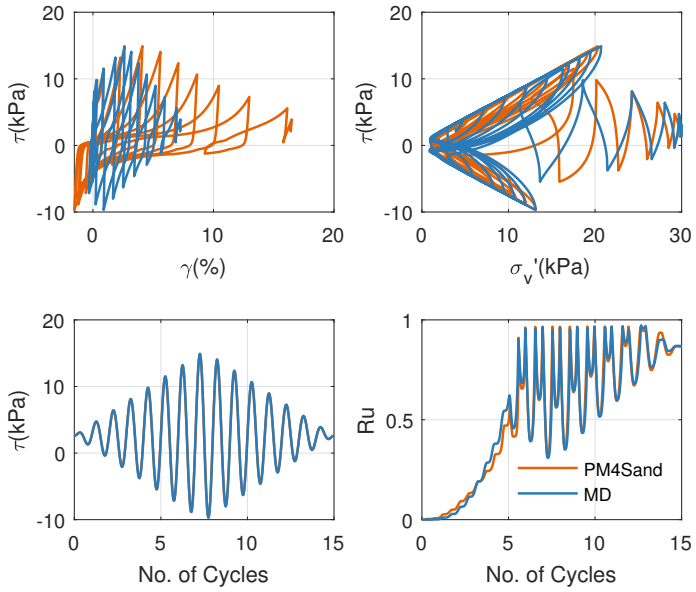

Figure B.8: Type-A prediction results for $\sigma'_v = 30\,kPa$ and $CSR = 0.41$.

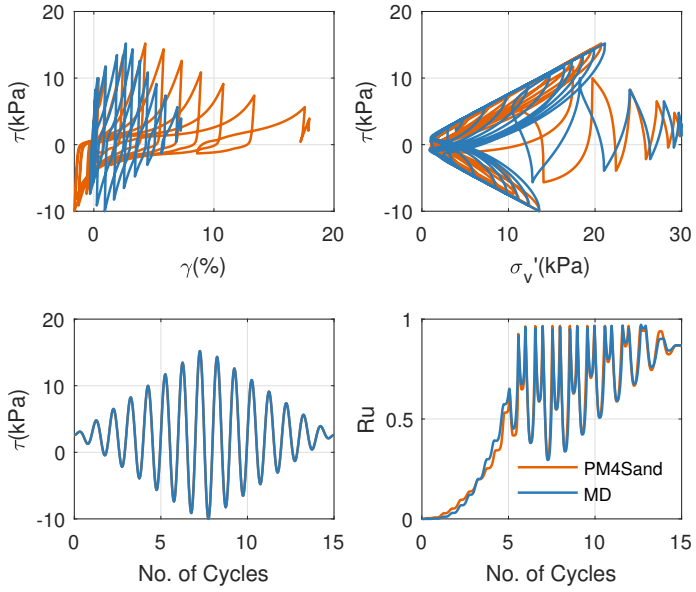

Figure B.9: Type-A prediction results for $\sigma'_v = 30\,kPa$ and $CSR = 0.42$.

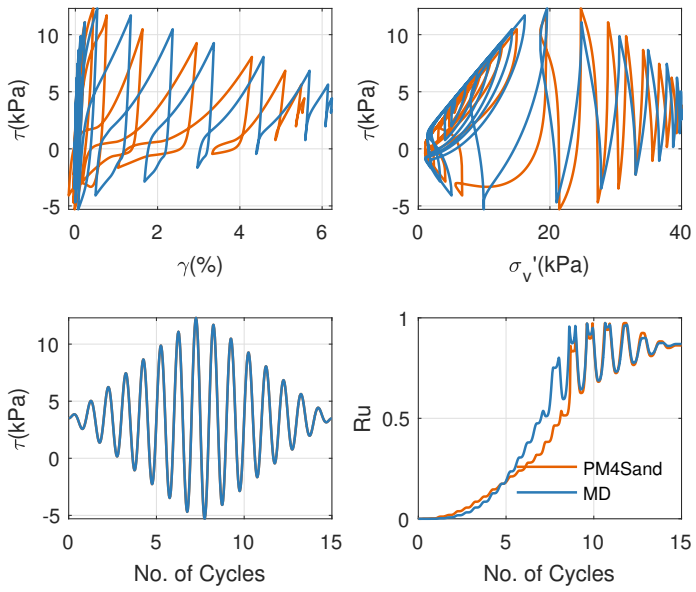

Figure B.10: Type-A prediction results for $\sigma'_v = 40\,kPa$ and $CSR = 0.22$.

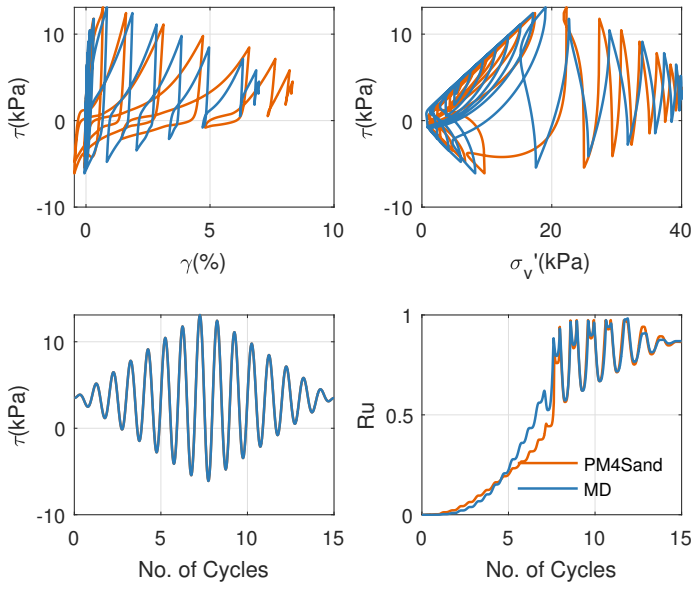

Figure B.11: Type-A prediction results for $\sigma'_v = 40\,kPa$ and $CSR = 0.24$.

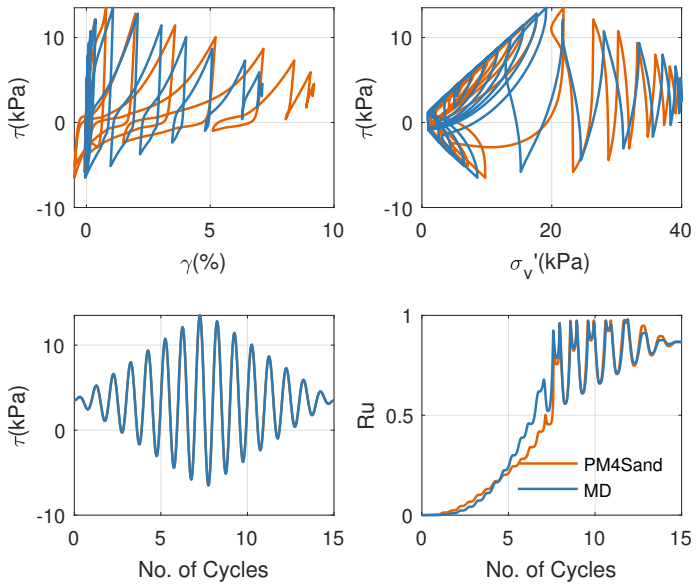

Figure B.12: Type-A prediction results for $\sigma'_v = 40\,kPa$ and $CSR = 0.25$.

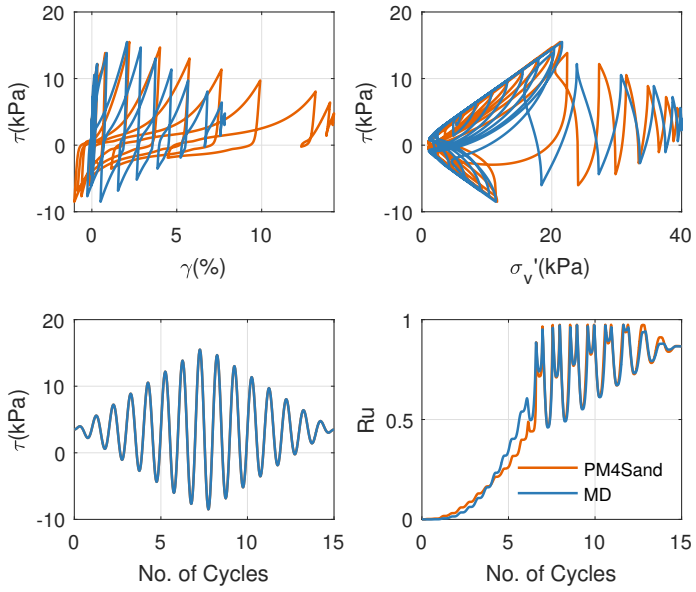

Figure B.13: Type-A prediction results for $\sigma'_v = 40\,kPa$ and $CSR = 0.30$.

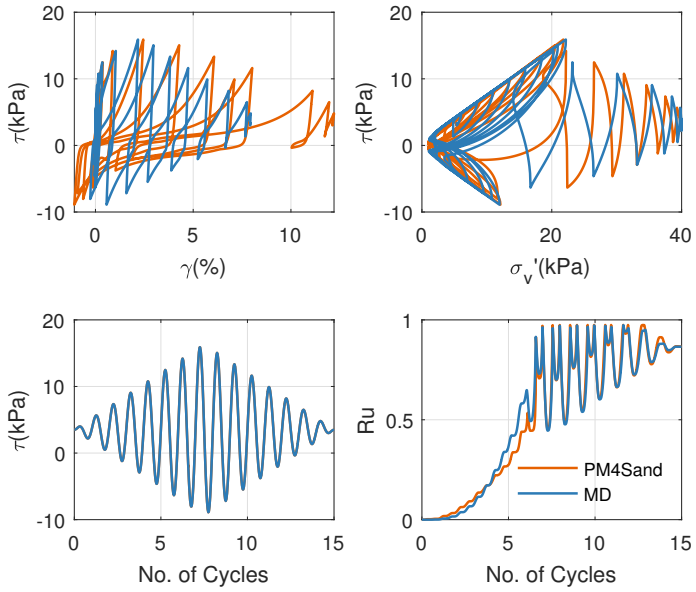

Figure B.14: Type-A prediction results for $\sigma'_v = 40\,kPa$ and $CSR = 0.31$.

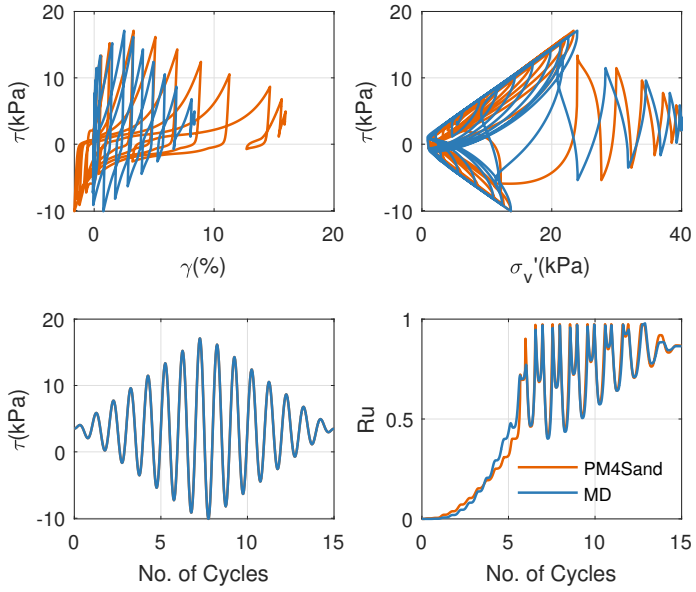

Figure B.15: Type-A prediction results for $\sigma'_v = 40\,kPa$ and $CSR = 0.34$.

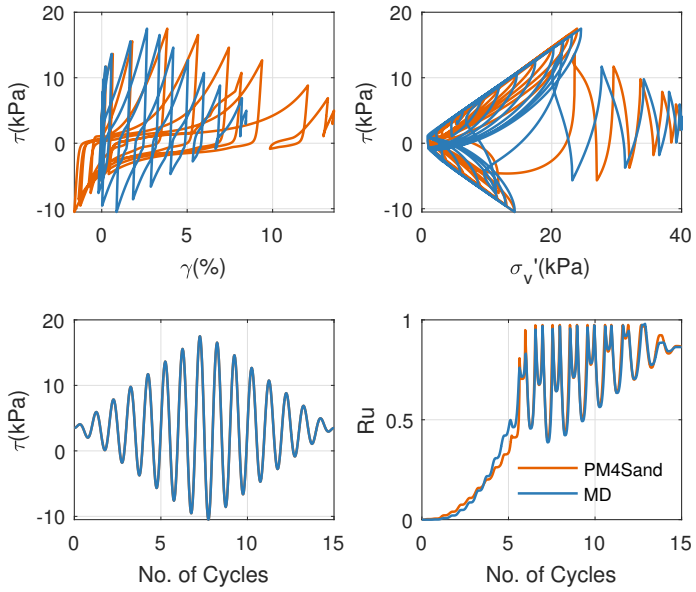

Figure B.16: Type-A prediction results for $\sigma'_v = 40\,kPa$ and $CSR = 0.35$.

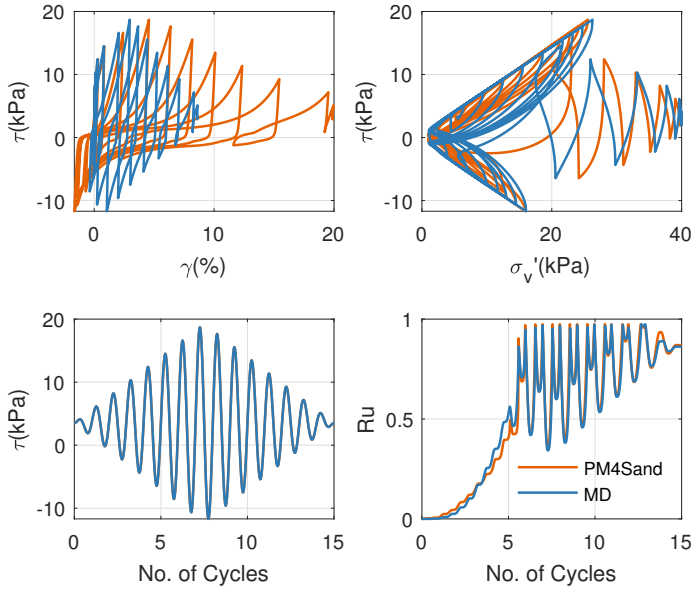

Figure B.17: Type-A prediction results for $\sigma'_v = 40\,kPa$ and $CSR = 0.38$.

Appendix C

ADDITIONAL LEAP2020 PHASE B PREDICTION RESULTS

C.1 EU-2

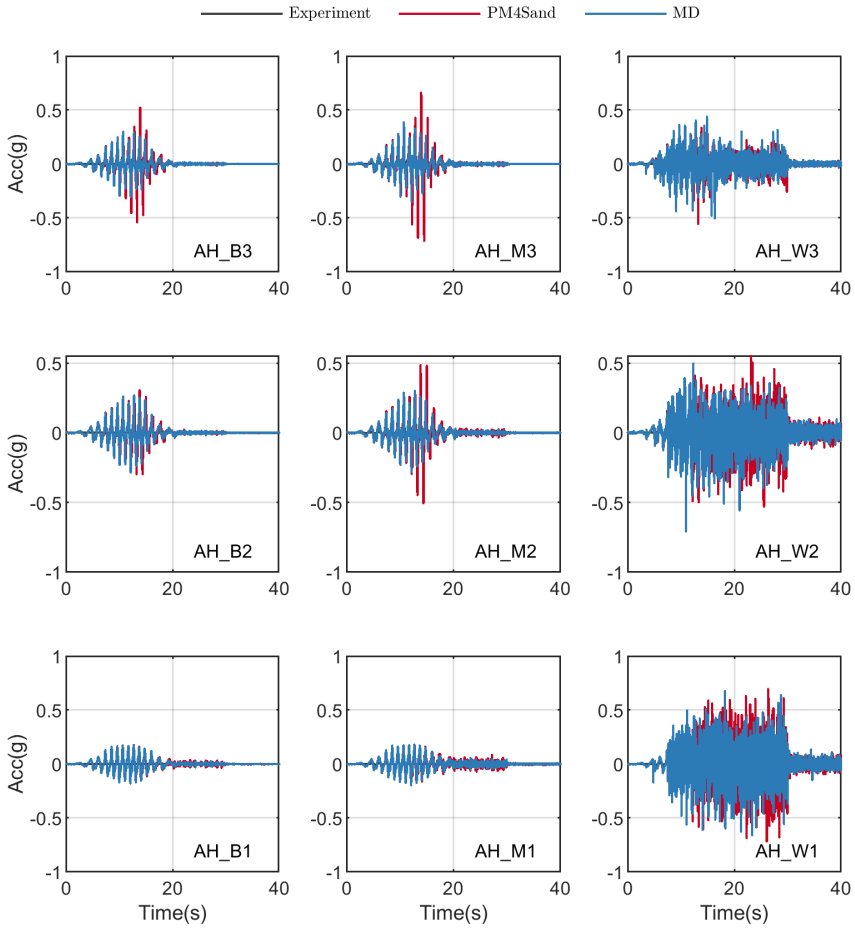

Figure C.1: Comparison of acceleration time histories between centrifuge and simulation results of EU-2 case at accelerometer arrays B-W. - see Fig. 9.1 for location of the sensors.

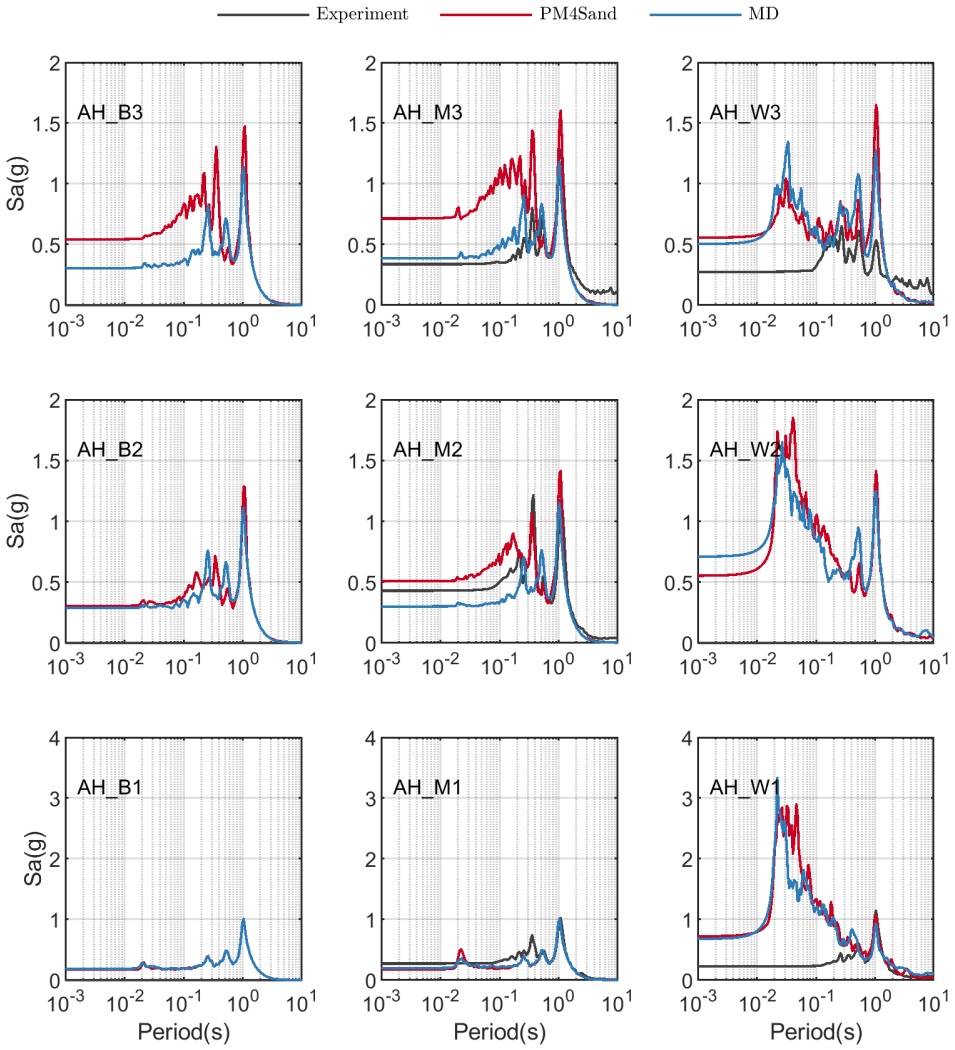

Figure C.2: Comparison of acceleration response spectra (5% damping) between centrifuge and simulation results of EU-2 case at accelerometer arrays B-W. - see Fig. 9.1 for location of the sensors.

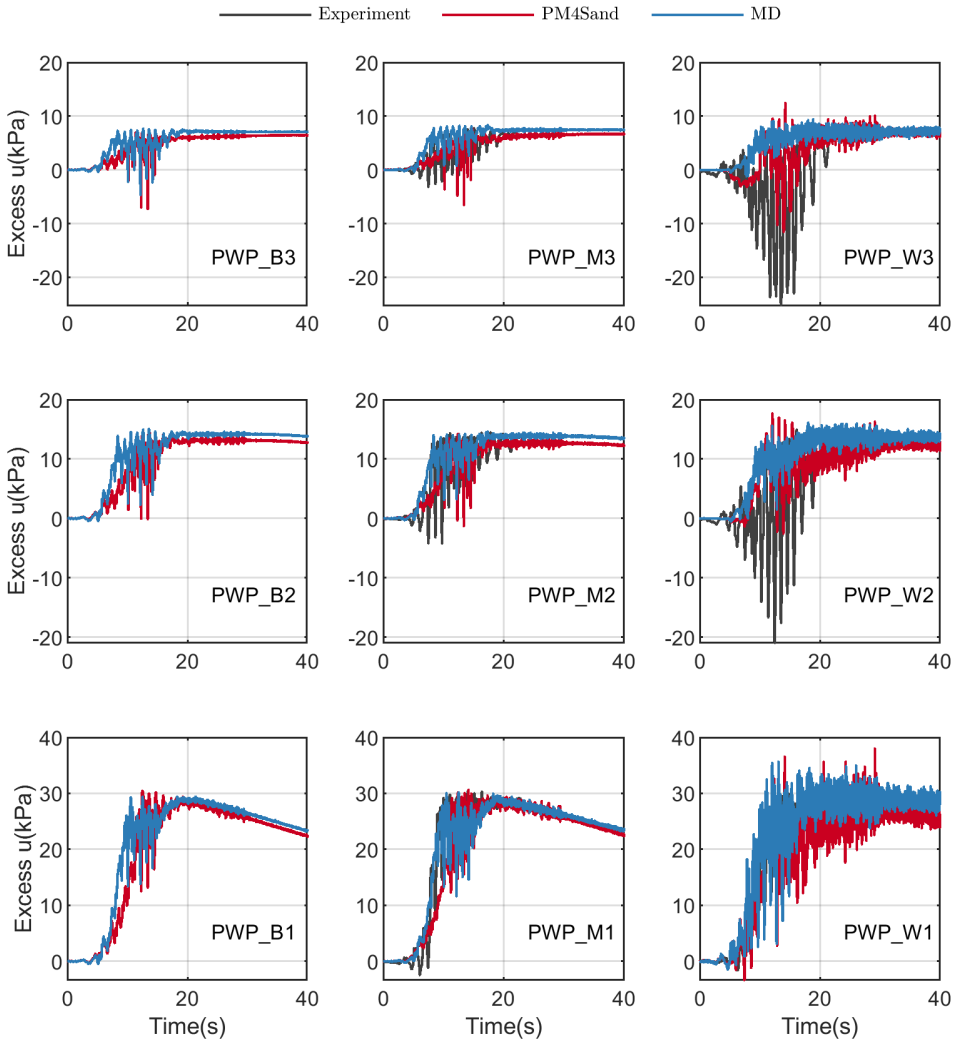

Figure C.3: Comparison of evolution of pwp between centrifuge and simulation results of EU-2 case at transducer arrays B-W. - see Fig. 9.1 for location of the sensors.

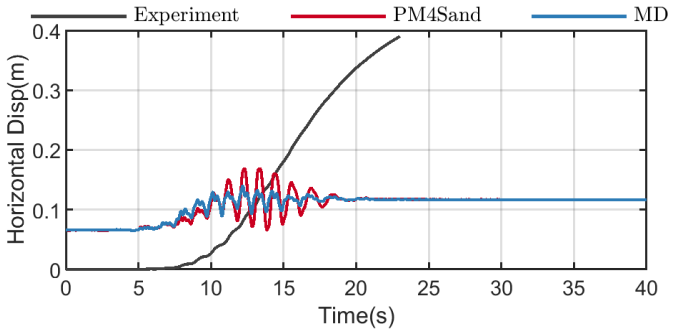

Figure C.4: Comparison of lateral displacements of sheetpile wall between centrifuge and simulation results at elevation of 5 m of EU-2 case.

C.2 KAIST-2

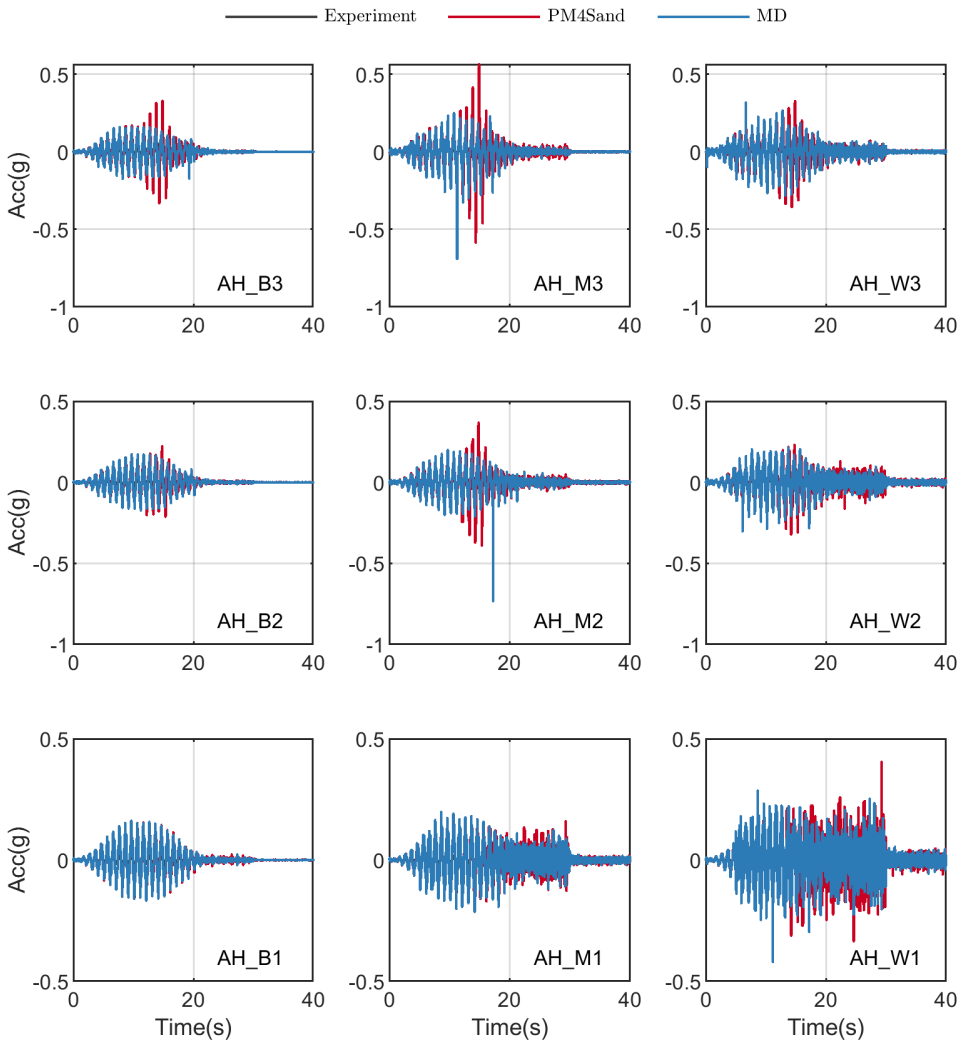

Figure C.5: Comparison of acceleration time histories between centrifuge and simulation results of KAIST-2 case at accelerometer arrays B-W. - see Fig. 9.1 for location of the sensors.

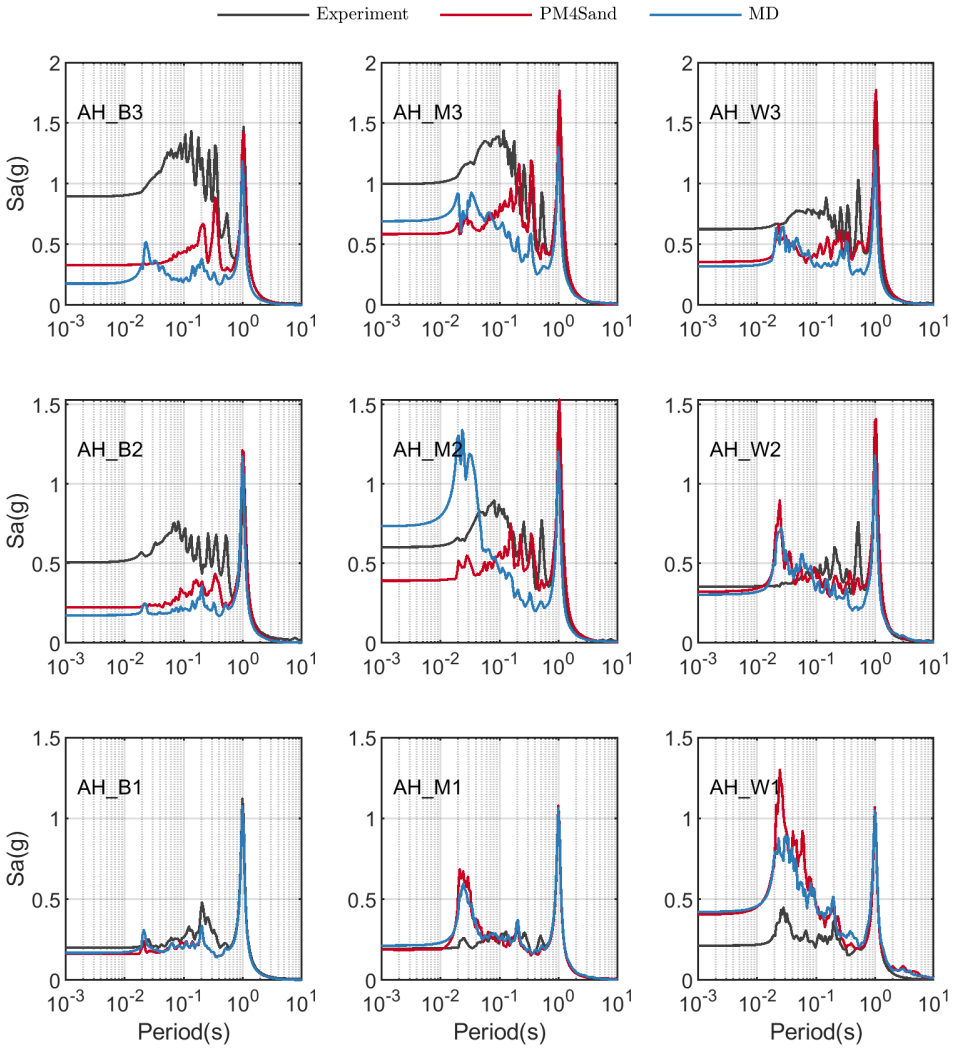

Figure C.6: Comparison of acceleration response spectra (5% damping) between centrifuge and simulation results of KAIST-2 case at accelerometer arrays B-W. - see Fig. 9.1 for location of the sensors.

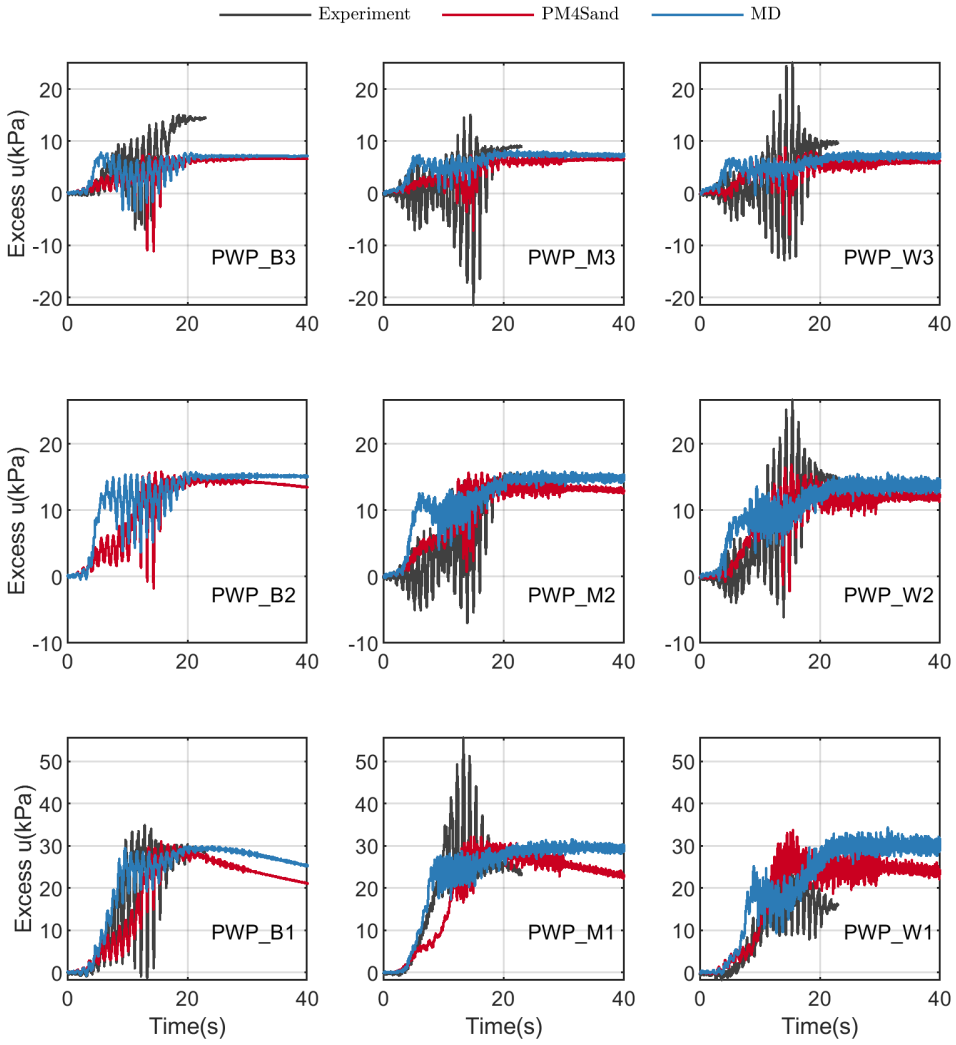

Figure C.7: Comparison of evolution of pwp between centrifuge and simulation results of KAIST-2 case at transducer arrays B-W. - see Fig. 9.1 for location of the sensors.

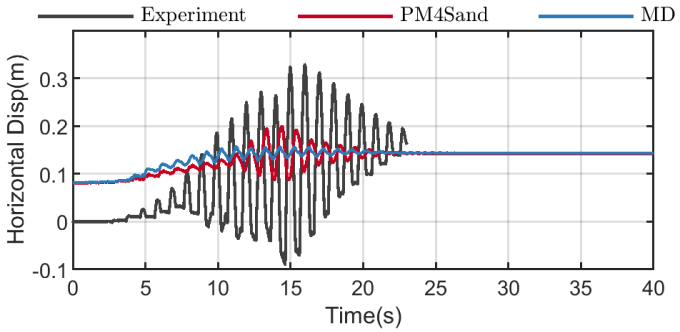

Figure C.8: Comparison of lateral displacements of sheetpile wall between centrifuge and simulation results at elevation of 5 m of KAIST-2 case.

C.3 KyU-1

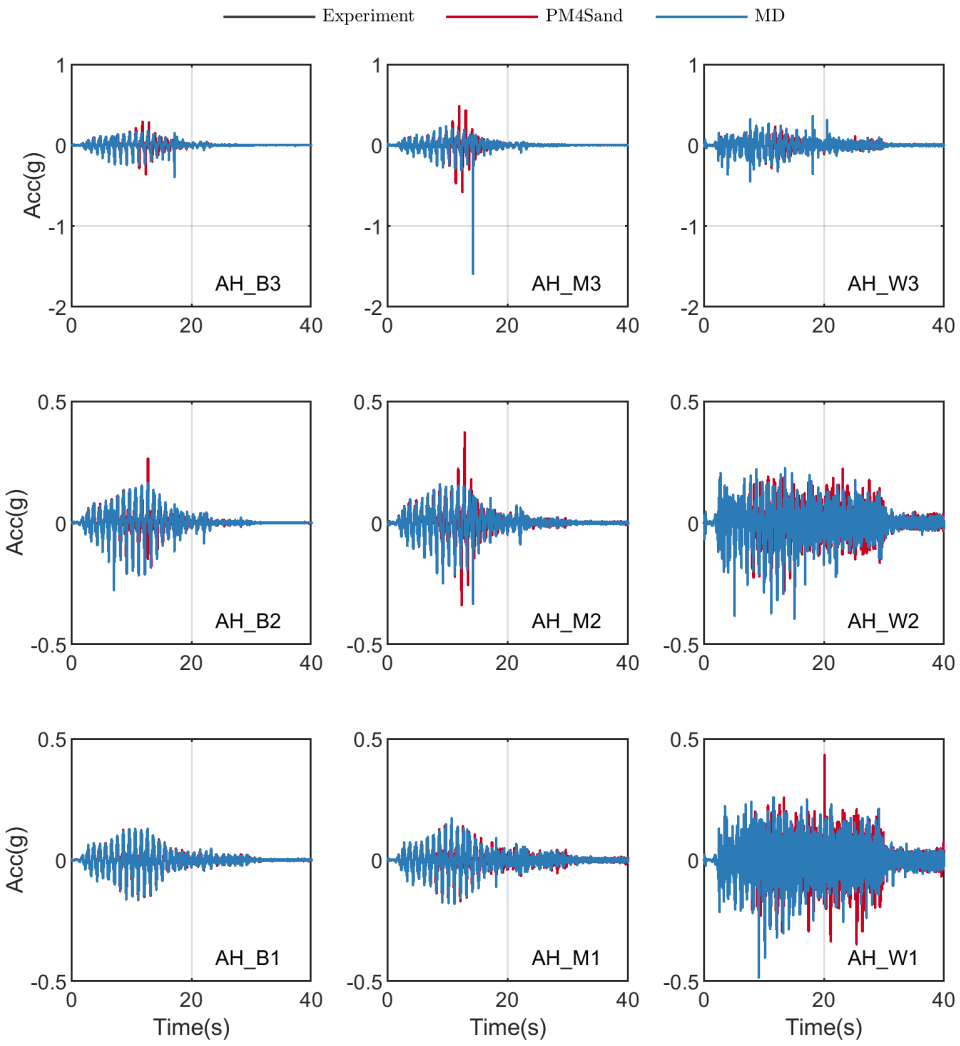

Figure C.9: Comparison of acceleration time histories between centrifuge and simulation results of KyU-1 case at accelerometer arrays B-W. - see Fig. 9.1 for location of the sensors.

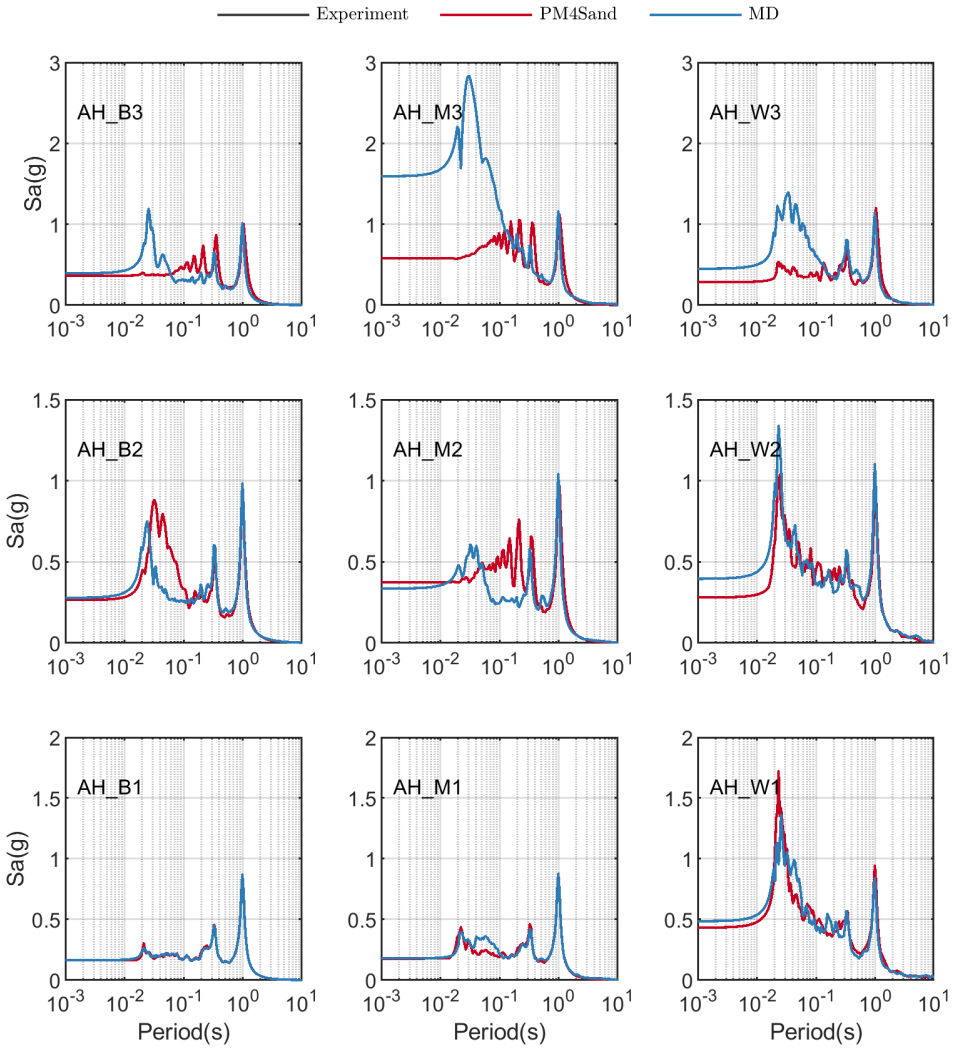

Figure C.10: Comparison of acceleration response spectra (5% damping) between centrifuge and simulation results of KyU-1 case at accelerometer arrays B-W. - see Fig. 9.1 for location of the sensors.

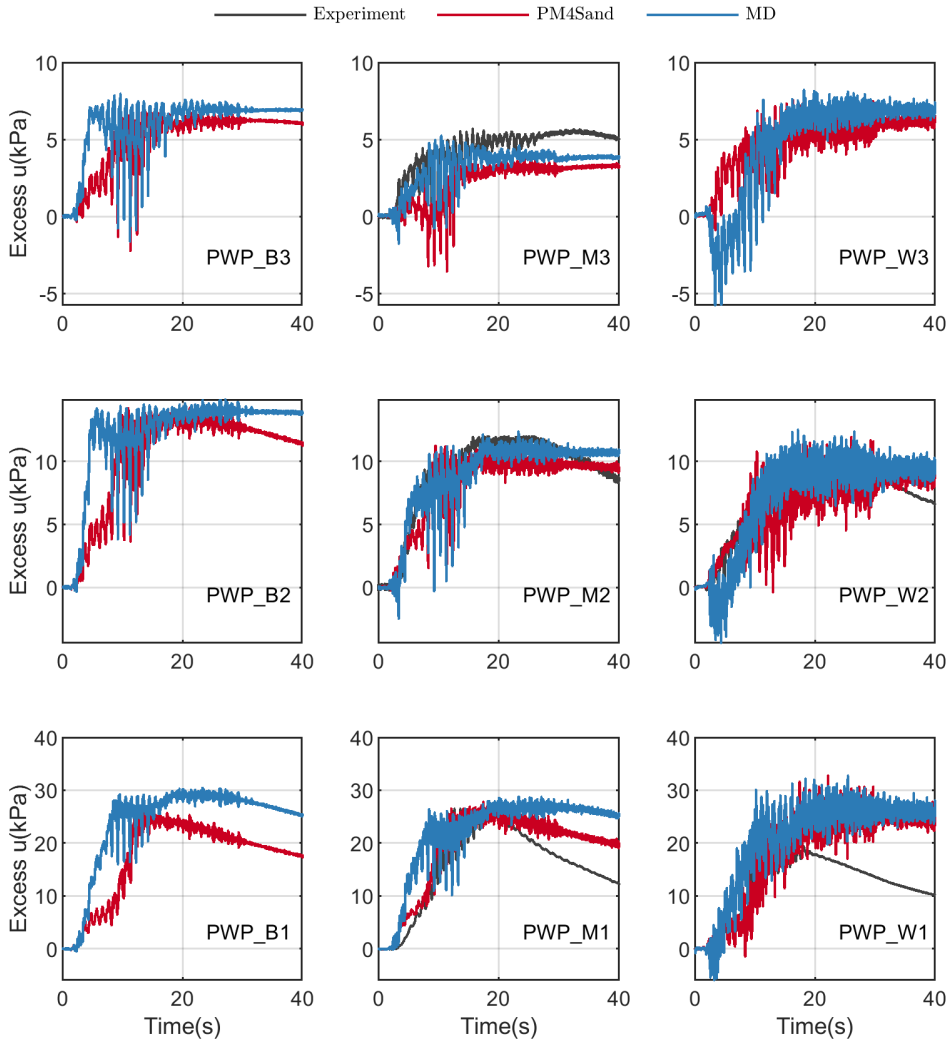

Figure C.11: Comparison of evolution of pwp between centrifuge and simulation results of KyU-1 case at transducer arrays B-W. - see Fig. 9.1 for location of the sensors.

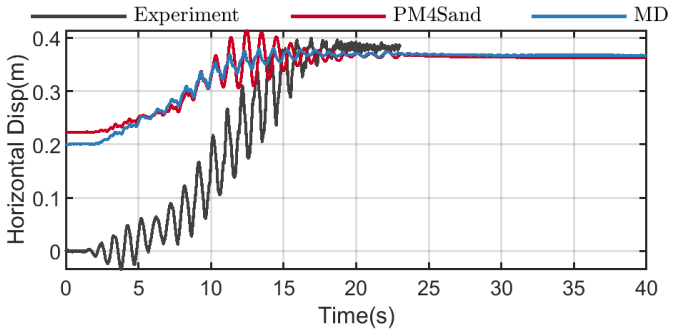

Figure C.12: Comparison of lateral displacements of sheetpile wall between centrifuge and simulation results at elevation of 5 m of KyU-1 case.

C.4 KyU-3

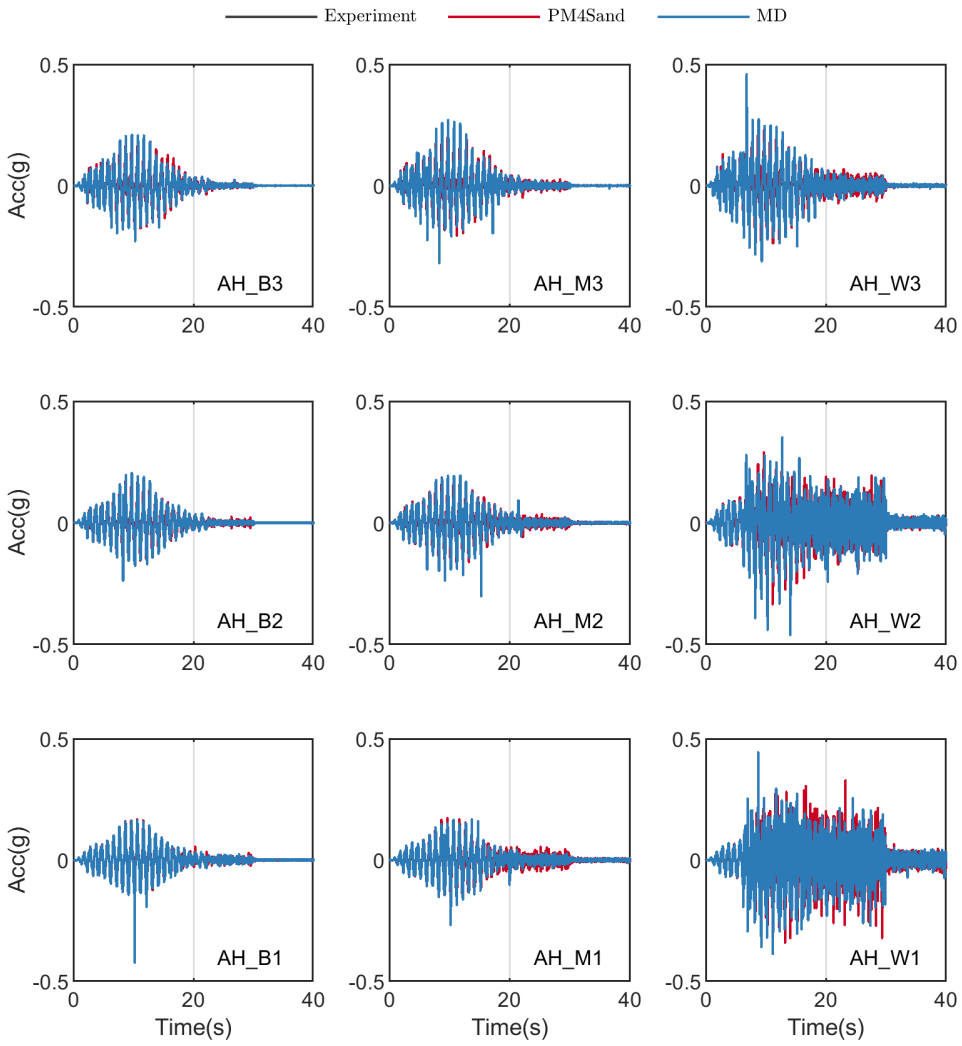

Figure C.13: Comparison of acceleration time histories between centrifuge and simulation results of KyU-3 case at accelerometer arrays B-W. - see Fig. 9.1 for location of the sensors.

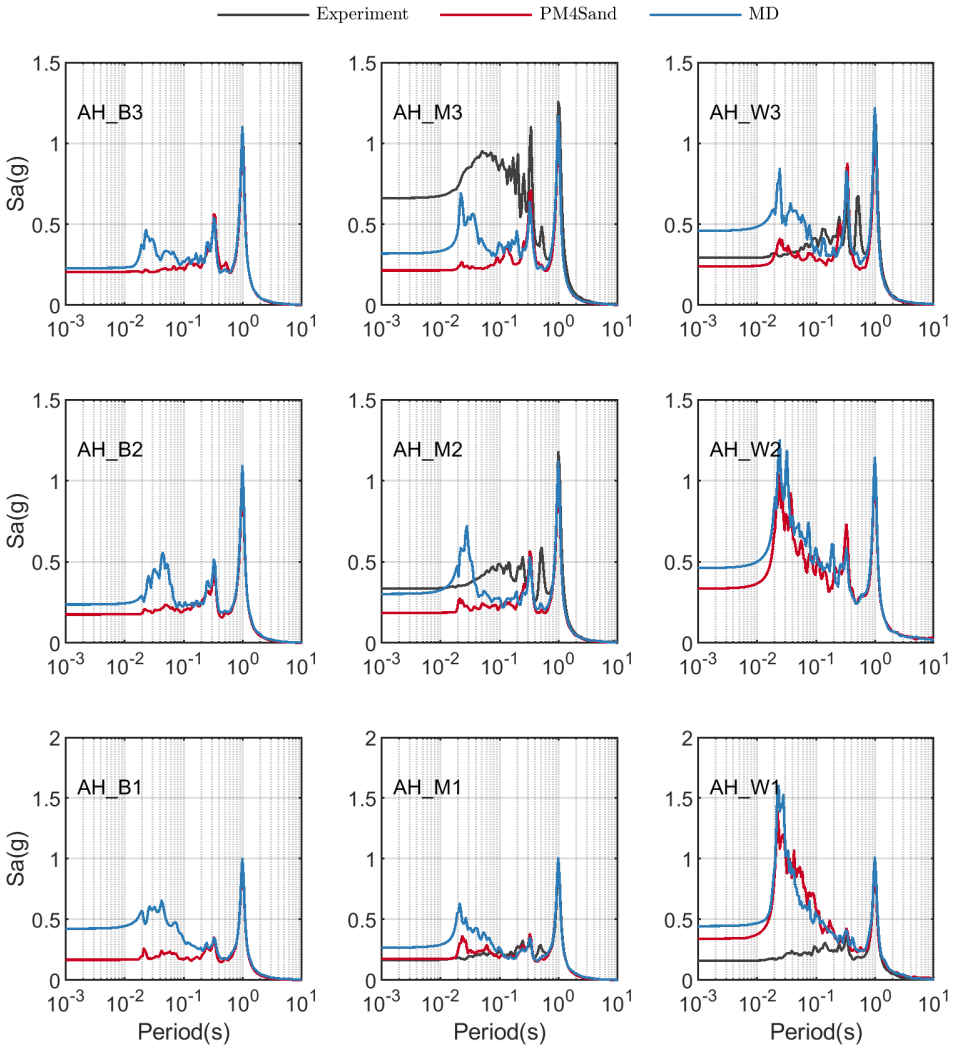

Figure C.14: Comparison of acceleration response spectra (5% damping) between centrifuge and simulation results of KyU-3 case at accelerometer arrays B-W. - see Fig. 9.1 for location of the sensors.

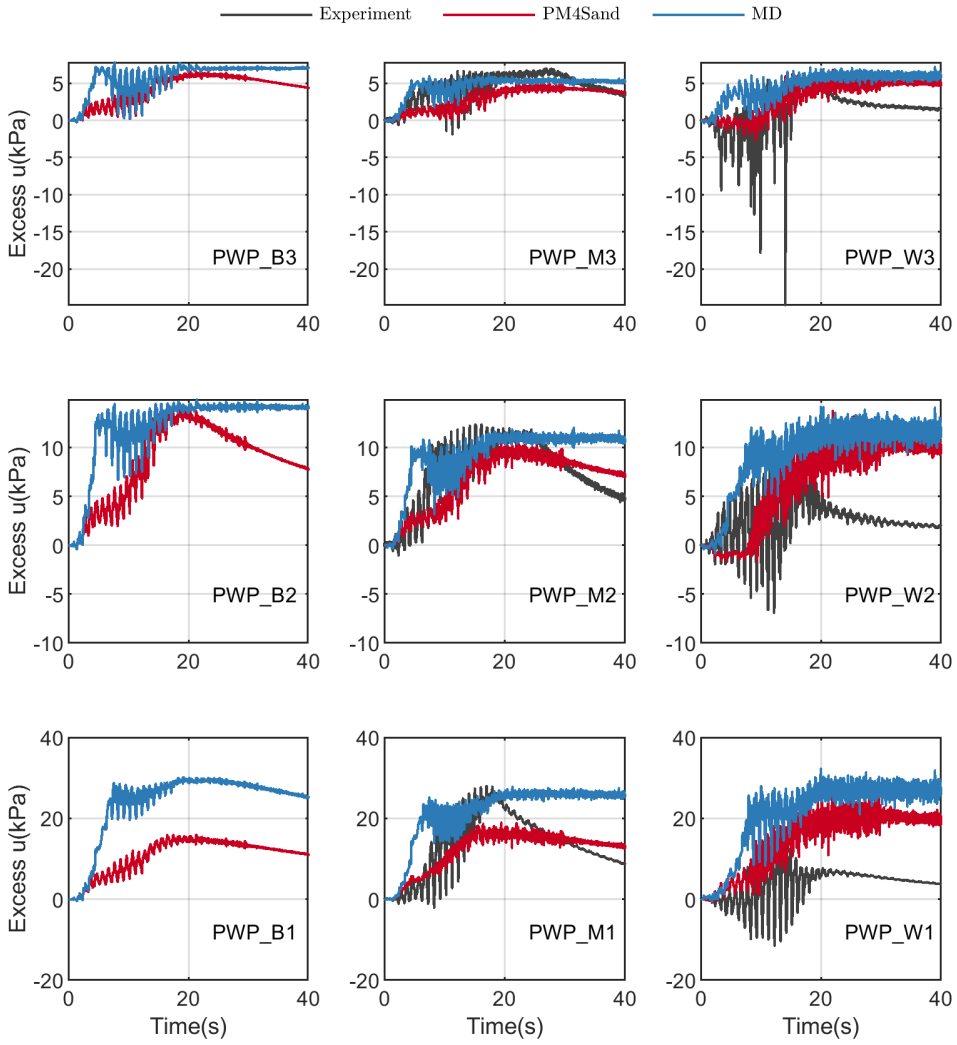

Figure C.15: Comparison of evolution of pwp between centrifuge and simulation results of KyU-3 case at transducer arrays B-W. - see Fig. 9.1 for location of the sensors.

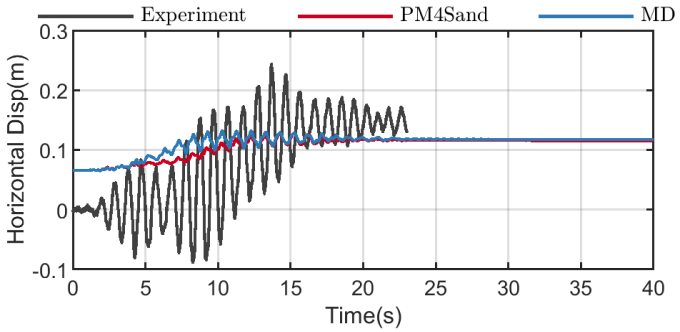

Figure C.16: Comparison of lateral displacements of sheetpile wall between centrifuge and simulation results at elevation of 5 m of KyU-3 case.

C.5 RPI-10

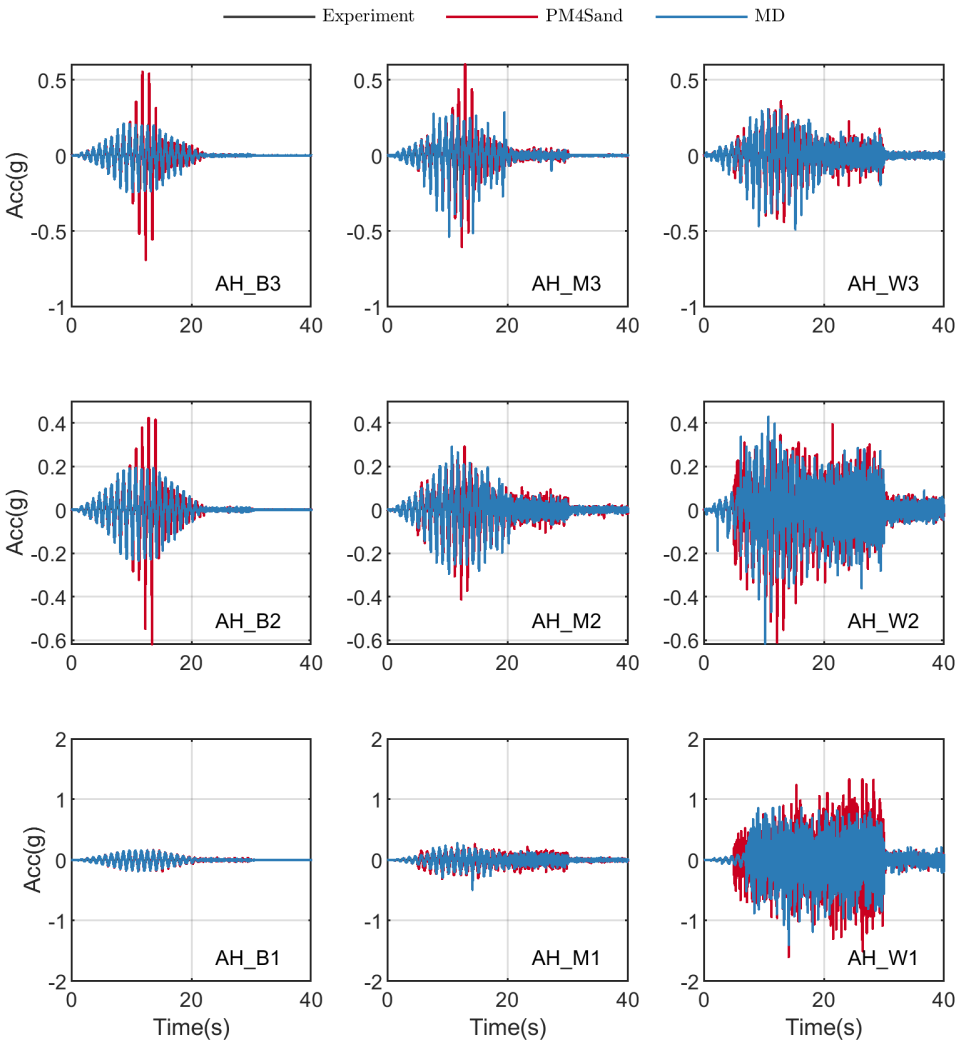

Figure C.17: Comparison of acceleration time histories between centrifuge and simulation results of RPI-10 case at accelerometer arrays B-W. - see Fig. 9.1 for location of the sensors.

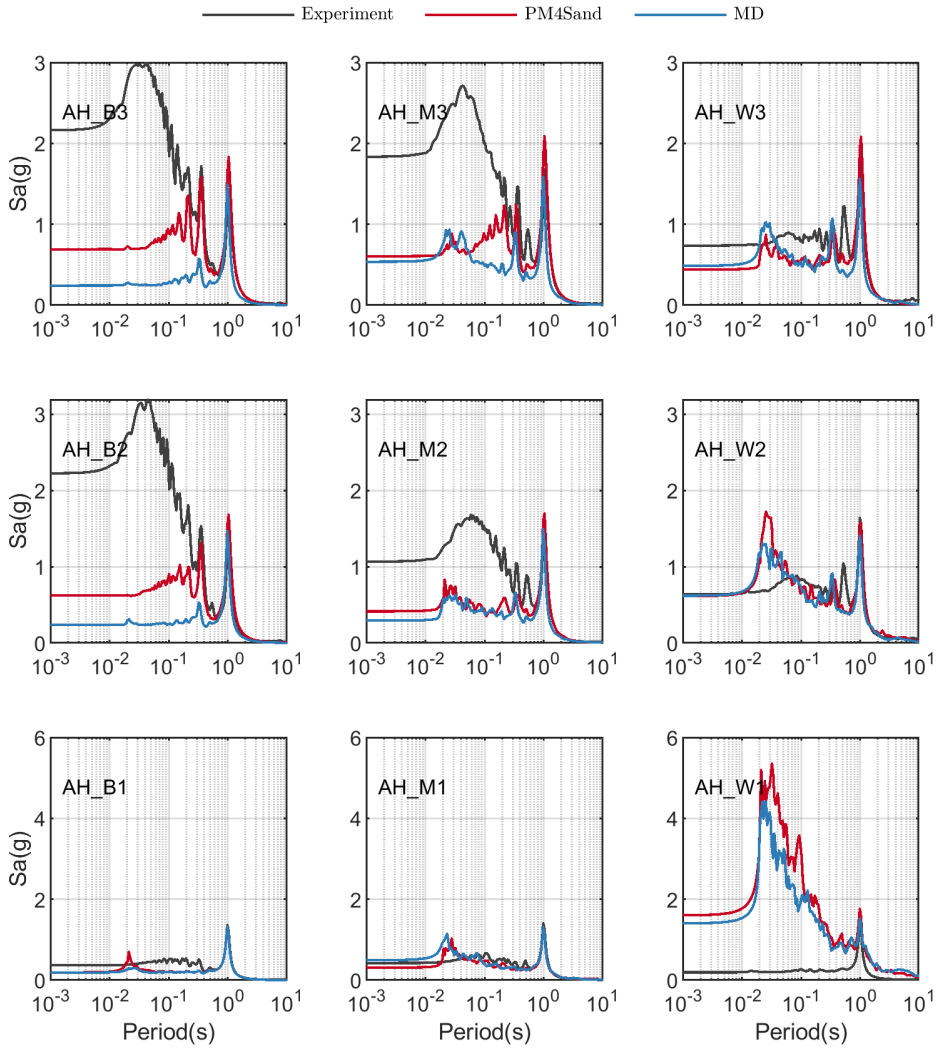

Figure C.18: Comparison of acceleration response spectra (5% damping) between centrifuge and simulation results of RPI-10 case at accelerometer arrays B-W. - see Fig. 9.1 for location of the sensors.

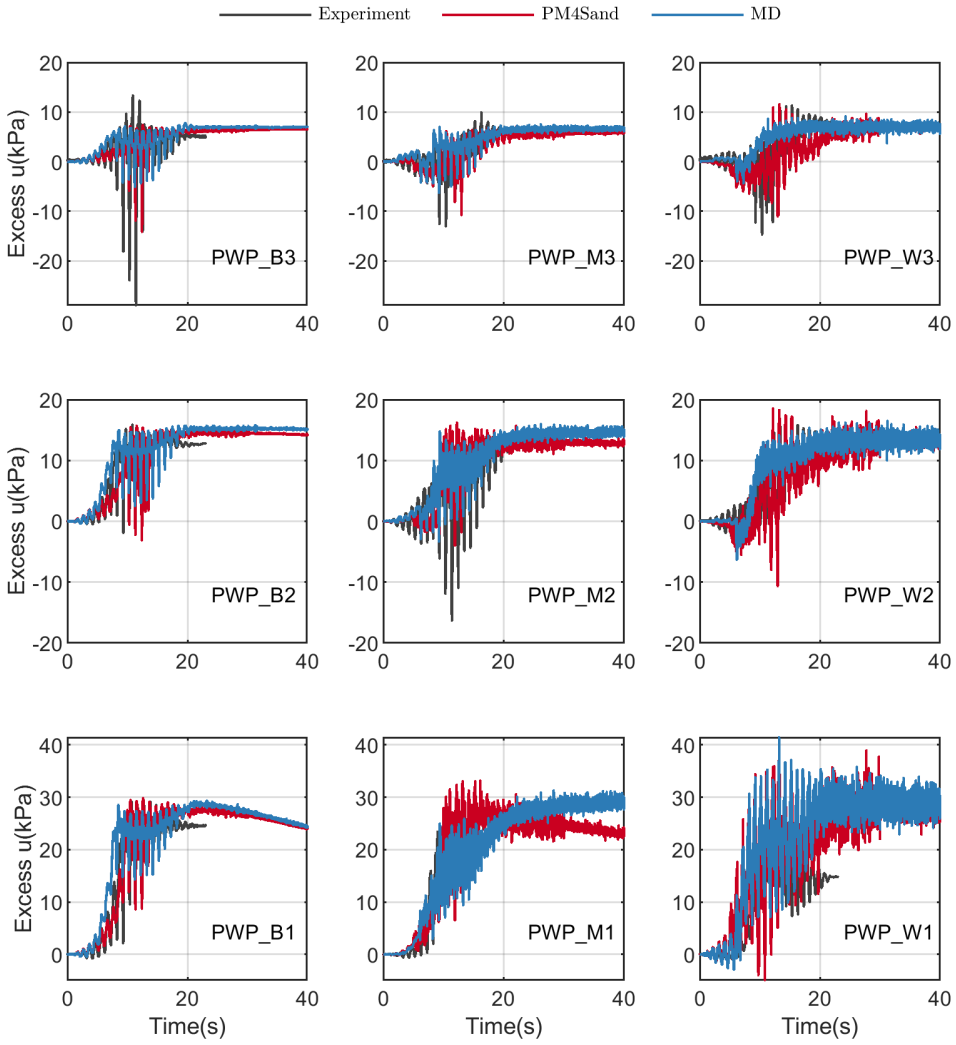

Figure C.19: Comparison of evolution of pwp between centrifuge and simulation results of RPI-10 case at transducer arrays B-W. - see Fig. 9.1 for location of the sensors.

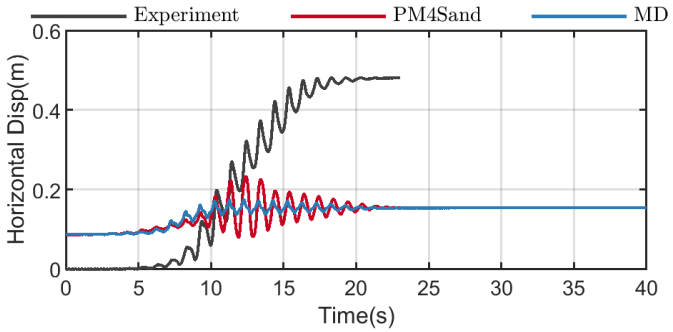

Figure C.20: Comparison of lateral displacements of sheetpile wall between centrifuge and simulation results at elevation of 5 m of RPI-10 case.

C.6 RPI-11

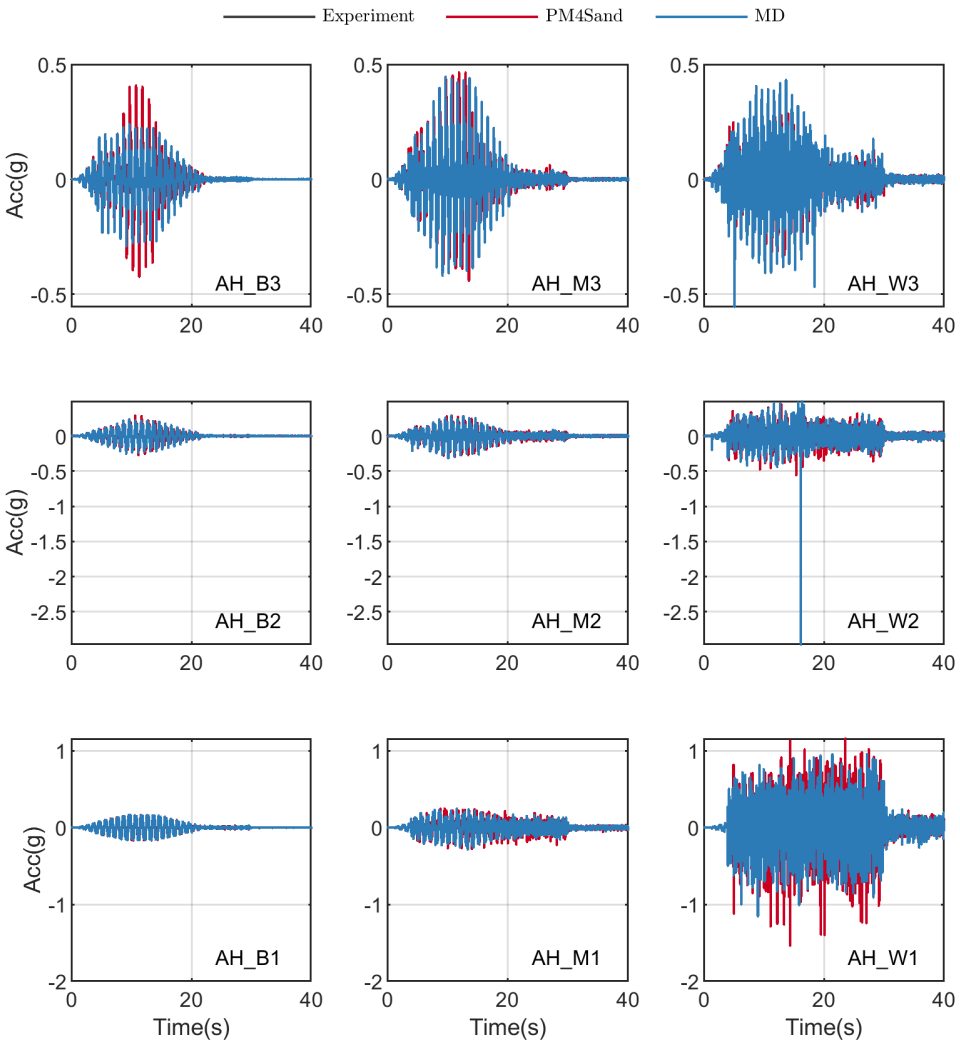

Figure C.21: Comparison of acceleration time histories between centrifuge and simulation results of RPI-11 case at accelerometer arrays B-W. - see Fig. 9.1 for location of the sensors.

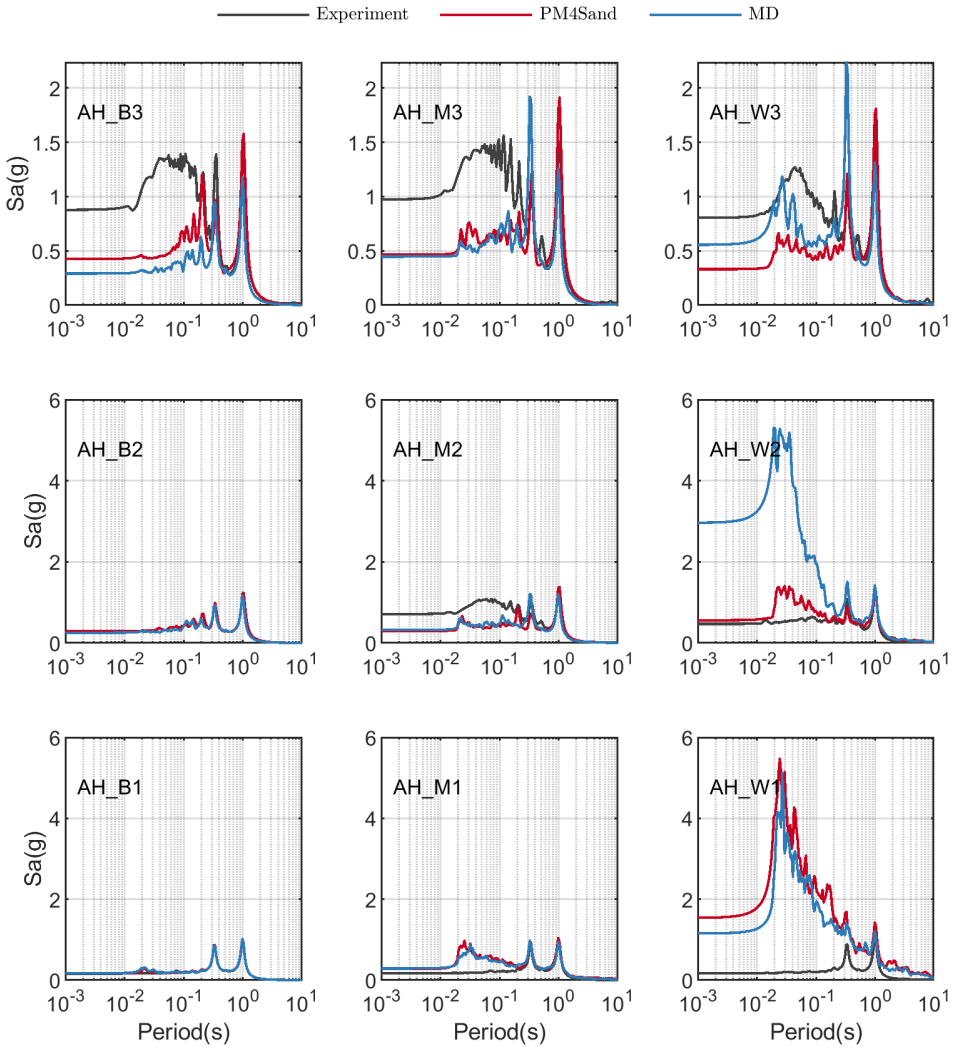

Figure C.22: Comparison of acceleration response spectra (5% damping) between centrifuge and simulation results of RPI-11 case at accelerometer arrays B-W. - see Fig. 9.1 for location of the sensors.

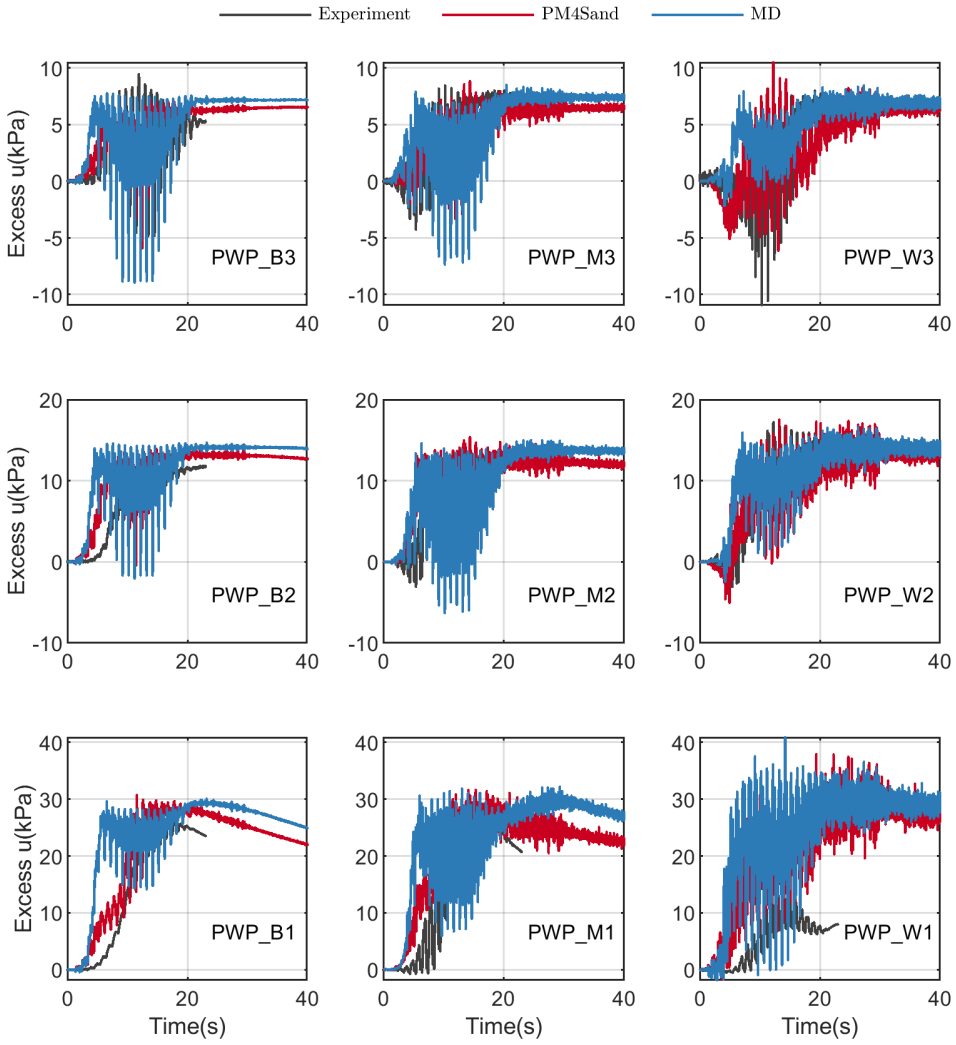

Figure C.23: Comparison of evolution of pwp between centrifuge and simulation results of RPI-11 case at transducer arrays B-W. - see Fig. 9.1 for location of the sensors.

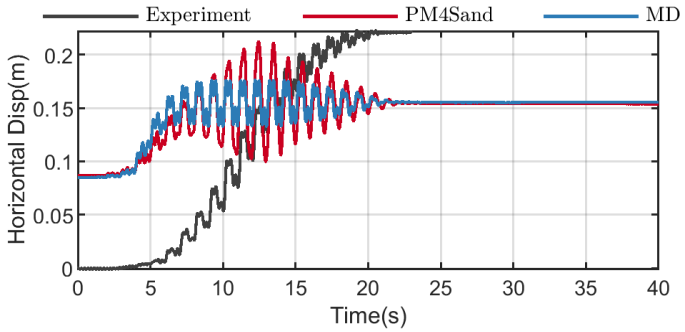

Figure C.24: Comparison of lateral displacements of sheetpile wall between centrifuge and simulation results at elevation of 5 m of RPI-11 case.

C.7 RPI-12

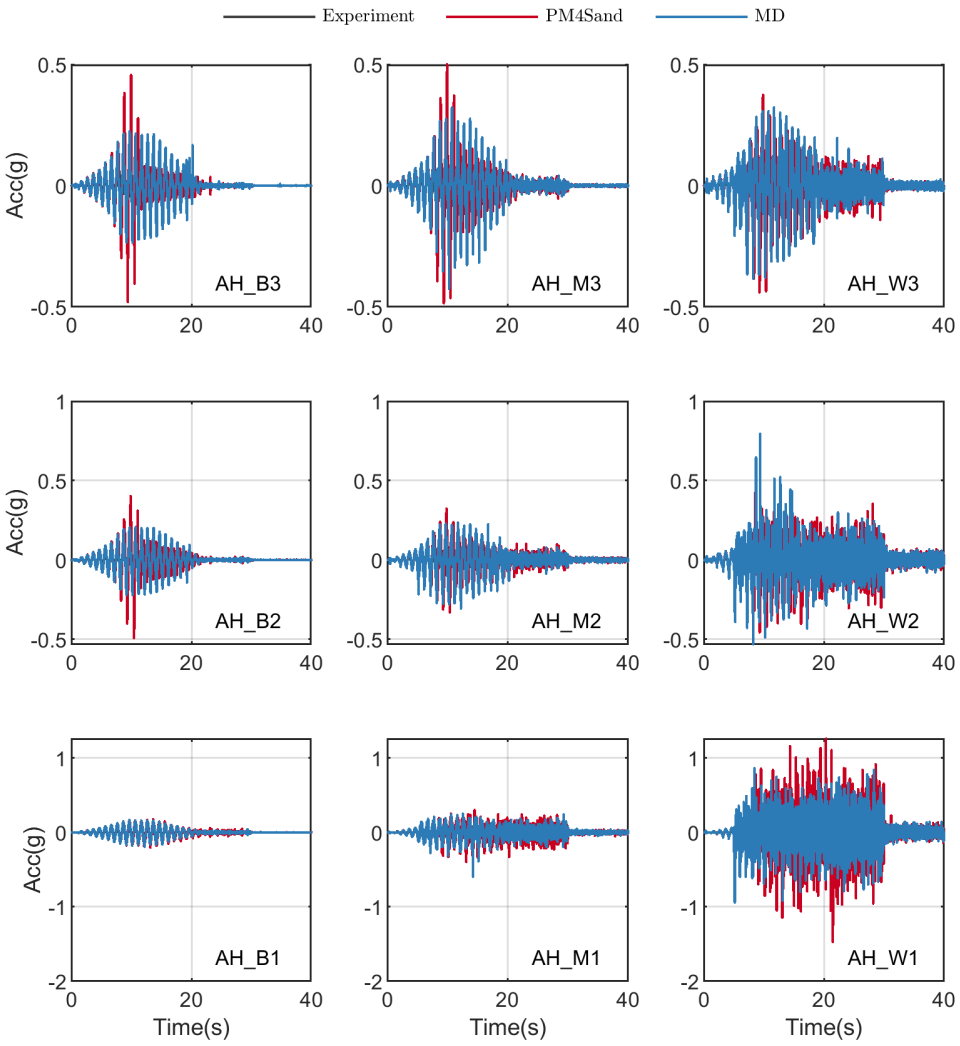

Figure C.25: Comparison of acceleration time histories between centrifuge and simulation results of RPI-12 case at accelerometer arrays B-W. - see Fig. 9.1 for location of the sensors.

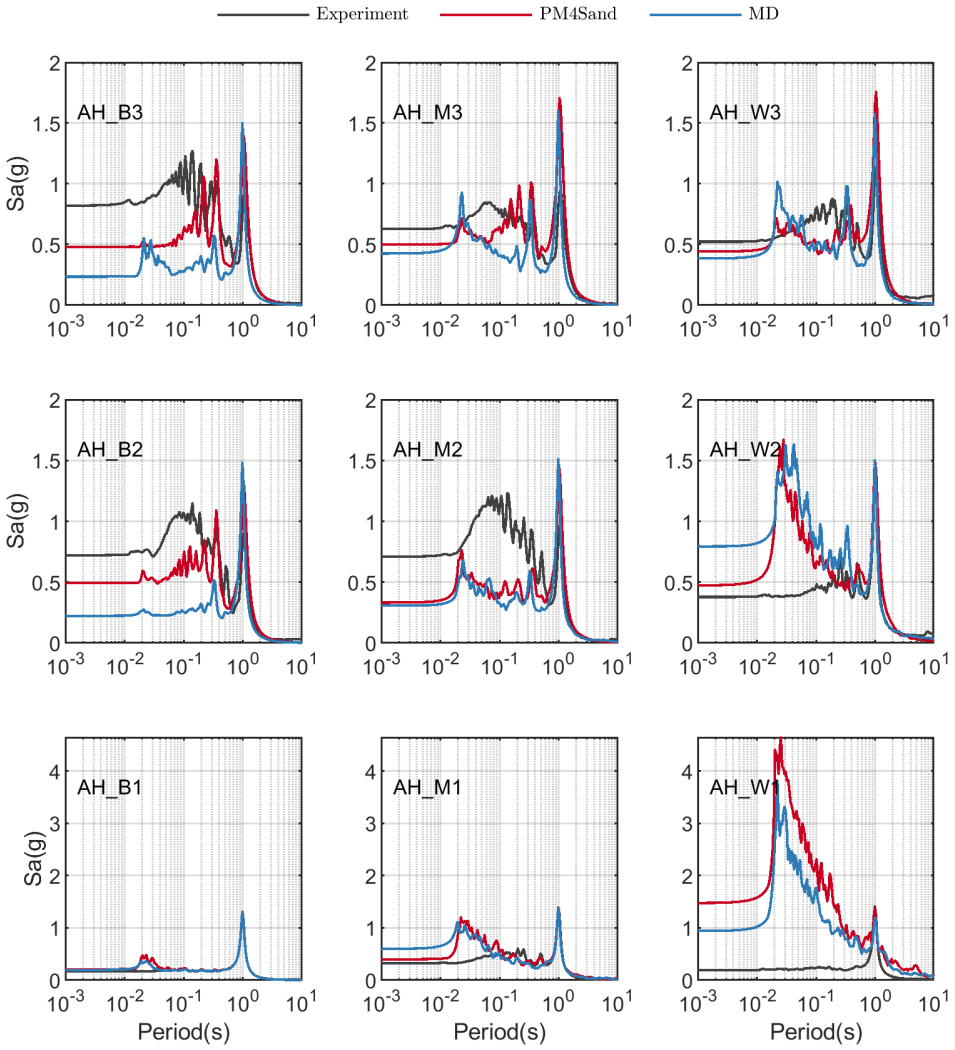

Figure C.26: Comparison of acceleration response spectra (5% damping) between centrifuge and simulation results of RPI-12 case at accelerometer arrays B-W. - see Fig. 9.1 for location of the sensors.

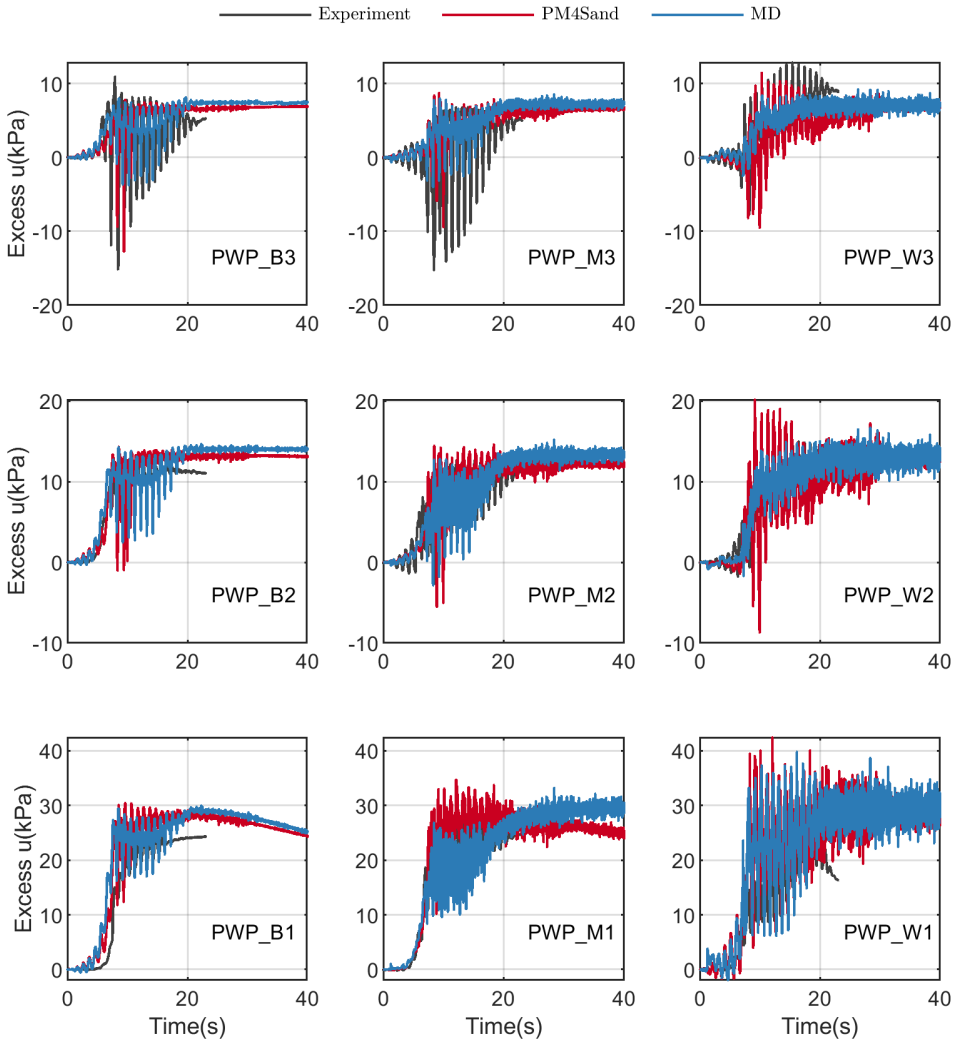

Figure C.27: Comparison of evolution of pwp between centrifuge and simulation results of RPI-12 case at transducer arrays B-W. - see Fig. 9.1 for location of the sensors.

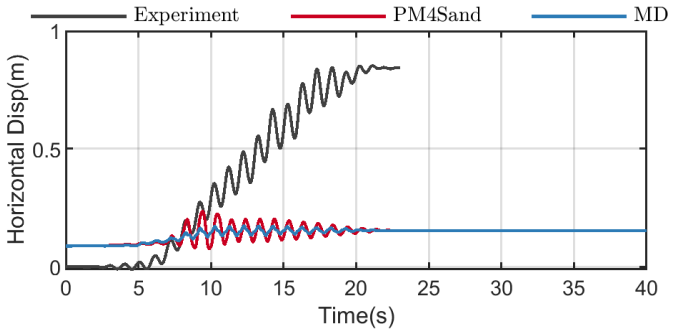

Figure C.28: Comparison of lateral displacements of sheetpile wall between centrifuge and simulation results at elevation of 5 m of RPI-12 case.

C.8 RPI-13

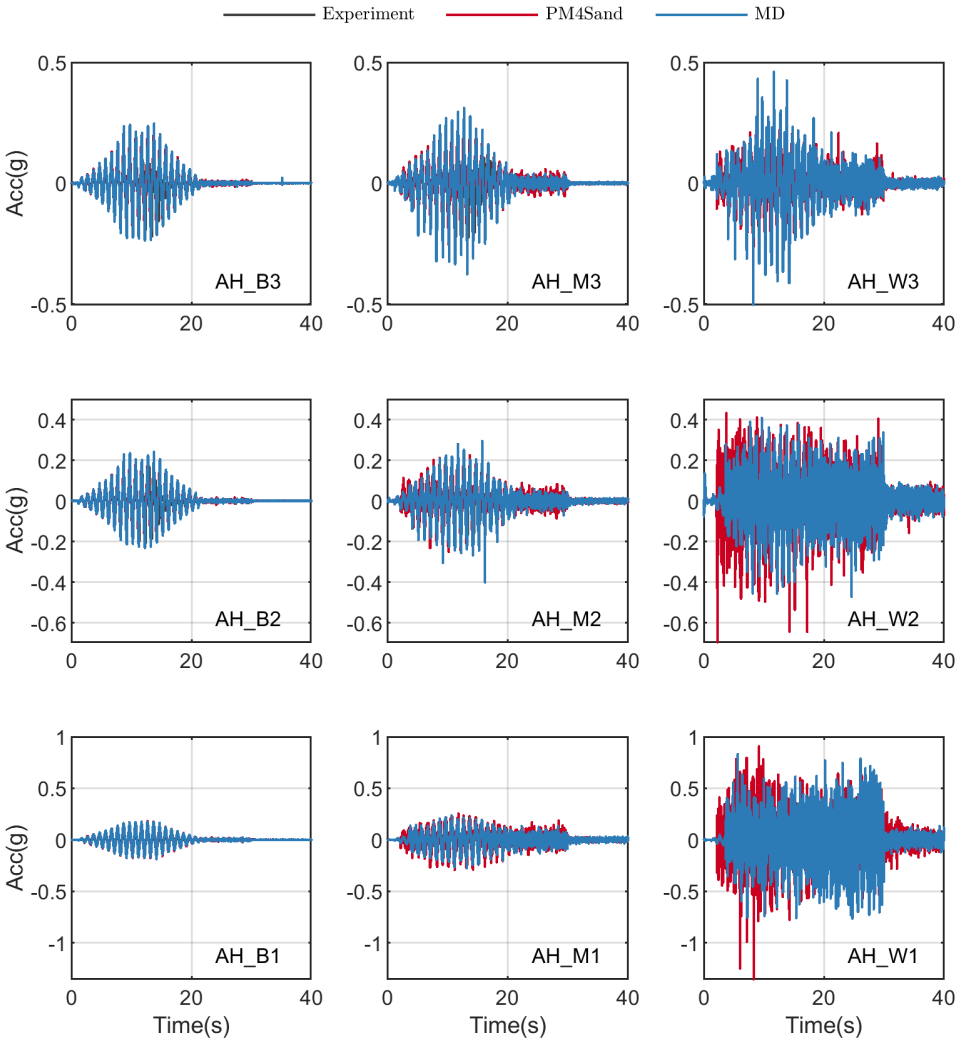

Figure C.29: Comparison of acceleration time histories between centrifuge and simulation results of RPI-13 case at accelerometer arrays B-W. - see Fig. 9.1 for location of the sensors.

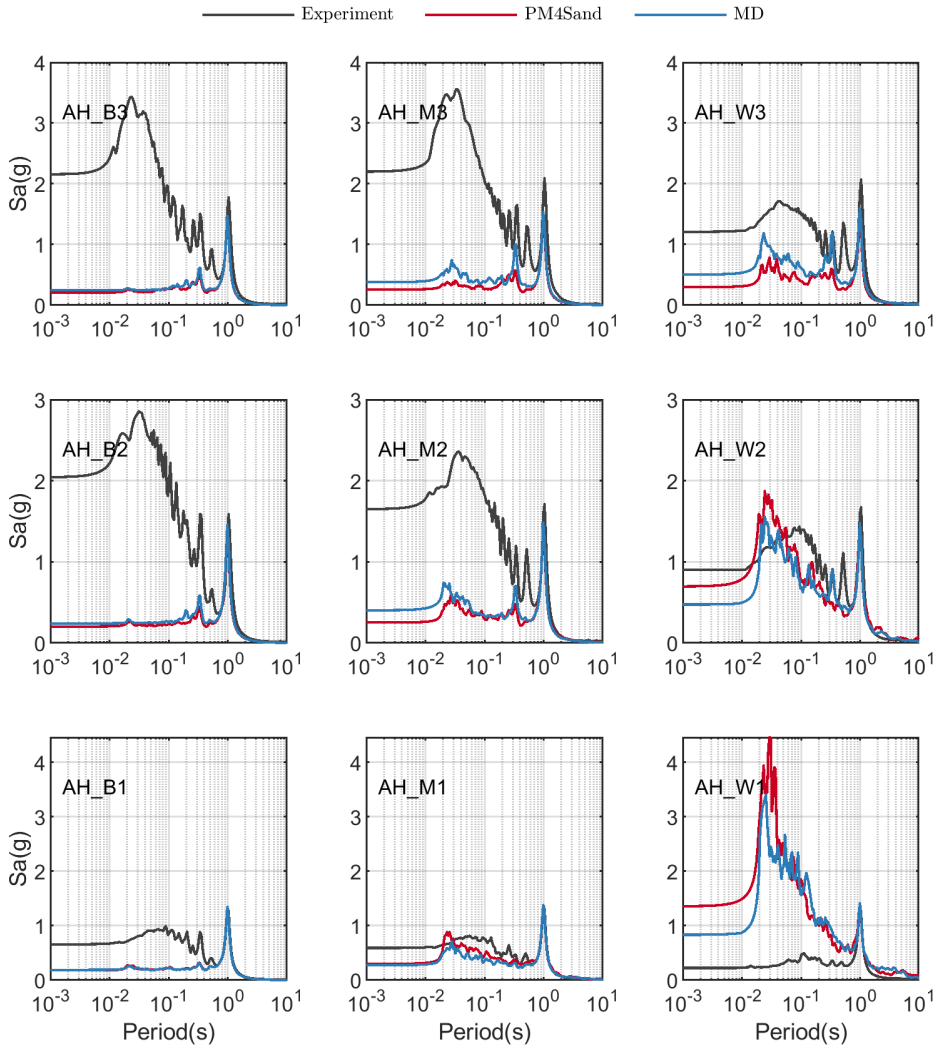

Figure C.30: Comparison of acceleration response spectra (5% damping) between centrifuge and simulation results of RPI-13 case at accelerometer arrays B-W. - see Fig. 9.1 for location of the sensors.

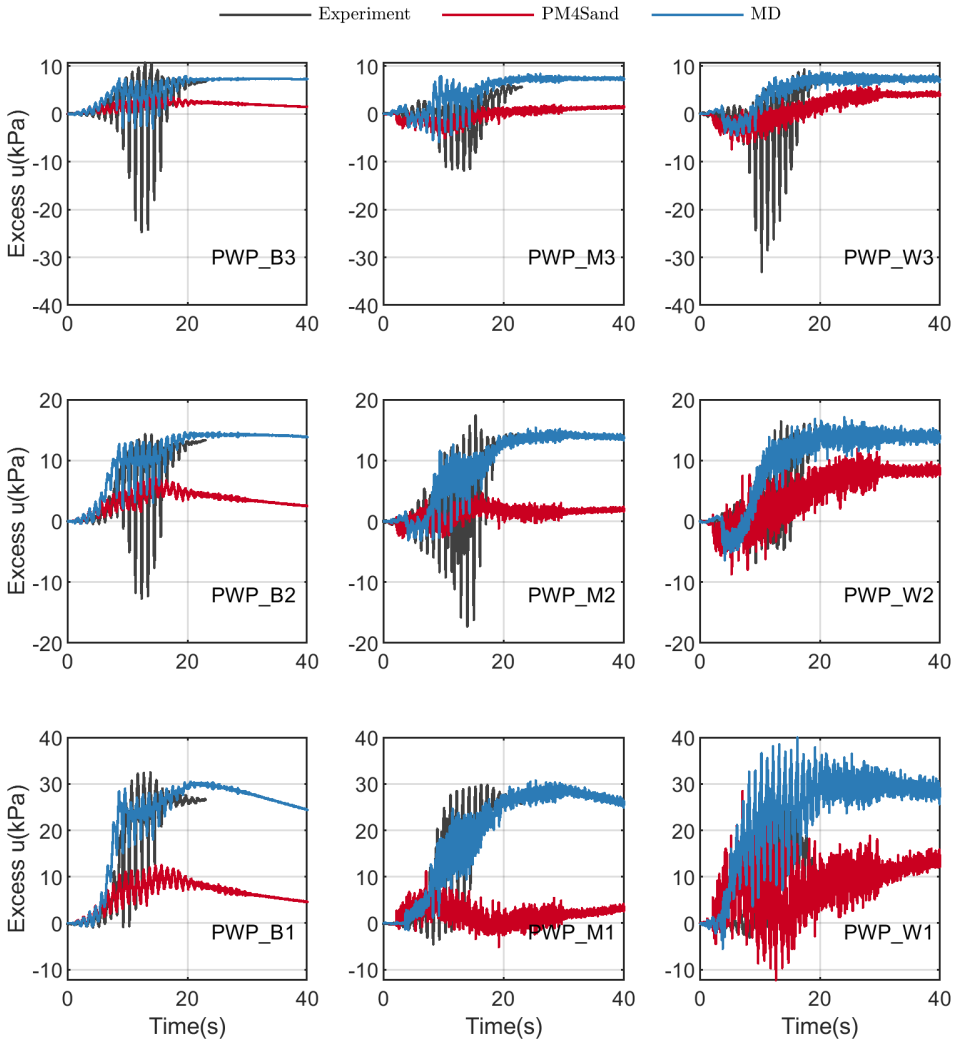

Figure C.31: Comparison of evolution of pwp between centrifuge and simulation results of RPI-13 case at transducer arrays B-W. - see Fig. 9.1 for location of the sensors.

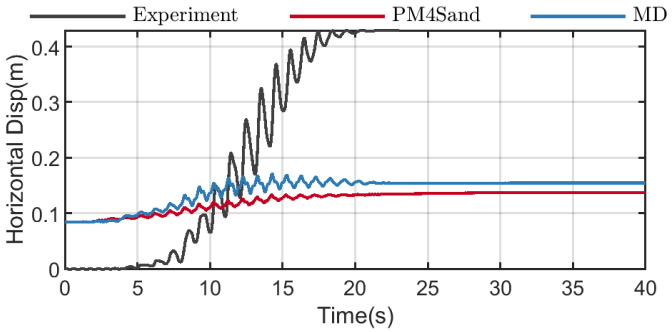

Figure C.32: Comparison of lateral displacements of sheetpile wall between centrifuge and simulation results at elevation of 5 m of RPI-13 case.

C.9 ZJU-1

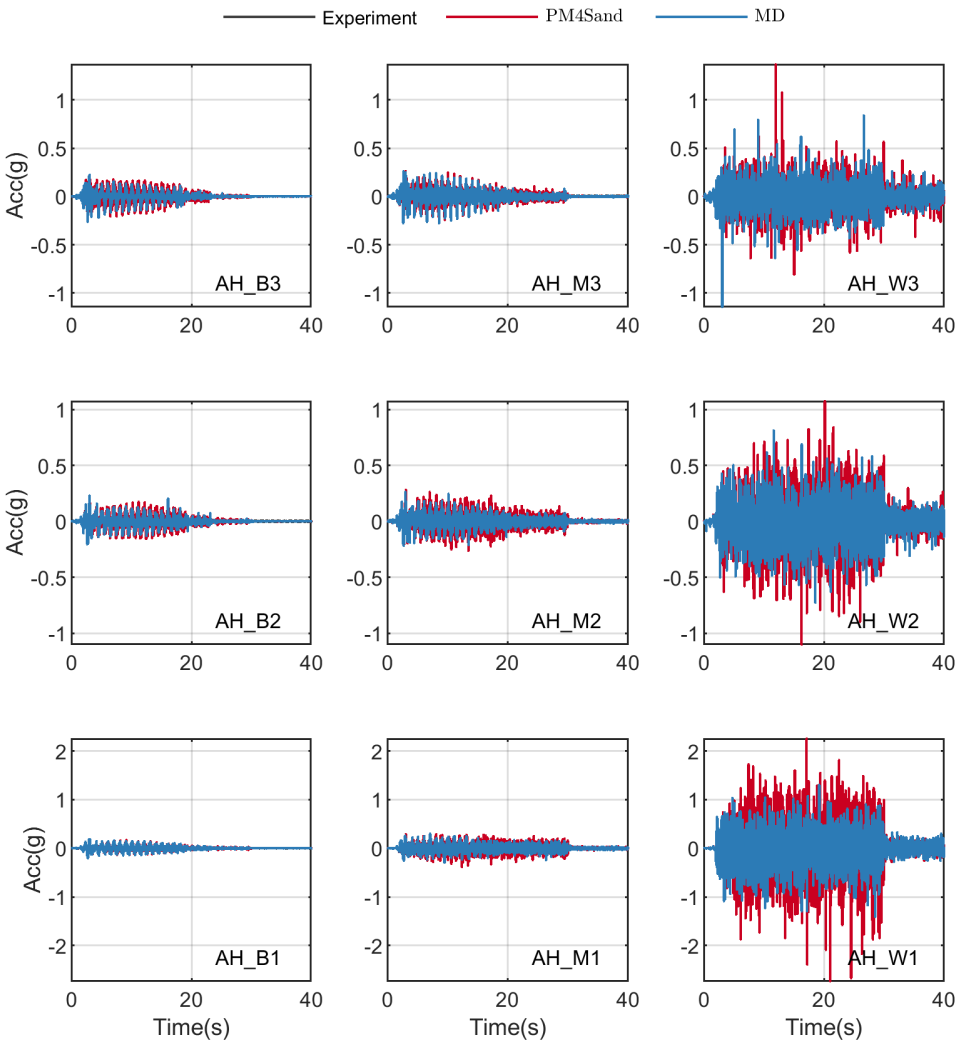

Figure C.33: Comparison of acceleration time histories between centrifuge and simulation results of ZJU-1 case at accelerometer arrays B-W. - see Fig. 9.1 for location of the sensors.

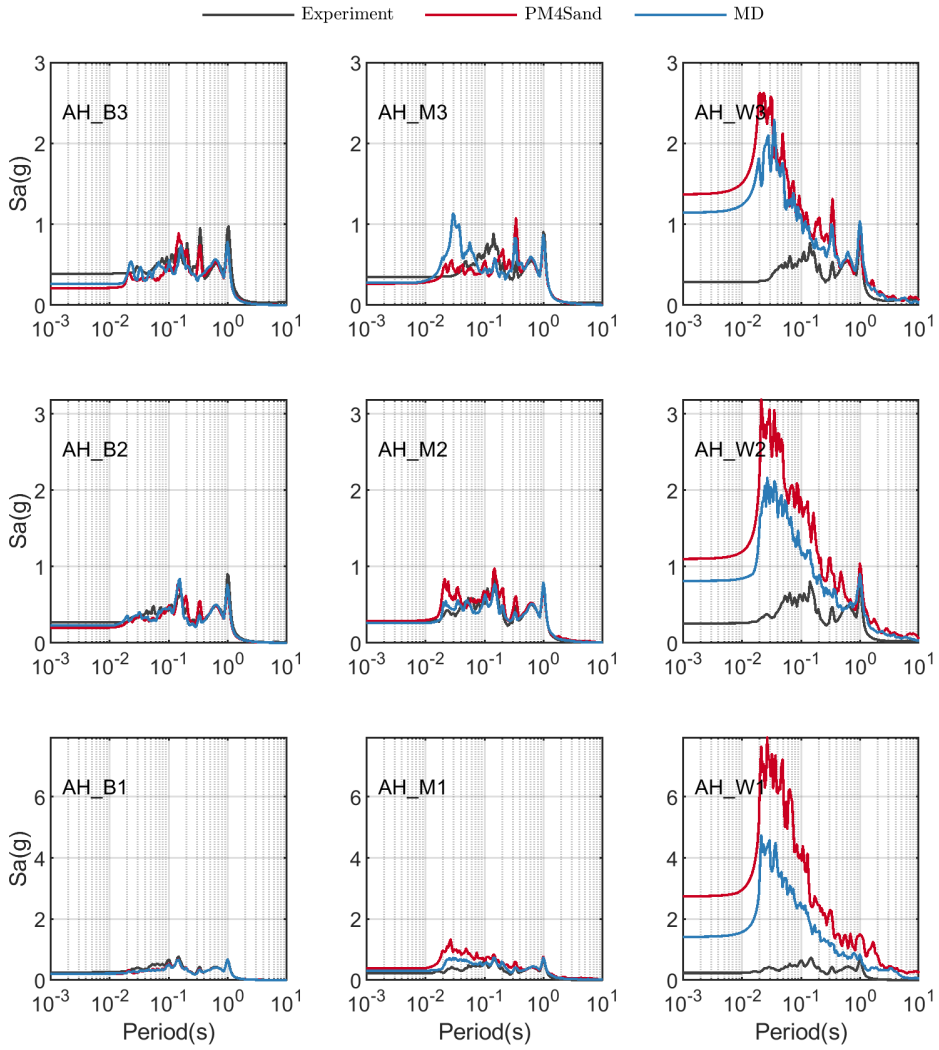

Figure C.34: Comparison of acceleration response spectra (5% damping) between centrifuge and simulation results of ZJU-1 case at accelerometer arrays B-W. - see Fig. 9.1 for location of the sensors.

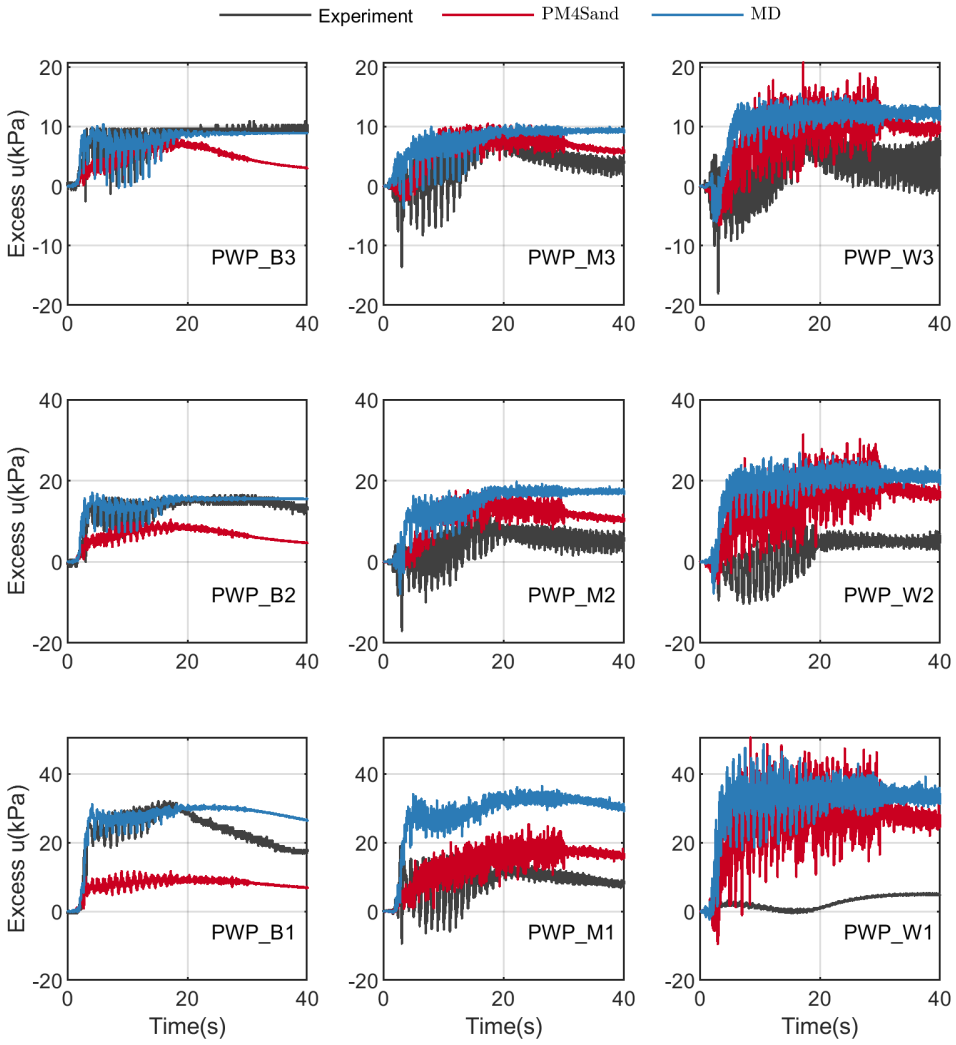

Figure C.35: Comparison of evolution of pwp between centrifuge and simulation results of ZJU-1 case at transducer arrays B-W. - see Fig. 9.1 for location of the sensors.

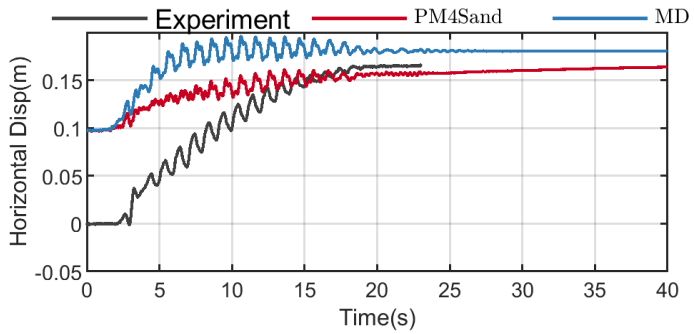

Figure C.36: Comparison of lateral displacements of sheetpile wall between centrifuge and simulation results at elevation of 5 m of ZJU-1 case.

Appendix D

INPUT MOTIONS SELECTED FOR ÇARK CANAL SITE

Table D.1: Summary of scaled input motion intensity measures

Motion	PGA (g)	PGV (m/s)	Ia (m/s)	CAV5 (m/s)	CAV (m/s)	Sa(T=0.5s)	Sa(T=1.0s)
1	0.30	0.32	1.05	6.97	7.69	0.75	0.54
2	0.32	0.32	0.65	4.64	5.04	0.72	0.41
3	0.28	0.55	1.78	10.80	11.07	0.82	0.52
4	0.25	0.78	1.65	11.66	11.86	0.78	0.37
5	0.30	0.23	0.62	5.51	6.07	0.65	0.31
6	0.31	1.08	1.65	13.49	14.19	0.55	0.90
7	0.26	0.35	1.59	16.36	17.81	0.51	0.35
8	0.27	0.41	2.24	15.78	17.30	0.62	0.31
9	0.36	0.55	1.01	8.07	9.15	0.71	0.50
10	0.28	0.65	1.22	8.81	9.28	0.48	0.40
SKR	0.40	0.45	1.81	10.75	10.96	0.44	0.39

Table D.2: Summary of additional input motions selected in this study

Result ID	Spectral Ordinate	Record Sequence Number	Mean Squared Error	Scale Factor	Tp-Pulse Period (s)	5-75% Duration (s)	5-95% Duration (s)	Arias Intensity (m/s)	Earthquake Name	Year	Magnitude	Mechanism	Rjb (km)	Rrup (km)	Vs30 (m/s)
1	H1	1106	0.0697	0.3539	1.092	4.3	9.5	8.4	"Kobe, Japan"	1995	6.9	strike slip	0.94	0.96	312
2	H1	1119	0.0412	0.4612	1.806	2.2	4.6	3.9	"Kobe, Japan"	1995	6.9	strike slip	0	0.27	312
3	H1	1120	0.0286	0.4525	1.554	6	11.3	8.7	"Kobe, Japan"	1995	6.9	strike slip	1.46	1.47	256
4	H1	1176	0.0416	1.1135	4.949	7	15.1	1.3	"Kocaeli, Turkey"	1999	7.51	strike slip	1.38	4.83	297
5	H1	1602	0.0496	0.4089	0.882	2.6	9	3.7	"Duzce, Turkey"	1999	7.14	strike slip	12.02	12.04	293.57
6	H1	2114	0.0506	0.9344	3.157	9.1	29.5	1.9	"Denali, Alaska"	2002	7.9	strike slip	0.18	2.74	329.4
7	H1	6887	0.0537	1.6544	12.621	11	28.5	0.9	"Darfield, New Zealand"	2010	7	strike slip	18.05	18.05	187
8	H1	6897	0.034	1.0423	7.826	13	19.6	2.1	"Darfield, New Zealand"	2010	7	strike slip	5.28	8.46	295.74
9	H1	6906	0.0749	0.4734	6.23	5.6	16	4.7	"Darfield, New Zealand"	2010	7	strike slip	1.22	1.22	344.02
10	H1	6911	0.0431	0.6174	9.919	7	9.5	3.2	"Darfield, New Zealand"	2010	7	strike slip	7.29	7.29	326.01

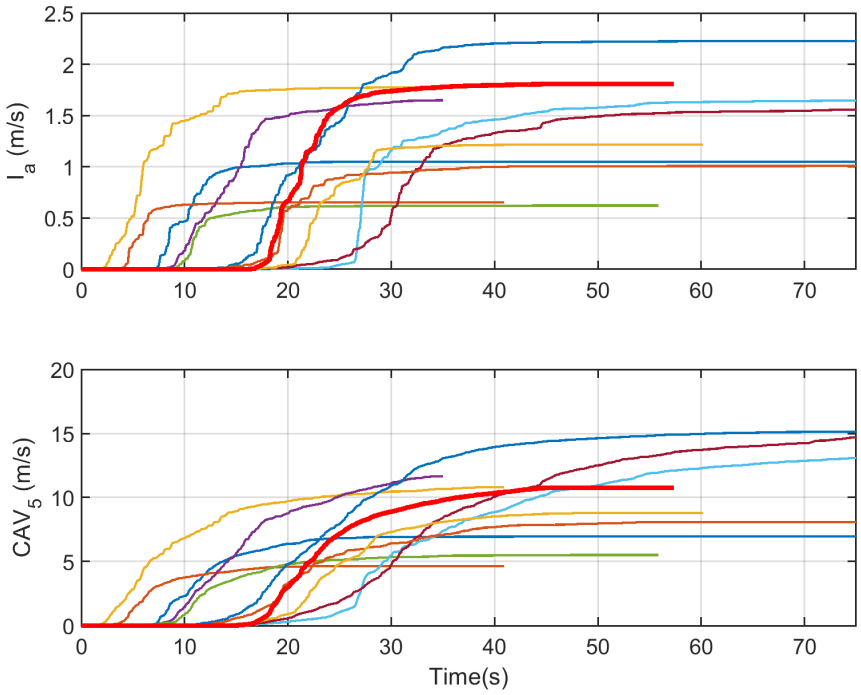

Figure D.1: Arias intensity and CAV_5 of all motions. SKR shown in red.

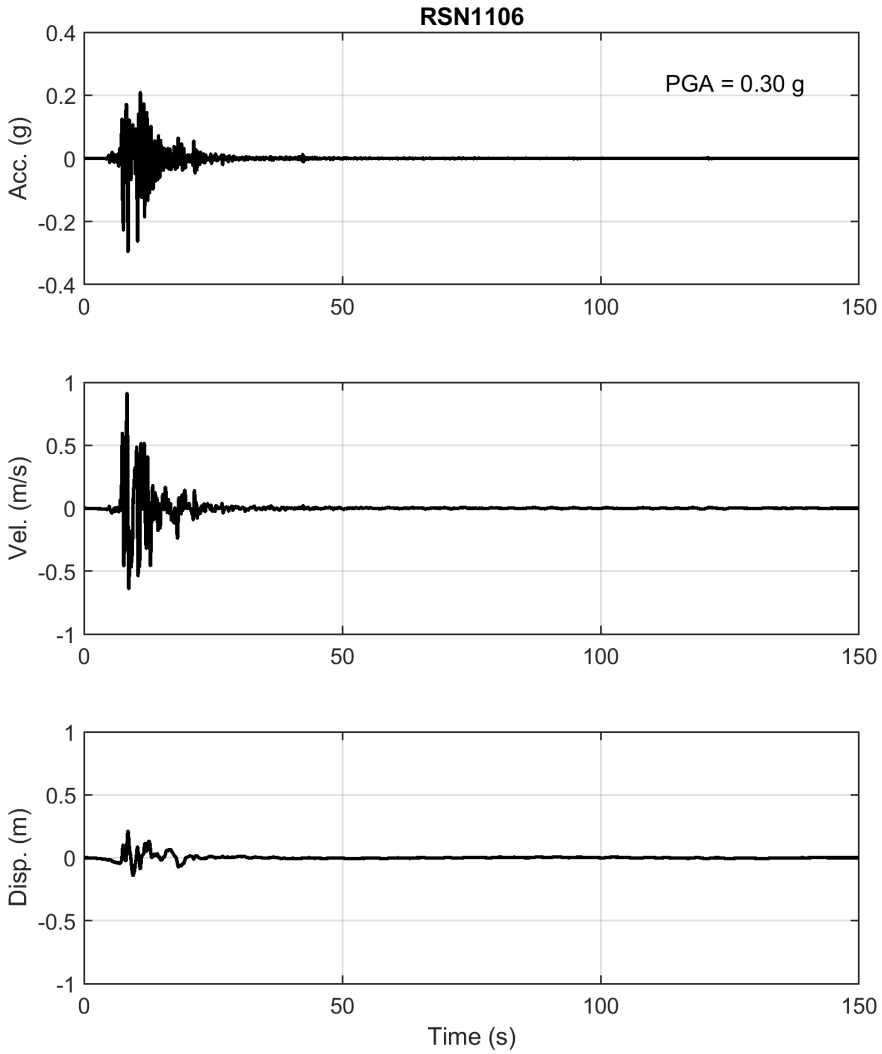

Figure D.2: Acceleration, velocity, and displacement time histories of motion RSN1106.

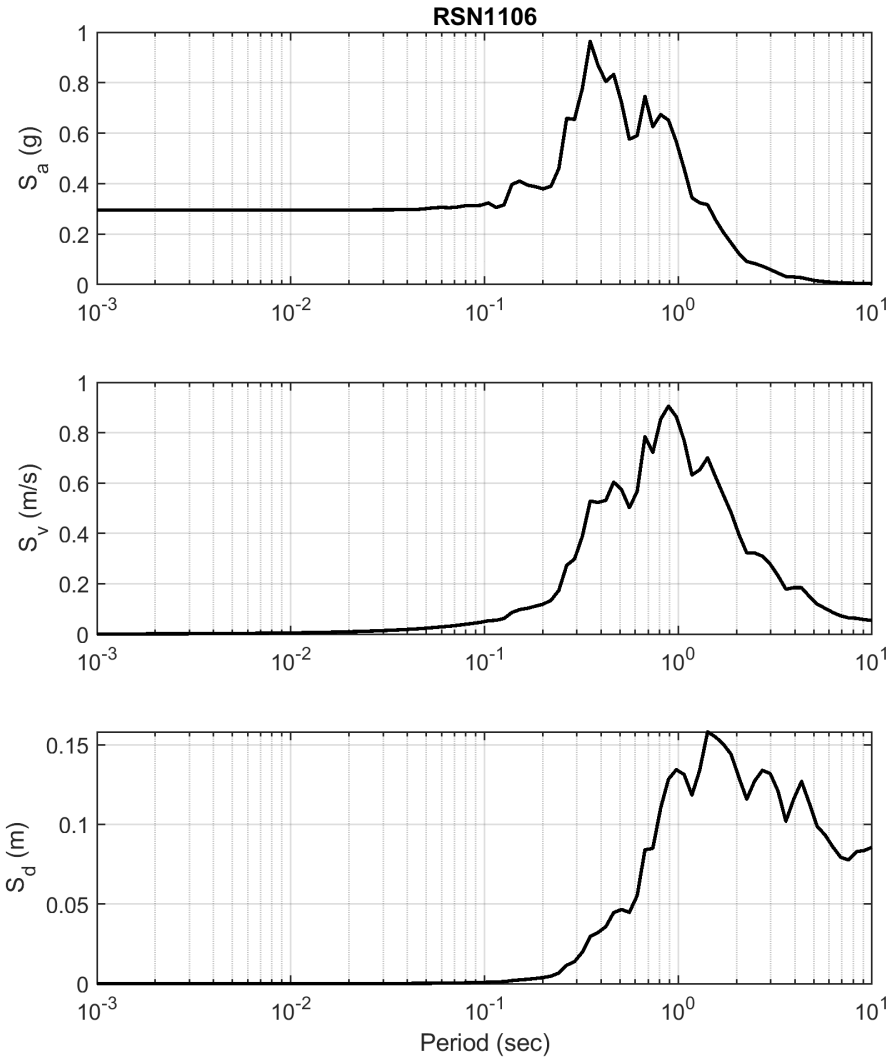

Figure D.3: Acceleration, velocity, and displacement response spectra of motion RSN1106.

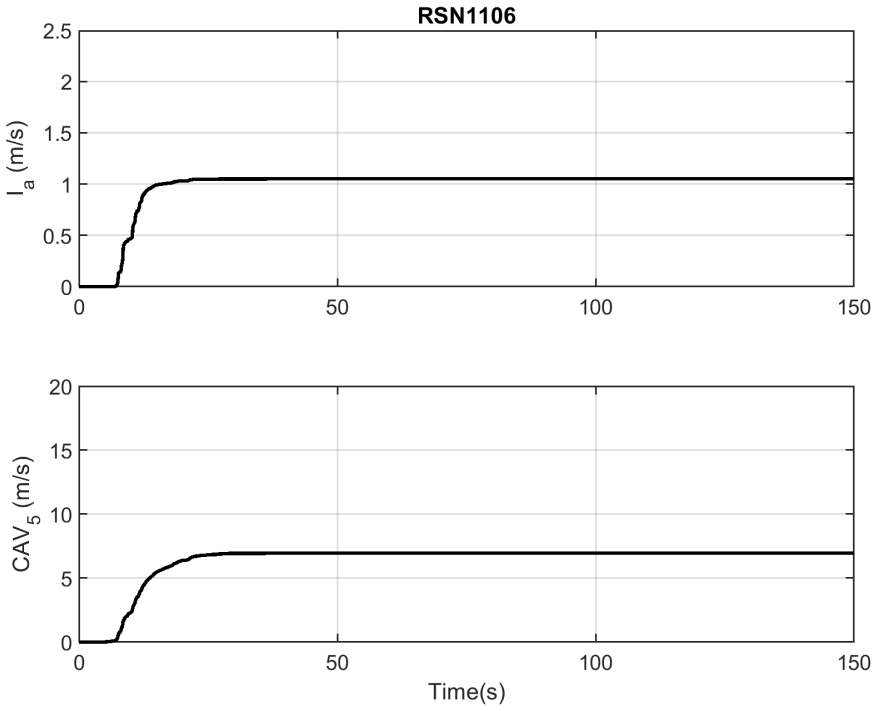

Figure D.4: Arias intensity and CAV_5 of motion RSN1106.

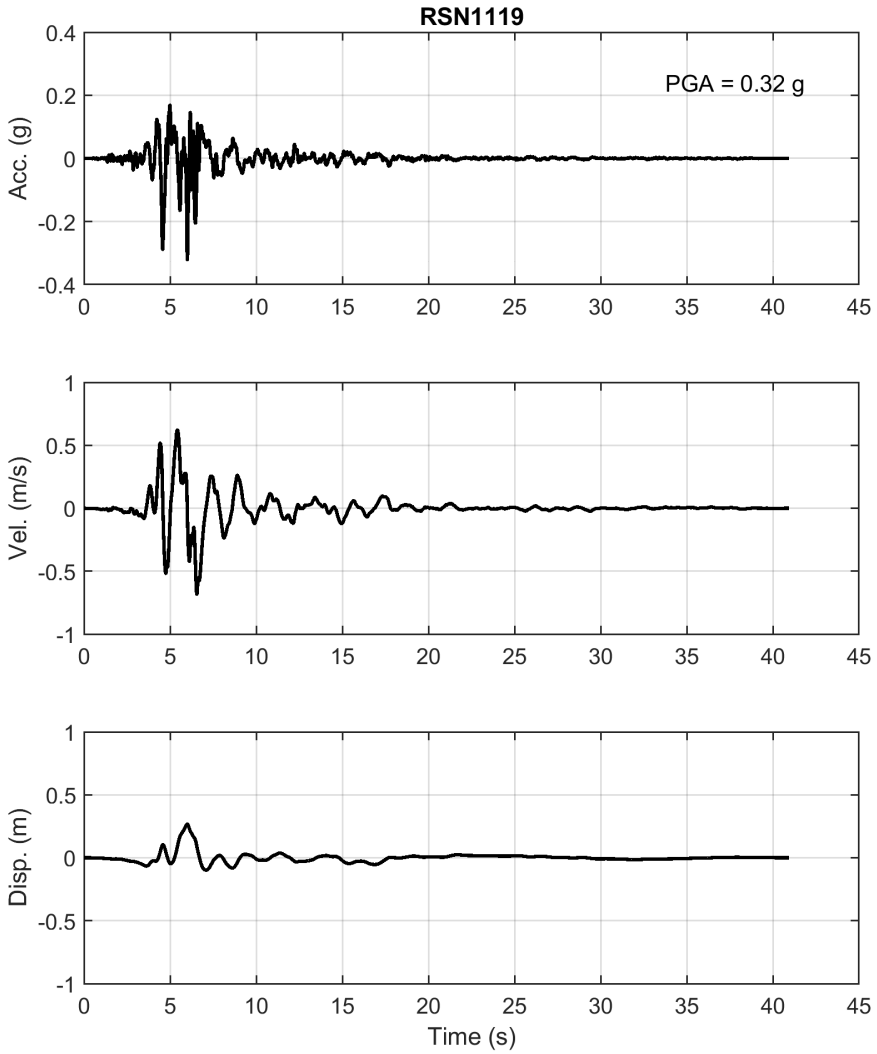

Figure D.5: Acceleration, velocity, and displacement time histories of motion RSN1119.

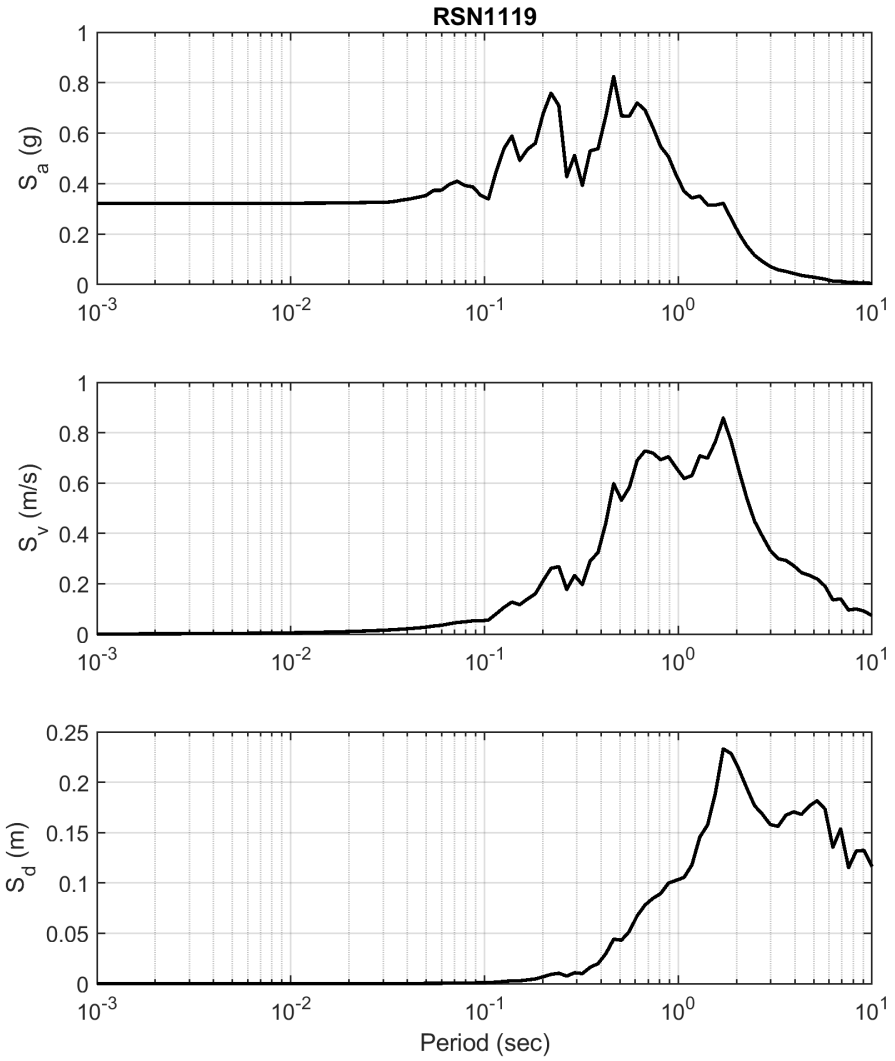

Figure D.6: Acceleration, velocity, and displacement response spectra of motion RSN1119.

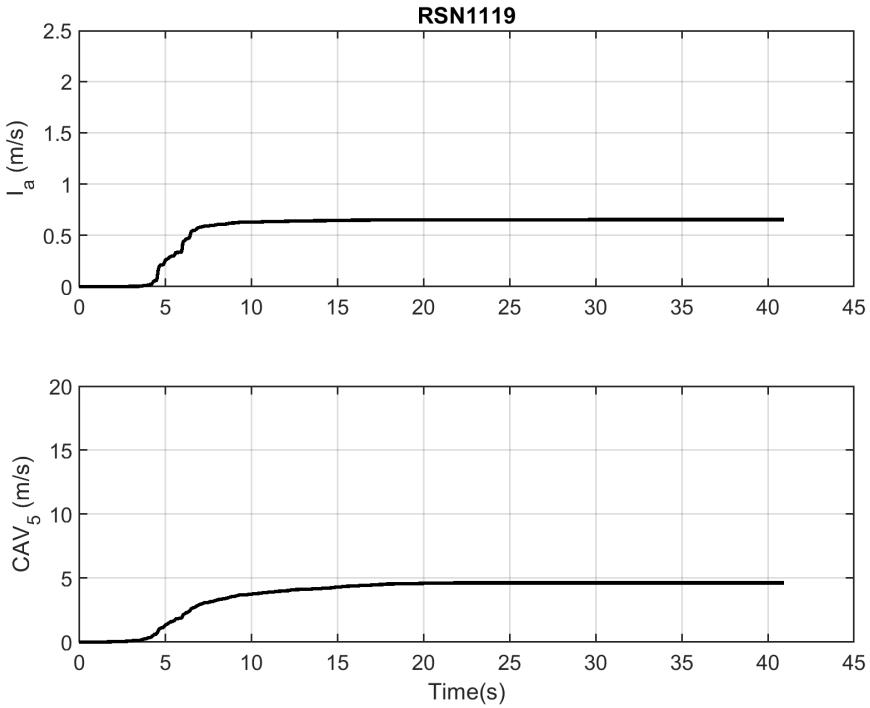

Figure D.7: Arias intensity and CAV_5 of motion RSN1119.

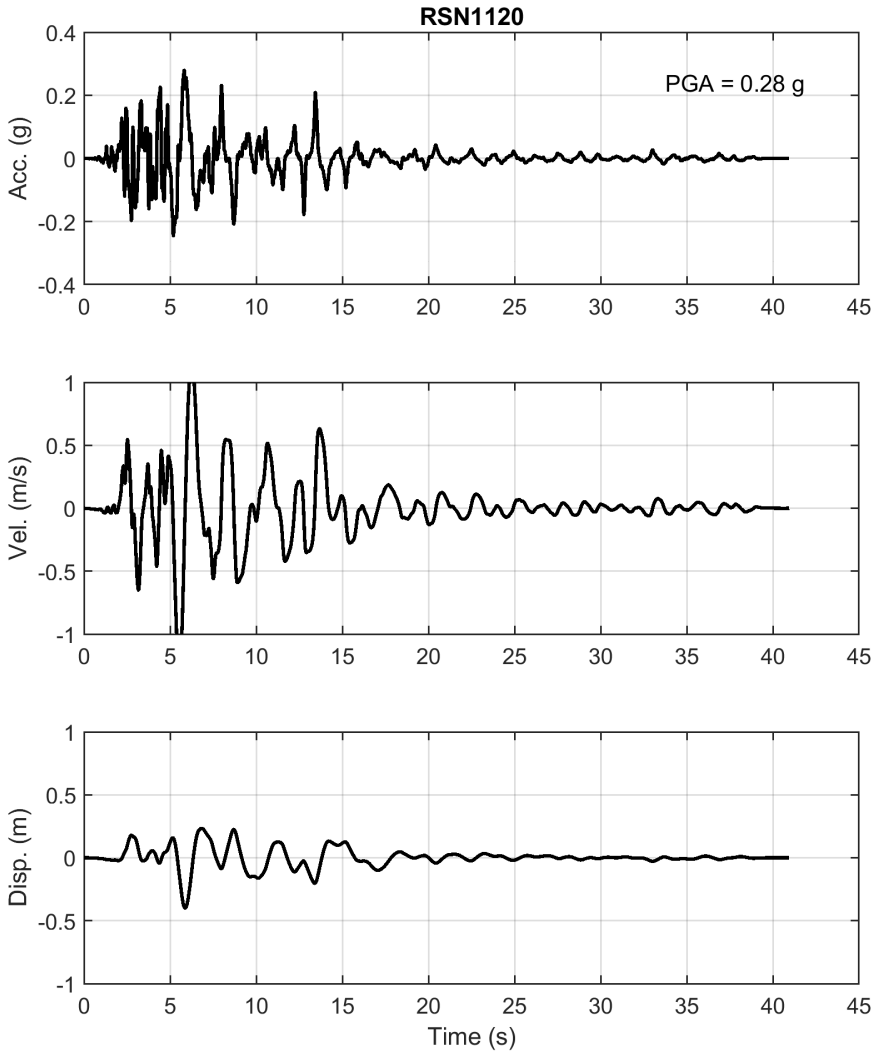

Figure D.8: Acceleration, velocity, and displacement time histories of motion RSN1120.

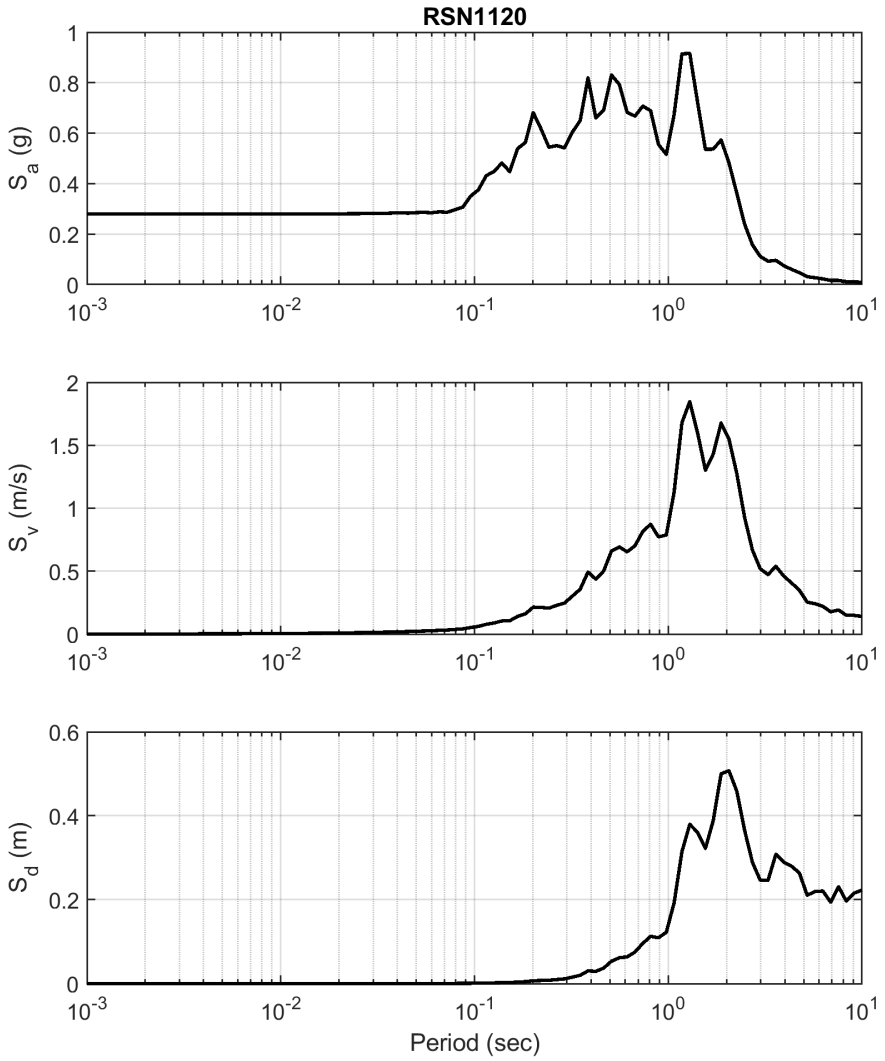

Figure D.9: Acceleration, velocity, and displacement response spectra of motion RSN1120.

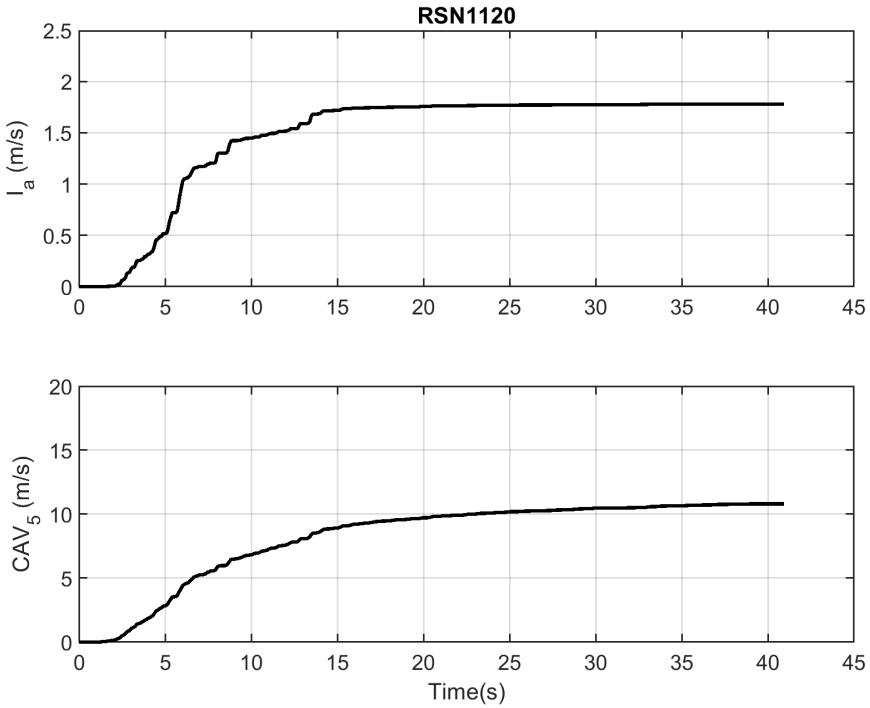

Figure D.10: Arias intensity and CAV_5 of motion RSN1120.

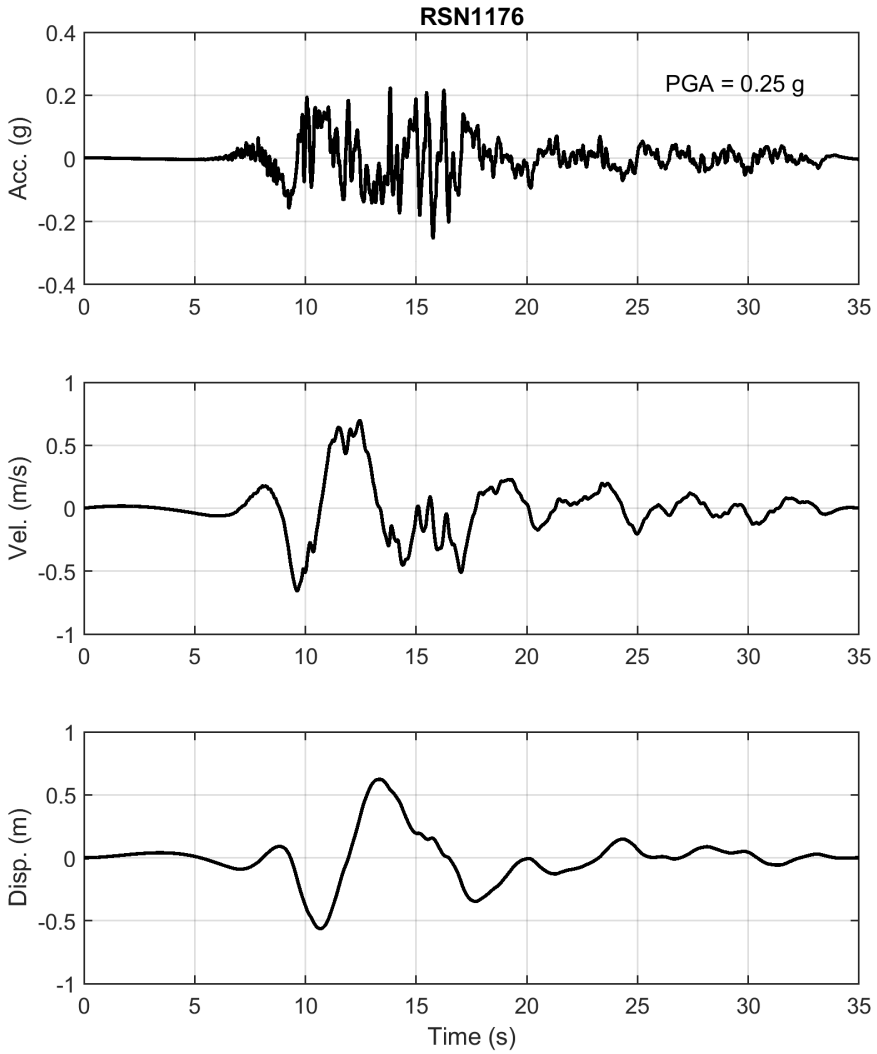

Figure D.11: Acceleration, velocity, and displacement time histories of motion RSN1176.

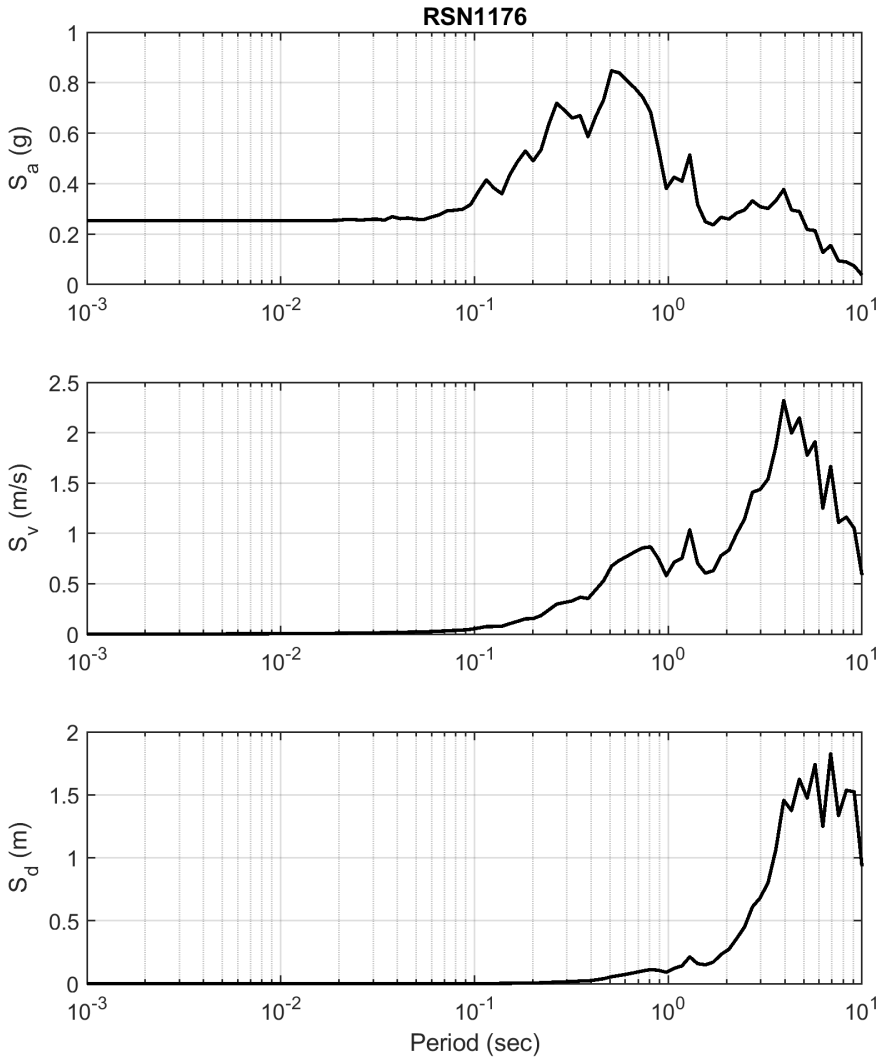

Figure D.12: Acceleration, velocity, and displacement response spectra of motion RSN1176.

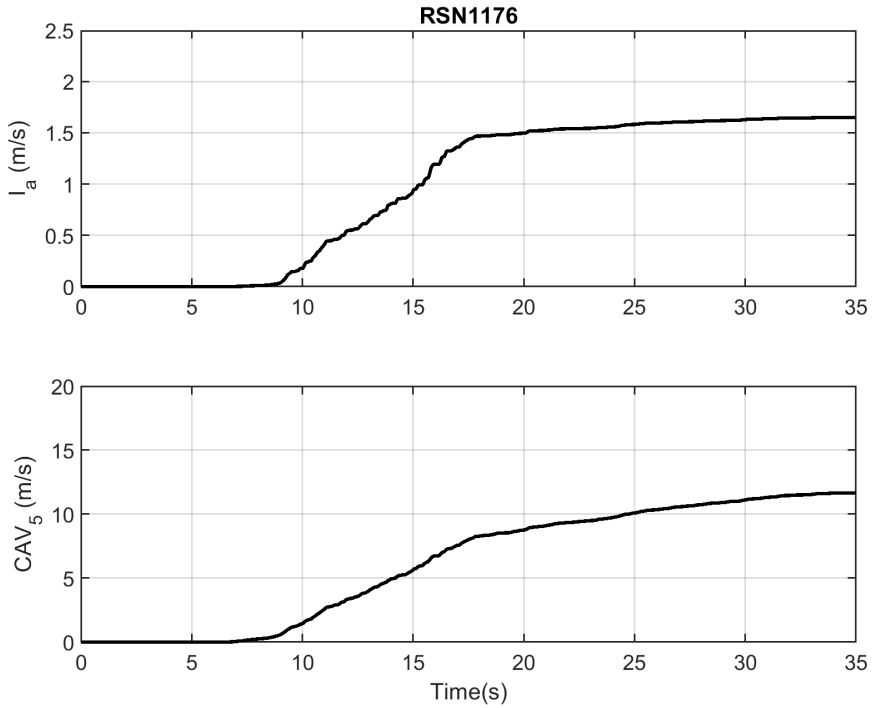

Figure D.13: Arias intensity and CAV_5 of motion RSN1176.

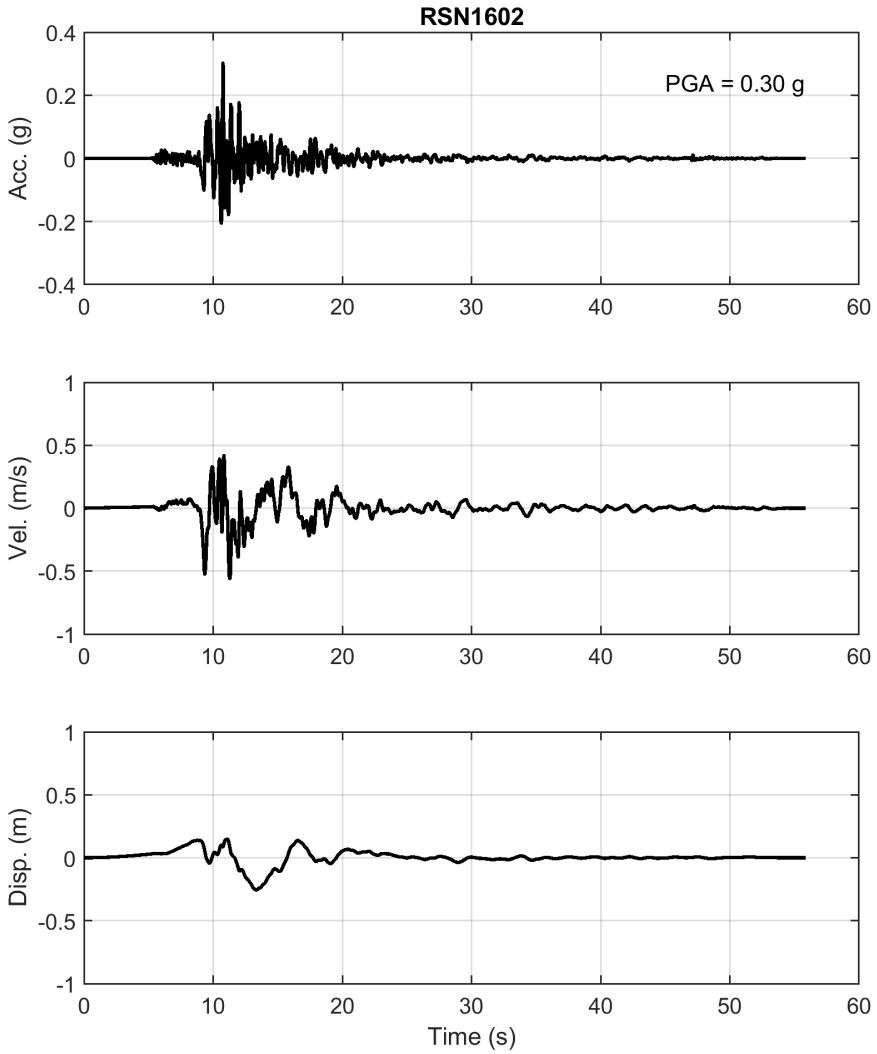

Figure D.14: Acceleration, velocity, and displacement time histories of motion RSN1602.

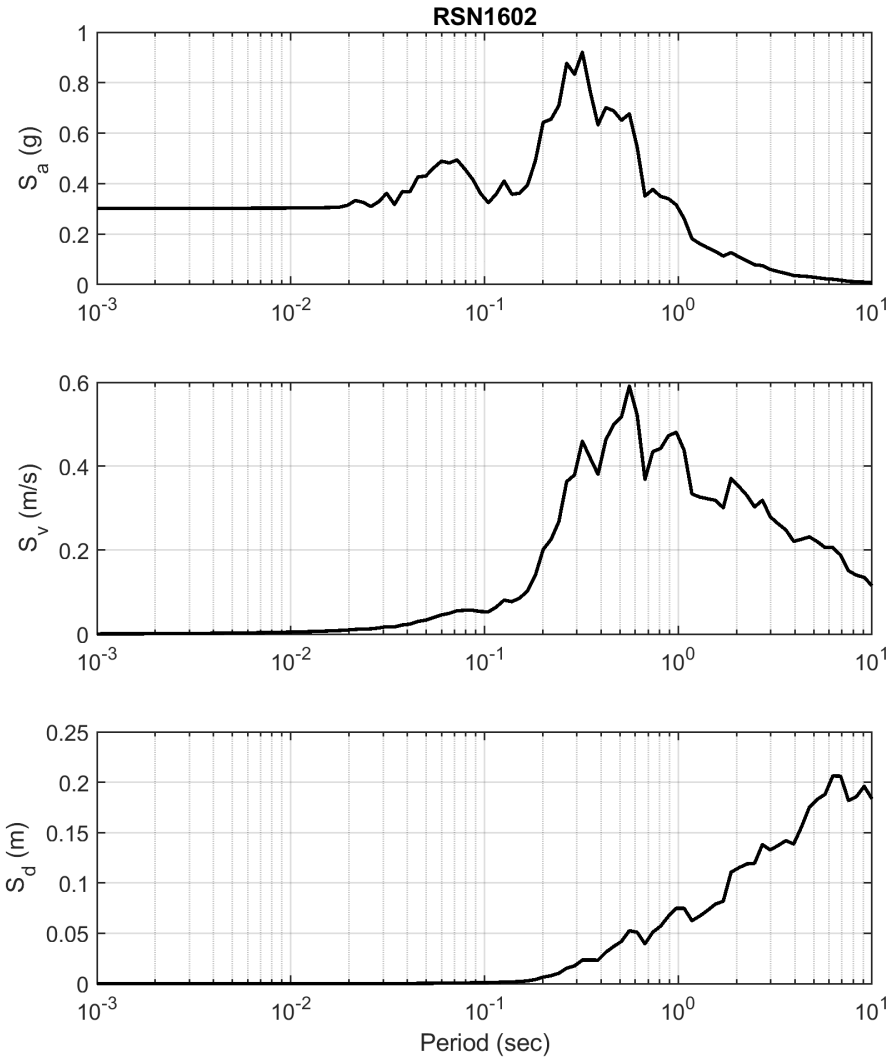

Figure D.15: Acceleration, velocity, and displacement response spectra of motion RSN1602.

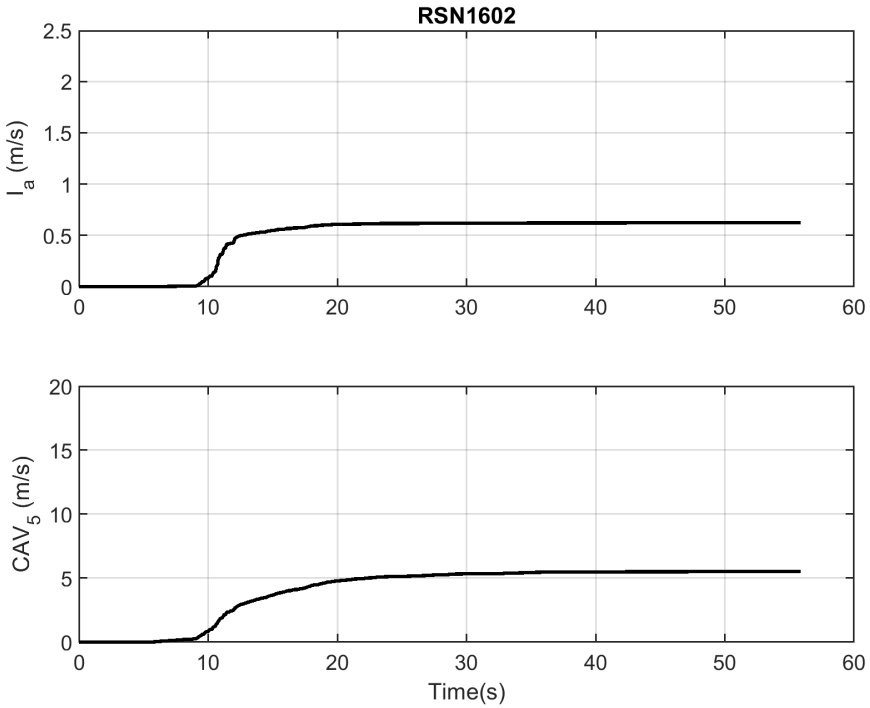

Figure D.16: Arias intensity and CAV_5 of motion RSN1602.

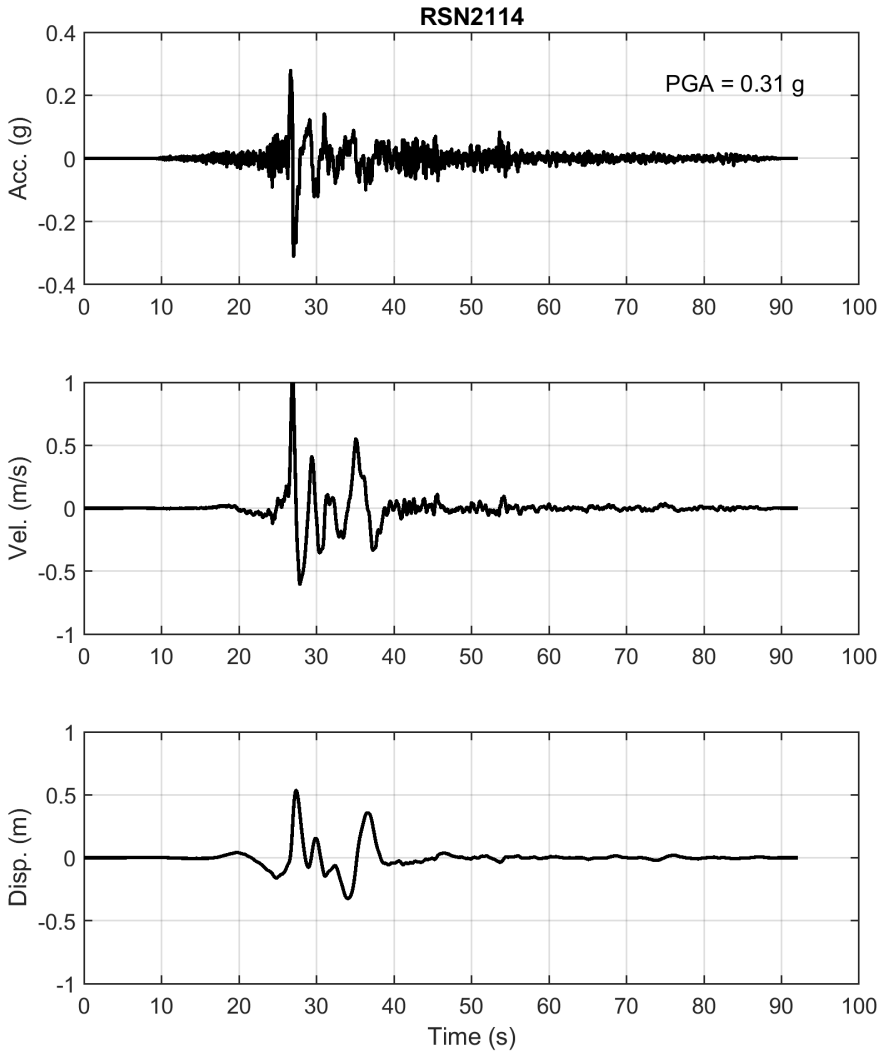

Figure D.17: Acceleration, velocity, and displacement time histories of motion RSN2114.

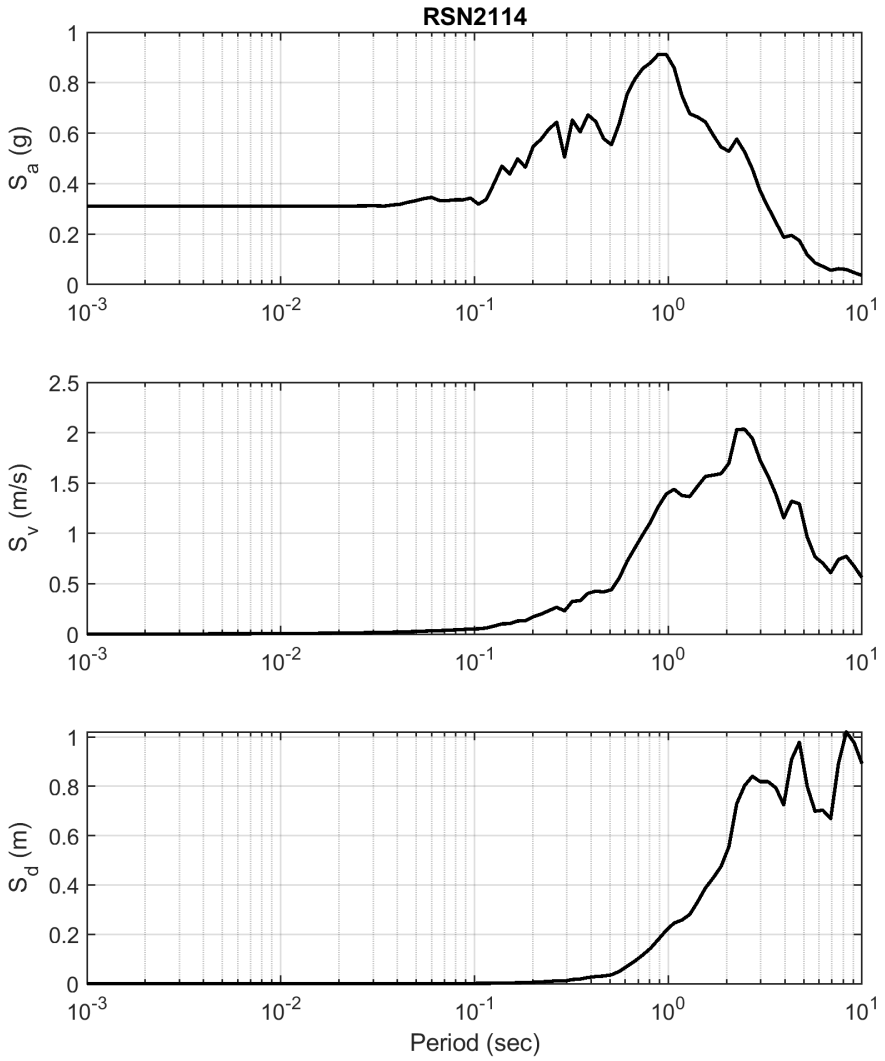

Figure D.18: Acceleration, velocity, and displacement response spectra of motion RSN2114.

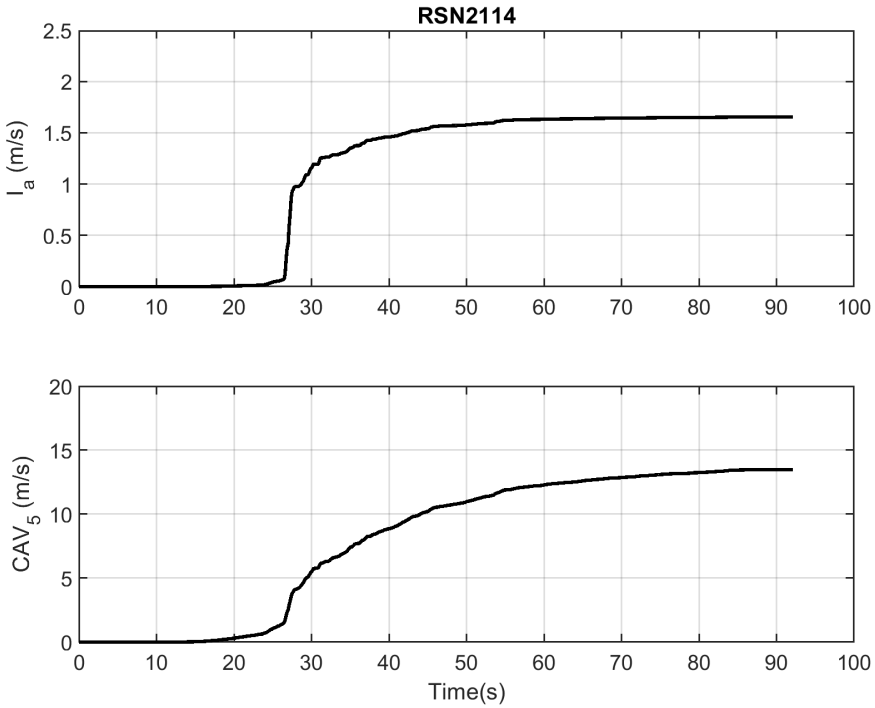

Figure D.19: Arias intensity and CAV_5 of motion RSN2114.

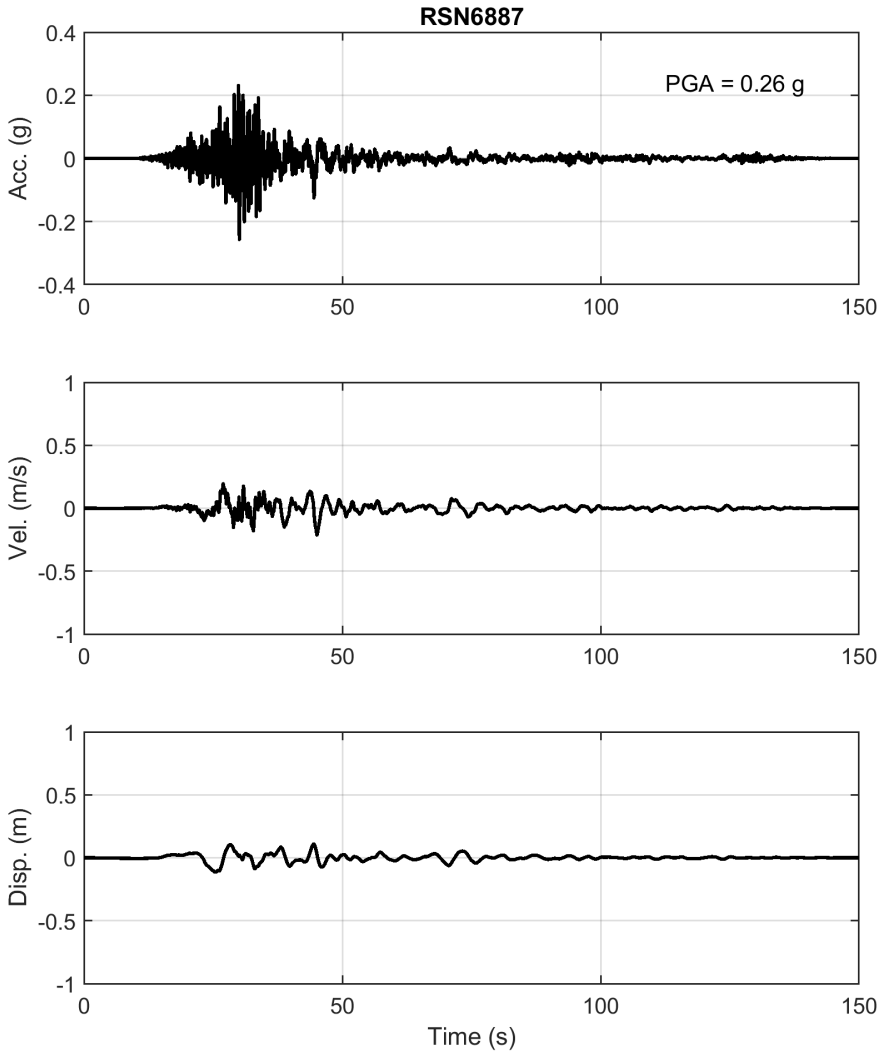

Figure D.20: Acceleration, velocity, and displacement time histories of motion RSN6887.

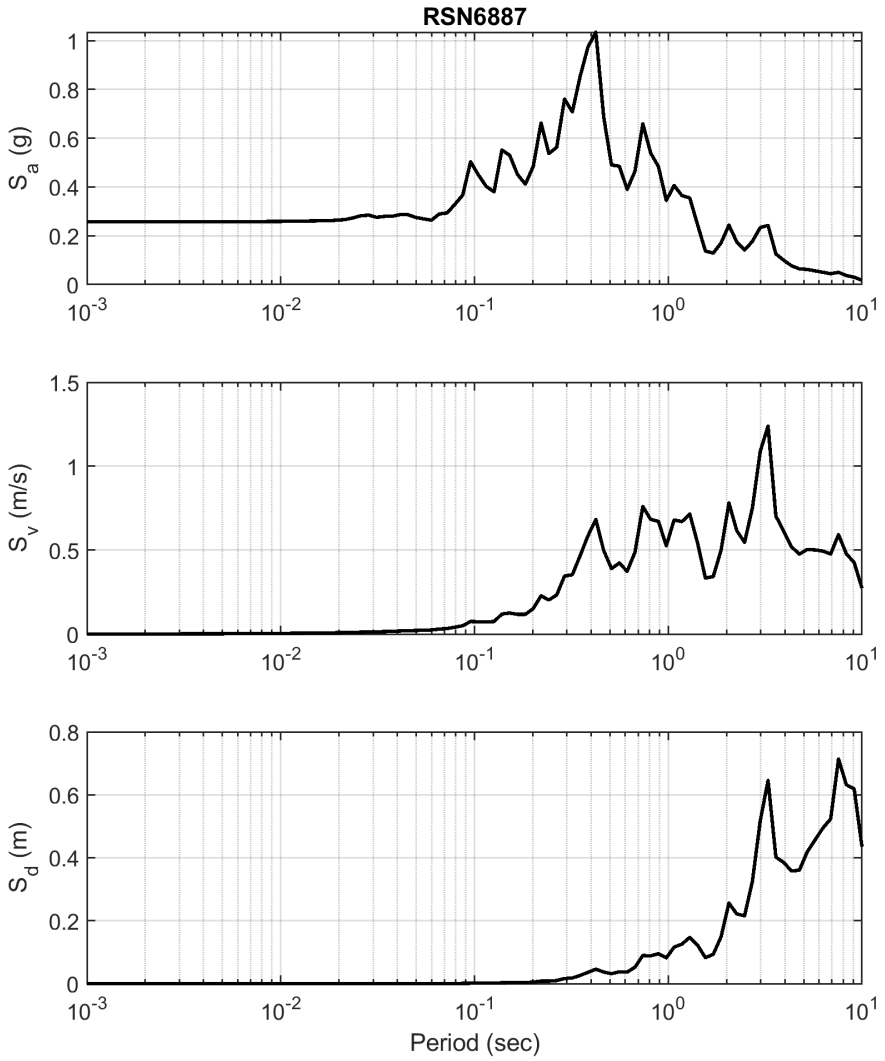

Figure D.21: Acceleration, velocity, and displacement response spectra of motion RSN6887.

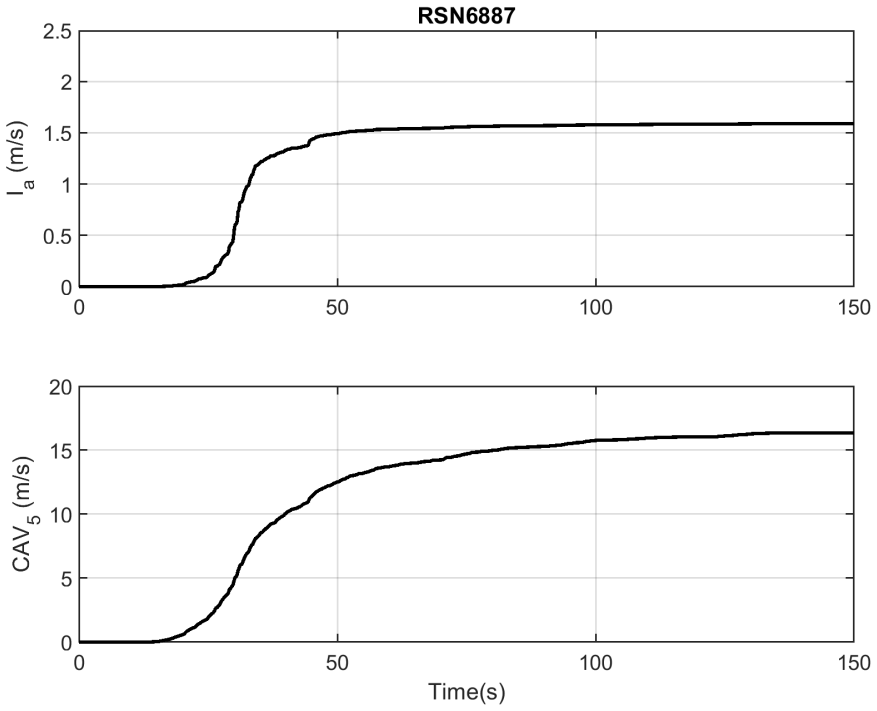

Figure D.22: Arias intensity and CAV_5 of motion RSN6887.

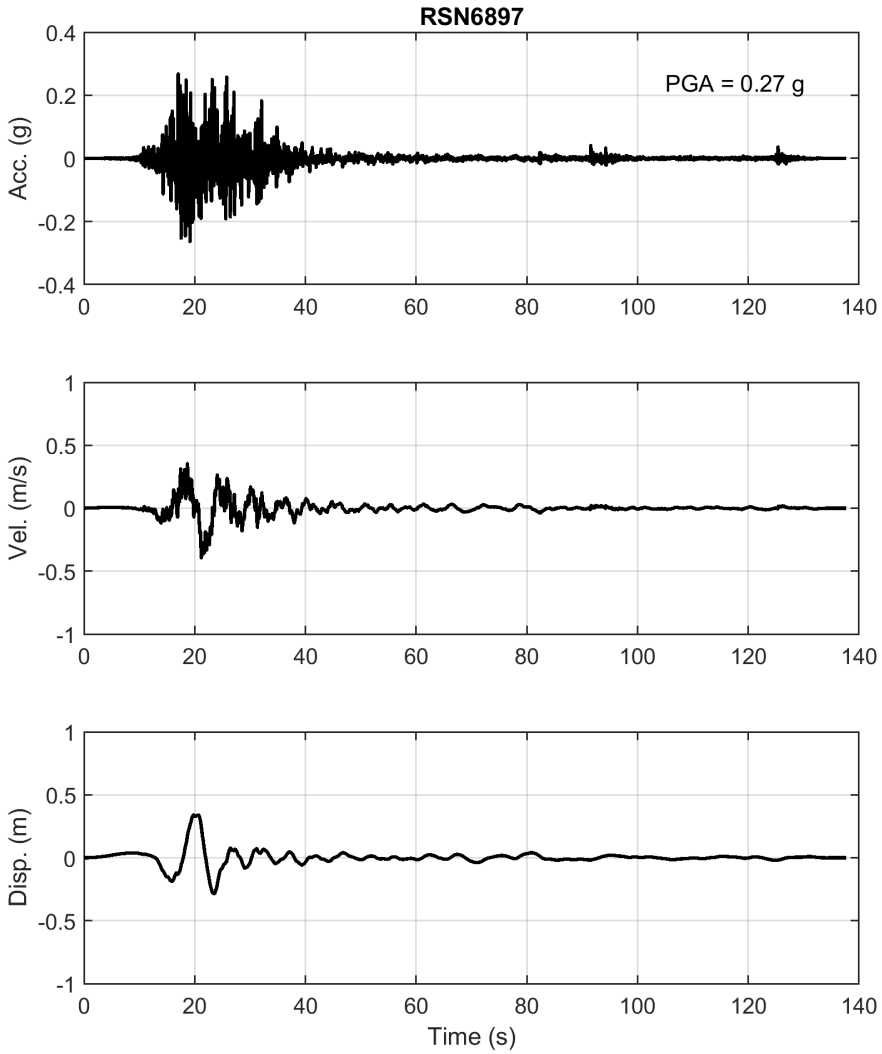

Figure D.23: Acceleration, velocity, and displacement time histories of motion RSN6897.

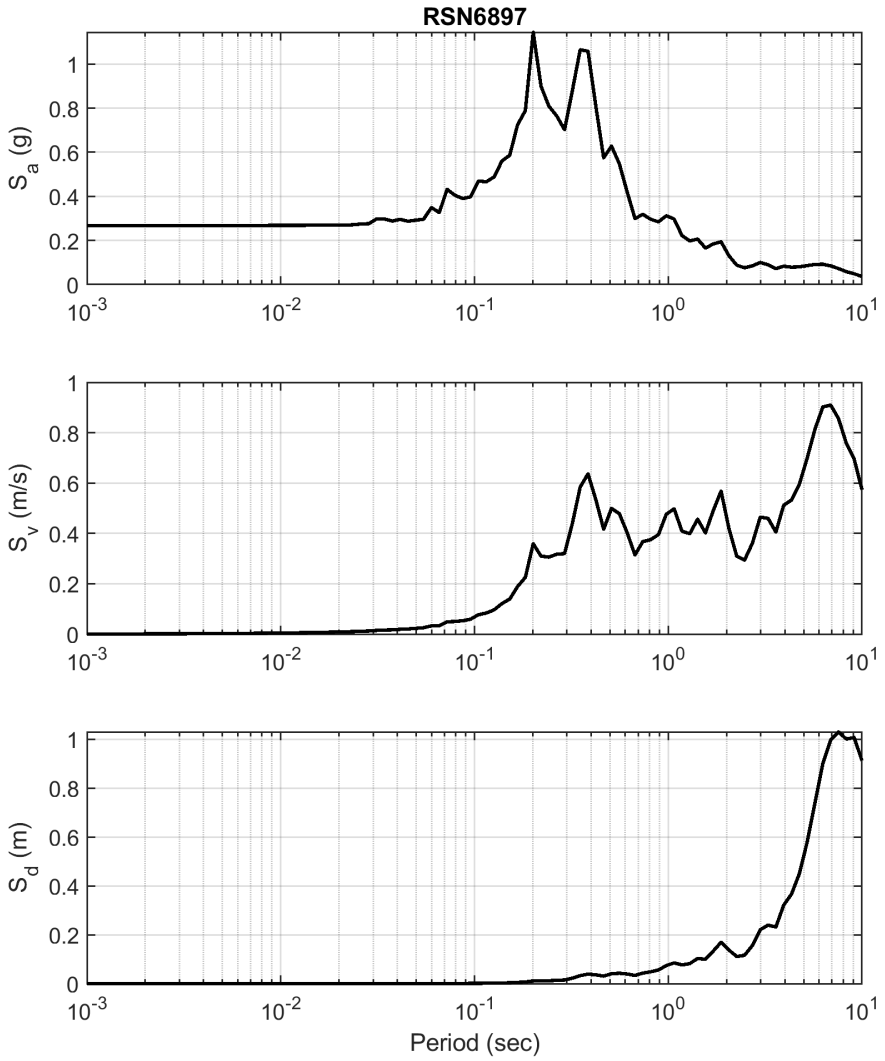

Figure D.24: Acceleration, velocity, and displacement response spectra of motion RSN6897.

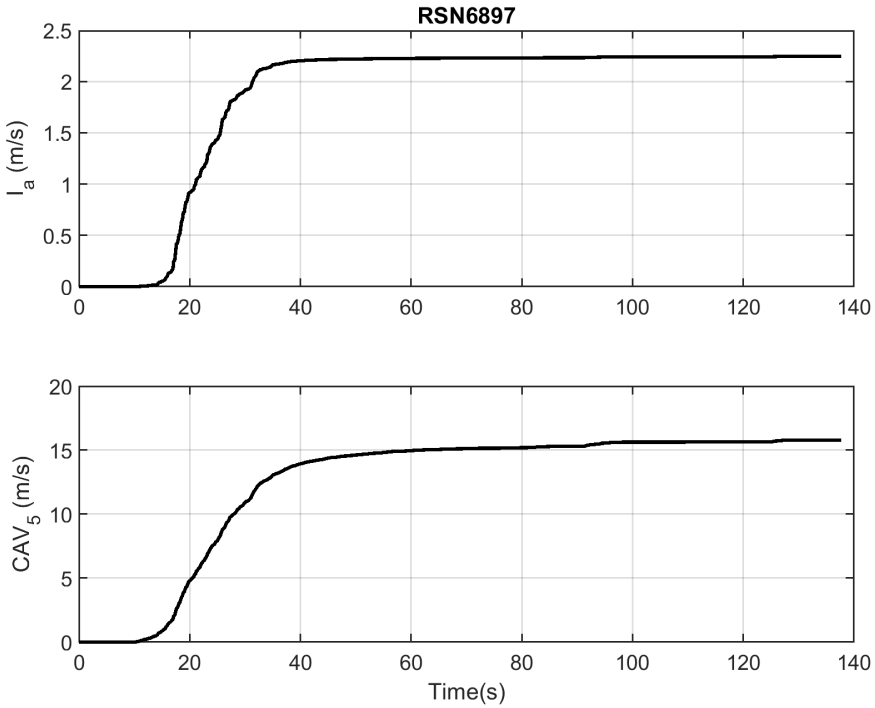

Figure D.25: Arias intensity and CAV_5 of motion RSN6897.

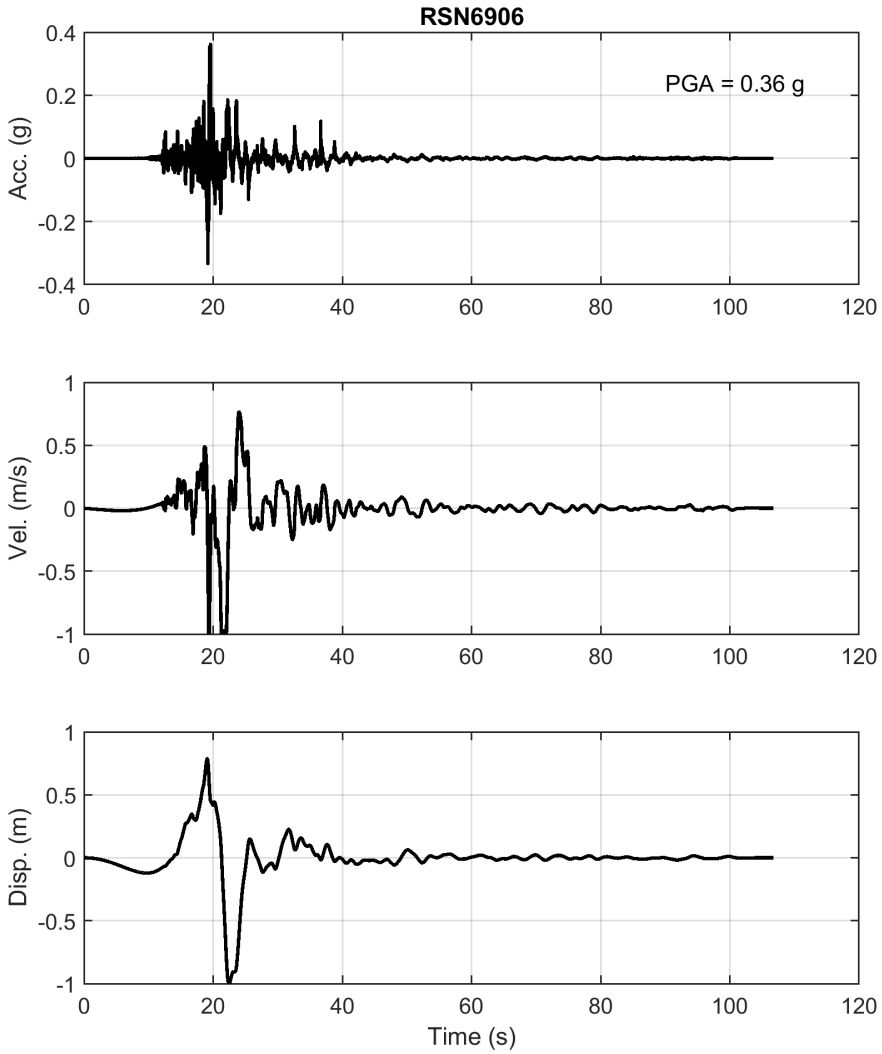

Figure D.26: Acceleration, velocity, and displacement time histories of motion RSN6906.

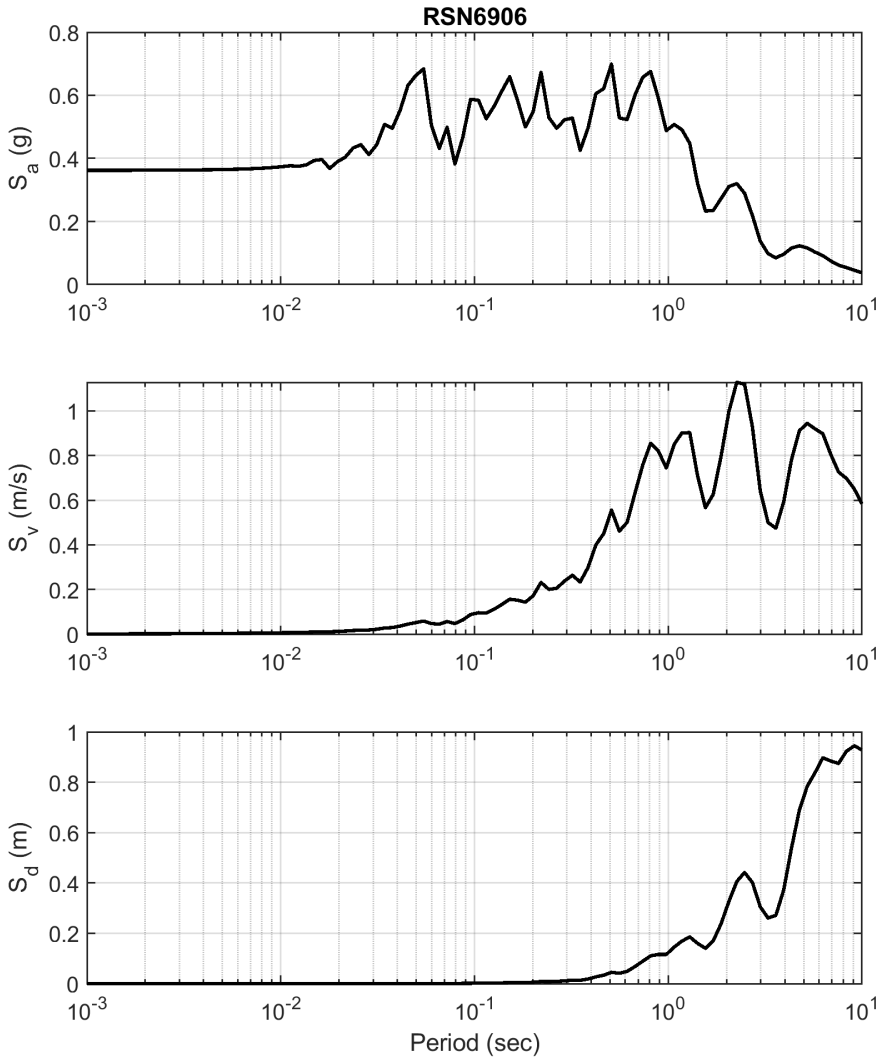

Figure D.27: Acceleration, velocity, and displacement response spectra of motion RSN6906.

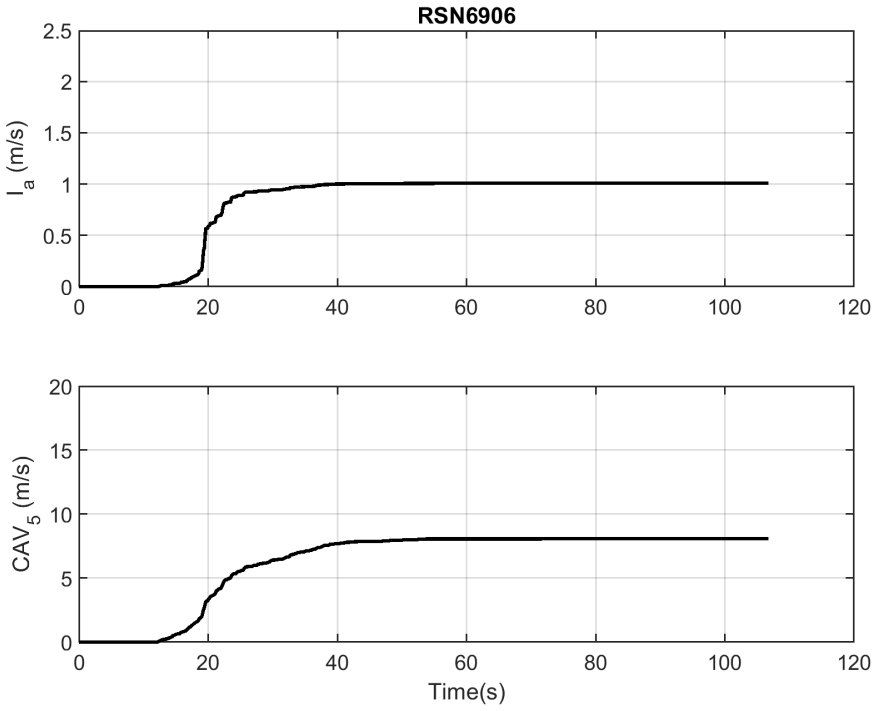

Figure D.28: Arias intensity and CAV_5 of motion RSN6906.

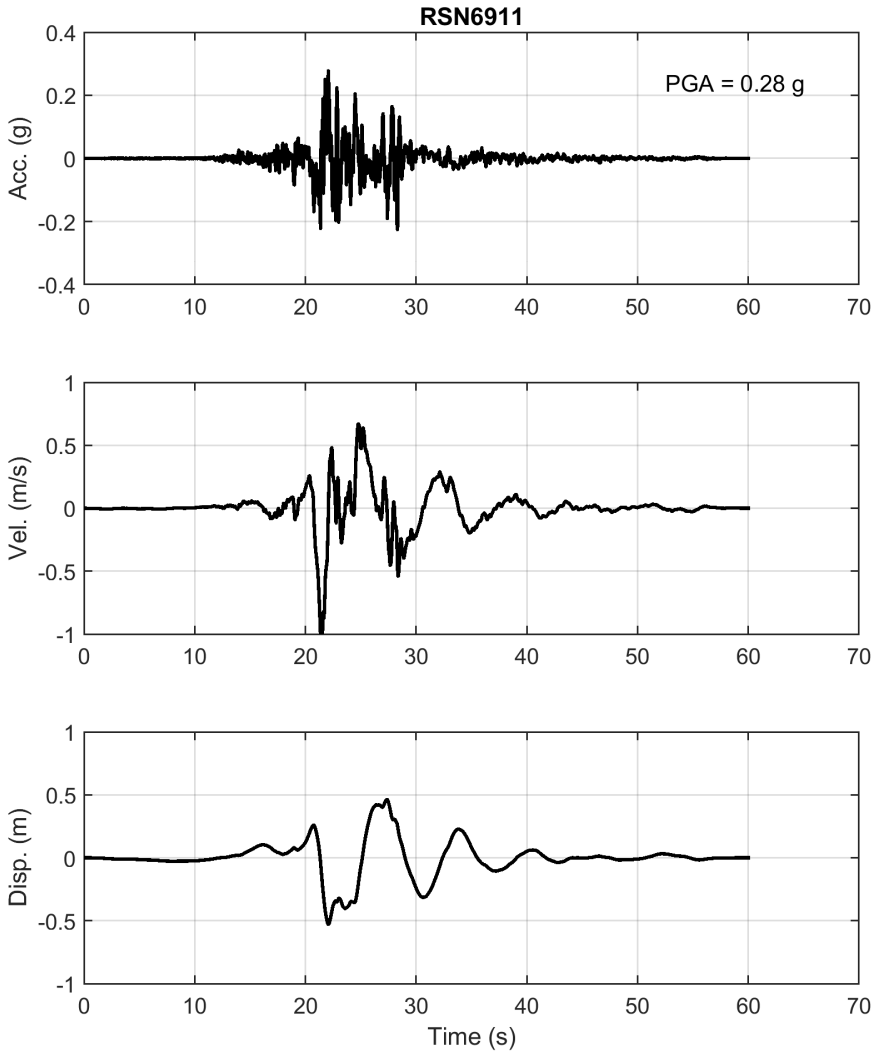

Figure D.29: Acceleration, velocity, and displacement time histories of motion RSN6911.

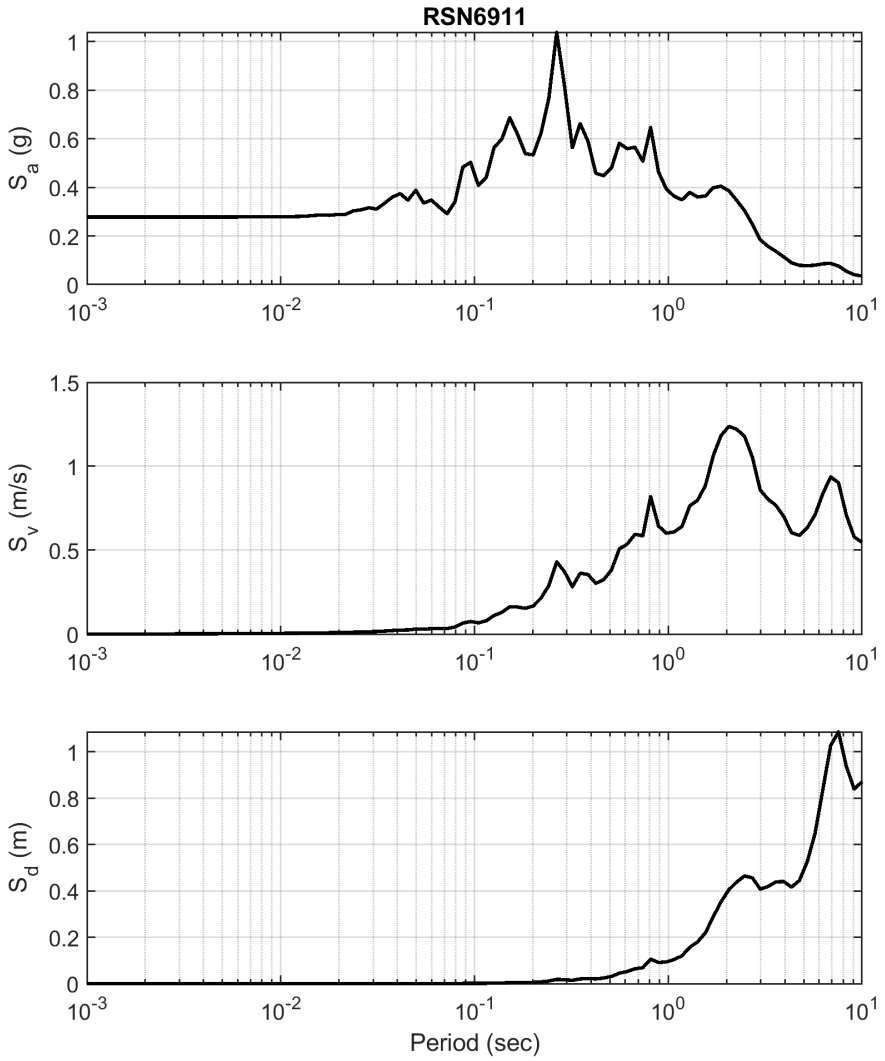

Figure D.30: Acceleration, velocity, and displacement response spectra of motion RSN6911.

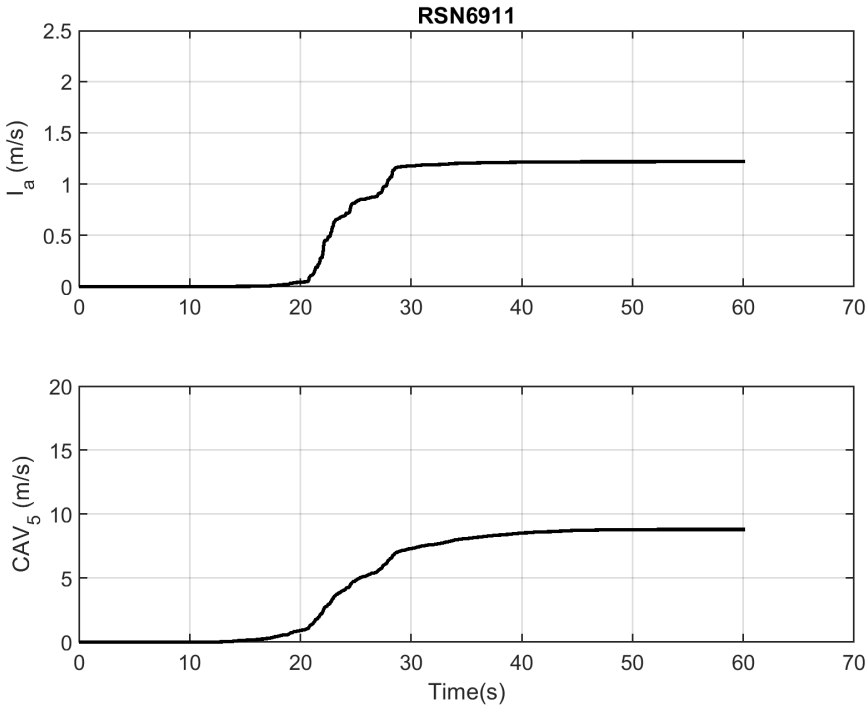

Figure D.31: Arias intensity and CAV_5 of motion RSN6911.

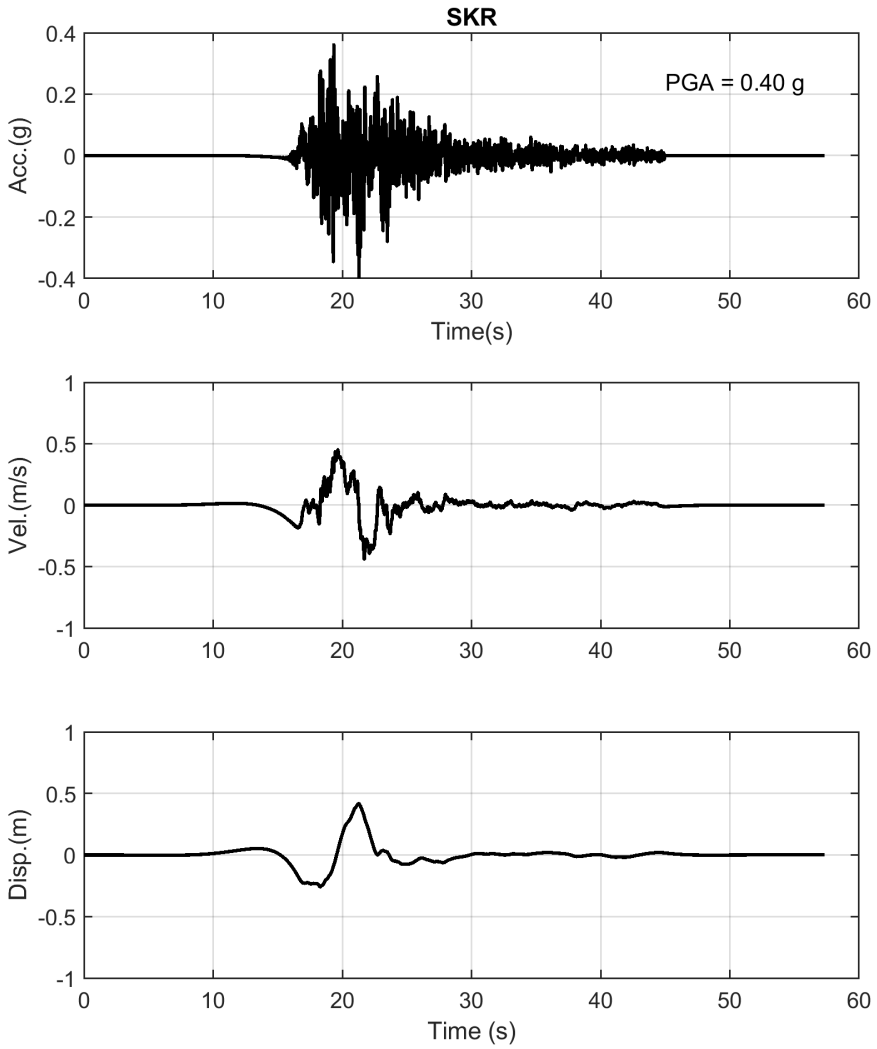

Figure D.32: Acceleration, velocity, and displacement time histories of motion SKR.

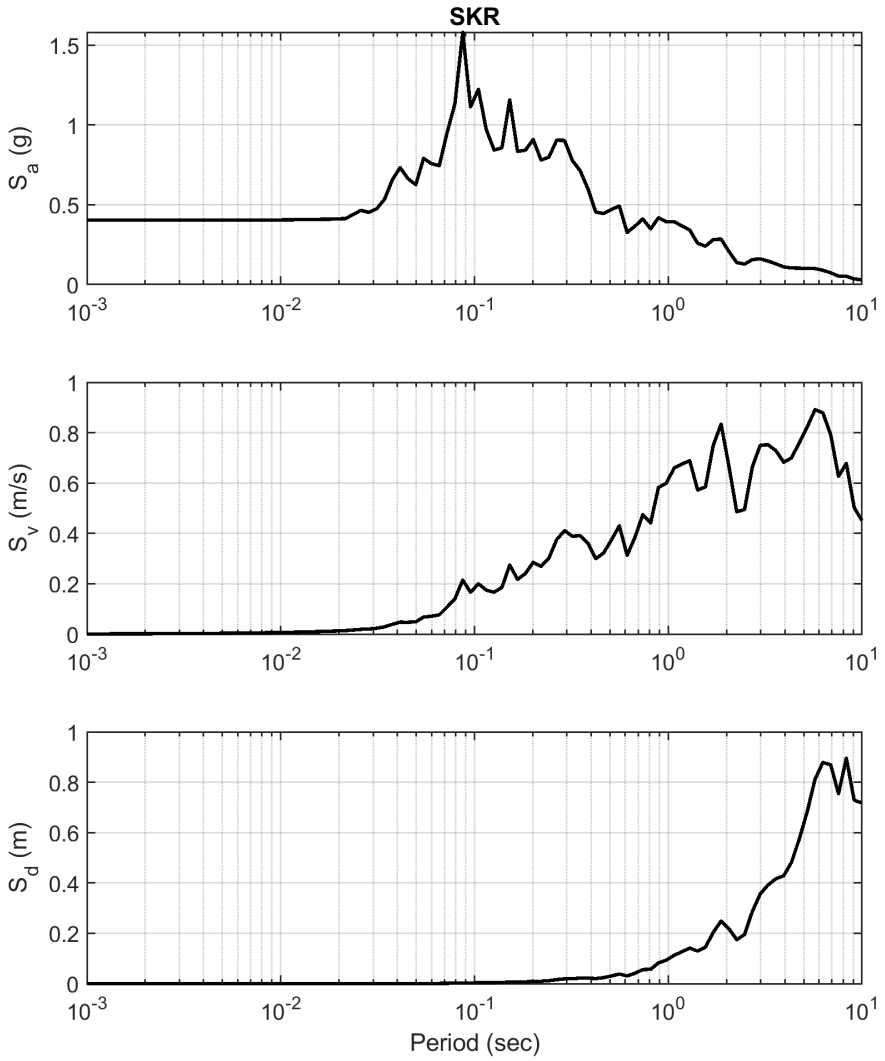

Figure D.33: Acceleration, velocity, and displacement response spectra of motion SKR.

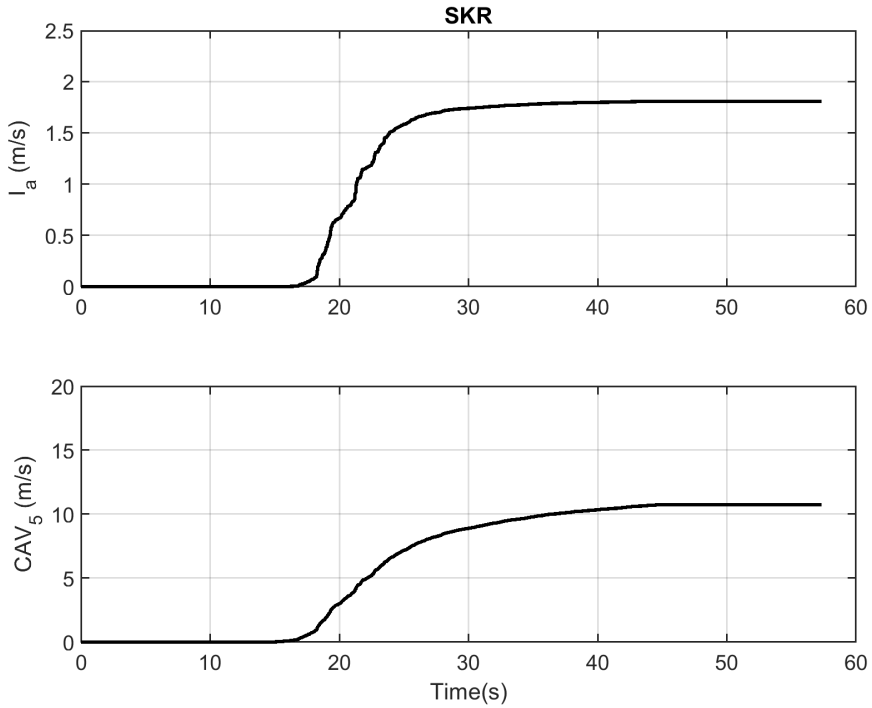

Figure D.34: Arias intensity and CAV_5 of motion SKR.